ON THE ROLE OF DEFECT INCOMPATIBILITIES ON MECHANICAL PROPERTIES OF POLYCRYSTALLINE AGGREGATES: A MULTI-SCALE STUDY

A Thesis
Presented to
The Academic Faculty

by

Manas Vijay Upadhyay

In Partial Fulfillment
of the Requirements for the Degree
Doctor of Philosophy in the
School of Mechanical Engineering

Georgia Institute of Technology
December 2014

ON THE ROLE OF DEFECT INCOMPATIBILITIES ON MECHANICAL PROPERTIES OF POLYCRYSTALLINE AGGREGATES: A MULTI-SCALE STUDY

Approved by:

Professor Laurent Capolungo, Advisor
School of Mechanical Engineering
Georgia Institute of Technology

Professor David McDowell
Department of Mechanical
Engineering & Materials Science and
Engineering
Georgia Institute of Technology

Professor Mohammed Cherkaoui
Department of Mechanical
Engineering
Georgia Institute of Technology

Professor Claude Fressengeas
Université de Lorraine
LEM3/CNRS France

Professor Hamid Garmestani
Department of Materials Science and
Engineering
Georgia Institute of Technology

Date Approved: 1 October 2014

To my parents,

Vijay Ishwarlal Upadhyay and Shweta Vijay Upadhyay,

and my sister,

Trusha Vijay Upadhyay,

for their unwavering support throughout this journey.

ACKNOWLEDGEMENTS

TABLE OF CONTENTS

LIST OF TABLES

LIST OF FIGURES

xviii

SUMMARY

The main objective of this thesis is to obtain critical insight on the role of crystalline incompatibilities in strain and curvature, induced in presence of line defects i.e. dislocations and disclinations, on the energy and geometry of specific features of the local microstructure, and on the bulk mechanical response of nanocrystalline/ultra-fine grained materials. To that end, studies are performed at the (1) inter-atomic and fine scale, and (2) at the mesoscale. The modelling approach is based on the field dislocation and disclination mechanics theory of continuously represented dislocations and disclinations. New, thermodynamically rigorous, multi-scale elastic constitutive laws based on the couple stress theory are developed to capture the effect of strain and curvature incompatibilities on the Cauchy and couple stresses. A new meso-scale elasto-viscoplastic constitutive model of defect incompatibilities based on a fast Fourier transform technique is developed. The desired scale transitioning is achieved via novel phenomenological defect density transport equations and the newly developed elastic constitutive laws.

At the fine scale, the model is applied to study energetic interactions between strain and curvature incompatibilities associated with grain boundaries and their influence on triple line energies. Results reveal that incompatible lattice strains have the most significant contribution to the energy. Incompatible lattice curvatures have negligible energetic contributions but are necessary to characterize the geometry of grain boundaries. Finally, both incompatible lattice strains and curvatures are necessary to capture the structure sensitive mechanical behavior of grain boundaries.

At the mesoscale, deformation of nanocrystalline aggregates characterized by

residual curvatures is studied to identify the impact of the latter's presence on the local and bulk mechanical response of the aggregate. Relaxation of local stresses generated from residual curvatures reproduces the effect of GB dislocation emission. Uniaxial tensile loading of nanocrystalline microstructures containing residual curvatures reveals a softening in the yield stress which could explain the breakdown in Hall-Petch law in the nanocrystalline regime.

Next, the possibility of characterizing incompatibilities using X-ray or neutron diffraction techniques is tested. Results reveal that only strains and their gradients contribute to the broadening of diffraction peaks; curvatures and their gradients have no contribution. This study leads to the development of a new multi-scale averaged strain based Fourier technique for generating virtual diffraction peaks.

CHAPTER I

INTRODUCTION

Nanotechnology, which involves creating useful materials, devices and systems through manipulation of matter at the nano-meter scale, has garnered a lot of interest from researchers in various scientific disciplines such as physics, chemistry, biology and engineering. The idea of miniaturization for enhanced applications was originlly conceived by Dr. Richard Feynman in 1950's, three decades before its fundamental beginnings. Today, nanotechnology is already making materials lighter, stronger, and more durable.

Research in this field strives at developing new material systems for practical usage as well as improve upon existing materials that are already in use. As an example of a promising new material system that is currently at the research stage is a piezo-electric nano-generator that uses a ZnO nanocrystal to harvest the mechanical energy (possibly from varied sources such as wind, wave, human movements, cars, etc.) and convert it into electricity [474, 441]. A deeper understanding of the mechanical and electrical behavior of these nano-sized piezoelectric generators could potentially unlock very useful applications such as in the biomedical industry for manufacturing self-powered gadgets that can be used as implantable devices to monitor blood flow, heart-rate, etc.

Nanotechnology has been successfully implemented in many diverse fields with applications at different length scales – inter-atomic ($10^{-10}-10^{-9}m$), fine ($10^{-8}-10^{-7}m$) to meso- ($10^{-6}-10^{-5}m$) and macro- ($> 10^{-5}m$) scales (shown in figure 1.3). For example, nano-sized quantum dot semiconductors [10, 194], micron-sized synthetic lipid membranes [373], among many others. While the process of technology transfer in

several of these fields largely remains at the laboratory stage, some nano-engineered material systems have indeed found their way towards practical applications. One such application is the use of carbon fiber reinforced composites, having carbon nanotubes as additives, for structural applications in aircrafts.

In the present work, the focus is on the mechanical properties of metals. Nanostructuring of conventional coarse grained materials has several mechanical benefits such as ultrahigh strength and hardness, increased strain rate sensitivity, superior fatigue and wear resistance, among others [146, 225, 83, 72]. Fabrication techniques for single phase nano-structured materials include gas-phase condensation of particulates and consolidation [146, 72, 349], electrodeposition [104], equal channel angular pressing [363], high pressure torsion [483], etc. Furthermore, it is possible to engineer nano-structured alloys through emerging techniques such as accumulated roll bonding [347, 213] where two or more different materials, or phases of the same material, are rolled together to form one single medium. Materials processed in such a manner possess properties that are more enhanced than their individual nano-sized components. For example, Cu-Nb nano-composite laminates [438, 171] formed using accumulated roll bonding process can achieve strengths upto 2.5 GPa for multi-layer widths of $\approx$ 2 - 5 nanometers, much significantly larger than the strengths of equivalent individual components. In general, however, development of nano-structured materials remains largely at the laboratory stage; a sufficient level of understanding on their bulk mechanical response is yet to be reached. Primary reason for this is the incomplete knowledge base on the deformation mechanisms in nano grained materials; the latter's typical microstructures are significantly different from those of their coarse grained counterparts. In this thesis, the work done is particularly relevant to microstructures of face centered cubic (FCC) equi-axed bulk 1) nc (nc) metals with average grain size less than 100 nm, fabricated through gas-phase condensation of

particulates and consolidation [146, 72, 349] or electrodeposition [104] and, 2) ultra-fine grained (ufc) metals with average grain size between 100 nm - 1 μm, fabricated using severe plastic deformation techniques such as equal channel angular pressing [363], accumulated roll bonding [347, 213] or high pressure torsion [483].

A typical microstructure of FCC equi-axed nc/ufg metals consists of 1) fine grains or crystallites with low number of dislocation defects in the bulk of the material, 2) a large volume fraction of grain boundaries (GBs), and 3) triple junctions (TJs) or triple lines between grains. For the sake of illustration, consider the microstructure of a Ni disc subjected to high pressure torsion [483]. The central part of the disc after 5 rotations and 1 GPa pressure exhibits a ufg microstructure (refer to figure 1.1(a)). The disc edges after 5 rotations and 1 GPa or 6 GPa pressure exhibit ufg (figure 1.1(b)) or nc (figure 1.1(c)) microstructures. The hardness values reported for the central, edge at 1 GPa, and edge at 6 GPa microstructures were $\approx$ 2.4 GPa, 3.1 GPa and 3.5 GPa, respectively.

1.1 Motivation

Experiments and atomistic simulations have revealed that the role of GB interfaces on governing the plastic deformation becomes increasingly important with decreasing average grain size in the nc regime [348, 391, 357, 477, 256, 208, 463, 66]. This role of GB interfaces manifests itself through microstructural geometric and energetic features at the inter-atomic, fine, and meso- scales. At the inter-atomic and fine scales these include GB structure and misorientation, their energy and free volume, TJ geometry and stresses, defect content, net defect polarity of the domain, etc. At the meso-scale these are grain orientation distribution, grain morphology, GB misorientation, interface-to-volume ratio, defect distribution and associated internal stresses, among others. Furthermore, the inter-atomic features define the meso-scale microstructural properties and in turn the collective meso-scale behavior influences
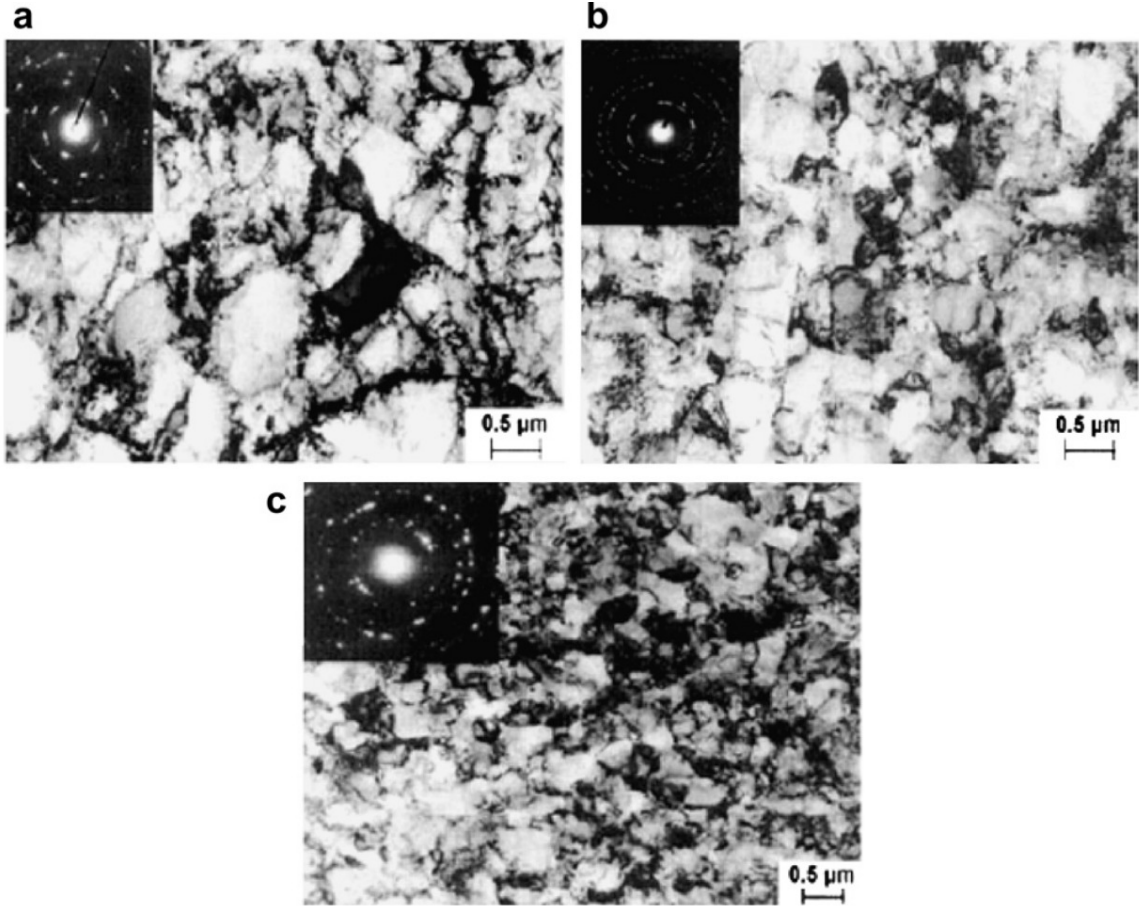
Figure 1.1: Microstructure of nickel discs subjected to high pressure torsion for (a) the central part of the disk after 5 rotations at 1 GPa pressure, (b) the edge of the disk after 5 rotations at 1 GPa and (c) the edge of the disk after 5 rotations at 6 GPa: Inset are the selective area electron diffraction patterns that were taken with an aperture size of 1.8 μm. (Adapted from Zhilyaev and Langdon *et al.* [483])

the local response at the inter-atomic scale. Of particular importance to the present work is to understand the role of lattice curvatures on the bulk mechanical response of nc/ufg materials. Lattice curvatures typically manifest themselves at interfaces in these materials. These interfaces, typically large angle GBs, are defects that accommodate rotational jump across two grains, thus inducing an incompatibility in the lattice curvature (or local elastic curvature) [251, 366]. These interfaces are also sources and sinks for dislocations. As the average grain size decreases, the interface thickness increases resulting in the accummulation of residual curvatures along with

strains in the vicinity of GBs. Furthermore, residual curvatures are also induced in the presence of dislocations. Interestingly, the role of curvatures on the local and bulk mechanical response of nc/ufg materials at the inter-atomic, fine or meso scales has never been studied.

Advances in modern experimental material characterization techniques such as *in situ* high resolution transmission electron microscopy [189], 3-dimensional *in situ* high energy X-ray and neutron diffraction [49], etc., are making it possible to access the structural information stored at the inter-atomic scale and highlight the potential significance of curvatures in defining the state of nc/ufg materials. Recent experimental observations using high resolution transmission electron microscopy on nc metals generated using severe plastic deformation techniques (Fe [291], Cu-Nb powder [244], Au [254], Pd [341]) suggested that incompatible lattice curvature inducing line defects *i.e.* disclinations [436], can be generated during nano-structuring of conventional coarse grained materials. These defects manifest themselves in the form of dipoles or quadrupoles in the vicinity of GBs and TJs; for example, Rösner *et al.* [341] found a rotational jump along a $\Sigma 9$ GB bounded by a triple and a quadruple junction in nc Pd (shown in figure 1.2). Disclinations could have a crucial impact on the stability of nc/ufg metals and alloys, as well as GB mediated plasticity mechanisms [291, 254, 341]. These could help identify deformation related phenomena such as possible sites for nucleation of grains, shear bands, cracks or twins. Furthermore, in ufg materials, in which plasticity is at a transition between dislocation slip and interface driven, disclinations may play a critical role in the formation of different structures; for example, micro shear bands [333].

Analysing the information obtained from experimental studies in a manner that meaningfully (i.e. thermodynamically and mechanically rigorous) interprets deformation behavior, requires models based at the inter-atomic scale, fine scale as well as meso-scale.

(a) (b)
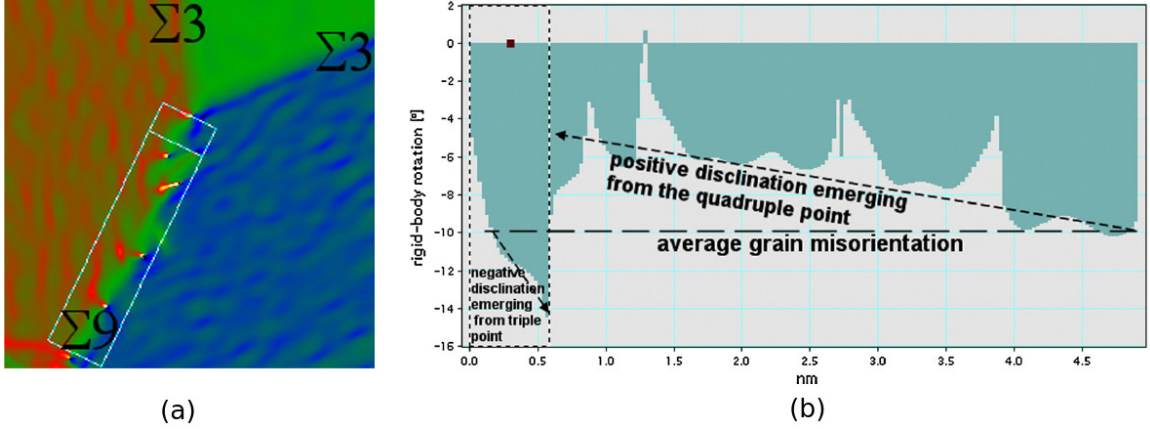
Figure 1.2: (a) View of the region along the Σ9 GB including the TJ and the quadruple point. Different boundaries are indicated, (b) Rigid body rotation measured in the form of a line profile along the Σ9 boundary and averaged over the width of the box. Two gradients of opposite sign emerge from the TJ and the quadruple point, respectively. The dotted line indicates the average grain misorientation. Due to the wavy character of the Σ9 boundary the rigid body rotation occurs as a periodically modulated signal along its length. Note the jump in rigid body rotation at ≈ 0.6 nm (adapted from Rösner *et al.* [341]).
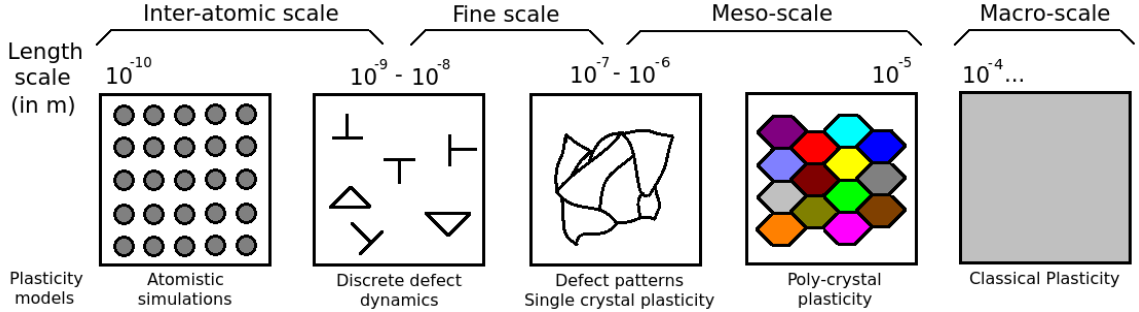
Figure 1.3: Schematic of different length scales and their associated plasticity. (Adapted from Cherkaoui and Capolungo [72])

With respect to modelling based on disclinations at the inter-atomic or fine-scale, there have been very limited contributions to understanding their role on the energy and geometry of local microstructure in nc materials. For static applications, disclinations have been successfully used to represent GBs [251, 366, 139] and TJs [44, 45, 46, 47]. GB energies [23] were computed based on closed form solutions of disclinations in an infinite isotropic medium [97, 333]. Kinematics of disclinations was introduced in the work of Mura [289]. Romanov [340, 335] proposed a kinetic model

6

an equivalent Orowan's law for plastic strain rate as a function of disclination density and strength. Theoretical models based on disclinations have also been proposed to describe several structural phenomena occurring in nc/ufg materials [333]. However, the energetic or geometric contributions of lattice curvatures were never taken into account. Furthermore, a rigorous treatment of the dynamics of dislocations and disclinations is lacking in these models; although, it should be noted that a significant step in this direction was made in the contribution by Clayton *et al.* [77].

At the meso-scale continuum based plasticity models are prominent approaches to model the bulk mechanical response of nc/ufg materials. These include phase field models based on non-linear Ginzburg Landau theory of superconductivity [160, 188, 247, 464, 155, 155], macro and meso-scale crystal plasticity constitutive models based on dislocation slip [329, 401, 182, 18, 315, 177, 27], and more recent advances include the meso-scale strain gradient plasticity models [9, 120, 123, 121, 304, 138, 156, 4, 28, 122, 157, 153, 124, 267]. However, these models, which are typically based on a lattice strain formulation, do not account for the contribution of curvature incompatibilities to plasticity.

In light of the above, the main objective of this thesis is *to assess the role of lattice curvature incompatibilities, necessarily defined at different length scales, on local enery and geometry, and the bulk mechanical response of nc/ufg materials.*

1.1.1 Challenges

In order to achieve the main objective, a continuum based constitutive modelling approach is adopted. The constitutive approach requires a kinematically and thermomechanically rigorously framework that is capable of capturing (1) fine scale properties such as the role of interface and TJ geometry on the energy of the microstructure, and use this information to model (2) the collective dynamic behavior of interfaces at the meso-scale.

The first challenge is to adopt and/or develop such a kinematically and thermomechanically rigorous theoretical framework. To that end, motivation is derived from a recently proposed dynamic field model of dislocations and disclinations by Fressengeas *et al.* [134]. These defects are represented, in a continuous manner, using their respective polar defect densities which are governed by kinematic conservation laws. Defect motion is described by transport equations on these defect densities. A dynamic interplay between dislocations and disclinations occurs through a disclination-induced source term in the transport equation for dislocations. Defect velocities are obtained based on thermo-mechanical considerations. The model is based on a higher order equilibrium involving couple stresses; equilibrium equations are obtained by conservation of mass, momentum and moment of momentum. The model accounts for incompatibilities in both elastic strains and curvatures. However, the field disclination and dislocation mechanics model is an open framework that needs to be closed by prescribing elastic constitutive laws that (1) account for the contribution of incompatibilities in both strain and curvature on the static response of the microstructure. A part of the present work is dedicated to developing these laws based on a thermo-mechanically rigorous approach.

A crucial aspect of modelling the mechanical response of nc/ufg materials is the passage of information between quantities defined at different length scales. From a geometric point of view, spatial averaging of fine scale kinematic quantites representative of the defect content in the local microstructure should appropriately represent the same kinematic quantities defined at the meso-scale. From a statics point of view, the modelling framework should allow capturing, with sufficient detail, the structural and energetic information on GBs at the inter-atomic and fine scales such that it correctly reflects the textural information at the meso-scale. From a dynamics point of view, the effect of geometric and energetic state of the local microstructure on the motion of defects at inter-atomic, fine and meso-scales should correctly represent the

bulk mechanical response of nc/ufg materials at the macro-scale. This requires using multi-scale metrics that can act as conduits to pass information between different scales. For example, a meso-incompatibility tensor introduced in the work of Clayton *et al.* [77] is used to provide a statistical indication on the heterogeneity in local (meso-scale) elastic deformations. In a recent work, Acharya and Roy [6] introduced plastic slip rate tensor as a multi-scale metric to capture the role of statistical dislocations on the fine-scale transport of dislocations. For nc/ufg materials, additional metrics that account for the presence of disclinations may be necessary to correctly reflect the GB geometry at the meso-scale. The present work is organized such that at the end of the study indications will be provided on whether lattice curvatures can be used as metrics for such transfer of information on plasticity across the scales in nc/ufg materials.

The next challenge is to develop a meso-scale constitutive model than can use the information transmitted through the aforementioned multi-scale metrics to model the bulk mechanical response. To that end, motivation is derived from the work of Acharya and Roy [6] on the phenomenological field dislocation mechanics model which accounts for contributions of both geometrically necessary and statistically stored dislocations. The phenomenology is extended to propose a meso-scale plastic curvature rate that allows modelling the evolution of statistically stored disclinations.

The final challenge is to test if incompatibilities in both strain and curvature can be characterized using experimental techniques such as X-ray or neutron diffraction.

1.2 Scope of the thesis

The current work strives to provide a rigorous continuum based multi-scale model for dislocations and disclinations with focus at the inter-atomic, fine and the meso scales. In order to facilitate the application of the model to nc/ufg aggregates, the developments made in this thesis are based on the small strain hypothesis. Considering the

fact that several phenomena related to disclinations are not particularly well known and that the proposed modelling framework is in its nascent form, a very careful approach is followed which consists of first understanding dislocations and disclinations from a continuous perspective and then tackling the challenges discussed in the previous section. The thesis is organised in the following manner:

Chapter 2 is dedicated to reviewing the essentials of theory of dislocations and disclinations from the point of their conception more than a century ago to present day understanding. The motivation behind using a continuum based representation of dislocations and disclinations is highlighted followed by a rigorous development of the incompatible kinematic theory of stationary continuously distributed defects adopting the latest interpretation of incompatibilities in the context of Acharya [2] and Fressengeas *et al.* [134].

In chapter 3 the objective is to solve, from a multi-scale perspective, the (1) static problem of finding stress fields that result from the presence of disclinations and dislocations, and the (2) dynamic problem of motion of these defects under the action of self and applied stresses. The chapter begins by developing new multi-scale elastic constitutive laws, based on thermo-mechanical considerations, to account for the incompatibilities induced in elastic curvatures and strains at the inter-atomic, fine (henceforth inter-atomic and fine scales will be addressed just using fine scale, unless at instances the distinction is deemed necessary) and meso scales as well as the compatible lattice strains and curvatures due to external loading and equilibrium conditions at fine and meso scales. These laws are then combined with the fine scale kinematic field theory of dislocations and disclinations to obtain the dynamic field dislocation and disclination mechanics model. Next, a meso-scale extension to the fine-scale dynamic model is proposed. This ends the theoretical development of the multi-scale constitutive model of dislocations and disclinations.

Chapter 4 focuses on assessing the role of incompatibilities in elastic strain and

curvature on the local microstructure of nc materials. To that end the mutli-scale model is applied to the case of <001> symmetric tilt GBs in a static case to understand the role of compatible lattice curvatures and then its application in a fully continuous setting is highlighted to understand the contribution of incompatibilities to GB energy and the role of elastic constitutive laws developed in this work in capturing this contribution. Following this, TJs constructed from <001> symmetric tilt GBs are studied in the discrete static case. The focus here is on understanding the relationship between TJ geometry (*i.e.* dihedral angles and GB misorientations) and energy.

Chapter 5 focuses on applying the meso-scale model to study plasticity in bulk nc materials. The objective here is to highlight the contribution of residual curvatures on the elasto-plastic response of these materials, with particular importance given to understanding their contribution to the local stresses. Furthermore, their contribution to grain rotation through the generation of geometrically necessary dislocations and disclinations during plastic curvature evolution is also highlighted; these are not accounted for in strain based crystal plasticity models. The numerical implementation of the model is based on using the state-of-the-art fast Fourier transform technique [239]. The framework is designed such that it accounts for (a) residual curvatures, and (b) elastic and plastic anisotropy and heterogeneity.

Chapter 6 is dedicated to test theoretically and computationally if incompatibilities can be characterized using X-ray and neutron diffraction. This could help facilitate comparison of the multi-scale model with experiments, atomistics and other continuum based plasticity models.

Finally, conclusions of this thesis are discussed in chapter 7.

1.3   Nomenclature

This section presents the generic nomenclature used in this work. These notations are also described at the location of their first appearance in the text. Chapter/section specific nomenclature exist and is directly presented in text of the associated chapter/section.

Tensorial quantities are represented using either a bold symbol or in their component form with rectangular Cartesian components. These notations shall be used interchangeably or together depending on the context. Vectors are distinguished from other tensors by representing them with an overhead arrow. Spatial derivatives in the component form are denoted using a comma followed by the component index. A superimposed dot represents a material time derivative.

1.3.1   Superscripts and subscripts

$e, p -$ Elastic and plastic components of a tensor

$s, a -$ Symmetric and anti-symmetric components of a tensor

$H, D -$ Hydrostatic and deviatoric components of a tensor

$T -$ Transpose of a tensor

$\parallel, \perp -$ Compatible (curl-free) and incompatible (divergence-free) components

of a tensor

$\odot, \vdash -$ Screw and edge components

1.3.2   Mathetical notations and formulae

Let ϕ_i, υ_{ij} and ς_{ijk} be arbitrary first, second and third order tensors, respectively, used to describe the .

$$\nabla \vec{r} - \text{Second order unit dyadic}$$

$$\mathrm{I}, \delta_{ij} - \text{Kronecker delta function}$$

$$\boldsymbol{X}, e_{ijk} - \text{Levi-Civita permutation symbol}$$

$$\upsilon_{(ij)} = \upsilon^s - \text{Symmetry of a tensor over a pair of indices}$$

$$\upsilon_{[ij]} = \upsilon^a - \text{Anti-symmetry of a tensor over a pair of indices}$$

$$tr\left(\upsilon\right) = \upsilon_{ii} - \text{Trace of a tensor}$$

$$\boldsymbol{grad}\upsilon = \left(\nabla\upsilon\right)_{ijk} = \upsilon_{ij,k} - \text{Gradient of a tensorial quantity}$$

$$\boldsymbol{div}\upsilon = \left(\nabla\cdot\upsilon\right)_i = \upsilon_{ij,j} - \text{Divergence of a 2nd order tensor}$$

$$\boldsymbol{curl}\upsilon = \left(\nabla\times\upsilon\right)_{ij} = e_{jkl}\upsilon_{il,k} - \text{Curl of a 2nd order tensor}$$

$$\boldsymbol{X}\left(\upsilon\right) = -\frac{1}{2}\upsilon : \boldsymbol{X} = -\frac{1}{2}e_{ijk}\upsilon_{ij} - \text{Rotation of 2nd order tensor to obtain a vector}$$

$$\{\phi\} = -\boldsymbol{X}\cdot\phi = -e_{ijk}\phi_k - \text{Rotation of a vector to obtain a 2nd order tensor}$$

$$\boldsymbol{X}\left(\varsigma\right) = -\frac{1}{2}\boldsymbol{X} : \varsigma = -\frac{1}{2}e_{mni}\varsigma_{mnj} - \text{Rotation of a 3rd order tensor to obtain}$$

$$\text{a 3rd order tensor}$$

$$\{\upsilon\} = -\boldsymbol{X}\cdot\upsilon = -e_{ijl}\upsilon_{lk} - \text{Rotation of a 2nd order tensor to obtain}$$

$$\text{a 3rd order tensor}$$

1.3.3   Field variables

$$\rho - \text{Material mass density}$$

$$\vec{r}, \vec{\boldsymbol{x}} - \text{Spatial position}$$

$$\vec{v} - \text{Material velocity}$$

$$V - \text{Volume of a body}$$

$$\boldsymbol{S} - \text{Surface of a body}$$

$$\vec{\boldsymbol{u}}, u_i - \text{Displacement vector}$$

$$\vec{\boldsymbol{\omega}}, \omega_i - \text{Rotation vector}$$

$$\boldsymbol{\eta} - \text{Incompatibility tensor}$$

$$\boldsymbol{U}, U_{ij} - \text{Distortion tensor}$$

$\boldsymbol{\epsilon}, \epsilon_{ij}$ — Strain tensor

$\boldsymbol{\omega}, \omega_{ij}$ — Rotation tensor

$\boldsymbol{\kappa}^a, \kappa_{[ij]k}$ — Third order curvature tensor

$\tilde{\boldsymbol{\kappa}}, \tilde{\kappa}_{ij}$ — Second order curvature tensor

G, G_{ijk} — 2-distortion tensor

$\boldsymbol{\alpha}, \alpha_{ij}$ — Geometrically necessary dislocation density tensor

$\boldsymbol{\theta}, \theta_{ij}$ — Geometrically necessary disclination density tensor

$\boldsymbol{\pi}, \pi_{ijk}$ — Geometrically necessary G-disclination density tensor

$\boldsymbol{C}$ — 4th order elasticity tensor

$\boldsymbol{B}, \boldsymbol{D}$ — 5th order elasticity tensors

$\boldsymbol{A}$ — 6th order elasticity tensor

λ, G — Lamé constants

$\boldsymbol{\sigma}, \sigma_{ij}$ — Asymmetric force stress tensor

M, M_{ijk} — 3rd order hyper stress tensor

$\tilde{M}, M_{ij}$ — Second order couple stress tensor

ψ — Helmholtz free energy density

$\vec{\boldsymbol{t}}$ — Traction vector

$\vec{\boldsymbol{m}}$ — Moment vector

CHAPTER II

INCOMPATIBLE THEORY OF LINE CRYSTAL DEFECTS

The purpose of this chapter is to present the state of the art on the theory of stationary line crystal defects *i.e.* dislocations and disclinations. The discussion begins by first understanding, from a mathematical standpoint, the geometry (stationary equivalent of kinematics) *i.e.* displacement, distortion, strain, rotation and curvature fields, and the statics of discrete line defects. Following this, the geometric equivalence between dislocations and disclinations is highlighted. The discussion is then directed towards connecting line defects to crystallography with emphasis on disclinations. From these discussions, the motivation behind adopting a continuous representation for line crystal defects is presented. The ensuing discussion then begins by recalling the geometry of a compatible body, *i.e.* a body containing no defects. This serves as the basis for the incompatible theory of continuously distributed defects. The latter, which was introduced in the work of Kröner [216] and deWit [94], is then presented with the equations refined in such a manner that they encompass the most recent developments [2, 134] in this theory. The chapter is concluded with a discussion giving perspective on incompatibility, as presented in this work, in comparison with other works.

2.1 *Discrete line defects*

The first treatise on line defects was presented by Volterra [436] in 1907, almost half a century before the first experimental evidence on these type of defects. Volterra postulated six types of line defects in a discrete form, (a) three of these were translational

type known as dislocations, and (b) the remaining three of rotational type known as disclinations. The discrete defects were embedded in an infinitely long cylindrical domain with the defect line located along its axis. The domain was assumed to be continuous everywhere except in the immediate vicinity of the defect line where the material is removed in order to avoid dealing with the severe distortions induced by the presence of defect. This region was called the defect core. The defects were characterized by a planar surface cut (shown as AA'BB' in figure 2.1) bounded by the defect line and extending into the cylindrical medium. The material on one side of the surface cut was then either translated with respect to the other to obtain a dislocation, or rotated with respect to the other to obtain a disclination.

Dislocations are characterized by the Burgers vector ($\vec{b}$) which is representative of the jump induced in the displacement field ($\vec{u}$),

$$[\vec{u}] = \vec{b} \tag{2.1}$$

where [ ] is representative of the discontinuity. The dislocations whose Burgers vectors are parallel to the defect line direction are identified as screw dislocations and those who having the Burgers vector perpendicular to the line are identified as edge dislocations.

Similarly, disclinations are characterized by a Frank's vector ($\vec{\Omega}$) representative of a jump in the rotation field ($\vec{\omega}$),

$$[\vec{\omega}] = \vec{\Omega} \tag{2.2}$$

When the Frank's vector is parallel to the defect line, the disclination has a wedge character and when it is perpendicular to the defect line, it has a twist character.

Figure 2.1 (adapted from Romanov and Kolesnikova [333]) pictorially describes Volterra's conceptualization of dislocations and disclinations. For a defect line with dislocation character, there are two types of edge dislocations possible (see figures 2.1(c) and 2.1(d)). The first one forms when surface A'B' is displaced in the direction

normal to the surface AB as shown in figure 2.1(c) and the second one forms when A'B' is displaced in the direction perpendicular to both the dislocation line and the normal to the surface AB as shown in figure 2.1(d). Figure 2.1(b) shows a screw dislocation formed when the surface AB is displaced in the direction of the defect line. When the defect line has disclination character, there are two types of twist disclinations that can be formed (see figures (2.1)(f) and (2.1)(g)). The first one shown in figure (2.1)(f) is formed when surface A'B' is rotated in the direction normal to the disclination line about an axis which is located at a distance r_ω in the direction perpendicular to the disclination line. The second twist disclination shown in figure (2.1)(g) is formed when the surface A'B' is rotated about an axis which is perpendicular to, and coplanar with, the disclination line. A wedge disclination as shown in figure (2.1)(e) is formed when the surface A'B' is rotated with respect to AB about the disclination line.
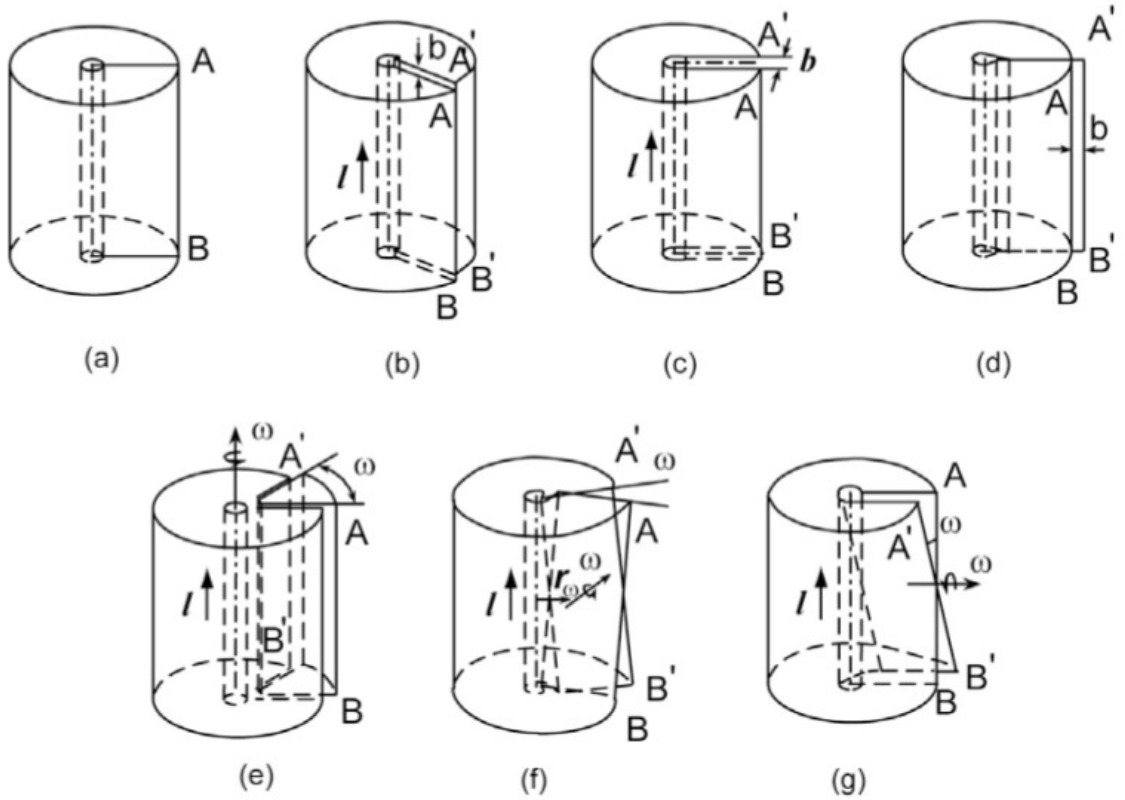
Figure 2.1: Volterra's dislocations and disclinations (adapted from Romanov and Kolesnikova [333]). Note here that $|\vec{\Omega}| = \omega$

From figure 2.1, for the case of dislocations it can be visualized that the jump in displacement is constant everywhere across ABA'B'. However, in the case of disclinations, the displacement jump evolves depending on (a) the location of the position vector with respect to the disclination line and (b) the Frank's vector. deWit [97], and Kroupa and Lejcek [223] have shown that this jump in displacement can be defined as,

$$[\vec{u}] = \vec{\Omega} \times (\vec{r}_\omega - \vec{r}) \tag{2.3}$$

where $\vec{r}$ is the radius-vector and $\vec{r}_\omega$ is the position for the rotation axis. Note that this could be different from the defect line; an example is shown in figure 2.1(f) for a twist disclination.

An evolving dislocation jump as shown in equation (2.3) can be most easily visualized in the case of a wedge disclination where an additional wedge of material can be inserted or removed from the elastic medium. Figure 2.2 depicts a negative wedge disclination (represented using a ∇; a positive wedge is denoted using Δ) where a wedge of angle ω can be imagined to be inserted into the region between faces A'B' and AB of figure 2.1. Due to the opening created by the wedge disclination, the displacement jump between faces A'B' and AB increases with an increase in the distance away from, and perpendicular to, the disclination line. Note that the displacement jump remains the same along the disclination line. In the case of twist disclinations it is more complicated to visualize the exact evolution of the displacement jump but from figure (2.1) it can be deduced that a component of the displacement jump evolves as a function of the distance along the disclination line direction.

A general defect line having mixed dislocation and disclination character was proposed in the works of Nabarro [294] and deWit [95, 96, 97]. The general line defect is characterized by both Burgers and Frank's vectors and its presence induces

18
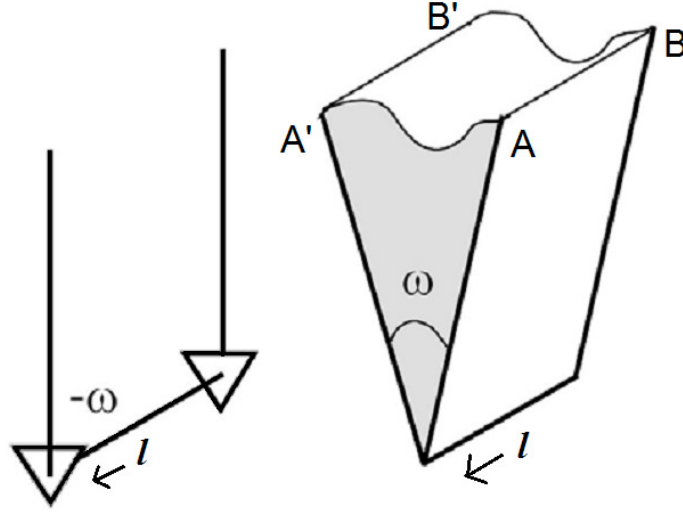
Figure 2.2: Negative wedge disclination of strength $|\vec{\Omega}| = -\omega$ inserted into the region between the cut faces ABA'B' of figure 2.1

a jump in both displacement and rotation fields,

$$[\vec{u}] = \vec{b} + \vec{\Omega} \times (\vec{r}_\omega - \vec{r}) \tag{2.4}$$

$$[\vec{\omega}] = \vec{\Omega} \tag{2.5}$$

Such a formulation was motivated from Weingarten's theorem. This theorem is based on the definition of a multiply connected body. Such a body consists of one or more regions around which any arbitrary circuit is irreducible to a single point in the domain, for example a domain containing voids or cracks. Weingarten's theorem states that: "*On following around an irreducible circuit in a multiply-connected body satisfying the classical compatibility conditions, the rotation and displacement change by an amount that would be possible for a rigid body*" [95].

deWit [94, 95, 96, 97] proposed to develop expressions for the geometric fields of a general line defect in a simply connected body. This body, unlike a multiply connected body, is the one where every closed path in the domain is reducible to a point. deWit postulated that in a simply connected medium the classical equilibrium conditions should be respected everywhere in the domain, including the defect core and the defect line.

19

In order to obtain the geometric fields associated with line defects in an infinitely extended simply connected continuous medium, deWit [95] rephrased the problem as an extended formulation of the Eshelbian inclusion problem [112]. The Eshelby problem involves solving for the stress field of an inclusion or inhomogeneity embedded in an otherwise infinite homogeneous matrix. Consider an inclusion of volume V' embedded inside an infinite matrix. Let this inclusion be subjected to a permanent deformation such that it results in a stress free or eigen strain. In reality, the inclusion is embedded inside the matrix and cannot undergo such a stress free transformation. Instead, both the inclusion and the matrix will deform and experience an elastic stress field. Eshelby inclusion problem then requires finding the stress, strain and displacement fields both in the inclusion and in the matrix. deWit argued that a plastic strain induced in the presence of a line defect can be viewed as an eigenstrain. Then the statement of the problem is posed without specifying the nature of the defect [95] as: "Given an infinitely extended homogeneous anisotropic body with the plastic strain ϵ^p given as a prescribed function of space. To find the resulting total displacement $\boldsymbol{u}$ throughout the body".

The solution begins by rephrasing the problem such that it is similar to the classical elasticity problem but without the true body force. The equilibrium equation to be solved is given as:

$$\mathbf{div}\, \boldsymbol{\sigma}^s(\vec{\boldsymbol{r}}) = \nabla \cdot \boldsymbol{\sigma}^s(\vec{\boldsymbol{r}}) = 0 \quad \text{or} \quad \sigma^s_{ij,j}(\vec{\boldsymbol{r}}) = 0 \tag{2.6}$$

where $\boldsymbol{\sigma}^s$ is the symmetric Cauchy stress and $\vec{\boldsymbol{r}}$ is the position vector of a field point in the Cartesian coordinate system. The stress is related to the symmetric elastic strain ϵ^e via the classical Hooke's law,

$$\boldsymbol{\sigma}^s(\vec{\boldsymbol{r}}) = \boldsymbol{C} : \boldsymbol{\epsilon}^e(\vec{\boldsymbol{r}}) \quad \text{or} \quad \sigma^s_{ij}(\vec{\boldsymbol{r}}) = C_{ijkl}\epsilon^e_{kl}(\vec{\boldsymbol{r}}) \tag{2.7}$$

where $\boldsymbol{C}$ is the 4th order anisotropic elasticity tensor. The symmetry of Cauchy stress and elastic strain imposes the symmetry on the indices of the elasticity tensor

20

as $C_{ijkl} = C_{jikl} = C_{ijlk}$. Recalling that the total strain which is defined as the symmetric part of the gradient of total displacement *i.e.* $\epsilon_{kl}(\vec{r}) = \frac{1}{2}(u_{kl}(\vec{r}) + u_{lk}(\vec{r}))$ is the sum of the elastic and plastic strains, the equilibrium equation in absence of body forces can be written as,

$$C_{ijkl}u_{k,lj}(\vec{r}) = C_{ijkl}\epsilon^p_{kl,j}(\vec{r}) \qquad (2.8)$$

To integrate this equation, the Green's tensor function $G_{ij}(\vec{r})$ is used, which represents the displacement in x_i direction at a field point $\vec{r}$ due to a point force in the x_j direction. The problem to be solved is then written as,

$$C_{ijkl}G_{kn,lj}(\vec{r}) + \delta_{in}\boldsymbol{\delta}(\vec{r}) = 0 \qquad (2.9)$$

where δ_{in} is the Kronecker delta and $\boldsymbol{\delta}(\vec{r})$ is the three-dimensional Dirac delta function. Solving this equation gives the expression of the total displacement field in an anisotropic elastic solid as a function of plastic strain (for details please refer to [95]),

$$u_n(\vec{r}) = -\int_{V'} C_{ijkl}G_{in,j}(\vec{r} - \vec{r'})\epsilon^p_{kl}(\vec{r'})dV' \qquad (2.10)$$

Explicit expressions for the Green's tensor are known for an isotropic material in terms of the modulus of rigidity or shear modulus G and Poisson's ratio ν,

$$G_{in}(\vec{r}) = \frac{1}{8\pi G}\left(\delta_{in}r_{,qq} - \frac{1}{2(1-\nu)}r_{,in}\right) \qquad (2.11)$$

here r is the magnitude of the position vector. The elastic constants C_{ijkl} have the following expression in isotropic elasticity,

$$C_{ijkl} = \lambda\delta_{ij}\delta_{kl} + G\left(\delta_{ik}\delta_{jl} + \delta_{il}\delta_{jk}\right) \qquad (2.12)$$

where $\lambda = \frac{2G\nu}{1-2\nu}$ and G are the Lamé constants with G being the shear modulus.

2.1.1 Statics of discrete dislocations

In the case when dislocations are present in the medium, the entire plastic distortion, which is the sum of the anti-symmetric plastic rotation ($\boldsymbol{\omega}^p$) and the symmetric

plastic strain $\boldsymbol{U}^p = \boldsymbol{\epsilon}^p + \boldsymbol{\omega}^p$, is prescribed. The double dot product of the anti-symmetric plastic rotation tensor with the elasticity tensor is equal to zero ($C_{ijkl}\omega_{kl}^p = 0$). Therefore the expression for the total displacement can be written as,

$$u_n(\boldsymbol{r}) = -\int_{V'} C_{ijkl}G_{in,j}(\boldsymbol{r} - \boldsymbol{r}')U_{kl}^p(\boldsymbol{r}')dV' \tag{2.13}$$

In the presence of a continuous distribution of dislocations, this expression is the same as that obtained by Mura [288]. The plastic distortion of a discrete dislocation can be defined as a function of the Burgers vector and an arbitrarily shaped defect surface $\boldsymbol{S}$ with normal $\vec{\boldsymbol{n}}$ [95],

$$U_{kl}^p = -\delta_k(\boldsymbol{S})b_l \tag{2.14}$$

where $\delta_k(\boldsymbol{S})$ attains the value 1 on the surface $\boldsymbol{S}$ and 0 everywhere else. deWit [95] proposed a general 3-dimensional defect surface which was a generalized form of the Volterra surface cut. The defect surface is allowed to take any arbitrary shape as long as it is bounded by the defect line. An arbitrary shape is allowed because it does not affect the continuity of elastic distortion and strain fields. However, the displacement fields are multi-valued everywhere on this surface. Figure 2.3 shows an infinitely long curved dislocation line $\boldsymbol{l}$ with Burgers vector $\boldsymbol{b}$ bounded by an arbitrary curved defect surface $\boldsymbol{S}$ and traversing an arbitrary curved Burgers surface σ which is bounded by the Burgers circuit in the sense shown by $\boldsymbol{\lambda}$. The displacement is discontinuous at the point of intersection of $\boldsymbol{S}$ and $\boldsymbol{\lambda}$. The discontinuity is in the direction of the Burgers vector.

The final expression for the displacement field is obtained by substituting (2.14) in (2.13),

$$u_n(\boldsymbol{r}) = -\int_{S'} C_{ijkl}G_{in,j}(\boldsymbol{r} - \boldsymbol{r}')b_l dS_k' \tag{2.15}$$

Equation (2.15) represents the displacement field of a curved dislocation line of
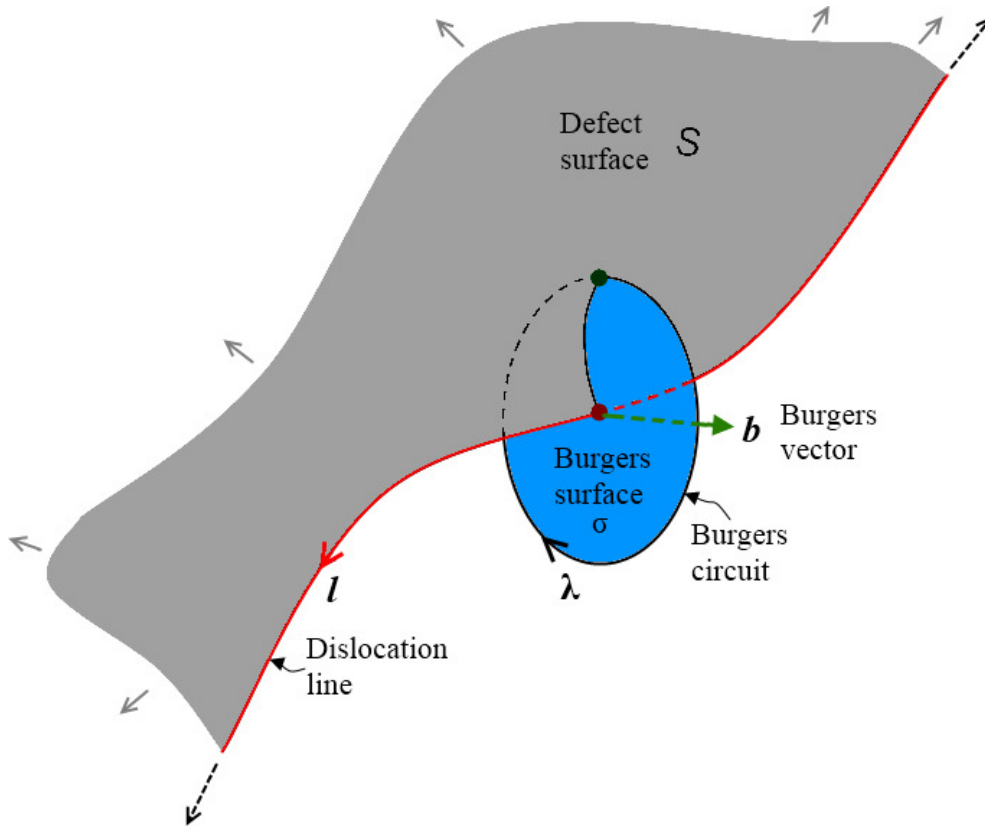
Figure 2.3: A curved dislocation line l with a general Burgers vector b in an infinite continuous medium, bounded by an arbitrarily shaped defect surface S and encircled by an arbitrarily shaped Burgers circuit λ, traverses the Burgers surface σ at an arbitrary angle. The grey and black dotted arrows indicate the possible extensions of S and l, respectively. The line direction and the sense of λ make the crossings between l and σ negative according to the right-hand rule.

finite length in an infinitely extended anisotropic elastic medium. Taking the derivatives of this field gives the distortion, strain, rotation and curvature fields.

In this work, we are interested in developing the closed form solutions for an infinitely long straight dislocation line in an infinitely extended isotropic medium. In this case, the defect surface becomes a planar semi-infinite surface cut. This is in spirit with the planar surface cut described in the hollow cylindrical domain by Volterra in figure 2.1 except that in deWit's work the surface cut enters into the defect core and is bounded by the defect line. In the present work, similar to the work of deWit [95], the dislocation line is placed along the z axis and bounds the

planar surface cut which lies in the xz plane such that its normal is in the negative y direction, and extends to infinity along the positive and negative z axis and the negative x axis as shown in figure 2.4(a). Since for a dislocation the jump in the displacement field remains constant everywhere on the defect surface, considering the geometric fields at the $z = 0$ plane is representative of all planes belonging to the same family. In this case the surface cut is represented by a semi-infinite line in the xy plane. Generally, the surface cut is allowed to attain any arbitrary rotation. However, giving a particular orientation to the surface cut is necessary to define the displacement field. In the present work, it is chosen to be along the negative x axis as illustrated in figure 2.4(b). This is in spirit with the work of deWit [97]. The angle ϕ is defined with respect to the chosen orientation of the surface cut and ranges from $(-\pi, \pi)$ with a jump of 2π across the $-x$ axis. With such a definition, the functional relationship of ϕ is given as $\phi(x, y) = \tan^{-1}(y/x) + \pi H(-x)\left[H(y) - H(-y)\right]$, where H is the Heaviside step function.

The closed-form solution of the compatible displacement field in two-dimensional isotropic case is then given as follows,

$$u_x = b_x \left[\frac{\phi}{2\pi} + \frac{xy}{4\pi(1-\nu)\rho^2}\right] + \frac{b_y}{4\pi(1-\nu)}\left[(1-2\nu)\ln\rho + \frac{y^2}{\rho^2}\right] \qquad (2.15a)$$

$$u_y = -\frac{b_x}{4\pi(1-\nu)}\left[(1-2\nu)\ln\rho + \frac{x^2}{\rho^2}\right] + b_y\left[\frac{\phi}{2\pi} - \frac{xy}{4\pi(1-\nu)\rho^2}\right] \qquad (2.15b)$$

$$u_z = \frac{b_z\phi}{2\pi} \qquad (2.15c)$$

where $b_i(i = x, y, z)$ is the Burgers vector component in direction i, ν is the Poisson's ratio, and $\rho = \sqrt{x^2 + y^2}$ is the distance from the defect line to an arbitrary point in the $x - y$ plane.

deWit [95] labels the displacements in equation (2.16) as the total displacements. The argument being that within the framework of solving an Eshelby type problem using the Green's function method, such is the necessary outcome of the solution. On the other hand, elsewhere in the literature these multi-valued displacements are
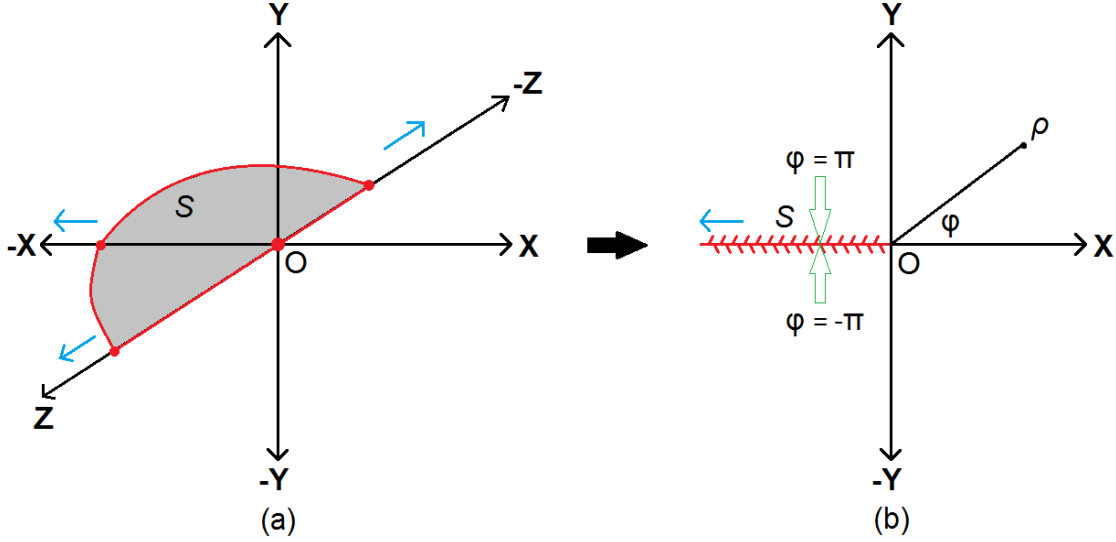
Figure 2.4: Semi-infinite defect surface along the $-x$ axis and bounded by the infinitely long straight defect along the z-axis in (a) 3-dimensions. Blue arrows indicate the directions of infinite extension of S and the red dots indicate the critical points of intersection of the surface with the coordinate axes. (b) $z = 0$ plane showing the defect surface represented as a semi-infinite line bounded at the origin and extending along the $-x$ axis. ϕ defines the angular position of the point ρ in the xy plane, $\phi \in [-\pi, \pi]$

referred to as the elastic displacements, for example in the work of Nabarro [294]. In this work we follow the latter nomenclature and identify the displacements in equation (2.16) and the preceding equations as elastic ($\vec{u}^e$). The reasoning is based on the continuity of the material which requires that the total displacements are well-defined everywhere in the domain. Due to the multi-valued nature of the displacements in equation (2.16), these cannot be deemed as total displacements. However, it is to be noted that deWit's work differs only in terminology; equations (2.16) give the same solution as those available elsewhere in the literature [436, 294, 15].

An illustration of these displacement fields for pure edge and pure screw dislocations are shown in the case of an infinitely extended continuous medium in figures 2.5 and 2.6, respectively. The Burgers vector is taken as $\vec{b} = (001)$ for the screw dislocation and $\vec{b} = (100)$ for the edge dislocation with magnitudes equal to 3.615 Å. The Poisson's ratio is taken as $\nu = 0.34$. Note the jump induced in the displacement

field across the surface cut. The x-component of the displacement (u_x) goes from $-|\vec{\boldsymbol{b}}|/2$ to $|\vec{\boldsymbol{b}}|/2$ across this surface cut for an edge dislocation. In the case of a screw dislocation, the z-component goes from $-|\vec{\boldsymbol{b}}|/2$ to $|\vec{\boldsymbol{b}}|/2$.

(a) u_x^e (m) (b) u_y^e (m)
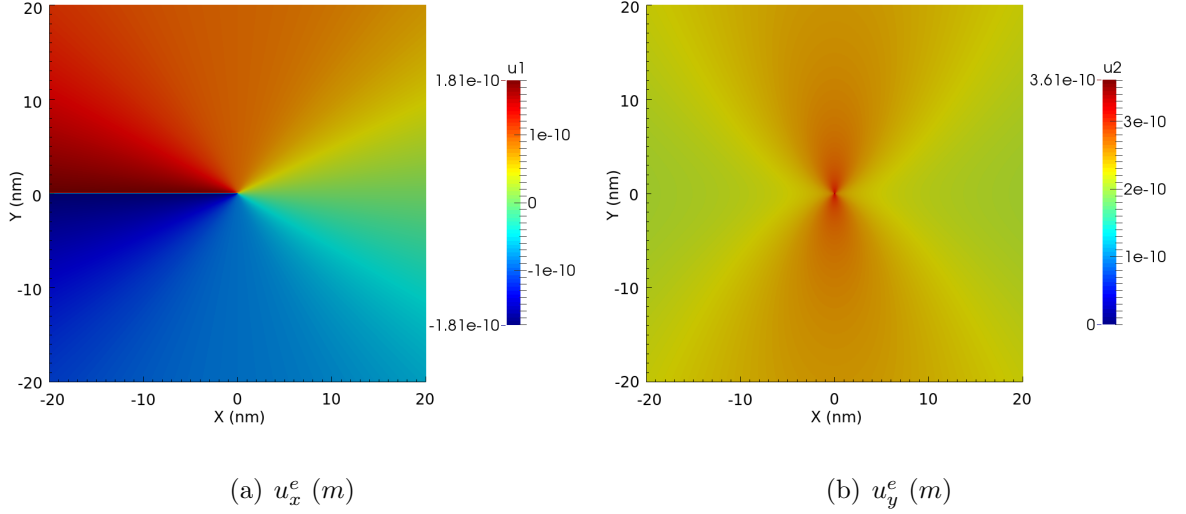
Figure 2.5: Non-zero components of elastic displacement fields (in m) (a) u_x^e and (b) u_y^e of an infinitely long straight single edge dislocation along the z-axis in an infinite continuous medium with $\vec{\boldsymbol{b}} = (\boldsymbol{100})$. The magnitude of the Burgers vector is taken to be 3.615 Å and the Poisson's ratio is $\nu = 0.34$.

The elastic distortion $\boldsymbol{U^e}$ is obtained by taking the gradient of the elastic displacement $U_{ij}^e = u_{i,j}^e$. Recall that the elastic displacement field is a discontinuous function. Taking its gradient requires neglecting the discontinuous part. This operation results into a smooth continuous elastic distortion field. This field is termed as compatible. The component of elastic distortion which cannot be accessed due to the multi-valued nature of the elastic displacement field is called the incompatible elastic distortion. The implications of this shall be discussed in the forthcoming section. For present purposes, we focus the discussion on compatible elastic distortions.

A remark on the notations employed in defining the compatible elastic distortion: note that this is in spirit with the nomenclature used in this work and differs from
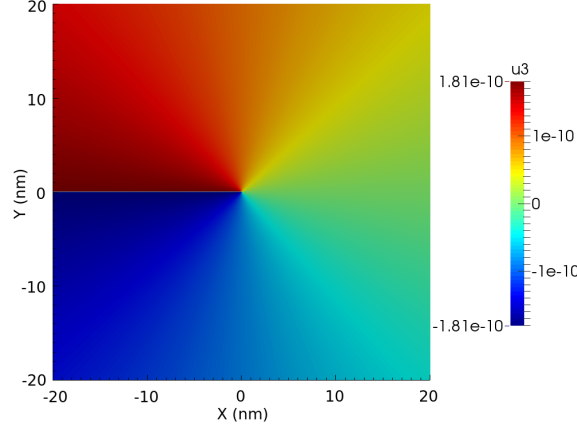
Figure 2.6: Non-zero component of the elastic displacement field u_z^e (in m) of an infinitely long straight single screw dislocation along the z-axis in an infinite continuous medium with $\vec{b} = (001)$. The magnitude of the Burgers vector is taken to be 3.615 Å and the Poisson's ratio is $\nu = 0.34$

that used in the work of deWit [97]. Taking this under consideration, the compatible elastic distortion is defined as,

$$U_{xx}^{e\parallel} = -\frac{b_x}{4\pi(1-\nu)}\left[(1-2\nu)\frac{y}{\rho^2} + 2\frac{x^2y}{\rho^4}\right] + \frac{b_y}{4\pi(1-\nu)}\left[(1-2\nu)\frac{x}{\rho^2} - 2\frac{xy^2}{\rho^4}\right] \quad (2.16)$$

$$U_{yy}^{e\parallel} = -\frac{b_x}{4\pi(1-\nu)}\left[(1-2\nu)\frac{y}{\rho^2} - 2\frac{x^2y}{\rho^4}\right] + \frac{b_y}{4\pi(1-\nu)}\left[(1-2\nu)\frac{x}{\rho^2} + 2\frac{xy^2}{\rho^4}\right] \quad (2.16a)$$

$$U_{zz}^{e\parallel} = 0 \quad (2.16b)$$

$$U_{xy}^{e\parallel} = \frac{b_x}{4\pi(1-\nu)}\left[(3-2\nu)\frac{x}{\rho^2} - 2\frac{xy^2}{\rho^4}\right] + \frac{b_y}{4\pi(1-\nu)}\left[(1-2\nu)\frac{y}{\rho^2} + 2\frac{x^2y}{\rho^4}\right] \quad (2.16c)$$

$$U_{yx}^{e\parallel} = -\frac{b_x}{4\pi(1-\nu)}\left[(1-2\nu)\frac{x}{\rho^2} + 2\frac{xy^2}{\rho^4}\right] - \frac{b_y}{4\pi(1-\nu)}\left[(3-2\nu)\frac{y}{\rho^2} - 2\frac{x^2y}{\rho^4}\right] \quad (2.16d)$$

$$U_{yz}^{e\parallel} = 0 \quad (2.16e)$$

$$U_{zy}^{e\parallel} = \frac{b_z x}{2\pi\rho^2} \quad (2.16f)$$

$$U_{xz}^{e\parallel} = 0 \quad (2.16g)$$

$$U_{zx}^{e\parallel} = -\frac{b_z y}{2\pi\rho^2} \quad (2.16h)$$

where the superscript '$\parallel$' denotes the compatible component. Note that it is possible

to integrate equations (2.16) to obtain an expression of a vectorial field, say '$\vec{v}$'. However, $\vec{v}$ will be a continuous function and would not correspond to the discontinuous elastic displacement field in equations (2.16). Furthermore, integrating the compatible elastic distortions would lead to a compatible elastic displacement field which is unique only up to a constant vector field.

The symmetric part of the compatible elastic distortion is the compatible elastic strain $\boldsymbol{\epsilon}^{e\|}$ whose components are given as,

$$\epsilon_{xx}^{e\|} = -\frac{b_x}{4\pi(1-\nu)}\left[(1-2\nu)\frac{y}{\rho^2} + 2\frac{x^2 y}{\rho^4}\right] + \frac{b_y}{4\pi(1-\nu)}\left[(1-2\nu)\frac{x}{\rho^2} - 2\frac{xy^2}{\rho^4}\right] \qquad (2.17)$$

$$\epsilon_{yy}^{e\|} = -\frac{b_x}{4\pi(1-\nu)}\left[(1-2\nu)\frac{y}{\rho^2} - 2\frac{x^2 y}{\rho^4}\right] + \frac{b_y}{4\pi(1-\nu)}\left[(1-2\nu)\frac{x}{\rho^2} + 2\frac{xy^2}{\rho^4}\right] \qquad (2.17a)$$

$$\epsilon_{zz}^{e\|} = 0 \qquad (2.17b)$$

$$\epsilon_{xy}^{e\|} = \epsilon_{yx}^{e\|} = \frac{b_x}{4\pi(1-\nu)}\left[\frac{x}{\rho^2} - 2\frac{xy^2}{\rho^4}\right] - \frac{b_y}{4\pi(1-\nu)}\left[\frac{y}{\rho^2} - 2\frac{x^2 y}{\rho^4}\right] \qquad (2.17c)$$

$$\epsilon_{yz}^{e\|} = \epsilon_{zy}^{e\|} = \frac{b_z x}{4\pi\rho^2} \qquad (2.17d)$$

$$\epsilon_{xz}^{e\|} = \epsilon_{zx}^{e\|} = -\frac{b_z y}{4\pi\rho^2} \qquad (2.17e)$$

The expressions for compatible elastic distortions and strains highlight their singular nature at the line of the defect. Furthermore, at distances less than the Burgers vector magnitude (usually taken as the radius of the core of the dislocation) these expressions are not valid.

The well known expressions for Cauchy stresses are then obtained by substituting equations (2.17) and (2.12) in the Hooke's law (2.7),

$$\sigma_{xx}^{e\|} = -\frac{Gb_x}{2\pi(1-\nu)}\left[\frac{y}{\rho^2} + 2\frac{x^2 y}{\rho^4}\right] + \frac{Gb_y}{2\pi(1-\nu)}\left[\frac{x}{\rho^2} - 2\frac{xy^2}{\rho^4}\right] \qquad (2.18)$$

$$\sigma_{yy}^{e\|} = -\frac{Gb_x}{2\pi(1-\nu)}\left[\frac{y}{\rho^2} - 2\frac{x^2 y}{\rho^4}\right] + \frac{Gb_y}{2\pi(1-\nu)}\left[\frac{x}{\rho^2} + 2\frac{xy^2}{\rho^4}\right] \qquad (2.18a)$$

$$\sigma_{zz}^{e\|} = -\frac{G\nu}{2\pi(1-\nu)}\left[2\frac{b_x y}{\rho^2} - 2\frac{b_y x}{\rho^2}\right] \qquad (2.18b)$$

$$\sigma_{xy}^{e\|} = \sigma_{yx}^{e\|} = \frac{Gb_x}{2\pi(1-\nu)}\left[\frac{x}{\rho^2} - 2\frac{xy^2}{\rho^4}\right] - \frac{Gb_y}{2\pi(1-\nu)}\left[\frac{y}{\rho^2} - 2\frac{x^2 y}{\rho^4}\right] \qquad (2.18c)$$

$$\sigma_{yz}^{e\|} = \sigma_{zy}^{e\|} = \frac{Gb_z x}{2\pi\rho^2} \qquad (2.18d)$$
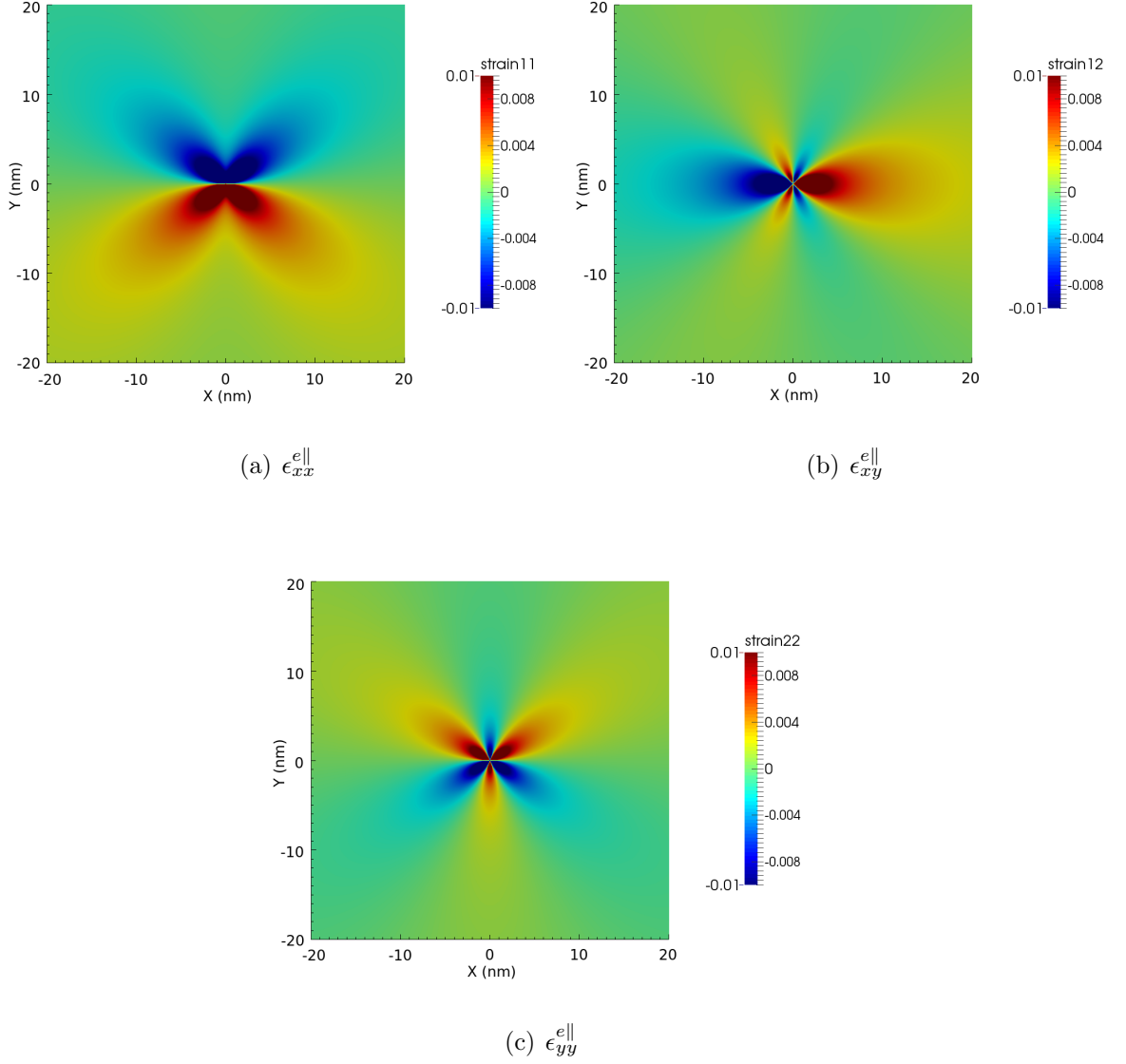
(a) $\epsilon_{xx}^{e\|}$

(b) $\epsilon_{xy}^{e\|}$

(c) $\epsilon_{yy}^{e\|}$

Figure 2.7: Non-zero components of compatible elastic strain fields (a) $\epsilon_{xx}^{e\|}$, (b) $\epsilon_{xy}^{e\|}$ and (c) $\epsilon_{yy}^{e\|}$ of an infinitely long straight single edge dislocation along the z-axis in an infinite continuous medium with $\vec{b} = (100)$. The magnitude of the Burgers vector is taken to be 3.615 Å and the Poisson's ratio is $\nu = 0.34$.

$$\sigma_{xz}^{e\|} = \sigma_{zx}^{e\|} = -\frac{Gb_z y}{2\pi\rho^2} \tag{2.18e}$$

Upon substituting the Cauchy stress into the equilibrium equation (2.6), it is found that $\sigma_{ij,j} = 0$ is respected everywhere in the domain, including the defect line
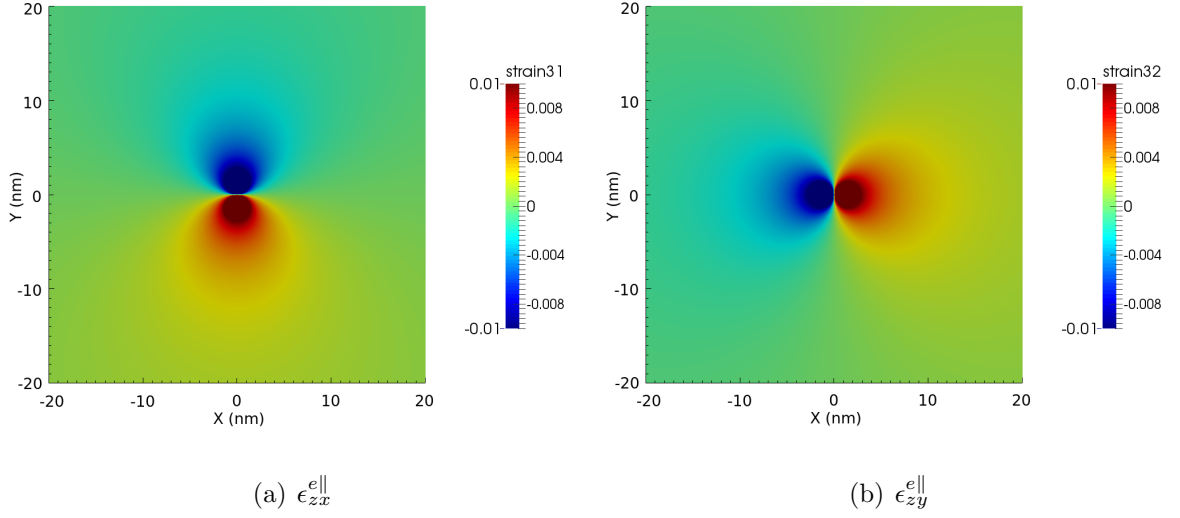
(a) $\epsilon_{zx}^{e\parallel}$

(b) $\epsilon_{zy}^{e\parallel}$

Figure 2.8: Non-zero components of compatible elastic strain fields (a) $\epsilon_{zx}^{e\parallel}$ and (b) $\epsilon_{zy}^{e\parallel}$ of an infinitely long straight single screw dislocation along the z-axis in an infinite continuous matrix with $\vec{b} = (001)$. The magnitude of the Burgers vector is taken to be 3.615 Å and the Poisson's ratio is $\nu = 0.34$.

where equation (2.18) is singular.

The elastic rotations for a dislocation are also compatible. This can be deduced from the fact that dislocations are translational type of defects. The compatible elastic rotation are given as follows,

$$\omega_x^{e\parallel} = \frac{b_z x}{4\pi\rho^2} \tag{2.19}$$

$$\omega_y^{e\parallel} = \frac{b_z y}{4\pi\rho^2} \tag{2.19a}$$

$$\omega_z^{e\parallel} = -\frac{b_x x}{2\pi\rho^2} - \frac{b_y y}{2\pi\rho^2} \tag{2.19b}$$

The compatible elastic curvatures $\boldsymbol{\kappa}^{e\parallel}$, which are defined as the gradients of the elastic rotation, are then derived as,

$$\kappa_{xx}^{e\parallel} = \frac{b_z}{4\pi}\left[\frac{1}{\rho^2} - \frac{2x^2}{\rho^4}\right] \tag{2.20}$$

$$\kappa_{xy}^{e\parallel} = -\frac{b_z xy}{2\pi\rho^4} \tag{2.20a}$$

$$\kappa_{xz}^{e\parallel} = 0 \tag{2.20b}$$

30

$$\kappa_{yx}^{e\parallel} = -\frac{b_z xy}{2\pi\rho^4} \tag{2.20c}$$

$$\kappa_{yy}^{e\parallel} = \frac{b_z}{4\pi}\left[\frac{1}{\rho^2} - \frac{2y^2}{\rho^4}\right] \tag{2.20d}$$

$$\kappa_{yz}^{e\parallel} = 0 \tag{2.20e}$$

$$\kappa_{zx}^{e\parallel} = -\frac{b_x}{2\pi}\left[\frac{1}{\rho^2} - \frac{2x^2}{\rho^4}\right] + \frac{b_y xy}{\pi\rho^4} \tag{2.20f}$$

$$\kappa_{zy}^{e\parallel} = \frac{b_x xy}{\pi\rho^4} - \frac{b_y}{2\pi}\left[\frac{1}{\rho^2} - \frac{2y^2}{\rho^4}\right] \tag{2.20g}$$

$$\kappa_{zz}^{e\parallel} = 0 \tag{2.20h}$$

Note that $\kappa_{yx}^{e\parallel} = \kappa_{xy}^{e\parallel}$ for an infinitely long straight dislocation. In general, the curvature tensor is asymmetric. This shall be evidenced in the case of disclinations.

(a) $\kappa_{zx}^{e\parallel}$ (m^{-1})   (b) $\kappa_{zy}^{e\parallel}$ (m^{-1})
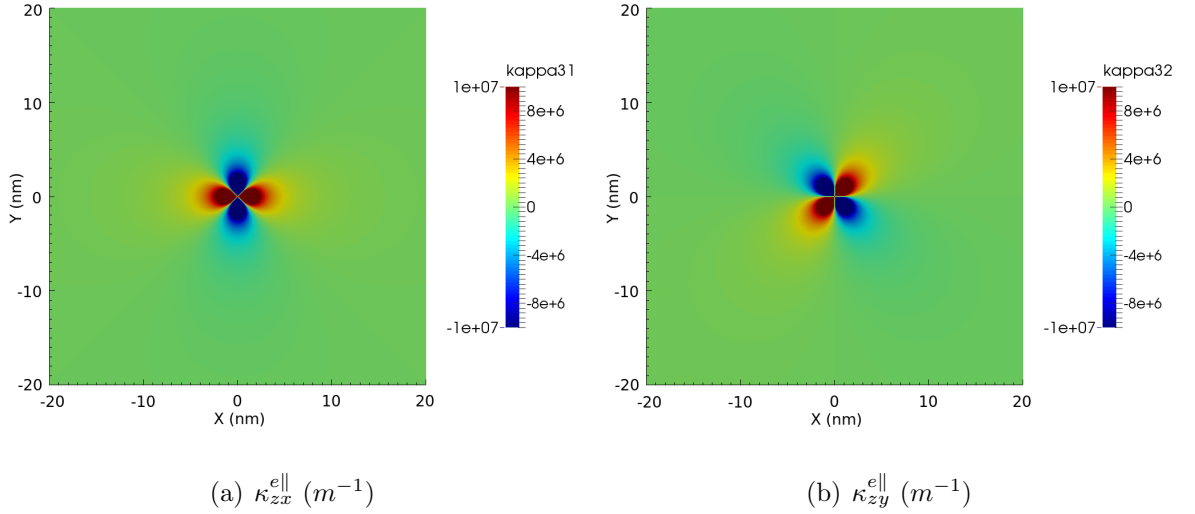
Figure 2.9: Non-zero compatible elastic curvature fields (in m^{-1}) (a) $\kappa_{zx}^{e\parallel}$ and (b) $\kappa_{zy}^{e\parallel}$ of an infinitely long straight single edge dislocation along the z-axis in an infinite continuous medium with $\vec{b} = (100)$. The magnitude of the Burgers vector is taken to be $3.615A^{\text{o}}$ and the Poisson's ratio is $\nu = 0.34$.

2.1.2   Statics of discrete disclinations

In the same work as dislocations, deWit [95, 96, 97] also developed the statics of discrete disclinations. Recall from equation (2.3) that the jump in elastic displacement

31
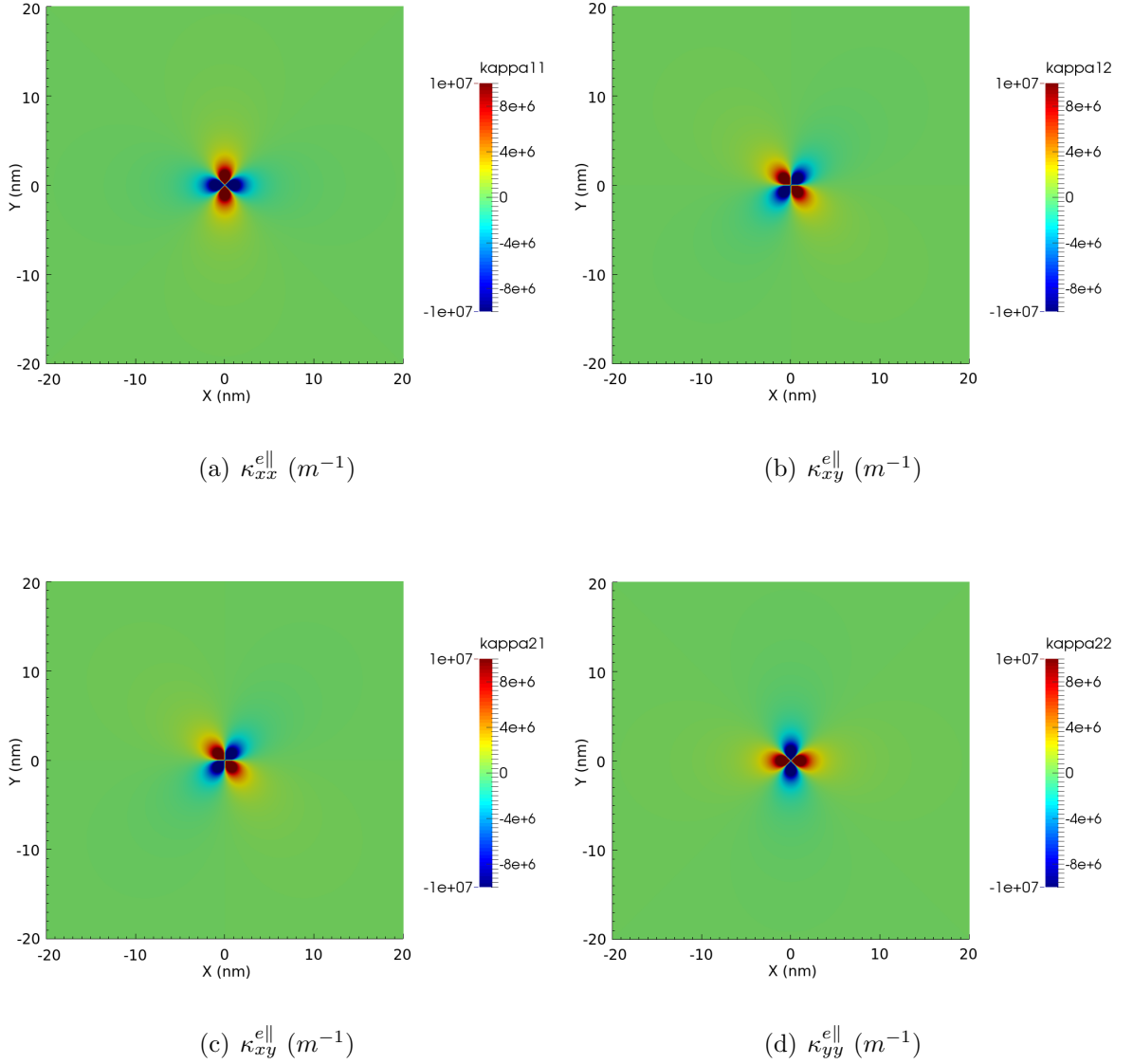
Figure 2.10: Non-zero compatible elastic curvature fields (in m^{-1}) (a) $\kappa_{xx}^{e\parallel}$, (a) $\kappa_{xy}^{e\parallel}$, (a) $\kappa_{yx}^{e\parallel}$ and (d) κ_{yy} of an infinitely long straight single screw dislocation along the z-axis in an infinite continuous medium with $\vec{b} = \mathbf{(001)}$. The magnitude of the Burgers vector is taken to be $3.615 A^o$ and the Poisson's ratio is $\nu = 0.34$.

in the presence of a disclination is given as $[u_l] = e_{lqr}\Omega_q(x_r - x_r^o)$. The plastic distortion of a discrete disclination is then defined as a function of the Frank's vector [290, 95],

$$U_{kl}^p = -\delta_k(S)e_{lqr}\Omega_q(x_r - x_r^o) \tag{2.21}$$

32

Then the expression for the elastic displacement field from equation (2.13) can be written as,

$$u_n(\boldsymbol{r}) = \int\limits_{V'} C_{ijkl} G_{in,j}(\boldsymbol{r} - \boldsymbol{r'}) \delta_k(S) e_{lqr} \Omega_q (x_r - x_r^o)(\boldsymbol{r'}) dV' \tag{2.22}$$

This elastic displacement solely arises from the rotational discontinuity induced by the disclination. The defect surface is defined in the same manner as in the case of a dislocation. Figure 2.11 shows a curved disclination line with Frank's vector $\boldsymbol{\Omega}$. It is bounded by the arbitrarily shaped surface $\boldsymbol{S}$ and traverses an arbitrarily shaped Frank's surface σ that terminates into a circuit $\boldsymbol{\lambda}$. The Frank's circuit has a positive sense according to the right hand rule. The rotation axis is displaced by a vector $\boldsymbol{r_\omega}$ from the point of intersection of $\boldsymbol{l}$ and σ. This implies that a disclination line has a de-localized defect core *i.e.* for a non-null $\boldsymbol{r_\omega}$, the core may not be centered on the disclination line; in some cases it is also possible that disclination line may not lie within the core.

The geometric fields for an infinitely long straight discrete disclination line are derived in a manner similar to the dislocation case. Let the disclination with Frank's vector $\vec{\Omega}$ lie along the z-axis in 3D Cartesian space. It is bounded by a planar surface cut similar to the case of dislocations shown in figure 2.4. The elastic displacements are then given as,

$$u_x^e = \frac{\Omega_x z}{4\pi(1-\nu)} \left[(1-2\nu) \ln \rho + \frac{y^2}{\rho^2} \right] + \Omega_y z \left[\frac{\phi}{2\pi} + \frac{xy}{4\pi(1-\nu)\rho^2} \right]$$
$$- \Omega_z \left[\frac{y\phi}{2\pi} - \frac{(1-2\nu)x(\ln\rho - 1)}{4\pi(1-\nu)} \right] \tag{2.23}$$

$$u_y^e = -\Omega_x z \left[\frac{\phi}{2\pi} - \frac{xy}{4\pi(1-\nu)\rho^2} \right] - \frac{\Omega_y z}{4\pi(1-\nu)} \left[(1-2\nu) \ln \rho + \frac{x^2}{\rho^2} \right]$$
$$+ \Omega_z \left[\frac{x\phi}{2\pi} + \frac{(1-2\nu)y(\ln\rho - 1)}{4\pi(1-\nu)} \right] \tag{2.23a}$$

$$u_z^e = \Omega_x \left[\frac{y\phi}{2\pi} - \frac{(1-2\nu)x(\ln\rho - 1)}{4\pi(1-\nu)} \right] - \Omega_y \left[\frac{x\phi}{2\pi} + \frac{(1-2\nu)y(\ln\rho - 1)}{4\pi(1-\nu)} \right] \tag{2.23b}$$

Note that even in the case of disclinations the displacements are always a function of the surface cut. Figure 2.12 and 2.13 illustrate the non-zero displacement vector
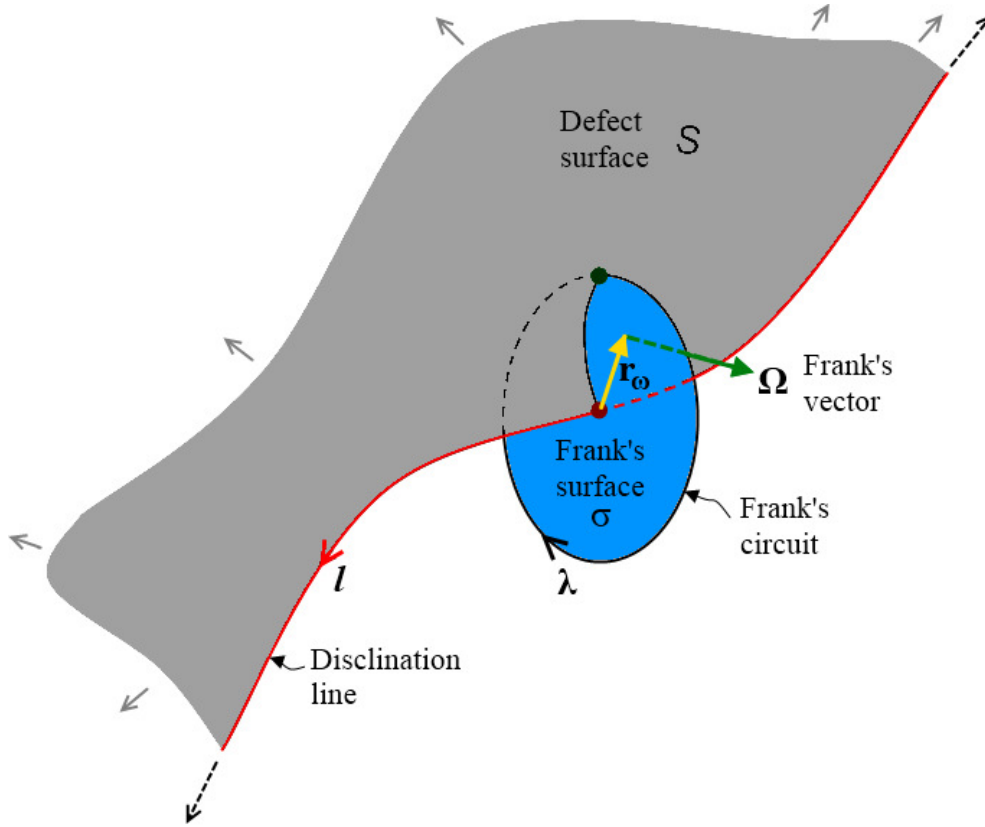
Figure 2.11: A curved disclination line l with a Frank's vector Ω in an infinite continuous medium, bounded by an arbitrarily shaped defect surface S and encircled by an arbitrarily shaped Frank's circuit λ, traverses the Frank's surface σ at an arbitrary angle. The grey and black dotted arrows indicate the possible extensions of S and l, respectively. r_ω is the vector denoting the position of the rotation axis. The line direction and the sense of λ make the crossings between l and σ negative according to the right-hand rule.

components on the $z = 0$ plane in the presence of an infinitely long straight wedge $\vec{\Omega} = (001)$ and twist $\vec{\Omega} = (100)$ disclination line respectively, lying along the z-axis in an infinite continuous medium (Poisson's ratio $\nu = 0.34$). The strength of the disclination is taken as $|\vec{\Omega}| = 3°$ which is in the same order as those obtained for disclination dipoles from experimental measurements [333].

As shown in figure 2.12(b) for the case of a wedge disclination, the jump in displacements across the surface cut increases along the direction perpendicular to the disclination line and the normal to the surface cut. This result is in accordance with

(a) u_x^e (m)

(b) u_y^e (m)
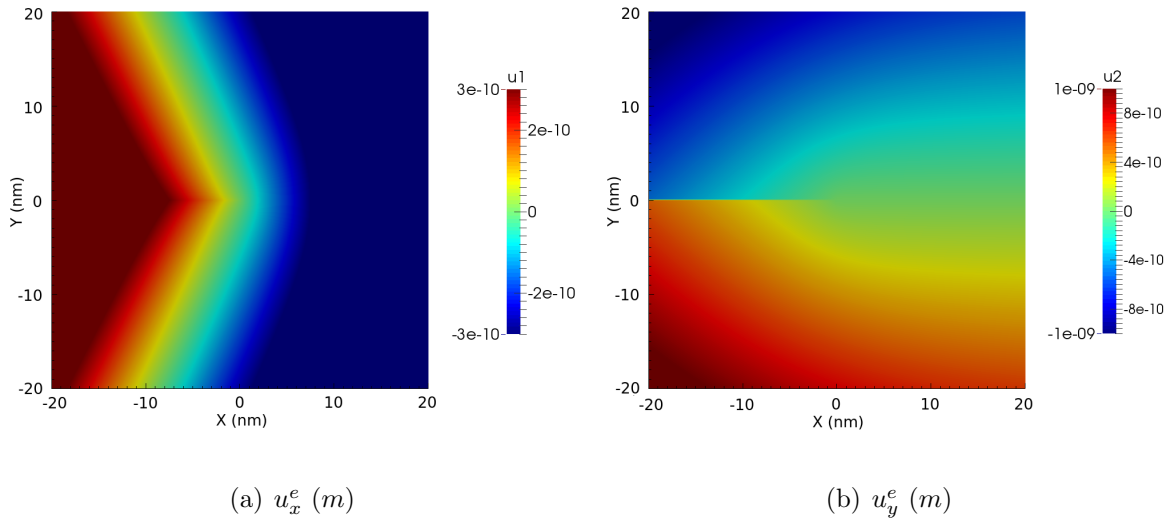
Figure 2.12: Non-zero components of elastic displacement fields (in m) (a) u_x^e and (b) u_y^e at $z = 0$ of an infinitely long straight single wedge disclination along the z-axis in an infinite continuous medium, having Poisson's ratio $\nu = 0.34$, with Frank's vector magnitude $|\vec{\Omega}| = 3^\circ$ along the direction **(001)**.

(a) u_z^e (m)
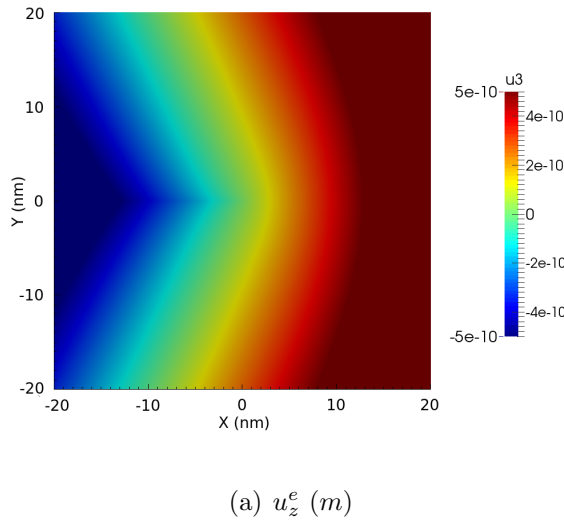
Figure 2.13: Non-zero component of displacement fields (in m) u_z at $z = 0$ an infinitely long straight single twist disclination along the z-axis in an infinite continuous medium, having Poisson's ratio $\nu = 0.34$, with Frank's vector magnitude $|\vec{\Omega}| = 3^\circ$ along the direction **(100)**.

35

the discussion earlier in this chapter on the figure 2.2. Note from equations (2.23) that the displacement for a wedge disclination is independent of the direction z. However, for twist disclinations there is a z component that makes the displacements vary along the direction of the disclination line, also in accordance with the discussion earlier in this section.

The elastic distortion U_{ij}^e has an antisymmetric component related to the elastic rotation field as $U_{[ij]}^e = -e_{ijk}\omega_k^e$, where $[\ ]$ on the indices represents the anti-symmetric component. The elastic distortion is therefore dependent on the surface cut orientation and is not compatible. This is reflected from the presence of ϕ, H and δ functions in the following expression of the elastic distortion field,

$$U_{xx}^e = -\frac{\Omega_x z}{4\pi(1-\nu)}\left[(1-2\nu)\frac{x}{\rho^2} - 2\frac{xy^2}{\rho^4}\right] - \frac{\Omega_y z}{4\pi(1-\nu)}\left[(1-2\nu)\frac{y}{\rho^2} + 2\frac{x^2 y}{\rho^4}\right]$$
$$+ \frac{\Omega_z}{4\pi(1-\nu)}\left[(1-2\nu)\ln\rho + \frac{y^2}{\rho^2}\right] \tag{2.24}$$

$$U_{xy}^e = -\frac{\Omega_x z}{4\pi(1-\nu)}\left[(1-2\nu)\frac{y}{\rho^2} + 2\frac{x^2 y}{\rho^4}\right] + \frac{\Omega_y z}{4\pi(1-\nu)}\left[(3-2\nu)\frac{x}{\rho^2} - 2\frac{xy^2}{\rho^4}\right]$$
$$+ \Omega_y z H(-x)\delta(y) - \Omega_z\left[\frac{\phi}{2\pi} + \frac{xy}{4\pi(1-\nu)\rho^2}\right] \tag{2.24a}$$

$$U_{xz}^e = -\frac{\Omega_x}{4\pi(1-\nu)}\left[(1-2\nu)\ln\rho + \frac{y^2}{\rho^2}\right] + \Omega_y\left[\frac{\phi}{2\pi} + \frac{xy}{4\pi(1-\nu)\rho^2}\right] \tag{2.24b}$$

$$U_{yx}^e = \frac{\Omega_x z}{4\pi(1-\nu)}\left[(3-2\nu)\frac{y}{\rho^2} - 2\frac{x^2 y}{\rho^4}\right] - \frac{\Omega_y z}{4\pi(1-\nu)}\left[(1-2\nu)\frac{x}{\rho^2} + 2\frac{xy^2}{\rho^4}\right]$$
$$+ \Omega_z\left[\frac{\phi}{2\pi} - \frac{xy}{4\pi(1-\nu)\rho^2}\right] \tag{2.24c}$$

$$U_{yy}^e = -\frac{\Omega_x z}{4\pi(1-\nu)}\left[(1-2\nu)\frac{x}{\rho^2} + 2\frac{xy^2}{\rho^4}\right] - \Omega_x z H(-x)\delta(y)$$
$$- \frac{\Omega_y z}{4\pi(1-\nu)}\left[(1-2\nu)\frac{y}{\rho^2} - 2\frac{x^2 y}{\rho^4}\right]$$
$$+ \frac{\Omega_z}{4\pi(1-\nu)}\left[(1-2\nu)\ln\rho + \frac{x^2}{\rho^2}\right] + \Omega_z x H(-x)\delta(y) \tag{2.24d}$$

$$U_{yz}^e = \Omega_x\left[\frac{\phi}{2\pi} - \frac{xy}{4\pi(1-\nu)\rho^2}\right] - \frac{\Omega_y}{4\pi(1-\nu)}\left[(1-2\nu)\ln\rho + \frac{x^2}{\rho^2}\right] \tag{2.24e}$$

$$U_{zx}^e = -\frac{\Omega_x}{4\pi(1-\nu)}\left[(1-2\nu)\ln\rho + \frac{y^2}{\rho^2}\right] - \Omega_y\left[\frac{\phi}{2\pi} - \frac{xy}{4\pi(1-\nu)\rho^2}\right] \tag{2.24f}$$

$$U_{zy}^e = \Omega_x\left[\frac{\phi}{2\pi} + \frac{xy}{4\pi(1-\nu)\rho^2}\right] - \frac{\Omega_y}{4\pi(1-\nu)}\left[(1-2\nu)\ln\rho + \frac{x^2}{\rho^2}\right]$$

$$-\Omega_y x H(-x)\delta(y) \tag{2.24g}$$

$$U_{zz}^e = 0 \tag{2.24h}$$

Eliminating the discontinuous anti-symmetric component of the elastic distortion gives a smooth compatible elastic strain field,

$$\epsilon_{xx}^{e\parallel} = -\frac{\Omega_x z}{4\pi(1-\nu)}\left[(1-2\nu)\frac{x}{\rho^2} - 2\frac{xy^2}{\rho^4}\right] - \frac{\Omega_y z}{4\pi(1-\nu)}\left[(1-2\nu)\frac{y}{\rho^2} + 2\frac{x^2 y}{\rho^4}\right]$$
$$+ \frac{\Omega_z}{4\pi(1-\nu)}\left[(1-2\nu)\ln\rho + \frac{y^2}{\rho^2}\right] \tag{2.25}$$

$$\epsilon_{yy}^{e\parallel} = -\frac{\Omega_x z}{4\pi(1-\nu)}\left[(1-2\nu)\frac{x}{\rho^2} + 2\frac{xy^2}{\rho^4}\right] - \Omega_x z H(-x)\delta(y)$$
$$- \frac{\Omega_y z}{4\pi(1-\nu)}\left[(1-2\nu)\frac{y}{\rho^2} - 2\frac{x^2 y}{\rho^4}\right]$$
$$+ \frac{\Omega_z}{4\pi(1-\nu)}\left[(1-2\nu)\ln\rho + \frac{x^2}{\rho^2}\right] + \Omega_z x H(-x)\delta(y) \tag{2.25a}$$

$$\epsilon_{zz}^{e\parallel} = 0 \tag{2.25b}$$

$$\epsilon_{xy}^{e\parallel} = \frac{\Omega_x z}{4\pi(1-\nu)}\left[\frac{y}{\rho^2} - 2\frac{x^2 y}{\rho^4}\right] + \frac{\Omega_y z}{4\pi(1-\nu)}\left[\frac{x}{\rho^2} - 2\frac{xy^2}{\rho^4}\right] - \frac{\Omega_z xy}{4\pi(1-\nu)\rho^2} \tag{2.25c}$$

$$\epsilon_{xz}^{e\parallel} = -\frac{\Omega_x}{4\pi(1-\nu)}\left[(1-2\nu)\ln\rho + \frac{y^2}{\rho^2}\right] + \frac{\Omega_y xy}{4\pi(1-\nu)\rho^2} \tag{2.25d}$$

$$\epsilon_{yz}^{e\parallel} = \frac{\Omega_x xy}{4\pi(1-\nu)\rho^2} - \frac{\Omega_y}{4\pi(1-\nu)}\left[(1-2\nu)\ln\rho + \frac{x^2}{\rho^2}\right] \tag{2.25e}$$

Similar to elastic displacements for twist disclinations, the elastic strain evolves as a function of the position along the disclination line. Equations (2.25) confirm that the strains do not contain ϕ, H or δ functions and are therefore well defined everywhere in the domain except the dislocation line where they are singular. However, these expressions also reveal a logarithmic dependence of elastic strain on the distance from the defect line highlighting their diverging nature in the presence of a single disclination. This is illustrated in figures 2.14 and 2.15 for the same wedge and twist disclination cases used to demonstrate the displacements and curvatures.

The Cauchy stresses induced in the presence of a single disclination are obtained by substituting equations (2.25) and (2.12) in the Hooke's law (2.7),

$$\sigma_{xx}^{e\parallel} = -\frac{Gb_x}{2\pi(1-\nu)}\left[\frac{y}{\rho^2} + 2\frac{x^2 y}{\rho^4}\right] + \frac{Gb_y}{2\pi(1-\nu)}\left[\frac{x}{\rho^2} - 2\frac{xy^2}{\rho^4}\right] \tag{2.26}$$
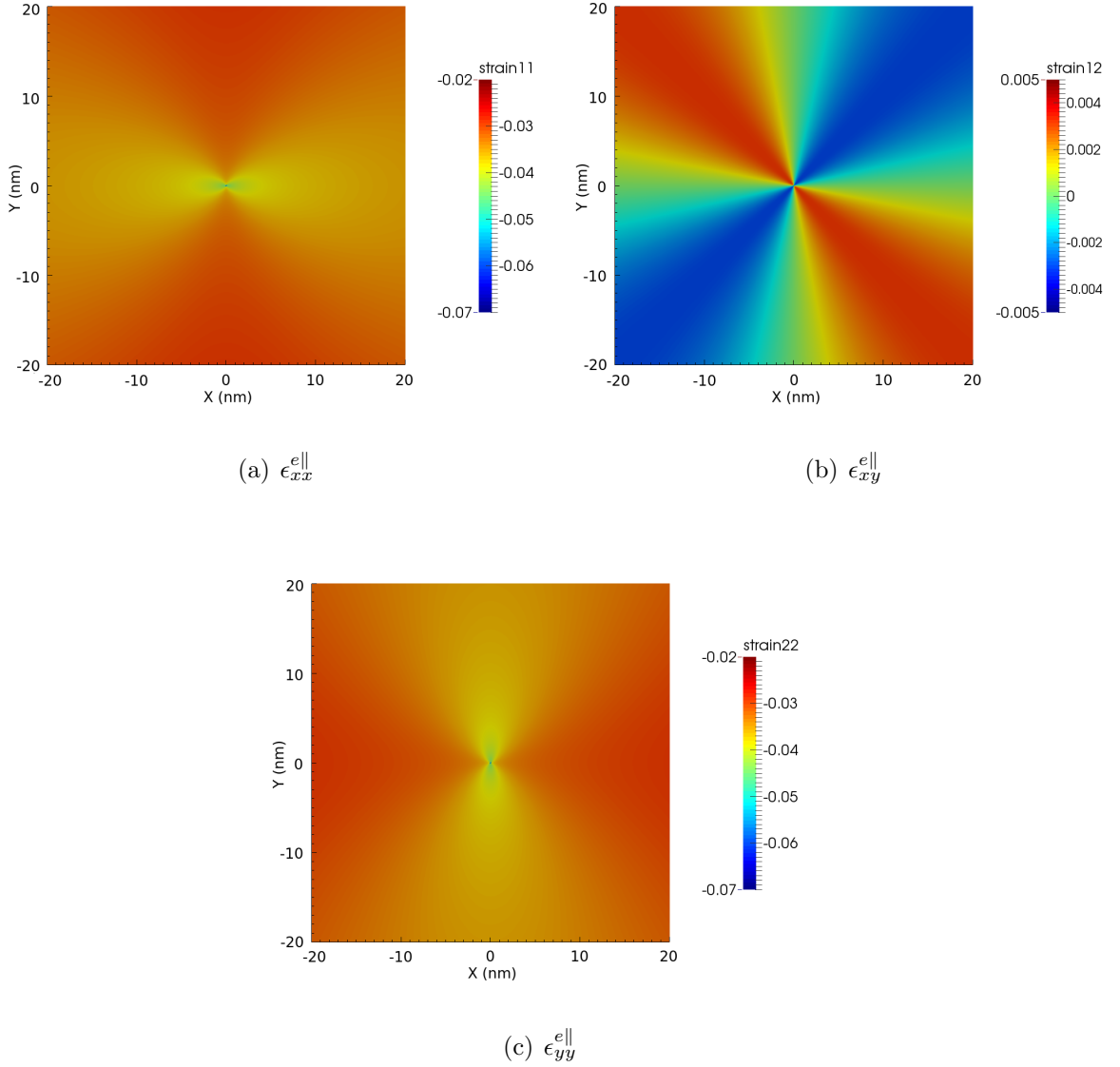
(a) $\epsilon_{xx}^{e\parallel}$

(b) $\epsilon_{xy}^{e\parallel}$

(c) $\epsilon_{yy}^{e\parallel}$

Figure 2.14: Non-zero components of elastic strain fields (a) $\epsilon_{xx}^{e\parallel}$, (b) $\epsilon_{xy}^{e\parallel}$ and (c) $\epsilon_{yy}^{e\parallel}$ of an infinitely long straight single wedge disclination along the z-axis in an infinite continuous medium, having Poisson's ratio $\nu = 0.34$, with Frank's vector magnitude $|\vec{\Omega}| = 3^\circ$ along the direction **(001)**.

$$\sigma_{yy}^{e\parallel} = -\frac{Gb_x}{2\pi(1-\nu)}\left[\frac{y}{\rho^2} - 2\frac{x^2y}{\rho^4}\right] + \frac{Gb_y}{2\pi(1-\nu)}\left[\frac{x}{\rho^2} + 2\frac{xy^2}{\rho^4}\right] \qquad (2.26a)$$

$$\sigma_{zz}^{e\parallel} = -\frac{G\nu}{2\pi(1-\nu)}\left[2\frac{b_xy}{\rho^2} - 2\frac{b_yx}{\rho^2}\right] \qquad (2.26b)$$

$$\sigma_{xy}^{e\parallel} = \sigma_{yx}^{e\parallel} = \frac{Gb_x}{2\pi(1-\nu)}\left[\frac{x}{\rho^2} - 2\frac{xy^2}{\rho^4}\right] - \frac{Gb_y}{2\pi(1-\nu)}\left[\frac{y}{\rho^2} - 2\frac{x^2y}{\rho^4}\right] \qquad (2.26c)$$

(a) $\epsilon_{xz}^{e\parallel}$ (b) $\epsilon_{yz}^{e\parallel}$
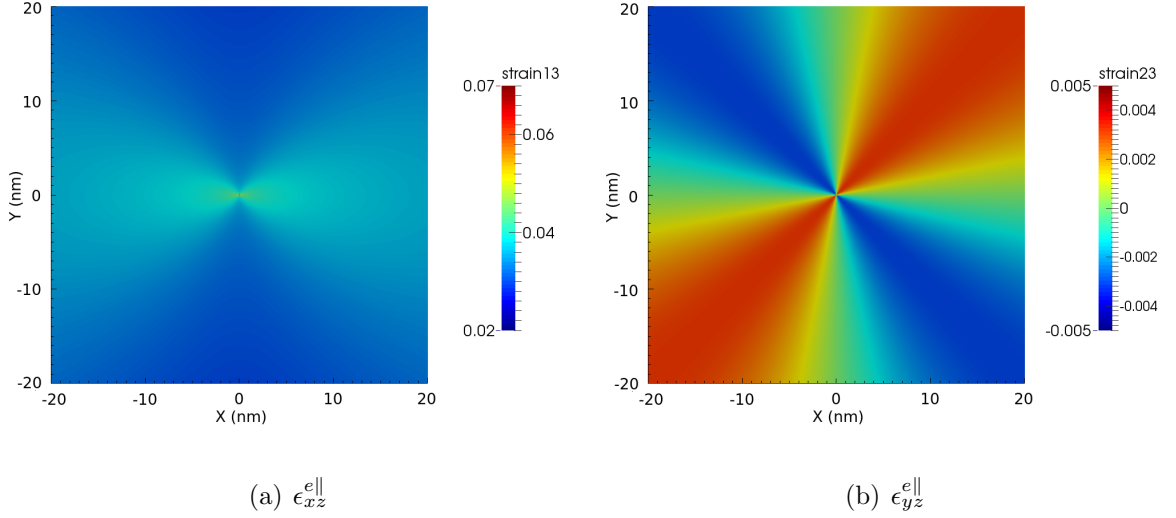
Figure 2.15: Non-zero components of elastic strain fields (a) $\epsilon_{xz}^{e\parallel}$ and (b) $\epsilon_{yz}^{e\parallel}$ of an infinitely long straight single twist disclination along the z-axis in an infinite continuous medium, having Poisson's ratio $\nu = 0.34$, with Frank's vector magnitude $|\vec{\Omega}| = 3^\circ$ along the direction **(100)**.

$$\sigma_{yz}^{e\parallel} = \sigma_{zy}^{e\parallel} = \frac{Gb_z x}{2\pi\rho^2} \tag{2.26d}$$

$$\sigma_{xz}^{e\parallel} = \sigma_{zx}^{e\parallel} = -\frac{Gb_z y}{2\pi\rho^2} \tag{2.26e}$$

Next, the discontinuous elastic rotation fields are given as,

$$\omega_x^e = \frac{\Omega_x \phi}{2\pi} - \frac{1}{2}\Omega_y x H(-x)\delta(y) \tag{2.27}$$

$$\omega_y^e = \frac{\Omega_y \phi}{2\pi} \tag{2.27a}$$

$$\omega_z^e = -\frac{\Omega_x yz}{2\pi\rho^2} - \frac{\Omega_y xz}{2\pi\rho^2} - \frac{1}{2}\Omega_y H(-x)\delta(y) + \frac{\Omega_z \phi}{2\pi} \tag{2.27b}$$

where ϕ is defined the same way as shown in figure 2.4. Notice that, contrary to the case of a dislocation, these elastic rotations are no longer compatible. A closer look at equations (2.27) reveals that the rotation field of a twist disclination depends on the position in the direction of the disclination line. This implies that the rotation jump across the defect surface is evolving as a function of the position along the twist disclination line. This is counter-intuitive because one would expect the rotational

39

jump to be constant along the disclination line by deriving analogy from the case of a dislocation having a constant displacement jump.

Taking the gradient of the elastic rotations in equation (2.27) gives the compatible elastic curvature field as follows,

$$\kappa_{xx}^{e\parallel} = -\frac{\Omega_x y}{2\pi\rho^2} \tag{2.28}$$

$$\kappa_{xy}^{e\parallel} = -\frac{\Omega_x x}{2\pi\rho^2} \tag{2.28a}$$

$$\kappa_{xz}^{e\parallel} = 0 \tag{2.28b}$$

$$\kappa_{yx}^{e\parallel} = -\frac{\Omega_y y}{2\pi\rho^2} \tag{2.28c}$$

$$\kappa_{yy}^{e\parallel} = \frac{\Omega_y x}{2\pi\rho^2} \tag{2.28d}$$

$$\kappa_{yz}^{e\parallel} = 0 \tag{2.28e}$$

$$\kappa_{zx}^{e\parallel} = -\frac{\Omega_x xyz}{\pi\rho^4} - \frac{\Omega_y z}{2\pi}\left[\frac{1}{\rho^2} - 2\frac{x^2}{\rho^4} + \pi\delta(\rho)\right] - \frac{\Omega_z y}{2\pi\rho^2} \tag{2.28f}$$

$$\kappa_{zy}^{e\parallel} = \frac{\Omega_x z}{2\pi}\left[\frac{1}{\rho^2} - 2\frac{y^2}{\rho^4} + \pi\delta(\rho)\right] + \frac{\Omega_y xyz}{\pi\rho^4} + \frac{\Omega_z x}{2\pi\rho^2} \tag{2.28g}$$

$$\kappa_{zz}^{e\parallel} = \frac{\Omega_x y}{2\pi\rho^2} - \frac{\Omega_y x}{2\pi\rho^2} \tag{2.28h}$$

Figures 2.16 and 2.17 show the non-vanishing components of the elastic curvature fields for a pure wedge and a pure twist disclination, respectively, on the $z = 0$ plane. The disclinations have a strength of $|\vec{\Omega}| = 3^\circ$ and the medium has a Poisson's ratio of $\nu = 0.34$.

2.2 Discussion

2.2.1 Geometric equivalence between disclinations and dislocations

Geometric equivalence between disclinations and dislocations was first shown in the work of Kröner [215]. Following an argument made in the work of Peach and Koehler [313], Kröner derived the displacement field of a dislocation using a procedure analogous to the line integral approach used to derive the Biot-Savart law in electromagnetism. The resulting strain is a function of the difference between rotational

(a) $\kappa_{zx}^{e\|}$ (m^{-1}) (b) $\kappa_{zy}^{e\|}$ (m^{-1})
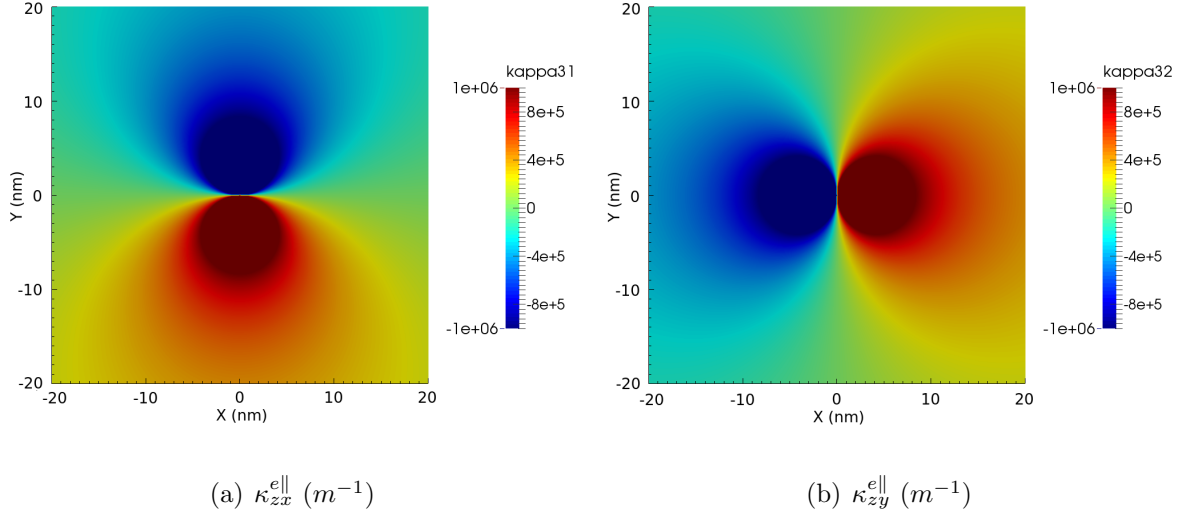
Figure 2.16: Non-zero components of compatible elastic curvature fields (in m^{-1}) (a) $\kappa_{zx}^{e\|}$ and (b) $\kappa_{zy}^{e\|}$ at $z = 0$ of an infinitely long straight single wedge disclination along the z-axis in an infinite continuous medium (Poisson's ratio of $\nu = 0.34$) with Frank's vector magnitude $|\vec{\Omega}| = 3°$ along the direction **(001)**.

components of two defect lines separated by a finite distance. This rotational component is identified as the disclination dipole and the distance separating them is the disclination dipole arm length. An example is shown in figure 2.18 where a wedge disclination dipole of strength $|\vec{\Omega}| = \pm\omega$ having a very small dipole arm $\vec{t}$ is represented using an equivalent dislocation with Burgers vector,

$$\vec{b} = \vec{t} \times \vec{\Omega} \qquad (2.29)$$

deWit [97] showed that both the compatible elastic strain and the compatible elastic curvature fields induced in the presence of a disclination dipole and its equivalent dislocation are the same. For the sake of illustration consider the following example of a wedge disclination dipole of strength $|\vec{\Omega}| = \pm 36.87°$ and arm length $|\vec{t}| = 0.28202$ nm. Figures 2.19 and 2.20 illustrate the ϵ_{xx} component of elastic strain and κ_{zx} component of the curvature fields, respectively, of the wedge disclination dipole and its equivalent edge dislocation, computed using equations (2.17), (2.20),

41

(a) $\kappa_{xx}^{e\parallel}$ (m^{-1})

(b) $\kappa_{xy}^{e\parallel}$ (m^{-1})

(c) $\kappa_{zz}^{e\parallel}$ (m^{-1})
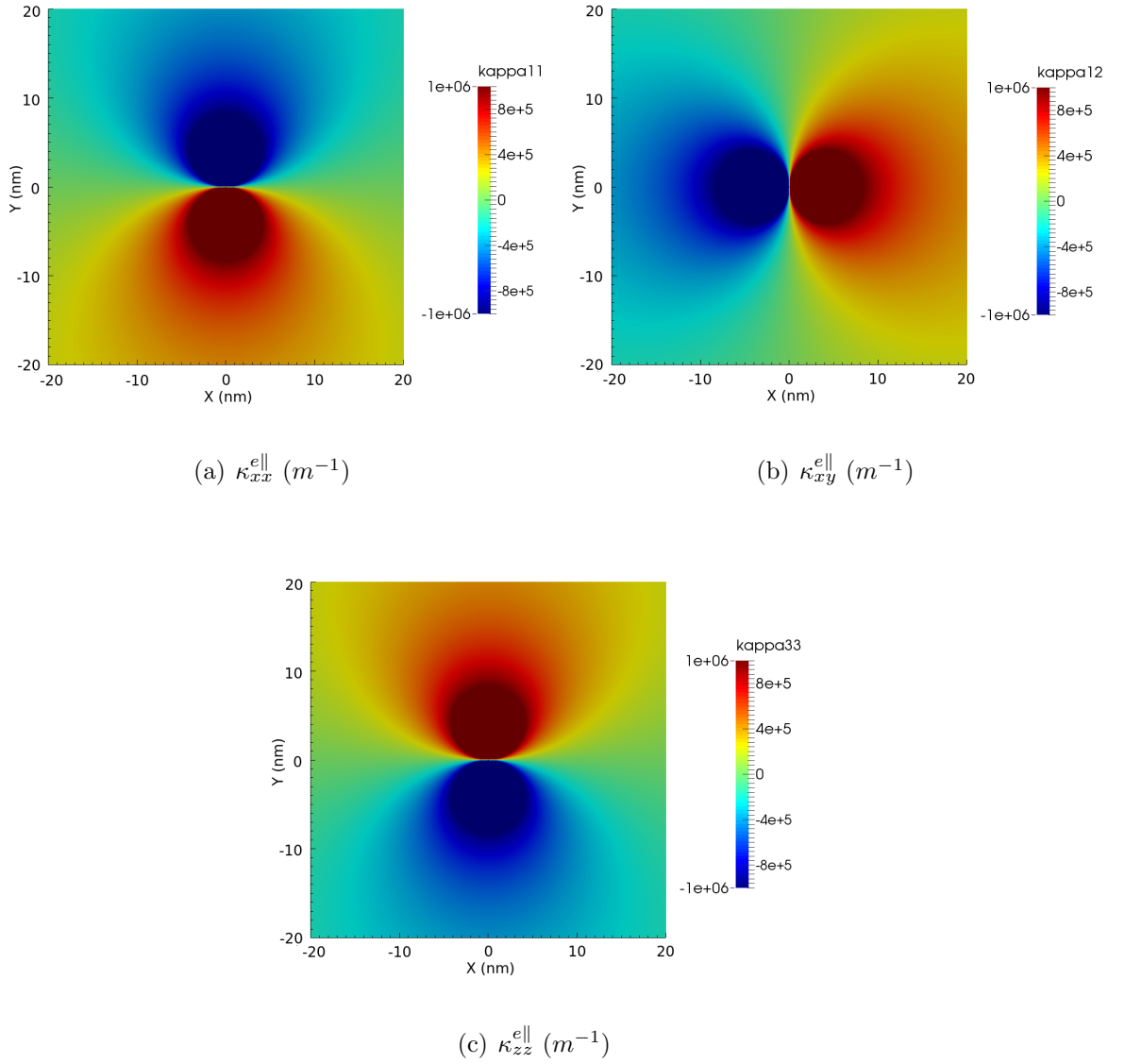
Figure 2.17: Non-zero component of compatible elastic curvature fields (in m^{-1}) (a) $\kappa_{xx}^{e\parallel}$, (b) $\kappa_{xy}^{e\parallel}$, and (c) $\kappa_{zz}^{e\parallel}$ at $z = 0$ an infinitely long straight single twist disclination along the z-axis in an infinite Cu matrix (Poisson's ratio $\nu = 0.34$) with Frank's vector magnitude $|\vec{\Omega}| = 3^{\circ}$ along the direction **(100)**.

(2.28) and (2.25); the equivalent Burgers vector thus obtained has a magnitude of $|\vec{b}| = 0.18148$ nm. The two disclinations are placed equidistantly from the origin and are aligned along the y-axis such that the equivalent dislocation lies at the origin and its Burgers vector is along the positive x-axis.
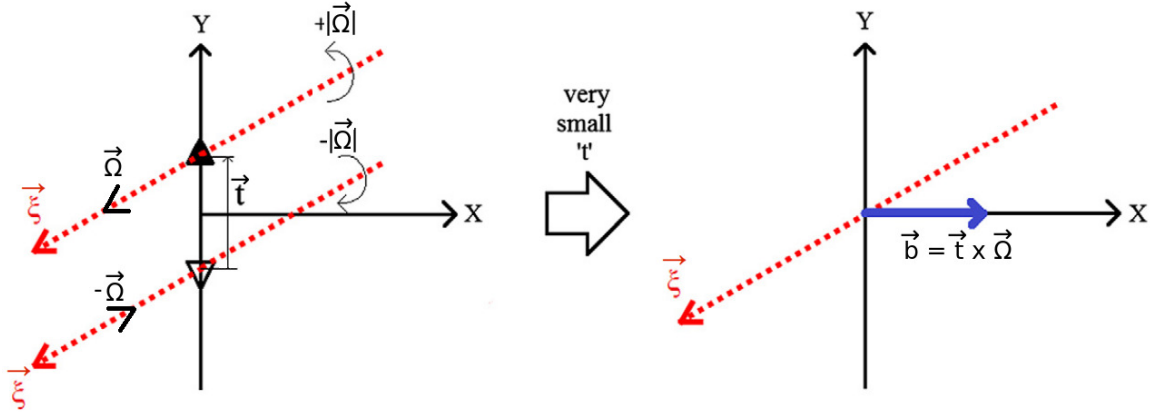
Figure 2.18: A wedge disclination dipole with line direction $\vec{\xi}$, arm strength $|\vec{\Omega}|$ and arm length $|\vec{t}|$ and its equivalent dislocation with line direction $\vec{\xi}$ and Burgers vector $\vec{b}$

(a) $\epsilon_{xx}^{e\|}$ (disclination dipole)   (b) $\epsilon_{xx}^{e\|}$ (dislocation)
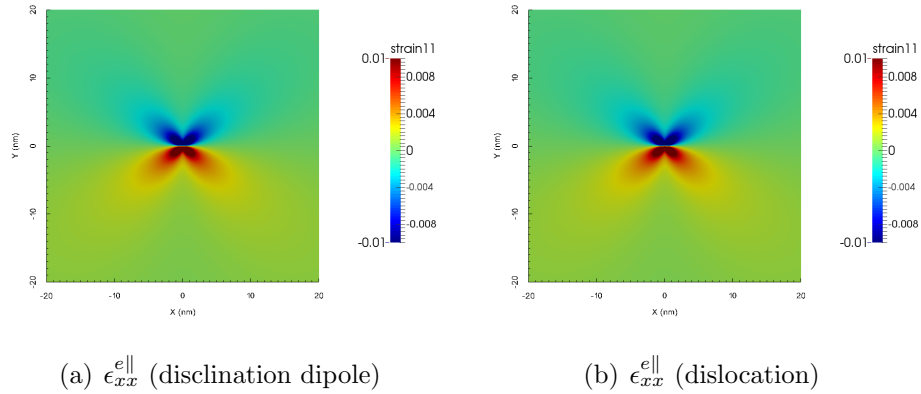
Figure 2.19: Comparison of compatible elastic strain fields $\epsilon_{xx}^{e\|}$ for (a) a wedge disclination dipole of strength $|\vec{\Omega}| = 36.87°$ and arm length $|\vec{t}| = 0.28202$ nm and (b) for an edge dislocation of equivalent Burgers vector magnitude $|\vec{b}| = 0.18148$ nm.

Figures 2.19 and 2.20 show the out of core elastic strain and curvature contributions for the wedge disclination dipole and its equivalent edge dislocation. Their closeness is asserted by the very low (less than 0.0001 %) averaged relative error. Note that the elastic strain fields, which are diverging for the case of single disclinations, are diminishing with distance for the case of a disclination dipole. This is due to the partial screening of the elastic strain fields that leads to their decay (at a rate faster

(a) $\kappa_{zx}^{e\parallel}$ (disclination dipole) (b) $\kappa_{zx}^{e\parallel}$ (dislocation)
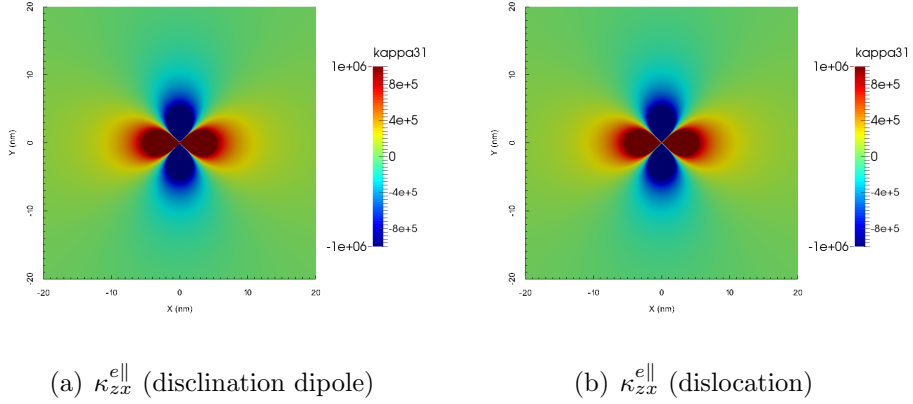
Figure 2.20: Comparison of compatible elastic curvature fields $\kappa_{zx}^{e\parallel}$ and $\kappa_{zy}^{e\parallel}$ for (a), (c) a wedge disclination dipole of strength $|\vec{\Omega}| = 36.87°$ and arm length $|\vec{t}| = 0.28202$ nm and (b), (d) for an edge dislocation of equivalent Burgers vector magnitude $|\vec{b}| = 0.18148$ nm.

than $1/r$) at large distances.

Romanov and co-workers [339, 333] elaborated the discussion on the dislocation-disclination equivalence by conceiving several types of disclination dipoles based on three degrees of freedom (DOF) in the form of (i) position of the rotation axis, (ii) position of the disclination line, and (iii) the magnitude and direction of Frank's vector. One example is a twist disclination dipole that can be formed by a single disclination line and two rotation axes as shown in figure 2.21(a). In such a configuration, the disclination lines coincide and the rotation axes with Frank's vector magnitudes $|\vec{\Omega}| = -\omega$ and $|\vec{\Omega}| = \omega$ are separated by a distance t such that it forms an equivalent edge dislocation with Burgers vector as shown in equation (2.29).

If the disclination dipole arm length is much larger than the interatomic spacing then the Burgers vector may have a magnitude quite large for a single dislocation to exist in a stable form in a crystal lattice. In such a case, the dipole can be represented by an equivalent dislocation wall. This was remarked by Li [250, 251] who proved that the strain and stress fields of a wedge disclination dipole with a large dipole arm length

44

is equal to that of an equivalent edge dislocation wall. The wall consists of dislocations having equal Burgers vectors and the summation of these Burgers vectors gives the equivalent Burgers vector obtained from equation (2.29). Such an equivalent edge dislocation wall is shown in figure 2.21(b). Another disclination dipole configuration is a two-line one-rotation-axis dipole as shown in figure 2.21(c). It demonstrates the properties of a dislocation quadrupole [333].
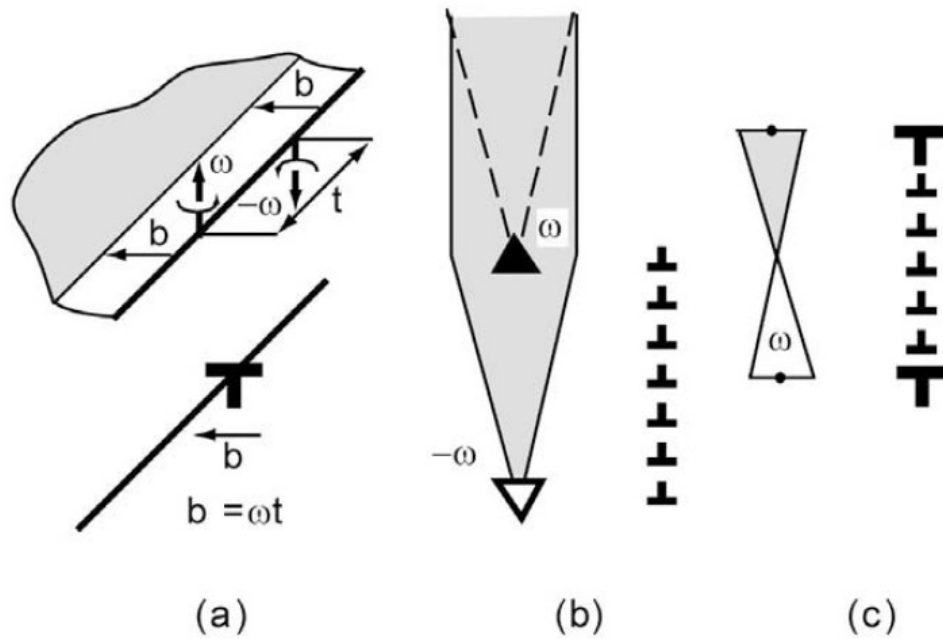
Figure 2.21: Disclination dipoles and their dislocation analogues (adapted from Romanov and Kolesnikova [333]), (a) single-line, two-rotation-axes dipole of twist disclinations, (b) two-lines, two-axes wedge disclination dipole and (c) one-axis wedge disclination dipole

A disclination can also be represented using a superposition of dislocations, and vice versa. This can be most simply illustrated for a wedge disclination. Reconsider the case of a negative wedge disclination shown in figure 2.2(a). This disclination has one rotation axis that is aligned along the disclination line. Such a disclination can be formed at the tip of an additional wedge of a material inserted into a continuous domain (see figure 2.22(b)). This wedge can be imagined in the form of a set of half-planes of atoms inserted into the material and arranged as shown in figure 2.22(c).

These half-planes induce a semi-infinite wall of dislocations which terminates at the tip of the wedge (see figure 2.22(d)) *i.e.* at the original disclination line.
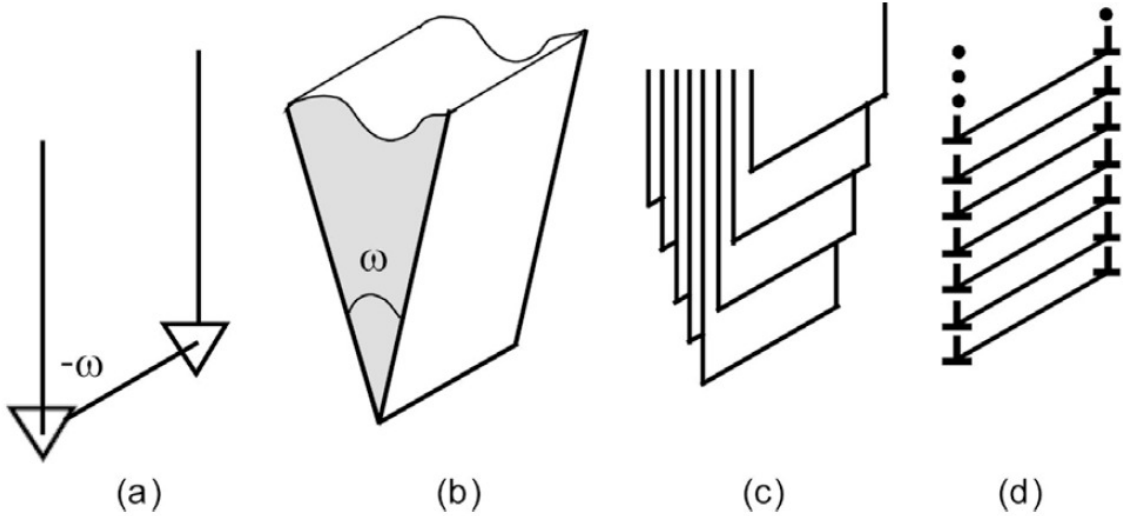
Figure 2.22: Relation between wedge disclinations and terminated edge dislocation walls: (a) negative wedge disclination with strength $-\omega$, (b) wedge of angle ω which has to be inserted to create the disclination, (c) a set of half-planes representing the wedge, and (d) terminated wall of equidistant edge dislocations (adopted from Romanov and Kolesnikova [333])

Romanov and coworkers [339, 333, 316] also discuss disclination loop configurations. A twist disclination loop, which is formed from a closed disclination line encircling a planar surface with the Frank's vector perpendicular to this surface, can be represented using a set of screw dislocations as shown in figure 2.23. A disclination loop can also be formed when the Frank's vector is contained in the planar surface encircled by the disclination line. In the literature, it is usually referred to as a wedge disclination loop [333]. Although, strictly speaking, such a configuration has a mixed wedge/twist character. A square type of a wedge disclination loop [316] is shown in figure 2.24. The rectangular shape is interesting because such a disclination loop can be easily transformed into other disclination defects such as an angular disclination, a disclination dipole, a U-shaped defect or a linear disclination.

In general, the compatible elastic strain and curvature fields are the same for all the
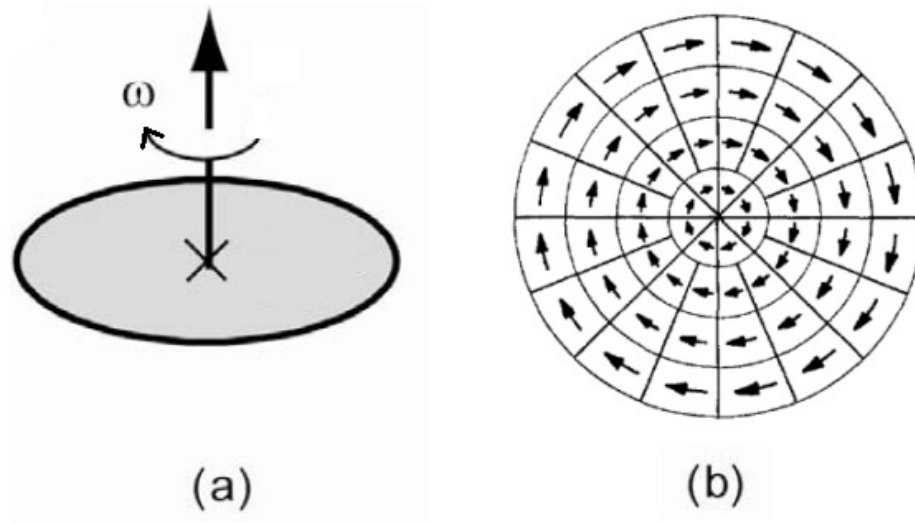
Figure 2.23: (a) A twist disclination loop and (b) an equivalent representation using screw discloations (adapted from Li [251])
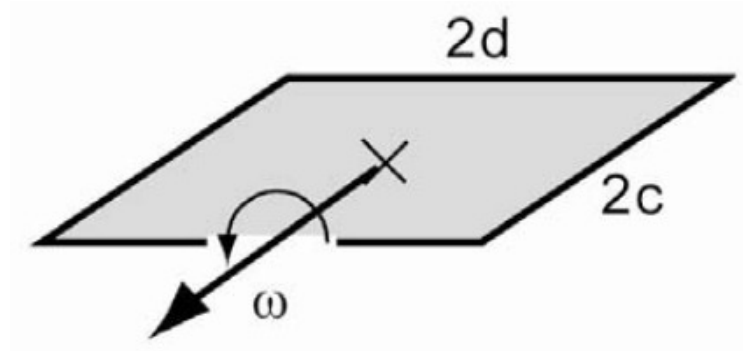
Figure 2.24: Rectangular pure wedge disclination loop (adapted from Pertsev *et al.* [316])

aforementioned disclination dipole/equivalent dislocation configurations. However, these are defined outside the core of the defects (recall the closed form solutions of deWit [97]), the same may not be true within the defect cores. Closed form expressions for elastic fields within the defect core exist but only in the case of discrete dislocations [314]. To the author's knowledge no such expressions for discrete disclinations are available.

2.2.2 Connecting disclinations to crystallography: State of the art

Volterra's treatise [436] gave a mathematical understanding on the geometry of line defects and provided the basis to connect them to crystallography. Such a connection was first established for dislocation in the pioneering works of Taylor and Elam [398, 399], Schmid [354], Orowan [308], Polanyi [318], Taylor [400, 397], Burgers [54, 55], Read [324], among others. Orowan [308], Polanyi [318], Taylor [400] and Burgers [54] considered the dislocation as a discrete line singularity in a crystal lattice. They proved that for dislocations to exist in a material, the Burgers vector must be a lattice vector corresponding to the translational symmetry of the material. The presence of a dislocation results in a discontinuity (jump) in the lattice (elastic) displacement field. This discontinuity has the magnitude and direction of the Burgers vector. In order to maintain the continuity of the material, lattice strains are generated. These in turn give rise to internal stresses in order to satisfy equilibrium conditions. These pioneering works led to the development of the theory of dislocations [93, 95, 97, 306, 216, 38, 40, 39, 217, 457] which along with early experimental observations of dislocation activity during plastic deformation [133, 432, 129, 85, 184, 270, 185, 312, 172, 435, 191, 40, 143] generated significant interest in understanding the plasticity of materials from a dislocation perspective.

The present work, focuses on the connection of disclinations to crystallography. For a detailed understanding on the theory of crystal dislocations and plasticity due to dislocation motion, the reader is referred to the works of Hull and Bacon [190], Nabarro [294], Hirth and Lothe [187], to name a few.

Thus far, disclinations in crystalline solids have received relatively less attention in comparison to dislocations. Following the treatise of Volterra [436], the first notable mention of disclinations was in association with liquid crystals [132, 332, 294]. Frank [132] conceived a disclination to be an isolated line defect in an otherwise perfect crystal. Nabarro [294] identified these disclination lines as either "screw-" type with

Frank's vector parallel to the disclination line or "edge-" type with Frank's vector perpendicular to the disclination line; these later came to be known as wedge and twist disclinations, respectively. Nabarro remarked that the rigid-body displacement forming a general line crystal defect may be resolved uniquely into a translational part $\vec{b}$ and a rotational part $\vec{\Omega}$ (recall the discussion on displacement jumps at the beginning of this section). The passage from continuum to a crystalline medium imposes restrictions on the values of $\vec{b}$ and $\vec{\Omega}$. If a line defect were to exist in a crystalline material, then the surface cut characterizing this defect can attain only those orientations in the crystal that do not change its essential properties, *i.e.* $\vec{b}$ and $\vec{\Omega}$. Focusing on the Frank's vector, it has to be in the order of $|\vec{\Omega}| = 2p\pi, p = 0, \pm 1, \pm 2 \ldots$, for a disclination to exist in a crystal possessing rotational axes corresponding to 1-fold rotational symmetry. Lattices of higher symmetry have rotation axes of higher order and correspondingly smaller values of $|\vec{\Omega}|$. In general an s-fold rotation axis leads to the permissible values of $|\vec{\Omega}| = \frac{2p\pi}{s}$ ($p = 0, \pm 1, \pm 2 \ldots$). These type of disclinations which are a function of the lattice rotational symmetry are known as full disclinations. Figure 2.25 shows full wedge disclinations with strengths $|\vec{\Omega}| = \pm 2\pi, \pm \pi, \pm \pi/2$ and $\pm \pi/3$. Such type of disclinations can exist only if the crystal has 1-fold, 2-fold, 4-fold or 6-fold rotational symmetry. For example, it is mathematically possible for a lattice with cubic symmetry to have disclinations of strengths $|\vec{\Omega}| = \pm 2\pi, \pm \pi, \pm 2\pi/3$ and $\pm \pi/2$ corresponding to its 1-fold, 2-fold, 3-fold and 4-fold rotational symmetries, respectively.

A closer examination of figure 2.25 (where the black lines are used to denote lattice planes) indicates that the lattice strains are not reducing to zero at large distances. In fact, the formulae in equation (2.25) indicate that they increase logarithmically as can be visualized from figure 2.14. Nabarro explained this by performing a physical experiment using rubber models of crystals. He remarked that attempts to make rubber models of crystals with full disclinations indicated that such configurations are
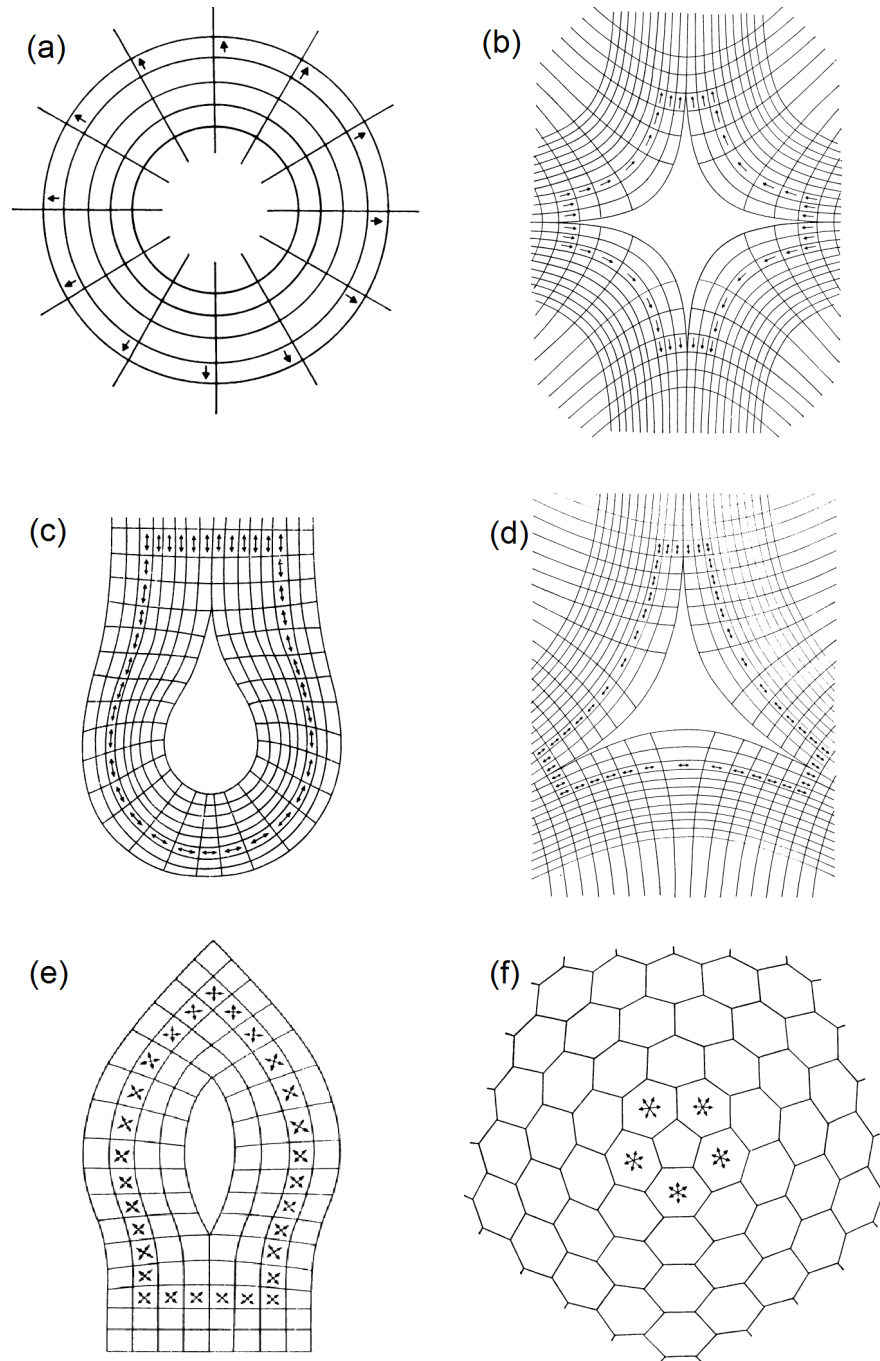
Figure 2.25: Nabarro's [294] representation of crystalline disclinations associated with s-fold crystal symmetry axis: (a),(b) Positive and negative wedge disclinations with 1-fold symmetry ($|\vec{\Omega}| = \pm 2\pi$), (c),(d) positive and negative wedge disclinations with 2-fold symmetry ($|\vec{\Omega}| = \pm\pi$), (e) positive wedge disclination with 4-fold symmetry ($|\vec{\Omega}| = \pm\pi/2$), and (f) positive wedge disclination with 6-fold symmetry ($|\vec{\Omega}| = \pm\pi/3$). Symmetry axes indicated by single or double arrow heads.

not likely to occur in crystalline solids. However, models made using a pile of cards (which are allowed to slide over one another) revealed that disclinations could exist in materials where the lattice planes were not restricted to maintain lateral registry. For example, consider the negative wedge disclination with the 2-fold symmetry shown in figure 2.25(d). The lattice maintains a uniform order of arrangement of atoms which leads to diverging lattice strains. However, if the planes were allowed to move laterally then this would lead to a more relaxed structure such as that shown in figure 2.26. Such is usually not the case in crystalline solids but it is possible in liquid crystals. For example, such patterns were found in nematic liquid crystals held between two parallel sheets of glass; patterns for $p = -2, -1, 0, 1, 2$ and 4 were reported [332, 294].
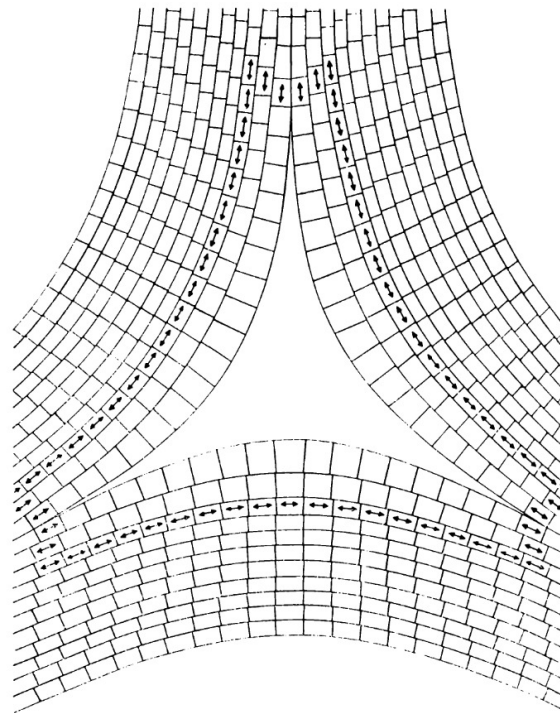
Figure 2.26: The negative screw disclination of figure 2.25(d) redrawn so that the lattice planes are no longer in lateral registry. Such configurations occur in liquid crystals.

Li [251] and Shih and Li [366] advocated the presence of disclinations in crystalline solids but not in the sense of full disclinations as proposed in the work of Frank [132] or Nabarro [294]. They proposed a disclination representation of GBs to study the elastic

51

energy and GB misorientation correlation in crystalline solids. At the time their model was proposed, it had become generally accepted that GBs should be represented using dislocations based on an earlier work by Read and co-workers [323, 324]. These workers suggested a dislocation based representation of low angle symmetric tilt GBs where the boundary consisted of a periodic arrangement of equally spaced dislocations of Burgers vector magnitude $b = \theta d$ where θ is the misorientation of the boundary and d is the spacing between adjacent dislocations. Their work was based on experimental evidence where equally spaced etch pits were observed along a low angle GB in rocksalt [13]. The relationship between Burgers vector and dislocation spacing was confirmed in the work of Vogel *et al.* [435] who observed GB dislocations in Germanium crystals. Aust and Chalmers [21], measured the elastic energy of GB dislocations in tin and found this to match with the one predicted by the dislocation based model [323]. Li [251] remarked that while the dislocation model is appropriate for low angle tilt GBs, such may not be the case for high angle GBs. As the GB misorientation increases, the spacing between dislocations decreases until a misorientation is reached when the cores start overlapping. At that point, while it is geometrically possible to define the Burgers vector and dislocation line in the coincidence site lattice, the energy values predicted by the dislocation model are incorrect. In fact, it is possible to obtain a negative GB energy estimate due to overlapping of dislocation cores. Furthermore, the dislocation based model was not able to predict the energy of twin boundaries or coincidence boundaries where the atoms fit well at the coincident lattice sites and therefore dislocations don't manifest themselves. Li suggested to replace the dislocations with their geometrically equivalent disclination dipoles.

The GB model of Li [251] and Shih and Li [366] used disclinations whose strengths were not equal to those of a full disclination. Such type of disclinations are identified as partial disclinations. Li represented a GB using a pair of partial disclination dipoles. The strengths of these dipoles were equal to the difference between misorientations of

reference GBs. These reference GBs are chosen from those generating energy cusps in the GB energy vs. misorientation plots. The dipole arm lengths were chosen such that the misorientation of the GB is conserved. For example, if θ_1 and θ_2 are the misorientations of GBs corresponding to the energy cusps, then one period H of a boundary with misorientation θ ($\theta_1 < \theta < \theta_2$) can be represented using two dipoles of strengths θ_1 and θ_2 with arm lengths $2L_1$ and $2L_2$ such that $H = 2(L_1 + L_2)$. For the GB misorientation θ to be conserved, the following relationship needs to be satisfied,

$$\theta = \frac{2L_1\theta_1 + 2L_2\theta_2}{2(L_1 + L_2)} \tag{2.30}$$

Li [251] proposed an expression for the strain energy per unit area of a disclination dipole wall as,

$$E = \frac{G(\Delta\theta)^2}{8\pi(1-\nu)}\frac{H}{2\pi}f(\lambda_1) \tag{2.31}$$

with

$$f(\lambda) = -16\int_0^\lambda (\lambda - \psi)\ln(2\sin\psi)d\psi$$
$$\lambda_1 = 2\pi L_1/H$$
$$\lambda_2 = 2\pi L_2/H = \pi - \lambda_1 \tag{2.32}$$

where $f(\lambda)$ is a function which depends on the interaction force between disclination dipoles. Using this relationship, Shih and Li [366] were able to recreate the cusps in GB vs. misorientation plots and provided a satisfactory match with from experiments on commercial purity face centered cubic Aluminium [174] and Copper [144]. Figure 2.27 shows the GB energy vs. misorientation plot for [001] symmetric tilt GBs in Copper obtained from the disclination model of Li [251] and Shih and Li [366]. Their results are compared with the experimental results of Gjostein and Rhines [144]. This was the first time a continuum based model was able to provide an acceptable match with experiments. However, Li remarked that the results required choosing

53

a combination of lengths L_1 and L_2 in order to fit the curves. There exist multiple combinations of L_1 and L_2 which satisfy the equation (2.30). This is because there are multiple ways for choosing reference boundaries θ_1 and θ_2 corresponding to cusp misorientations. For example, consider the 22.63º [001] symmetric tilt GB in a face centered cubic material with a period H. If the reference cusp misorientations are taken as $\theta_1 = 0$º and $\theta_2 = 90$º then from equation (2.30) the ratio L_2/L_1 is 2.977. If now the reference cusp misorientations are taken as $\theta_1 = 0$º and $\theta_2 = 36.87$º (as is done in the work of Shih and Li [366]) the same ratio becomes 0.63. These two choices for L_1 and L_2 would give the same length of the GB period H but the GB energy vs. misorientation curve would be different. The model of Li [251] is not self-contained *i.e.* it lacks selection rules for specifying the appropriate dipole arrangement that geometrically represents the GB structure and relies on computer fitting of experimental data to predict the appropriate structure.

At the time Li [251] and Shih and Li [366] developed their model, the state of the art of representing GBs was using the coincidence-ledge-dislocation model proposed in the works of Bishop and Chalmers [42] and Chalmers and Gleiter [65]. The coincidence-ledge-dislocation model proposed that the GB core was made up of periodically repeating arrangements of atoms called structural units. For one family of GBs with the same tilt axis, the coincidence-ledge-dislocation model identified those GBs in which the lattices forming the boundary are exactly coincident *i.e.* belonging to the coincident site lattice (CSL). These came to be known as special or favoured boundaries. For example, in the case of [001] symmetric tilt GBs in a face centered cubic metal the special GBs were identified as those having misorientations 0º, 22.6º, 28.1º, 36.9º, 53.13º and 90º (shown in figure 2.28). These correspond to the boundaries associated with energy cusps in the GB energy vs. misorientation plots. Bishop and Chalmers [42] suggested that all the other non-special or non-favoured GBs in the misorientation range can be formed using structural units of the special GBs.
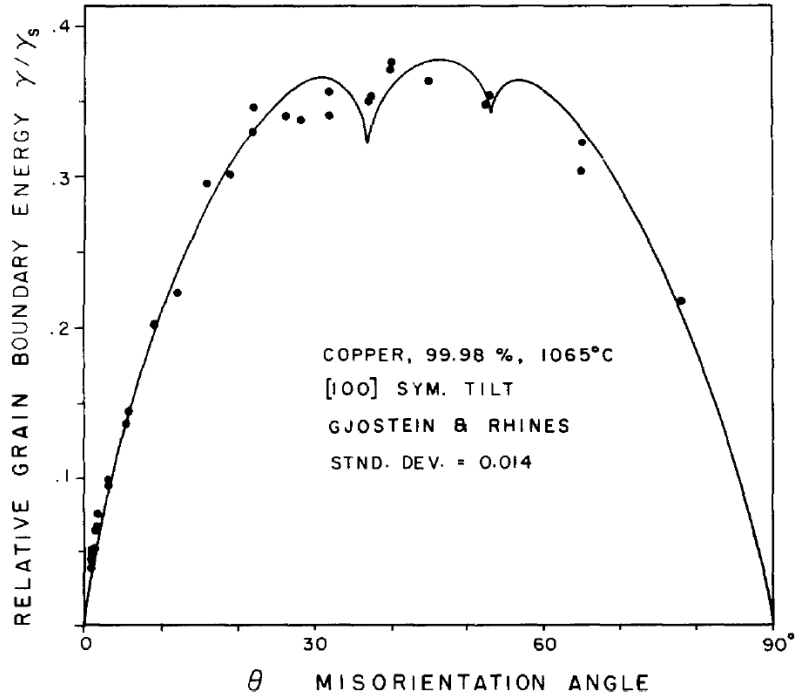
Figure 2.27: GB energy vs. misorientation plot for commercially pure Cu (adapted from Shih and Li [366]). The solid line generated using the disclination model [366] is computer fit with experimental results obtained from the work of Gjostein and Rhines [144].

However, they faced a similar problem as in the work of Li [251], and Shih and Li [366], in that their model was unable to identify, from a multitude of possibilities, the correct type of structural units to represent a particular boundary.
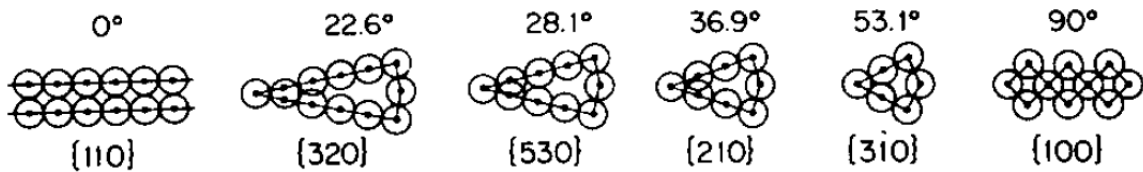
Figure 2.28: Special [001] symmetric tilt GBs with misorientations 0°, 22.6°, 28.1°, 36.9°, 53.13° and 90° with their respective boundary planes {110}, {320}, {530}, {210}, {310} and {100}.

This problem was resolved in the work of Sutton *et al.* [387, 388, 389, 437] where a molecular statics method was used to determine the equilibrium atomic structures of several symmetric and asymmetric tilt GBs in metals. The resulting atomistic

55

structural unit model defined rules for determining the GB structure. The model identifies special boundaries as those which correspond to low Σ values; for a GB plane with miller indices hkl, $\Sigma = h^2 + k^2 + l^2$ for a centered boundary *i.e.* boundary with more than one coincidence site lattice and $\Sigma = \frac{1}{2}(h^2 + k^2 + l^2)$ for a non-centered boundary. The selection criteria for special boundaries is dependent on the interatomic potential of the material which quite interestingly does not always predict the lowest Σ value boundaries as special. For example, $\Sigma = 27(115)$ and $\Sigma = 11(113)$ are favoured $[1\bar{1}0]$ symmetric tilt GBs in Aluminium but $\Sigma = 9(114)$ is not. At the same time, boundaries that can be deemed special may vary for different metals with the same crystal structure. In order to maintain structural continuity throughout the misorientation range, all the non-special boundaries should consist of a periodically reproduced sequence of structural units from their nearest special boundaries. For example, in the case of [001] symmetric tilt GBs in Copper having 0° $\Sigma = 1$, 36.9° $\Sigma = 5$, 53.13° $\Sigma = 5$ and 90° $\Sigma = 1$ as special boundaries, a non-special GB with misorientation 16.26°, should contain structural units of special boundaries 0° and 36.9°.

In order to compute the elastic energy vs. misorientation curve, the following procedure is used. The structure of every non-special GB is first identified. Considering the case of 16.26° [001] symmetric tilt GB, if the structural units of the associated special boundaries are identified as A (for 0°) and B(for 36.9°) then one period of the 16.26° boundary is represented as |AAAB.AAAB| (the dot indicates a centered boundary [420]). The larger number of the same type of units in the boundary are called majority units and the smaller number are called minority units. The structural unit model postulates that the minority units in a non-special GB can be conceived as strain inducing perturbations in an otherwise uniform structure of the special boundary of majority units. Lattice strains are generated due to the presence of secondary GB dislocations lying at the core of the perturbing minority

units. These secondary GB dislocations belong to the DSC lattice and are different from the primary dislocations of the GB, belonging to the crystal lattice. For the special boundaries, no such minority units exist and they can be represented using just the primary GB dislocations.

Quite interestingly, Sutton and Vitek [387] reported that the cores of secondary GB dislocations are smaller than the separation between them (*i.e.* the characteristic length of the majority units) such that no "core overlap" occurs. As a consequence the argument of Li [251] on the overlapping of dislocation cores at higher GB misorientations does not hold. However, Gertsman *et al.* [139] recalled the original argument of Li [251] on disclinations and GBs being rotational type of defects, and proposed to build upon the dislocation based structural unit model by representing the secondary GB dislocations with their equivalent disclination dipoles. These dipoles have arm lengths equal to the characteristic length of a minority unit and their strengths equal to $\Delta\theta = \pm(\theta_1 - \theta_2)$ such that the net Burgers vector of the secondary GB dislocations is conserved. This is known as the disclination structural unit model. For example, consider a model |AABABABAB| boundary shown in figure 2.29. The B units are identified as the minority units of characteristic length d_2' associated with the special boundary of misorientation θ_2 while the A units are the majority units of characteristic length d_1' associated with the special boundary having misorientation θ_1. When the minority and majority units are mixed such that they form the |AABABABAB|, the characteristic lengths of each unit are changed such that they attain new values d_1 and d_2 (here it is assumed that all the structural units of the same type change by the same amount). Then the minority B units can be represented using disclination dipoles of strength $\Delta\theta = \pm(\theta_1 - \theta_2)$ as shown in figure 2.29. This model has been used to recreate the GB energy vs misorientation plots with an excellent match with experiments and atomistic simulations for the case of non equilibrium GBs in Aluminium [300], symmetric tilt GBs in diamond [296, 297], and in Nickel and Copper [297, 23],
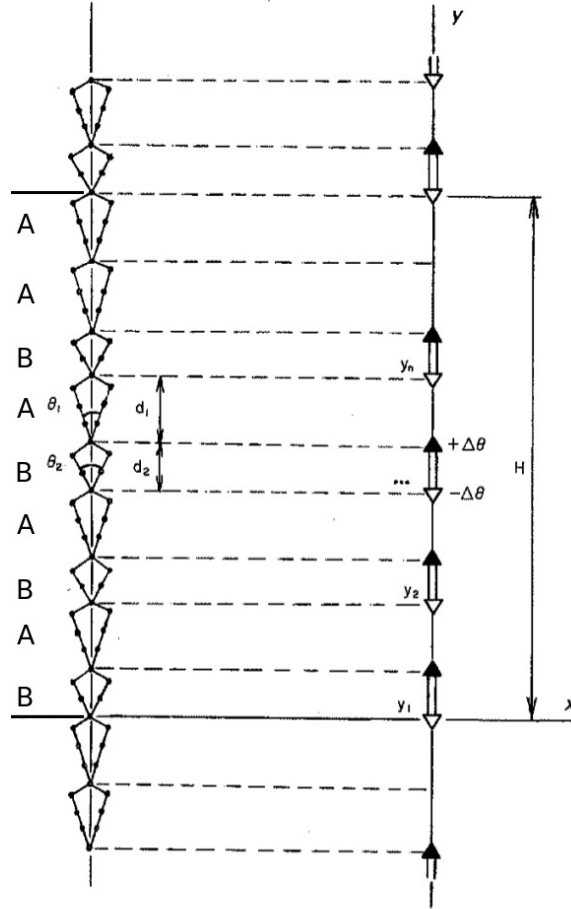
Figure 2.29: A model GB with one period represented as |AABABABAB| where A are the majority units belonging to a special boundary θ_1 and B are the minority units belonging to the special boundary θ_2. In the disclination structural unit model, the minority B units are represented using disclination dipoles of strength $\Delta\theta = \pm(\theta_1 - \theta_2)$ with arm length equal to the characteristic length of the minority unit (adapted from Gertsman *et al.* [139])

quasi-periodic tilt boundaries of finite extent [276], etc. The disclination structural unit forms the basis for representing GBs in the present work and is described with more details in chapter 4.

A disclination based approach has also been used to describe the geometry of TJs in the work of Bollmann [44, 45, 46, 47]. This work was motivated by the experimental study of Palumbo and Aust [309, 310] who reported observing evidence of

disclinations along GBs by studying etched recrystallized high purity Nickel. Boll-mann proposed a methodology to test the possibility of a disclination forming at a TJ. This involved using the dislocation based O-lattice representation of GBs that form the TJ. The O-lattice method describes the GBs as mathematical interfaces of infinitesimal thickness which separate two lattices by a linear translation. This translation is between the nearest neighbouring points of the two lattices such that it leads to the minimal dislocation content in the GB. Consider three GBs of infinitesimal thickness which form a triple-line between grains 1, 2 and 3. Let $\boldsymbol{P}$, $\boldsymbol{Q}$ and $\boldsymbol{R}$ denote the transformation matrix of the nearest neighbour relation that transforms a unit cell from grain 1 to 2, grain 2 to 3, and grain 3 to 1, respectively. Starting from a unit cell of grain 1, passing through grain 2 to grain 3 and finally arriving back at grain 1 by means of the matrix product $\boldsymbol{RQP}$ there are two possibilities that can arise: (i) The sequence arrives at the same unit cell from which it started. In that case $\boldsymbol{RQP} = \boldsymbol{I}$, where $\boldsymbol{I}$ is the identity matrix, or (ii) the sequence could lead to a different unit cell such that $\boldsymbol{RQP} = \boldsymbol{U}$. Here, $\boldsymbol{U}$ is a uni-modular matrix that preserves the volume of the unit cell *i.e.* $\det(\boldsymbol{U}) = 1$. The latter case occurs when dislocation balance at the triple line is not satisfied. In this case, large long range stresses are induced in the medium. Bollmann [47] called this triple-line a U-line and remarked that it possessed the characteristics of a full disclination. In the event that the dislocation content is balanced at the triple-line there is no disclination formed. Such a triple-line is called an I-line. For example, triple-lines with tilt GBs having misorientations $+30^\circ$, -15° and -15° would give an I-line $+30^\circ - 15^\circ - 15^\circ = 0^\circ$. On the other hand, tilt GBs having misorientations $+30^\circ$, $+15^\circ$ and $+15^\circ$ would give a U-line $+30^\circ + 15^\circ + 15^\circ = 60^\circ$.

Shekhar and King [365] attempted at obtaining the stress fields of tri-crystals separated in orientation via small angle symmetric grain boundaries of misorientations -4°, 2°, 2°. They used a dislocation based representation of these boundaries to

obtain the stress fields of the triple junction. Figure 2.30 shows the shear stress σ_{xy} plot for a -4°, 2°, 2°. According to the *U*-line model of Bollmann [47], this configuration corresponds to an *I*-line *i.e.* there should be no disclination forming at the triple line. However, Shekhar and King [365] report diverging stress fields as shown for the component σ_{xy} in figure 2.30 which is very similar to the ϵ_{xy} profile of a wedge disclination shown in figure 14(b). They remarked that the strength of the partial disclination is dependent on the position of the GB dislocations shown in figure 2.30.
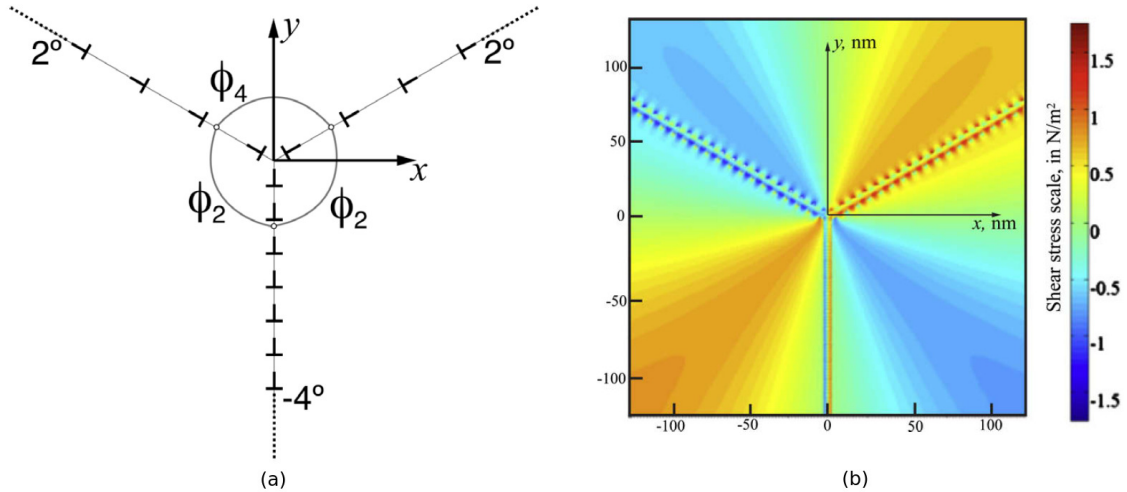
Figure 2.30: Shear stress σ_{xy} (b) for a -4°, 2°, 2° TJ (a) (adapted from Shekhar and King [365]). ϕ represent the dihedral angles.

The disclination structural unit model [139] and the disclination based TJ models [44, 45, 46, 47, 365] define the state of the art of connecting mathematical disclinations to crystallography. Interestingly, while disclinations have already been used to describe diverse phenomena such as misorientation in hetero-epitaxial diamond films [273], phase transformation history in epitaxial ferroelectric thin films [130], displacements of Earth's crust [73], polarization effects and diffraction of electromagnetic waves [305], etc., their to contribution to plasticity has not been widely documented. This may have been due to the success of dislocation based plasticity models at the

meso-scale, or the success of the original structural unit model in predicting mechanisms associated with GB mediated plasticity at the atomistic scale, or even due to general scepticism met by the argument that remotely hints towards presence of disclinations in crystalline solids, one can only speculate.

2.2.3 Experimental observation of disclinations

In the past decade, increasing experimental evidence has appeared that provides sufficient proof of the presence of defect structures that exhibit a disclination type nature in polycrystalline materials, especially those having nano-sized grains. Klemm *et al.* [207, 206, 205] reported the presence of screened partial disclinations in cold rolled Cu, down to 50% of original thickness for a polycrystalline sample, and 70% thickness reduction of a single crystal Cu. The analysis was performed on Kikuchi patterns obtained from TEM micro-diffraction experiments. Partial disclinations of mixed (both twist and wedge) type were found to be arranged in the form of a quadrupole at the site of a microband (see figure 2.31). Their strengths were reported to be between $1^\circ - 3^\circ$. For an extensive review of experimental indications towards presence of disclinations in metallic and non-metallic ultra-fine grained materials, the readers are directed towards the work of Romanov and co-workers [337, 333].

Murayama *et al.* [291] used HRTEM to observe dislocations terminating at partial disclinations in nc body centered cubic Fe prepared by mechanical milling. Figure 2.32 shows the terminating dislocations in the encircled region of a 20.5 nm width image of nc Fe having approximately 6 nm thick crystals. Murayama *et al.* remarked that the presence of disclinations confirms that crystals can rotate and undergo turbulent behavior during severe plastic deformation due to the action of partial disclinations, as was suggested in the work of Romanov and Vladimirov [339]. Similar disclination structures were reported in the work of Lei *et al.* [244] on ball milled Cu-Nb powders. Liu *et al.* [254] reported the formation of a wedge disclination to accommodate grain
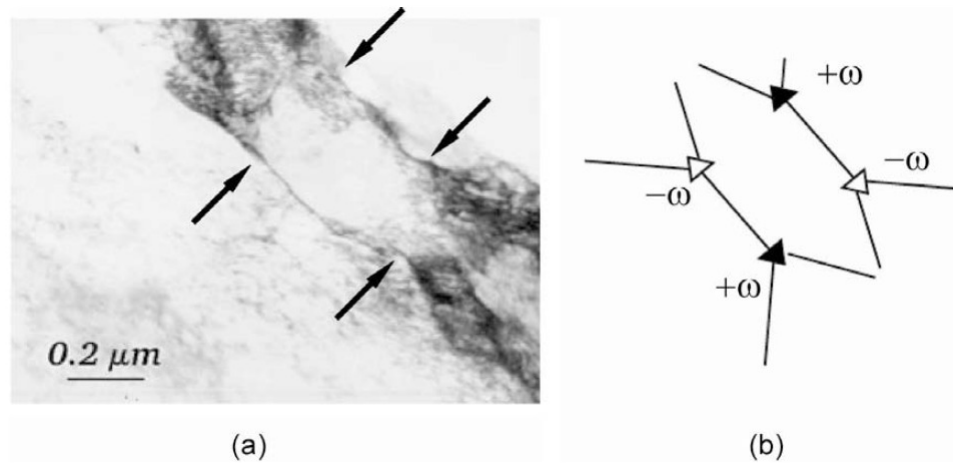
Figure 2.31: Microbands in deformed materials and their disclination interpretation: (a) TEM micrograph of a microband in Cu single crystal rolled down to 70% thickness reduction at room temperature, Klemm et al. [207], (b) schematics showing cell wall junctions with disclination quadrupole configuration [333].
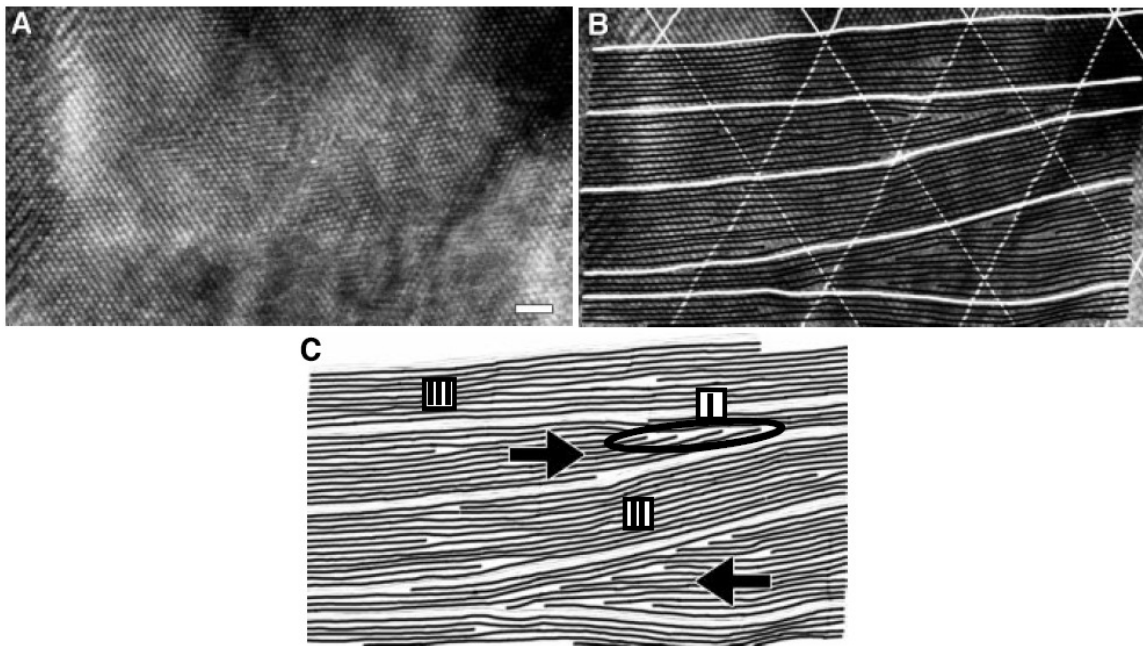
Figure 2.32: (A) Experimental HRTEM image of mechanically milled, nc Fe powder taken in a JEM-4000EX microscope near Scherzer defocus. (B) White lines shown superimposed periodically on the three sets of 110 planes in (A) to highlight the distortion of the nearly horizontal set of 110 planes. Black lines are also superimposed on this set of planes to clearly indicate their position. (C) The nearly horizontal black and white lines in (B) removed from the HRTEM image so that they are more clearly visible. Scale bar in (A), 1.0 nm. (adapted from Murayama *et al.* [291])

rotation in nc gold thin films. A study on nc Pd prepared by severe plastic deforma-tion of an inert gas condensate, Rösner *et al.* [341] observed a disclination dipole along a $\Sigma 9$ GB bounded by a TJ formed with two $\Sigma 3$ twin boundaries and a quadrupole point formed with three $\Sigma 3$ boundaries. Using an aberration corrected transmission electron microscope, the Rösner and co-workers [341] were able to identify a positive disclination emerging from the triple junction line along the $\Sigma 9$ boundary that was balanced by a negative disclination emerging from the quadrupole point. Upon mea-suring the rotation change along the $\Sigma 9$ boundary, a jump in the elastic rotation was observed (shown in figure 1.2). The study concluded that a disclination dipole existed along the $\Sigma 9$ boundary and was essential for stabilizing the structure observed. Al-though from the equivalence between dislocations and disclinations discussed in the previous subsection, it may be argued that structures exhibiting a disclination nature could be specific arrangements of dislocations that are geometrically equivalent to a disclination [333]. A clear understanding on whether a disclination is a charac-teristic defect or a degenerate arrangement of dislocations or both, is still an open question. Nevertheless, these experimental observations highlight the importance of understanding the contribution of disclinations to plasticity.

The aforementioned experimental studies indicate towards the presence of sta-tistical disclinations in the microstructure. A method to quantify the disclination densities was only recently proposed in the work of Beausir and Fressengeas [30]. These workers measured the polar disclination density from orientation maps gen-erated from ultra-fined grain Cu and nc Al thin films. The ultra-fine grained Cu sample was prepared by subjecting the coarse grained Cu sample to equi-channel angular pressing (ECAP) process at room temperature that resulted in an average shear strain of $\gamma = 2$ after the first pass. Orientation mapping was carried out on a grid with a 0.2 μm step (detailed description of the experimental procedure is given in Toth *et al.* [405]). Figure 2.33 shows the quantification of norm of the polar

disclination density $\sqrt{\theta_{11}^2 + \theta_{22}^2 + \theta_{33}^2}$ and the scalar dislocation measure $\sqrt{\alpha_{13}^2 + \alpha_{23}^2}$ obtained from the main map in figure 2.33(a) along a high angle grain boundary - figures 2.33(b), (c) and (d) - and low angle grain boundary - figure 2.33(e) -. Absolute value of maximum polar disclination density component θ_{33} in the high angle grain boundary was reported as $5 \times 10^{12}/\mu m^2$.

2.2.4 Need for a fully continuous approach

The advent of high resolution transmission electron microscopy has made it possible to detect disclinations in polycrystalline materials. Related studies indicate that disclinations usually manifest themselves in their screened form at crystalline interfaces within polycrystals that have undergone severe plastic deformation [207, 206, 205, 291, 341]. However, the information on formation of these disclination structures, or plastic deformation involving disclinations, could not be extracted from the experimental observations.

Theoretical models [344, 179, 340, 301, 302, 334, 303, 424, 362, 166, 164, 165, 337, 336, 333, 338] have suggested the inception of disclinations during grain fragmentation of coarse grained polycrystalline metals and alloys undergoing large strain plastic deformation. Rybin [344] and Romanov and Vladimirov [339] suggested that formation of disclination dipoles and misorientation bands usually takes place near stress concentrators such as non-equilibrium GBs. In another work, TJs have been identified as sources of disclination nucleation [345]. The nucleation of disclinations in the vicinity of TJs has a combined contribution coming from the rotation induced due to changes in misorientation occurring from accumulation of plastic strain near GBs and the abrupt orientation change across GB [333]. Gutkin *et al.* [164] proposed a discrete disclination dynamics model to provide estimates for the critical shear stress required to nucleate disclinations. Romanov and co-workers [339, 340] proposed to modify the Taylor hardening law ($\sigma = \alpha G b \sqrt{\rho}$, where α is dependent on the active
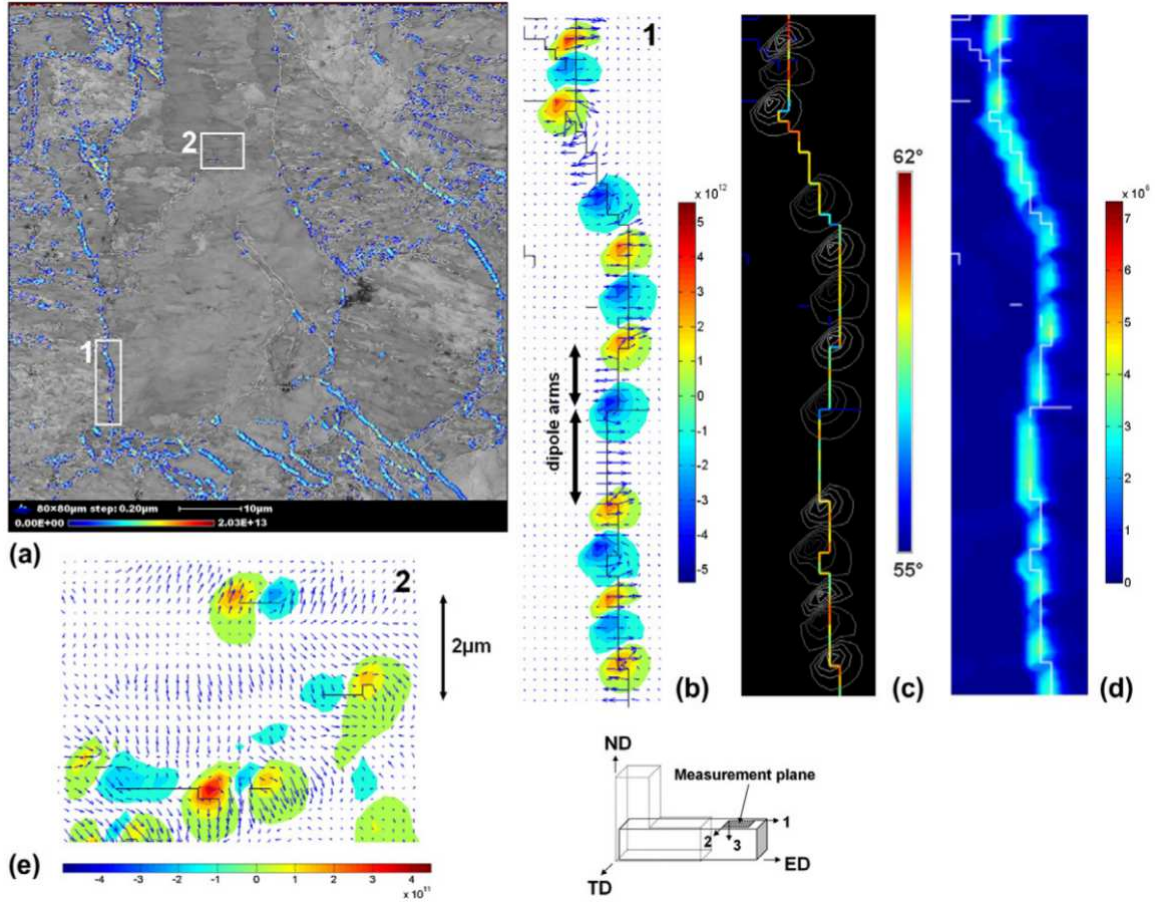
Figure 2.33: Pure Cu ECAPed, one pass. Shear strain $\gamma = 2$. The main map (a) represents the scalar disclination measure $\theta = \sqrt{\theta_{11}^2 + \theta_{22}^2 + \theta_{33}^2}$ in rad/m^{-2}. The close-up maps (b), (c) and (d) show respectively the density of wedge disclinations θ_{33} (in rad/m^{-2}), the disorientation and the scalar dislocation measure $\sqrt{\alpha_{13}^2 + \alpha_{23}^2}$ in m^{-1} (*i.e.* the length of the local Burgers vector per unit surface resulting from the dislocation densities $(\alpha_{13}, \alpha_2 3)$) along a high angle grain boundary, while the close-up map (e) shows θ_{33} (in rad/m^{-2}) along low angle sub-grain boundaries. In the subsets (b,e), the arrows represent the local Burgers vectors: their horizontal and vertical components are respectively α_{13} and α_{23} (in m^{-1}). A continuous line indicates the presence of a disorientation of at least $5°$. The disorientation lies in the range $55°62°$ along the grain boundary shown in subsets (b,c,d). The black arrows in subset (b) highlight two successive dipoles with vertical arm lengths, horizontal Burgers vectors (normal to the arm length) and inverse polarities. Note the inversion of the Burgers vectors direction in the dipoles interiors. (adapted from Beausir and Fressengeas [30])

slip systems in a crystal and ρ is the statistical dislocation density of the crystal) to account for hardening due to disclinations. This was used in the work of Seefeldt [362] where an extensive analysis of the work-hardening mechanisms at large strains

was performed using a discrete dislocation and disclination approach. Valiev et al. [424] and Nazarov et al. [302] discuss the disclination induced long-range stress fields emerging from non-equilibrium GBs and their interaction with dislocations which modify the mechanical properties of nanocrystals such as root mean square strain, dilatation and stored energy. For instance, the disclination contribution to dilatation in ultra-fine grained Al (average grain size 100 nm) was reported to be in the order of 10^{-4}. Junction disclinations are also responsible for long range stresses in nanocrystals [303]. They appear as a result of incompatibility of plastic strain in neighbouring grains [345]. For further details the author would like to direct the reader towards the review article by Romanov and Kolesnikova [333].

The common feature between all the models mentioned in this section is their reliance on a discrete representation of dislocations and disclinations. The geometric and stress fields reported by these models are computed using either the general integral forms for curved defects in anisotropic elasticity or, in the limiting case, closed form solutions in isotropic elasticity similar to the ones presented in section 2.1. As remarked earlier in the section on discrete line defects, the integral or closed form solutions are valid only outside the defect core. If these defects are used to represent GBs in nc materials, then ignoring the defect core may lead to ignoring the energetic contribution of the defected volume; this contribution is significant as will be shown later in this work. In a recent atomistic study [268], it was noted that the elasto-plastic response of nc materials is highly dependent on the core structure of their constituent GBs. For example, the core structure of GBs and their associated excess free volumes have been shown to influence the nucleation of dislocations at GBs [411] and shear coupled GB migration [79]. Modelling such structure sensitive behavior using a discrete defect approach would improperly estimate the bulk mechanical response due to the information lost by neglecting the core, irrespective of the GB representation approach chosen (dislocation or disclination structural unit

model).

Furthermore, in the discrete approach the compatible elastic strain and curvature fields are derived from multi-valued elastic displacement and rotation fields as shown in section 2.1. This could also have consequences. In presence of dislocations, an incompatibility is induced in the elastic distortion field due to the discontinuous elastic displacement field. Similarly, in the presence of disclinations, an incompatibility is induced in the elastic curvature field due to the discontinuous elastic rotation field. In representing dislocations (disclinations) with their equivalent disclinations (dislocations), as discussed in section 2.2.1, the out-of-core compatible elastic strain and curvature may be equivalent but the elastic displacement or rotation fields and the corresponding incompatibilities in elastic strain and curvature fields are fundamentally different. This information is lost in using just the compatible elastic strain and curvature fields.

The present work proposes to use a fully continuous representation of dislocations and disclinations. This approach defines defects using their representative polar densities [306, 216, 288, 94, 289] which in the discrete representation of defects are singular but in the continuous representation are attributed a finite volume. Such an approach can account for the structure sensitive response of GBs.

An alternative approach would be to incorporate atomic features into the continuum approach such as the Peierls-Nabarro [314, 293, 187] model. This model is developed to understand the motion of dislocations during their slip over the crystal lattice and proposes expressions for geometric fields that are valid within the dislocation core. However, no such model exists for disclinations; although efforts towards this are underway.

2.3 Continuously distributed line defects

This section presents the geometry of continuously represented line crystal defects in a simply connected domain. The discussion begins by first understanding the geometry of a compatible body *i.e.* a simply connected body containing no defects. The compatibility of the medium is ensured by respecting the Saint-Venant's compatibility condition on the elastic strain. Failure of Saint-Venant's compatibility condition introduces an incompatibility in the material which may arise in the elastic distortion in presence of dislocations or in the elastic strain and curvature in the presence of both dislocations and disclinations. The focus is then on deriving the various compatible and incompatible geometric quantities. This section can be thought of as an extension to the incompatible theory of dislocations and disclinations of deWit [94] deriving motivation from the work of Acharya [2] and Fressengeas *et al.* [134]. The derivations are shown using three notations (del operator in textual format, del operator in mathematical format, and the Einstein notation) that are frequently used in the literature in order to facilitate readability for readers accustomed to any of these notations. Finally, this section proposes the geometric relationships assuming that equilibrium is respected everywhere in defect-free or defected simply connected domain. The derivation of equilibrium equations is left for the next chapter.

2.3.1 Geometric fields of a compatible body

Consider a defect-free simply connected body with volume V and bounded by a surface $\boldsymbol{S}$ (with normal $\vec{\boldsymbol{n}}$) undergoing an elastic deformation. This state of the body can be characterized by an elastic displacement vector $\vec{\boldsymbol{u}}^{e}$ that is point-wise continuous *i.e.* single valued everywhere in the domain and hence compatible. Therefore, the elastic distortion, strain, rotation, curvature and higher order gradients of the displacement are all compatible. In the following, the superscript $\parallel$ identifying the compatible components is suppressed and will reappear during the discussion on defects where a

distinction between compatibilities and incompatibilities becomes crucial.

Since the displacement field is single-valued, a compatible elastic distortion field can be defined as the gradient of the compatible elastic displacement field,

$$\boldsymbol{U}^e = \mathbf{grad}\ \vec{\boldsymbol{u}}^e = \nabla\vec{\boldsymbol{u}}^e \quad \text{or} \quad U_{ij}^e = u_{i,j}^e \tag{2.33}$$

This expression of distortion provides the first compatibility condition for the material. Assuming that $\vec{\boldsymbol{u}}^e$ exists, the definition in equation (2.33) implies that $\boldsymbol{U}^e$ satisfy the following condition,

$$\mathbf{curl}\ \boldsymbol{U}^e = \nabla\times\boldsymbol{U}^e = 0 \quad \text{or} \quad e_{jkl}U_{il,k}^e = 0 \tag{2.34}$$

Conversely, by the potential theory [295] the condition in equation (2.34) is sufficient to ensure the existence of a single-valued continuous elastic displacement field from equation (2.33) up to a constant rigid body translation.

The compatible elastic strain is defined as the symmetric part of the compatible elastic distortion and is given as,

$$\boldsymbol{\epsilon}^e = \frac{1}{2}\left(\mathbf{grad}\ \vec{\boldsymbol{u}}^e + \mathbf{grad}^T\ \vec{\boldsymbol{u}}^e\right) = \frac{1}{2}\left(\nabla\vec{\boldsymbol{u}}^e + \vec{\boldsymbol{u}}^e\nabla\right) \quad \text{or} \quad \epsilon_{ij}^e = U_{(ij)}^e = \frac{1}{2}(u_{ij}^e + u_{ji}^e) \tag{2.35}$$

where "()" on the indices denote the symmetric part of the tensor. The compatible elastic rotation tensor is given as the anti-symmetric part of the compatible elastic distortion,

$$\boldsymbol{\omega}^e = \frac{1}{2}\left(\mathbf{grad}\ \vec{\boldsymbol{u}}^e - \mathbf{grad}^{\ eT}\vec{\boldsymbol{u}}^e\right) = \frac{1}{2}\left(\nabla\vec{\boldsymbol{u}}^e - \vec{\boldsymbol{u}}^e\nabla\right) \quad \text{or} \quad \omega_{ij}^e = U_{[ij]}^e = \frac{1}{2}(u_{ij}^e - u_{ji}^e) \tag{2.36}$$

Then the compatible elastic distortion tensor is defined as

$$\boldsymbol{U}^e = \boldsymbol{\epsilon}^e + \boldsymbol{\omega}^e \quad \text{or} \quad U_{ij}^e = \epsilon_{ij}^e + \omega_{ij}^e \tag{2.37}$$

The elastic rotation rotation can also be described using a vector as follows,

$$\vec{\boldsymbol{\omega}}^e = \frac{1}{2}\mathbf{curl}\ \vec{\boldsymbol{u}}^e \quad \text{or} \quad \omega_i^e = \frac{1}{2}e_{ijk}u_{k,j}^e \tag{2.38}$$

From the above relationship it can be deduced that in the compatible case the elastic rotations are rigid body rotations. The compatible elastic rotation vector is related to the compatible elastic rotation tensor as,

$$\vec{\omega}^e = X(\boldsymbol{\omega}^e) \quad \text{or} \quad \omega_k^e = -\frac{1}{2}e_{ijk}\omega_{ij}^e \tag{2.39}$$

$$\boldsymbol{\omega}^e = \{\vec{\omega}^e\} \quad \text{or} \quad \omega_{ij}^e = -e_{ijk}\omega_k^e \tag{2.40}$$

From this definition of compatible elastic strain, the Saint-Venant compatibility condition can be deduced as,

$$\mathbf{curl}\,\mathbf{curl}^T\,\boldsymbol{\epsilon}^e = \nabla \times \boldsymbol{\epsilon}^e \times \nabla = 0 \quad \text{or} \quad e_{nmj}e_{jkl}\epsilon_{ik,l}^e = 0 \tag{2.41}$$

A compatibility condition on the elastic rotation can also be deduced as,

$$\mathbf{div}\,\vec{\omega}^e = \nabla \cdot \vec{\omega}^e = 0 \quad \text{or} \quad \omega_{i,i}^e = 0 \tag{2.42}$$

These compatibility conditions can also be deduced by combining equations (2.37) and (2.40) to give,

$$\mathbf{curl}\,(\boldsymbol{\epsilon}^e + \boldsymbol{\omega}^e) = \mathbf{curl}\,\boldsymbol{\epsilon}^e + (\mathbf{div}\,\vec{\omega}^e)\boldsymbol{I} - \mathbf{grad}^T\,\vec{\omega}^e = 0 \quad \text{or}$$

$$\nabla \times (\boldsymbol{\epsilon}^e + \boldsymbol{\omega}^e) = \nabla \times \boldsymbol{\epsilon}^e + (\nabla \cdot \vec{\omega}^e)\boldsymbol{I} - \vec{\omega}^e\nabla = 0 \quad \text{or}$$

$$e_{jkl}\epsilon_{il,k}^e + \omega_{k,k}^e\delta_{ij} - \omega_{j,i}^e = 0 \tag{2.43}$$

where $\boldsymbol{I}$ is a unit dyadic or the Kronecker delta function. Taking the trace of this expression gives the equation (2.42). Substituting equation (2.42) in equation (2.43) gives the following expression,

$$\mathbf{curl}\,\boldsymbol{\epsilon}^e - \mathbf{grad}^T\,\vec{\omega}^e = \nabla \times \boldsymbol{\epsilon}^e - \vec{\omega}^e\nabla = 0 \quad \text{or} \quad e_{jkl}\epsilon_{il,k}^e - \omega_{j,i}^e = 0 \tag{2.44}$$

The transpose of this is also true for a compatible body,

$$-\mathbf{curl}\,\boldsymbol{\epsilon}^e - \mathbf{grad}\,\vec{\omega}^e = -\nabla \times \boldsymbol{\epsilon}^e - \nabla\vec{\omega}^e = 0 \quad \text{or} \quad -e_{jkl}\epsilon_{il,k}^e - \omega_{i,j}^e = 0 \tag{2.45}$$

deWit [94] then considers the converse problem of obtaining the compatible elastic displacement from the compatibility conditions (2.41) and (2.42). It is found that these conditions are necessary for the existence of the compatible elastic displacement but they are not sufficient. Obtaining a unique expression for the compatible elastic displacement is not the aim of this work, for this the interested reader can derive motivation from the work of deWit [94].

The second order compatible elastic curvature tensor is defined as the gradient of the compatible elastic rotation vector as,

$$\boldsymbol{\kappa}^e = \mathbf{grad}\,\vec{\boldsymbol{\omega}}^e = \nabla\vec{\boldsymbol{\omega}}^e \quad \text{or} \quad \kappa_{ij}^e = \omega_{i,j}^e \qquad (2.46)$$

At times this elastic curvature tensor is also identified as the bend/twist (the off-diagonal components correspond to 'bend' and the diagonal components correspond to 'twist') tensor in order to differentiate it from the Nye's curvature tensor [306]. However, in this work the latter shall be addressed as the contortion tensor and the gradient of the elastic rotation field as the elastic curvature.

The compatibility condition on the compatible elastic curvature can then be obtained as,

$$\mathbf{curl}\,\boldsymbol{\kappa}^e = \nabla \times \boldsymbol{\kappa}^e = 0 \quad \text{or} \quad e_{jkl}\kappa_{il,k}^e = 0 \qquad (2.47)$$

This condition is sufficient to ensure the solution of a rotation field up to a constant rigid body rotation. Another compatibility condition can be obtained by combining equations (2.45) and (2.47) to give,

$$\boldsymbol{\kappa}^e = -\mathbf{curl}^T\,\boldsymbol{\epsilon}^e = \boldsymbol{\epsilon}^e \times \nabla \quad \text{or} \quad \kappa_{ij}^e = e_{jkl}\epsilon_{ik,l}^e \qquad (2.48)$$

The third compatibility condition on the compatible elastic curvature tensor follows from the above equation through the vanishing of its trace

$$\mathrm{tr}(\boldsymbol{\kappa}^e) = 0 \quad \text{or} \quad \kappa_{ii}^e = 0 \qquad (2.49)$$

71

Another expression useful in this work, which goes beyond deWit's treatment of the compatible elasticity problem is of the compatible third order elastic curvature tensor defined as the gradient of the compatible elastic rotation tensor proposed in the work of Kröner [218],

$$\tilde{\boldsymbol{\kappa}}^e = \mathbf{grad}\,\boldsymbol{\omega}^e = \frac{1}{2}\mathbf{grad}\,\left(\mathbf{grad}\,\vec{\boldsymbol{u}}^e - \mathbf{grad}^T\,\vec{\boldsymbol{u}}^e\right) = \nabla\boldsymbol{\omega}^e = \frac{1}{2}\nabla\left(\nabla\vec{\boldsymbol{u}}^e - \vec{\boldsymbol{u}}^e\nabla\right) \quad \text{or}$$

$$\kappa_{ijk}^e = \omega_{ij,k}^e = U_{[ij],k}^e = \frac{1}{2}(u_{i,jk}^e - u_{j,ik}^e) \tag{2.50}$$

Finally, the relationship between the second and third order compatible elastic curvatures is given as follows,

$$\tilde{\boldsymbol{\kappa}}^e = \{\boldsymbol{\kappa}^e\} \quad \text{or} \quad \tilde{\kappa}_{ijk}^e = -e_{ijl}\kappa_{lk}^e \tag{2.51}$$

$$\boldsymbol{\kappa}^e = X(\tilde{\boldsymbol{\kappa}}^e) \quad \text{or} \quad \kappa_{ij}^e = -\frac{1}{2}e_{mni}\tilde{\kappa}_{mnj}^e \tag{2.52}$$

The conditions on compatible elastic distortion, strain, rotation and curvature together prove the existence of a compatible elastic displacement and rotation field up to a constant rigid body elastic displacement and rotation, respectively. Note that for a body undergoing elastic deformation, the compatible elastic geometric quantities are always equal to the total geometric quantities. Therefore, the equations (2.33) - (2.52) hold true for total field quantities.

2.3.2 Geometric fields of continuously distributed dislocations

When defects are present and possibly moving within the simply connected domain, the total geometric field variables have a contribution coming from both elastic and plastic components. The compatibility conditions on total field quantities (2.34), (2.41), (2.42), (2.43), (2.44) and (2.47) are always true, but those on the elastic and plastic components may not be true depending on the type of defect in the material. In the following, this is tested in the case of geometrically necessary or polar dislocations. The geometric field equations derived are in harmony with the work of Acharya [2] and deWit [94].

Let the elastically deformed simply connected body contain an arbitrary distribution of continuous dislocations with polar density $\boldsymbol{\alpha}$. Due to the presence of dislocations, a local incompatible plastic distortion $\boldsymbol{U^{p\perp}}$ is induced in the body. This leads to the generation of an incompatible elastic distortion $\boldsymbol{U^{e\perp}}$ in order to maintain the continuity of the material. The elastic deformation induced due to external loads results into a compatible elastic distortion field in the medium. A compatible elastic distortion may also arise from the necessity of maintaining local equilibrium. In the following, these compatible elastic distortions will be denoted in a combined form using $\boldsymbol{U^{e\|}}$. The entire elastic distortion tensor is then given as,

$$\boldsymbol{U^e} = \boldsymbol{U^{e\|}} + \boldsymbol{U^{e\perp}} \quad \text{or} \quad U^e_{ij} = U^{e\|}_{ij} + U^{e\perp}_{ij} \tag{2.53}$$

Note that due to presence of an incompatible elastic distortion, the combined elastic distortion tensor can no longer be defined as the gradient of the elastic displacement as in equation (2.34). This in spirit with the definition of general elastic distortions in the work of Bilby [37]. The body could also contain a compatible plastic distortion distribution such that the combined plastic distortion too can no longer be defined as a gradient of plastic displacement,

$$\boldsymbol{U^p} = \boldsymbol{U^{p\|}} + \boldsymbol{U^{p\perp}} \quad \text{or} \quad U^p_{ij} = U^{p\|}_{ij} + U^{p\perp}_{ij} \tag{2.54}$$

The elastic (2.53) and plastic (2.54) distortions combine to give the total distortion as follows,

$$\boldsymbol{U} = \boldsymbol{U^e} + \boldsymbol{U^p} = \boldsymbol{U^{e\|}} + \boldsymbol{U^{e\perp}} + \boldsymbol{U^{p\|}} + \boldsymbol{U^{p\perp}} \quad \text{or}$$

$$U_{ij} = U^e_{ij} + U^p_{ij} = U^{e\|}_{ij} + U^{e\perp}_{ij} + U^{p\|}_{ij} + U^{p\perp}_{ij} \tag{2.55}$$

This equation along with the necessary condition (2.34) on the compatibility of total distortion gives the following relationship,

$$\boldsymbol{U^{e\perp}} + \boldsymbol{U^{p\perp}} = 0 \quad \text{or} \quad U^{e\perp}_{ij} + U^{p\perp}_{ij} = 0 \tag{2.56}$$

73

Then from this equation the polar dislocation density is defined as,

$$\mathbf{curl}\,\boldsymbol{U^{e\perp}} = \nabla \times \boldsymbol{U^{e\perp}} = \boldsymbol{\alpha} \quad \text{or} \quad e_{jkl}U^{e\perp}_{il,k} = \alpha_{ij}$$

$$\mathbf{curl}\,\boldsymbol{U^{p\perp}} = \nabla \times \boldsymbol{U^{p\perp}} = -\boldsymbol{\alpha} \quad \text{or} \quad e_{jkl}U^{p\perp}_{il,k} = -\alpha_{ij} \tag{2.57}$$

From the Stokes-Helmholtz decomposition of the plastic distortion induced in the presence of dislocations, the incompatible component is defined as the curl of a vector field. Therefore, the divergence of incompatible plastic distortion is equal to zero which further implies that its component normal to the surface of the body should vanish everywhere on the surface. These augmented conditions are necessary to ensure that the incompatible plastic distortion vanishes identically throughout the body when the polar dislocation density is equal to zero.

$$\mathbf{div}\,\boldsymbol{U^{p\perp}} = \nabla \cdot \boldsymbol{U^{p\perp}} = 0 \quad \text{or} \quad U^{p\perp}_{ij,j} = 0, \quad \text{in } V \quad \text{and}$$

$$\boldsymbol{U^{p\perp}} \cdot \vec{\boldsymbol{n}} = 0 \quad \text{or} \quad U^{p\perp}_{ij}n_j = 0, \quad \text{on } \boldsymbol{S} \tag{2.58}$$

From the Stokes-Helmholtz decomposition of the elastic distortion arising from the presence of dislocations, the compatible component belongs to the divergence space and can be defined as a gradient of a continuous vector field. This along with the definition of the induced elastic distortion from elastic deformation in equation (2.34) implies that the combined compatible elastic distortion can be defined as a gradient of a displacement vector field. Therefore, its curl will be equal to zero. The same holds true for the compatible plastic distortion. This provides the compatibility condition on compatible elastic and plastic distortion as,

$$\mathbf{curl}\,\boldsymbol{U^{e\|}} = \nabla \times \boldsymbol{U^{e\|}} = 0 \quad \text{or} \quad e_{jkl}U^{e\|}_{il,k} = 0$$

$$\mathbf{curl}\,\boldsymbol{U^{p\|}} = \nabla \times \boldsymbol{U^{p\|}} = 0 \quad \text{or} \quad e_{jkl}U^{p\|}_{il,k} = 0 \tag{2.59}$$

Equations (2.57) and (2.59) can then be combined to retrieve the definition of the polar dislocation density as proposed in the works of Kröner [216], Mura [288], and

deWit [94],

$$\mathbf{curl}\, \boldsymbol{U^e} = \nabla \times \boldsymbol{U^e} = \boldsymbol{\alpha} \quad \text{or} \quad e_{jkl}U^e_{il,k} = \alpha_{ij}$$

$$\mathbf{curl}\, \boldsymbol{U^p} = \nabla \times \boldsymbol{U^p} = -\boldsymbol{\alpha} \quad \text{or} \quad e_{jkl}U^p_{il,k} = -\alpha_{ij} \tag{2.60}$$

The geometric meaning of the equation (2.60) is that in the presence of dislocation distributions $\boldsymbol{\alpha}$, incompatible elastic distortion $\boldsymbol{U^e}$ is generated to ensure the continuity of the material. This equation along with (2.58) implies that dislocations are the sources of incompatible elastic distortion in the medium. Due to the presence of incompatibility, the elastic distortion cannot be related to a displacement field as defined in equation (2.33). In the absence of dislocations in the medium, $\boldsymbol{\alpha}$ and consequently the incompatible component of elastic distortion vanish. Then the compatible elastic distortion can be related to the displacement tensor using equation (2.33).

The polar dislocation density needs to respect the following continuity condition,

$$\mathbf{div}\, \boldsymbol{\alpha} = \nabla \cdot \boldsymbol{\alpha} = 0 \quad \text{or} \quad \alpha_{ij,j} = 0 \tag{2.61}$$

This condition implies that dislocations do not terminate inside the simply connected body. Note that if the body also contains other type of defects, then this condition may not be satisfied. This shall be evidenced in the next section where the case of a simply connected body containing both dislocations and disclinations is considered.

The solution to both equations (2.57) and (2.60) provide uniquely the incompatible elastic and plastic distortions along with a gradient term that belongs to the null space of the curl operator.

The elastic and plastic distortions can be separated into symmetric strain and anti-symmetric rotation components. In the presence of dislocations, the elastic and plastic rotations remain compatible. However, the elastic and plastic strains have

both compatible and incompatible components,

$$\boldsymbol{\epsilon}^e = \boldsymbol{\epsilon}^{e\|} + \boldsymbol{\epsilon}^{e\perp} \quad \text{or} \quad \epsilon_{ij}^e = \epsilon_{ij}^{e\|} + \epsilon_{ij}^{e\perp} \tag{2.62}$$

$$\boldsymbol{\epsilon}^p = \boldsymbol{\epsilon}^{p\|} + \boldsymbol{\epsilon}^{p\perp} \quad \text{or} \quad \epsilon_{ij}^p = \epsilon_{ij}^{p\|} + \epsilon_{ij}^{p\perp} \tag{2.63}$$

The elastic and plastic strains combine to give the total strain as

$$\boldsymbol{\epsilon} = \boldsymbol{\epsilon}^e + \boldsymbol{\epsilon}^p = \boldsymbol{\epsilon}^{e\|} + \boldsymbol{\epsilon}^{e\perp} + \boldsymbol{\epsilon}^{p\|} + \boldsymbol{\epsilon}^{p\perp} \quad \text{or}$$

$$\epsilon_{ij} = \epsilon_{ij}^e + \epsilon_{ij}^p = \epsilon_{ij}^{e\|} + \epsilon_{ij}^{e\perp} + \epsilon_{ij}^{p\|} + \epsilon_{ij}^{p\perp} \tag{2.64}$$

The compatible components of elastic and plastic strain are also a combination of a contribution coming from respecting the equilibrium conditions and a contribution from external stresses. The combined elastic and plastic strain and rotation give,

$$\boldsymbol{U}^e = \boldsymbol{\epsilon}^{e\|} + \boldsymbol{\epsilon}^{e\perp} + \boldsymbol{\omega}^{e\|} \quad \text{or} \quad U_{ij}^e = \epsilon_{ij}^{e\|} + \epsilon_{ij}^{e\perp} + \omega^{e\|}$$

$$\boldsymbol{U}^p = \boldsymbol{\epsilon}^{p\|} + \boldsymbol{\epsilon}^{p\perp} + \boldsymbol{\omega}^{p\|} \quad \text{or} \quad U_{ij}^p = \epsilon_{ij}^{p\|} + \epsilon_{ij}^{p\perp} + \omega^{p\|} \tag{2.65}$$

with the following condition on elastic and plastic incompatible strains,

$$\boldsymbol{\epsilon}^{e\perp} + \boldsymbol{\epsilon}^{p\perp} = 0 \quad \text{or} \quad \epsilon_{ij}^{e\perp} + \epsilon_{ij}^{p\perp} = 0 \tag{2.66}$$

This condition ensures that the total geometric fields always remain compatible. Note that in the presence of dislocations, the elastic and plastic rotations are compatible. Therefore, the incompatible elastic and plastic distortions are equal to the incompatible elastic and plastic strain,

$$\boldsymbol{U}^{e\perp} = \boldsymbol{\epsilon}^{e\perp} \quad \text{or} \quad U_{ij}^{e\perp} = \epsilon_{ij}^{e\perp}$$

$$\boldsymbol{U}^{p\perp} = \boldsymbol{\epsilon}^{p\perp} \quad \text{or} \quad U_{ij}^{p\perp} = \epsilon_{ij}^{p\perp} \tag{2.67}$$

Substituting the elastic and plastic distortions from equation (2.65) into equation (2.60) gives the following expressions for polar dislocation density,

$$\mathbf{curl}\,\boldsymbol{\epsilon}^{e\perp} + (\mathbf{div}\,\vec{\boldsymbol{\omega}}^{e\|})\boldsymbol{I} - \mathbf{grad}^T\,\vec{\boldsymbol{\omega}}^{e\|} = \nabla \times \boldsymbol{\epsilon}^{e\perp} + (\nabla \cdot \vec{\boldsymbol{\omega}}^{e\|})\boldsymbol{I} - \vec{\boldsymbol{\omega}}^{e\|}\nabla = \boldsymbol{\alpha} \quad \text{or}$$

$$e_{jkl}\epsilon^{e\perp}_{il,k} + \omega^{e\|}_{k,k}\delta_{ij} - \omega^{e\|}_{j,i} = \alpha_{ij} \tag{2.68}$$

$$\mathbf{curl}\,\boldsymbol{\epsilon}^{p\perp} + (\mathbf{div}\,\vec{\boldsymbol{\omega}}^{p\|})\boldsymbol{I} - \mathbf{grad}^T\,\vec{\boldsymbol{\omega}}^{p\|} = \nabla \times \boldsymbol{\epsilon}^{p\perp} + (\nabla \cdot \vec{\boldsymbol{\omega}}^{p\|})\boldsymbol{I} - \vec{\boldsymbol{\omega}}^{p\|}\nabla = -\boldsymbol{\alpha} \quad \text{or}$$

$$e_{jkl}\epsilon^{p\perp}_{il,k} + \omega^{p\|}_{k,k}\delta_{ij} - \omega^{p\|}_{j,i} = -\alpha_{ij} \tag{2.69}$$

Taking the trace of the above equations (2.68) and (2.69) one gets,

$$\mathbf{div}\,\vec{\boldsymbol{\omega}}^{e\|} = \nabla \cdot \vec{\boldsymbol{\omega}}^{e\|} = \frac{1}{2}\mathrm{tr}(\boldsymbol{\alpha}) \quad \text{or} \quad \omega^{e\|}_{i,i} = \frac{1}{2}\alpha_{jj} \tag{2.70}$$

$$\mathbf{div}\,\vec{\boldsymbol{\omega}}^{p\|} = \nabla \cdot \vec{\boldsymbol{\omega}}^{p\|} = -\frac{1}{2}\mathrm{tr}(\boldsymbol{\alpha}) \quad \text{or} \quad \omega^{p\|}_{i,i} = -\frac{1}{2}\alpha_{jj} \tag{2.71}$$

Note that contrary to the case of a defect free body, in the presence of dislocations the trace of the elastic rotation tensor is non-vanishing.

Taking motivation from the Saint-Venant compatibility condition (2.41), the equations (2.68) and (2.69) can be combined with equation (2.70) to obtain the following relationship,

$$\mathbf{grad}\,\vec{\boldsymbol{\omega}}^{e\|} = \nabla\vec{\boldsymbol{\omega}}^{e\|} = \mathbf{curl}^T\,\boldsymbol{\epsilon}^{e\perp} + \boldsymbol{K} = \boldsymbol{\epsilon}^{e\perp} \times \nabla + \boldsymbol{K} \quad \text{or} \quad \omega^{e\|}_{i,j} = e_{jkl}\epsilon^{e\perp}_{il,k} + K_{ij} \tag{2.72}$$

$$\mathbf{grad}\,\vec{\boldsymbol{\omega}}^{p\|} = \nabla\vec{\boldsymbol{\omega}}^{p\|} = \mathbf{curl}^T\,\boldsymbol{\epsilon}^{p\perp} - \boldsymbol{K} = \boldsymbol{\epsilon}^{p\perp} \times \nabla - \boldsymbol{K} \quad \text{or} \quad \omega^{p\|}_{i,j} = e_{jkl}\epsilon^{p\perp}_{il,k} - K_{ij} \tag{2.73}$$

where $\boldsymbol{K}$ is the Nye's curvature tensor [306] or the contortion tensor. Recall that this is not the same as the second order curvature tensor nor equivalent to the third order curvature tensor described in this work. It is defined as,

$$\boldsymbol{K} = \frac{1}{2}\mathrm{tr}(\boldsymbol{\alpha})\boldsymbol{I} - \boldsymbol{\alpha}^T \quad \text{or} \quad K_{ij} = \frac{1}{2}\alpha_{kk}\delta_{ij} - \alpha_{ji} \tag{2.74}$$

Recalling the definition of the second order curvature tensor as the gradient of the rotation, one obtains a relationship between the elastic and plastic curvatures and the contortion tensor as,

$$\boldsymbol{\kappa}^{e\|} = \mathbf{curl}^T\,\boldsymbol{\epsilon}^{e\perp} + \boldsymbol{K} = \boldsymbol{\epsilon}^{e\perp} \times \nabla + \boldsymbol{K} \quad \text{or} \quad \kappa^{e\|}_{ij} = e_{jkl}\epsilon^{e\perp}_{il,k} + K_{ij} \tag{2.75}$$

$$\boldsymbol{\kappa}^{p\|} = \mathbf{curl}^T\,\boldsymbol{\epsilon}^{p\perp} - \boldsymbol{K} = \boldsymbol{\epsilon}^{p\perp} \times \nabla - \boldsymbol{K} \quad \text{or} \quad \kappa^{p\|}_{ij} = e_{jkl}\epsilon^{p\perp}_{il,k} - K_{ij} \tag{2.76}$$

In the presence of dislocations, the elastic and plastic third order curvature are compatible $\tilde{\boldsymbol{\kappa}}^{e,p\|}$ and are related to the elastic and plastic second order curvature, respectively, via equations (2.51) and (2.52).

The contortion tensor is sometimes used to estimate the curvature tensors by neglecting the contribution of incompatible elastic and plastic strains. Such an approximation has already been employed in experimental analysis to estimate the polar dislocation density [103, 119, 311] using the relationship,

$$\boldsymbol{\alpha} = \text{tr}(\boldsymbol{K})\boldsymbol{I} - \boldsymbol{K^T} \quad \text{or} \quad \alpha_{ij} = K_{kk}\delta_{ij} - K_{ji} \tag{2.77}$$

If in addition the incompatible elastic strain contribution were to be recovered (for example using data from electron diffraction studies [454, 195, 433]) then the dislocation density can be more accurately estimated.

Taking the curl of equations (2.72) and (2.73) gives the compatibility conditions on elastic and plastic curvatures,

$$\textbf{curl}\,\boldsymbol{\kappa}^{e\|} = \nabla \times \boldsymbol{\kappa}^{e\|} = \textbf{curl}\,\textbf{curl}^T\,\boldsymbol{\epsilon}^{e\perp} + \textbf{curl}\,\boldsymbol{K} = \nabla \times \boldsymbol{\epsilon}^{e\perp} \times \nabla + \nabla \times \boldsymbol{K} = 0 \quad \text{or}$$

$$e_{jkl}\kappa^{e\|}_{il,k} = e_{jmn}e_{nkl}\epsilon^{e\perp}_{ik,l} + e_{jkl}K_{il,k} = 0 \tag{2.78}$$

$$\textbf{curl}\,\boldsymbol{\kappa}^{p\|} = \nabla \times \boldsymbol{\kappa}^{p\|} = \textbf{curl}\,\textbf{curl}^T\,\boldsymbol{\epsilon}^{p\perp} - \textbf{curl}\,\boldsymbol{K} = \nabla \times \boldsymbol{\epsilon}^{p\perp} \times \nabla - \nabla \times \boldsymbol{K} = 0 \quad \text{or}$$

$$e_{jkl}\kappa^{p\|}_{il,k} = e_{jmn}e_{nkl}\epsilon^{p\perp}_{ik,l} - e_{jkl}K_{il,k} = 0 \tag{2.79}$$

In a defect-free simply connected medium, the Saint-Venant's compatibility condition (2.41) on elastic strain is well respect everywhere. However, in the presence of dislocations this condition is no longer respected and an incompatibility $\boldsymbol{\eta}$ is introduced in the medium at the location where the dislocation densities are non-zero. The incompatibility tensor $\boldsymbol{\eta}$ is defined as,

$$\textbf{curl}\,\textbf{curl}^T\,\boldsymbol{\epsilon}^{e\perp} = \nabla \times \boldsymbol{\epsilon}^{e\perp} \times \nabla = \boldsymbol{\eta} \quad \text{or} \quad e_{jmn}e_{nkl}\epsilon^{e\perp}_{ik,l} = \eta_{ij} \tag{2.80}$$

78

From equations (2.66) and (2.80) the following relationship between the incompatibility tensor and incompatible plastic strain can be deduced,

$$\mathbf{curl\,curl}^T\,\epsilon^{p\perp} = \nabla \times \boldsymbol{\epsilon}^{p\perp} \times \nabla = -\boldsymbol{\eta} \quad \text{or} \quad e_{jmn}e_{nkl}\epsilon^{p\perp}_{ik,l} = -\eta_{ij} \qquad (2.81)$$

A relationship between contortion tensor and the incompatibility tensor can be deduced from equations (2.78), (2.79), (2.80) and (2.81) as follows,

$$\mathbf{curl\,K} = \nabla \times \boldsymbol{K} = \boldsymbol{\eta} \quad \text{or} \quad e_{jkl}K_{il,k} = \eta_{ij} \qquad (2.82)$$

And lastly, the relationship between the incompatibility tensor and the dislocation density tensor can be obtained from equation (2.80) and the curl of equation (2.68),

$$(\mathbf{curl}^T\,\boldsymbol{\alpha})^s = (\boldsymbol{\alpha} \times \nabla)^s = \boldsymbol{\eta} \quad \text{or} \quad \frac{1}{2}(e_{jkl}\alpha_{ik,l} + e_{ikl}\alpha_{jk,l}) = \eta_{ij} \qquad (2.83)$$

The continuity condition on incompatibility tensor is given as,

$$\mathbf{div}\,\boldsymbol{\eta} = \nabla \cdot \boldsymbol{\eta} = 0 \quad \text{or} \quad \eta_{ij,j} = 0 \qquad (2.84)$$

The geometric meaning of this equation is that the incompatibility is conserved in the body. Equations (2.80) to (2.83) show that when the incompatible elastic strain, dislocation density and the contortion point-wise vanish everywhere in the domain, the incompatibility $\boldsymbol{\eta}$ also vanishes.

The Burgers vector for a simply-connected body containing dislocations is defined as,

$$\vec{\boldsymbol{b}} = \oint_C d\mathbf{r} \cdot \boldsymbol{U}^e \quad \text{or} \quad b_i = \oint_C dr_j U^e_{ij} \qquad (2.85)$$

where C is a closed curve called the Burgers circuit similar to that shown in figure (2.3). Recalling the Stokes theorem where the line integral of a tensor field is equal to the surface integral of the curl of that tensor field, from equations (2.60) and (2.85) the Burgers vector can be related to the polar dislocation density,

$$\vec{\boldsymbol{b}} = \int_S d\boldsymbol{S} \cdot \boldsymbol{\alpha} \quad \text{or} \quad b_i = \int_S dS n_j \alpha_{ij} \qquad (2.86)$$

where $\boldsymbol{S}$ is any (defect) surface inside the body bounded by C. From the above relationship (2.86), it can be deduced that the diagonal and off-diagonal components of the polar dislocation density correspond to the screw and edge components of the dislocation, respectively.

In order to respect the continuity condition (2.61) on the polar dislocation density, the net Burgers vector content in the simply connected body V should be equal to zero. If in equation (2.86) $\boldsymbol{S}$ is a closed surface bounding a volume V then using the divergence theorem and equation (2.61) it is found that,

$$\vec{\boldsymbol{b}}_{net} = \int_V dV \operatorname{div} \boldsymbol{\alpha} = \int_V dV \nabla \cdot \boldsymbol{\alpha} = 0 \quad \text{or} \quad b_i^{net} = \int_V dV \alpha_{ij,j} = 0 \qquad (2.87)$$

2.3.3 Geometric fields of continuously distributed dislocations and disclinations

Let the elastically deforming simply connected body now contain an arbitrary distribution of continuous dislocations and disclinations with polar densities $\boldsymbol{\alpha}$ and $\boldsymbol{\theta}$, respectively. Due to the presence of disclinations, a local incompatible plastic curvature $\boldsymbol{\kappa}^{p\perp}$ is induced in the body. This leads to the generation of an incompatible elastic curvature $\boldsymbol{\kappa}^{e\perp}$. A compatible elastic curvature may also arise from the necessity of maintaining local equilibrium and from elastic deformation inducing moments. This combined compatible elastic curvature is denoted by $\boldsymbol{\kappa}^{e\|}$. Similar to the elastic and plastic distortions in the sole presence of dislocations, in the combined presence of dislocations and disclinations the elastic and plastic strain tensors are defined as in equation (2.62) along with the elastic and plastic curvature tensors as follows,

$$\boldsymbol{\kappa}^e = \boldsymbol{\kappa}^{e\|} + \boldsymbol{\kappa}^{e\perp} \quad \text{or} \quad \kappa_{ij}^e = \kappa_{ij}^{e\|} + \kappa_{ij}^{e\perp} \qquad (2.88)$$

$$\boldsymbol{\kappa}^p = \boldsymbol{\kappa}^{p\|} + \boldsymbol{\kappa}^{p\perp} \quad \text{or} \quad \kappa_{ij}^p = \kappa_{ij}^{p\|} + \kappa_{ij}^{p\perp} \qquad (2.89)$$

The compatible elastic and plastic curvature are defined as the combination of the component necessary to satisfy equilibrium along with the contribution from the

imposed elastic deformation. In the presence of disclinations, both the compatible and incompatible components of the second $\boldsymbol{\kappa}^{e,p}$ and third $\tilde{\boldsymbol{\kappa}}^{e,p}$ order compatible elastic and plastic curvatures are also related via equations (2.51) and (2.52). The elastic and plastic curvatures combine to give the total curvature as follows,

$$\boldsymbol{\kappa} = \boldsymbol{\kappa}^e + \boldsymbol{\kappa}^p = \boldsymbol{\kappa}^{e\|} + \boldsymbol{\kappa}^{e\perp} + \boldsymbol{\kappa}^{p\|} + \boldsymbol{\kappa}^{p\perp} \quad \text{or}$$

$$\kappa_{ij} = \kappa_{ij}^e + \kappa_{ij}^p = \kappa_{ij}^{e\|} + \kappa_{ij}^{e\perp} + \kappa_{ij}^{p\|} + \kappa_{ij}^{p\perp} \tag{2.90}$$

This equation along with the necessary condition (2.47) on the compatibility of total curvature gives the following relationship,

$$\boldsymbol{\kappa}^{e\perp} + \boldsymbol{\kappa}^{p\perp} = 0 \quad \text{or} \quad \kappa_{ij}^{e\perp} + \kappa_{ij}^{p\perp} = 0 \tag{2.91}$$

From here the polar disclination density can be defined as,

$$\mathbf{curl}\,\boldsymbol{\kappa}^{e\perp} = \nabla \times \boldsymbol{\kappa}^{e\perp} = \boldsymbol{\theta} \quad \text{or} \quad e_{jkl}\kappa_{il,k}^{e\perp} = \theta_{ij}$$

$$\mathbf{curl}\,\boldsymbol{\kappa}^{p\perp} = \nabla \times \boldsymbol{\kappa}^{p\perp} = -\boldsymbol{\theta} \quad \text{or} \quad e_{jkl}\kappa_{il,k}^{p\perp} = -\theta_{ij} \tag{2.92}$$

Then the compatibility condition on polar disclination density is given as,

$$\mathbf{div}\,\boldsymbol{\theta} = \nabla \cdot \boldsymbol{\theta} = 0 \quad \text{or} \quad \theta_{ij,j} = 0 \tag{2.93}$$

This condition implies that disclinations do not end inside the simply connected body.

Similar to the previous case of plastic distortions, the incompatible plastic curvature should vanish identically throughout the body when the polar disclination density is equal to zero. This enforces augmented conditions on the incompatible plastic curvature,

$$\mathbf{div}\,\boldsymbol{\kappa}^{p\perp} = \nabla \cdot \boldsymbol{\kappa}^{p\perp} = 0 \quad \text{or} \quad \kappa_{ij,j}^{p\perp} = 0, \quad \text{in } V \quad \text{and}$$

$$\boldsymbol{\kappa}^{p\perp} \cdot \vec{\boldsymbol{n}} = 0 \quad \text{or} \quad \kappa_{ij}^{p\perp} n_j = 0, \quad \text{on } \boldsymbol{S} \tag{2.94}$$

As a consequence of incompatibilities in elastic and plastic curvature, the elastic and plastic rotation fields are undefined and consequently from equation (2.65) the

elastic and plastic distortion fields are undefined. Therefore in the presence of discli-
nations only the elastic and plastic strain and curvature fields and their gradients
should be considered. The presence of disclinations entails the following augmented
conditions on plastic strain (instead of those on plastic distortion as shown in equation
2.58),

$$\textbf{div }\boldsymbol{\epsilon^{p\perp}} = \nabla \cdot \boldsymbol{\epsilon^{p\perp}} = 0 \quad \text{or} \quad \epsilon^{p\perp}_{ij,j} = 0, \quad \text{in } V \quad \text{and}$$

$$\boldsymbol{\epsilon^{p\perp}} \cdot \vec{\boldsymbol{n}} = 0 \quad \text{or} \quad \epsilon^{p\perp}_{ij} n_j = 0, \quad \text{on } \boldsymbol{S} \tag{2.95}$$

The compatibility condition on compatible elastic and plastic curvature have al-
ready been presented in equations (2.78) and (2.79). These can then be combined
with equation (2.92) to retrieve the definition of the polar disclination density as
proposed in the work of deWit [94],

$$\textbf{curl }\boldsymbol{\kappa^e} = \nabla \times \boldsymbol{\kappa^e} = \boldsymbol{\theta} \quad \text{or} \quad e_{jkl}\kappa^e_{il,k} = \theta_{ij} \tag{2.96}$$

$$\textbf{curl }\boldsymbol{\kappa^p} = \nabla \times \boldsymbol{\kappa^p} = -\boldsymbol{\theta} \quad \text{or} \quad e_{jkl}\kappa^p_{il,k} = -\theta_{ij} \tag{2.97}$$

The geometric meaning of the equations (2.92) and (2.96) is that in the presence
of disclination distributions $\boldsymbol{\theta}$, incompatible elastic curvatures are generated to ensure
the continuity of the material. Consequently these equations combined with (2.91)
and (2.94) show that disclinations are sources of incompatible elastic curvature in
the medium. Due to the presence of incompatibility, the elastic curvature cannot
be related to an elastic rotation field as defined in equation (2.46). In the absence
of disclinations in the medium, $\boldsymbol{\theta}$ and consequently the incompatible component of
elastic curvature vanish. The elastic curvature can then be related to the elastic
rotation tensor using equation (2.46).

The solution to equations (2.92), (2.96) and (2.97) provide uniquely the incom-
patible elastic and plastic curvatures along upto a constant gradient term (belonging
to the null space of the curl operator).

The dislocation density equation (2.69) needs to be updated since the elastic and plastic rotations are undefined and the presence of incompatible elastic and plastic curvature need to be accounted for. Therefore,

$$\mathbf{curl}\,\boldsymbol{\epsilon}^{e\perp} + \mathrm{tr}(\boldsymbol{\kappa}^{e(\|+\perp)})\boldsymbol{I} - \boldsymbol{\kappa}^{e(\|+\perp)T} = \nabla \times \boldsymbol{\epsilon}^{e\perp} + \mathrm{tr}(\boldsymbol{\kappa}^{e(\|+\perp)})\boldsymbol{I} - \boldsymbol{\kappa}^{e(\|+\perp)T} = \boldsymbol{\alpha} \text{ or}$$

$$e_{jkl}\epsilon_{il,k}^{e\perp} + \kappa_{kk}^{e(\|+\perp)}\delta_{ij} - \kappa_{ji}^{e(\|+\perp)} = \alpha_{ij} \tag{2.98}$$

$$\mathbf{curl}\,\boldsymbol{\epsilon}^{p\perp} + \mathrm{tr}(\boldsymbol{\kappa}^{p(\|+\perp)})\boldsymbol{I} - \boldsymbol{\kappa}^{e(\|+\perp)T} = \nabla \times \boldsymbol{\epsilon}^{p\perp} + \mathrm{tr}(\boldsymbol{\kappa}^{p(\|+\perp)})\boldsymbol{I} - \boldsymbol{\kappa}^{e(\|+\perp)T} = \boldsymbol{\alpha} \text{ or}$$

$$e_{jkl}\epsilon_{il,k}^{p\perp} + \kappa_{kk}^{p(\|+\perp)}\delta_{ij} - \kappa_{ji}^{p(\|+\perp)} = -\alpha_{ij} \tag{2.99}$$

Equation (2.99) implies that an arbitrary plastic strain and curvature leads to dislocations. Note that it is the combined compatible and incompatible elastic and plastic curvatures that contribute to the dislocation density. The geometric meaning of the equations (2.96) and (2.98) is that in the presence of both dislocation and disclination distributions $\boldsymbol{\alpha}$ and $\boldsymbol{\theta}$, elastic strain $\boldsymbol{\epsilon}^e$ and curvature $\boldsymbol{\kappa}^e$ are generated to ensure the continuity of the material. Consequently these equations show that disclinations and dislocations are sources of elastic strain and curvature in the medium.

The contortion tensor in equation (2.75) too needs to be redefined to account for the incompatible elastic and plastic curvatures,

$$\boldsymbol{\kappa}^{e(\|+\perp)} = \mathbf{curl}^T\,\boldsymbol{\epsilon}^{e\perp} + \boldsymbol{K} = \boldsymbol{\epsilon}^{e\perp} \times \nabla + \boldsymbol{K} \quad \text{or} \quad \kappa_{ij}^{e(\|+\perp)} = e_{jkl}\epsilon_{il,k}^{e\perp} + K_{ij} \tag{2.100}$$

$$\boldsymbol{\kappa}^{p(\|+\perp)} = \mathbf{curl}^T\,\boldsymbol{\epsilon}^{p\perp} - \boldsymbol{K} = \boldsymbol{\epsilon}^{p\perp} \times \nabla - \boldsymbol{K} \quad \text{or} \quad \kappa_{ij}^{p(\|+\perp)} = e_{jkl}\epsilon_{il,k}^{p\perp} - K_{ij} \tag{2.101}$$

In the presence of both dislocations and disclinations, the incompatibility tensor is given as,

$$\boldsymbol{\eta} = \mathbf{curl}\,\boldsymbol{K} - \boldsymbol{\theta} = \nabla \times \boldsymbol{K} - \boldsymbol{\theta} \quad \text{or} \quad e_{jkl}K_{il,k} - \theta_{ij} = \eta_{ij} \tag{2.102}$$

$$\boldsymbol{\eta} = (\mathbf{curl}^T\,\boldsymbol{\alpha} - \boldsymbol{\theta})^s = (\boldsymbol{\alpha} \times \nabla - \boldsymbol{\theta})^s \quad \text{or} \quad \frac{1}{2}(e_{jkl}\alpha_{ik,l} + e_{ikl}\alpha_{jk,l}) - \theta_{(ij)} = \eta_{ij} \tag{2.103}$$

The continuity condition for polar dislocation density is given as,

$$\mathbf{div}\,\boldsymbol{\alpha} + 2\vec{\boldsymbol{\theta}} = \nabla \cdot \boldsymbol{\alpha} + 2\vec{\boldsymbol{\theta}} = 0 \quad \text{or} \quad \alpha_{ij,j} - e_{ikl}\theta_{kl} = 0 \tag{2.104}$$

83

Contrary to the case of sole presence of dislocations in the simply connected domain, the divergence of the dislocation density is not equal to zero when disclinations are also present in the medium. Equation (2.104) implies that dislocations terminate at disclinations. This was evidenced in the experimental work of Murayama *et al.* [291] where lines of partial dislocations terminated at disclinations in nc body centered cubic Fe as shown in figure 2.32 in section 2.2.2.

The relationship between contortion and the polar disclination density is derived as,

$$\mathbf{grad}\,(\mathrm{tr}\boldsymbol{K}) - \mathbf{div}^T\boldsymbol{K} + 2\vec{\boldsymbol{\theta}} = \nabla(\mathrm{tr}\boldsymbol{K}) - \boldsymbol{K}\cdot\nabla + 2\vec{\boldsymbol{\theta}} = 0 \quad \text{or}$$

$$K_{mm,i} - K_{ji,j} - e_{ikl}\theta_{kl} = 0 \tag{2.105}$$

From equations (2.103) and (2.104) it can be found that the continuity condition on incompatibility (2.84) is also respected in the presence of both dislocations and disclinations.

By virtue of Weingarten's theorem (recall from section 2.1), in the presence of both dislocations and disclinations it is possible to define the Frank's vector and the general Burgers vector in terms of the compatible and incompatible components of elastic curvatures and strains:

$$\vec{\boldsymbol{\Omega}} = \oint_C d\mathbf{r}\cdot\boldsymbol{\kappa}^{e(\|+\perp)} \text{ or } \Omega_i = \oint_C dr_j\kappa_{ij}^{e(\|+\perp)} \tag{2.106}$$

$$\vec{\boldsymbol{b}} = \oint_C d\mathbf{r}\cdot(\boldsymbol{\epsilon}^{e(\|+\perp)} - (\boldsymbol{\kappa}^{e(\|+\perp)T}\times\vec{\boldsymbol{r}})^T) \text{ or } b_i = \oint_C dr_j(\epsilon_{ij}^{e(\|+\perp)} - e_{ikl}\kappa_{kj}^{e(\|+\perp)}r_l) \tag{2.107}$$

Using Stokes' theorem, the Frank's and Burgers vector can be related to the polar defect densities by,

$$\vec{\boldsymbol{\Omega}} = \int_S d\boldsymbol{S}\cdot\boldsymbol{\theta} \quad \text{or} \quad \Omega_i = \int_S dSn_j\theta_{ij} \tag{2.108}$$

$$\vec{\boldsymbol{b}} = \int_S d\boldsymbol{S}\cdot(\boldsymbol{\alpha} - (\boldsymbol{\theta}^T\times\vec{\boldsymbol{r}})^T) \quad \text{or} \quad b_i = \int_S dSn_j(\alpha_{ij} - e_{ikl}\theta_{kj}r_l) \tag{2.109}$$

In section 2.3.2 it was shown that the diagonal and off-diagonal components of the polar dislocation density correspond to the screw and edge components of the

dislocation, respectively. Similarly, the diagonal and off-diagonal components of the disclination density tensor correspond to the wedge and twist components of the disclination.

The term $(\theta^T \times \vec{r})^T$ accounts for the delocalization of the disclination core discussed in section 2.1.2. The Burgers content within a volume bounded by the surface S is a function of the position of the disclination core.

If S is a closed surface bounding a volume V then using the divergence theorem it is found that,

$$\vec{\Omega}_{net} = \int_V dV \, \mathbf{div} \, \boldsymbol{\theta} = \int_V dV \nabla \cdot \boldsymbol{\theta} = 0 \quad \text{or} \quad \Omega_i^{net} = \int_V dV \theta_{ij,j} = 0 \quad (2.110)$$

$$\vec{b}_{net} = \int_V dV \, \mathbf{div} \, (\boldsymbol{\alpha} - (\boldsymbol{\theta}^T \times \mathbf{r})^T) = \int_V dV \nabla \cdot (\boldsymbol{\alpha} - (\boldsymbol{\theta}^T \times \mathbf{r})^T) = 0 \quad \text{or}$$

$$b_i^{net} = \int_V dV (\alpha_{ij,j} - \{e_{ikl}\theta_{kj}r_l\}_{,j}) = 0 \quad (2.111)$$

Thus, similar to the case of dislocations, the continuity conditions on polar defect densities ensures conservation of both Franks and Burgers vectors in the medium. Note that in the absence of disclinations, the Frank's vector is equal to zero everywhere in the domain and the net Burgers vector is conserved following from equation (2.87). In the absence of both dislocations and disclinations, both Burgers and Frank's vectors are zero everywhere in the domain. From here a general remark can be made that contributes to defining the characteristics of a simply connected body: For a defect-free or line defected body to be deemed simply connected, the conditions (2.110) and (2.111) on the net Burgers and Frank's vector need to be satisfied.

2.4 Understanding incompatibility

The term 'incompatibility' has evolved over the better part of the last century. The development shown in the previous section is its most recent interpretation which was introduced in the works of Acharya [2] and Fressengeas *et al.* [134]. It is important to

understand the differences between the original and current interpretations of incompatibility in order to characterize the presented incompatible theory of continuously distributed defects.

Origin of the term "incompatibility" finds its traces in the early work of Rießner [325] who studied the problem of the eigen or incompatible stress state of an elastic body. The body was assumed to possess an incompatible stress state due to a history of plastic deformation. At the time when the concept was introduced the connection of dislocation with crystallography had not yet been made. Then the generation of such a stress state was understood as follows. Let a stress free body V contain an element V' bounded by a surface S', as shown in figure 2.34. Let this element be cut out and isolated from the remainder of the body $(V - V')$. Now, let the element and the remainder of the body be subjected to plastic deformation while in isolation. Without the loss of generality, it can be assumed that each body undergoes a shape change in a manner different from the other one. Then an attempt at reassembling the two volumes would result into a set of non-fitting bodies. If the element V' and the remainder of the body $V - V'$ were to reform a compact body, then V' (or $V - V'$, or both) would have to subjected to external forces inducing elastic deformation such that it fits into the deformed cavity in $V - V'$. Upon removal of these forces, an incompatible stress state would necessarily generate in order to maintain the continuity of the medium. The final configuration in shown in figure 2.34(d).

The connection of an incompatible stress state with dislocations was proposed at the time of increasing experimental evidence for dislocations in the mid 1900's. The concept of incompatible elastic distortion was introduced in the works of Eckart [102], Kondo [211], Bilby and co-workers [38, 40, 39, 37], Eshelby [111], Kröner [217], among others. This incompatible elastic distortion was deemed to be induced as a result of geometrically necessary dislocations generated in order to maintain the
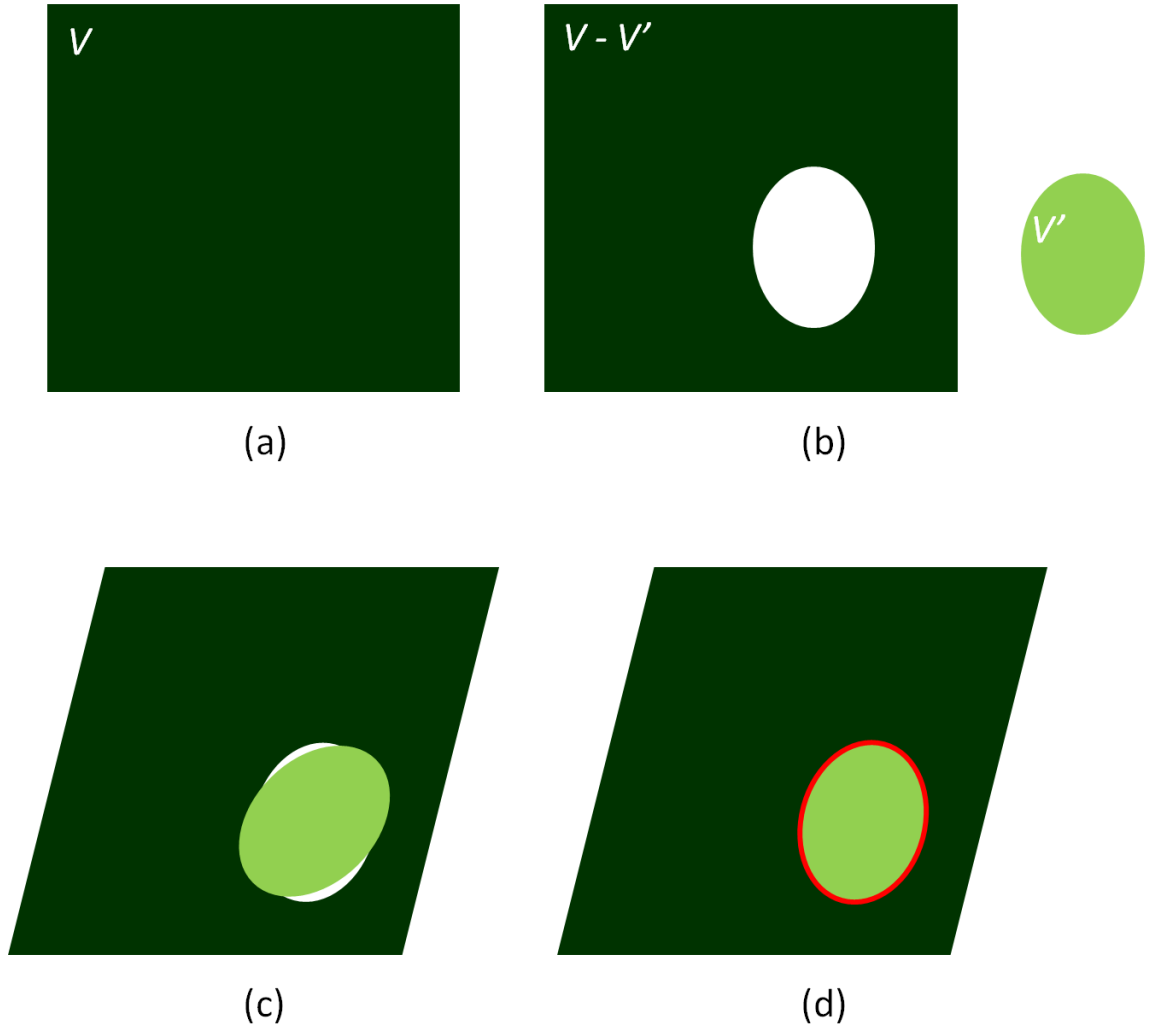
Figure 2.34: Understanding incompatibility as interpreted before the appearance of experimental evidence on dislocations: (a) A body of volume V, (b) with an element V' isolated from the remainer of the body $V - V'$ and subjected to plastic deformation such that both the sub-volumes are transformed into (c) non-fitting elements. External forces are applied on V' such that it fits into the cavity in $V - V'$. Upon removal of these forces, incompatibilities - shown in red (d) - are generated in order to maintain the continuity of the material.

continuity of the medium. Therefore, the incompatible elastic distortion resulted in the generation of the incompatible stress state of the medium. Such an incompatible elastic distortion – formerly termed as lattice correspondence function [37] – was introduced as a replacement for the deformation gradient used in classical elasticity. In general, this incompatible elastic distortion is not associated to any displacement field but in absence of dislocations it is equal to the gradient of elastic displacement. These early developments served as a basis for dislocation based finite strain crystal plasticity theories [329, 401, 182, 18, 315, 177, 27] at the meso-scale (sub-grain or single grain of size $\approx 10^{-7}m - 10^{-6}m$). The works of Kondo [211], Bilby [38], Kröner [217], and others also motivated the development of plasticity theories at the macro-scale [242, 25, 81, 275, 274, 352]. Recently, Clayton *et al.* [77] proposed a multi-scale plasticity model by building upon the incompatible elastic distortion proposed in the works of [102, 211, 38, 40, 111, 39, 217, 37] in order to study the internal state of a material while obtaining its macroscopic mechanical response. An extension to include disclinations was also proposed in the same work [77].

At the meso-scale, a typical realization of an incompatible stress state as interpreted by the aforementioned crystal plasticity models can be explained as follows. Reconsider the body V shown in figure 2.34. Let this body be simply connected containing an arbitrary distribution of defects such that it respects the conditions (2.110) and (2.111). Local stresses will be generated due to the presence of incompatible elastic strains and curvatures. Now let the surface $\boldsymbol{S'}$ bound a volume V' within the body such that it too contains an arbitrary distribution of defects but with a net polarity represented by non-zero $\vec{\boldsymbol{b}} = b_1$ and $\vec{\boldsymbol{\Omega}} = \Omega_1$. Then the remainder of the body $(V - V')$ will have a net polarity of $\vec{\boldsymbol{b}} = -\vec{\boldsymbol{b}}$ and $\vec{\boldsymbol{\Omega}} = -\vec{\boldsymbol{\Omega}}$ in order to conserve the Burgers and Frank's vectors in the whole body V. Now let the body V' be isolated from the remainder of the material $V - V'$ as shown in figure 2.35(b). Here it is assumed that the isolation process is isentropic *i.e.* does not produce a
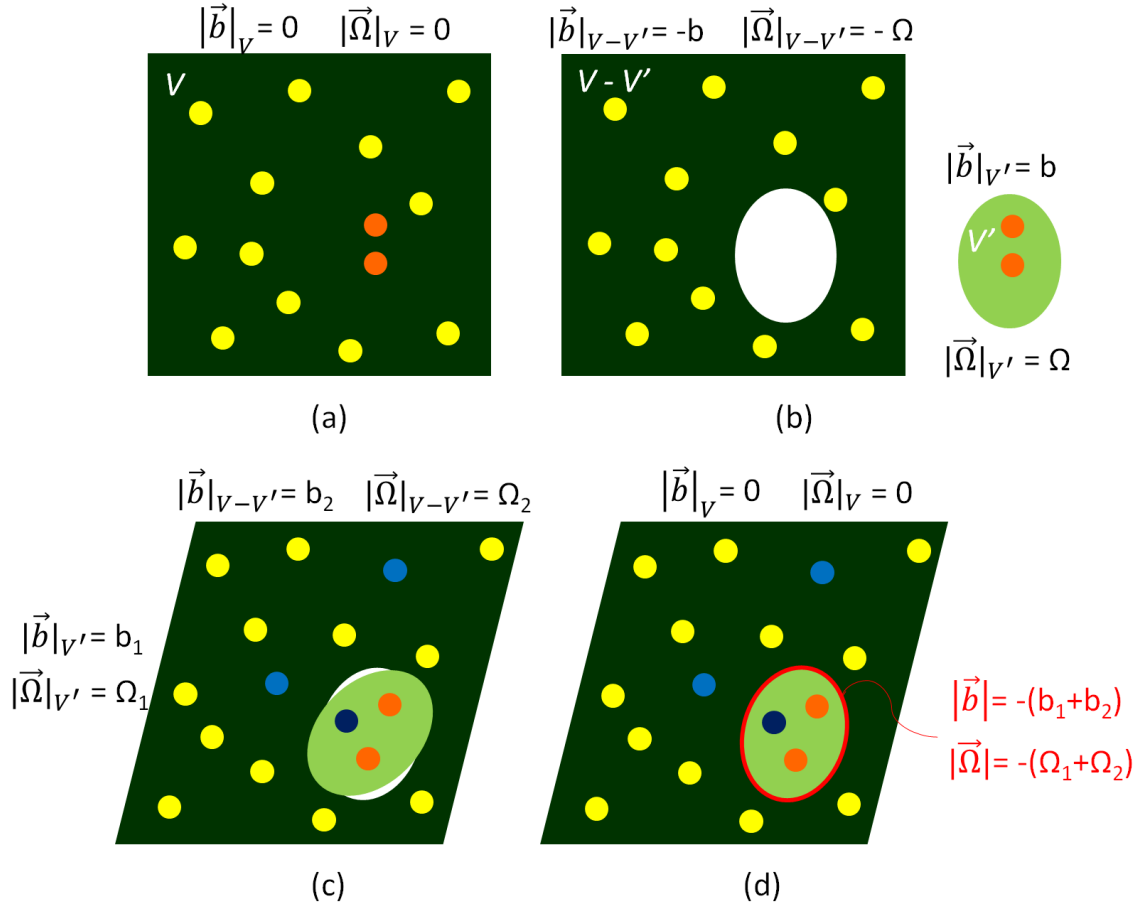
Figure 2.35: Understanding incompatibility as interpreted in the work of Bilby [37], Clayton *et al.* [77]: (a) A body of volume V with net Burgers and Franks vector equal to zero, (b) contains an element V' having $|\vec{b}| = b$ and $|\vec{b}| = \Omega$, respectively, is isolated from the remainer of the body $V - V'$ ($|\vec{b}| = -b$ and $|\vec{b}| = -\Omega$). These volumes are subjected to the same kind of plastic deformation such that both are transformed into (c) non-fitting elements with $|\vec{b}| = b_1$ and $|\vec{b}| = -\Omega_1$ in . External forces are applied on V' such that it fits into the cavity in $V - V'$. Upon removal of these forces, incompatibilities - shown in red (d) - are generated in order to maintain the continuity of the material. Color code for dots: yellow - original defects in $V - V'$, orange - original defects in V', cyan - new defects in $V - V'$ and navy blue - new defects in V'.

rearrangement of defects within the volume. Then body $V - V'$ becomes multiply connected, and the Burgers and Frank's vectors are not conserved in either of these bodies. Next both these isolated volumes are subjected to the same kind of plastic deformation process. In general, due to their arbitrary distribution, the defects would evolve in a different manner in each volume leading to some combination of rearranged, nucleated or annihilated defects as shown in figure 2.35(c). This provides an explanation for the shape changes which, in general, are different for both these volumes. Body V' and body $V - V'$ now are non-fitting elements. Without the loss of generality, let the new Burgers and Frank's vectors in V' be $\vec{b}_1$ and $\vec{\Omega}_1$ and those in $V - V'$ be $\vec{b}_2$ and $\vec{\Omega}_2$, respectively. The combined polarity of these volumes is represented by $\vec{b}_1 + \vec{b}_2$ and $\vec{\Omega}_1 + \vec{\Omega}_2$. Now, let both these volumes be elastically deformed under the action of external constraints such that they can be combined to reform a compact simply connected body V. Upon removal of these external constraints, incompatibilities should necessarily be generated to respect the continuity of the material. Furthermore, the conservation of Burgers and Frank's vectors in V would imply that these incompatibilities correspond a net polarity of $-(\vec{b}_1 + \vec{b}_2)$ and $-(\vec{\Omega}_1 + \vec{\Omega}_2)$. The final configuration is shown in figure 2.35(d). In general, a net non zero Burgers and Frank's vector result in the generation of polar dislocation and disclinations densities. Therefore, polar dislocations and disclinations are geometrically necessary to maintain the continuity of the medium.

Acharya [2] refined the meaning of compatibility and incompatibility by revisiting the definitions of incompatible elastic and plastic distortion. Starting from a mathematical argument, Acharya [2] proposed that the elastic distortion can be orthogonally decomposed in a unique fashion using the Stokes-Helmholtz decomposition such that one component belongs to the divergence space (*i.e.* its curl is equal to zero) and the other component belongs to the curl space (*i.e.* its gradient is zero). In general, any first or higher order tensor that is well-defined in a given domain

can be decomposed in such a manner. The term having a zero curl is defined as the compatible component (represented using ||) and can be defined using a gradient of a vector field (say $\vec{v}$), such that $\boldsymbol{U}^{e\parallel} = \nabla\vec{v}$. The component belonging to the curl space is defined as the incompatible component $\boldsymbol{U}^{e\perp}$. As seen in section 2.3.2, the incompatible elastic distortion $\boldsymbol{U}^{e\perp}$ is generated in the presence of a continuous distribution of dislocations of density $\boldsymbol{\alpha}$. The latter is related to the former via equation (2.57). Now, taking the curl of the entire elastic distortion tensor $\boldsymbol{U}^e$, which is defined as $\boldsymbol{U}^e = \boldsymbol{U}^{e\parallel} + \boldsymbol{U}^{e\perp}$, would give $\mathbf{curl}\,\boldsymbol{U}^e = \mathbf{curl}\,\boldsymbol{U}^{e\perp}$ which is a unique well-defined solution. The converse procedure, however, does not yield a unique solution. If the latter equality were to be integrated, the solution thus obtained would be exact but only up to a constant gradient term *i.e.* $\boldsymbol{U}^e = \nabla\vec{w} + \boldsymbol{U}^{e\perp}$. Acharya remarked that $\nabla\vec{w}$ is the compatible elastic distortion $\boldsymbol{U}^{e\parallel}$ (seen in section 2.3.2) which is necessary to respect the equilibrium condition on Cauchy stresses as shown in equation (2.6). If a simply connected body containing an arbitrary distribution of dislocations with density $\boldsymbol{\alpha}$ was undergoing an elastic deformation, then compatible elastic distortions would evolve (i) because of the external constraints and (ii) because of the necessity to respect local equilibrium conditions which depend on the new configuration.

Fressengeas *et al.* [134] extended the dislocation model of Acharya to account for both dislocations and disclinations. Recall that in the presence of disclinations, the elastic distortion is no longer defined since it is related to the undefined elastic rotation. In this case, Fressengeas *et al.* showed that the dislocation density is associated with the incompatible component of elastic and plastic strain and both compatible and incompatible components of elastic and plastic curvature as in equations (2.98) and (2.99).

Reconsidering the simply connected body with an arbitrary distribution of dislocations and disclinations shown in figure 2.35, each defect is associated with a non-zero

local compatible (shown in colored || signs) and incompatible elastic strain and curvature fields. In figure 2.36(a), the dots represent an arbitrary combination of $\boldsymbol{\alpha}$ and $\boldsymbol{\theta}$. Conservation of the Burgers and Frank's vector is ensured through the net incompatibility going to zero. However, the net compatible elastic strains and curvatures may not necessarily be zero. Next, the volume V' is isentropically isolated from the remainder of the body such that the incompatible content and arrangement would remain the same. However, the compatible fields are fully recoverable and in general they would change in order to satisfy equilibrium corresponding to the new isolated configurations as shown by the single apostrophes in figure 2.36(b). Plastic deformation of both volumes would lead to rearrangement and/or nucleation or annihilation of defects in the material changing the defect content in V' to $|\vec{\boldsymbol{b}}| = b_1$ and $|\vec{\boldsymbol{\Omega}}| = \Omega_1$ and in $V - V'$ to $|\vec{\boldsymbol{b}}| = b_2$ and $|\vec{\boldsymbol{\Omega}}| = \Omega_2$, without the loss of generality. The compatible elastic fields would also change in order to respect the equilibrium of the new configuration. These are shown by double apostrophes in the figure 2.36(c). Finally, upon reassembly of the simply connected body, a geometrically necessary incompatibility is generated at the interface whose strength corresponds to $|\vec{\boldsymbol{b}}| = -(b_1 + b_2)$ and $|\vec{\boldsymbol{\Omega}}| = -(\Omega_1 + \Omega_2)$ to ensure the conservation of Burgers and Frank's vectors, respectively. The overall compatible elastic field configuration is again transformed in order to respect the equilibrium in newly reformed simply connected domain. The final configuration of the system is shown in figure 2.36(d). Note that the along with compatible and incompatible elastic fields, the compatible and incompatible plastic fields too may be affected.

2.5 Summary and discussion

This chapter begins by providing a review on the development of the theory of line defects *i.e.* dislocations and disclinations, with special emphasis on disclinations and their connection with crystallography. The static theory of discrete dislocations and
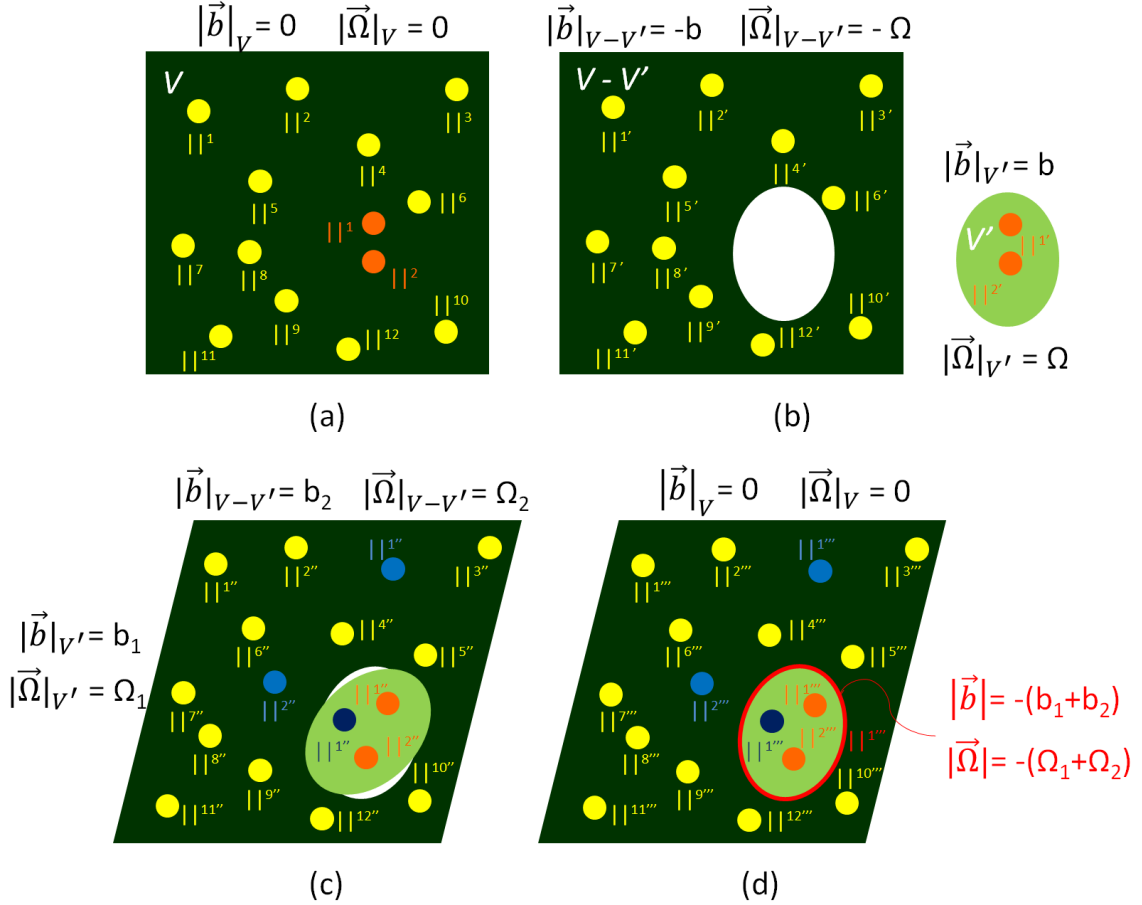
Figure 2.36: Understanding incompatibility as interpreted in the work of Acharya [2] and Fressengeas *et al.* [134]: (a) A body of volume V with net Burgers and Frank's vector equal to zero, (b) contains an element V' having $|\vec{b}| = b$ and $|\vec{b}| = \Omega$, respectively, is isolated from the remainer of the body $V - V'$ ($|\vec{b}| = -b$ and $|\vec{b}| = -\Omega$). These volumes are subjected to the same kind of plastic deformation such that both are transformed into (c) non-fitting elements with $|\vec{b}| = b_1$ and $|\vec{b}| = -\Omega_1$ in . External forces are applied on V' such that it fits into the cavity in $V - V'$. Upon removal of these forces, incompatibilities - shown in red (d) - are generated in order to maintain the continuity of the material. Color code for dots: yellow - original defects in $V - V'$, orange - original defects in V', cyan - new defects in $V - V'$ and navy blue - new defects in V'. $\|$ denotes some combination of compatible elastic strain and curvature fields and the apostrophes represent the changing compatible elastic field configurations.

disclinations as proposed in the work of deWit [95, 96, 97]. The equilibrium solutions and kinematic relationships for geometric fields *i.e.* elastic displacements, distortions, strains, rotations, curvatures, and the Cauchy stresses are derived assuming that equilibrium conditions are satisfied everywhere in the continuous domain, including the

defect lines. deWit's point of view on equilibrium being respected is with respect to a simply connected domain and is fundamentally different from the approaches taken by Volterra [436], Nabarro [294], etc. In the work of Volterra, and Nabarro, equilibrium expressions for the aforementioned geometric and stress fields are proposed outside of the defect core region delimited by a cut-off radius thus making the body multiply connected. The defect core region is assumed to not satisfy the equilibrium conditions. Both these approaches provide the same closed form solutions for the compatible geometric fields and their corresponding Cauchy stresses outside the core of the defects. While the method of Volterra, Nabarro and others is not applicable within the core, deWit's discrete approach too fails within the core region due to the singularity associated at the defect line. Furthermore, incompatible geometric fields are not being accommodated within this framework.

The continuous description of the defects within a simply connected body, which deWit [94, 95, 96, 97] used to propose closed form solutions in the discrete case, forms an appropriate basis to account for these incompatibilities induced in presence of dislocations and disclinations. This continuous approach reinterprets the core of defects in terms of zones of non-zero incompatibility. This associates the polar densities of dislocations and disclinations directly to the defect core. Using this description an incompatible theory of continuously distributed dislocations, and dislocations and disclinations was proposed in the work of Acharya [2] and Fressengeas *et al.* [134], respectively. This chapter recalls the continuous description of compatible and incompatible geometric fields associated with the presence of defects by assuming that equilibrium is satisfied everywhere in the simply connected domain. The derivations of these and connection of geometry of continuous defects with statics and dynamics is provided in the next chapter.

2.6 Conclusion

This chapter highlights the importance of modelling disclinations in nc materials and their relationship with dislocations. To that end, methodologies based on the discrete and continuous representation of these defects are presented. The latter approach which accounts for the incompatibilities in lattice strains and curvatures is found to be the most appropriate to achieve the aim of this thesis, i.e. capturing their role on the local geometry and energy, and the bulk mechanical properties of nc materials. To that end, the stationary form of kinematics, *i.e.* geometry, of these defects is developed by combining the linear theory of continuously distributed defects with the latest interpretation of incompatibilities. This theoretical framework forms the basis for the development of the dynamic theory of continuously distributed defects in the following chapter.

CHAPTER III

MULTI-SCALE STATIC AND DYNAMIC FIELD THEORY OF CONTINUOUSLY DISTRIBUTED DEFECTS

The objective of this chapter is to present the fine scale dynamic field theory of disclinations and dislocations developed in the work of Fressengeas *et al.* [134] and develop its extension to the meso-scale. In the previous chapter, expressions for compatible and incompatible geometric fields of a simply connected domain containing an arbitrary continuous distribution of dislocations and disclinations are derived by taking into account the most recent interpretation of an incompatibility. The derivation assumed that the stresses induced in the presence of defects respect equilibrium conditions everywhere in the domain.

The chapter is organised as follows, in section 3.1, the discussion begins by deriving these equilibrium conditions. Using these, new elastic constitutive laws that account for the incompatibilities are developed based on the requirements of non-negative mechanical dissipation for a body subjected to surface tractions and surface moments. This is followed by a discussion characterizing the proposed elastic constitutive laws. An explicit expression for these laws is proposed in an isotropic case. The elastic laws combined with the geometric fields of continuous defects from the previous chapter form the governing equations of the static field theory of dislocations and disclinations. A newly developed Fourier transform based solution algorithm is presented for the static case. Then, deriving motivation from the work of Fressengeas *et al.* [134], the extension to the dynamic case at fine scale is presented in section 3.3. Recalling these derivations provides a new perspective on the length scale at which the continuum is described in the present work. This is discussed in section

3.4. The length scale dependence of elasticity constants is also discussed along with the interpretation of incompatibilities at the meso-scale. In section 3.5 an extension of the fine scale dynamic field disclination and dislocation mechanics model to the meso-scale is presented. A meso-scale averaging procedure for fine scale field variables is discussed and phenomenological expressions pertaining to this extension are proposed. In section C, the discussion is directed towards understanding the implications, with respect to compatibility of geometric fields, of describing interfaces and junctions formed by these interfaces using a continuous description of dislocations and disclinations as opposed to a discrete representation.

3.1 *Higher order/grade multi-scale elastic constitutive laws*

In crystalline media, internal stresses are generated due to elastic displacements of atoms from their low-energy equilibrium positions. Such deformed configurations may result from (i) a compatible elastic deformation induced from external constraints, and/or (ii) the presence of line crystal defects – dislocations and disclinations – inducing compatible and incompatible fields of elastic strain and curvature. From causality, these compatible and incompatible elastic strains and curvatures are related to the internal stresses through a relationship known as an elastic constitutive law. These elastic fields along with the internal stresses contribute to the thermodynamic state of a material. This is measured in terms of a thermodynamic potential, known as the Helmholtz free energy density.

For a simply connected body undergoing elastic deformation, the classical theory of elasticity states that the Helmholtz free energy density of this system is a function of elastic strains and their work conjugates Cauchy stresses. If elastic curvatures are also generated in the medium, then the couple stress theory [281, 406] suggests that these too contribute to the Helmholtz free energy. Mindlin and Tiersten [281] and Toupin [406] define this contribution in terms of elastic curvatures and their work

conjugate couple stresses.

3.1.1 Elastic constitutive laws for a simply connected body subjected to tractions and moments

The procedure outlined below follows in the footsteps of Mindlin and Tiersten [281]. Consider a defect-free simply connected body of volume V and bounded by a surface $\boldsymbol{S}$. Let $\vec{\boldsymbol{n}}$ be the outward unit normal to the surface. Let a traction vector (force per unit area) $\vec{\boldsymbol{t}}$ and moment $\vec{\boldsymbol{m}}$ (couple per unit area) act on the surface of the body. The body forces and couples are neglected in this discussion.

Now let this body be subjected to elastic deformation. Conservation of mass and balance of momentum impose the following conditions:

$$\frac{d}{dt} \int_V \rho dV = 0 \tag{3.1}$$

$$\frac{d}{dt} \int_V \vec{\boldsymbol{v}} \rho dV = \int_S \vec{\boldsymbol{t}} d\boldsymbol{S} \tag{3.2}$$

where d/dt is the time derivative, $\vec{\boldsymbol{v}}$ is the velocity and ρ is the mass density. Considering the equilibrium of forces and moments on an arbitrary surface in an infinitesimal cubic volume leads to the definition of the asymmetric force $\boldsymbol{\sigma}$ and second order couple $\boldsymbol{M}$ stress tensors:

$$\vec{\boldsymbol{t}} = \boldsymbol{\sigma} \cdot \vec{\boldsymbol{n}} \quad \text{or} \quad t_i = \sigma_{ij} n_j, \quad \text{on } \boldsymbol{S} \tag{3.3}$$

$$\vec{\boldsymbol{m}} = \boldsymbol{M} \cdot \vec{\boldsymbol{n}} \quad \text{or} \quad m_i = M_{ij} n_j, \quad \text{on } \boldsymbol{S} \tag{3.4}$$

Substituting (3.3) for the traction vector equation into the right hand side of (3.2) and applying the divergence theorem (integral of the divergence of a field over the entire volume is equal to the surface integral of the component of this field resolved over the surface bounding this volume) gives,

$$\int_S \vec{\boldsymbol{t}} dS = \int_S \boldsymbol{\sigma} \cdot \vec{\boldsymbol{n}} dS = \int_V \mathbf{div}\, \boldsymbol{\sigma} dV \quad \text{or} \quad \int_S t_i dS = \int_S \sigma_{ij} n_j dS = \int_V \sigma_{ij,j} dV \tag{3.5}$$

Substituting this expression in the momentum balance equation (3.2) then gives

$$\int_V \left(\mathbf{div}\, \boldsymbol{\sigma} - \rho \dot{\vec{\boldsymbol{v}}} \right) dV = \int_V \left(\nabla \cdot \boldsymbol{\sigma} - \rho \dot{\vec{\boldsymbol{v}}} \right) dV = 0 \quad \text{or} \quad \int_V \left(\sigma_{ij,j} - \rho \dot{v}_i \right) dV = 0 \tag{3.6}$$

Assuming that the body is stationary, the following three equilibrium equations on force stresses are obtained,

$$\mathbf{div}\,\boldsymbol{\sigma} = \nabla \cdot \boldsymbol{\sigma} = 0 \quad \text{or} \quad \sigma_{ij,j} = 0 \tag{3.7}$$

In order to obtain the equilibrium equation on couple stresses, the conservation of moment of momentum is revisited,

$$\frac{d}{dt} \int_V \vec{r} \times \vec{v} \rho dV = \int_S \left(\vec{r} \times \vec{t} + \vec{m} \right) dS \quad \text{or}$$
$$\frac{d}{dt} \int_V e_{ijk} r_j v_k \rho dV = \int_S \left(e_{ijk} r_j t_k + m_i \right) dS \tag{3.8}$$

Solving each term of (3.8) individually gives the following equation for the conservation of moment of momentum of a stationary body,

$$\int_V \vec{r} \times \mathbf{div}\,\boldsymbol{\sigma} dV + \int_V \left(\mathbf{div}\,\boldsymbol{M} + 2\mathrm{X}\left(\boldsymbol{\sigma}\right) \right) \rho dV$$
$$= \int_V \vec{r} \times \nabla \cdot \boldsymbol{\sigma} dV + \int_V \left(\nabla \cdot \boldsymbol{M} + 2\mathrm{X}\left(\boldsymbol{\sigma}\right) \right) \rho dV = 0 \quad \text{or}$$
$$\int_V e_{ijk} r_j \sigma_{kl,l} dV + \int_V \left(M_{ij,j} - e_{ijk} \sigma_{jk} \right) \rho dV = 0 \tag{3.9}$$

Substituting the force stress equilibrium equation (3.7) in the above equation provides the equilibrium equations for couple stresses,

$$\mathbf{div}\,\boldsymbol{M} + 2\mathrm{X}\left(\boldsymbol{\sigma}\right) = \nabla \cdot \boldsymbol{M} + 2\mathrm{X}\left(\boldsymbol{\sigma}\right) = 0 \quad \text{or} \quad M_{ij,j} - e_{ijk} \sigma_{jk} = 0 \tag{3.10}$$

Decomposing the asymmetric force stress tensor into its symmetric and anti-symmetric parts,

$$\boldsymbol{\sigma} = \boldsymbol{\sigma}^s + \boldsymbol{\sigma}^a \quad \text{or} \quad \sigma_{ij} = \sigma_{ij}^s + \sigma_{ij}^a = \sigma_{(ij)} + \sigma_{[ij]} \tag{3.11}$$

The superscript "s" and symmetric operation ( ) will be used interchangeably throughout the text (similarly for "a" and [ ]). The anti-symmetric part of the force stresses is defined as,

$$\boldsymbol{\sigma}^a = \{\boldsymbol{X}\left(\boldsymbol{\sigma}\right)\} \quad \text{or} \quad \sigma_{ij}^a = \frac{1}{2} e_{ijk} e_{mnk} \sigma_{mn} \tag{3.12}$$

99

Substituting (3.12) in (3.10) gives,

$$\boldsymbol{\sigma}^a = -\frac{1}{2}\{\textbf{div } \boldsymbol{M}\} \quad \text{or} \quad \sigma_{ij}^a = \frac{1}{2}e_{ijk}M_{kl,l} \tag{3.13}$$

From the equation (3.13), the couple stresses are related to the anti-symmetric component of the force stresses. In the absence of couple stresses, the force stresses are equal to the symmetric Cauchy stresses and the equilibrium (3.7) needs to be balanced only on the Cauchy stresses. However, in the presence of couple stresses, the equilibrium equation (3.7) is satisfied by both symmetric part (Cauchy stress) and the anti-symmetric part of the force stresses.

Equations (3.7) and (3.10) are the governing equations of the couple stress theory [281]. In the present framework, the total displacements are the only DOFs; the rotations being rigid body in nature cannot be considered as explicit DOFs. Therefore the six equilibrium equations and the three total displacements make the combined system of equations overdetermined. A determinate system can be obtained by combining these equilibrium equations through the anti-symmetric part of the force stresses. Substituting equation (3.13) into (3.7) gives,

$$\textbf{div}\left(\boldsymbol{\sigma}^s - \frac{1}{2}\{\textbf{div } \boldsymbol{M}\}\right) = \nabla \cdot \left(\boldsymbol{\sigma}^s - \frac{1}{2}\{\nabla \cdot \boldsymbol{M}\}\right) = 0 \text{ or } \sigma_{ij,j}^s + \frac{1}{2}e_{ijk}M_{kl,lj} = 0 \tag{3.14}$$

Now, consider the balance of the internal energy per unit mass of the body. For a body undergoing elastic deformation, the second law of thermodynamics requires that the mechanical power dissipated is equal to zero *i.e.* the stored free energy is equal to the external work done on surfaces

$$D = \int_S \left(\vec{v} \cdot \vec{t} + \dot{\vec{\omega}} \cdot \vec{m}\right) dS - \int_V \dot{\psi} dV = 0 \text{ or } \int_S \left(v_i t_i + \dot{\omega}_i m_i\right) dS - \int_V \dot{\psi} dV = 0 \tag{3.15}$$

where D is the dissipation and ψ is the Helmholtz free energy density. From equations (3.3) and (3.4),

$$D = \int_S \left(\vec{v} \cdot \boldsymbol{\sigma} \cdot \vec{n} + \dot{\vec{\omega}} \cdot \boldsymbol{M} \cdot \vec{n}\right) dS - \int_V \dot{\psi} dV = 0 \text{ or}$$

$$D = \int_S \left(v_i \sigma_{ij} n_j + \dot{\omega}_i M_{ij} n_j \right) dS - \int_V \dot{\psi} dV = 0 \tag{3.16}$$

Applying the divergence theorem yields,

$$D = \int_V \left(\mathbf{grad}\, \vec{v} : \boldsymbol{\sigma} + \vec{v}^t \cdot \mathbf{div}\, \boldsymbol{\sigma} + \mathbf{grad}\, \dot{\vec{\omega}} : \boldsymbol{M} + \dot{\vec{\omega}} \cdot \mathbf{div}\, \boldsymbol{M} \right) dV - \int_V \dot{\psi} dV$$

$$= \int_V \left(\nabla \vec{v} : \boldsymbol{\sigma} + \vec{v}^t \cdot (\nabla \cdot \boldsymbol{\sigma}) + \nabla \dot{\vec{\omega}} : \boldsymbol{M} + \dot{\vec{\omega}} \cdot (\nabla \cdot \boldsymbol{M}) \right) dV - \int_V \dot{\psi} dV = 0$$

$$\text{or } D = \int_V \left(v_{i,j} \sigma_{ij} + v_i \sigma_{ij,j} + \omega_{i,j} : M_{ij} + \dot{\omega}_i M_{ij,j} \right) dV - \int_V \dot{\psi} dV = 0 \tag{3.17}$$

Using relationship (2.39) for rotation vector and tensor, and equilibrium equations (3.7) and (3.10) and performing some algebra gives,

$$D = \int_V \left(\mathbf{grad}\, \vec{v} : \boldsymbol{\sigma} + \mathbf{grad}\, \dot{\vec{\omega}} : \boldsymbol{M} - \dot{\boldsymbol{\omega}} : \boldsymbol{\sigma} \right) dV - \int_V \dot{\psi} dV$$

$$= \int_V \left(\nabla \vec{v} : \boldsymbol{\sigma} + \nabla \dot{\vec{\omega}} : \boldsymbol{M} - \dot{\boldsymbol{\omega}} : \boldsymbol{\sigma} \right) dV - \int_V \dot{\psi} dV = 0$$

$$\text{or } D = \int_V \left(v_{i,j} \sigma_{ij} + \dot{\omega}_{i,j} M_{ij} - \dot{\omega}_{ij} \sigma_{ij} \right) dV - \int_V \dot{\psi} dV = 0 \tag{3.18}$$

The gradient of the velocity vector is equal to the sum of the rate of change of total distortion with respect to time. Then recalling the definition of the distortion as the sum of strain and rotation, the gradient of the velocity vector can be expressed as,

$$\mathbf{grad}\, \vec{v} = \mathbf{grad}\, \dot{\boldsymbol{u}} = \dot{\boldsymbol{U}} = \dot{\boldsymbol{\epsilon}} + \dot{\boldsymbol{\omega}} \tag{3.19}$$

Decomposing the force stress tensor into symmetric and anti-symmetric components gives the following expression for the dissipation,

$$D = \int_V \left(\dot{\boldsymbol{\epsilon}} : \boldsymbol{\sigma}^s + \dot{\boldsymbol{\omega}} : \boldsymbol{\sigma}^a + \mathbf{grad}\, \dot{\vec{\omega}} : \boldsymbol{M} - \dot{\boldsymbol{\omega}} : \boldsymbol{\sigma}^a \right) dV - \int_V \dot{\psi} dV$$

$$= \int_V \left(\dot{\boldsymbol{\epsilon}} : \boldsymbol{\sigma}^s + \dot{\boldsymbol{\omega}} : \boldsymbol{\sigma}^a + \nabla \dot{\vec{\omega}} : \boldsymbol{M} - \dot{\boldsymbol{\omega}} : \boldsymbol{\sigma}^a \right) dV - \int_V \dot{\psi} dV = 0$$

$$\text{or } D = \int_V \left(\dot{\epsilon}_{ij} \sigma_{ij}^s + \dot{\omega}_{ij} \sigma_{ij}^a + \dot{\omega}_{i,j} M_{ij} - \dot{\omega}_{ij} \sigma_{ij}^a \right) dV - \int_V \dot{\psi} dV = 0 \tag{3.20}$$

Note that the inner (double dot) product between a symmetric and anti-symmetric tensor is equal to zero. Therefore, in the products in equation (3.20), the symmetric

total strain rate tensor $\dot{\boldsymbol{\epsilon}}$ extracts only the symmetric part of the force stress tensor $\boldsymbol{\sigma}^s$ (Cauchy stress tensor) and the anti-symmetric total rotation rate tensor $\dot{\boldsymbol{\omega}}$ extracts only the anti-symmetric part of the force stress tensor $\boldsymbol{\sigma}^a$. The gradient of the rotation vector is a deviatoric tensor $i.e.$ $\omega_{i,i} = 0$. Therefore the gradient of rotation extracts only the deviatoric part of the couple stresses $\boldsymbol{M}^D$. Taking the gradient of the total rotation rate as the rate of change of the second order curvature (2.46) $i.e.$ $\dot{\omega}_{i,j} = \dot{\kappa}_{ij}$ and substituting in equation (3.20) gives

$$D = \int_V \left(\dot{\boldsymbol{\epsilon}} : \boldsymbol{\sigma}^s + \dot{\boldsymbol{\kappa}} : \boldsymbol{M}^D \right) dV - \int_V \dot{\psi} dV = 0$$
$$\text{or } D = \int_V \left(\dot{\epsilon}_{ij} \sigma_{ij}^s + \dot{\kappa}_{ij} M_{ij}^D \right) dV - \int_V \dot{\psi} dV = 0 \qquad (3.21)$$

Equation (3.21) represents the balance of mechanical power dissipated for a body in equilibrium under the action of surface tractions and moments. During elastic deformation the defects existing in the medium are motionless; the plastic strain and curvature rates are equal to zero. Therefore, the total strain and curvature rates are equal to their elastic counterparts. Thus, irrespective of the presence or absence of defects, equation (3.21) reduces to,

$$D = \int_V \left(\dot{\boldsymbol{\epsilon}}^e : \boldsymbol{\sigma}^s + \dot{\boldsymbol{\kappa}}^e : \boldsymbol{M}^D \right) dV - \int_V \dot{\psi} dV = 0$$
$$\text{or } D = \int_V \left(\dot{\epsilon}_{ij}^e \sigma_{ij}^s + \dot{\kappa}_{ij}^e M_{ij}^D \right) dV - \int_V \dot{\psi} dV = 0 \qquad (3.22)$$

From here it can be deduced that the Helmholtz free energy density has contributions coming only from the elastic strain and curvature. These contributions include both the compatible and incompatible components.

Note that by accounting for the incompatible components of elastic strain and curvature fields, the dissipation formulation accounts for defect core contributions to free energy of the medium without introducing singularities in the kinematic and stress fields. This formulation is restricted at the fine-scale treatments of defects. At the meso-scale, where inter-granular boundaries are treated as singular interfaces, the

dissipation formulation should account for the discontinuity in kinematic fields across the interface. This is presented in section C.1. As shall be seen in later chapters, for the sake of simplicity of applications at meso-scale, the dissipation framework involving interfaces is abandoned. Meso-scale elastic laws are adopted from the couple stress theory framework [281] without an explicit dissipation formulation.

In order to satisfy the equation (3.22), the free energy density has to be a function of elastic strain and curvature:

$$\psi = \psi\left(\boldsymbol{\epsilon}^e, \tilde{\boldsymbol{\kappa}}^e\right) \quad \text{or} \quad \psi = \psi\left(\epsilon_{ij}^e, \kappa_{ij}^e\right) \tag{3.23}$$

Differentiating equation (3.23) with respect to time gives

$$\dot{\psi} = \frac{\partial \psi}{\partial \boldsymbol{\epsilon}^e} : \dot{\boldsymbol{\epsilon}}^e + \frac{\partial \psi}{\partial \tilde{\boldsymbol{\kappa}}^e} : \dot{\tilde{\boldsymbol{\kappa}}}^e \quad \text{or} \quad \dot{\psi} = \frac{\partial \psi}{\partial \epsilon_{ij}^e} \dot{\epsilon}_{ij}^e + \frac{\partial \psi}{\partial \kappa_{ij}^e} \dot{\kappa}_{ij}^e \tag{3.24}$$

Comparing equations (3.22) with (3.24) gives,

$$\boldsymbol{\sigma}^s = \frac{\partial \psi}{\partial \boldsymbol{\epsilon}^e} \quad \text{or} \quad \sigma_{ij}{}^s = \frac{\partial \psi}{\partial \epsilon_{ij}{}^e} \tag{3.25}$$

$$\boldsymbol{M}^D = \frac{\partial \psi}{\partial \boldsymbol{\kappa}^e} \quad \text{or} \quad M_{ij}^D = \frac{\partial \psi}{\partial \kappa_{ij}{}^e} \tag{3.26}$$

Equations (3.25) and (3.26) represent the symmetric Cauchy components of the force stresses and deviatoric components of the couple stresses, respectively. These expressions from $\boldsymbol{\sigma}^s$ and $\boldsymbol{M}^D$ are valid for compatible or incompatible anisotropic simply connected bodies undergoing elastic deformation. From equilibrium equations (3.7) and (3.10), the entire force and couple stress tensors are necessary to maintain the equilibrium of the medium but only the symmetric Cauchy stress components of force stresses and deviatoric components of couple stresses contribute to the free energy density. Hence the existence of anti-symmetric force stresses and hydro-static couple stresses does not follow from elastic constitutive laws.

Following the usual norm of the literature, constitutive laws are proposed in the case of linear elasticity. A convex quadratic expression of the free energy density

is adopted, similar to that in the work of Kröner [218]. Only the first and second gradients of displacement are taken as dependent state variables for the free energy density. The displacement itself does not enter the expression of free energy density because a rigid body translation of the body should not affect its internal stress state. Similarly, rigid body rotations also do not contribute to the free energy density.

First, the compatible case is considered. When a defect-free simply connected body undergoes elastic deformation, the displacements are single valued everywhere in the body. Equations (3.25) and (3.26) impose that only the symmetric part of the first gradient of displacement and the anti-symmetric part of the second gradient of displacement enter the expression of the free energy density,

$$
\begin{aligned}
\psi = \psi & \left(\frac{1}{2} \left(\mathbf{grad}\ \boldsymbol{u}^{e\|} + \mathrm{grad}^T \boldsymbol{u}^{e\|} \right), \frac{1}{2}\mathbf{grad}\ \left(\mathbf{grad}\ \boldsymbol{u}^{e\|} - \mathrm{grad}^T \boldsymbol{u}^{e\|} \right) \right) \\
& = \psi(u^{e\|}_{(i,j)}, u^{e\|}_{[i,j]k})
\end{aligned}
\tag{3.27}
$$

Its expression is,

$$
\begin{aligned}
\psi = {} & \frac{1}{2} u^{e\|}_{(i,j)} C_{(ij)(kl)} u^{e\|}_{(k,l)} + u^{e\|}_{(i,j)} B_{(ij)[kl]m} u^{e\|}_{[k,l]m} \\
& + u^{e\|}_{[i,j]k} D_{[ij]k(lm)} u^{e\|}_{(l,m)} + \frac{1}{2} u^{e\|}_{[i,j]k} A_{[ij]k[lm]n} u^{e\|}_{[l,m]n}
\end{aligned}
\tag{3.28}
$$

In order to demonstrate the symmetries or anti-symmetries associated with the elasticity tensors, in the following only the Einstein notation is utilized to represent tensors of all orders. The bold-font notation will be taken up later.

The independent state variables in equation (3.28) are the second order symmetric strain tensor and the third order anti-symmetric curvature tensor obtained using equation (2.52). Such a choice intentionally differs from the expression proposed in equation (3.23). As shall be seen later in this section, it allows deducing a relationship between the third order hyper-stresses, *i.e.* the work conjugates of the third order anti-symmetric second gradient of elastic displacements, and the second order couple stresses, *i.e.* the work conjugates of the second order elastic curvatures.

104

The symmetric elastic strain tensor and the anti-symmetric third order curvature tensor impose symmetry and anti-symmetry conditions on the indices of the elasticity tensors $\boldsymbol{A}, \boldsymbol{B}, \boldsymbol{C}$ and $\boldsymbol{D}$. An elastic constant is symmetric over the indices that are shared with elastic strain and anti-symmetric with those shared with the anti-symmetric third order curvature tensor. The quadratic form of the free energy density imposes additional conditions on the elasticity tensors resulting in the following symmetries or anti-symmetries:

$$C_{(ij)(kl)} = C_{(ji)(kl)} = C_{(ij)(lk)} = C_{(kl)(ij)} \tag{3.29}$$

$$A_{[ij]k[lm]n} = -A_{[ji]k[lm]n} = -A_{[ij]k[ml]n} = A_{[ji]k[ml]n} = A_{[lm]n[ij]k} \tag{3.30}$$

$$B_{(ij)[kl]m} = B_{(ji)[kl]m} = -B_{(ij)[lk]m} = -B_{(ji)[lk]m} \tag{3.31}$$

$$D_{[ij]k(lm)} = -D_{[ji]k(lm)} = D_{[ij]k(ml)} = -D_{[ji]k(ml)} \tag{3.32}$$

Taking the partial derivatives of the free energy density, first with respect to the symmetric elastic displacement gradient and second with respect to the third order anti-symmetric second gradient of elastic displacement gives the elastic constitutive laws on Cauchy and couple stresses, respectively,

$$\sigma_{(pq)} = \frac{\partial \psi}{\partial u_{(p,q)}^{e\|}} = C_{(pq)(kl)} u_{(k,l)}^{e\|} + B_{(pq)[kl]m} u_{[k,l]m}^{e\|} + u_{[i,j]k}^{e\|} D_{[ij]k(pq)} \tag{3.33}$$

$$\tilde{M}_{[pq]r} = \frac{\partial \psi}{\partial u_{[p,q]r}^{e\|}} = u_{(i,j)}^{e\|} B_{(ij)[pq]r} + D_{[pq]r(lm)} u_{(l,m)}^{e\|} + A_{[pq]r[lm]n} u_{[l,m]n}^{e\|} \tag{3.34}$$

The tensorial partial derivatives of the free energy density should necessarily be taken with tensors having indices other than i, j, k, l and m. The anti-symmetric part of the second gradient of elastic displacements $u_{[i,j]k}^{e\|}$ is the anti-symmetric third order elastic curvature tensor $\tilde{\kappa}_{[ij]k}^{e\|}$. Therefore the third order anti-symmetric hyper-stress tensor can also be defined as $\tilde{M}_{[pq]r} = \frac{\partial \psi}{\partial \tilde{\kappa}_{[pq]r}^{e\|}}$. Substituting equation (2.51) in this relationship and rearranging the terms gives $-e_{pqs} \tilde{M}_{[pq]r} = \frac{\partial \psi}{\partial \kappa_{sr}^{e\|}}$. On comparison with equation (3.26) a relationship between the second order deviatoric couple stress tensor

and the third order anti-symmetric hyper-stress tensor is established:

$$\boldsymbol{M}^D = 2\boldsymbol{X}\left(\tilde{\boldsymbol{M}}\right) = -\boldsymbol{X} : \tilde{\boldsymbol{M}} \quad \text{or} \quad M_{il} = -e_{ijk}\tilde{M}_{[jk]l} \tag{3.35}$$

$$\tilde{\boldsymbol{M}} = \frac{1}{2}\left\{\boldsymbol{M}^D\right\} \quad \text{or} \quad \tilde{M}_{[ij]k} = -\frac{1}{2}e_{ijl}M_{lk} \tag{3.36}$$

Equations (3.35) and (3.36) are consistent with the assumed relationships proposed in the work of Kröner [218] and the micropolar elasticity model by Eringen [105]. When equation (3.36) is substituted in the equilibrium equation of couple stresses (3.10), the resulting equation corresponds to the form of equilibrium equation proposed by Eringen and Suhubi [110] where the anti-symmetric part of the third order hyper-stress tensor is identified as the first stress moment.

In the sole presence of dislocations within the body, an additional incompatible component of the symmetric elastic distortion contributes to the free energy density along with the compatible elastic distortion and compatible curvature. Thus the internal state variable in the expression for the Helmholtz free energy density corresponding to the symmetric part of the gradient of the elastic displacement is replaced by an elastic distortion having compatible and incompatible components. Furthermore, the anti-symmetric component of the second gradient of elastic displacement remains compatible. The anti-symmetric component of the compatible gradient of elastic displacement is defined as the anti-symmetric component of the compatible elastic distortion. Therefore, the compatible anti-symmetric component of the second gradient of displacement (*i.e.* $u_{i,jk}^{e\|}$) is replaced by the gradient of compatible elastic distortion (*i.e.* $U_{[ij],k}^{e\|}$).

$$\psi = \psi\left(\boldsymbol{U}^{e(\|+\perp)s}, \mathbf{grad}\, \boldsymbol{U}^{e\|a}\right) = \psi\left(U_{(ij)}^{e(\|+\perp)}, U_{[ij],k}^{e\|}\right) \tag{3.37}$$

$$\psi = \frac{1}{2}U_{(ij)}^{e(\|+\perp)}C_{(ij)(kl)}U_{(kl)}^{e(\|+\perp)} + U_{(ij)}^{e(\|+\perp)}B_{(ij)[kl]m}U_{[kl],m}^{e\|}$$

$$+ U_{[ij],k}^{e\|}D_{[ij]k(lm)}U_{(lm)}^{e(\|+\perp)} + \frac{1}{2}U_{[ij],k}^{e\|}A_{[ij]k[lm]n}U_{[lm],n}^{e\|} \tag{3.38}$$

This is the most general form of the quadratic free energy density of a body containing an arbitrary distribution of dislocations. The constitutive relationships

for the Cauchy and third order couple stresses are obtained by taking the partial derivatives with respect to the distortion and its gradient respectively:

$$\sigma_{(pq)} = \frac{\partial \psi}{\partial U_{(pq)}^{e(\|+\perp)}} = C_{(pq)(kl)} U_{(kl)}^{e(\|+\perp)} + B_{(pq)[kl]m} U_{[kl],m}^{e\|} + U_{[ij],k}^{e\|} D_{[ij]k(pq)} \tag{3.39}$$

$$M_{[pq]r} = \frac{\partial \psi}{\partial U_{[pq],r}^{e\|}} = U_{(ij)}^{e(\|+\perp)} B_{(ij)[pq]r} + D_{[pq]r(lm)} U_{(lm)}^{e(\|+\perp)} + A_{[pq]r[lm]n} U_{[lm],n}^{e\|} \tag{3.40}$$

In the presence of both disclinations and dislocations, the curvature has an additional incompatible component along with the compatible component. The elastic distortion is undefined and therefore its symmetric component is replaced with the elastic strain. The elastic strain also has contributions coming from its compatible and incompatible components.

$$\psi = \psi(\boldsymbol{\epsilon}^{e(\|+\perp)s}, \tilde{\boldsymbol{\kappa}}^{e(\|+\perp)a}) = \psi(\epsilon_{(ij)}^{e(\|+\perp)}, \tilde{\kappa}_{[ij]k}^{e(\|+\perp)}) \tag{3.41}$$

$$\psi = \begin{bmatrix} \frac{1}{2} \epsilon_{(ij)}^{e(\|+\perp)} C_{(ij)(kl)} \epsilon_{(kl)}^{e(\|+\perp)} + \epsilon_{(ij)}^{e(\|+\perp)} B_{(ij)[kl]m} \tilde{\kappa}_{[kl]m}^{e(\|+\perp)} \\ + \tilde{\kappa}_{[ij]k}^{e(\|+\perp)} D_{[ij]k(lm)} \epsilon_{(lm)}^{e(\|+\perp)} + \frac{1}{2} \tilde{\kappa}_{[ij]k}^{e(\|+\perp)} A_{[ij]k[lm]n} \tilde{\kappa}_{[lm]n}^{e(\|+\perp)} \end{bmatrix} \tag{3.42}$$

The constitutive relationships are obtained from the expression (3.42) by taking partial derivatives of the elastic energy density with respect to $\epsilon_{(pq)}^{e(\|+\perp)}$ and $\tilde{\kappa}_{[pq]r}^{e(\|+\perp)}$ respectively,

$$\sigma_{(pq)} = \frac{\partial \psi}{\partial \epsilon_{(pq)}^{e(\|+\perp)}} = C_{(pq)(kl)} \epsilon_{(kl)}^{e(\|+\perp)} + B_{(pq)[kl]m} \tilde{\kappa}_{[kl]m}^{e(\|+\perp)} + \tilde{\kappa}_{[ij]k}^{e(\|+\perp)} D_{[ij]k(pq)} \tag{3.43}$$

$$M_{[pq]r} = \frac{\partial \psi}{\partial \tilde{\kappa}_{[pq]r}^{e(\|+\perp)}} = \epsilon_{(ij)}^{e(\|+\perp)} B_{(ij)[pq]r} + D_{[pq]r(lm)} \epsilon_{(lm)}^{e(\|+\perp)} + A_{[pq]r[lm]n} \tilde{\kappa}_{[lm]n}^{e(\|+\perp)} \tag{3.44}$$

Comparing the expressions for the free energy density in the case when no defects, only dislocations, and both dislocations and disclinations are present in the medium, it can be deduced that the order of the incompatibility increases with increasing order of the defects.

The proposed elastic laws can also be formulated in terms of 4th order elasticity tensors. Then the third order elastic curvatures are replaced by the second order

elastic curvatures. The derivations are shown in the appendix B.1.1. The transformed elastic laws are:

$$\boldsymbol{\sigma}^s = \boldsymbol{C} : \boldsymbol{\epsilon}^{e(\|+\perp)} + \boldsymbol{B} : \boldsymbol{\kappa}^{e(\|+\perp)} \quad \text{or} \quad \sigma_{(pq)} = C_{(pq)(kl)}\epsilon^{e(\|+\perp)}_{(kl)} + B_{(pq)nm}\kappa^{e(\|+\perp)}_{nm}$$

$$\boldsymbol{M}^D = \boldsymbol{D} : \boldsymbol{\epsilon}^{e(\|+\perp)} + \boldsymbol{A} : \boldsymbol{\kappa}^{e(\|+\perp)} \quad \text{or} \quad M^D_{sr} = D_{sr(nm)}\epsilon^{e(\|+\perp)}_{nm} + A_{srnm}\kappa^{e(\|+\perp)}_{nm} \quad (3.45)$$

here the 4th order tensors $\boldsymbol{B}$ and $\boldsymbol{D}$ represent a combination of their 5th order counterparts. The free energy density is then given as:

$$\psi = \psi\left(\epsilon^{e(\|+\perp)}_{ij}, \kappa^{e(\|+\perp)}_{ij}\right) = \epsilon^{e(\|+\perp)}_{ij}C_{(ij)(kl)}\epsilon^{e(\|+\perp)}_{kl} + \epsilon^{e(\|+\perp)}_{ij}B_{(ij)kl}\kappa^{e(\|+\perp)}_{kl}$$

$$+\kappa^{e(\|+\perp)}_{ij}D_{ij(kl)}\epsilon^{e(\|+\perp)}_{kl} + \kappa^{e(\|+\perp)}_{ij}A_{ijkl}\kappa^{e(\|+\perp)}_{kl} \quad (3.46)$$

From the above equation, the following relationship between 4th order elasticity tensors $\boldsymbol{B}$ and $\boldsymbol{D}$ can be deduced:

$$B_{(ij)kl} = D_{(kl)ij} \quad (3.47)$$

In the following sections, the 4th and 5th order representations of elasticity tensors $\boldsymbol{B}$ and $\boldsymbol{D}$ will be used interchangeably without further justification.

3.1.2 Scale dependence of higher order elastic constants: non-locality

Cauchy stresses are described in units of Pascals Pa (also N/m^2) and strains are dimensionless. Therefore, the 4th order elasticity tensor $\boldsymbol{C}$ has the same units as Cauchy stress. On the other hand, couple stresses are described in units of N/m and curvatures in $1/m$ which from the constitutive equations implies that the elasticity tensors $\boldsymbol{B}$, $\boldsymbol{D}$ and $\boldsymbol{A}$ are of dimensions N/m, N/m and N, respectively. The elasticity tensors $\boldsymbol{B}$, $\boldsymbol{D}$ and $\boldsymbol{A}$ are more frequently defined in terms of the order of shear modulus and a length scale l such that $\boldsymbol{B} = \alpha_1\mu l$, $\boldsymbol{D} = \alpha_2\mu l$ and $\boldsymbol{A} = \alpha_3\mu l^2$. The distance l is the internal length scale that sets the characteristic dimension of the area over which inhomogeneity of the elastic curvature/strains induces a significant Cauchy/couple stress component. Kröner [218] proposed that such an inhomogeneity occurs within

the core of the defect and therefore proposed to use $l \approx b$ as an estimate for the value. The order of this estimate is in general agreement with those provided elsewhere in the literature; for example, in a recent work [264] on non-locality in Cu, an estimate of $l = 0.5A°$ was provided. For the applications in the upcoming sections, α_1, α_2 and α_3 will be taken as 1 and $l = b$ unless mentioned otherwise.

The origin of the non-locality of elasticity lies in the concurrent presence of disclinations and dislocations in the lattice, as implied by the definition of Burgers vector in equation (2.107). The strong variations of the incompatible elastic curvature tensor within the defected area induce incompatible elastic strains $\boldsymbol{\epsilon}^{e'} = (\boldsymbol{\kappa}^{eT} \times \vec{\boldsymbol{r}})^T$, which combines with the compatible and incompatible elastic strain $\boldsymbol{\epsilon}^e$ arising from the presence of dislocations. Therefore, Cauchy stress components are induced by the variations of elastic curvature in the defect core. The corresponding length scale must be of the order of size of the core region. Therefore, it is expected that, symmetrically the strong variations of the incompatible elastic strain tensor in the core region result in elastic curvatures $\boldsymbol{\kappa}^{e'} = \vec{\boldsymbol{r}} \times \boldsymbol{\epsilon}^e / r^2$ which along with the compatible and incompatible elastic curvature $\boldsymbol{\kappa}^e$ contribute to couple stresses.

3.1.3 Classification of higher order/grade elastic laws

In this part, the elastic constitutive laws developed in the previous subsection are benchmarked with respect to existing elastic constitutive laws. The latter can generally be classified into two groups: i) models based on compatible theory and ii) models based on incompatible theory. The discussion begins with the compatible models.

One of the most widely used compatible models is the classical linear elasticity model (Hooke's law). In this framework, the mechanical response of a body is characterized by the compatible elastic strains and their work conjugates, *i.e.* the Cauchy stresses. The three elastic displacements are taken as the only DOF. Hooke's law is applied to study the macroscopic mechanical response of systems subjected to

traction boundary conditions. At the macroscopic scale, defect inhomogeneities are neglected, and deformation of the body is assumed to be compatible everywhere. The present model reduces to the Hooke's law in the compatible case where no defect is present in the body and the contributions of compatible curvatures to the free energy density are ignored.

In the Cosserat approach [80], the mechanical response is characterized by the elastic strains and second order curvatures and their work conjugates, the Cauchy and couple stresses, respectively. The Cosserat model was initially developed to study the elastic response during bending of beams, torsion of shafts, etc. When the medium is in static equilibrium, the Cosserat model corresponds to the micropolar elasticity model [105]. In this model, both the displacements and rotations are taken as independent DOF. The independent rotations have a compatible component corresponding to the rigid body rotation (the curl of the displacement) and a multi-valued incompatible component corresponding to the local rotation of material points. However, the Cosserat model does not account for the contributions of incompatible elastic strains and compatible elastic curvatures to the elastic energy density. The proposed model goes beyond the Cosserat or micropolar framework by incorporating contributions from both the compatible and incompatible components of the elastic strains and curvatures. In the couple stress model by Mindlin-Tiersten [281] and Toupin [406], the rotations are taken as rigid body rotations and are thus dependent on the displacements. Therefore, only the compatible components of elastic strain and curvature enter the expression of the free energy density. Hence, the present constitutive model reduces to the couple stress model [281, 406] when assuming a defect-free body. A similar form of the free energy density having elastic strains and third order curvature tensors as internal state variables for an infinite medium containing uniformly distributed infinitely long dislocations is proposed by Kröner [218]. However, Kröners model [218] ignores the incompatibility induced in elastic strain in

the presence of dislocations, and it is thus equivalent to the couple stress model. The compatible strain gradient elasticity model proposed by Mindlin and Eshel [280] takes the gradient of compatible elastic strain as an additional state variable along with compatible elastic strain and compatible elastic curvature, and hence faces similar shortcomings as the other compatible models in dealing with line crystal defects.

The generalized micromorphic continuum model [278, 110] postulates that each material point is deformable and has its own finite volume as opposed to the Cosserat model, which assumes that material points can translate or rotate without deforming *i.e.* they are rigid. The material points in a micromorphic continuum are attributed twelve independent DOF: three macro-displacements, three micro-rotations and six micro-deformations (three micro-dilatations and three micro-shears). This model is developed to study the mechanical response of a body containing inhomogeneities such as inclusions. A relative strain tensor $\boldsymbol{\gamma}$ correlates the macro and micro strains of the body. The compatible strains and rotations from the present model can be related to the macro-strains and macro-rotations of the micromorphic model, and the incompatible strains and rotations can be correlated with the micro-strains and micro-rotations. The geometric equations derived in section 2.3.1 for a compatible body are respected everywhere in the micromorphic medium. Incompatible or micro variables are introduced in the presence of defects and are localized within the region where the defect distribution is non-zero. The relative strain tensor which can be decomposed into compatible macro-strains and incompatible micro-strains, corresponds to the compatible and incompatible elastic strains, respectively, of the present model. A similar correlation exists between the macro and micro curvatures in the micromorphic model and the compatible and incompatible curvatures in the present model.

In the micromorphic framework [278, 110], the free energy density is taken as the function of both, relative and macro strains. Such a consideration could induce redundancies since the relative strain has macro-strain as one of its dependent variables.

Table 1 [421] summarizes the constitutive laws proposed in some of the aforementioned compatible linear elasticity models in comparison with those proposed in the present model in absence of defects.

Table 1: Free energy density and elastic laws of linear compatible models

MODEL	ELASTIC ENERGY DENSITY	ELASTIC LAWS AND EQUILIBRIUM EQUATIONS
Hooke's law	$\psi = \psi\left(\boldsymbol{\epsilon}^{e\parallel}\right) = \frac{1}{2}\boldsymbol{\sigma}^s : \boldsymbol{\epsilon}^{e\parallel}$ or $\psi = \psi\left(\epsilon_{ij}^{e\parallel}\right) = \frac{1}{2}\sigma_{ij}^s\epsilon_{ij}^{e\parallel}$	$\boldsymbol{\sigma}^s = \frac{\partial\psi}{\partial\boldsymbol{\epsilon}^{e\parallel}}$ or $\sigma_{ij}^s = \frac{\partial\psi}{\partial\epsilon_{ij}^{e\parallel}}$ $\mathbf{div}\,\boldsymbol{\sigma}^s = \nabla\cdot\boldsymbol{\sigma}^s = 0$ or $\sigma_{ij,j}^s = 0$
Cosserat[80] Micropolar model [105] Couple stress theory [281, 406]	$\psi = \psi\left(\boldsymbol{\epsilon}^{e\parallel}, \boldsymbol{\kappa}^{e\parallel}\right)$ $= \frac{1}{2}\boldsymbol{\sigma}^s : \boldsymbol{\epsilon}^{e\parallel} + \frac{1}{2}\boldsymbol{M^D} : \boldsymbol{\kappa}^{e\parallel}$ or $\psi = \psi\left(\epsilon_{ij}^{e\parallel}, \kappa_{ij}^{e\parallel}\right)$ $= \frac{1}{2}\sigma_{ij}^s\epsilon_{ij}^{e\parallel} + \frac{1}{2}M_{ij}^D\kappa_{ij}^{e\parallel}$ The cross terms are assumed equal to zero	$\boldsymbol{\sigma}^s = \frac{\partial\psi\left(\boldsymbol{\epsilon}^{e\parallel},\boldsymbol{\kappa}^{e\parallel}\right)}{\partial\boldsymbol{\epsilon}^{e\parallel}}$ or $\sigma_{ij}^s = \frac{\partial\psi\left(\epsilon_{ij}^{e\parallel},\kappa_{ij}^{e\parallel}\right)}{\partial\epsilon_{ij}^{e\parallel}}$ $\boldsymbol{M^D} = \frac{\partial\psi\left(\boldsymbol{\epsilon}^{e\parallel},\boldsymbol{\kappa}^{e\parallel}\right)}{\partial\boldsymbol{\kappa}^{e\parallel}}$ or $M_{ij}^D = \frac{\partial\psi\left(\epsilon_{ij}^{e\parallel},\kappa_{ij}^{e\parallel}\right)}{\partial\kappa_{ij}^{e\parallel}}$ $\mathbf{div}\,\boldsymbol{\sigma}^s = \nabla\cdot\boldsymbol{\sigma}^s = 0$ or $\sigma_{ij,j}^s = 0$ $\mathbf{div}\,\boldsymbol{M^D} + 2X(\boldsymbol{\sigma}^a)$ $= \nabla\cdot\boldsymbol{M^D} + 2X(\boldsymbol{\sigma}^a) = 0$ or $M_{ij,j}^D - e_{ijk}\sigma_{jk}^a = 0$
Kröners model [218]	$\psi = \psi\left(\boldsymbol{\epsilon}^{e\parallel}, \tilde{\boldsymbol{\kappa}}^{e\parallel}\right)$ $= \frac{1}{2}\boldsymbol{\sigma^s} : \boldsymbol{\epsilon}^{e\parallel} + \frac{1}{2}\tilde{\boldsymbol{M}} : \tilde{\boldsymbol{\kappa}}^{e\parallel}$ or $\psi = \psi\left(\epsilon_{ij}^{e\parallel}, \tilde{\kappa}_{ijk}^{e\parallel}\right)$ $= \frac{1}{2}\sigma_{ij}^s\epsilon_{ij}^{e\parallel} + \frac{1}{2}\tilde{M}_{[ij]k}\tilde{\kappa}_{[ij]k}^{e\parallel}$ The cross terms are assumed equal to zero	$\boldsymbol{\sigma}^s = \frac{\partial\psi\left(\boldsymbol{\epsilon}^{e\parallel},\tilde{\boldsymbol{\kappa}}^{e\parallel}\right)}{\partial\boldsymbol{\epsilon}^{e\parallel}}$ or $\sigma_{ij}^s = \frac{\partial\psi\left(\epsilon_{ij}^{e\parallel},\tilde{\kappa}_{[ij]k}^{e\parallel}\right)}{\partial\epsilon_{ij}^{e\parallel}}$ $\tilde{\boldsymbol{M}} = \frac{\partial\psi\left(\boldsymbol{\epsilon}^{e\parallel},\boldsymbol{\kappa}^{e\parallel}\right)}{\partial\tilde{\boldsymbol{\kappa}}^{e\parallel}}$ or $\tilde{M}_{[ij]k} = \frac{\partial\psi\left(\epsilon_{ij}^{e\parallel},\tilde{\kappa}_{[ij]k}^{e\parallel}\right)}{\partial\tilde{\kappa}_{ijk}^{e\parallel}}$ $\mathbf{div}\,\boldsymbol{\sigma}^s = \nabla\cdot\boldsymbol{\sigma}^s = 0$ or $\sigma_{ij,j}^s = 0$ $\mathbf{div}\,\boldsymbol{M^D} + 2X(\boldsymbol{\sigma}^a)$ $= \nabla\cdot\boldsymbol{M^D} + 2X(\boldsymbol{\sigma}^a) = 0$ or $M_{ij,j}^D - e_{ijk}\sigma_{jk}^a = 0$
Micromorphic model [278, 110]	$\psi = \psi\left(\boldsymbol{\epsilon}^{e\parallel}, \boldsymbol{\gamma}^{e\parallel}, \boldsymbol{\chi}^{e\parallel}\right)$ $= \frac{1}{2}\boldsymbol{\sigma}^s : \boldsymbol{\epsilon}^{e\parallel} + \frac{1}{2}\boldsymbol{M} : \boldsymbol{\chi}^{e\parallel}$ $+\frac{1}{2}\boldsymbol{\tau} : \boldsymbol{\gamma}^{e\parallel}$	$\boldsymbol{\sigma}^s = \frac{\partial\psi\left(\boldsymbol{\epsilon}^{e\parallel},\boldsymbol{\gamma}^{e\parallel},\boldsymbol{\chi}^{e\parallel}\right)}{\partial\boldsymbol{\epsilon}^{e\parallel}}$ or $\sigma_{ij}^s = \frac{\partial\psi\left(\epsilon_{ij}^{e\parallel},\gamma_{ij}^{e\parallel},\chi_{ijk}^{e\parallel}\right)}{\partial\epsilon_{ij}^{e\parallel}}$; $\boldsymbol{M} = \frac{\partial\psi\left(\boldsymbol{\epsilon}^{e\parallel},\boldsymbol{\gamma}^{e\parallel},\boldsymbol{\chi}^{e\parallel}\right)}{\partial\boldsymbol{\chi}^{e\parallel}}$ or $M_{ijk} = \frac{\partial\psi\left(\epsilon_{ij}^{e\parallel},\gamma_{ij}^{e\parallel},\chi_{ijk}^{e\parallel}\right)}{\partial\chi_{ijk}^{e\parallel}}$;

Continued on next page

Table 1 – *Continued from previous page*

MODEL	ELASTIC ENERGY DENSITY	ELASTIC LAWS AND EQUILIBRIUM EQUATIONS
	or $\psi = \psi\left(\epsilon_{ij}^{e\parallel}, \gamma_{ij}^{e\parallel}, \chi_{ijk}^{e\parallel}\right)$ $= \frac{1}{2}\sigma_{ij}^s\epsilon_{ij}^{e\parallel} + \frac{1}{2}\tau_{ij}^s\gamma_{ij}^{e\parallel}$ $+\frac{1}{2}M_{ijk}\chi_{ijk}^{e\parallel}$ The cross terms are assumed equal to zero	$\boldsymbol{\tau} = \dfrac{\partial\psi\left(\boldsymbol{\epsilon}^{e\parallel},\boldsymbol{\gamma}^{e\parallel},\boldsymbol{\chi}^{e\parallel}\right)}{\partial\boldsymbol{\gamma}^{e\parallel}}$ or $\tau_{ij} = \dfrac{\partial\psi\left(\epsilon_{ij}^{e\parallel},\gamma_{ij}^{e\parallel},\chi_{ijk}^{e\parallel}\right)}{\partial\gamma_{ij}^{e\parallel}}$ $\mathbf{div}\left(\boldsymbol{\sigma}^s + \boldsymbol{\tau}\right) = \nabla\cdot\left(\boldsymbol{\sigma}^s + \boldsymbol{\tau}\right) = 0$ or $\sigma_{ij,j}^s + \tau_{ij,j} = 0$; $\mathbf{div}\,\boldsymbol{M}^D + 2X(\boldsymbol{\tau}^a) = 0$ or $M_{ij,j}^D - e_{ijk}\tau_{jk} = 0$
Proposed model without defects	$\psi = \psi\left(\boldsymbol{\epsilon}^{e\parallel}, \boldsymbol{\kappa}^{e\parallel}\right)$ $= \frac{1}{2}\boldsymbol{\sigma}^s : \boldsymbol{\epsilon}^{e\parallel}$ $+\frac{1}{2}\boldsymbol{M}^D : \boldsymbol{\kappa}^{e\parallel}$ or $\psi = \frac{1}{2}\sigma_{ij}^s\epsilon_{ij}^{e\parallel}$ $+\frac{1}{2}M_{ij}^s\kappa_{ij}^{e\parallel}$	$\boldsymbol{\sigma}^s = \dfrac{\partial\psi\left(\boldsymbol{\epsilon}^{e\parallel},\boldsymbol{\kappa}^{e\parallel}\right)}{\partial\boldsymbol{\epsilon}^{e\parallel}}$ or $\sigma_{ij}^s = \dfrac{\partial\psi\left(\epsilon_{ij}^{e\parallel},\kappa_{ij}^{e\parallel}\right)}{\partial\epsilon_{ij}^{e\parallel}}$ $\boldsymbol{M}^D = \dfrac{\partial\psi\left(\boldsymbol{\epsilon}^{e\parallel},\boldsymbol{\kappa}^{e\parallel}\right)}{\partial\boldsymbol{\kappa}^{e\parallel}}$ or $M_{ij}^D = \dfrac{\partial\psi\left(\epsilon_{ij}^{e\parallel},\kappa_{ij}^{e\parallel}\right)}{\partial\kappa_{ij}^{e\parallel}}$ $\mathbf{div}\,\boldsymbol{\sigma}^s = \nabla\cdot\boldsymbol{\sigma}^s = 0$ or $\sigma_{ij,j}^s = 0$ $\mathbf{div}\,\boldsymbol{M}^D + 2X(\boldsymbol{\sigma}^a)$ $= \nabla\cdot\boldsymbol{M^D} + 2X(\boldsymbol{\sigma}^a) = 0$ or $M_{ij,j}^D - e_{ijk}\sigma_{jk}^a = 0$

In the class of incompatible elastic constitutive models, we can find the non-local micropolar elasticity models [107, 108] which derive their motivation from the non-local elasticity theories [219, 106, 109]. Recall that in non-local elasticity, the material points undergo translational motion as in the classical elasticity case, but the Cauchy stresses at a point depend on the elastic strains in the region near that point. The non-local micropolar elasticity models extend this concept to include couple stresses and curvatures. Gradient micropolar elasticity models [231, 232, 237] based on non-local micropolar elasticity [107, 108] introduce higher gradients of the elastic strains

and curvatures and their work conjugates in order to account for the presence of dislocations and disclinations. Strain gradient elasticity models [163, 234, 162, 8, 233, 237] have proposed analytical solutions to the elastic strain and Cauchy stresses in the case when dislocations [163, 234, 162, 8, 233, 237] and disclinations [233, 162] are present in the material. In the incompatible strain gradient elasticity model [233] incompatible elastic strains were introduced as state variables. Second order strain gradient theory [279, 236] has been proposed whereby the elastic strain and its first and second gradients are taken as the dependent variables. The contribution of cross terms associated with compatible and incompatible curvatures to the stress fields is, however, beyond the scope of these strain gradient models. An incompatible micromorphic approach [235] was proposed where the incompatible components of micro strain, relative strain and elastic curvature were taken as state variables. Similar to the compatible micromorphic approach [278, 110], redundancies are introduced while incorporating both the micro strain and the relative strain as state variables.

In yet another approach accounting for the presence of defects, defect density tensors are introduced as direct state variables in the elastic laws [125, 157, 77, 158, 267, 221, 382, 230, 7]. The elastic energy is separated into contributions coming from a compatible part (elastic strains and/or elastic curvatures) and a defect density part (defect energy as a function of the dislocation density). In the elasto-viscoplastic model by Forest *et al.* [125], geometrically necessary and statistically stored dislocation densities, and kinematic hardening variables along with compatible strain and curvature are taken as internal state variables in the expression of the elastic energy. A similar expression of the free energy density was proposed by Gurtin [157] where the elastic strain and geometrically necessary dislocation density are taken as internal state variables. The micro-curl model [19] based on the micromorphic model, takes the macro-strain, relative plastic strain and curl of the plastic micro-deformation (which accounts for the dislocation density) as internal state variables for the free

energy density in the presence of defects. The relative plastic strains and the curl of the plastic micro-deformation set-up the respective micro-stresses and couple stresses. From the definition of geometrically necessary dislocation density in equation (2.60), the curvature and geometrically necessary dislocation density are related and thus a redundancy is induced in considering the explicit contribution of both. Similar arguments can be provided for the micropolar single crystal plasticity model [267], **curl** H^p model [159] and small strain elasto-viscoplastic framework [126]. The present thermo-mechanically consistent framework differs fundamentally from the models incorporating defect densities or plastic strains as internal state variables. Table 2 [421] summarizes some of the prominent elasticity models that account for the presence of defects in the body. The superscripts $\parallel$ and $\perp$ are suppressed when both compatible and incompatible components are present.

Table 2: Free energy density and elastic laws of linear incompatible models

MODEL	ELASTIC ENERGY DENSITY	ELASTIC LAWS AND EQUILIBRIUM EQUATIONS
non-local micropolar elasticity [107, 108]	$\psi = \psi\left(\boldsymbol{\gamma}^e, \boldsymbol{\kappa}^e\right)$ $= \frac{1}{2}\boldsymbol{\sigma}^* : \boldsymbol{\gamma}^e + \frac{1}{2}\boldsymbol{M}^* : \boldsymbol{\kappa}^e$ or $\psi = \psi\left(\gamma_{ij}^e, \kappa_{ij}^e\right)$ $= \frac{1}{2}\sigma_{ij}^* \gamma_{ij}^e + \frac{1}{2}M_{ij}^* \kappa_{ij}^e$	$\boldsymbol{\sigma}^* = \int_{V'} \boldsymbol{\beta}^*(\boldsymbol{r} - \boldsymbol{r}')\boldsymbol{\sigma}(\boldsymbol{r}')dV'$ $\boldsymbol{M}^* = \int_{V'} \boldsymbol{\beta}^*(\boldsymbol{r} - \boldsymbol{r}')\boldsymbol{M}(\boldsymbol{r}')dV'$ $\mathbf{div}\,\boldsymbol{\sigma}^* = \nabla \cdot \boldsymbol{\sigma}^* = 0$ or $\sigma_{ij,j}^* = 0$ $\mathbf{div}\,\boldsymbol{M}^D + 2X(\boldsymbol{\sigma}^*)$ $= \nabla \cdot \boldsymbol{M}^* + 2X(\boldsymbol{\sigma}^*) = 0$ or $M_{ij,j}^* - e_{ijk}\sigma_{jk}^* = 0$
Gradient micropolar elasticity	$\psi = \psi\left(\boldsymbol{\gamma}^e, \boldsymbol{\kappa}^e, \nabla\boldsymbol{\gamma}^e, \nabla\boldsymbol{\kappa}^e\right)$ $= \frac{1}{2}\boldsymbol{\sigma}^* : \boldsymbol{\gamma}^e + \frac{1}{2}\boldsymbol{M}^* : \boldsymbol{\kappa}^e$ $+\frac{1}{2}\boldsymbol{G}^* : \nabla\boldsymbol{\gamma}^e + \frac{1}{2}\boldsymbol{\lambda}^* : \nabla\boldsymbol{\kappa}^e$	$\boldsymbol{\sigma}^* = \int_{V'} \boldsymbol{\beta}^*(\boldsymbol{r} - \boldsymbol{r}')\boldsymbol{\sigma}(\boldsymbol{r}')dV'$ $\boldsymbol{M}^* = \int_{V'} \boldsymbol{\beta}^*(\boldsymbol{r} - \boldsymbol{r}')\boldsymbol{M}(\boldsymbol{r}')dV'$ $\boldsymbol{G}^* = \int_{V'} \boldsymbol{\beta}^*(\boldsymbol{r} - \boldsymbol{r}')\boldsymbol{G}(\boldsymbol{r}')dV'$

Continued on next page

Table 2 – *Continued from previous page*

MODEL	ELASTIC ENERGY DENSITY	ELASTIC LAWS AND EQUILIBRIUM EQUATIONS
[231, 232] [237]	or $\psi = \frac{1}{2}\sigma^*_{ij}\gamma^e_{ij} + \frac{1}{2}M^*_{ij}\kappa^e_{ij}$ $\frac{1}{2}G^*_{ijk}\gamma^e_{ij,k} + \frac{1}{2}\lambda^*_{ijk}\kappa^e_{ij,k}$	$\boldsymbol{\lambda}^* = \int_{V'}\boldsymbol{\beta}^*(\boldsymbol{r}-\boldsymbol{r'})\boldsymbol{\lambda}(\boldsymbol{r'})dV'$ $\mathbf{div}\,\boldsymbol{\sigma}^s - \mathbf{div}\,\mathbf{div}\,\boldsymbol{G}^* = \nabla\cdot\boldsymbol{\sigma}^s - \nabla\cdot\nabla\cdot G^* = 0$ or $\sigma^*_{ij,j} - G^*_{ijk,jk} = 0$ $\mathbf{div}\,(\boldsymbol{M}^* - \mathbf{div}\,\boldsymbol{\lambda}^*) + 2X(\boldsymbol{\sigma}^* - \mathbf{div}\,\boldsymbol{G}^*)$ $= \nabla\cdot(\boldsymbol{M}^* - \nabla\cdot\boldsymbol{\lambda}^*) + 2X(\boldsymbol{\sigma}^* - \nabla\cdot\boldsymbol{G}^*) = 0$ or $M^*_{ij,j} - \lambda^*_{ijk,jk} - e_{ijk}(\sigma^*_{jk} - G^*_{jkl,l}) = 0$
Second strain gradient elasticity [236]	$\psi = \psi\left(\boldsymbol{\epsilon}^e, \nabla\boldsymbol{\epsilon}^e, \nabla\nabla\boldsymbol{\epsilon}^e\right)$ $= \frac{1}{2}\boldsymbol{\sigma}^s : \boldsymbol{\epsilon}^e + \frac{1}{2}\boldsymbol{M^s} : \nabla\boldsymbol{\epsilon}^e$ $+ \frac{1}{2}\boldsymbol{Y}^s : \nabla\nabla\boldsymbol{\epsilon}^e$ or $\psi = \frac{1}{2}\sigma^s_{ij}\epsilon^e_j + \frac{1}{2}M_{(ij)k}\epsilon^e_{ij,k}$ $+ \frac{1}{2}M_{(ij)kl}\epsilon^e_{ij,kl}$	$\boldsymbol{\sigma}^s = \frac{\partial\psi(\boldsymbol{\epsilon}^e,\mathbf{grad}\,\boldsymbol{\epsilon}^e,\mathbf{grad}\,\mathbf{grad}\,\boldsymbol{\epsilon}^e)}{\partial\boldsymbol{\epsilon}^e}$ $= \frac{\partial\psi(\boldsymbol{\epsilon}^e,\nabla\boldsymbol{\epsilon}^e,\nabla\nabla\boldsymbol{\epsilon}^e)}{\partial\boldsymbol{\epsilon}^e}$ or $\sigma^s_{ij} = \frac{\partial\psi\left(\epsilon^e_{ij},\epsilon^e_{ij,k},\epsilon^e_{ij,kl}\right)}{\partial\epsilon^e_{ij}}$ $\boldsymbol{M}^s = \frac{\partial\psi(\boldsymbol{\epsilon}^e,\mathbf{grad}\,\boldsymbol{\epsilon}^e,\mathbf{grad}\,\mathbf{grad}\,\boldsymbol{\epsilon}^e)}{\partial\mathbf{grad}\,\boldsymbol{\epsilon}^e}$ $= \frac{\partial\psi(\boldsymbol{\epsilon}^e,\nabla\boldsymbol{\epsilon}^e,\nabla\nabla\boldsymbol{\epsilon}^e)}{\partial\mathbf{grad}\,\boldsymbol{\epsilon}^e}$ or $M^s_{ijk} = \frac{\partial\psi\left(\epsilon^e_{ij},\epsilon^e_{ij,k},\epsilon^e_{ij,kl}\right)}{\partial\epsilon^e_{ij,k}}$ $\boldsymbol{Y}^s = \frac{\partial\psi(\boldsymbol{\epsilon}^e,\mathbf{grad}\,\boldsymbol{\epsilon}^e,\mathbf{grad}\,\mathbf{grad}\,\boldsymbol{\epsilon}^e)}{\partial\mathbf{grad}\,\mathbf{grad}\,\boldsymbol{\epsilon}^e}$ $= \frac{\partial\psi(\boldsymbol{\epsilon}^e,\nabla\boldsymbol{\epsilon}^e,\nabla\nabla\boldsymbol{\epsilon}^e)}{\partial\mathbf{grad}\,\mathbf{grad}\,\boldsymbol{\epsilon}^e}$ or $Y^s_{ijkl} = \frac{\partial\psi\left(\epsilon^e_{ij},\epsilon^e_{ij,k},\epsilon^e_{ij,kl}\right)}{\partial\epsilon^e_{ij,kl}}$ $\mathbf{div}\,(\boldsymbol{\sigma}^s - \mathbf{div}\,\boldsymbol{M}^s - \mathbf{div}\,\mathbf{div}\,\boldsymbol{Y}^s)$ $= \nabla\cdot(\boldsymbol{\sigma}^s - \nabla\cdot\boldsymbol{M}^s - \nabla\cdot\nabla\cdot\boldsymbol{Y}^s) = 0$ or $\sigma^s_{ij,j} - M^s_{ijk,jk} - Y^s_{ijkl,jkl} - = 0$
Gradient plasticity model [157]	$\psi = \psi\left(\boldsymbol{\epsilon}^{e\parallel}\right) + \psi\left(\boldsymbol{\alpha}\right)$ $= \frac{1}{2}\boldsymbol{\sigma}^s : \boldsymbol{\epsilon}^{e\parallel} + \boldsymbol{T}^\alpha : \boldsymbol{\alpha}$ or $\psi = \frac{1}{2}\sigma^s_{ij}\epsilon^{e\parallel}_{ij} + T^\alpha_{ij}\alpha_{ij}$	$\boldsymbol{\sigma}^s = \frac{\partial\psi\left(\boldsymbol{\epsilon}^{e\parallel}\right)}{\partial\boldsymbol{\epsilon}^{e\parallel}}$ or $\sigma^s_{ij} = \frac{\partial\psi\left(\epsilon^{e\parallel}_{ij}\right)}{\partial\epsilon^{e\parallel}_{ij}}$ $\boldsymbol{T}^\alpha = \frac{\partial\psi(\boldsymbol{\alpha})}{\partial\boldsymbol{\alpha}} = t^\alpha_\odot\boldsymbol{s}^\alpha\otimes\boldsymbol{s}^\alpha + t^\alpha_\vdash\boldsymbol{l}^\alpha\otimes\boldsymbol{s}^\alpha + \boldsymbol{K}$ or $T^\alpha = t^\alpha_\odot s^\alpha_i s^\alpha_j + t^\alpha_\vdash l^\alpha_i s^\alpha_j + K_{ij}$ $\mathbf{div}\,\boldsymbol{\sigma}^s = \nabla\cdot\boldsymbol{\sigma}^s = 0 \quad$ or $\quad \sigma_{ij,j} = 0$
Elasto-viscoplastic Cosserat	$\psi = \psi\left(\boldsymbol{\epsilon}^{e\parallel}, \boldsymbol{\kappa}^{e\parallel}\right)$ $+ \psi\left(\boldsymbol{\alpha}, \rho^s_S, \rho^s_G\right) = \frac{1}{2}\boldsymbol{\sigma}^s : \boldsymbol{\epsilon}^{e\parallel}$ $+ \boldsymbol{T}^\alpha : \boldsymbol{\alpha} + r^{sl}\rho^s_S + r^{sl}_G\rho^s_G$	$\boldsymbol{\sigma}^s = \frac{\partial\psi\left(\boldsymbol{\epsilon}^{e\parallel}\right)}{\partial\boldsymbol{\epsilon}^{e\parallel}}$ or $\sigma^s_{ij} = \frac{\partial\psi\left(\epsilon^{e\parallel}_{ij}\right)}{\partial\epsilon^{e\parallel}_{ij}}$ $\boldsymbol{T}^\alpha = \frac{\partial\psi(\boldsymbol{\alpha})}{\partial\boldsymbol{\alpha}} = t^\alpha_\odot\boldsymbol{s}^\alpha\otimes\boldsymbol{s}^\alpha + t^\alpha_\vdash\boldsymbol{l}^\alpha\otimes\boldsymbol{s}^\alpha + \boldsymbol{K}$ or $T^\alpha = t^\alpha_\odot s^\alpha_i s^\alpha_j + t^\alpha_\vdash l^\alpha_i s^\alpha_j + K_{ij}$

Table 2 – *Continued from previous page*

MODEL	ELASTIC ENERGY DENSITY	ELASTIC LAWS AND EQUILIBRIUM EQUATIONS
model [125]	or $\psi = \frac{1}{2}\sigma_{ij}^s \epsilon_{ij}^{e\parallel} + T_{ij}^\alpha \alpha_{ij}$ $+ r^{sl}\rho_S^s + r_G^{sl}\rho_G^s$	$r^{sl} = \frac{\partial\psi(\rho_S^s)}{\partial\rho_S^s}; r_G^{sl} = \frac{\partial\psi(\rho_G^s)}{\partial\rho_G^s}; \chi^{sl} = \frac{\partial\psi(\alpha^s)}{\partial\alpha^s}$ **div** $\boldsymbol{\sigma}^s = \nabla \cdot \boldsymbol{\sigma}^s = 0$ or $\sigma_{ij,j} = 0$ **div** $\boldsymbol{M}^D + 2X(\boldsymbol{\sigma}^a)$ $= \nabla \cdot \boldsymbol{M}^D + 2X(\boldsymbol{\sigma}^a) = 0$ or $M_{ij,j}^D - e_{ijk}\sigma_{jk}^a = 0$
Micro-curl model [19]	$\psi = \psi\left(\boldsymbol{\epsilon}^{e\parallel}, \boldsymbol{\epsilon}^p, \boldsymbol{K}^\circ\right)$ $= \frac{1}{2}\boldsymbol{\sigma}^s : \boldsymbol{\epsilon}^{e\parallel} + \frac{1}{2}H_\phi\boldsymbol{\epsilon}^p : \boldsymbol{\epsilon}^p$ $+ \frac{1}{2}A\boldsymbol{K}^\circ : \boldsymbol{K}^\circ$ or $\psi = \frac{1}{2}\sigma_{ij}^s\epsilon_{ij}^{e\parallel} + T_{ij}^\alpha\alpha_{ij}$ $+ r^{sl}\rho_S^s + r_G^{sl}\rho_G^s$	$\boldsymbol{\sigma}^s = \frac{\partial\psi\left(\boldsymbol{\epsilon}^{e\parallel}\right)}{\partial\boldsymbol{\epsilon}^{e\parallel}}$ or $\sigma_{ij}^s = \frac{\partial\psi\left(\epsilon_{ij}^{e\parallel}\right)}{\partial\epsilon_{ij}^{e\parallel}}$ $\boldsymbol{s} = H_\phi\boldsymbol{\epsilon}^p$ or $s_{ij} = H_\phi\epsilon_{ij}^p$ $\boldsymbol{M}^\circ = A\boldsymbol{K}$ or $M_{ij}^\circ = AK_{ij}$ **div** $\boldsymbol{\sigma}^s = \nabla \cdot \boldsymbol{\sigma}^s = 0$ or $\sigma_{ij,j} = 0$ **curl** $\boldsymbol{M}^\circ + \boldsymbol{s} = 0$ or $e_{jkl}M_{il,k} + s_{ij} = 0$
Proposed model with disclinations	$\psi = \psi\left(\boldsymbol{\epsilon}^{e(\parallel+\perp)}, \boldsymbol{\kappa}^{e(\parallel+\perp)}\right)$ $= \frac{1}{2}\boldsymbol{\sigma}^s : \boldsymbol{\epsilon}^{e(\parallel+\perp)}$ $+ \frac{1}{2}\boldsymbol{M}^D : \boldsymbol{\kappa}^{e(\parallel+\perp)}$ or $\psi = \frac{1}{2}\sigma_{ij}^s\epsilon_{ij}^{e(\parallel+\perp)}$ $+ \frac{1}{2}M_{ij}^s\kappa_{ij}^{e(\parallel+\perp)}$	$\boldsymbol{\sigma}^s = \frac{\partial\psi\left(\boldsymbol{\epsilon}^{e(\parallel+\perp)}, \boldsymbol{\kappa}^{e(\parallel+\perp)}\right)}{\partial\boldsymbol{\epsilon}^{e(\parallel+\perp)}}$ or $\sigma_{ij}^s = \frac{\partial\psi\left(\epsilon_{ij}^{e(\parallel+\perp)}, \kappa_{ij}^{e(\parallel+\perp)}\right)}{\partial\epsilon_{ij}^{e(\parallel+\perp)}}$ $\boldsymbol{M}^D = \frac{\partial\psi\left(\boldsymbol{\epsilon}^{e(\parallel+\perp)}, \boldsymbol{\kappa}^{e(\parallel+\perp)}\right)}{\partial\boldsymbol{\kappa}^{e(\parallel+\perp)}}$ or $M_{ij}^D = \frac{\partial\psi\left(\epsilon_{ij}^{e(\parallel+\perp)}, \kappa_{ij}^{e(\parallel+\perp)}\right)}{\partial\kappa_{ij}^{e(\parallel+\perp)}}$ **div** $\boldsymbol{\sigma}^s = \nabla \cdot \boldsymbol{\sigma}^s = 0$ or $\sigma_{ij,j}^s = 0$ **div** $\boldsymbol{M}^D + 2X(\boldsymbol{\sigma}^a)$ $= \nabla \cdot \boldsymbol{M}^D + 2X(\boldsymbol{\sigma}^a) = 0$ or $M_{ij,j}^D - e_{ijk}\sigma_{jk}^a = 0$

Similar to the couple stress [281] and micropolar model [105], the present model allows for the prescription of moments and rotations along with the tractions and

displacements on the surface of a body. In addition, higher order Dirichlet and Neumann boundary conditions can be prescribed on the surface. The present formulation deals with standard boundary conditions which are easier to prescribe as compared to non-standard boundary conditions, such as dislocation slip rates [157].

Therefore, the elastic laws presented in this work can be classified as higher order and higher grade. Note that the higher order here does not hold the same interpretation as that proposed in the work of Forest and Sievert [127] where the order is related to the DOF associated with the medium *i.e.* classical or couple stress continuum (3), Cosserat or micropolar continuum (6) and micromorphic medium (6). The higher order is with respect to the incompatible components of elastic and plastic distortions, strains and curvatures which are not considered in the traditional couple stress theory of Mindlin and Tiersten [281]. In the present work, classification with respect to DOF is deemed as a rank based classification and in that context the present model has the same rank as the couple stress continuum. The governing equilibrium equations of the medium are the same as the couple stress theory. The proposed elastic laws are higher grade with respect to the gradients of displacement that can be prescribed; in the present work these are limited to the second derivative of displacement.

3.1.4 Isotropic case - elasticity tensors and constitutive relationships

In the following, the focus is on the mathematical formulation of the elastic constitutive laws in the special case of isotropy. Such laws have also been proposed in the work of Lazar [230]. The ensuing study is performed on a body subjected to surface tractions and moments. First, the expressions of elasticity tensors $\boldsymbol{A}$, $\boldsymbol{B}$, $\boldsymbol{C}$ and $\boldsymbol{D}$ are developed in an isotropic case. Then, the final expressions of the elastic laws for compatible and incompatible deformation of an isotropic body containing dislocations and disclinations are derived.

An isotropic tensor is defined as a tensor which has the same components in all

orthogonally rotated coordinate systems [230, 364, 226]. A general n^{th} order elasticity tensor has 3^n non-zero independent terms. However, in the isotropic case there is a significant reduction in the number of non-zero independent terms because of the various associated symmetries. The procedure to obtain an expression for an nth order isotropic tensor presented in the work of Suiker and Chang [385] is briefly reviewed here. These authors begin by first defining a formal orthogonal invariant polynomial function [192]. A homogeneous polynomial function $T\left(\boldsymbol{u^{(1)}}, \boldsymbol{u^{(2)}}, ..., \boldsymbol{u^{(N)}}\right)$ of N vectors $\boldsymbol{u^{(N)}}$ with $N \geqslant 1$, has a formal orthogonal invariant form when it can be expressed as a linear combination of the independent basic invariants of the orthogonal group consisting of the scalar products $\boldsymbol{u^{(i)}}.\boldsymbol{u^{(j)}}$ and $\det\left[\boldsymbol{u^{(i)}}\boldsymbol{u^{(j)}}...\boldsymbol{u^{(k)}}\right]$. The even formal orthogonal invariant polynomial functions can be expressed as a combination of scalar products, and the odd formal orthogonal invariant polynomial functions as the sum of $\det\left[\boldsymbol{u^{(p)}}\boldsymbol{u^{(q)}}...\boldsymbol{u^{(r)}}\right] T^*$ terms, where the vectors $\boldsymbol{u^{(p)}}, \boldsymbol{u^{(q)}}, ..., \boldsymbol{u^{(r)}}$ belong to the vector space $\boldsymbol{u^{(1)}}, \boldsymbol{u^{(2)}}, ..., \boldsymbol{u^{(N)}}$, and T^* is an even formal orthogonal invariant. In an orthogonal coordinate system the scalar product is the Kronecker delta δ_{ij}

$$\delta_{ij} = \boldsymbol{u^{(i)}} \cdot \boldsymbol{u^{(j)}} \tag{3.48}$$

and the $\det\left[\boldsymbol{u^{(i)}}\boldsymbol{u^{(j)}}...\boldsymbol{u^{(m)}}\right] = e_{ij...k}u_i^{(1)}u_j^{(2)}...u_k^{(m)}$ where, $e_{ij...k}$ is the permutation tensor defined as,

$$e_{ij...k} = \begin{cases} +1 \text{ if ij...k is an even permutation of } 1,2,...,\text{m} \\ -1 \text{ if ij...k is not an even permutation of } 1,2,...,\text{m} \\ 0 \text{ otherwise} \end{cases} \tag{3.49}$$

Suiker and Chang [385] prove that the isotropy of a tensor is a necessary and sufficient condition for it to be expressed in terms of a formal orthogonal invariant polynomial function:

$$T(\boldsymbol{u^{(1)}}, \boldsymbol{u^{(2)}}, ..., \boldsymbol{u^{(N)}}) = T_{ij...k}u_i^{(1)}u_j^{(2)}...u_k^{(N)} \tag{3.50}$$

where $T_{ij...k}$ is constructed solely from δ_{ij} and $e_{ij...k}$ for the odd and even isotropic tensors.

In the literature, sometimes along with isotropy an additional symmetry is imposed on the elasticity tensors in the form of centro-symmetry. A material is centro-symmetric when there exists an inversion center in the crystal such that for every point (x, y, z) in a unit cell there exists an indistinguishable point $(-x, -y, -z)$.

In what follows the expressions of the free energy density components for a simply connected body undergoing elastic deformation are presented in an isotropic case, and where pertinent with an additional assumption of centro-symmetry. The physical implications of centro-symmetry shall be highlighted in the ensuing discussion. The expression for the 4th order isotropic tensor $\boldsymbol{C}$ is re-developed using the methodology proposed by Suiker and Chang [385]. The expressions for the 5th order and 6th order isotropic tensors have been presented in other works [230, 192] and are derived in Appendix B.

3.1.4.1 Free energy density contributions coming from terms with 4th order elasticity tensors

From equations (3.28), (3.38), and (3.42), the only 4th order tensor elasticity tensor contributing to the free energy density is $\boldsymbol{C}_{ijkl}$, associated with the elastic strains and the Cauchy stresses. In the most general case, $\boldsymbol{C}_{ijkl}$ has $3^4 = 81$ non-zero coefficients. In the isotropic case, these reduce to just three independent non-zero coefficients.

Following the discussion at the beginning of this section, the relationship between the isotropic tensor $\boldsymbol{C}_{ijkl}$ and the formal orthogonal invariant polynomial function $C\left(\boldsymbol{u}^{(1)}, \boldsymbol{u}^{(2)}, \boldsymbol{u}^{(3)}, \boldsymbol{u}^{(4)}\right)$ associated with vectors $\boldsymbol{u}^{(1)}$, $\boldsymbol{u}^{(2)}$, $\boldsymbol{u}^{(3)}$, $\boldsymbol{u}^{(4)}$ is,

$$C\left(\boldsymbol{u}^{(1)}, \boldsymbol{u}^{(2)}, \boldsymbol{u}^{(3)}, \boldsymbol{u}^{(4)}\right) = C_{ijkl} u_i^{(1)} u_j^{(2)} u_k^{(3)} u_l^{(4)} \tag{3.51}$$

The 4th ordered function $\boldsymbol{C}\left(\boldsymbol{u}^{(1)}, \boldsymbol{u}^{(2)}, \boldsymbol{u}^{(3)}, \boldsymbol{u}^{(4)}\right)$ can be written as a linear combination of the independent basic invariants [385] as;

$$\boldsymbol{C}\left(\boldsymbol{u}^{(1)}, \boldsymbol{u}^{(2)}, \boldsymbol{u}^{(3)}, \boldsymbol{u}^{(4)}\right) = \boldsymbol{C}_1 \boldsymbol{u}^{(1)} \cdot \boldsymbol{u}^{(2)} \boldsymbol{u}^{(3)} \cdot \boldsymbol{u}^{(4)} + \boldsymbol{C}_2 \boldsymbol{u}^{(1)} \cdot \boldsymbol{u}^{(3)} \boldsymbol{u}^{(2)} \cdot \boldsymbol{u}^{(4)}$$
$$+ \boldsymbol{C}_3 \boldsymbol{u}^{(1)} \cdot \boldsymbol{u}^{(4)} \boldsymbol{u}^{(2)} \cdot \boldsymbol{u}^{(3)} \tag{3.52}$$

which from equations (3.48) and (3.50) gives,

$$C_{ijkl} = C_1 \delta_{ij}\delta_{kl} + C_2 \delta_{ik}\delta_{jl} + C_3 \delta_{il}\delta_{jk} \tag{3.53}$$

The elasticity tensor $\boldsymbol{C}$ is decomposed into symmetric and anti-symmetric parts with respect to indices ij and kl,

$$C_{ijkl} = C_{(ij)(kl)} + C_{(ij)[kl]} + C_{[ij](kl)} + C_{[ij](kl)} \tag{3.54}$$

From the symmetries of the quadratic expression of the free energy density for a defect free (3.28), dislocated (3.38) and both dislocated and disclinated (3.42) crystal, the only component of $\boldsymbol{C}$ which contributes to the elastic energy is $C_{(ij)(kl)}$. Using this symmetry over the indices ij and kl, the three independent coefficients in equation (3.53) reduce to only two independent coefficients

$$C_{ijkl} = C_1 \delta_{ij}\delta_{kl} + C_2(\delta_{ik}\delta_{jl} + \delta_{il}\delta_{jk}) \tag{3.55}$$

The constants C_1 and C_2 are identified as the Lamé constants λ and G, respectively.

In the absence of defects, the compatible component of the elastic strain can be defined as the symmetric part of the gradient of elastic displacement. In the presence of dislocations, the elastic strain is defined as the symmetric component of the compatible and incompatible elastic distortion. Therefore, the expression of the free energy density for a defect-free or defected body undergoing elastic deformation is given by

$$\frac{1}{2}\boldsymbol{\epsilon}^e : \boldsymbol{C} : \boldsymbol{\epsilon}^e = \frac{\lambda}{2}(\mathrm{Tr}\,(\boldsymbol{\epsilon}^e))^2 + G\boldsymbol{\epsilon}^e : \boldsymbol{\epsilon}^e \quad \text{or} \quad \frac{1}{2}\epsilon_{ij}^e C_{(ij)(kl)}\epsilon_{kl}^e = \frac{\lambda}{2}(\epsilon_{kk}^e)^2 + G\epsilon_{ij}^e\epsilon_{ij}^e \tag{3.56}$$

The expression of the 5th order isotropic tensor B_{ijklm} is given by equation (B.3). The symmetry of the elastic strain tensor and anti-symmetry of the third order curvature tensor associated with B_{ijklm} impose the symmetry and anti-symmetry on the indices ij and kl respectively. The symmetries on the indices are obtained from equation (3.31) as $B_{(ij)[kl]m}$. Using the expression for isotropic tensor $B_{(ij)[kl]m}$ from the appendix gives:

$$B_{(ij)[kl]m} = \frac{1}{4} \left[\begin{array}{l} B_1^{'} \left(e_{ikl}\delta_{jm} + e_{jkl}\delta_{im} \right) \\[2mm] + B_2^{'} \left(e_{ikm}\delta_{jl} - e_{ilm}\delta_{jk} + e_{jkm}\delta_{il} - e_{jlm}\delta_{ik} \right) \\[2mm] + B_3^{'} e_{klm}\delta_{ij} \end{array} \right] \tag{3.57}$$

Recalling from equation (3.57), the anti-symmetric component of the second gradient of the compatible elastic displacements is the compatible third order anti-symmetric elastic curvature tensor. In the sole presence of dislocations, the latter is defined as the gradient of the compatible elastic rotation. In the presence of both dislocations and disclinations, the third order anti-symmetric elastic curvature has an additional incompatible component. The term involving $\boldsymbol{B}$ in the expression of the free energy density of a defect-free or defected body is,

$$\epsilon_{ij}^e B_{(ij)[kl]m} \tilde{\kappa}_{[kl]m}^e = \frac{1}{4} \left[\begin{array}{l} B_1^{'} \left(e_{ikl}\epsilon_{ij}^e \tilde{\kappa}_{[kl]j}^e + e_{jkl}\epsilon_{ij}^e \tilde{\kappa}_{[kl]i}^e \right) \\[2mm] + B_2^{'} (e_{ikm}\epsilon_{ij}^e \tilde{\kappa}_{[kj]m}^e - e_{ilm}\epsilon_{ij}^e \tilde{\kappa}_{[jl]m}^e \\[2mm] + e_{jkm}\epsilon_{ij}^e \tilde{\kappa}_{[ki]m}^e - e_{jlm}\epsilon_{ij}^e \tilde{\kappa}_{[il]m}^e) \\[2mm] + B_3^{'} e_{klm}\epsilon_{ii}^e \tilde{\kappa}_{[kl]m}^e \end{array} \right] \tag{3.58}$$

After substituting the second order elastic curvature tensor for the third order anti-symmetric elastic curvature tensor by using equation (2.52) and performing some algebra, the simplified expression reads:

$$\epsilon_{ij}^e B_{(ij)[kl]m} \tilde{\kappa}_{[kl]m}^e = \frac{1}{4} \left(-4B_1^{'} \epsilon_{ij}^e \kappa_{ij}^e - 4B_2^{'} \left(\epsilon_{ij}^e \kappa_{ij}^e - \epsilon_{ii}^e \kappa_{jj}^e \right) - 2B_3^{'} \epsilon_{ii}^e \kappa_{jj}^e \right) \tag{3.59}$$

From the equation of dissipation (3.22), the second order curvature tensor is deviatoric. Therefore its trace is equal to zero. Taking $B_1 = -\left(B_1' + B_2'\right)$, the final expression of equation (3.58) is given as

$$\epsilon_{ij}^e B_{(ij)[kl]m} \tilde{\kappa}_{[kl]m}^e = B_1 \epsilon_{ij}^e \kappa_{ij}^e = B_1 \boldsymbol{\epsilon}^e : \boldsymbol{\kappa}^e \tag{3.60}$$

Hence, an independent elastic constant couples the elastic strains and second order elastic curvature in the free energy density term associated with elasticity tensor $\boldsymbol{B}$.

Similar to tensor $\boldsymbol{B}$, the symmetries associated with the indices of tensor $\boldsymbol{D}$ are expressed in equation (B.17) in the Appendix. The term associated with $\boldsymbol{D}$ that contributes to the free energy density can be computed in a similar way to give the following expression

$$\tilde{\kappa}_{[ij]k}^e D_{[ij]k(lm)} \epsilon_{lm}^e = D_1 \kappa_{ij}^e \epsilon_{ij}^e = D_1 \boldsymbol{\kappa}^e : \boldsymbol{\epsilon}^e \tag{3.61}$$

In this contribution, the symmetric elastic strains extract the symmetric part of the asymmetric second order curvature tensor. Of course, the contributions from the cross terms (3.60) and (3.61) are the same, under the condition that the coefficients are equal. Similar expressions for cross-terms have been proposed in the work of Lazar [230].

For the isotropic centro-symmetric case the tensors $\boldsymbol{B}$ and $\boldsymbol{D}$ have an additional symmetry imposed on their indices: $B_{ijklm} = B_{lmkij}$ and $D_{ijklm} = D_{lmkij}$. Substituting this in equation (3.57) reveals that $B_{ijklm}, D_{ijklm} = 0$ *i.e.* the cross term has no contribution to the stresses or the energy in those parts of the material where centro-symmetry is respected. This is in accordance with the work of Kröner [218], Mindlin [278] and Forest *et al.* [125]. It highlights a very important result *i.e.* the cross terms extract only the incompatible components of the elastic strain and curvature. The presence or absence of the contribution of tensors $\boldsymbol{B}$ and $\boldsymbol{D}$ are directly associated with the presence or absence of defects in the medium. The cross term contribution

can therefore be rewritten as,

$$\epsilon^e_{ij} B_{(ij)[kl]m} \tilde{\kappa}^e_{[kl]m} = B_1 \epsilon^{e\perp}_{ij} \tilde{\kappa}^{e\perp}_{ij} = B_1 \boldsymbol{\epsilon}^{e\perp} : \tilde{\boldsymbol{\kappa}}^{e\perp} \tag{3.62}$$

$$\tilde{\kappa}^e_{[ij]k} D_{[ij]k(lm)} \varepsilon^e_{lm} = D_1 \tilde{\kappa}^e_{ij} \epsilon^e_{ij} = D_1 \tilde{\boldsymbol{\kappa}}^{e\perp} : \boldsymbol{\epsilon}^{e\perp} \tag{3.63}$$

3.1.4.3 Free energy density contributions coming from terms with 6th order elasticity tensors

Using the expression of the 6th order isotropic elasticity tensor A_{ijklmn} and its associated anti-symmetries from equation (B.26),

$$
\begin{aligned}
A_{[ij]k[lm]n} &= A'_1 \left(\delta_{il}\delta_{jk}\delta_{mn} + \delta_{ik}\delta_{jm}\delta_{nl} - \delta_{ik}\delta_{jl}\delta_{nm} - \delta_{im}\delta_{jk}\delta_{\ln} \right) \\
&+ A'_2 \left(\delta_{il}\delta_{jn}\delta_{km} + \delta_{in}\delta_{jm}\delta_{kl} - \delta_{im}\delta_{jn}\delta_{kl} - \delta_{in}\delta_{jl}\delta_{km} \right) \\
&+ A'_3 \left(\delta_{il}\delta_{jm}\delta_{kn} - \delta_{im}\delta_{jl}\delta_{kn} \right)
\end{aligned}
\tag{3.64}
$$

The expression of tensor $\boldsymbol{A}$ in equation (3.64) corresponds to the 6th elastic tensor in the work of Lazar, M [230]. Adopting similar arguments from the previous section and taking the third order anti-symmetric elastic curvatures as components of the free energy density term associated with $\boldsymbol{A}$ gives the following expression:

$$
\begin{aligned}
&\frac{1}{2} \tilde{\kappa}^e_{[ij]k} A_{[ij]k[lm]n} \tilde{\kappa}^e_{[lm]n} \\
&= \frac{1}{2} \left(
\begin{array}{l}
A'_1 \left(\tilde{\kappa}^e_{[ij]j} \tilde{\kappa}^e_{[im]m} + \tilde{\kappa}^e_{[ij]i} \tilde{\kappa}^e_{[lj]l} - \tilde{\kappa}^e_{[ij]i} \tilde{\kappa}^e_{[jm]m} - \tilde{\kappa}^e_{[ij]j} \tilde{\kappa}^e_{[li]l} \right) \\
+A'_2 \left(\tilde{\kappa}^e_{[ij]k} \tilde{\kappa}^e_{[ik]j} + \tilde{\kappa}^e_{[ij]k} \tilde{\kappa}^e_{[kj]i} - \tilde{\kappa}^e_{[ij]k} \tilde{\kappa}^e_{[ki]j} - \tilde{\kappa}^e_{[ij]k} \tilde{\kappa}^e_{[jk]i} \right) \\
+A'_3 \left(\tilde{\kappa}^e_{[ij]k} \tilde{\kappa}^e_{[ij]k} - \tilde{\kappa}^e_{[ij]k} \tilde{\kappa}^e_{[ji]k} \right)
\end{array}
\right)
\end{aligned}
\tag{3.65}
$$

Substituting the second order elastic curvature tensor for the third order antisymmetric elastic curvature tensor by using equation (2.52) and performing some algebra gives the final expression,

$$\frac{1}{2} \tilde{\kappa}^e_{[ij]k} A_{[ij]k[lm]n} \tilde{\kappa}^e_{[lm]n} = \frac{1}{2} \left(A_1 \kappa^e_{ij} \kappa^e_{ij} - A_2 \kappa^e_{ji} \kappa^e_{ij} \right) \tag{3.66}$$

where $A_1 = \left(4A'_1 + 4A'_2 + 2A'_3 \right)$ and $A_2 = 4A'_1$. The curvatures are compatible in the absence of disclinations. In the presence of both disclinations and dislocations,

124

an additional incompatible component contributes to the free energy density and the couple stresses. Notice that the 6th order elasticity tensor is non-vanishing in an isotropic centro-symmetric case.

3.1.4.4 Elastic laws

The general form of the free energy density of a defect-free, dislocated or both dislocated and disclinated body undergoing elastic deformation reduces to the following form in an isotropic case,

$$
\begin{aligned}
\psi &= \frac{1}{2}\boldsymbol{\epsilon}^e : \boldsymbol{C} : \boldsymbol{\epsilon}^e + \boldsymbol{\epsilon}^{e\perp} : \boldsymbol{B} : \tilde{\boldsymbol{\kappa}}^{e\perp} + \tilde{\boldsymbol{\kappa}}^{e\perp} : \boldsymbol{D} : \boldsymbol{\epsilon}^{e\perp} + \frac{1}{2}\tilde{\boldsymbol{\kappa}}^e : \boldsymbol{A} : \tilde{\boldsymbol{\kappa}}^e \\
&= \frac{\lambda}{2}(\mathrm{Tr}\,(\boldsymbol{\epsilon}^e))^2 + G\boldsymbol{\epsilon}^e : \boldsymbol{\epsilon}^e + (B_1 + D_1)\boldsymbol{\epsilon}^{e\perp} : \boldsymbol{\kappa}^{e\perp} + \frac{1}{2}\left(A_1\boldsymbol{\kappa}^e : \boldsymbol{\kappa}^e - A_2\boldsymbol{\kappa}^{eT} : \boldsymbol{\kappa}^e\right) \quad \text{or} \\
\psi &= \frac{1}{2}\epsilon^e_{ij}C_{(ij)(kl)}\epsilon^e_{kl} + \epsilon^e_{ij}B_{(ij)[kl]m}\tilde{\kappa}^e_{[kl]m} + \tilde{\kappa}^e_{[ij]k}D_{[ij]k(lm)}\epsilon^e_{(lm)} + \frac{1}{2}\tilde{\kappa}^e_{[ij]k}A_{[ij]k[lm]n}\tilde{\kappa}^e_{[lm]n} \\
&= \frac{\lambda}{2}(\epsilon^e_{kk})^2 + G\epsilon^e_{ij}\epsilon^e_{ij} + (B_1 + D_1)\epsilon^{e\perp}_{ij}\kappa^{e\perp}_{ij} + \frac{1}{2}\left(A_1\kappa^e_{ij}\kappa^e_{ij} - A_2\kappa^e_{ji}\kappa^e_{ij}\right) \quad (3.67)
\end{aligned}
$$

The cross terms show an interesting coupling between the symmetric elastic strain and the deviatoric second order elastic curvature. The symmetric elastic strain can be orthogonally decomposed into hydrostatic and deviatoric components as $\left(\boldsymbol{\epsilon}^{e\perp}\right)^s = \left(\left(\boldsymbol{\epsilon}^{e\perp}\right)^s\right)^H + \left(\left(\boldsymbol{\epsilon}^{e\perp}\right)^s\right)^D$. Similarly, the deviatoric second order elastic curvature can be orthogonally decomposed into symmetric and anti-symmetric components as $\left(\boldsymbol{\kappa}^{e\perp}\right)^D = \left(\left(\boldsymbol{\kappa}^{e\perp}\right)^D\right)^s + \left(\left(\boldsymbol{\kappa}^{e\perp}\right)^D\right)^a$. The inner product between hydrostatic and deviatoric tensors vanishes. Also, the inner product between symmetric and anti-symmetric tensors is also equal to zero. Hence the only components of the elastic strain and curvature that can be extracted from the cross-terms are $\left(\left(\boldsymbol{\epsilon}^{e\perp}\right)^s\right)^D : \left(\left(\tilde{\boldsymbol{\kappa}}^{e\perp}\right)^D\right)^s$. Finally taking $E_1 = B_1 + D_1$, the expression of the free energy density reads as:

$$
\begin{aligned}
\psi &= \frac{\lambda}{2}(\mathrm{Tr}\,(\boldsymbol{\epsilon}^{es}))^2 + G\boldsymbol{\epsilon}^{es\perp} : \boldsymbol{\epsilon}^{es} + E_1\boldsymbol{\epsilon}^{es\perp} : \boldsymbol{\kappa}^{eD\perp} + \frac{1}{2}\left(A_1\boldsymbol{\kappa}^{eD} : \boldsymbol{\kappa}^{eD} - A_2\boldsymbol{\kappa}^{eTD} : \boldsymbol{\kappa}^{eD}\right) \quad \text{or} \\
&= \frac{\lambda}{2}(\epsilon^{es}_{kk})^2 + G\epsilon^{es}_{ij}\epsilon^{es}_{ij} + E_1\kappa^{eD\perp}_{ij}\epsilon^{es\perp}_{ij} + \frac{1}{2}\left(A_1\kappa^{eD}_{ij}\kappa^{eD}_{ij} - A_2\kappa^{eD}_{ji}\kappa^{eD}_{ij}\right) \quad (3.68)
\end{aligned}
$$

The Cauchy and couple stresses are derived from the elastic energy density by taking the partial derivatives with respect to elastic strain and second order elastic

curvature,

$$\boldsymbol{\sigma}^s = \lambda \mathrm{Tr}(\boldsymbol{\epsilon}^e)^s \boldsymbol{I} + 2G(\boldsymbol{\epsilon}^e)^s + E_1\Big(\big(\boldsymbol{\kappa}^{e\perp}\big)^D\Big)^s \qquad (3.69)$$

$$\boldsymbol{M}^D = E_1\big(\big(\boldsymbol{\epsilon}^{e\perp}\big)^s\big)^D + A_1(\boldsymbol{\kappa}^e)^D - A_2\big(\boldsymbol{\kappa}^{eT}\big)^D \qquad (3.70)$$

The contribution from the cross terms is consistent with the symmetry of the Cauchy stresses and the deviatoric nature of the couple stresses. Only one independent non-zero elastic coefficient couples the elastic strains and curvatures and enters the expression of both Cauchy and couple stresses. Along with λ and G, three independent elastic coefficients A_1, A_2 and E_1 contribute to the free energy density. In the isotropic centro-symmetric case, the present model conforms to the micropolar model by Lubarda [257]. In this case, the couple stress tensor becomes anti-symmetric by assuming $A_1 = A_2$. Such a form of the couple stresses is presented in the work of Hadjesfandiari and Dargush [169]. Table 3 [421] lists some of the models that have proposed the expressions of elastic energy in an isotropic case.

Table 3: Isotropic elastic laws for compatible and incompatible media

MODEL	ISOTROPIC ELASTIC LAWS
Hooke's law	$\boldsymbol{\sigma}^s = \lambda \mathrm{Tr}(\boldsymbol{\epsilon}^{e\|s})\boldsymbol{I} + 2G(\boldsymbol{\epsilon}^{e\|s})$ or $\sigma_{ij}^s = \lambda\epsilon_{kk}^{e\|s} + 2G\epsilon_{ij}^{e\|s}$
Kröner's model [218]	$\boldsymbol{\sigma}^s = \lambda \mathrm{Tr}(\boldsymbol{\epsilon}^{e\|s})\boldsymbol{I} + 2G(\boldsymbol{\epsilon}^{e\|s})$ or $\sigma_{ij}^s = \lambda\epsilon_{kk}^{e\|s} + 2G\epsilon_{ij}^{e\|s}$ $\boldsymbol{M}^D = \alpha\mathrm{Tr}(\boldsymbol{K})\boldsymbol{I} + 2\beta(\boldsymbol{K}) + 2\gamma(\boldsymbol{K})^T$ or $M_{ij}^D = \alpha K_{kk} + 2\beta K_{ij} + 2\gamma K_{ji}$
Couple stress model [281]	$\boldsymbol{\sigma}^s = \lambda \mathrm{Tr}(\boldsymbol{\epsilon}^{e\|s})\boldsymbol{I} + 2G(\boldsymbol{\epsilon}^{e\|s})$ or $\sigma_{ij}^s = \lambda\epsilon_{kk}^{e\|s} + 2G\epsilon_{ij}^{e\|s}$ $\boldsymbol{M}^D = 4\alpha(\boldsymbol{\kappa}^{e\|D}) + 2\beta(\boldsymbol{\kappa}^{e\|D})^T$ or $M_{ij}^D = 4\alpha\kappa_{ij}^{e\|D} + 4\beta\kappa_{ji}^{e\|D}$
Cosserat model Forest [124]	$\boldsymbol{\sigma} = \lambda \mathrm{Tr}(\boldsymbol{\epsilon}^{e\|})\boldsymbol{I} + 2G(\boldsymbol{\epsilon}^{e\|s}) + 2G_c(\boldsymbol{\epsilon}^{e\|a})$ or $\sigma_{ij}^s = \lambda\epsilon_{kk}^{e\|s} + 2G\epsilon_{ij}^{e\|s}$

Continued on next page

Table 3 – *Continued from previous page*

MODEL	ELASTIC LAWS AND EQUILIBRIUM EQUATIONS
	$\boldsymbol{M} = \alpha\mathrm{Tr}(\boldsymbol{\kappa}^{e\|})\boldsymbol{I} + 2\beta(\boldsymbol{\kappa}^{e\|s}) + 2\gamma(\boldsymbol{\kappa}^{e\|a})$ or $M_{ij} = \alpha\kappa_{kk}^{e\|} + 2\beta\kappa_{ij}^{e\|s} + 2\gamma\kappa_{ij}^{e\|a}$
Micropolar model [257]	$\boldsymbol{\sigma}^s = \lambda\mathrm{Tr}(\boldsymbol{\epsilon}^{e\|s})\boldsymbol{I} + 2G(\boldsymbol{\epsilon}^{e\|s})$ or $\sigma_{ij}^s = \lambda\epsilon_{kk}^{e\|s} + 2G\epsilon_{ij}^{e\|s}$ $\boldsymbol{M}^D = 4\alpha(\boldsymbol{\kappa}^{e\perp D}) + 2\beta(\boldsymbol{\kappa}^{e\perp D})^T$ or $M_{ij}^D = 4\alpha\kappa_{ij}^{e\perp D} + 4\beta\kappa_{ji}^{e\perp D}$
Proposed model with disclinations	$\boldsymbol{\sigma}^s = \lambda\mathrm{Tr}(\boldsymbol{\epsilon}^{e(\|+\perp)s})\boldsymbol{I} + 2G(\boldsymbol{\epsilon}^{e(\|+\perp)s}) + E_1(\boldsymbol{\kappa}^{e\perp D})$ or $\sigma_{ij}^s = \lambda\epsilon_{kk}^{e(\|+\perp)s} + 2G\epsilon_{ij}^{e(\|+\perp)s} + E_1(\kappa_{ij}^{e\perp D})$ $\boldsymbol{M}^D = E_1(\boldsymbol{\epsilon}^{e\perp s}) + A_1(\boldsymbol{\kappa}^{e(\|+\perp)D}) - A_2(\boldsymbol{\kappa}^{e(\|+\perp)D})^T$ or $M_{ij}^D = E_1(\epsilon_{ij}^{e\perp s}) + A_1(\kappa_{ij}^{e(\|+\perp)D}) - A_2(\kappa_{ji}^{e(\|+\perp)D})^T$

3.1.4.5 Discussion - Isotropy, centro-symmetry and elasticity tensors

In the model by Kröner [218], couple stresses are defined as functions of Nye's curvature tensor which is related to the transpose of the dislocation density tensor and its trace via the equation (2.74). Forming the trace of the dislocation density tensor from equation (2.68) and substituting in equation (2.74) gives the relationship between the contortion tensor, and elastic curvature and strain tensors as $\boldsymbol{K} = \boldsymbol{\kappa}^e - (\mathbf{curl}\,\boldsymbol{\epsilon}^e)^T$. The elastic strain is symmetric and hence the trace of its curl is equal to zero. Moreover, the second order elastic curvature is deviatoric. Hence the trace of the contortion tensor in the equation of couple stresses in Kröner's model [218] in table 3 vanishes. The couple stresses are thus deviatoric in nature and also have a contribution coming from the deviatoric symmetric elastic strains. In the Cosserat model proposed by Forest [124], the rotation is independent of the displacement. Therefore the trace of the rotation tensor may not necessarily be equal to zero. Thus, a non-zero hydrostatic component of the second order elastic curvature is introduced in the expression

of the couple stresses. This feature contradicts the condition imposed by mechanical dissipation on the couple stresses that only the deviatoric component of the latter enters the expression of free energy density.

Another main difference between the proposed model and the other models listed in table 3 arises in the treatment of isotropy. Most of these models propose elastic laws in an isotropic centro-symmetric case. This is perhaps to apply these models to the most commonly known and widely used isotropic centro-symmetric materials which are cubic crystals, particularly face centered cubic and body centered cubic. As shown earlier in this section, centro-symmetry is related to the presence or absence of defects in the body. In presence of line crystal defects, large distortions induced in the vicinity of the defect could result in the breaking of centro-symmetry within the defect core.

Materials that are isotropic but do not possess centro-symmetry are classified as hemitropic, chiral, acentric or non-centro-symmetric materials [230, 364, 226]. Chirality, or non-centrosymemtry, is a characteristic of complex material systems such as bones, composites with helical or screw shaped inclusions [226]. In classical elasticity, chirality does not affect the elastic properties of a material. This is mainly due to the fact that in classical elasticity the stress is related to the strain by a 4th order tensor which is invariant to inversion. In fact, all even ordered tensors remain unaffected by chirality. On the other hand, odd ranked tensors vanish if there is centro-symmetry [281, 278]. They, however, have a non-zero contribution if there is chirality. Higher order higher grade models including the proposed model are capable of dealing with such symmetries.

Elastic constants of a material are dependent on the interatomic cohesive energy. The latter is the energy required to disassemble a crystal into its constituent parts *i.e.* atoms. This energy has a contribution coming from an attractive force in the event that the distance between two atoms is larger than the equilibrium interatomic

distance and a repulsive force in the event that the distance becomes smaller than the equilibrium interatomic distance. In the vicinity of a line crystal defect, the interatomic distances, and hence cohesive forces, are different from those corresponding to equilibrium interatomic spacing of the medium. This creates a local change in the elastic properties of the material. Thus, similar to the inclusions in composites, the defects act as inhomogeneities in an otherwise uniform crystalline matrix. A change in elastic moduli of the bulk material was observed in the study of superlattices of <001>twist GBs by Wolf and Lutsko [462] and Wolf and Kluge [461]. They found that in the vicinity of the GBs the elastic moduli (especially the Youngs modulus and shear modulus) were strongly influenced by the GB structure. While considering the local effect of defects on elastic constants in a linear model would not seem tractable, in a purely mathematical formulation, introducing higher order elastic constants may facilitate the capture of some, if not all, of these local effects.

However, determining the higher (5th and 6th) order material constants is not straightforward. The difficulty particularly arises when incompatibilities are induced in the curvature. Atomistic computations have been performed to obtain the higher order elastic constants in the case of single crystal and polycrystalline Cu [99], β-tin [266] and dysprosium [372]. Ultrasonic testing has been used where the dependence of ultrasonic wave velocity on the stresses in materials is utilized to extract the higher order elastic compliance constants from an Aluminium alloy A5052 [202]. These methods are, however, restricted to the specific case where the elastic energy density is a function of just the strain (or stress in the ultrasonic case). To the author's knowledge, higher order elastics constants associated with the elastic curvature are yet to be determined. The atomistic [99, 266, 372] and ultrasonic [202] techniques have shown promising results and may prove useful in tackling this problem. For the moment, however, there appears to be no clear route to experimentally validate the model.

3.2 Fine scale static field theory of disclinations and dislocations

The higher order elastic constitutive laws proposed in the previous section together with the geometric incompatible theory of defects presented in the previous chapter constitute the state of the art of field theory of disclination and dislocation statics. In this section, a historical perspective leading to the development of this theory is presented along with the governing equations.

3.2.1 Governing equations

The static field theory of disclinations and dislocations can trace its roots back to the non-linear elastic theory of continuously distributed dislocations (ECDD) [456]. The approach involves first laying down the equations for elastic distortions generated in the material in presence of a continuous distribution of dislocations and then connected them with non-linear and anisotropic elasticity to obtain the Cauchy stresses. The expression for distortions obtained was similar to the work of Mura [288] (please refer to equation (2.60)), however the procedure to obtain stresses was fundamentally different. Mura [288], who solved a dynamic problem without body forces, extended the stationary formulation of Burgers [54] by employing a time dependent Green's function to obtain the stress field of a single moving dislocation and then to obtain the result for a continuous distribution of dislocations by superposition. On the other hand, Willis [456], for the stationary case, proposed to solve the field equations associated with the continuous distribution of dislocations. The methodology adopted by Willis gives a direct solution to the stress field of a crystal containing a continuous distribution of dislocations rather than being deduced from superposition as in the work of Mura [288].

Acharya [2] however argued that the ECDD framework is not sufficient to obtain a unique solution for the stress state. As seen in the discussion at the end of the

previous chapter, the argument of Acharya was that solving the field equation for dislocation density, the plastic distortion can be uniquely obtained only up to a gradient of the vector field. Acharya proposed to prescribe the null-space component *i.e.* the compatible plastic strain $\boldsymbol{U}^{p\|}$ by associating it with the classical plastic slip tensor. In order to account for the contribution of incompatible elastic distortions, Acharya [2] proposed an extension to the classical Hooke's law by incorporating both compatible and incompatible components of the elastic distortion into the equation. If curvature incompatibilities are taken into account then the extended ECDD model can be generalized to a static theory of field dislocations and disclinations. The governing equations of the static theory of field dislocations and disclinations are:

$$\mathbf{curl}\,\boldsymbol{\kappa}^{\boldsymbol{p}\perp} = \nabla \times \boldsymbol{\kappa}^{\boldsymbol{p}\perp} = -\boldsymbol{\theta} \quad \text{or} \quad e_{jkl}\kappa^{p\perp}_{il,k} = -\theta_{ij}$$

$$\mathbf{curl}\,\boldsymbol{\epsilon}^{\boldsymbol{p}\perp} + \mathrm{tr}(\boldsymbol{\kappa}^{\boldsymbol{p}(\|+\perp)})\boldsymbol{I} - \boldsymbol{\kappa}^{\boldsymbol{e}(\|+\perp)\boldsymbol{T}} = \nabla \times \boldsymbol{\epsilon}^{\boldsymbol{p}\perp} + \mathrm{tr}(\boldsymbol{\kappa}^{\boldsymbol{p}(\|+\perp)})\boldsymbol{I} - \boldsymbol{\kappa}^{\boldsymbol{e}(\|+\perp)\boldsymbol{T}} = \boldsymbol{\alpha} \quad \text{or}$$

$$e_{jkl}\epsilon^{p\perp}_{il,k} + \kappa^{p(\|+\perp)}_{kk}\delta_{ij} - \kappa^{p(\|+\perp)}_{ji} = -\alpha_{ij}$$

$$\mathbf{div}\left(\boldsymbol{\sigma}^s - \frac{1}{2}\{\mathbf{div}\,\boldsymbol{M}\}\right) = \nabla \cdot \left(\boldsymbol{\sigma}^s - \frac{1}{2}\{\nabla \cdot \boldsymbol{M}\}\right) = 0 \quad \text{or} \quad \sigma^s_{ij,j} + \frac{1}{2}e_{ijk}M_{kl,lj} = 0$$

$$\sigma_{(pq)} = C_{(pq)(kl)}\epsilon^{e(\|+\perp)}_{(kl)} + B_{(pq)[kl]m}\kappa^{e(\|+\perp)}_{[kl]m} + \kappa^{e(\|+\perp)}_{[ij]k}D_{[ij]k(pq)}$$

$$M_{[pq]r} = \epsilon^{e(\|+\perp)}_{(ij)}B_{(ij)[pq]r} + D_{[pq]r(lm)}\epsilon^{e(\|+\perp)}_{(lm)} + A_{[pq]r[lm]n}\kappa^{e(\|+\perp)}_{[lm]n}$$

$$\vec{\boldsymbol{t}} = \boldsymbol{\sigma} \cdot \vec{\boldsymbol{n}} \quad \text{or} \quad t_i = \sigma_{ij}n_j, \quad \text{on } \boldsymbol{S}$$

$$\vec{\boldsymbol{m}} = \boldsymbol{M} \cdot \vec{\boldsymbol{n}} \quad \text{or} \quad m_i = M_{ij}n_j, \quad \text{on } \boldsymbol{S}$$

$$\vec{\boldsymbol{u}}(\vec{\boldsymbol{x}}) = \vec{\boldsymbol{u}}, \quad \text{on } \boldsymbol{S} \tag{3.71}$$

The field disclination and dislocation statics problem involves finding the compatible elastic strain and curvature fields and Cauchy and couple stresses associated with a given dislocation and disclination density fields.

3.3 Fine scale dynamic field theory of disclinations and dislocations

This section presents the fine scale field disclination and dislocation mechanics model (FDDM) proposed in the work of Fressengeas *et al.* [134]. The equations for statics presented in the previous section are extended to the dynamic case to obtain the FDDM model with a slight modification. In that, a disclination source term is added to account for the generation/annihilation of disclinations. In the absence of the source term, the proposed equations are exactly the same as presented in the work of Fressengeas *et al.* [134].

3.3.1 Governing equations

Consider a material surface $\boldsymbol{S}$ with normal $\vec{\boldsymbol{n}}$ and bounded by a closed curve C. Let $\boldsymbol{f}^{\alpha}$ and $\boldsymbol{f}^{\theta}$ be the dislocation and disclination fluxes that measure the rate of inflow of dislocations and disclination lines, respectively, into $\boldsymbol{S}$. Let the dislocations and disclinations with Burgers $\vec{\boldsymbol{b}}$ and Frank's vector $\vec{\boldsymbol{\Omega}}$, respectively, comprise of a line element $\boldsymbol{dx}$ on the curve C. Focusing first on the disclinations, let $\vec{\boldsymbol{V}}^{\theta}$ be their velocity and $\vec{\boldsymbol{\xi}}$ be their line direction. The disclination density tensor is then given as $\boldsymbol{\theta} = \vec{\boldsymbol{\Omega}} \times \vec{\boldsymbol{\xi}}$. If $\boldsymbol{k}^{\theta}$ represents the source term for disclination generation then the conservation of the Frank's vector dictates that the rate of change of the Frank's vector of all disclination lines threading the surface $\boldsymbol{S}$ be equal to the sum of the total disclination flux across curve C and the disclination source term,

$$\frac{d}{dt} \int_S \boldsymbol{\theta} \cdot \vec{\boldsymbol{n}} dS = \int_C \boldsymbol{f}^{\theta} \cdot \boldsymbol{dx} + \int_S \boldsymbol{k}^{\theta} \cdot \vec{\boldsymbol{n}} dS \text{ or}$$
$$\frac{d}{dt} \int_S \theta_{ij} \cdot n_j dS = \int_C f_{ij}^{\theta} \cdot dx_j + \int_S k_{ij}^{\theta} \cdot n_j dS \qquad (3.72)$$

Using Stokes' theorem, the following expression for the rate of disclination density evolution is obtained,

$$\dot{\boldsymbol{\theta}} = \mathbf{curl}\, \boldsymbol{f}^{\theta} + \boldsymbol{k}^{\theta} = \nabla \times \boldsymbol{f}^{\theta} + \boldsymbol{k}^{\theta} \quad \text{or} \quad \theta_{ij} = e_{jkl} f_{il,k}^{\theta} + k_{ij}^{\theta} \qquad (3.73)$$

The rate of inflow of Frank's vector across the surface $d\boldsymbol{S} = \vec{\boldsymbol{\xi}} \times d\boldsymbol{x}$ is given as,

$$\boldsymbol{f} \cdot d\boldsymbol{x} = \vec{\boldsymbol{\Omega}}(\vec{\boldsymbol{V}}^\theta \cdot d\boldsymbol{S}) \quad \text{or} \quad f_{ij}dx_j = \Omega_i V_k^\theta dS_k \tag{3.74}$$

Substituting for $d\boldsymbol{S}$ gives,

$$\begin{aligned}
\boldsymbol{f} \cdot d\boldsymbol{x} &= \vec{\boldsymbol{\Omega}}(\vec{\boldsymbol{V}}^\theta \cdot \vec{\boldsymbol{\xi}} \times d\boldsymbol{x}) &\quad \text{or} \quad& f_{ij}dx_j = \Omega_i V_k^\theta e_{klm}l_l dx_m \\
&= \vec{\boldsymbol{\Omega}}(\vec{\boldsymbol{V}}^\theta \times \vec{\boldsymbol{\xi}} \cdot d\boldsymbol{x}) &\quad \text{or} \quad& f_{ij}dx_j = \Omega_i e_{mkl} V_k^\theta l_l dx_m \\
&= (\vec{\boldsymbol{\Omega}} \otimes \vec{\boldsymbol{V}}^\theta \times \vec{\boldsymbol{\xi}}) \cdot d\boldsymbol{x} &\quad \text{or} \quad& f_{ij}dx_j = |\vec{\boldsymbol{\Omega}}|e_{mkl}V_k^\theta l_l e_i \otimes e_m |d\boldsymbol{x}| \\
&= -(\vec{\boldsymbol{\Omega}} \otimes \vec{\boldsymbol{\xi}} \times \vec{\boldsymbol{V}}^\theta) \cdot d\boldsymbol{x} &\quad \text{or} \quad& f_{ij} = -|\vec{\boldsymbol{\Omega}}|e_{mlk}V_k^\theta l_l e_i \otimes e_j |d\boldsymbol{x}| \tag{3.75}
\end{aligned}$$

Recalling that $\boldsymbol{\theta} = \vec{\boldsymbol{\Omega}} \times \vec{\boldsymbol{\xi}}$ and substituting it in equation (3.75) gives,

$$\boldsymbol{f} = -\boldsymbol{\theta} \times \vec{\boldsymbol{V}}^\theta \quad \text{or} \quad f_{ij} = e_{jkl}\theta_{ik}V_l^\theta \tag{3.76}$$

Then the local polar disclination density evolution is given by,

$$\dot{\boldsymbol{\theta}} = -\mathbf{curl}\,(\boldsymbol{\theta} \times \vec{\boldsymbol{V}}^\theta) + \boldsymbol{k}^\theta = -\nabla \times (\boldsymbol{\theta} \times \vec{\boldsymbol{V}}^\theta) + \boldsymbol{k}^\theta \quad \text{or}$$

$$\dot{\theta}_{ij} = -e_{jkl}e_{lmn}\left(\theta_{im}V_n^\theta\right)_{,k} + k_{ij}^\theta \tag{3.77}$$

Comparing equation (3.77) with the time derivative of equation (2.97) reveals that the plastic curvature rate is given by,

$$\dot{\boldsymbol{\kappa}}^p = \boldsymbol{\theta} \times \vec{\boldsymbol{V}}^\theta \quad \text{or} \quad \dot{\kappa}_{ij}^p = e_{jkl}\theta_{ik}V_l^\theta \tag{3.78}$$

Compatible plastic curvatures $\boldsymbol{\kappa}^{p\|}$ are developed during the transport of defects. These accumulate to form the plastic curvature history in the material [134].

Equation (3.77) is the transport equation on disclination density. Its geometric meaning is that the incompatible component of plastic curvature $\dot{\boldsymbol{\kappa}}^{p\perp}$ incrementally contributes to the disclination density along with other possible sources or sinks. The same expression without the source term is proposed in the work of Mura [289] but the formulation does not distinguish between the compatible and incompatible components and relates the disclination density tensor with gradients of plastic distortion.

This also neglects the fact that elastic and plastic distortions are undefined in the presence of disclinations.

In section 2.2.2 the models suggesting possible sites and sources for disclination nucleation were discussed [344, 179, 340, 301, 302, 334, 303, 424, 362, 166, 164, 165, 337, 336, 333, 338]. It was suggested that the disclination nucleation could partly be aided by local plastic rotations induced due to the accumulation of plastic strain in the vicinity of a disclination. Therefore a component of the source term for disclinations should be associated with plastic slip history, specifically the local rotation induced due to plastic slip. The source term k^θ accounts for all possible sources leading to disclination nucleation as well as annihilation, apart for those arising from the evolution of plastic curvature. In the present work, however the disclination source term k^θ is neglected.

Deriving motivation from the work of Mura [289], Acharya [2] proposed a similar expression as equation (3.77) for transport of polar dislocation densities in terms of the plastic distortion. Since in the presence of both disclinations and dislocations the plastic distortion is undefined, therefore the new modified transport equation for polar dislocations is given by taking the time derivative of equation (2.99),

$$\dot{\boldsymbol{\alpha}} = -\mathbf{curl}\,\dot{\boldsymbol{\epsilon}}^p + \dot{\boldsymbol{\kappa}}^{pT} - \mathrm{tr}(\dot{\boldsymbol{\kappa}}^p)\boldsymbol{I} + \boldsymbol{k}^\alpha = -\nabla \times \dot{\boldsymbol{\epsilon}}^p + \dot{\boldsymbol{\kappa}}^{pT} - \mathrm{tr}(\dot{\boldsymbol{\kappa}}^p)\boldsymbol{I} + \boldsymbol{k}^\alpha \quad \text{or}$$

$$\dot{\alpha}_{ij} = -e_{jkl}\dot{\epsilon}^p_{il,k} + \dot{\kappa}^p_{ji} - \dot{\kappa}^p_{kk}\delta_{ij} + k^\alpha_{ij} \tag{3.79}$$

with the plastic strain rate given as,

$$\dot{\boldsymbol{\epsilon}}^p = \frac{1}{2}\left(\boldsymbol{\alpha} \times \vec{\boldsymbol{V}}^\alpha + (\boldsymbol{\alpha} \times \vec{\boldsymbol{V}}^\alpha)^T\right) \quad \text{or} \quad \dot{\epsilon}^p_{ij} = \frac{1}{2}\left(e_{jkl}\alpha_{ik}V^\alpha_l + e_{ikl}\alpha_{jk}V^\alpha_l\right) \tag{3.80}$$

where $\vec{\boldsymbol{V}}^\alpha$ is the dislocation velocity. Polar dislocation density has an incremental contribution coming from the incompatible plastic strain along with a disclination source term $\boldsymbol{s}^\theta = \dot{\boldsymbol{\kappa}}^{pT} - \mathrm{tr}(\dot{\boldsymbol{\kappa}}^p)\boldsymbol{I}$. The source term $\boldsymbol{s}^\theta$ implies that dislocations are nucleated as a consequence of the transport of disclinations. These could result in

stress relaxations in the vicinity of dislocations [339, 204, 333]. The source term $\boldsymbol{k^\alpha}$ accounts for sources of dislocations besides transport of disclinations.

Similar to compatible plastic curvature $\boldsymbol{\kappa^{p\parallel}}$, compatible plastic strains $\boldsymbol{\epsilon^{p\parallel}}$ are also developed during the transport of defects. These accumulate to form the plastic strain history in the material [2].

In the work of Acharya [2], the dislocation density is associated with individual slip systems in a grain. With such a formulation the field dislocation mechanics model is capable to probe at fine scales ($\approx 10^{-9} - 10^{-7}m$). With the introduction of disclinations, FDDM is capable of probing magnitudes of Frank's vectors leading to displacements at or below the interatomic spacing. Burgers vector causing these displacements can be associated with the DSC lattice which allows lower magnitudes than Burgers vectors of the crystal lattice. These type of lattices are used to describe the structure of GBs within the framework of the dislocation structural unit model [387] as well as the disclination structural unit model [139]. The FDDM model can therefore be combined with these GB representation models to probe the interatomic-scale along with the fine scale through dislocations.

Modeling the transport of dislocations and disclinations requires appropriate constitutive relationships connecting the defect velocities with the stress state. In order to obtain these, the mechanical dissipation formulation is revisited for the case of a simply connected body containing an arbitrary distribution of dislocations and disclinations and undergoing plastic deformation under the action of surface traction and moments. In this case, the second law of thermodynamics dictates that the mechanical power dissipation is positive *i.e.* the net work done to bring the system from state A to B is more than the change in internal energy of the system. In fact the energy stored is used to elastically deform the material; the power dissipated corresponds to the rate of plastic work done. Recalling from the dissipation equation (3.21) and

135

substituting for the internal energy density from (3.23) gives:

$$D = \int_V \left(\dot{\boldsymbol{\epsilon}}^{\boldsymbol{p}} : \boldsymbol{\sigma}^s + \dot{\boldsymbol{\kappa}}^{\boldsymbol{p}} : \boldsymbol{M}^D \right) dV \quad \text{or} \quad D = \int_V \left(\dot{\epsilon}^p_{ij} \sigma^s_{ij} + \dot{\kappa}^p_{ij} M^D_{ij} \right) dV \quad (3.81)$$

Substituting equations (3.78) and (3.80) for plastic curvature and strain rates gives,

$$D = \int_V \left(\frac{1}{2} \left(\boldsymbol{\alpha} \times \vec{\boldsymbol{V}}^{\boldsymbol{\alpha}} + (\boldsymbol{\alpha} \times \vec{\boldsymbol{V}}^{\boldsymbol{\alpha}})^T \right) : \boldsymbol{\sigma}^s + \left(\boldsymbol{\theta} \times \vec{\boldsymbol{V}}^{\boldsymbol{\theta}} \right) : \boldsymbol{M}^D \right) dV \text{ or}$$

$$D = \int_V \left(\frac{1}{2} \left(e_{jkl} \alpha_{ik} V^\alpha_l + e_{ikl} \alpha_{jk} V^\alpha_l \right) \sigma^s_{ij} + e_{jkl} \theta_{ik} V^\theta_l M^D_{ij} \right) dV \quad (3.82)$$

The symmetric force stress or the Cauchy stress tensor extracts only the symmetric component of the plastic strain rate, therefore the dissipation equation can be rewritten as,

$$D = \int_V \left(\left(\boldsymbol{\alpha} \times \vec{\boldsymbol{V}}^{\boldsymbol{\alpha}} \right) : \boldsymbol{\sigma}^s + \left(\boldsymbol{\theta} \times \vec{\boldsymbol{V}}^{\boldsymbol{\theta}} \right) : \boldsymbol{M}^D \right) dV = \int_V \left(\vec{\boldsymbol{F}}^{\boldsymbol{\alpha}} \cdot \vec{\boldsymbol{V}}^{\boldsymbol{\alpha}} + \vec{\boldsymbol{F}}^{\boldsymbol{\theta}} \cdot \vec{\boldsymbol{V}}^{\boldsymbol{\theta}} \right) dV \text{ or}$$

$$D = \int_V \left(e_{jkl} \alpha_{ik} V^\alpha_l \sigma^s_{ij} + e_{jkl} \theta_{ik} V^\theta_l M^D_{ij} \right) dV = \int_V \left(F^\alpha_i V^\alpha_i + F^\theta_j V^\theta_j \right) dV \quad (3.83)$$

where $\vec{\boldsymbol{F}}^{\boldsymbol{\alpha}}$ and $\vec{\boldsymbol{F}}^{\boldsymbol{\theta}}$ are the driving forces for dislocations and disclinations, respectively and are given as,

$$\vec{\boldsymbol{F}}^{\boldsymbol{\alpha}} = -2X(\boldsymbol{\sigma}^s \cdot \boldsymbol{\alpha}) \quad \text{or} \quad F^\alpha_i = e_{ijk} \sigma^s_{lj} \alpha_{lk} \quad (3.84)$$

$$\vec{\boldsymbol{F}}^{\boldsymbol{\theta}} = -2X(\boldsymbol{M}^{\boldsymbol{D}} \cdot \boldsymbol{\theta}) \quad \text{or} \quad F^\theta_i = e_{ijk} M^D_{lj} \theta_{lk} \quad (3.85)$$

Acharya [2] has shown the relationship of $\vec{\boldsymbol{F}}^{\boldsymbol{\alpha}}$ to the Peach-Köhler force driving the dislocations either on their glide or non-glide planes by using the dyadic notation $\boldsymbol{\alpha} = \vec{\boldsymbol{b}} \otimes \vec{\boldsymbol{\xi}}$ to give,

$$\vec{\boldsymbol{F}}^{\boldsymbol{\alpha}} = \boldsymbol{\sigma}^s \cdot \vec{\boldsymbol{b}} \times \vec{\boldsymbol{\xi}} \quad \text{or} \quad F^\alpha_i = e_{jkl} \sigma^s_{ij} b_k \xi_l \quad (3.86)$$

It can be seen that with such a formulation the dislocation density tensors can be directly connected to crystallography; the dislocation density is no longer infinitely large and the Burgers vectors is no longer infinitely small as is usually assumed in the case of a structureless continuum approach [288].

A relationship, similar to $\vec{F}^{\alpha}$, can be obtained for $\vec{F}^{\theta}$ by substituting $\boldsymbol{\theta} = \vec{\Omega} \otimes \vec{\xi}$,

$$\vec{F}^{\theta} = \boldsymbol{M}^{D} \cdot \vec{\Omega} \times \vec{\xi} \quad \text{or} \quad F_i^{\theta} = e_{jkl} M_{ij}^{D} \Omega_k \xi_l \qquad (3.87)$$

$\vec{F}^{\theta}$ can be thought of as an equivalent moment force. Note that the connection between disclination motion and crystallography is not completely understood. However, it is known that movement of disclinations does not have an analogous restriction to particular slip systems. Also, note that since couple stresses are related to only the anti-symmetric component of the force stresses, the Peach-Köhler type relationship still holds in the presence of disclinations showing that the dislocation motion is insensitive to couple stresses. In general, this agrees well with the success of dislocation based plasticity models that are formulated based on the classical Hooke's law, for example, the field dislocation mechanics model [2].

A phenomenological relationship between the defect velocities and the driving forces can be proposed as [2, 134],

$$\vec{F}^{\alpha} = B^{\alpha} \vec{V}^{\alpha} \quad \text{or} \quad F_i^{\alpha} = B^{\alpha} V_l^{\alpha} \qquad (3.88)$$

$$\vec{F}^{\theta} = B^{\theta} \vec{V}^{\theta} \quad \text{or} \quad F_i^{\theta} = B^{\theta} V_l^{\theta} \qquad (3.89)$$

B^{α} and B^{θ} are material parameters which in general are positive definite second order tensors that account for the temperature dependence of the motion of defects and the non-locality induced in presence of defects. For example, it is possible that the mobility of disclinations is dependent on the concentration of polar dislocations in its vicinity, and vice versa, which is accounted for by these tensors. Their physical dimensions are those of stress divided by a length and a velocity. In the present work, B^{α} and B^{θ} are taken as scalar constants. In Equations (3.88) and (3.89) assume that a linear viscous drag may be applicable at relatively high loading rate and would require modification to account for thermally-activated motion of defects which usually occurs at low loading rates.

Finally, the complete set of governing equations for the elasto-plastic FDDM are given as,

$$\boldsymbol{\theta} = -\mathbf{curl}\,\boldsymbol{\kappa}^{p\perp} = -\nabla \times \boldsymbol{\kappa}^{p\perp} \quad \text{or} \quad \theta_{ij} = -e_{jkl}\kappa_{il,k}^{p\perp} \tag{3.90}$$

$$\boldsymbol{\alpha} = -\mathbf{curl}\,\boldsymbol{\epsilon}^{p\perp} + \mathrm{tr}(\boldsymbol{\kappa}^{p(\|+\perp)})\boldsymbol{I} - \boldsymbol{\kappa}^{p(\|+\perp)T} = -\nabla \times \boldsymbol{\epsilon}^{p\perp} + \mathrm{tr}(\boldsymbol{\kappa}^{p(\|+\perp)})\boldsymbol{I} - \boldsymbol{\kappa}^{p(\|+\perp)T}$$

$$\text{or } \alpha_{ij} = -e_{jkl}\epsilon_{il,k}^{p\perp} + \kappa_{kk}^{p(\|+\perp)}\delta_{ij} - \kappa_{ji}^{p(\|+\perp)} \tag{3.91}$$

$$\boldsymbol{\kappa}^{p\|} = \hat{\boldsymbol{\kappa}}^{p\|} \quad \text{or} \quad \kappa_{ij}^{p\|} = \hat{\kappa}_{ij}^{p\|} \tag{3.92}$$

$$\boldsymbol{\epsilon}^{p\|} = \hat{\boldsymbol{\epsilon}}^{p\|} \quad \text{or} \quad \epsilon_{ij}^{p\|} = \hat{\epsilon}_{ij}^{p\|} \tag{3.93}$$

$$\dot{\boldsymbol{\kappa}}^{p} = \boldsymbol{\theta} \times \vec{\boldsymbol{V}}^{\theta} \quad \text{or} \quad \dot{\kappa}_{ij}^{p} = e_{jkl}\theta_{ik}V_{l}^{\theta} \tag{3.94}$$

$$\dot{\boldsymbol{\epsilon}}^{p} = \frac{1}{2}\left(\boldsymbol{\alpha} \times \vec{\boldsymbol{V}}^{\alpha} + (\boldsymbol{\alpha} \times \vec{\boldsymbol{V}}^{\alpha})^{T}\right) \quad \text{or} \quad \dot{\epsilon}_{ij}^{p} = \frac{1}{2}\left(e_{jkl}\alpha_{ik}V_{l}^{\alpha} + e_{ikl}\alpha_{jk}V_{l}^{\alpha}\right) \tag{3.95}$$

$$\mathbf{div}\left(\boldsymbol{\sigma}^{s} - \frac{1}{2}\{\mathbf{div}\,\boldsymbol{M}\}\right) = \nabla \cdot \left(\boldsymbol{\sigma}^{s} - \frac{1}{2}\{\nabla \cdot \boldsymbol{M}\}\right) = 0 \text{ or } \sigma_{ij,j}^{s} + \frac{1}{2}e_{ijk}M_{kl,lj} = 0 \tag{3.96}$$

$$\dot{\boldsymbol{\theta}} = -\mathbf{curl}\,(\boldsymbol{\theta} \times \vec{\boldsymbol{V}}^{\theta}) + \boldsymbol{k}^{\theta} = -\nabla \times (\boldsymbol{\theta} \times \vec{\boldsymbol{V}}^{\theta}) + \boldsymbol{k}^{\theta} \quad \text{or}$$

$$\dot{\theta}_{ij} = -e_{jkl}e_{lmn}\left(\theta_{im}V_{n}^{\theta}\right)_{,k} + k_{ij}^{\theta} \tag{3.97}$$

$$\dot{\boldsymbol{\alpha}} = -\mathbf{curl}\,\dot{\boldsymbol{\epsilon}}^{p} + \dot{\boldsymbol{\kappa}}^{pT} - \mathrm{tr}(\dot{\boldsymbol{\kappa}}^{p})\boldsymbol{I} + \boldsymbol{k}^{\alpha} = -\nabla \times \dot{\boldsymbol{\epsilon}}^{p} + \dot{\boldsymbol{\kappa}}^{pT} - \mathrm{tr}(\dot{\boldsymbol{\kappa}}^{p})\boldsymbol{I} + \boldsymbol{k}^{\alpha} \quad \text{or}$$

$$\dot{\alpha}_{ij} = -e_{jkl}\dot{\epsilon}_{il,k}^{p} + \dot{\kappa}_{ji}^{p} - \dot{\kappa}_{kk}^{p}\delta_{ij} + k_{ij}^{\alpha} \tag{3.98}$$

$$\sigma_{(pq)} = C_{(pq)(kl)}\epsilon_{(kl)}^{e(\|+\perp)} + B_{(pq)[kl]m}\kappa_{[kl]m}^{e(\|+\perp)} + \kappa_{[ij]k}^{e(\|+\perp)}D_{[ij]k(pq)} \tag{3.99}$$

$$M_{[pq]r} = \epsilon_{(ij)}^{e(\|+\perp)}B_{(ij)[pq]r} + D_{[pq]r(lm)}\epsilon_{(lm)}^{e(\|+\perp)} + A_{[pq]r[lm]n}\kappa_{[lm]n}^{e(\|+\perp)} \tag{3.100}$$

$$\vec{\boldsymbol{V}}^{\alpha} = -\frac{2}{B^{\alpha}}X(\boldsymbol{\sigma}^{s} \cdot \boldsymbol{\alpha}) \quad \text{or} \quad V_{i}^{\alpha} = \frac{1}{B^{\alpha}}e_{ijk}\sigma_{lj}^{s}\alpha_{lk} \tag{3.101}$$

$$\vec{\boldsymbol{V}}^{\theta} = -\frac{2}{B^{\theta}}X(\boldsymbol{M}^{D} \cdot \boldsymbol{\theta}) \quad \text{or} \quad V_{i}^{\theta} = \frac{1}{B^{\theta}}e_{ijk}M_{lj}^{D}\theta_{lk} \tag{3.102}$$

with constraints (2.88), (2.89), (2.90), (2.91), (2.93), (2.104) and augmented conditions (2.94), (2.95). Also, recall the relationship between third order and second order curvatures and couple stresses, (2.52) and (3.35).

In the following, the numerical scheme to solve the FDDM problem as presented in the work of Fressengeas *et al.* is briefly discussed. The author would like to highlight that this methodology is used in the FEM simulations (relevant to the present work and briefly discussed in the coming chapters) performed by Dr. Vincent Taupin from

the LEM3 laboratory of CNRS, in France.

In the FDDM model, the unknowns are the displacement $\vec{u}$ fields. Assuming that the disclination and dislocation densities are known at a step in time gives the incompatible component of κ^p from equation (3.90) (using the side conditions mentioned in relation with equation (2.94)), but finding the incompatible part of ϵ^p from equation (3.91) requires knowledge of the history-dependent compatible part of κ^p. Therefore, the algorithm is as follows. Suppose an arbitrary distribution of dislocations and disclinations is known at the initial time and let the compatible part of the plastic curvature and plastic strain tensors arbitrarily set to zero, without loss of generality. Then, the incompatible parts of κ^p and ϵ^p can be determined from equations (3.90) and (3.91) respectively. Then, using the constitutive relations (3.99) and (3.100), the equilibrium equation (3.96) can be solved for the displacement vector fields, which are obtained uniquely, up to a rigid body motion. In addition, the plastic strain rate and curvature rate can be computed from equations (3.94), (3.95) using dislocation and disclination velocities (3.101) and (3.102), respectively. These are utilized to update the plastic strain and curvature. In this algorithm, only the compatible parts of the plastic strain and curvature are needed for the update. Finally, the dislocation and disclination densities are updated using transport equations (3.97) and (3.98), and the procedure can therefore be iterated at the next time step.

The rate form of the governing equations leads to a simpler incremental algorithm, at the expense of an arbitrary initial distribution of crystal defects. Taking the time derivative of equations (3.96), (3.99), and (3.100) the rate equations are:

$$\mathbf{div}\left(\dot{\boldsymbol{\sigma}}^s - \frac{1}{2}\{\mathbf{div}\,\dot{\boldsymbol{M}}\}\right) = \nabla \cdot \left(\dot{\boldsymbol{\sigma}}^s - \frac{1}{2}\{\nabla \cdot \dot{\boldsymbol{M}}\}\right) = 0 \tag{3.103}$$

$$\dot{\boldsymbol{\kappa}}^p = \boldsymbol{\theta} \times \vec{\boldsymbol{V}}^\theta \tag{3.104}$$

$$\dot{\boldsymbol{\epsilon}}^p = \frac{1}{2}\left(\boldsymbol{\alpha} \times \vec{\boldsymbol{V}}^\alpha + (\boldsymbol{\alpha} \times \vec{\boldsymbol{V}}^\alpha)^T\right) \tag{3.105}$$

$$\dot{\boldsymbol{\theta}} = -\mathbf{curl}\,\dot{\boldsymbol{\kappa}}^p + \boldsymbol{k}^\theta = -\nabla \times \dot{\boldsymbol{\kappa}}^p + \boldsymbol{k}^\theta \tag{3.106}$$

$$\dot{\boldsymbol{\alpha}} = -\mathbf{curl}\,\dot{\boldsymbol{\epsilon}}^p + \dot{\boldsymbol{\kappa}}^{pT} - \mathrm{tr}(\dot{\boldsymbol{\kappa}}^p)\boldsymbol{I} + \boldsymbol{k}^{\alpha} = -\nabla \times \dot{\boldsymbol{\epsilon}}^p + \dot{\boldsymbol{\kappa}}^{pT} - \mathrm{tr}(\dot{\boldsymbol{\kappa}}^p)\boldsymbol{I} + \boldsymbol{k}^{\alpha} \quad (3.107)$$

$$\dot{\boldsymbol{\sigma}}^s = \boldsymbol{C} : (\dot{\boldsymbol{\epsilon}} - \dot{\boldsymbol{\epsilon}}^p) + \boldsymbol{B} : (\dot{\boldsymbol{\kappa}} - \dot{\boldsymbol{\kappa}}^p) \quad (3.108)$$

$$\dot{\boldsymbol{M}}^D = \boldsymbol{D} : (\dot{\boldsymbol{\epsilon}} - \dot{\boldsymbol{\epsilon}}^p) + \boldsymbol{A} : (\dot{\boldsymbol{\kappa}} - \dot{\boldsymbol{\kappa}}^p) \quad (3.109)$$

$$\vec{\boldsymbol{V}}^{\alpha} = -\frac{2}{B^{\alpha}} X(\boldsymbol{\sigma}^s \cdot \boldsymbol{\alpha}) \quad (3.110)$$

$$\vec{\boldsymbol{V}}^{\theta} = -\frac{2}{B^{\theta}} X(\boldsymbol{M}^D \cdot \boldsymbol{\theta}) \quad (3.111)$$

Suppose that all fields are known at a given step in time. For the next time step, the unknowns are the material velocity fields $\vec{\boldsymbol{v}}$. They are solutions to the rate of equilibrium problem (3.103), (3.108) and (3.108). In these equations, the plastic strain rate and curvature are obtained from the dislocation/disclination densities and stress/couple-stress tensors by using equations (3.104) and (3.105) and (3.110) and (3.111). Once the dislocation and disclination densities are updated using equations (3.106) and (3.107), the rate of equilibrium procedure can be iterated at the following time step. In this incremental scheme, the determination of the incompatible parts of the plastic curvature and strain arising from an initial distribution of crystal defects is avoided. Hence, in contrast with the first algorithm, there is no continuity requirement on the plastic curvature and strain, but only on their rates. Therefore, the solutions obtained from these two algorithms might turn out to be somewhat different. If the choice is made to also avoid the initial determination of the incompatible part of the plastic curvature and strain, then the relaxation of an arbitrarily chosen configuration of plastic strain and curvature may be used to define workable initial conditions.

A Galerkin least-square weak solution of the transport equation along with Galerkin weak formulation for the equilibrium equations as proposed in the work of Varadhan *et al.* [430] is used to solve the dynamic FDDM problem. The methodology is not shown here since it was not developed during the course of the present thesis work. Interested readers are directed towards the work of Varadhan *et al.* [430].

From a computational standpoint, the continuous approach has an advantage over

the discrete approach. Using the finite element scheme in a continuous approach [2, 6, 343] incurs a fixed computational cost because the system's DOF remain the same; the continuous fields of defects are always defined at every point in the domain and can attain any value without incurring any additional computational cost. On the other hand, finite element based discrete defect models [224, 92, 479, 360, 142, 449, 53, 36] have an increasing cost due to the evolution of defects and nucleation of new defects which increases the DOF of the problem.

3.4 Incompatibilities at meso-scale

The fine scale FDDM model allows incompatibilities defined at the interatomic scale or fine scale to be associated with individual defects. Taking the Burgers and Frank's circuit about the defect core would give the net polar defect density from which it is possible to characterize the defect as a dislocation, disclination or mixed type satisfying equations (2.108) and (2.109). The velocities of the defect are also known through equations (3.101) and (3.102), and using these it is possible to know their position at any given time. Therefore, at the fine and interatomic length scales, the incompatibilities can be directly used to characterize individual defects.

However, at the meso-scale, where defect cores are indistinguishable, incompatibility cannot be associated with an individual defect. At such length scales, the Burgers and Frank's circuits are generally threaded by an ensemble of defects with different polarities and orientations. The net incompatibility may reduce or become equal to zero. In this case, the dislocation and disclination densities, as defined in equations (2.92) and (2.98), would be referred to as statistical defect densities. Consider the example shown in figure 3.1 for a dislocated crystal viewed at the meso-scale. Burgers circuits are drawn around randomly chosen regions and the net polarity is measured. This helps identify regions having net Burgers vectors greater than, equal to or less than zero. A region having net Burgers vector equal to zero is not necessarily devoid

of defects. On the other hand, a region having a net positive or negative polarity when viewed at the fine scale may contain a significant portion of the volume where the defect density is equal to zero. However, at the meso-scale the entire region is identified by a dislocation density corresponding to the net non-zero polarity.
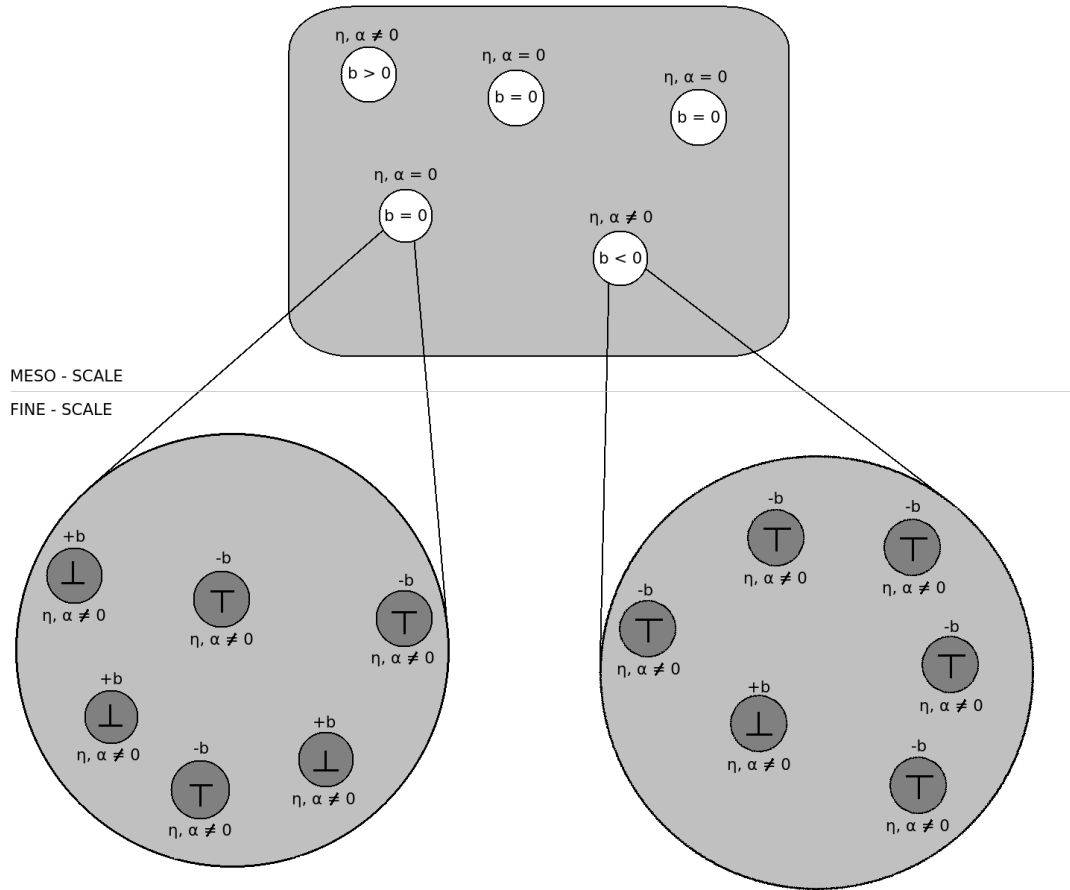
Figure 3.1: Incompatibilities and net polarity at the fine and meso- scales

3.5 Meso-scale dynamic field disclination and dislocation mechanics

At the meso-scale, performing statistical averaging of polar densities of defects threading the Burgers or Frank's circuits drawn around any region in the volume could lead to a vanishing net incompatibility. However, the statistical defect content of this

region may not necessarily be zero. In addition, it is possible that some of these statistical defects are mobile and can evolve under the influence of stresses. In their present form, equations (3.78) and (3.80) are not able to capture plastic curvature and strain rates arising from statistical defects. Furthermore, the defect velocities at meso-scale are defined as a statistical average and equations (3.101) and (3.102) may not appropriately reflect the mobility of ensembles of defects.

To that end, an extension to the FDDM needs to be introduced in order to account for the evolution of statistical defects such that (1) the stress field of average, polar dislocation and disclination densities that do not vanish at the meso-scale, (2) plastic strain and curvature rate arising from the temporal evolution of these densities, and (3) the effect of polar densities on the strength of the material. Such an extension was proposed in the case of dislocations by Acharya and Roy [6] and is extended to the general case of dislocations and disclinations in this work. Figure 3.2 pictorially describes the above discussion for the case of dislocations.

3.5.1 Phenomenological meso-scale fields

Acharya and Roy [6] proposed to extend the plastic strain rate having only the polar dislocation density contribution in equation (3.80) by introducing the term $\boldsymbol{L}^p$ to account for statistical dislocations as an additional contribution at the meso-scale:

$$\dot{\boldsymbol{\epsilon}}^p = \left(\boldsymbol{\alpha} \times \vec{\boldsymbol{V}}^\alpha + \boldsymbol{L}^p \right)^s \quad \text{or} \quad \dot{\epsilon}^p_{ij} = \frac{1}{2} \left(e_{jkl}\alpha_{ik}V_l^\alpha + e_{ikl}\alpha_{jk}V_l^\alpha + L^p_{ij} + L^p_{ji} \right) \quad (3.112)$$

The statistical term $\boldsymbol{L}^p$ is phenomenologically associated with the conventional plastic slip rate tensor, which reads:

$$\boldsymbol{L}^p = \sum_s \dot{\gamma}^p_s \vec{\boldsymbol{m}}_s \otimes \vec{\boldsymbol{n}}_s = \sum_s \dot{\gamma}^p_s \boldsymbol{P}_s \quad \text{or} \quad L^p_{ij} = \sum_s \dot{\gamma}^p_s m_i^s \otimes n_j^s = \sum_s \dot{\gamma}^p_s P^s_{ij} \quad (3.113)$$

where $\dot{\gamma}^p_s$ is the shear rate on slip plane s of slip direction $\vec{\boldsymbol{m}}_s$ and normal $\vec{\boldsymbol{n}}_s$. $\boldsymbol{P}_s$ is the Schmid tensor. Note that, plastic strain generated from the transport of dislocations or disclinations is not considered here. Plastic slip on system s is activated by the
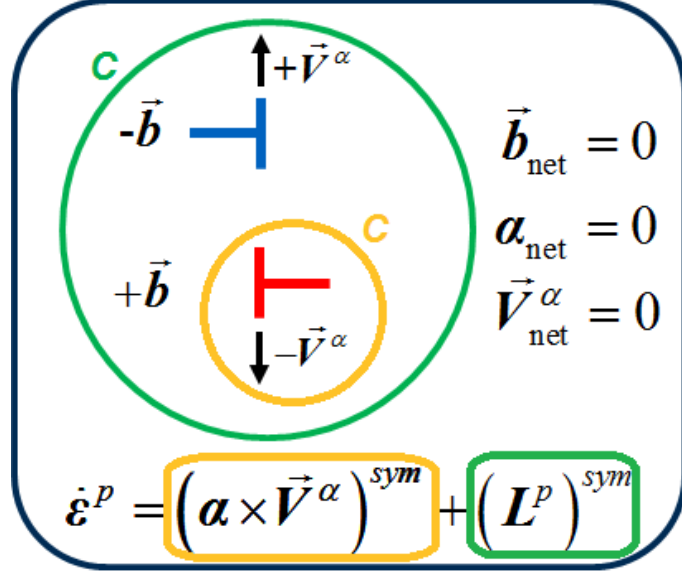
Figure 3.2: Illustration of plastic flow as a function of spatial resolution scale. At the fine or interatomic scale resolution sketched by the orange Burgers, the plastic strain rate produced by the expansion of a dislocation dipole with velocity $\vec{V}^{\alpha}$ is resolved by the mobility of polar dislocation densities. At the meso-scale resolution sketched by the green circuits, the net polarity of the dislocation dipole is zero, resulting in a statistical dislocation density. The plastic strain rate produced by the expansion of the dislocation dipole cannot be resolved by the mobility of polar dislocation densities and must be accounted for by a statistical rate term.

resolved shear stress $\tau_s = \boldsymbol{\sigma}^s : \boldsymbol{P}_s$ through the relation:

$$\dot{\gamma}_s^p = \dot{\gamma}_0^p (|\tau_s/\tau_0|)^n sign(\tau_s) \tag{3.114}$$

where $\dot{\gamma}_0^p$, τ_0 and n are the reference plastic strain rate, critical resolved shear stress and power law exponent, respectively.

Forest *et al.* [125] and Mayeur *et al.* [267] suggested that the motion of dislocations also results in the evolution of plastic curvature rate. In their Cosserat [125]/micropolar [267] strain gradient plasticity models, expressions were proposed for the plastic curvature rate as a function of GND evolution during dislocation slip [267]:

144

$$\dot{\boldsymbol{\kappa}}_{GND}^p = \sum_s \left[\vec{\boldsymbol{t}}^{\,s} \otimes \hat{\boldsymbol{b}}^{\,s} \frac{\dot{\phi}_0}{L^s} \left(\frac{\left\langle |\boldsymbol{M} : \vec{\boldsymbol{t}}^{\,s} \otimes \hat{\boldsymbol{b}}^{\,s}| / L^s - \sigma_y^s \right\rangle}{g^s} \right)^n sgn\left(\boldsymbol{M} : \vec{\boldsymbol{t}}^{\,s} \otimes \hat{\boldsymbol{b}}^{\,s} \right) \right]_{edge}$$

$$+ \left[\hat{\boldsymbol{b}}^{\,s} \otimes \hat{\boldsymbol{b}}^{\,s} \frac{\dot{\phi}_0}{L^s} \left(\frac{\left\langle |\boldsymbol{M} : \hat{\boldsymbol{b}}^{\,s} \otimes \hat{\boldsymbol{b}}^{\,s}| / L^s - \sigma_y^s \right\rangle}{g^s} \right)^n sgn\left(\boldsymbol{M} : \hat{\boldsymbol{b}}^{\,s} \otimes \hat{\boldsymbol{b}}^{\,s} \right) \right]_{screw} \qquad (3.115)$$

where $\vec{\boldsymbol{t}}^{\,s} = \hat{\boldsymbol{b}}^{\,s} \times \vec{\boldsymbol{n}}^s$ is a slip system (s) vector that is orthogonal to the unit slip vector or unit Burgers vector $\hat{\boldsymbol{b}}^{\,s}$ and the normal $\vec{\boldsymbol{n}}^s$ to the slip plane. The *edge* and *screw* components correspond to additive decomposition of the polar dislocation density tensor $\boldsymbol{\alpha} = b \sum_s \alpha_{edge}^s \hat{\boldsymbol{b}}^{\,s} \otimes \vec{\boldsymbol{n}}^s + \alpha_{screw}^s \hat{\boldsymbol{b}}^{\,s} \otimes \hat{\boldsymbol{b}}^{\,s}$. $\dot{\phi}_0$ is the rotation rate, L^s is the characteristic plastic length scale, σ_y is the yield strength, g^s is the threshold couple stress.

Mayeur *et al.* [267] later proposed a single plastic flow criterion (similar to the power law formulation in equation (3.115))for both plastic strain and curvature rates based on the argument that additive decomposition of polar dislocation density tensor into edge and screw components may not be appropriate for finite deformation plasticity models [17, 286].

In both the single- and multi-criterion (different plastic flow rules for strain and curvature rate) models, generation of polar disclinations due to plastic curvature evolution is not taken into consideration. Polar disclination evolution is a direct consequence of the kinematic relationship shown in equation (3.97). Furthermore, while spatial averaging results in a net zero polar disclination density, the number density of disclinations is non-zero *i.e.* they become statistical in nature. Evolution of these statistical disclinations could have additional contributions to the plastic curvature. This can also be understood from the illustration shown in figure 3.3. Even further, due to the non-locality associated with disclinations, GNDs may be generated (refer to figure 3.3) that do not evolve as a function of the slip system. This could become particularly important in nc materials where plasticity via dislocation

145

slip becomes energetically unfavorable and GB mechanisms are activated.
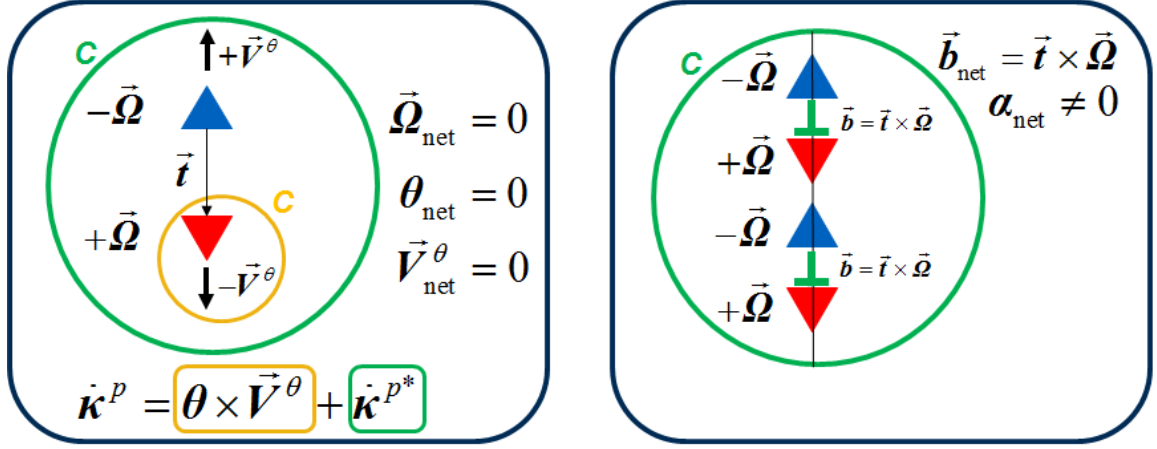
Figure 3.3: Illustration of plastic curvature rate as a function of spatial resolution scale ($\dot{\boldsymbol{\kappa}}^p_{GND}$ is not shown). At the fine or interatomic scale resolution sketched by the orange Frank's circuit, the plastic curvature rate produced by the expansion of a disclination dipole with velocity $\vec{V}^\theta$ is resolved by the mobility of polar dislocation densities. At the meso-scale resolution sketched by the green circuits, the net polarity of the disclination dipole is zero, resulting in a statistical disclination density. The plastic curvature rate produced by expansion of the disclination dipole cannot be resolved by the mobility of polar disclination densities and must be accounted for by a statistical rate term. Non-locality associated with disclinations results in the generation of polar dislocations that may not evolve as a function of slip systems and need to be taken into account.

In light of the above, a phenomenological extension to the fine-scale plastic curvature rate equation (3.94) is proposed to account for plastic curvature evolution coming from GNDs generated due to plastic slip ($\dot{\boldsymbol{\kappa}}^p_{GND}$) and evolution of statistical disclinations and non-local polar dislocations at the meso-scale as:

$$\dot{\boldsymbol{\kappa}}^p = \boldsymbol{\theta} \times \vec{V}^\theta + \dot{\boldsymbol{\kappa}}^p_{GND} + \dot{\boldsymbol{\kappa}}^{p*} \quad \text{or} \quad \dot{\kappa}^p_{ij} = e_{jkl}\theta_{ik}V^\theta_l + \dot{\kappa}^p_{GND_{ij}} + \dot{\kappa}^{p*}_{ij} \quad (3.116)$$

where $\dot{\boldsymbol{\kappa}}^{p*}$ represents the statistical plastic curvature rate. Deriving motivation from the power law formulation proposed in the Cosserat/micropolar strain gradient plasticity models of Forest *et al.* [125] and Mayeur *et al.* [267], respectively, an expression for $\dot{\boldsymbol{\kappa}}^{p*}$ is proposed as:

$$\dot{\boldsymbol{\kappa}}^{p*} = k\frac{\boldsymbol{M}^D}{||\boldsymbol{M}^D||} \quad \text{or} \quad \dot{\kappa}^p_{ij} = k\frac{M^D_{ij}}{\sqrt{M^D_{kl}M^D_{kl}}} \quad (3.117)$$

146

where k is assumed to have the simplest power law relationship as:

$$k = \dot{\kappa}_0^p \left(\frac{||\boldsymbol{M}^D||}{M_0} \right)^n \quad \text{or} \quad k = \dot{\kappa}_0^p \left(\frac{\sqrt{M_{ij}^D M_{ij}^D}}{M_0} \right)^n \tag{3.118}$$

where $\dot{\boldsymbol{\kappa}}_0^p$, M_0 and n are the reference plastic curvature rate, reference couple stress and the power exponent, respectively. Note that with such a formulation, the present framework becomes multi-criterion. This is necessary to account for the plastic curvature contribution coming from both statistical disclinations and non-local polar dislocations, which is different from GND evolution due to dislocation slip. The use of a multi-criterion model [17, 286] is also facilitate by the present framework based on a small strain hypothesis; it allows for the additive decomposition of the polar dislocation density into screw and edge components discussed in equation (3.115).

The motion of disclinations is not bound to a particular slip direction. Therefore, unlike the case of Cauchy stresses in plastic strain rate and couple stresses in $\dot{\boldsymbol{\kappa}}_{GND}^p$, the couple stresses in $\dot{\boldsymbol{\kappa}}^{p*}$ are not resolved in direction of a slip system and as a first estimate k is taken as a function of the norm of couple stress thus making it frame invariant. A similar expression was proposed in the work of Romanov and Vladimirov [339] to account for relaxation of moments via GB rotation.

The term $\dot{\kappa}_0$ has dimensions of $(1/m)$ and can be expressed as a function of an evolving reference plastic rotation rate $(\dot{\omega}/L_c)$ where $\dot{\omega}$ is a rotation rate and L_c is the characteristic plastic length scale. This has the same form but different significance than the reference curvature rate $(\dot{\phi}/L^s)$ in equation (3.115). The latter corresponds to lattice rotation fields induced in the presence of polar dislocations generated from dislocation slip that have a much larger distribution than the incompatible rotation fields associated with disclinations. This in turn should be reflected from the characteristic length scales L_c and L^s which have to satisfy the inequality $L_c < L^s$. The threshold couple stress has dimensions (N/m) similar to the component g^s in equation (3.115).

In the present work, the focus is on highlighting the possible role of statistical disclination evolution during plastic deformation. Mayeur *et al.* [267] reported that stress v/s strain curves plotted for the plastic deformation of a single crystal while allowing plastic curvature evolution results in a reduction of slope in plastic regime compared to the conventional elasto-viscoplastic case for metals. Relaxation of Cauchy stresses due to grain rotations should be expected due to $\dot{\boldsymbol{\kappa}}^{p*}$ evolution. This is tested in chapter 5 where the applications to polycrystalline materials are studied. Note that the intent here is not to quantify the amount of plastic deformation accommodated via curvature evolution. Therefore, the contributions of $\dot{\boldsymbol{\kappa}}^{p}_{GND}$ will not be considered and henceforth any reference to the phenomenological or meso-scale plastic curvature rate shall be to $\dot{\boldsymbol{\kappa}}^{p*}$. Appropriate estimates for $\dot{\kappa}_0$ and M_0 based on microstructural conditions shall be chosen for the sake of illustration.

The transport equations for polar disclination and dislocation densities, equations (3.97) and (3.98), now read as:

$$\dot{\boldsymbol{\theta}} = -\mathbf{curl}\,(\boldsymbol{\theta} \times \vec{\boldsymbol{V}}^{\theta} + \boldsymbol{\kappa}^{p*}) + \boldsymbol{k}^{\theta} = -\nabla \times (\boldsymbol{\theta} \times \vec{\boldsymbol{V}}^{\theta} + \boldsymbol{\kappa}^{p*}) + \boldsymbol{k}^{\theta} \quad \text{or}$$

$$\dot{\theta}_{ij} = -e_{jkl}e_{lmn}\left(\theta_{im}V_n^{\theta}\right)_{,k} + e_{jkl}\kappa^{p*}_{il,k} + k_{ij}^{\theta} \tag{3.119}$$

$$\dot{\boldsymbol{\alpha}} = -\mathbf{curl}\,(\dot{\boldsymbol{\epsilon}}^p + (\boldsymbol{L}^p)^s) + (\dot{\boldsymbol{\kappa}}^{\boldsymbol{p}} + \dot{\boldsymbol{\kappa}}^{\boldsymbol{p*}})^T - \mathrm{tr}(\dot{\boldsymbol{\kappa}}^{\boldsymbol{p}} + \dot{\boldsymbol{\kappa}}^{\boldsymbol{p*}})\boldsymbol{I} + \boldsymbol{k}^{\alpha}$$

$$\quad = -\nabla \times (\dot{\boldsymbol{\epsilon}}^{\boldsymbol{p}} + (\boldsymbol{L}^p)^s) + (\dot{\boldsymbol{\kappa}}^{\boldsymbol{p}} + \dot{\boldsymbol{\kappa}}^{\boldsymbol{p*}})^T - \mathrm{tr}(\dot{\boldsymbol{\kappa}}^{\boldsymbol{p}} + \dot{\boldsymbol{\kappa}}^{\boldsymbol{p*}})\boldsymbol{I} + \boldsymbol{k}^{\alpha} \quad \text{or}$$

$$\dot{\alpha}_{ij} = -e_{jkl}(\dot{\epsilon}^p_{il,k} + L^p{}_{(il),k}) + \dot{\kappa}^p_{ji} + \dot{\kappa}^{p*}_{ji} - (\dot{\kappa}^p_{kk} + \dot{\kappa}^{p*}_{kk})\delta_{ij} + k_{ij}^{\alpha} \tag{3.120}$$

The meso-scale field disclination and dislocation mechanics model is expected to be useful in material systems where dislocation-mediated plasticity is limited, either because the average grain size becomes too small, as in ultrafinegrained or nano-crystalline materials, or because the material does not have enough slip systems, like Olivine which has an orthorhombic crystal structure.

3.5.2 Plasticity beyond dislocations

The concept of plastic curvature evolution was first treated in the work of Forest *et al.* [125]. This work follows a similar approach, albeit within the relatively simpler couple stress theory framework, but introduces a generic form of the plastic curvature rate to allow capturing both statistical dislocation and disclination contributions to lattice curvature which result in the generation of geometrically necessary disclinations and dislocations. Such a contribution to the latter is in addition to external loading conditions (bending or torsion), internal sources of plastic inhomogeneity and elastic heterogeneity across interfaces.

With respect to disclination contribution to plasticity, a handful of experimental studies [291, 254, 244] and theoretical considerations [333] have suggested that disclinations nucleate in order to accommodate plasticity in materials undergoing severe plastic deformation via grain rotation. This mechanism is in addition to the grain rotation caused due to GB sliding and shear coupled GB migration. Furthermore, the metastable equilibrium state associated with the presence of disclinations could lead to driving forces that may contribute to the nucleation of new grains, twins, cracks, etc. The proposed meso-scale model is the first model that is capable to account for the contribution of disclinations to plasticity in a kinematically and thermo-mechanially rigorous manner. In addition to nucleation/annihilation of disclinations, the proposed meso-scale model provides the necessary basis for capturing GB related mechanisms at the meso-scale by accounting for both plastic strain and curvature conrbutions to plasticity.

The strain gradient plasticity models [9, 120, 123, 121, 304, 138, 156, 4, 28, 122, 157, 153, 124, 267] and field dislocation mechanics model of Acharya [2] have shown that incompatible elastic/plastic strains can definitely be introduced as multi-scale metrics encompassing the fine, meso- and macro scales. They have also introduced polar dislocation densities, capturing the contribution of strains at the fine and meso-

scales, as multi-scale metrics. The present framework augments this definition of polar dislocation densities through the introduction of incompatible elastic/plastic curvatures. Whether these can directly be treated as multi-scale metrics will be put to test in the applications of the meso-scale field dislocation and disclination mechanics model in section 5.

Finally, with respect to the classification of the proposed meso-scale model, it belongs to the higher order multi-criterion crystal plasticity models. Such a classification finds its roots in the work of Forest and co-workers [125, 124] who introduced couple stresses, which are generated due to presence of plastic curvature, as a back stress in the yield criterion, and the viscoplastic relationship between plastic strain rate and Cauchy stress. Forest [124] proposed that the evolution of plastic curvature followed an independent yield criterion than the plastic strain and suggested an extension of Von Mises (VM) plasticity thus making their model multi-criterion. This contrasts a single-criterion crystal plasticity model which augments the VM plasticity model to obtain a combined equivalent stress and equivalent strain measures [126, 267]. In its present form, the proposed model presumes that Cauchy and couple stresses follow different plastic evolution laws and may be interpreted as a multi-criterion model. However, it is important to note that the equilibrium relationship (3.14), the geometric constraint on polar dislocation and disclination densities and the fact that both plastic strain and curvature lead to the generation of geometrically necessary dislocations, suggest that the yield criteria for Cauchy and couple stresses should be correlated. Development of a single criterion model, however, is beyond the scope of present work.

3.6   *Discussion*

This chapter continues with the discussion on the continuous description of defects following the previous chapter. Following the development of the compatible and

incompatible geometric fields, the beginning of this chapter focuses on developing new elastic constitutive laws that account for the presence of both compatible and incompatible elastic strains and distortions associated with the presence of dislocations and disclinations. These are higher order with respect to the type of incompatibility that they are capable to account for and higher grade with respect to equivalent gradients of displacement that are considered (in this case up to the second gradient is considered). These laws are rigorously derived based on thermo-mechanical dissipation considerations and satisfy the balance of mass, momentum and moment of momentum. The dissipation based formulation can be used to extend these elastic constitutive laws to account for more general phenomena such as higher order defects (for example G-disclinations which induce incompatibilities in elastic distortion [5, 421]), piezoelectric effect [396] on stresses, etc. Such problems may arise in the case for those theories that are specially tailored to solve a very specific problem within the domain of dislocation and/or disclination theory; for example the model of Gurtin [157] which requires specifying non-standard boundary conditions.

In order to develop these elastic laws it is necessary to impose appropriate boundary conditions that allow for the description of both dislocations and disclinations. These are surface traction and moments along with rigid body displacements and/or rotations. Imposing both traction and moments lead to the generation of Cauchy and couple stresses in the domain. A coupling between Cauchy and couple stresses is obtained through the equilibrium equation which is in tandem with the coupling between these stresses through the elastic constitutive laws. The robustness of these elastic laws is also observed in the simplest of symmetries associated with elasticity *i.e.* linear isotropic elasticity. The framework upon which is such that in the linear isotropic elastic case, the shape of the constitutive laws is affected by the presence or absence of defects. In the latter case, the material has an additional point symmetry which is lost when defects are present in the domain; albeit only in those regions

where the incompatibility is non-zero. The linear isotropic elastic laws are able to capture this difference through cross terms that couple the incompatible components of elastic strain and curvature without any *ad hoc* assumptions. The presence or absence of defects directly affects this coupling which in the latter case vanishes due to the absence of incompatible elastic strains and curvatures.

The higher order elastic constitutive laws form a crucial component of the field theory of dislocation and disclination mechanics [134]. This theory is based on in-compatible description of continuously represented defects and models the motion of these defects using transport equations. The dislocation velocities are phenomeno-logically described using the Peach Koehler force which is a function of the Burgers vectors and the Cauchy stresses. In the presence of disclinations, the Burgers vector becomes a spatial function of the incompatible curvature through equations (2.107) and (2.109). The dislocation density, which is a function of the Burgers vector, also becomes spatially dependent, invariably transferring this property to the incompat-ible elastic strains and curvatures through equation (2.98). In order for the Cauchy and couple stresses to appropriately reflect the non-locality associated with the core (through the incompatibility), an appropriate definition of the elasticity tensors needs to be accounted for. This is naturally achieved via the length scale dependence of the higher order elasticity tensors. The length factor in higher order elasticity tensors $\boldsymbol{A}$, $\boldsymbol{B}$ and $\boldsymbol{D}$ can be directly associated with the characteristic length of defects in the domain. Such estimates have been provided in the works of Kröner [218], Maranganti and Sharma [264], among others, which will be used in the following chapters to study the role of incompatibilities at the fine and meso-scales. Focusing back on the defect velocities, the non-locality associated with the Burgers vector and the Cauchy stress should affect the transport of dislocations. Similarly, for the transport of disclina-tions, a similar non-local effect should be observed through its dependence on the couple stresses and hence their associated elasticity tensors. This will be put to test

in the next chapter where the dynamic model is applied to study shear coupled GB migration [58] of <001> symmetric tilt GBs.

The multi-scale nature of the elastic laws arises from their capacity to account for the incompatible elastic strains and curvatures. At the length scale of defects (or the fine scale), where incompatibilities can be associated with individual defects, these laws have non-vanishing cross terms. However, at the meso-scale where spatial averaging leads to a zero net incompatibility of the medium, these laws are still capable of predicting the stresses through the compatible elastic strains and curvatures. Quite interestingly, the fact that incompatibilities are associated with individual defects in the current framework, requires the definition of the continuous framework at the length scale of these defects. Consider the case of disclinations, these are used to describe GB interfaces that can be as thin as 1 nm. In order for to apply the proposed model, the continuum approximation must be made at the interatomic length scale. Furthermore, at this scale the continuum should allow the balance of mass, momentum and moment of momentum in order to satisfy the equilibrium conditions everywhere in the domain. This type of a continuum is proposed and used in this chapter. The implications of this approximation will be studied in the next chapter.

Focusing at the meso-scale, while spatial averaging could lead to a net zero incompatibility in the domain, it is possible and very likely that during plastic deformation polar defect densities are generated within the medium. In this case, incompatibilities in elastic strain and curvature are induced, however, these can no longer be attributed to individual defects. Rather they are indicative of the net polarity of the region where there are defined and induce a stress field of their own. It is crucial to account for their contributions to plasticity along with the contribution of mobile statistical defects present in the medium. To that end, the phenomenological field disclination and dislocation mechanics model is proposed which combines the contributions of both plastic slip and plastic curvature due to statistical defects and models

the transport of polar defects in the medium. Such a theoretical construction paves way for a transfer of information on field variables between the fine scale and the meso-scale. This will be particularly useful in studying the influence of motion of GB interfaces on the meso-scale response and vice versa.

3.7 Conclusion

New higher order/grade elastic constitutive laws, based on the incompatible framework developed in the previous chapter, are proposed to account for the contribution of incompatibilities in elastic strain and curvature at the fine and meso scales. These laws form an integral part of the fine scale field disclination and dislocation mechanics theory that accounts for the transport of polar dislocation and disclination contributions to local plasticity. A meso-scale phenomenological field disclination and dislocation mechanics model is proposed that accounts for statistical dislocation and disclination contributions to plasticity, in addition to those coming from polar defect densities. The fine and meso scale models allow for a kinematically rigorous continuous treatment of interfaces and junctions at both these scales by respecting compatibility conditions on elastic and plastic strain and curvature at the interfaces.

CHAPTER IV

TOWARDS A CONTIUOUS STRUCTURE SENSITIVE MODEL OF GRAIN BOUNDARIES: APPLICATIONS TO <001> SYMMETRIC TILT GBS AND TJS

The aim of this chapter is understand (1) the contribution of strain and curvature incompatibilities to grain boundary energy and (2) the relationship between triple junction geometry and energy.

To that end, the multi-scale field disclination and dislocation mechanics model developed in the previous chapter will be applied to $< 001 >$ symmetric tilt GBs (STGBs) and TJs in face centered cubic (FCC) materials. In order to understand the role of incompatibilities, GB energy vs. misorientation plots for <001> STGBs are created and compared with those obtained from atomistic simulations and experiments. Section 4.1 begins with first giving a detailed description of the discrete disclination structural unit model (DSUM) [139] to represent the <001> STGBs. Then the GB energy vs. misorientation curve is generated using just the out-of-core compatible components of elastic strain and curvature; recall that core contributions from disclinations are beyond the scope of a discrete approach. Next the discrete approach is compared with the energy vs. misorientation curve generated using a fully continuous approach that uses both compatible and incompatible contributions of strain and curvature. From here it is possible to obtain an estimate on the incompatible contributions to GB energy. The crucial role of elastic constitutive laws, developed in section 3.1, is highlighted in capturing the non-local behavior that is necessary to drive the shear coupled GB migration in <001> STGBs.

In section 4.2, the focus is directed towards TJs constructed from STGBs. New

155

kinematic constraints on the TJ dihedral and misorientation angles are developed based on the tangential continuity considerations discussed in the previous chapter in section C.0.2. New 2-dimensional maps of TJ energy vs. misorientations are generated for TJs formed between <001> STGBs.

4.1 Incompatibility contribution to energy of <001> STGBs

4.1.1 Disclination structural unit model

The DSUM framework to represent GBs was briefly reviewed in section 2.2.2 and is detailed in the following discussion for the case of <001> STGBs.

As originally proposed by Li, any perfect planar STGB, with misorientation θ such that $\theta_1 < \theta < \theta_2$, can be represented by a sequence of special boundaries separated by disclination dipoles of alternating Frank's vector magnitude (strengths) $\Delta\theta = \pm(\theta_2 - \theta_1)$. Therefore, a set of specific reference misorientations $(\theta_1, \theta_2, \ldots, \theta_n)$ – identifying special GBs – has to be selected. In the case of symmetric tilt boundaries about the <001> axis, the reference misorientations are 0º, 36.87º, 53.13º and 90º to which the structural units A, B, C and D are assigned, respectively. Each of these misorientations is composed of only one repeated structural unit [387]. Structural continuity throughout the misorientation range entails that all non-favoured boundaries – *i.e.* boundaries with misorientation different from that of the reference special boundaries – consist of a periodically reproduced sequence of structural units pertaining to the two nearest favoured boundaries. As such, all boundaries with misorientation between 0° and 36.87° are composed of only A and B structural units. The period of a given boundary will be composed of 'm' majority units and 'n' minority units.

Consider a GB of misorientation θ such that $\theta_1 < \theta < \theta_2$, where θ_1 and θ_2 are misorientations associated with its adjacent special boundaries. The GB is thus composed of majority and minority units associated with misorientation θ_1 and θ_2.

156

Let d_1 and d_2 denote the rest length of each structural unit. Transitions from a majority to a minority unit define the locations of disclination dipoles with strength $\pm\Delta\theta = \theta_1 - \theta_2$ and length d_2'. Each dipole is separated by majority units with length equal to an integral multiple of their characteristic length d_1' [139]. The period vector of a non-special GB can be decomposed into the sum of the period vectors of its associated special GBs. Figure 4.1 shows the decomposition of a period of a generic STGB into structural units.
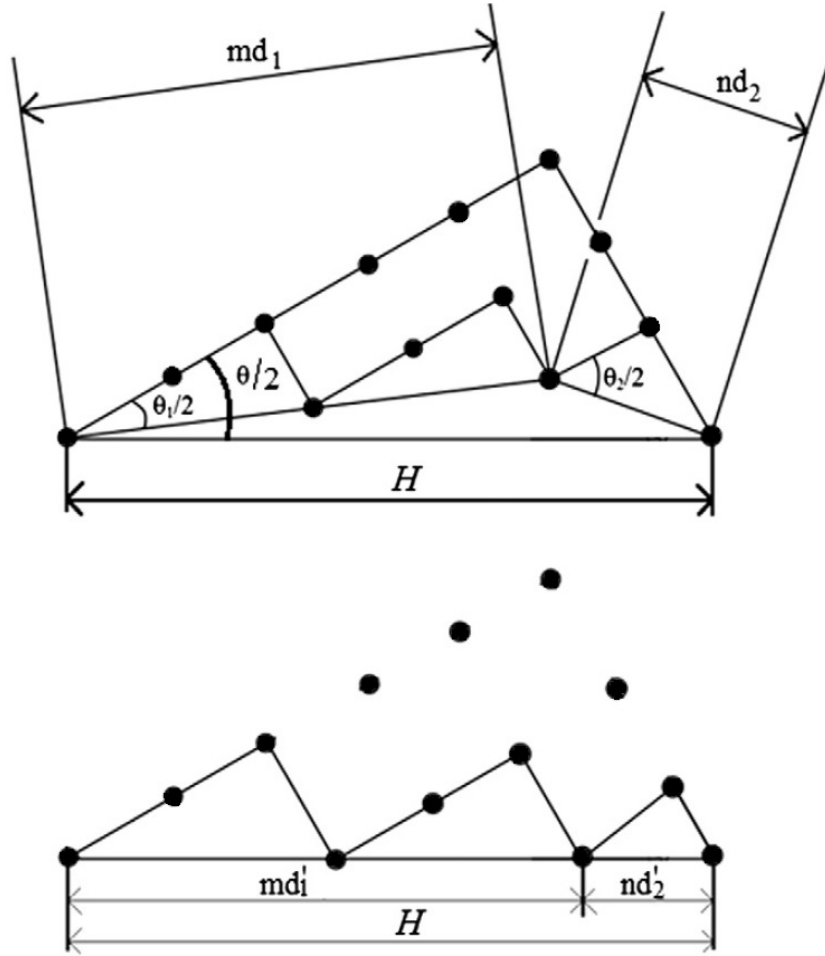
Figure 4.1: Projection of the structural units of a non planar GB.

The length of the period H is given by the following equations,

$$H = md_1' + nd_2' \neq md_1 + nd_2 \tag{4.1}$$

157

$$H = \left\{ (md_1)^2 + (nd_2)^2 + 2mnd_1d_2 \cos\left(\frac{\theta_2 - \theta_1}{2}\right) \right\}^{1/2} \qquad (4.2)$$

$$H \sin\left(\frac{\theta}{2}\right) = md_1 \sin\left(\frac{\theta_1}{2}\right) + nd_2 \sin\left(\frac{\theta_2}{2}\right) \qquad (4.3)$$

$$d_1' = d_1 \cos\left(\frac{\theta - \theta_1}{2}\right) \qquad (4.4)$$

$$d_2' = d_2 \cos\left(\frac{\theta_2 - \theta}{2}\right) \qquad (4.5)$$

The structural units in figure 4.1 have undergone a geometric distortion from their rest boundary lengths d_1 (majority unit) and d_2 (minority unit) to d_1' and d_2' due to the geometric constraints (4.1) on the period H. The distorted units in the decomposed structure are thus the projection of the undistorted structural units on the GB plane.

A series of 29 misorientations – between $0°$ and $90°$ – are considered in the case of <001> STGBs. The dipole arm lengths are computed from equations (4.1). These boundaries along with their period vectors, GB planes and structural decomposition of the period are shown in table 4. The vertical lines denote a single period of the GB and the dot represents a centered boundary – *i.e.* a boundary with more than one CSL in its period.

Table 4: Structural unit decomposition of symmetric tilt
GBs about the [001] axis

θ (deg)	GB plane	Σ	Structural Decomposition of the period	Period vector
3.95	(15 14 0)	421	|AAAAAAAAAAAAAB.AAAAAAAAAAAAAB|	[$\bar{1}$4 15 0]
6.03	(15 14 0)	181	|AAAAAAAB.AAAAAAAB|	[$\bar{9}$ 10 0]
12.68	(5 4 0)	41	|AAAB.AAAB|	[$\bar{4}$ 5 0]
16.26	(4 3 0)	25	|AAB.AAB|	[$\bar{3}$ 4 0]

Continued on next page

Table 4 – *Continued from previous page*

θ (deg)	GB plane	Σ	Structural Decomposition of the period	Period vector
20.02	(10 7 0)	149	|AABABAB.AABABAB|	$[\bar{7}\ 10\ 0]$
22.62	(3 2 0)	13	|AB.AB|	$[\bar{2}\ 3\ 0]$
25.06	(11 7 0)	85	|ABABABB|	$\frac{1}{2}[\bar{7}\ 11\ 0]$
28.07	(5 3 0)	17	|ABB|	$\frac{1}{2}[\bar{3}\ 5\ 0]$
30.51	(7 4 0)	65	|ABBB.ABBB|	$[\bar{4}\ 7\ 0]$
33.40	(13 7 0)	109	|ABBBBBB|	$\frac{1}{2}[\bar{7}\ 13\ 0]$
35.30	(29 15 0)	533	|ABBBBBBBBBBBBBB|	$\frac{1}{2}[\bar{15}\ \ 29\ 0]$
36.87	(2 1 0)	5	|B.B|	$[\bar{1}\ 2\ 0]$
39.60	(17 8 0)	353	|BBBBBBBC.BBBBBBBC|	$[\bar{8}\ 17\ 0]$
42.08	(9 4 0)	97	|BBBC.BBBC|	$[\bar{4}\ 9\ 0]$
43.60	(7 3 0)	29	|BBC|	$\frac{1}{2}[\bar{3}\ 7\ 0]$
46.40	(5 2 0)	29	|BC.BC|	$[\bar{2}\ 5\ 0]$
48.89	(8 3 0)	73	|BBC.BBC|	$[\bar{3}\ 8\ 0]$
51.11	(17 6 0)	325	|BCCCCC.BCCCCC|	$[\bar{6}\ 17\ 0]$
53.13	(3 1 0)	5	|C|	$\frac{1}{2}[\bar{1}\ 3\ 0]$
54.95	(19 6 0)	397	|CCCCCCD.CCCCCCD|	$[\bar{6}\ 19\ 0]$
56.60	(10 3 0)	109	|CCCD.CCCD|	$[\bar{3}\ 10\ 0]$
58.11	(7 2 0)	53	|CCD.CCD|	$[\bar{2}\ 7\ 0]$
61.93	(4 1 0)	17	|CD.CD|	$[\bar{1}\ 4\ 0]$
64.94	(9 2 0)	85	|CDCDD.CDCDD|	$[\bar{2}\ 9\ 0]$
67.38	(5 1 0)	13	|CDD|	$\frac{1}{2}[\bar{1}\ 5\ 0]$

Continued on next page

Table 4 – *Continued from previous page*

θ (deg)	GB plane	Σ	Structural Decomposition of the period	Period vector
71.08	(6 1 0)	37	|CDDD.CDDD|	$[\bar{1}\ 6\ 0]$
73.74	(7 1 0)	25	|CDDDD|	$\frac{1}{2}[\bar{1}\ 7\ 0]$
78.58	(10 1 0)	101	|CDDDDDDD.CDDDDDDD|	$[\bar{1}\ 10\ 0]$
82.37	(15 1 0)	113	|CDDDDDDDDDDDDD|	$\frac{1}{2}[\bar{1}\ 15\ 0]$

The sequence of arrangement of the structural units is unique to each boundary. The arrangement of the structural units has to fulfil the following two conditions:

(1) The spacing between minority units must be maximized.

(2) The arrangement should form a periodic sequence continuous with the neighbouring boundary structures.

A periodic sequence of 'm' majority units and 'n' minority units can be formed in $(m + n - 1)!/m!n!$ ways, and only one sequence fulfils the above conditions. The generation of this particular sequence is detailed in Sutton and Vitek [387] and is performed in two steps. For the sake of illustration, consider the $\theta = 20.02^{\text{o}}$ boundary. Its delimiting boundaries are the $0°$ and $36.87°$ boundaries. It is a centered boundary with period vector $[\bar{7}\ 10\ 0]$ and the period vectors of the 0° and 36.87^{o} boundaries are $1/2[\bar{1}\ 1\ 0]$ and $[\bar{1}\ 2\ 0]$ such that the decomposition of the half period of 20.02^{o} boundary is:

$$\frac{1}{2}[\bar{7}\ 10\ 0] = \frac{4}{2}[\bar{1}\ 1\ 0] + \frac{3}{2}[\bar{1}\ 2\ 0]$$

First, the majority units are associated with minority units such that each minority unit is separated by the same number of majority units. With $m = 4$ and $n = 3$ one obtains ABABAB.ABABAB. Second, from the remaining majority units, if any, each

one is associated to an equal number of minority units. The sequence for the 20.02º boundary is therefore AABABAB.AABABAB. The characteristic length of the B unit is 0.28202 nm. Two pairs of these B units are separated by a majority A unit with characteristic length 0.17757 nm and every third pair is separated by two A units with the distance between the B units being twice the characteristic length of the majority units *i.e.* 0.35514 nm.

The magnitude of the Frank's vector and the characteristic lengths of the majority and minority units of all the 29 boundaries shown in table 4 are presented in table 5.

Table 5: Characteristic length of the majority and minority units and the Frank's vectors

θ (deg)	Majority units 'm' in 1 period	Minority units 'n' in 1 period	d'_1 (nm)	d'_2 (nm)	Frank's vector Ω in degrees
3.95	13(A)	1(B)	0.18021	0.27341	±36.87
6.03	8(A)	1(B)	0.18006	0.27484	±36.87
12.68	3(A)	1(B)	0.17921	0.27877	±36.87
16.26	2(A)	1(B)	0.17850	0.28050	±36.87
20.02	4(A)	3(B)	0.17757	0.28202	±36.87
22.62	1(A)	1(B)	0.17681	0.28290	±36.87
25.06	4(B)	3(A)	0.28358	0.17602	±36.87
28.07	2(B)	1(A)	0.28426	0.17493	±36.87
30.51	3(B)	1(A)	0.28466	0.17396	±36.87
33.40	6(B)	1(A)	0.28497	0.17271	±36.87
35.30	14(B)	1(A)	0.28507	0.17182	±36.87

Continued on next page

Table 5 – *Continued from previous page*

θ (deg)	Majority units 'm' in 1 period	Minority units 'n' in 1 period	d'_1 (nm)	d'_2 (nm)	Frank's vector Ω in degrees
36.87	1(B)	0(A)	–	–	± 36.87
39.60	7(B)	1(C)	0.28502	0.40038	± 16.26
42.08	3(B)	1(C)	0.28480	0.40132	± 16.26
43.60	2(B)	1(C)	0.28461	0.40180	± 16.26
46.40	1(B)	1(C)	0.28411	0.40250	± 16.26
48.89	7(C)	1(B)	0.40291	0.28353	± 16.26
51.11	5(C)	1(B)	0.40313	0.28290	± 16.26
53.13	1(C)	0(B)	–	–	± 16.26
54.95	6(C)	1(D)	0.40314	0.12158	± 36.87
56.60	3(C)	1(D)	0.40301	0.12212	± 36.87
58.11	2(C)	1(D)	0.40281	0.12260	± 36.87
61.93	1(C)	1(D)	0.40200	0.12369	± 36.87
64.94	3(D)	2(C)	0.12446	0.40105	± 36.87
67.38	2(D)	2(C)	0.12502	0.40008	± 36.87
71.08	3(D)	1(C)	0.12577	0.39825	± 36.87
73.74	4(D)	1(C)	0.12622	0.39669	± 36.87
78.58	7(D)	1(C)	0.12687	0.39330	± 36.87
82.37	12(D)	1(C)	0.12722	0.39014	± 36.87

4.1.2 GB energy in discrete static case: contribution of compatible elastic strains and curvatures

The DSUM has already been implemented using a discrete representation in a static case to compute the energy of <001> STGBs in FCC Cu and Ni [23], and of [$1\bar{1}00$] STGBs in hexagonal closed packed (HCP) metals [466] based on the structural unit model in HCP by Farkas [116]. Closed-form analytical solutions were derived by Wu [465] for the elastic strain and Cauchy stress fields of a periodic array of interfacial wedge disclination dipoles in a bi-crystal under transversely isotropic conditions. Interestingly, thus far the contribution of elastic curvatures and couple stresses to the elastic energy of GBs, have never been accounted for.

In light of the above, <001> STGBs represented using DSUM are studied in a 2-dimensional static case. Infinitely long discrete disclination dipoles of strengths shown in table 5 are used to represent the 29 <001> STGBS shown in table 4. The DSUM uses a discrete representation of disclinations and therefore the GB elastic energy computed here will have contributions coming from the out-of-core compatible elastic strains and curvatures. Explicit expressions for these are given by equations (2.25) and (2.28). The elastic laws are considered in an isotropic centro-symmetric case. In this case, the cross terms associated with elasticity tensors $\boldsymbol{B}$ and $\boldsymbol{D}$ vanish. The elastic energy is then given as,

$$E^{el} = E^{cauchy} + E^{couple} \tag{4.6}$$

$$E^{cauchy} = \frac{1}{2}\sigma_{ij}^{s}\epsilon_{ij}^{e\parallel} = \frac{1}{2}\epsilon_{ij}^{e\parallel}C_{ijkl}\epsilon_{kl}^{e\parallel} \tag{4.7}$$

$$E^{couple} = \frac{1}{2}M_{ij}^{D}\kappa_{ij}^{e\parallel} = \frac{1}{2}\kappa_{ij}^{e\parallel}A_{ijkl}\kappa_{kl}^{e\parallel} \tag{4.8}$$

Figure 4.2 shows the procedure used to compute the elastic energy of GBs in the discrete static case. A GB – of height of 10 μm – is placed at the centre of a rectangular area of height equal to that of the GB and of width 100 nm. The energy is computed in a rectangular area centred in the domain. It has a height equal to two

163

times the period vector of the boundary and a width 20 nm – $i.e.$ 10 nm on each side of the GB. A two dimensional 4-point Gauss quadrature method is used to integrate the energy of the GB. The two parameters of importance to reach the desired accuracy are the mesh size and box size, both of which were optimized to reach convergence. Note that, as the GB has a finite height, the width of the integration box is limited. For the sake of accuracy, a very fine square mesh, of size 0.1 nm, is used to compute the box energy. As illustrated in figure 4.2, showing the energy field associated with the 20.02° boundary, it is found that using a width of 20 nm is sufficient to ensure convergence. Finally, a core cut-off radius equal to the Burgers vector magnitude for the (111) slip plane in FCC Copper is chosen; this is 0.255 nm. As expected the GB energies obtained are finite and independent of the integration box size chosen.
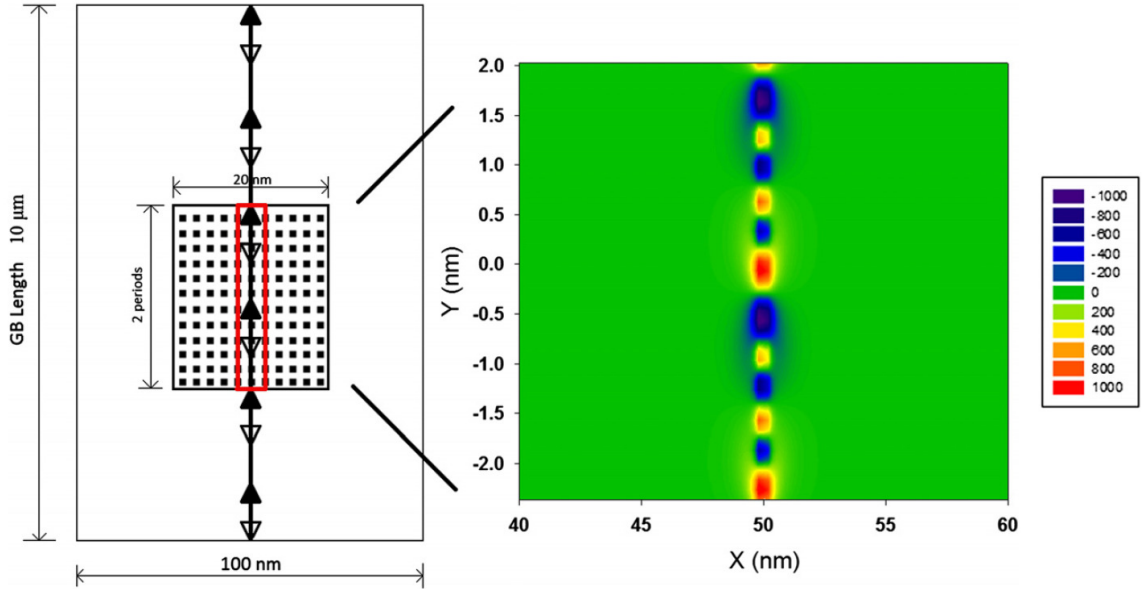
Figure 4.2: Integration mesh and box dimensions (not to scale) and the disclination arrangement in a 20.02° misorientation boundary. The red box denotes the area that falls in the cut-off region whose half width is equal to the Burgers vector magnitude for the <111> slip planes in FCC Cu. The right hand side of the figure shows the σ_{xx} (MPa) component of the stress field.

The material constants taken here are those of Cu: $G = 48$ GPa, $\nu = 0.34$, $A_1 = Gb^2$, $A_2 = 0$, with $b = 2.551$ Å. The magnitude of $\boldsymbol{A}$ has been adopted from

Kröners estimate [218]. As such, the present estimate of the curvature contributions allows only for a description of its contribution to the GB energy shape and for an appreciation of the relative orders of magnitude between the contributions from strains and curvatures.

The numerical accuracy of the integration procedure is shown in figure 4.3(a), presenting a comparison of the evolution of the elastic energy – E^{cauchy} – with respect to the misorientation angle obtained from the numerical integration procedure described above and the analytical formulae in the work of Bachurin *et al.* [23]. The numerical approach is in good agreement with analytical proofs.
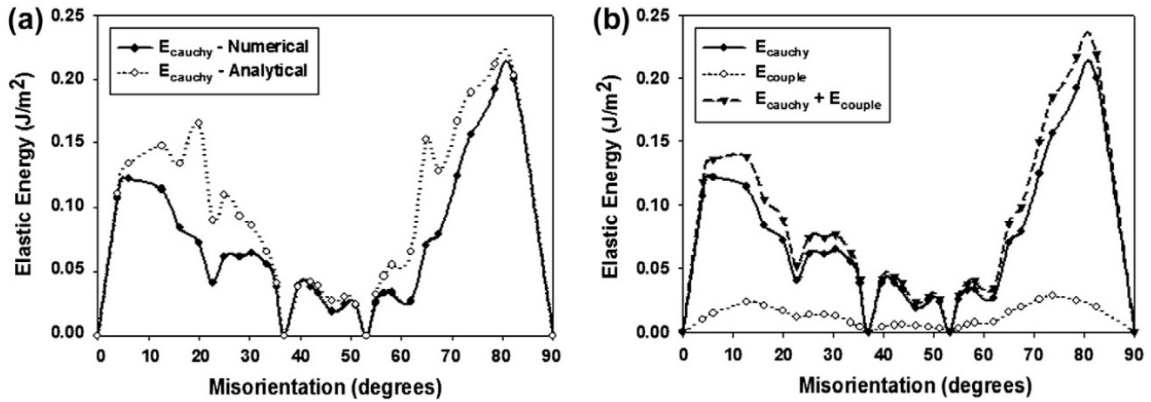
Figure 4.3: (a) Comparison between the Cauchy part of the elastic strain energy obtained from analytical derivations and numerically as a function of misorientation angles, (b) evolution of the total and Cauchy stresses and couple-stresses contributions to the GB energy as a function of misorientation.

Figure 4.3(b) shows the evolution of E^{cauchy} and E^{couple}, obtained via numerical integration, as a function of GB misorientation. It is found that the contribution of couple-stresses mimics that of Cauchy stresses. Furthermore, the contribution of couple-stresses to the total elastic energy is not negligible. When compared with the total energy obtained from atomistic simulations (shown in figure 4.4), however, it is found that there is a huge difference in the elastic energy obtained from the numerical procedure. In the DSUM – both in the case of infinite [139] and of finite [276] boundaries – the total GB energy is taken as the sum of the elastic energy, the
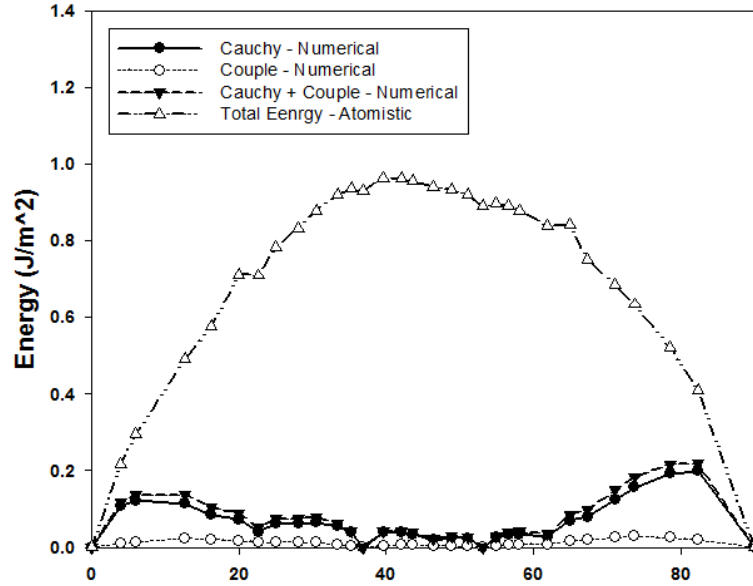
Figure 4.4: Comparison between the elastic energy obtained from numerical procedure shown in figure 4.2 and the total energy obtained from molecular statics simulations (points were digitized from [23]). The large difference in energy comes from neglecting the core region when using a discrete representation of the GB.

average of the specific energies of each reference structural unit and the core energy of each disclination dipole. These specific energies and core contributions are arbitrarily chosen in order to fit the energies obtained from atomistic simulations. The huge difference in the energies indicates that the core contributions are not negligible. Accounting for these requires using a fully continuous approach.

4.1.3 GB energy in continuous dynamic case: contribution of incompatible elastic strains and curvatures

This section is presented to briefly highlight the role of incompatibilities in elastic strain and curvatures on the grain boundaries. This study was led by Dr. Vincent Taupin and was directly motivated from the present work. Furthermore, the results obtained in that work are important

Continuous representations of the GBs were obtained by representing the disclination dipole walls that are used in the discrete DSUM model. The presence of these continuous densities induces incompatible curvatures which result in the generation of

Cauchy and couple stresses through the elastic constitutive relationship described in section 3.1. The GBs are then allowed to relax under their own stress fields resulting and the energies of the relaxed structures are plotted to re-create the <001> STGB energy vs misorientation plot. Quite interestingly, the energies obtained from the relaxed structures were found to be exceedingly small when compared with atomistic predictions. This difference arises from using the DSUM representation of GBs in the continuous approach. Reconsider the <001> STGBS shown in table 5. It can be seen that the non-special GBs in the range 22.62º – 64.94º are referred with respect to the boundaries 36.87º and 53.13º. The latter, which are special boundaries, are devoid of any minority units and, hence, disclination dipoles. Therefore, they have no contribution to the elastic energy of the GB. In the work of Bachurin *et al.* [23], the energies of these special boundaries are assigned a conveniently chosen value in order to fit the cusp energies with those obtained from experiments or atomistic simulations. However, such a fit is completely arbitrary. Furthermore, the energies are computed using a discrete representation of disclination dipoles.

A new methodology to represent GBs was developed in the work of Fressengeas Fressengeas *et al.* [135] with the aim to conform with the atomistic arrangements within GBs as well as energetically match with atomistic simulations and experiments. This is achieved by establishing a crossover between a discrete atomistic GB configuration and an equivalent continuous disclination density field. The result is shown in figure 4.5. Excellent agreement is found at all misorientations. Energy cusps are obtained for the $\Sigma5(310)$ and $\Sigma5(210)$ boundaries of misorientation 36.9° and 53.1°, respectively, in agreement with experimental data and atomistic predictions. This method was used to simulate shear coupled grain boundary migration in <001> STGBs by Taupin *et al.* [394]. The simulations also performed by Dr. Taupin were directly motivated from the static and dynamic cases presented in the previous section. Figure 4.6 shows the coupling factor predicted by the FDDM model for the

shea coupled boundary migration of <001> STGBs. The simulations revealed that the elastic constitutive laws presented developed by the author (refer to section 3.1) were crucial in modelling the dynamic behavior of defects; the cross terms $\boldsymbol{B}$ and $\boldsymbol{D}$ captured the non-local behavior that is induced in presence of disclinations, and were necessary to initiate and drive the motion of GBs.
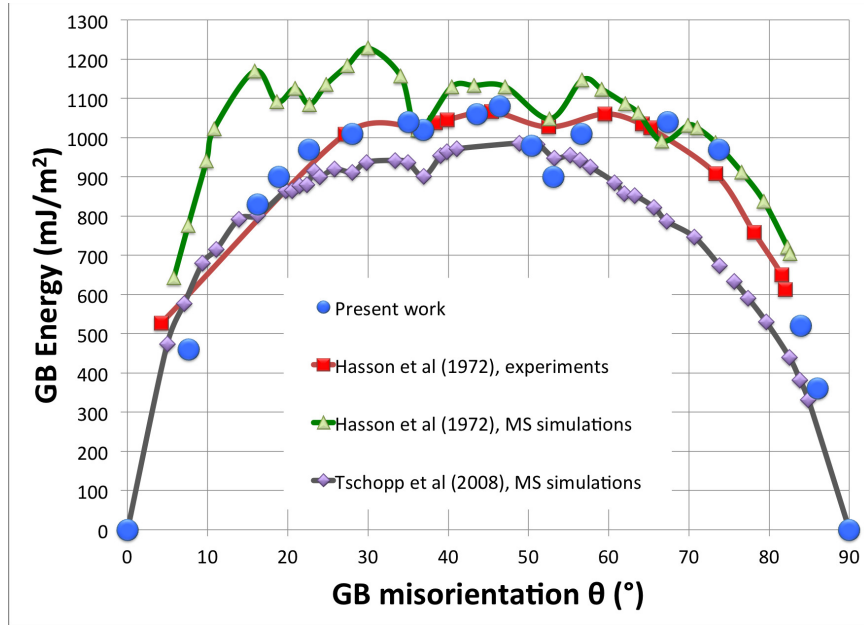
Figure 4.5: Elastic energy density per unit length of <001> tilt boundaries in copper, as a function of misorientation. Blue circles: present work, red squares/green triangles: experimental estimates/molecular statics predictions from [174], purple diamonds: molecular statics predictions from [408]. (Adapted from [135])

4.1.4   Continuous modelling at interatomic scale: rationalization

Based on all the results shown above, Fressengeas *et al.* [135] have provided a deep insight on the meaning of continuous modelling at the interatomic scale which is in accordance with most of the results shown in present work and is recalled in the following.

The current understanding is that the assumption of continuity of the field variables is no longer valid at or below the interatomic scale where the discrete atomistic
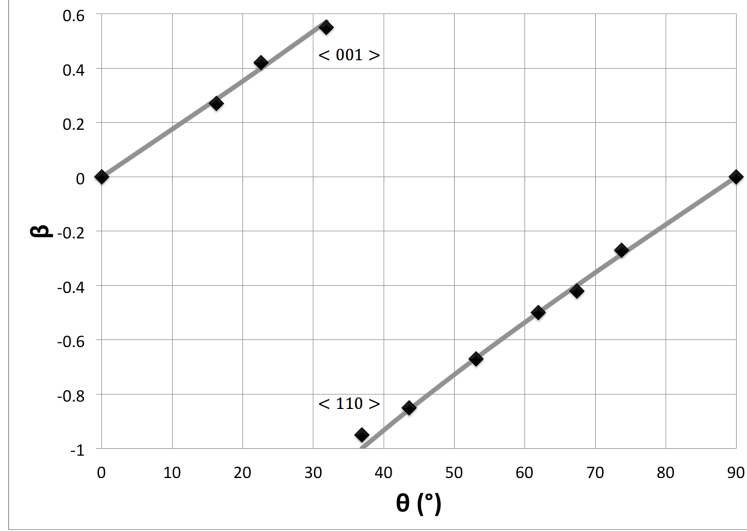
Figure 4.6: Shear-coupling factor as a function of misorientation. The dots represent the values obtained by the present simulations. The two solid lines represent the values predicted by the <001> and <110> shear deformation modes defined in [58]. (Adapted from [394])

nature of matter becomes apparent. Therefore, it is generally believed that continuum mechanics fails to appropriately capture the physical phenomena pertaining to this length scale. The present results demonstrate that an appropriate, non-local continuum description involving smooth fields of displacement and crystal defect densities can be adequate for the purpose of capturing the physical phenomena at this length scale, and may usefully complement atomistic representations.

Using a continuous approach at length scales below the elementary lattice parameters is certainly meaningful from the point of view of the differential geometry of continua. However, the fundamental reason for the ability of the present framework to describe physical properties at nanoscale is that it deals with the breaking of lattice symmetry and non-locality of the elastic behavior resulting from fluctuations of inter-atomic forces that take place in the core of crystal defects. It is interesting to note that accounting for the non-linearity of elasticity is not as essential as considering its non-local character. Although elastic dilatations as high as 20% are found

in the present calculations, using linear elasticity does not prevent from accurately retrieving the elastic energy of the GB. Furthermore, this excellent agreement was obtained without introducing any *ad hoc* fitting parameter in the formulation.

A continuous description of lattice defects may be considered as more attractive than discrete approaches for various reasons. Smoothness is desirable from the point of view of mathematical analysis and numerical computation, and because it allows coping with core properties. When viewed at a sufficiently small scale, lattice defects and the corresponding distributions of elastic strain and energy are better described by suitably localized smooth density fields than by a singularity. Furthermore, (ii) using continuous density fields to model crystal defect ensembles comes rather naturally from the structure of their conservation laws, *i.e.*, equations (3.97) and (3.98). From a kinematic point of view, the latter provide a rational framework for the dynamics of defects. In the present work, this feature is used to set out a boundary value problem for the displacement and dislocation/disclination density fields. This gives rise to the non-locality in space and time in the standard variables of conventional continuum mechanics. This non-local generalization of the latter, leads to well-posed problems in dislocation and disclination dynamics. In addition, (iii), this approach has a potential for computational efficiency because it does not have to resolve atomic vibrations. The kinetic energy of atomic and subatomic vibrations is time-averaged over periods of microseconds, and characterized as dissipation. Thus, by time coarse-graining, the atoms and their fast vibrations are replaced with the dissipative evolution of smooth dislocation/disclination density fields embedded in an elastic continuum. As a result, finite element simulations may allow considering the dynamics of crystal defects over time scales in the μs or more, under realistic loading rates and stresses.

Finally, (iv), a continuous approach of crystal defects at nanoscale like the present one provides a natural basis for the derivation of a continuous theory of crystal defect ensembles at meso-scale through appropriate averaging techniques. This was

170

proposed in section 3.5 where the structure of the meso-scale theory was derived by defining space-time averaged field variables as weighted, running averages of the corresponding nano-scale field variables over a domain whose scale is determined by the desired spatial and temporal resolution [22, 6, 343]. From the results shown above, several features can be anticipated that help understand implications of the present results at nanoscale on the structure of an averaged theory whose resolution length scale is too large to resolve GBs. Firstly, the averaged plastic strain/curvature rates defined in the coarse-graining process involve not only the averaged strain/curvature rates associated with the motion of signed defects (polar dislocations/disclinations) (3.95, 3.94), but also the strain/curvature rates ($\boldsymbol{L}^p, \dot{\boldsymbol{\kappa}}^{p*}$) associated with statistical dislocation/disclination densities of no polarity. Secondly, the conservation of the Frank and Burgers vectors implies the jump conditions (seen in section C.0.2) on the meso-scopic plastic curvature rate and strain rate, respectively, at the GB. These have a consequence on the non-locality of these field variables which affects the transport of defects for the case of shear coupled GB migration [394].

With a careful implementation of the continuum at the inter-atomic length scake, this approach can provide a basis for developing multi-scale models that encompass the inter-atomic, fine, meso- and macro- scales. This could be a potential alternative to coupled atomistic-continuum models such as the "coupling length scales" method [1], quasicontinuum method [392], "coupled atomistic and dislocation dynamics" method [367, 368], and the more recent "concurrent atomistic-continuum" method [471, 468, 469, 470].

4.2 TJs from <001> STGBs

In this section, a special case of TJs (TJs) – constructed from <001> STGBs – is considered. The discussion begins by deriving the kinematic constraints that are imposed

on the TJ dihedral angles and associated GB misorientations due to the available degrees of freedom to represent a TJ using STGBs in 2-dimensions. Then compatibility conditions are derived based on tangential continuity of elastic curvature at the TJ. Energies of TJs are plotted as a function of dihedral angles and misorientations. These are compared with energies obtained from TJ configurations respecting to kinematic constraints, compatibility conditions and Herring's relationship, respectively.

4.2.1 Kinematics

11 DOF are required to construct a TJ: 5 to define a first boundary, 5 to define a second boundary and 1 to define the orientation of the third boundary, which is left with only one rotation degree of freedom as it initiates at the intersection of the two other boundaries. If additionally, one considers the kinematic constraints imposed by the closure condition on a circuit mapped around a TJ, solely 8 DOF are required to uniquely define a TJ. These are reduced to 4 in the 2-dimensional case (*i.e.* each grain orientation and GB orientation less the circuit closure constraint). If only those TJs that are built from STGBs are considered – such as in the present case – then a relationship between the dihedral angles of the GBs and their misorientations can be obtained.

For the sake of illustration, figure 4.7 depicts a 2-dimensional TJ built from the intersection of tilt boundaries where the dihedral angles and the angle of orientation of each crystal with respect to the x-axis are denoted by β_i and ϕ_i with $i \in [1, 3]$, respectively. Let $[\psi_{ij}]$ denote the disorientation between grains i and j. Let β_{ij} be the dihedral angles between GBs i and j with $i, j \in [1, 3]$. The relationship between misorientation and dihedral angles can be expressed with relatively simple geometrical considerations shown in the following.
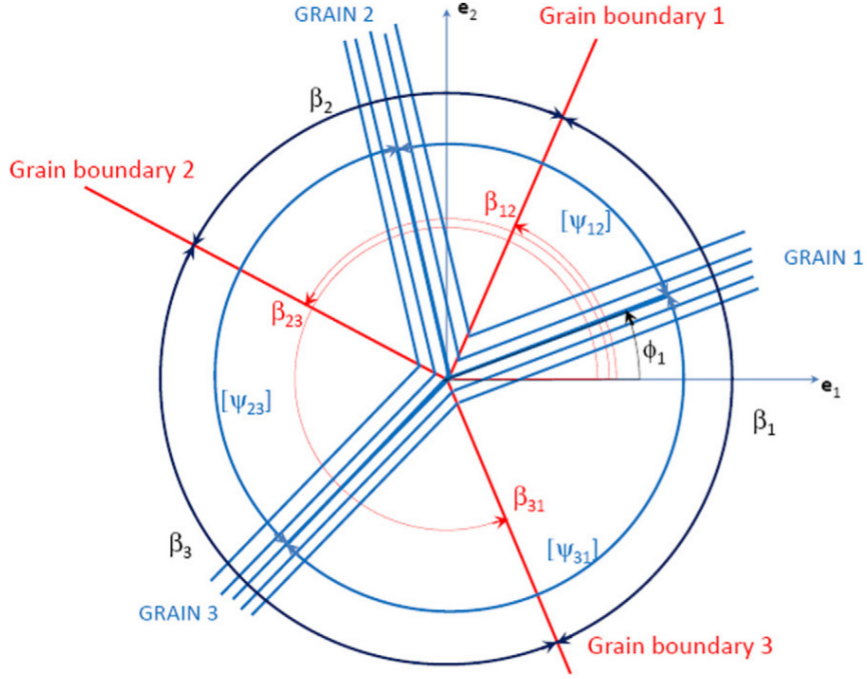
Figure 4.7: Schematic of the TJ geometry.

If the rotation transforming grain m into grain n is denoted as $\boldsymbol{R}_{mn}$ then:

$$\boldsymbol{R}_{mn} = \begin{pmatrix} \cos\left[\psi_{mn}\right] & \sin\left[\psi_{mn}\right] & 0 \\ -\sin\left[\psi_{mn}\right] & \cos\left[\psi_{mn}\right] & 0 \\ 0 & 0 & 1 \end{pmatrix} \tag{4.9}$$

In order to avoid the formation of a U-line [45, 46, 47] (discussed in section 2.2.2), the following constraint must be respected:

$$\boldsymbol{I} = \boldsymbol{R}_{31}.\boldsymbol{R}_{23}.\boldsymbol{R}_{12} \tag{4.10}$$

where $\boldsymbol{I}$ denotes the identity matrix. Combining equations (4.9) and (4.10), the following condition is obtained:

$$[\psi_{12}] + [\psi_{23}] + [\psi_{31}] = 2\pi n \quad \text{with } n = 0, 1 \tag{4.11}$$

As seen in figure 4.7, the orientation of each boundary is given by:

$$\beta_{12} = \frac{[\psi_{12}]}{2} + \phi_1 \tag{4.12}$$

$$\beta_{23} = \beta_{12} + \frac{[\psi_{12}]}{2} + \frac{[\psi_{23}]}{2} \tag{4.13}$$

$$\beta_{31} = \beta_{23} + \frac{[\psi_{23}]}{2} + \frac{[\psi_{31}]}{2} \tag{4.14}$$

Therefore the dihedral angles of the boundaries are given by:

$$\beta_1 = \beta_{31} - \beta_{23} = \frac{[\psi_{23}] + [\psi_{31}]}{2} \tag{4.15}$$

$$\beta_3 = \beta_{23} - \beta_{12} = \frac{[\psi_{12}] + [\psi_{23}]}{2} \tag{4.16}$$

$$\beta_2 = 2\pi - (\beta_1 + \beta_3) \tag{4.17}$$

equations (4.9) to (4.17) show that a TJ built from STGBs essentially has two degrees of freedom. Henceforth, TJs respecting equations (4.9) to (4.17) will be addressed as kinematically constrained TJs.

In the case of <001> STGBs, the geometric duality in the misorientation range 0° – 90° imposes additional constrains on the misorientations. Consider the (001) plane having a [001] STGB with [100] planes forming the misorientation angle $[\psi_{ij}]$ between grains i and j. If the misorientation, $[\psi_{ij}]$ is greater than 90° the corresponding misorientation between the [010] lattice planes of these grains will be less than 90° giving:

$$\left[\psi'_{ij}\right] = \pi - [\psi_{ij}] \tag{4.18}$$

ψ'_{ij} is the true misorientation of the GB.

4.2.2 Compatibility conditions

Interfacial tangential continuity conditions and multi-junction compatibility conditions developed in the appendix C.0.2 are derived here in the specific case of 2-dimensional TJs constructed using <001> STGBs.

Reconsider the plane edge-wedge model presented at the beginning of this chapter. In an orthonormal reference frame $(\vec{e}_1, \vec{e}_2, \vec{e}_3)$, let the disclination tensor be: $\boldsymbol{\theta} = \theta_{33}\vec{e}_3 \otimes \vec{e}_3$, all components other than θ_{33} being zero. Recall that the only relevant

elastic and plastic curvature components are $(\kappa_{31}^e, \kappa_{32}^e)$ and $(\kappa_{31}^p, \kappa_{32}^p)$. A plane dislocation distribution involving the edge densities α_{13} and α_{23}: $\alpha_{13} = \alpha_{13}(x_1, x_2), \alpha_{23} = \alpha_{23}(x_1, x_2)$ is consistent with this disclination distribution, in the sense that it allows satisfying the equilibrium and continuity equations. Furthermore, transport of these edge dislocations in the plane $(\vec{e}_1, \vec{e}_2)$ induces a plane plastic strain state $(\epsilon_{11}^p, \epsilon_{12}^p, \epsilon_{22}^p)$, with the strain rates $(\dot{\epsilon}_{11}^p, \dot{\epsilon}_{12}^p, \dot{\epsilon}_{22}^p)$, respectively.

Now, assume that an interface $\mathcal{I}$ (shown in figure C.1) is existing between the crystals (D^-, D^+), with normal $\vec{n} = \vec{e}_2$ oriented from D^- toward D^+. Provisionally, let the surface-dislocation and surface-disclination distributions $(\boldsymbol{\alpha}(\mathcal{I}), \boldsymbol{\theta}(\mathcal{I}))$ exist in the interface. Then, specializing equation (C.7), any tangential discontinuity of the elastic curvature along the interface: $\left[\kappa_{31}^e\right]$ is found to be accommodated by a wedge surface-disclination density $\theta_{33}(\mathcal{I})$:

$$\left[\kappa_{31}^e\right] = \theta_{33}(\mathcal{I}) \tag{4.19}$$

However, if continuous modeling of the boundary is adopted and surface-disclinations discarded, this relation transforms into the the tangential continuity condition:

$$\left[\kappa_{31}^e\right] = 0 \tag{4.20}$$

According to equation (C.9), a normal discontinuity $\left[\kappa_{32}^e\right]$ may also exist:

$$\left[\kappa_{32}^e\right] = \left[\psi\right] \tag{4.21}$$

where $\left[\psi\right]$ sets the disorientation of the crystals (D^-, D^+) across the interface. Hence, the latter appears to be representing a tilt boundary. The discontinuity (4.21) implies that discontinuity of the disclination density θ_{33} may occur at the interface.

If the reference point is chosen to lie in the interface, such that $\vec{r}_0 = 0$, specializing equation (C.15) shows that any tangential discontinuity of the elastic strain across the interface is accommodated by edge surface-dislocations $\alpha_{13}(\mathcal{I})$ and $\alpha_{23}(\mathcal{I})$:

$$\left[\epsilon_{11}^e\right] = -\alpha_{13}(\mathcal{I}) \tag{4.22}$$

$$\left[\epsilon_{21}^e\right] \quad = \quad -\alpha_{23}(\mathcal{I}) \tag{4.23}$$

However, if continuous modeling prevails, equations (4.22) and (4.23) reduce to:

$$\left[\epsilon_{11}^e\right] \quad = \quad 0 \tag{4.24}$$

$$\left[\epsilon_{21}^e\right] \quad = \quad 0 \tag{4.25}$$

Analogous relations are obtained from equation (C.22) for the plastic strain rates:

$$\left[\dot{\epsilon}_{11}^p\right] \quad = \quad 0 \tag{4.26}$$

$$\left[\dot{\epsilon}_{21}^p\right] \quad = \quad 0 \tag{4.27}$$

These relations indicate that the plastic shear strain rate and extension rate must be continuous along the interface. Preventing the non-glide motion of α_{13} edges across the interface is sufficient to fulfil equation (4.26). Possible occurrence of a normal discontinuity of the plastic strain rate tensor is written as:

$$\left[\dot{\epsilon}_{22}^p\right] = \left[\dot{\chi}\right] \tag{4.28}$$

where $\left[\dot{\chi}\right]$ may be non-zero. This relation implies that discontinuity of the non-glide motion of α_{23} edges along the interface, e.g. by climb or atom shuffling, is consistent with the continuity conditions on the plastic strain rate.

Now, reconsider the 2-dimensional TJ shown in figure 4.7. The disorientation between grain i and grain j and the orientation angle of their interface $\mathcal{I}_{ij}$ with respect to the $\vec{e}_1$ axis are respectively denoted with $\left[\psi_{ij}\right]$ and β_{ij} ($\forall(i,j) \in \{1,3\}$), while the angle between the lattice orientation of grain i and the interface $\mathcal{I}_{ij}$ is taken as $\left[\psi_{ij}\right]$. The analysis shown above in equations (4.19) - (4.21) for the generic interface $\mathcal{I}$ is now reproduced in a local orthonormal frame $(\vec{u}_1, \vec{u}_2, \vec{e}_3)$ for each of the three interfaces $\mathcal{I}_{ij}$, with $(\vec{u}_1, \vec{e}_3)$ as the plane of the interface and $\vec{n} = -\vec{u}_2$ as its normal directed from grain i to grain j. Written in components of the elastic

curvature tensor in the local frame of the interface $\mathcal{I}_{ij}$, the results corresponding to equations (4.19) and (4.21) are:

$$\left[\kappa_{31}^e\right]_{ij} = \theta_{33}(\mathcal{I}_{ij}) \tag{4.29}$$

$$\left[\kappa_{32}^e\right]_{ij} = -\left[\psi_{ij}\right], \tag{4.30}$$

all the other components of the matrices $\left[\kappa_e\right]$ being zero. Rotating these matrices to project equation (C.25) on the common reference frame $(\vec{e}_1, \vec{e}_2, \vec{e}_3)$, it is found that:

$$\sum_{ij=12,23,31} \left[\psi_{ij}\right]sin\beta_{ij} + \theta_{33}(\mathcal{I}_{ij})cos\beta_{ij} = 0 \tag{4.31}$$

$$\sum_{ij=12,23,31} -\left[\psi_{ij}\right]cos\beta_{ij} + \theta_{33}(\mathcal{I}_{ij})sin\beta_{ij} = 0 \tag{4.32}$$

Along with equations (4.11), equations (4.31) and (4.32) set a system of algebraic linear equations for the three unknowns $\left[\psi_{ij}\right]$. As a first step in the solution of this system, assume tangential continuity of the elastic curvature at all interfaces: $\forall ij, \theta_{33}(\mathcal{I}_{ij}) = 0$, as required in a continuous model. With a non-zero determinant $D = sin(\beta_{23} - \beta_{31}) + sin(\beta_{31} - \beta_{12}) + sin(\beta_{12} - \beta_{23}) = -(sin\beta_1 + sin\beta_2 + sin\beta_3)$, the solutions are such that:

$$\frac{\left[\psi_{12}\right]}{sin\beta_3} = \frac{\left[\psi_{23}\right]}{sin\beta_1} = \frac{\left[\psi_{31}\right]}{sin\beta_2} = \frac{2\pi}{sin\beta_1 + sin\beta_2 + sin\beta_3} \tag{4.33}$$

Equation (4.33) is a sine law, formally similar to the Herring equation between the interfacial free energies and dihedral angles [180]. However, it is not a force balance equation. Its meaning is that TJs with dihedral angles $\beta_i, i \in \{1, 2, 3\}$ and disorientations $\left[\psi_{ij}\right]$ fulfill rotational compatibility. In particular, when all dihedral angles are $\beta_i = 2\pi/3, \forall i \in \{1, 2, 3\}$, equation (4.33) leads to: $\forall ij, \left[\psi_{ij}\right] = 2\pi/3$. This case corresponds to a compatible TJ with three-fold symmetry. TJs respecting these conditions shall henceforth be called "compatible TJs" or "TJs respecting compatibility conditions". In the context of singular modeling, the algebraic system of equations (4.11), (4.31) and (4.32) may be used to obtain information on the

177

surface-disclinations needed to accommodate arbitrary disorientations $[\psi_{ij}]$ in a TJ with dihedral angles β_i. The disorientations, in the presence of surface-disclinations at the interfaces, are:

$$[\psi_{12}] \quad = \quad \frac{2\pi \sin\beta_3 + \theta_{33}(\mathcal{I}_{12})(\cos\beta_2 - \cos\beta_1) + (\theta_{33}(\mathcal{I}_{23}) - \theta_{33}(\mathcal{I}_{31}))(1 - \cos\beta_3)}{sin\beta_1 + \sin\beta_2 + sin\beta_3} \tag{4.34}$$

$$[\psi_{23}] \quad = \quad \frac{2\pi \sin\beta_1 + \theta_{33}(\mathcal{I}_{23})(\cos\beta_3 - \cos\beta_2) + (\theta_{33}(\mathcal{I}_{31}) - \theta_{33}(\mathcal{I}_{12}))(1 - \cos\beta_1)}{sin\beta_1 + sin\beta_2 + sin\beta_3} \tag{4.35}$$

$$[\psi_{31}] \quad = \quad \frac{2\pi \sin\beta_2 + \theta_{33}(\mathcal{I}_{31})(\cos\beta_1 - \cos\beta_3) + (\theta_{33}(\mathcal{I}_{12}) - \theta_{33}(\mathcal{I}_{23}))(1 - \cos\beta_2)}{\sin\beta_1 + \sin\beta_2 + \sin\beta_3} \tag{4.36}$$

However, inverting these relations for the surface-disclinations is not possible, because of the involved determinant Δ:

$$\Delta = (\cos\beta_3 - \cos\beta_2)(\cos\beta_1 - cos\beta_3)(\cos\beta_2 - \cos\beta_1)$$

$$+ (1 - \cos\beta_1)(1 - \cos\beta_3)(\cos\beta_1 - \cos\beta_3)$$

$$+ (1 - \cos\beta_2)(1 - \cos\beta_3)(\cos\beta_3 - \cos\beta_2)$$

$$+ (1 - \cos\beta_1)(1 - \cos\beta_2)(\cos\beta_2 - \cos\beta_1) \tag{4.37}$$

is zero. As an example, consider arbitrary variations $[\delta\psi_{ij}]$ from the disorientations $[\psi_{ij}] = 2\pi/3$ obtained in the three-fold symmetric TJ. Then, equations (4.34), (4.35) and (4.36) become:

$$\sqrt{3}[\delta\psi_{12}] \quad = \quad \theta_{33}(\mathcal{I}_{23}) - \theta_{33}(\mathcal{I}_{31}) \tag{4.38}$$

$$\sqrt{3}[\delta\psi_{23}] \quad = \quad \theta_{33}(\mathcal{I}_{31}) - \theta_{33}(\mathcal{I}_{12}) \tag{4.39}$$

$$\sqrt{3}[\delta\psi_{31}] \quad = \quad \theta_{33}(\mathcal{I}_{12}) - \theta_{33}(\mathcal{I}_{23}) \tag{4.40}$$

Clearly, the only differences in surface-disclination densities are obtained from equations (4.38), (4.39) and (4.40). Hence, from singular modeling analysis, any arbitrary variation from the disorientations in a compatible TJ can be accommodated by surface-disclinations, but the densities of the latter are known up to a constant. In continuous modeling, departures from the compatible disorientations are accommodated in a finite-width layer across the interface by bulk disclination densities.

Now, consider the impact of fulfilling the compatibility condition (C.30) on the normal discontinuities of the plastic strain rates at the TJ. In the local frame of interface $\mathcal{I}_{ij}$, the relations reflecting tangential continuity and normal discontinuity of the plastic strain rate tensor, and corresponding to equations (4.26), (4.27) and (4.28) are:

$$\left[\dot{\epsilon}^p_{11}\right]_{ij} = 0 \tag{4.41}$$

$$\left[\dot{\epsilon}^p_{21}\right]_{ij} = 0 \tag{4.42}$$

$$\left[\dot{\epsilon}^p_{22}\right]_{ij} = -\left[\dot{\chi}\right]_{ij}, \tag{4.43}$$

where $\left[\dot{\chi}\right]_{ij}$ may be non zero, the other components of the matrices $\left[\dot{\epsilon}^p\right]_{ij}$ being zero in the local reference frame. Rotating these matrices to project equation (C.30) in the common reference frame $(\vec{e}_1, \vec{e}_2, \vec{e}_3)$, it is found that:

$$\sum_{ij=12,23,31} \left[\dot{\epsilon}^p_{22}\right]_{ij} \sin^2 \beta_{ij} = 0 \tag{4.44}$$

$$\sum_{ij=12,23,31} \left[\dot{\epsilon}^p_{22}\right]_{ij} \sin \beta_{ij} \cos \beta_{ij} = 0 \tag{4.45}$$

$$\sum_{ij=12,23,31} \left[\dot{\epsilon}^p_{22}\right]_{ij} \cos^2 \beta_{ij} = 0. \tag{4.46}$$

For the sake of convenience, let $\beta_{12} = 0$. Without loss of generality, it is found that the determinant D of this homogeneous set of algebraic linear equations, where the unknowns are the three extension rate discontinuities $\left[\dot{\epsilon}^p_{22}\right]_{ij}, ij = 12, 23, 31$, is $D = sin\beta_1 sin\beta_2 sin\beta_3$. Since D is usually non-zero, the unique solution to equations (4.44), (4.45) and 4.46) is: $\left[\dot{\epsilon}^p_{22}\right]_{ij} = 0, ij = 12, 23, 31$. Therefore normal continuity of the plastic strain rate tensor is generally required at such TJs, in addition to tangential continuity. In connection with equation (4.28), the interpretation of this result in terms of dislocation mobility is that non-glide motion along the interfaces is generally not kinematically allowed at compatible TJs. An exception to this rule is met when one of the dihedral angles is equal to π, say $\beta_2 = \pi$. Then a non-zero solution to equations (4.44), (4.45) and (4.46) is existing: $\left[\dot{\epsilon}^p_{22}\right]_{31} = 0, \left[\dot{\epsilon}^p_{22}\right]_{12} = -\left[\dot{\epsilon}^p_{22}\right]_{23} \neq 0$,

which indicates that non-glide motion of dislocations along the straight interface $(\mathcal{I}_{12}, \mathcal{I}_{23})$ is still possible at the TJ (see figure 4.7).

4.2.3 Relationship between TJ geometry and excess energy

Two-dimensional TJs (figure 4.7) are represented by assembling three-GBs according to their specified dihedral angles. As shown in figure 4.8, each GB is represented with help of the DSUM. Since GBs reaching the TJ are essentially semi-infinite, construction of the triple line raises the question of the initial positioning of the disclinations associated with each GB. Choice is made here to let all GBs start at the triple line. In the event that the GB length is not an integral multiple of its period, compensating disclinations are added at the ends of the GBs such as to maintain the misorientation. An alternative choice would consist of allowing for an offset in the position of the first disclination of each boundary with respect to the triple line. While this may reduce the energy of the boundary, the local misorientation across a GB near the triple line would be changed.

Elastic energy of the TJs is computed via a similar numerical integration technique used in the case of GBs. First, the elastic energy – containing both elastic strain and curvature contributions – of a square area centered at the TJ is computed using a 2D Gauss quadrature integration method (figure 4.8). The domain size is decomposed into elements of equal size. In the integration area, contributions from all disclination dipoles -for each GB- are accounted for. Each GB length is larger than the integration box size. Convergence tests are performed to determine the GB length and the integration box size yielding accurate values of the triple line energies. Figure 4.9 shows, for a fixed integration area and mesh size, the effect of the GB length on the elastic energy of a $4°$, $-2°$, $-2°$ TJ with fixed and equal dihedral angles for a constant box size of 17.24 nm. The elastic energy converges when the GB length is equal to or larger than 20 μm. An estimate of the maximum ratio of box size to the GB length
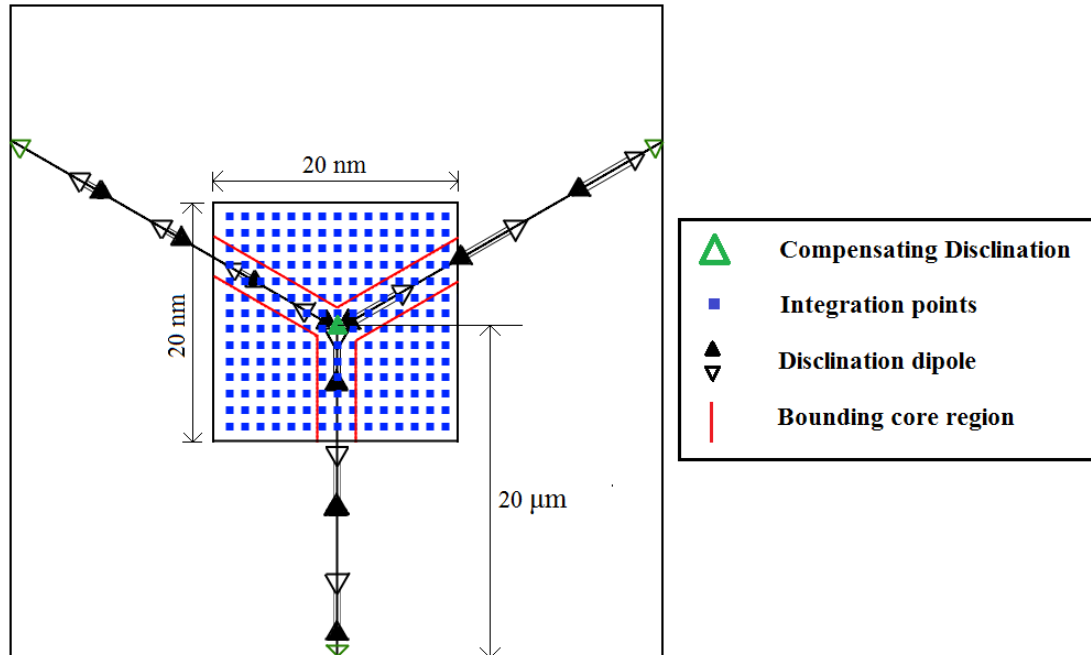
Figure 4.8: Overall Domain and Integration box used to compute the elastic energy of triple lines (not to scale). Compensating disclinations are added to maintain the misorientation of the GBs in the event that the length of the GB is not an integral multiple of its period.

to reach convergence yields a value of 8.623×10^{-4}.
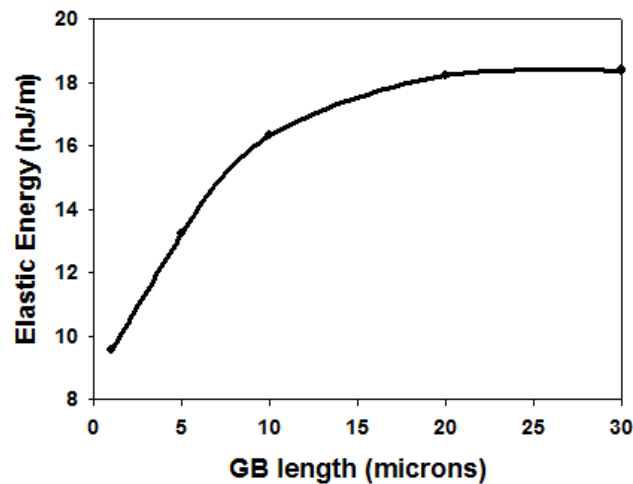
Figure 4.9: Evolution of total energy as a function of GB length for a $4°$, $-2°$, $-2°$ TJ with fixed and equal dihedral angles, keeping the box size constant ($17.24\ nm$).

181

Finally, the triple line excess energy is obtained by removing the elastic energy contribution of each GB from the total energy of the integration box. The former is obtained by multiplying the elastic energy per unit area of the infinitely long GB by the GB length.

The evolution of elastic energy with respect to the box size is studied such as to optimize the size of the integration box. In this case the GB length is kept constant at 20 μm and the maximum box size that can be chosen is 17.24 nm (in order to avoid end effects discussed above). The elastic energy and stress field evolution as a function of box size are shown in figure 4.10. Here, a triple line with GB misorientations 35°, 50°, −85° is considered and two geometries are studied (1) fixed dihedral angles and, (2) kinematically constrained by equations (4.9) to (4.17). As shown in figure 4.10 (a) and (c), the elastic energy of the unconstrained triple line appears to be diverging. This is also emphasized with the contribution of end-effects past box sizes of 17.24 nm. This is to be expected as incompatibilities are necessarily induced by the fact that the kinematic constraints are not respected. In the case where the kinematic constraints are respected, it is found that the computation of the excess elastic energies of triple lines is far less sensitive to the box size up to a certain point (varies for different TJ configurations) beyond which the end effects are non-negligible. This point is clearly marked in the Figure 4.10 (a) and (b). The global minimum in the elastic energy in the case of 35°, 50°, −85° kinematically constrained TJ occurs at a box size of 17.24 nm. It is to be noted that the box size leading to a global excess elastic energy at the triple line is dependent on the triple line geometry and GB misorientations.

As a result of the numerical study, in order to avoid end-effects, the GB length chosen is 20 μm and a fine mesh of size 0.1 nm (same as that for GBs) is chosen to achieve higher accuracy. The box size is fixed at 17.24 nm.

In order to understand the influence of the dihedral angles and GB misorientations on the excess energy of the TJ, three series of computations are performed:
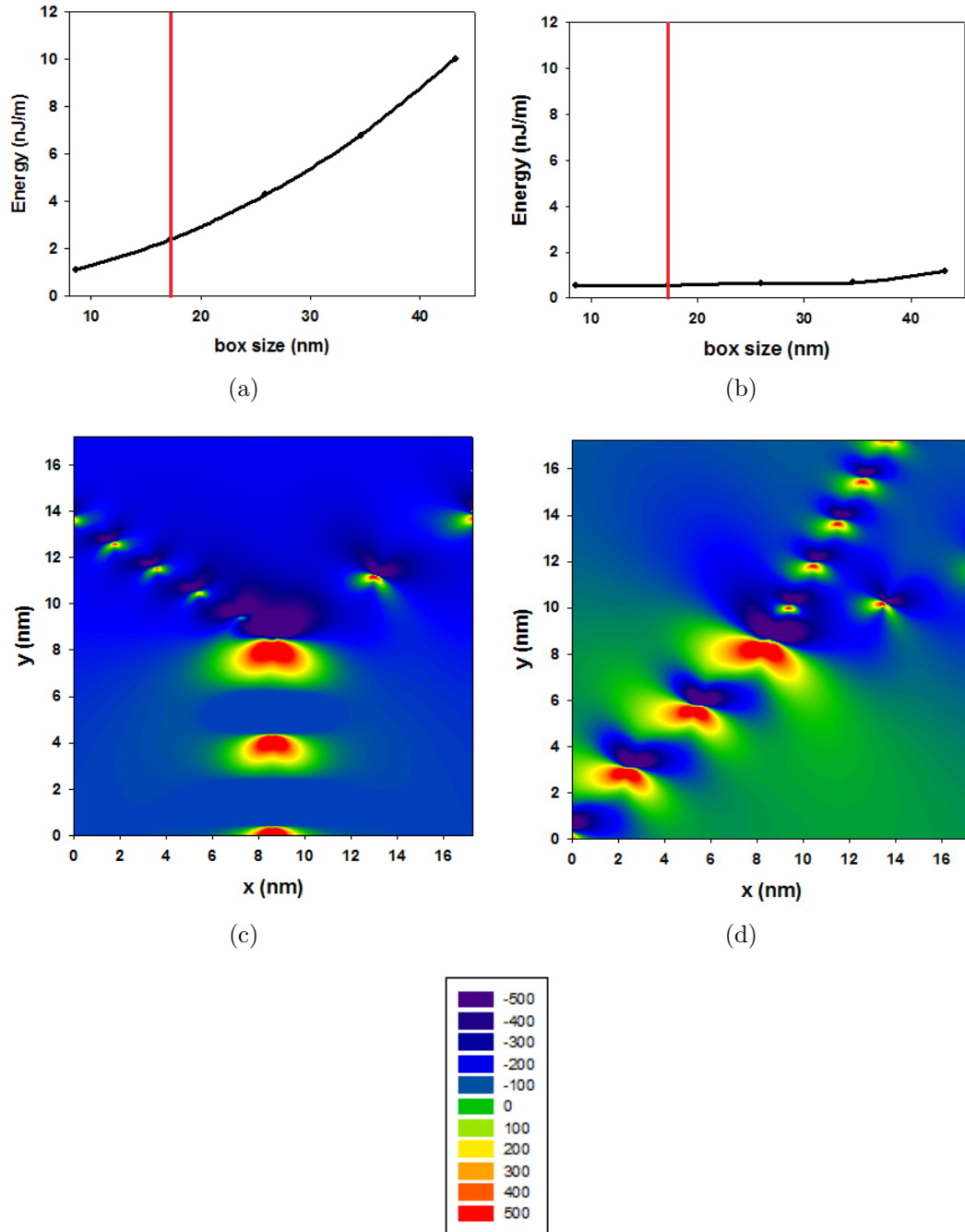
Figure 4.10: (a) Evolution of TJ energy and (c) stress field σ_{xx} (MPa) in the case of a 35°, 50°, −85° TJ with 120° dihedral angles, as a function of box size. (b) Evolution of TJ energy and (d) stress field σ_{xx} (MPa) in the case of a 35°, 50°, −85° kinematically constrained TJ, as a function of box size. The GB length is kept constant (20 μm) in all cases. The red line denotes the largest box size beyond which the end effects influence the elastic energy.

(1) First, the sole effect of misorientations is studied. The three dihedral angles are set equal to 120° and two of the misorientation angles are varied independently between −90° and 90°. The last misorientation angle is such that constraint (4.11) is respected. Clearly, in this case, the relations (4.13) through (4.17) are no longer respected – this implies that TJs constructed in these first virtual variations of the parameters should be composed of at least one non-symmetric boundary. Further, these variations of the misorientations are generally incompatible with either the Herring relation or the compatibility condition (4.33).

(2) In a second series of computations, the sole effect of dihedral angles is studied. For this purpose two of the misorientations are equal and the third one, $[\psi_{31}]$, is set according to the relationship obtained from (4.14). Two of the dihedral angles were varied independently from 90° degree to 150° and the third one is such that (4.17) is respected. Again, these virtual variations of the dihedral angles are generally incompatible with either the Herring relation or the compatibility condition (4.33).

(3) The last set of computations considers the case where all the kinematic constraints (4.13) to (4.17) are respected. Therefore in this case, there are only two degrees of freedom left. Misorientations $[\theta_{12}]$ and $[\theta_{23}]$ are varied; recall that by virtue of (4.15) to (4.17) the TJ dihedral angles are a consequence of the misorientation angles. As in the previous two cases, these variations of the misorientations are generally incompatible with either the Herring relation or the compatibility relation (4.33) except at one point.

4.2.3.1   The effect of misorientation changes on TJ excess energy

Figure 4.11 shows the evolution of total excess elastic energy as a function of GB misorientations with fixed and equal dihedral angles. Also, for the sake of completeness, figure 4.12 (a)-(b) separate the Cauchy and couple-stress related excess elastic

energy variations. Additionally, in both figures, TJ geometries respecting the kinematic, compatibility and equilibrium conditions of Herring are shown. Here, since all dihedral angles are equal, the corresponding kinematically constrained TJ coincides with that identified by both Herrings relation and the compatibility condition on curvature. Additionally, Figure 4.11 delineates GB misorientations corresponding to special cusp GBs; these are shown with straight lines. The minimum energy and negative energy points too are clearly identified in figures 4.11 and 4.12. Some combinations of TJs having misorientations equal to $n\pi/2$ ($n = 0, 1$ and 2) between two of the three associated grains correspond to the same crystal lattice orientation in both these grains and as such do not form a GB. The blanks in the figures 4.11, 4.12 (a) and (b) correspond to these TJs.

Observation of Figure 11 shows that the orders of magnitude of the predicted TJ excess energies are in general agreement with the few measures available to date [128]. It is essential to note in this figure that the compatibility, equilibrium and kinematic conditions described in the above do not correspond to global energy minima, but only to a local minimum of energy the total excess energy of the compatible TJ is predicted to be equal to 607.29 nJ/m from figure 4.12 - in either of figure 4.11 or 4.12. Note similarly that TJs constructed from two special cusp GBs do not correspond to local energy minima.

TJs corresponding to very low excess energies have a negative energy contribution coming from the couple stresses (see figure 4.12(b)). This suggests that couple stresses tend to stabilize some of the TJ configurations. However, it is to be noted that the TJ stability is necessarily related with the structure of the connected GBs. As such, if, during the course of loading, the local GB misorientations evolve in the neighbourhood of the TJ, the TJ excess energy will also change, and an *a priori* low energy TJ may, or may not, become a high energy one. Since they are not located in global energy minima, it is thus critical to understand their behavior using the dynamic FDDM
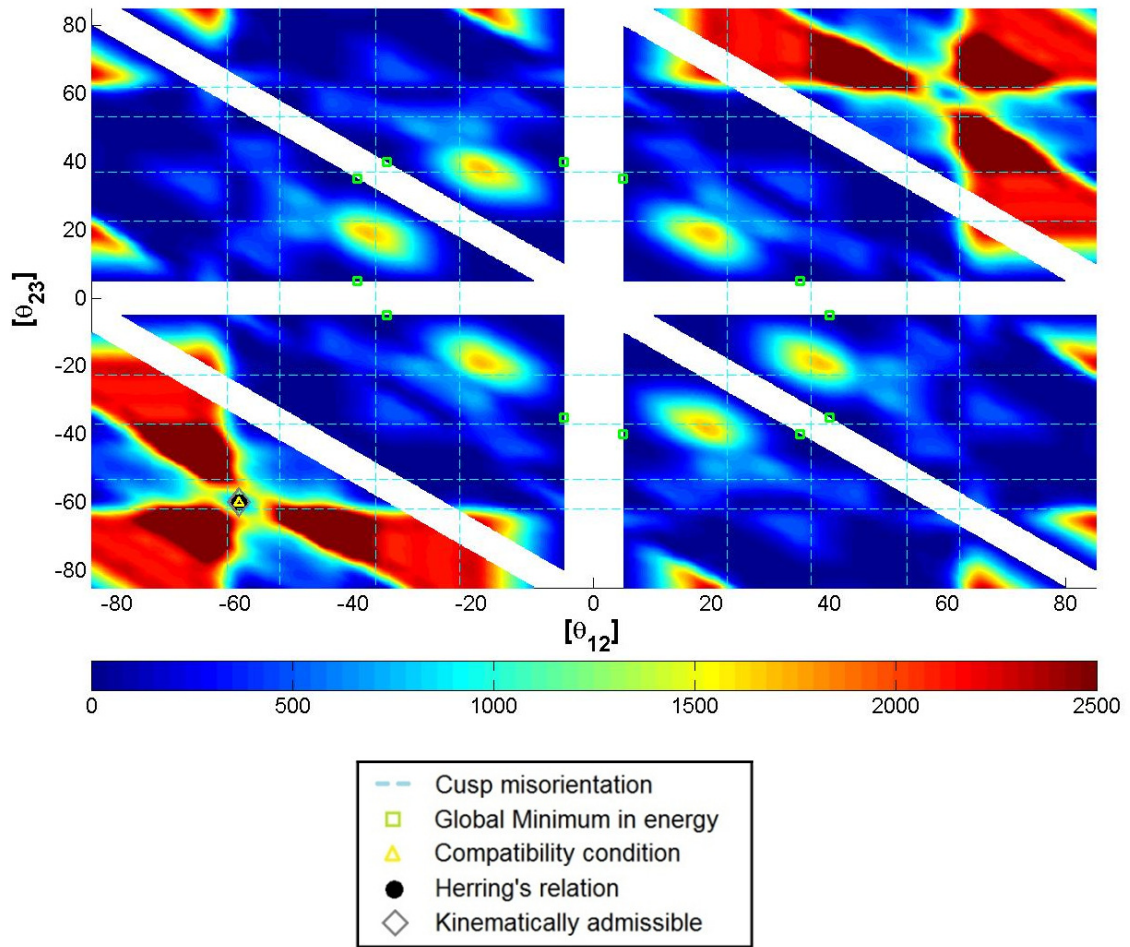
Figure 4.11: Evolution of the total excess elastic energy (nJ/m) with GB misorientation angles in the case of TJs with fixed and equal dihedral angles.

model.

The energy evolutions in both Figure 4.11 and 4.12 clearly exhibit a point symmetry that is a consequence of the crystal symmetry itself. The global minima indicated on these maps share the same energy value. The existence of multiple minima is a consequence of the crystal symmetry. Interestingly though, the central region of the plot exhibits a six fold symmetry where six regions of high excess energies can be identified. In attempting to connect the present results with the extension of the O-lattice theory of Bollmann [44] to the case of TJs two remarks are to be made. As discussed in the above and in [98], circuit mapping around a TJ and shrinking the

(a) E^{cauchy}

(b) E^{couple}
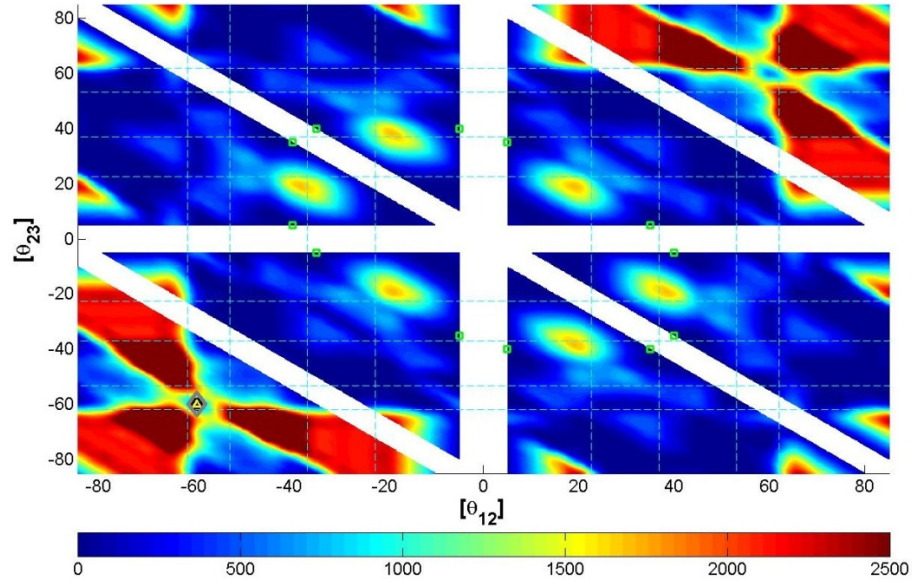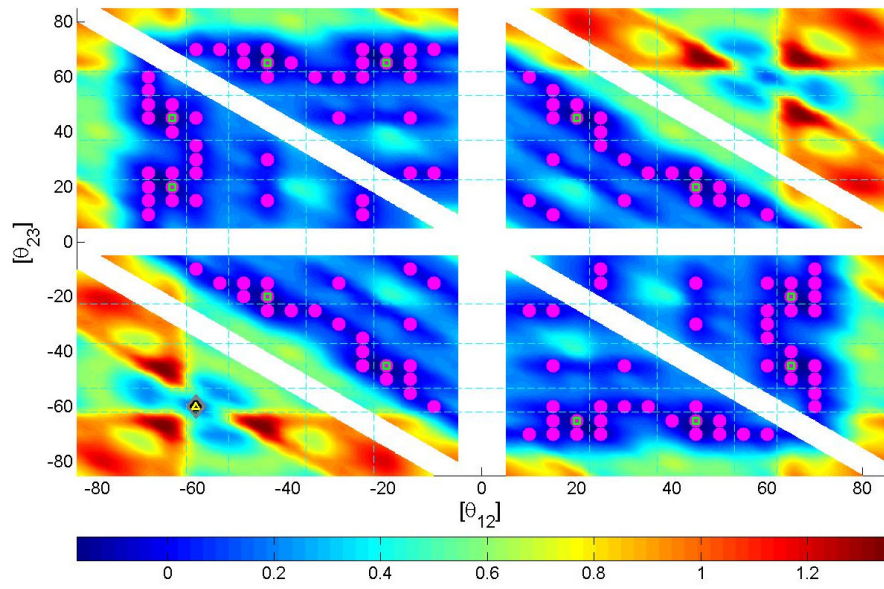
Legend:
- Cusp misorientation
- Negative energy
- Global Minimum in energy
- Compatibility condition
- Herring's relation
- Kinematically admissible

Figure 4.12: Evolution of the Cauchy (a) and Couple (b) stresses contribution excess elastic energy in (nJ/m) with GB misorientation angles in the case of TJs with fixed and equal dihedral angles.

circuit to a point yields a null enclosed area, which cannot act as a support either for dislocation or disclination densities. Therefore, it is to be pointed out that (regardless of the transformation operators used to perform circuit mapping around a triple line) a claim on the defect character of a triple line necessarily supposes that the circuit map is reduced to a small but non zero characteristic size ε. Connection with experimental measures – such as EBSD or HR-EBSD – also necessitates a reduction of the circuit map to a small but non-zero size, e.g. the smallest pixel size that can be detected by the experimental set-up. This experimental constraint is fortunately consistent with the present continuous approach. The very high-energy regions found in Figure 4.12 (a) and (b) may be associated to a net TJ disclination with non zero circuit size. In other words, the surface-disclination defect defined by equations (4.34), (4.35) and (4.36) is non zero only if $\varepsilon > 0$.

Upon comparing figure 4.12 (a) and (b) it is found that the contributions arising from the Cauchy stress are two to three orders of magnitude larger than those arising from couple-stresses. The fact that couple-stress contributions are much lower than that of Cauchy stress is not surprising as per the results on the relative contributions of couple-stresses on the GB elastic energy (see Figure 4.3). However, the difference in order of magnitude of each contribution suggests that significant disclination screening is occurring at TJs. Secondly, the comparison between Figure 4.12 (a) and (b) also shows that the couple and Cauchy stress contributions evolve in similar fashions *i.e.* the local minima in excess energy associated with contributions from Cauchy stress corresponds to local minima in the corresponding couple stress contributions.

4.2.3.2   Effects of dihedral angles

In order to study the effect of changes in the dihedral angles on the evolution of excess elastic energy at fixed misorientation angles-, two reference TJs are used. Note that as in the previous case, all structures studied do not respect the kinematical constraints

(4.9) to (4.17). The present study is thus to be regarded as purely parametric. The first TJ studied is built from GBs with low misorientation $4°$, $-2°$, $-2°$ and large period vectors while the second configuration studied corresponds to a TJ resulting from the intersection of relatively high angle GBs $20°$, $-10°$, $-10°$ and thus small period vectors.

Comparison between the two cases allows identification of general trends (if those exist) associated with the effect of dihedral angle evolutions. Results pertaining to the evolution of the total energy of the TJ in these simulations are presented in Figure 4.13 (a) to (b). In Figure 4.14 (a), (b) the evolution of Cauchy and couple-stress related parts of the excess energy, respectively, as a function of dihedral angles are shown for the first TJ, *i.e.* with $4°$, $-2°$, $-2°$ boundary misorientations. Similarly, results dedicated to the case of the second TJ considered are shown in Figure 4.14 (c) and (d). For the sake of clarity each plot is normalized by its absolute maximum. As in the previous case, TJs respecting kinematic constraints, compatibility conditions and Herring's relationship are shown with point symbols, as well as the minima of the plots. In the present case, as the dihedral angles are left free to vary and the GB misorientations are fixed and used to determine the unique boundary respecting Herrings relation, the kinematically constrained condition and the compatibility condition (4.33) will not yield the same point. From Figure 4.13, a comparison of the relationships between dihedral angles and TJ excess energy for both TJs studied, clearly shows that no general trend, *i.e.* independent on the GB misorientations, can be extrapolated. Considering only the case of Cauchy stresses, it is found that low dihedral angles correspond to low energy levels in the case of the $4°$, $-2°$, $-2°$ TJ while the same dihedral angles yield large values of the TJ excess energy for the large misorientations.

Note here, that the change in GB structure *i.e.* leading to an asymmetric boundary - resulting from a change in the dihedral angles is not accounted for. These changes

(a) $4°$, $-2°$, $-2°$ (E^{total})

(b) $20°$, $-10°$, $-10°$ (E^{total})

□ Global Minimum in energy
△ Compatibility condition
● Herring's relation
◇ Kinematically admissible
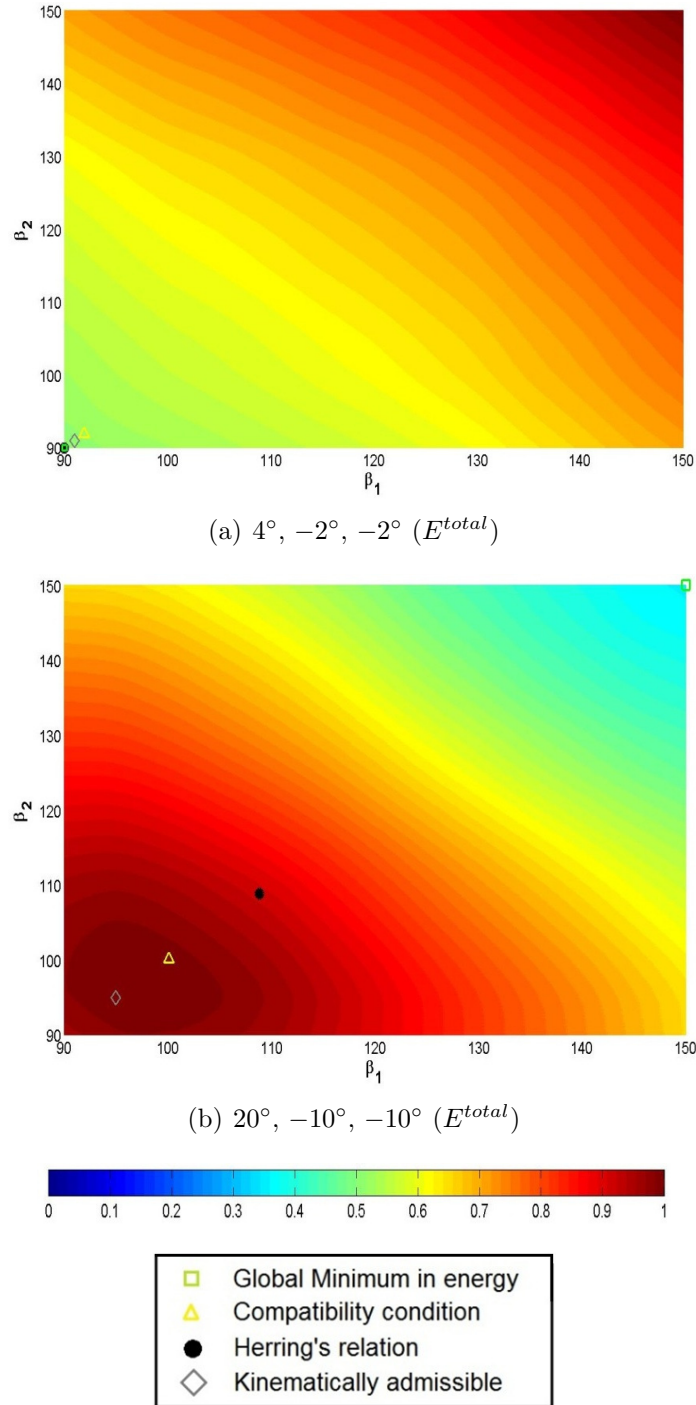
Figure 4.13: Normalized total triple line excess energy contributions for the $4°$, $-2°$, $-2°$ TJ (a) and $20°$, $-10°$, $-10°$ TJ (b).

are expected to be minor for (1) small changes in the dihedral angles and (2) long period vector boundaries such as the $4°$, $-2°$, $-2°$. Interestingly it is found that
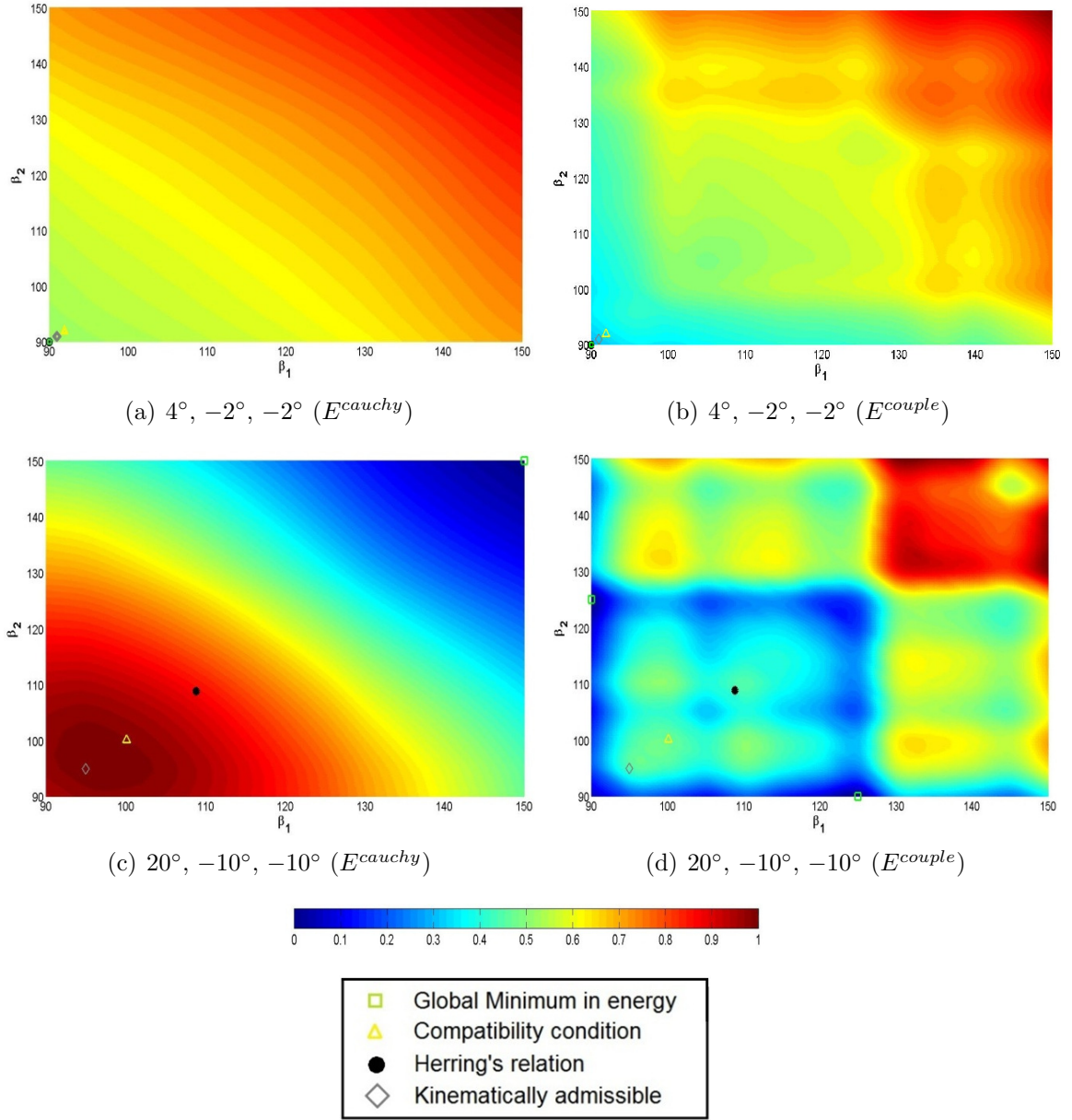
Figure 4.14: Normalized triple line excess energy contributions from the (a,c) Cauchy and (b,d) couple stresses with respect to the change in the dihedral angles for the $4°$, $-2°$, $-2°$ TJ (a,c) and $20°$, $-10°$, $-10°$ TJ (b,d).

in the case of this TJ, departure from the kinematically constrained configuration – which, in this case, corresponds to a change in dihedral angles – can lead to higher excess energy configurations. However, this is not the case for $20°$, $-10°$, $-10°$ TJ. In the latter case, deviating away from the kinematically constrained configuration

lowers the excess energy of the TJ, thus improving its stability.

Comparison between figures 4.14 (b) and (d) shows that in the case of both TJs, change in dihedral angles produce similar variations in the couple stress contribution to the excess energy. On the other hand, from figures 4.14 (a) and (c), this is clearly not the case for the Cauchy stress contribution to the excess energy. In general the Cauchy stress related part of the excess energy is much larger in magnitude than that of the couple stress contributions to the elastic energy. Therefore, similarity in the evolution of the total excess energy (figures 4.13 (a) and (b)) and Cauchy stress contribution to excess energy is expected.

4.2.3.3 Relationship between TJ excess energy and GB misorientations in the kinematically constrained case

In the case of kinematically constrained TJs resulting from the intersection of three STGBs, the evolution of the total excess energy as a function of two of the GB misorientations is shown in figure 4.15. In essence, the coupled effect of misorientations and dihedral variations is investigated. As in case (a), negative energy points, the global minimum TJ, TJ respecting Herrings relationship, and TJ respecting the compatibility condition are denoted with point symbols. Similar to the previous cases, dashed lines denote special cusp misorientations. Unlike the case of TJs with fixed dihedral angles a six-fold symmetry no longer exists for the kinematically constrained TJs.

It is found here that large variations in the energy levels appear. More interestingly, non negligible areas of the plots exhibit negative excess energies. From comparison with results obtained in cases (a) and (b) it is clear that this is the result of the coupling between dihedral angles and GB misorientations. Note however, that although it is often the case, the excess energy of the kinematically constrained TJ is not necessarily lower than that of the "iso" TJ with equal dihedral angles and same GB misorientation angles. Moreover, it is found here that neither the TJ identified by

192

Herrings relationship nor by the compatibility requirements corresponds to the global minimum energy TJ. Again, this result serves as a strong motivation for studying the dynamics of these structures.
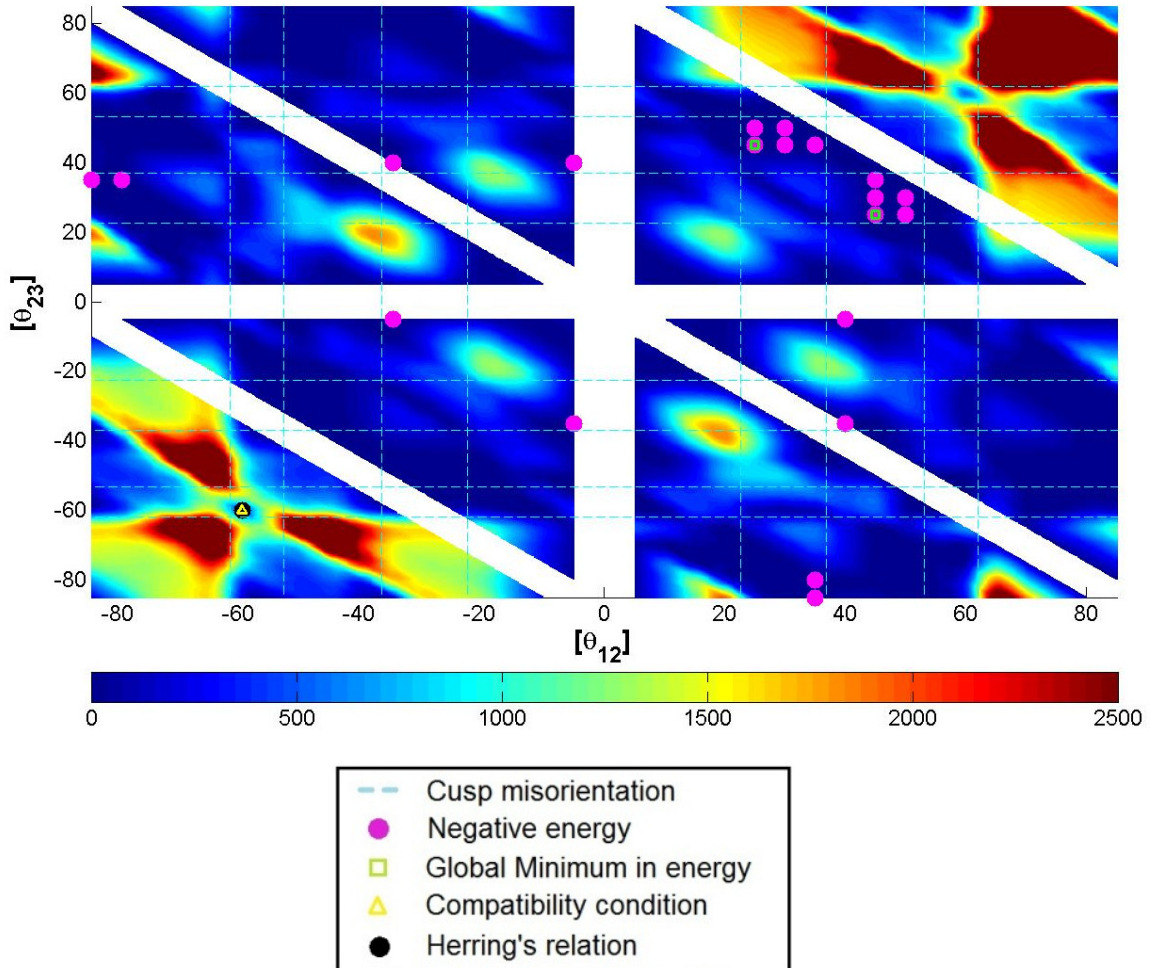
Figure 4.15: Total excess energy evolution with respect to the GB misorientations in the case of kinematically constrained TJ.

In order to appreciate the possible role of couple stresses on minimizing TJ energy, figure 4.16 presents the evolution of the ratio $r = |E_{couple}| / (|E_{couple}| + |E_{Cauchy}|)$ as a function of GB misorientations. It is found here that most points with negative excess energy correspond to large r values between 0.2 and 0.85. Moreover, the regions of large r values are rather diffuse. Thus, a local change in GB misorientation in these regions – for example, due to an externally applied load – would not drastically

change the TJ excess energy. This suggests that couple-stresses may play a key role in stabilizing TJs.
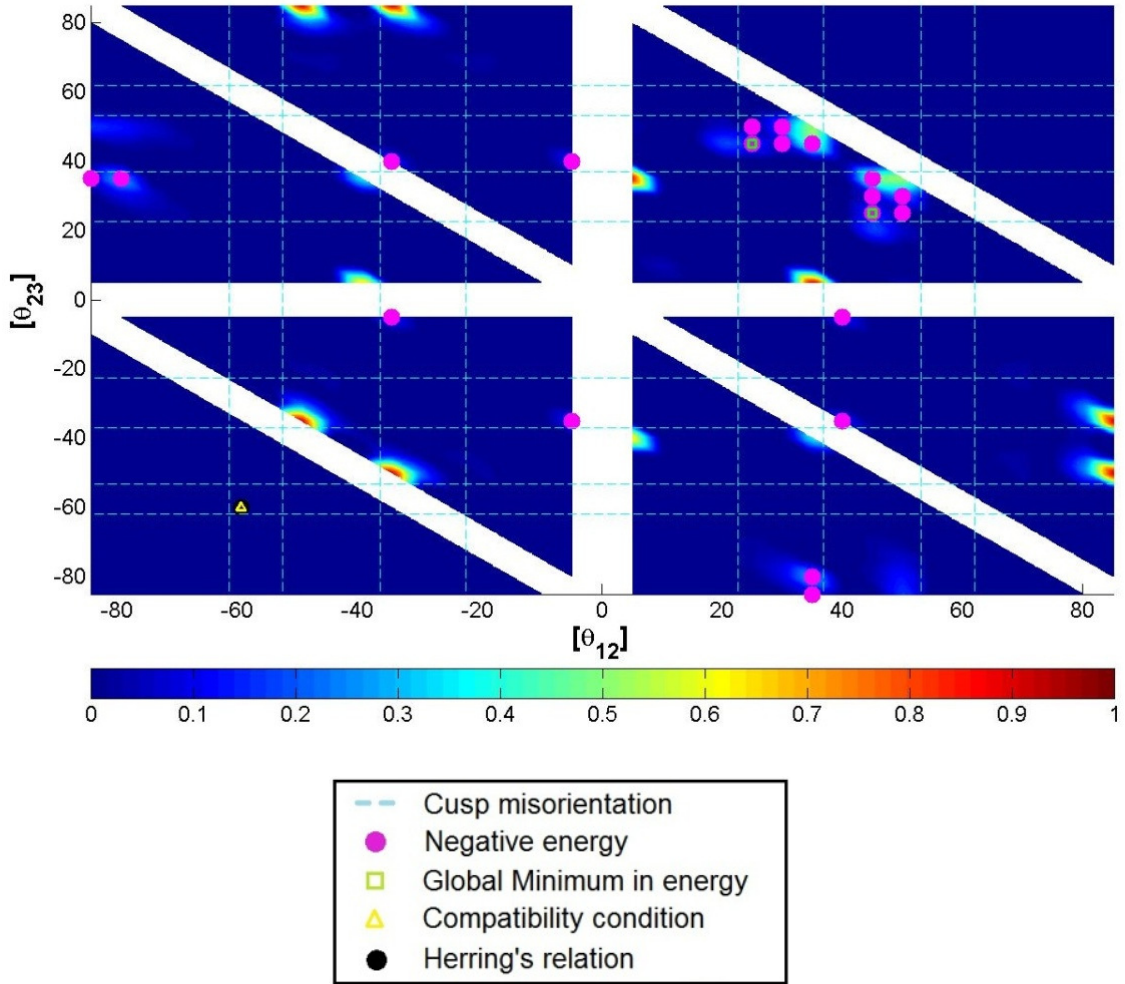
Figure 4.16: Evolution of the ratio: $r = |E_{couple}| / (|E_{couple}| + |E_{Cauchy}|)$ with respect to the GB misorientations.

This work shows that with the adopted TJ construction technique the energy levels vary significantly. First, very large TJ excess energies appear in a significant part of the geometries considered. These TJs are unlikely to be observed in a material; they should yield large driving forces associated with plasticity mechanisms resulting in lower energy local configurations. This is in agreement with molecular dynamics simulations [484]. Second, all TJ geometries with negative excess energies were identified. In those negative energy cases, the contribution of elastic curvatures (and

couple stresses) to the total system energy is comparable to that of elastic strains (and Cauchy stresses). Finally, kinematically admissible TJs, i.e. TJs satisfying the kinematic constraints and compatibility conditions on the normal discontinuities of elastic curvature, do not correspond to global but to local minima of the excess energy.

4.3   Discussion

This chapter began with the intention to demonstrate the advantages of using a disclination based continuous approach at the fine scale by applying it to the case of <001> STGBs and TJs constructed from these STGBs.

The disclination based approach has provided an important link between atomic and continuous representations of GBs. The FDDM model facilitated the development of a new fully continuous GB representation technique which allowed to recreate energy vs. misorientation curves for <001> STGBs that gave a close match with experimentally obtained curves; coming from a continuum based model, such a closeness is unprecedented without any *ad hoc* assumptions. The key to this result is in defining GB core structure using polar disclination densities which induce incompatibilities in elastic strain and curvature that contribute to the elastic energy. This ensures that the GB misorientation is preserved. Therefore, the disclination based continuous representation of GBs preserves both the energy and the misorientation of the GB.

FDDM's predictive capabilities for GB mechanisms are then tested in the case of shear coupled GB mechanism for <001> STGBs. The model very accurately predicts the geometric factor β associated with the motion of these boundaries. An important feature is highlighted during this study. The transport of defect densities is strongly dependent on the non-locality associated with the presence of disclinations at the inter-atomic scale. This is captured through the 5th order elasticity tensors associated with the cross terms in the elastic constitutive laws. Their importance can be understood from the fact that the GB motion could be achieved only when the

terms associated with these elasticity tensors were accounted for. This also highlights that a couple stress theory is necessary to study the mechanical properties of GBs.

Application to the case of TJs, although in the very specific case of those constructed from <001> STGBs in a static setting, have highlighted some important results. TJs that are thought to be energetically stable based on Herring's relationship or the newly presented kinematic and compatibility constraints are found to be at a local and not global minima in the TJ energy vs. GB misorientations maps. Some of these lower energy configurations have compensating disclinations at the location of the TJ. These are necessary to maintain the misorientation of the GBs and it is found that they do not always result in a net increase in the TJ energy. This indicates that disclination nucleation could be a possible relaxation mechanism. Such a conclusion is consistent with the recent experimental observations of disclination dipoles along a $\Sigma 9$ GB in nc Pd which was bounded on one side by a TJ. A deeper understanding of disclination nucleation processes could be understood using a dynamic approach such as the fine scale FDDM. This would also help understand phenomena such as TJ mobility and its effect on GB motion.

In the next chapter, the meso-scale field disclination and dislocation model is used to better understand polar disclination nucleation.

4.4 Conclusion

In this chapter a disclination based representation of <001> STGBs and TJs is used to understand the contribution of strain and curvature incompatibilities to GB energy and geometry of local microstructure. Incompatible elastic strains that manifest themselves within the defect cores are found to have the most significant contribution to the elastic energy. Their contribution to the elastic energy is captured through the higher order/grade elastic constitutive laws developed in this work. These elastic laws capture the non-locality associated with the presence of disclinations and play a

crucial role in modelling dynamics of disclinations and dislocations.

Static simulations were performed to generate TJ energy vs. misorientation maps for TJs constructured from <001> STGBs. Results revealed that TJ configurations corresponding to Herring's relationship, respecting kinematic constraints, and compatibility conditions on elastic strain and curvature, did not belong to a global minimum. The global minimum excess energy TJ configuration conisted of high angle GBs. Some TJ configurations were found to have a negative excess energy contribution. For these triple junctions the elastic curvature, and consequently couple stress, contribution to the elastic energy was notably large compared to higher energy TJ configurations. This suggests that elastic curvatures could be generated as a consequence of relaxation mechanisms possibly through the nucleation of sub-grain boundaries, new grains, disclinations, twins.

CHAPTER V

TOWARDS A CRYSTAL PLASTICITY MODEL BEYOND DISLOCATION SLIP: MESO-SCALE APPLICATIONS TO FCC POLYCRYSTALS

The aim of this chapter is to understand the contribution of lattice curvature to the bulk mechanical response of nc materials. To that end, the meso-scale phenomenological field disclination and dislocation mechanics model (PMFDDM), developed in section 3.5.1, is applied using using state-of-the-art fast Fourier transform (FFT) technique to study polycrystals. The chapter is organized as follows: The discussion begins by recollecting a recently developed method to determine the content of polar dislocation and disclination densities of electron backscattering diffraction (EBSD) orientation mapping of polycrystalline sample. This technique is used to set up initial elastic curvature and polar defect densities in the microstructure arising just from the elastic inhomogeneity. Following this the FFT technique based on continuous Fourier transforms (CFT) is presented along with the iterative procedure and algorithm. The advantages and disadvantages of FFT formulation over FEM are discussed. The PMFDDM FFT model is benchmarked with respect to the conventional elasto-viscoplastic (EVP) FFT model based on dislocation slip plasticity [239]. This serves as a motivation for developing a discrete Fourier transform method (DFT). Then relaxation of nc microstructures is studied by first activating only strain plasticity and then both strain and curvature plasticity, to understand the contribution of the latter. Finally, the The PMFDDM DFT model is applied to highlight the contributions of curvatures to nc/ufg plasticity. In these simulations, the defects generated during plasticity are stationary *i.e.* no defect transport. In this specific case, the

plastic curvature contribution to plasicity is via grain rotation and/or generation of geometrically necessary dislocations and disclinations.

5.1 Characterizing the microstructure: interfacial polar defect densities and curvature

In the previous chapter it was seen that at the fine-scale resolution GBs are characterized using disclination dipoles. At the meso-scale, spatial averaging of these dipoles results in a net zero polar disclination density. However, the polar dislocation densities are non-zero and need to be accounted for. The aim of this section is to present a numerical technique that can capture the polar dislocation content in the GBs described at the meso-scale and can be used as an initial condition to characterize the microstructure.

To that end, the following approach is taken. Recalling the discussion in section 3.5.1, GBs at the meso scale are modelled as singular surfaces accommodating the jump in orientation between two grains of the polycrystal. As a result of this orientation jump, incompatible elastic curvatures are generated. These curvatures are related to the polar dislocation densities through equation 2.98. If these elastic curvatures can be estimated then the nc microstructure can be characterized with polar dislocations.

In light of the above, the 2-dimensional methodology of Beausir and Fressengeas [30] to extract residual polar dislocation and disclination density fields from the EBSD maps is recalled and extended to a fully 3-dimensional setting. It is assumed that the lattice orientations are known at all points in the microstructure, possibly from experimental data, in order to set up the initial conditions. The local lattice orientations are characterized by a set of Euler angles (ϕ_1, ϕ, ϕ_2) and the associated sample-to-crystal rotation matrix $\boldsymbol{R}$. The disorientation between two points a and b in the body is given by the couple $(\vec{r}, \Delta\psi)$, where $\vec{r}$ is the axis of rotation and $\Delta\psi$ the disorientation angle around $\vec{r}$. In the cartesian coordinate system with sample

reference frame $(\vec{e}_1, \vec{e}_2, \vec{e}_3)$, the difference of elastic rigid body rotation vector $\boldsymbol{\Delta\omega}^e$ between points a and b satisfies:

$$\Delta\psi \, \vec{r} = \Delta\omega_i^e \, e_i. \tag{5.1}$$

If $\boldsymbol{R_a}$ and $\boldsymbol{R_b}$ denote the rotation matrices at points a and b, the disorientation matrix from point a to b can be calculated as $\Delta\boldsymbol{R} = \boldsymbol{R_a}^{-1} \cdot \boldsymbol{R_b}$. Then, the variation of elastic rigid body rotation $\Delta\omega_i^e$ is obtained from [311]:

$$\Delta\omega_i^e = -\frac{e_{ijk}\Delta R_{jk}\Delta\psi}{2sin(\Delta\psi)}. \tag{5.2}$$

As a final step, the elastic curvature tensor component κ_{ij}^e is approximated by the variation of the elastic rigid body rotation $\Delta\omega_i^e$ over a distance Δx_j:

$$\kappa_{ij}^e = \frac{\Delta\omega_i^e}{\Delta x_j}. \tag{5.3}$$

The initial polar disclination density associated with this elastic curvature field is then given by equation (2.92). Assuming that the curl of elastic strain tensor at the initial time is negligible and using equation (2.98), the initial polar dislocation density associated with elastic curvatures is:

$$\boldsymbol{\alpha} = -\boldsymbol{\kappa}_e^t + tr(\boldsymbol{\kappa}_e)\mathbf{I} \tag{5.4}$$

The elastic curvature contribution to polar dislocation density leads to the generation of geometrically necessary dislocations which are in addition to those generated from strain gradients arising due to geometry of loading [120, 123] or internal sources of plastic inhomogeneity [16].

A consequence of using this methodology is that there is an artificial jump induced in the elastic curvature fields that results in the generation of disclination densities that do not have a physical basis. However, this methodology is the best technique available to account for the contribution of residual curvatures.

5.2 PMFDDM using a continuous fast Fourier transform technique

The main purpose behind developing the meso-scale model is to study the influence of elastic inhomogeneity on disclination evolution and to capture the collective behavior of grain boundaries on polycrystalline plasicity. Achieving this requires a numerical technique that is capable of handling the local effects of inhomogeneous plasticity, elastic heterogeneity, rotational effects coming from both dislocation and disclination based plasticity, among many other aspects in a realistic time frame. This is difficult to achieve using an FEM based approach whose computational time complexity is $O(N^3)$, where N is the total number of simulation points. To that end, an FFT technique is developed as an alternative approach to solve the PMFDDM problem.

The FFT method was originally developed for linear elastic [283, 284], non-linear elasto-plastic [283, 284] and viscoplastic [271, 272] composites. It was then extended to linear and non polycrystals where the heterogeneity was associated with the spatial distribution of grains and orientation dependent mechanical properties [238, 239]. The FFT approach used in this work derives motivation from the elasto-viscoplastic (EVP) FFT model [239]. The numerical scheme involves solving the 'local problem' on a representative volume element to obtain the effective response of a polycrystal subjected to macroscopic geometric quantities and stresses.

In the following, first the compatible solution to the local problem is developed using continuous Fourier transform representation of Green's tensor for a heterogeneous anisotropic elastic material. Following which the FFT iterative procedure based on continuous transforms of derivatives is presented. Recall that at meso-scale incompatibilities are not associated with individual cores representative of defects. Recalling the argument from section 3.1 centro-symmetry is assumed to be respected everywhere within the domain, inluding the zones of incompatibility, the terms involving 5th order elasticity tensors $\boldsymbol{B}$ and $\boldsymbol{D}$ are neglected from the elastic constitutive

laws. Thus for present purposes the PMFDDM model is developed in the couple stress theory framework. For the sake of convenience, the superscripts 's' and 'D' for Cauchy and couple stresses and their respective polarization tensors will henceforth be dropped.

5.2.1 Modelling framework

The local problem consists of equilibrium equation (3.14), elastic constitutive laws (3.99) and (3.100), along with boundary and interface conditions. For the present purposes, it is assumed that all the differently oriented grains are perfectly bonded *i.e.* displacements, tractions and moments are continuous across GB interfaces. In order to treat the discontinuity of these fields at the boundaries, periodic boundary conditions are imposed. These can be understood in the following way. Let the total strain ($\epsilon(\vec{x})$) and curvature ($\kappa(\vec{x})$) fields be split into their volume averages E and K along with fluctuations in local fields $\epsilon^*(\vec{x})$ and $\kappa^*(\vec{x})$, respectively.

$$\epsilon(\vec{x}) = E + \epsilon^*(\vec{x})$$

$$\kappa(\vec{x}) = K + \kappa^*(\vec{x}) \tag{5.5}$$

The presence of continuous total strain and curvature fields implies that the body is simply connected and therefore a continuous displacement field ($\vec{u}(\vec{x})$) can be uniquely defined. This displacement can also be split into a mean field and a fluctuation field $\vec{u}^*(\vec{x})$. By assuming periodic boundary conditions it is assumed that the fluctuating displacement is $\vec{u}^*(\vec{x})$ is periodic. Furthermore, the total displacement is continuous everywhere in the domain. In order to satisfy the equilibrium equations the traction and moment vectors *i.e.* $\sigma \cdot \vec{n}$ and $M \cdot \vec{n}$, respectively, have the same magnitude but opposite direction for parallel surfaces of the microstructure.

The aforementioned local problem can then be solved in tandem with the general FFT framework established by Moulinec and Suquet [283, 284]. Let C° and A° be the 4th order elasticity tensors of a reference linear medium. Recalling that the

total strain and curvatures are defined as gradients of total displacements (equations (2.35), (2.38) and (2.46) for compatible elastic strains which are also always valid for total displacements), the Cauchy and couple stresses at a material point $\vec{x}$ can be represented by adding and subtracting an appropriate expression involving the reference elasticity tensors and displacements as,

$$\sigma_{ij}(\vec{x}) = \sigma_{ij}(\vec{x}) + C^{\circ}_{ijkl}u_{k,l}(\vec{x}) - C^{\circ}_{ijkl}u_{k,l}(\vec{x}) \tag{5.6}$$

$$M_{ij}(\vec{x}) = M_{ij}(\vec{x}) + \frac{1}{2}A^{\circ}_{ijkl}e_{kmn}u_{n,ml}(\vec{x}) - \frac{1}{2}A^{\circ}_{ijkl}e_{kmn}u_{n,ml}(\vec{x}) \tag{5.7}$$

Recall that the tensor C°_{ijkl} is symmetric over the indices ij and kl and therefore extracts only the symmetric component of $u_{k,l}$ making the term $C^{\circ}_{ijkl}u_{k,l}$ equal to $C^{\circ}_{ijkl}\epsilon_{kl}$. Defining the Cauchy stress polarization (τ_{ij}) and couple stress polarization (μ_{ij}) tensors as,

$$\tau_{ij}(\vec{x}) = \sigma_{ij}(\vec{x}) - C^{\circ}_{ijkl}u_{k,l}(\vec{x}) = \sigma_{ij}(\vec{x}) - C^{\circ}_{ijkl}\epsilon_{kl}(\vec{x}) \tag{5.8}$$

$$\mu_{ij}(\vec{x}) = M_{ij}(\vec{x}) - \frac{1}{2}A^{\circ}_{ijkl}e_{kmn}u_{n,ml}(\vec{x}) = M_{ij}(\vec{x}) - A^{\circ}_{ijkl}\kappa_{kl}(\vec{x}) \tag{5.9}$$

the local Cauchy and couple stresses can be redefined as,

$$\sigma_{ij}(\vec{x}) = \tau_{ij}(\vec{x}) + C^{\circ}_{ijkl}u_{k,l}(\vec{x}) \tag{5.10}$$

$$M_{ij}(\vec{x}) = \mu_{ij}(\vec{x}) + \frac{1}{2}A^{\circ}_{ijkl}e_{kmn}u_{n,ml}(\vec{x}) \tag{5.11}$$

The polarization tensors indicate the fluctuation, from the volume average, of the local stress fields. Substituting (5.10) and (5.11) in the equilibrium equation (3.14) gives

$$\sigma_{ij,j}(\vec{x}) + \frac{1}{2}e_{ijk}M_{kl,lj}(\vec{x}) = C^{\circ}_{ijkl}u_{k,lj}(\vec{x}) + \frac{1}{2}e_{ijk}A^{\circ}_{klmn}e_{mop}u_{p,onlj}(\vec{x})$$
$$+ \tau_{ij,j}(\vec{x}) + \frac{1}{2}e_{ijk}\mu_{kl,lj}(\vec{x}) = 0 \tag{5.12}$$

Let a fictitious body force $\vec{f}$ be defined as,

$$f_i(\vec{x}) = \tau_{ij,j}(\vec{x}) + \frac{1}{2}e_{ijk}\mu_{kl,lj}(\vec{x}) \tag{5.13}$$

then the displacement can be defined as a convolution of the Green's function $\boldsymbol{G}$ and the fictitious body force as,

$$u_k(\vec{\boldsymbol{x}}) = \int G_{ki}(\vec{\boldsymbol{x}} - \vec{\boldsymbol{x}}')f_i(\vec{\boldsymbol{x}}')d\vec{\boldsymbol{x}}' \tag{5.14}$$

Defining $F^\circ_{ijlnop} = \frac{1}{2}e_{ijk}A^\circ_{klmn}e_{mop}$ and substituting the displacement by the Green's function in the equilibrium equation (5.12) such that for a periodic unit cell with imposed average strain $\boldsymbol{E} = <\boldsymbol{\epsilon}>$ and curvature $\boldsymbol{K} = <\boldsymbol{\kappa}>$ the problem to be solved is,

$$C^\circ_{ijkl}G_{kq,lj}(\vec{\boldsymbol{x}} - \vec{\boldsymbol{x}}') + F^\circ_{ijlnop}G_{pq,onlj}(\vec{\boldsymbol{x}} - \vec{\boldsymbol{x}}') + \delta_{iq}\boldsymbol{\delta}(\vec{\boldsymbol{x}} - \vec{\boldsymbol{x}}') = 0 \tag{5.15}$$

where $\boldsymbol{\delta}$ is the Dirac delta function and δ_{iq} is the Kronecker delta. Replacing the index p by k, performing the Fourier transform and rearranging the terms gives the following expression for the Green's tensor,

$$\hat{G}_{ki}(\vec{\boldsymbol{k}}) = (k_l k_j C^\circ_{ijkl} - k_o k_n k_l k_j F^\circ_{ijlnok})^{-1} \tag{5.16}$$

where the superscript $\wedge$ represents the Fourier transform of a spatial function. $\vec{\boldsymbol{k}}$ represents a point in the Fourier space whose magnitude is equal to the angular frequency. Taking the Fourier transform of the fictitious body force in equation (5.13) gives,

$$\hat{f}_i(\vec{\boldsymbol{k}}) = ik_j\hat{\tau}_{ij}(\vec{\boldsymbol{k}}) - \frac{1}{2}e_{ijk}k_l k_j\hat{\mu}_{kl}(\vec{\boldsymbol{k}}) \tag{5.17}$$

Finally, the compatible local total strain and curvature, are

$$\epsilon_{ij}(\mathbf{x}) = E_{ij} + \frac{1}{2}FT^{-1}\left(ik_j\left(\hat{G}_{ik}(\vec{\boldsymbol{k}}) + \hat{G}_{ki}(\vec{\boldsymbol{k}})\right)\hat{f}_k(\vec{\boldsymbol{k}})\right) \tag{5.18}$$

$$\kappa_{ij}(\mathbf{x}) = K_{ij} - \frac{1}{2}e_{ikl}FT^{-1}\left(k_j k_k\hat{G}_{lm}(\vec{\boldsymbol{k}})\hat{f}_m(\vec{\boldsymbol{k}})\right) \tag{5.19}$$

where FT^{-1} is the inverse Fourier transform operator. Note here that these total compatible kinematic quantities have the contribution of both elastic and plastic components as defined by equations (2.64) and (2.90).

5.2.1.1   Curvature contribution to grain rotation

Prominent meso-scale crystal plasticity models such as the elasto-plastic, viscoplastic, elasto-viscoplastic self consistent and FFT models which are based on a plastic slip rate formulation account for grain rotation contribution coming from the anti-symmetric component of the plastic slip tensor $(L^p_{[ij]})$. This stems from the dislocation motion under the action of shear stresses which leads to a shape change that culminates into a reorientation of the grain. The anti-symmetric component of the plastic slip rate is the plastic rotation tensor that is used to update the Euler angles at each Fourier point at the end of every time step. These contrbutions are augmented with the plastic curvature contribution to rotation in the strain gradient plasticity models. However, plastic rotation contributions arisin from the evolution of disclinations have never been accounted for. The meso-scale field disclination and dislocation mechanics model is able to achieve this using the evolving plastic curvature $\dot{\boldsymbol{\kappa}}^p$ from equation (3.117). For the sake of simplicity focus is only given to plastic curvature contributions coming from disclinations; dislocation contributions are neglected.

From the Stokes-Helmholtz decomposition of $\dot{\boldsymbol{\kappa}}_p$, it can be defined as the sum of a curl-free component $\dot{\kappa}^{p\|}_{ij}$ and a divergence-free component $\dot{\kappa}^{p\perp}_{ij}$. The curl-free component $\dot{\kappa}^{p\|}_{ij}$ is the compatible plastic curvature rate which contributes to the rotation of grains. Recalling that the divergence of curl of any n^{th} ordered tensor is equal to zero, it can be deduced that the divergence of the plastic curvature rate is equal to the divergence of the compatible plastic curvature rate $(\dot{\kappa}^p_{ij} = \dot{\kappa}^{p\|}_{ij})$ with the side condition that the curl of the compatible plastic curvature rate is zero [134]. Defining the compatible plastic curvature rate $\dot{\kappa}^{p\|}_{ij}$ as the gradient of a plastic rotation rate,

$$\dot{\boldsymbol{\kappa}}^{\|}_p = \mathbf{grad}\ \dot{\boldsymbol{\omega}}_p \tag{5.20}$$

and taking the divergence of the above equation transforms the gradient operator on the plastic rotation into a Laplacian $(\dot{\kappa}^{p\|}_{ij,j} = \dot{\omega}^p_{i,kk})$. Taking its Fourier transform and

after performing some algebra gives the expression for the plastic rotation in the real space as,

$$\dot{\omega}_i^p = FT^{-1}\left(-\frac{i\xi_j \hat{\dot{\kappa}}_{ij}^p(\xi)}{\xi^2}\right) \tag{5.21}$$

The plastic rotation vector can be defined in terms of a second order tensor as $\boldsymbol{\omega}^p = -\mathbf{X} : \vec{\boldsymbol{\omega}}^p$. This second order compatible plastic rotation rate along with the rotation contribution from plastic slip rate is then subtracted from the total rotation (having contributions from both local and macro rotations) to obtain the compatible elastic rotation ($\boldsymbol{\omega}^{e\|}$) which contributes to grain rotation.

5.2.2 Numerical scheme

The FFT iterative procedure employs an Euler implicit time discretization scheme to solve the PMFDDM FFT problem. Using equations (2.64), (2.90), (3.25) and (3.26) and recalling that contributions from terms involving elasticity tensors $\boldsymbol{B}$ and $\boldsymbol{D}$ are neglected, the Cauchy and couple stresses at a material point $\vec{x}$ at time $t + \Delta t$ are expressed as:

$$\boldsymbol{\sigma}^{(t+\Delta t)}(\vec{x}) = \mathbf{C}(\vec{x}) : \left(\boldsymbol{\epsilon}^{(t+\Delta t)}(\vec{x}) - \boldsymbol{\epsilon}^{p(t)}(\vec{x}) - \dot{\boldsymbol{\epsilon}}^{p(t+\Delta t)}(\vec{x}, \boldsymbol{\sigma}^{(t+\Delta t)})\Delta t\right) \tag{5.22}$$

$$\boldsymbol{M}^{(t+\Delta t)}(\vec{x}) = \mathbf{A}(\vec{x}) : \left(\boldsymbol{\kappa}^{(t+\Delta t)}(\vec{x}) - \boldsymbol{\kappa}^{p(t)}(\vec{x}) - \dot{\boldsymbol{\kappa}}^{p(t+\Delta t)}(\vec{x}, \boldsymbol{M}^{(t+\Delta t)})\Delta t\right) \tag{5.23}$$

At the zeroeth time step, the elastic curvature obtained from the 3D technique based on EBSD orientation mapping (see section 5.1) is used to provide an initial guess for the couple stress tensor. The initial total curvature is assumed to be zero i.e. the microstructure is in an undeformed state. Therefore from equation (2.90) the accumulated local plastic curvature is assumed equal to the negative of the instantaneous elastic curvature. This provides an estimate for the polar defect content in the medium. If, however, the initial elastic curvature were not to be estimated then the initial defect densities and the guess for couple stress would be equal to zero.

The solution procedure which follows the above step is similar to the one proposed in the EVP FFT model of Lebensohn *et al.* [239]. The polarization tensors $\boldsymbol{\tau}$ and $\boldsymbol{\mu}$ are respective functions of $\boldsymbol{\epsilon}$ and $\boldsymbol{\kappa}$ and require an iterative approach to obtain a solution. Let $\boldsymbol{e}^{(i)}$, $\tilde{\boldsymbol{\kappa}}^{(i)}$, $\boldsymbol{\lambda}^{(i)}$ and $\boldsymbol{\phi}^{(i)}$ be the guesses for strain, curvature, Cauchy stress, and couple stress, respectively, at the iteration i. The polarization tensors at this iteration are given as,

$$\tau_{ij}^{(i)}(\vec{\boldsymbol{x}}) = \sigma_{ij}^{(i)}(\vec{\boldsymbol{x}}) - C_{ijkl}^{o} e_{kl}^{(i)}(\vec{\boldsymbol{x}}) \tag{5.24}$$

$$\mu_{ij}^{(i)}(\vec{\boldsymbol{x}}) = M_{ij}^{(i)}(\vec{\boldsymbol{x}}) - A_{ijkl}^{o} \tilde{\kappa}_{kl}^{(i)}(\vec{\boldsymbol{x}}) \tag{5.25}$$

Green's tensor and the $i + 1$ guess for the fictive body force in Fourier space are then computed using equations (E.17) and (5.17). These equations along with the polarization tensors in equations (5.24) and (5.25), the $(i + 1)$ guesses for compatible total strain and curvature are:

$$e_{ij}^{(i+1)}(\mathbf{x}) = E_{ij} + \frac{1}{2} FT^{-1} \left(ik_j \left(\hat{G}_{ik}(\mathbf{k}) + \hat{G}_{ki}(\mathbf{k}) \right) \hat{f}_k^{(i)}(\mathbf{k}) \right) \tag{5.26}$$

$$\tilde{\kappa}_{ij}^{(i+1)}(\mathbf{x}) = K_{ij} - \frac{1}{2} e_{ikl} FT^{-1} \left(k_j k_k \hat{G}_{lm}(\mathbf{k}) \hat{f}_m^{(i)}(\mathbf{k}) \right) \tag{5.27}$$

The stresses can then be computed using equations (5.22) and (5.23) where the plastic strain and curvature rates are computed using equations (3.114) and (3.117). However, such a direct computation does not ensure that the constitutively obtained stresses fulfil the equilibrium conditions, thus taking a lot of iterations to converge.

In order to achieve a faster convergence, an augmented Lagrangian scheme [271, 272] can be employed. The original scheme proposed in the work of Michel *et al.* adjusts two strain and stress fields such that one strain field is compatible (similar to the one in equation (5.18) but in classical elasticity) and one stress field satisfies equilibrium (only the components related to Cauchy stresses in equation (5.12)). The other strain and stress fields are constitutively related and the iterative procedure is designed such that the two strains and the two stresses converge to each other.

Following convergence, the method delivers a compatible strain field constitutively related to an equilibrated stress field. In the following, an extension of the augmented Lagrangian technique is employed where two of each: curvature, strain, Cauchy stress, and couple stress fields are utilized to achieve accelerated convergence.

The procedure involves first transforming the 3 x 3 Cauchy stress and strain tensors and the 3 x 3 x 3 x 3 stiffness tensor $\boldsymbol{C}$ into 6, 6 and 6 x 6 tensors, respectively, using the "Kelvin notation". This notation was introduced in the early work of Thompson [403] and is used as an alternative approach to the Voigt formulation [20]. The Kelvin decomposition allows to separate the stress and strain tensors into 5 deviatoric and 1 hydrostatic components [241] while preserving the norm of the stiffness, Cauchy and strain tensors as well as the energy of the system [88]. The 6 eigenvectors associated with the Kelvin decomposition are formulated in the form of 6 basis tensors as shown in the appendix B.1.1. An extension to the Kelvin formulation is developed for the case of couple stress, curvature and stiffness tensor $\boldsymbol{A}$ which due to the asymmetry of the couple stress and curvature tensor will be of the shape 9, 9, and 9 x 9, respectively. The 9 basis tensors are derived in the Appendix B.1.1.

For each material point $\vec{x}$, the enhanced augmented Lagrangian scheme requires minimizing the residual R_i:

$$R_i(\boldsymbol{\sigma}^{(i+1)}, \boldsymbol{M}^{(i+1)})(\vec{x}) = \sigma_k^{(i+1,j)}(\vec{x}) + C_{kl}^0 \epsilon_l^{(i+1)}(\vec{x}) - \lambda_k^{(i)}(\vec{x}) - C_{kl}^0 e_l^{(i+1)}(\vec{x}); k = 1,6$$

$$R_k(\boldsymbol{T}^{(i+1)}, \boldsymbol{M}^{(i+1)})(\vec{x})$$

$$= M_k^{(i+1,j)}(\vec{x}) + A_{kl}^0 \kappa_l^{(i+1)}(\vec{x}) - \mu_k^{(i)}(\vec{x}) - A_{kl}^0 \tilde{\kappa}_l^{(i+1)}(\vec{x}); k = 7,15 \qquad (5.28)$$

These 15 non-linear equations are solved using the Newton-Raphson iterative procedure as follows:

$$\sigma_k^{(i+1,j+1)} = \sigma_k^{(i+1,j)} - \left[\frac{\partial R_k}{\partial \sigma_l} \bigg|_{\boldsymbol{\sigma}^{(i+1,j)}, \boldsymbol{M}^{(i+1,j)}} \right]^{-1} R_l(\boldsymbol{\sigma}^{(i+1,j)}, \boldsymbol{M}^{(i+1,j)}) \qquad (5.29)$$

$$M_k^{(i+1,j+1)} = M_k^{(i+1,j)} - \left[\frac{\partial R_k}{\partial M_l} \bigg|_{\boldsymbol{\sigma}^{(i+1,j)}, \boldsymbol{M}^{(i+1,j)}} \right]^{-1} R_l(\boldsymbol{\sigma}^{(i+1,j)}, \boldsymbol{M}^{(i+1,j)}) \qquad (5.30)$$

where the residual computed at the $(j + 1)$ iteration of the Newton-Raphson loop is used to obtain the $(j+1)$ guess for the stress. The inverse term is the Jacobian which is a 15×15 tensor. Rearranging equations (5.22) and (5.23) in terms of the total strain and curvature and taking their derivatives with respect to Cauchy and couple stresses gives the following expression for the Jacobian:

$$\left.\frac{\partial R_k}{\partial T_l}\right|_{\boldsymbol{T}^{i+1,j},\boldsymbol{M}^{i+1,j}} = \delta_{kl} + C_{km}^0 C_{ml}^{-1} + C_{km}^0 \frac{\partial \dot{\epsilon}_m^p}{\partial T_l}\Delta t \; ; k = 1 - 6 \, , l = 1 - 6$$

$$\left.\frac{\partial R_k}{\partial T_l}\right|_{\boldsymbol{T}^{i+1,j},\boldsymbol{M}^{i+1,j}} = 0 \; ; k = 7 - 15 \, , l = 1 - 6$$

$$\left.\frac{\partial R_k}{\partial M_l}\right|_{\boldsymbol{T}^{i+1,j},\boldsymbol{M}^{i+1,j}} = 0 \; ; k = 1 - 6 \, , l = 7 - 15$$

$$\left.\frac{\partial R_k}{\partial M_l}\right|_{\boldsymbol{T}^{i+1,j},\boldsymbol{M}^{i+1,j}} = \delta_{kl} + A_{km}^0 A_{ml}^{-1} + A_{km}^0 \frac{\partial \dot{\kappa}_m^p}{\partial M_l}\Delta t \; ; k = 7 - 15 \, , l = 7 - 15 \text{ (5.31)}$$

where the partial derivative terms associated with Δt are the tangent compliance of the viscoplastic response $\frac{\partial \dot{\epsilon}_m^p}{\partial \sigma_l}$ from equation (3.114) and the plastic curvature compliance $\frac{\partial \dot{\kappa}_m^p}{\partial M_l}$ from equation (3.117). The critical resolved shear stress (CRSS) τ_0, which is a function of the stress dependent plastic strain, is taken as a function of stress $\tau_0^s(\boldsymbol{\epsilon}^p(\boldsymbol{\sigma})) = \tau_0^s(\boldsymbol{\sigma})$. On the other hand, M_0 is taken as a constant and :

$$\frac{\partial \dot{\epsilon}_i^p}{\partial \sigma_j} \approx n\dot{\gamma}_0 \sum_{s=1}^N \frac{m_i^s m_j^s}{\tau_0^s\left(\boldsymbol{\sigma}^{(i+1,j)}\right)} \left(\frac{|\boldsymbol{m}^s \cdot \boldsymbol{\sigma}|}{\tau_0^s\left(\boldsymbol{\sigma}^{(i+1,j)}\right)}\right)^{n-1} \tag{5.32}$$

$$\frac{\partial \dot{\kappa}_i^p}{\partial M_j} = \frac{\dot{\kappa}_0\|\boldsymbol{M}\|^{n-3}}{M_0^n}\left((n-1)M_j M_i + \delta_{ij}\|\boldsymbol{M}\|^2\right) \tag{5.33}$$

where $\boldsymbol{m}^s$ is the Schmid tensor $\mathbf{P}^s$ in Kelvin notation, subscripts $i, j = 1, \ldots, 9$. For the sake of simplicity, the plastic curvature compliance (5.33) can be approximated as a diagonal matrix, as follows:

$$\frac{\partial \dot{\kappa}_i^p}{\partial M_j} \approx \frac{n\dot{\kappa}_0}{M_0^n}\|\boldsymbol{M}\|^{n-1}\delta_{ij} \tag{5.34}$$

Once convergence is achieved, the new guess for auxiliary Cauchy and couple stress fields is given by,

$$\boldsymbol{\lambda}^{(i+1)}(\vec{\boldsymbol{x}}) = \boldsymbol{\lambda}^{(i)}(\vec{\boldsymbol{x}}) + \boldsymbol{C}^0 : \left(\boldsymbol{e}^{(i+1)}(\vec{\boldsymbol{x}}) - \boldsymbol{\epsilon}^{(i+1)}(\vec{\boldsymbol{x}})\right) \tag{5.35}$$

$$\boldsymbol{\phi}^{(i+1)}(\vec{x}) = \boldsymbol{\phi}^{(i)}(\vec{x}) + \boldsymbol{A}^0 : \left(\tilde{\boldsymbol{\kappa}}^{(i+1)}(\vec{x}) - \boldsymbol{\kappa}^{(i+1)}(\vec{x}) \right) \qquad (5.36)$$

The iterations are repeated until normalized average differences between $\boldsymbol{\sigma}(\vec{x})$ and $\boldsymbol{\lambda}(\vec{x})$, $\boldsymbol{M}(\vec{x})$ and $\boldsymbol{\phi}(\vec{x})$, $\boldsymbol{\epsilon}(\vec{x})$ and $\boldsymbol{e}(\vec{x})$, and $\boldsymbol{\kappa}(\vec{x})$ and $\tilde{\boldsymbol{\kappa}}(\vec{x})$, are smaller than a threshold. This ensures satisfaction of compatibility and equilibrium conditions, up to the threshold.

Higher order boundary conditions in the form of macroscopic total strain and curvature rate are imposed on the periodic microstructure such that at time step $t+1$ the macroscopic strain and curvature are given as,

$$E_{ij}^{(t+1)} = E_{ij}^{(t)} + \dot{E}_{ij}\Delta t \qquad (5.37)$$

$$K_{ij}^{(t+1)} = K_{ij}^{(t)} + \dot{K}_{ij}\Delta t \qquad (5.38)$$

In addition to these, macroscopic Cauchy $\boldsymbol{\Sigma}$ and couple $\boldsymbol{\Phi}$ stresses can be also be imposed. These boundary conditions allow for the simulation of pure tension/compression, pure shear, pure bending, pure torsion, creep (in tension, bending or torsion) and complex loading scenarii. Prescribing the macroscopic stresses requires modifying the macroscopic strain and curvature at each iteration $i+1$ by the following:

$$E_{ij}^{(t+1,i+1)} = E_{ij}^{(t+1,i)} + C_{ijkl}^{o-1}\alpha^{kl}\left(\Sigma_{kl} - \left\langle \lambda_{kl}^{(i+1)}(\mathbf{x}) \right\rangle \right) \dot{E}_{ij}\Delta t \qquad (5.39)$$

$$K_{ij}^{(t+1,i+1)} = K_{ij}^{(t+1,i)} + A_{ijkl}^{o-1}\beta^{kl}\left(\Phi_{kl} - \left\langle \phi_{kl}^{(i+1)}(\mathbf{x}) \right\rangle \right) \dot{K}_{ij}\Delta t \qquad (5.40)$$

where $\alpha^{kl} = 1$ and $\beta^{kl} = 1$ if components Σ_{kl} and Φ_{kl} are imposed, respectively, and zero otherwise.

The FFT technique has the following advantages and disadvantages: (i) It avoids the difficulties with meshing by solving the unit cell (local) problem. (ii) It is computationally faster than FEM; its computational cost is $O(N\log(N))$ which is much lower than the $O(N^3)$ of FEM based techniques. (iv) It uses a regularized periodic grid and its present form can be only applied to RVEs (iii) It is an N-site formulation, unlike self-consistent schemes [240], and does not require homogenization of

the RVE. Therefore, it provides an exact solution (within the bounds imposed by the discretization and the error allowed by the iterative procedure) to the combined problem involving equilibrium and compatibility conditions such that the final compatible strain and equilibrated stress satisfy the constitutive relationship. (v) The algorithm is based on piecewise continuous derivatives of kinematic quantities transformed in Fourier space and therefore assumes that the displacements, strains, curvatures and their derivatives are continuous everywhere in the domain. In its present form, it suffers from the Gibbs phenomenon *i.e.* it cannot handle jumps in the kinematic fields. Although this may be treated by using discrete finite differences instead of continuous derivatives, as shown in a recent work by Berbenni *et al.* [34]. Figure 5.1 shows the flowchart of the PMFDDM interative procedure described above.

Table 6: Legend for flowchart 1

NOTATION	DESCRIPTION
E	Macro strain
K	Macro curvature
$\Delta E = \dot{E}\Delta t$	Macro strain increment
$\Delta K = \dot{K}\Delta t$	Macro curvature increment
t	Previous time step
$t + \Delta t$	Current time step
N_{tot}	Total number of time steps
ε	Threshold value for error
ERR	Normalized error
N_{iter}	Maximum number of iterations
ΔK	Macro curvature increment
re, im	Real and imaginary components in Fourier space

Continued on next page

Table 6 – *Continued from previous page*

NOTATION	DESCRIPTION
ξ_i	Fourier space vector in component form
σ^{err}, M^{err}	Threshold errors in Cauchy and couple stresses
A, B	Normalized errors in Cauchy and couple stresses
wgt	volumetric weight function
VM	VM component
BCs	Boundary conditions
EA	Euler Angles
N1, N2, N3	Fourier points
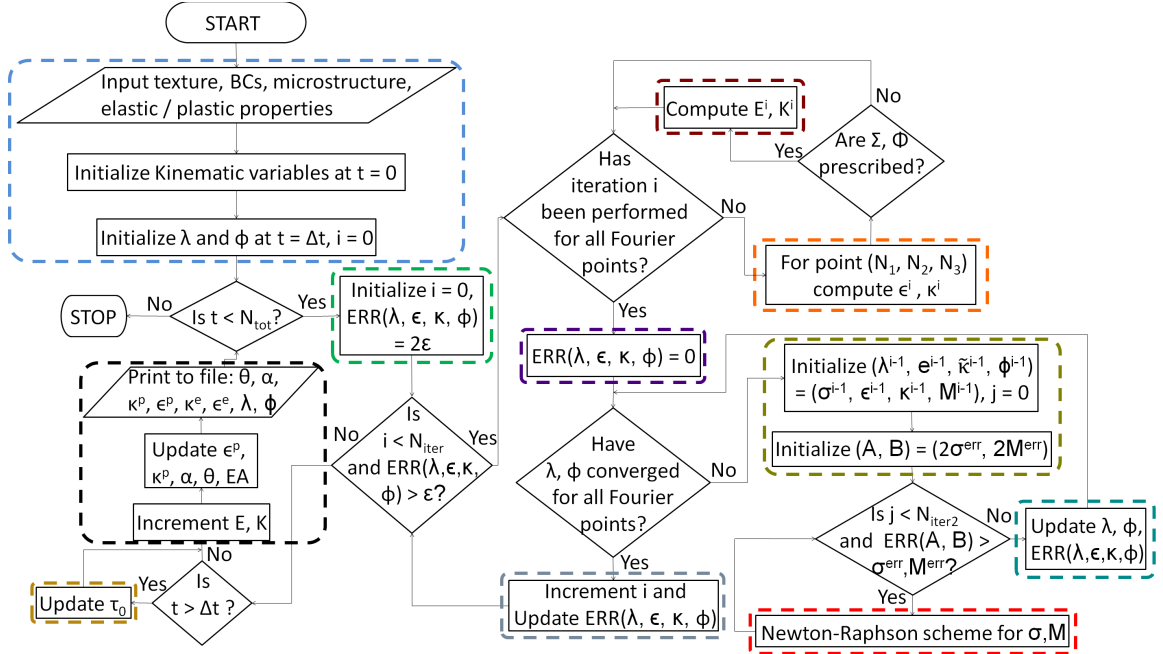
Figure 5.1: Flowchart of the PMFDDM FFT algorithm. Dashed colored boxes correspond to colored expressions in algorithm 1 shown in appendix G.

5.3 Capturing curvature contribution to polycrystalline response: strategy

The purpose of this section is to devise simulations that will demonstrate the contribution of residual curvatures to nc plastic response and to the evolution of polar dislocation and disclination densities. In the following, the simulation microstructure, boundary conditions and the different initial curvature cases studied to achieve this objective are described. Using these, the case studies to be performed are discussed.

5.3.1 Microstructures: elastic/plastic properties and geometry

The unit cell is attributed material properties of FCC Cu at room temperature. For the Cauchy stress elastic constitutive relationship, the elastic constants (in Voigt notation) are: C_{11} = 170.2 GPa, C_{12} = 114.9 GPa and C_{44} = 61.0 GPa [371, 239]. For Cauchy stress visco-plastic constitutive relationship, the reference plastic shear rate is taken as $\dot{\gamma}_0$ = 0.1/sec and the power exponent is n = 10. FCC Cu has 12 111<110> slip systems available and the Schmid's tensor is used to obtain the active slip systems. The CRSS is chosen according to the average grain size of the microstructure. An elastic-perfectly plastic response is modelled, therefore the CRSS remains constant during the entire simulation. For couple stress elastic constitutive response, the elasticity tensor $\boldsymbol{A}$ in the Voigt form has the diagonal values of $Gb^2 = 3.96653 \times 10^{-9}N$. This is the form of elastic constant proposed in the work of Kröner [218]. For couple stress plastic constitutive relationship, the reference plastic curvature is taken as $\dot{\kappa}$ = 100/$micron$, threshold couple stress as $M_0 = 10^{-7}$ N//μm and the power exponent as n = 10. The threshold couple stress remains constant throughout the simulation.

Two types of microstructures are studied: (a) polycrystalline RVE with 100 randomly oriented grains and (b) bicrystal. The first type, generated using Voronoi

tessellations, is shown in figure 5.2. The kinematic and stress fields of the microstructure are studied along the vertical line passing through the center of the cross-sectional area shown. The normal to this cross section is along the z axis. Points of interest are the intersections of the line with the interfaces. These are indicated by numbers shown in the figure. From a first glance there are 6 grains traversed by the line. A closer look reveals that there are other grains that emerge at the interfaces which have only one voxel belonging to the microstructure cross section. These could have an interesting consequence on the shape of the kinematic and stress profiles drawn. Identifying these individual voxels as protrusions from other grains, the total number of grains traversed by the line then increases to 9. These results in a total of 8 different interfaces traversed by the line. Further inspection of the cross-section reveals that the line follows the interface between points 1 and 2, making this zone a potential site of interest. Therefore the same interface is assigned two numbers. Finally, at point number 10, the line encounters a triple junction between grains that have already formed interfaces that were previously traversed by the line. This triple junction is of a lot of interest and is also assigned a number. Therefore, the total number of interface identifiers is now 10.

The second type of microstructure studied is the bicrystal. Two types of bicrystals are studied. The first one being a 2-dimensional bicrystal having tilt misorientation of 5° about the z axis, henceforth known as bicrystal-a, and the second one being a 3-dimensional columnar structure with randomly oriented grains, henceforth known as bicrystal-b. In both the cases, the grains are of the same size. Figure 5.3 shows the two bicrystals with their Euler angles.

In both these cases, the unit cell is cubic shaped and discretized using a $64 \times 64 \times 64$ grid (the same discretization will be adopted for all the simulations in this section). The "fourn" subroutine from the "Numerical Recipes 77" is used to solve the FFT problem. It requires the Fourier points to be in the order of $2^n; n \in \mathbb{Z}$. A good
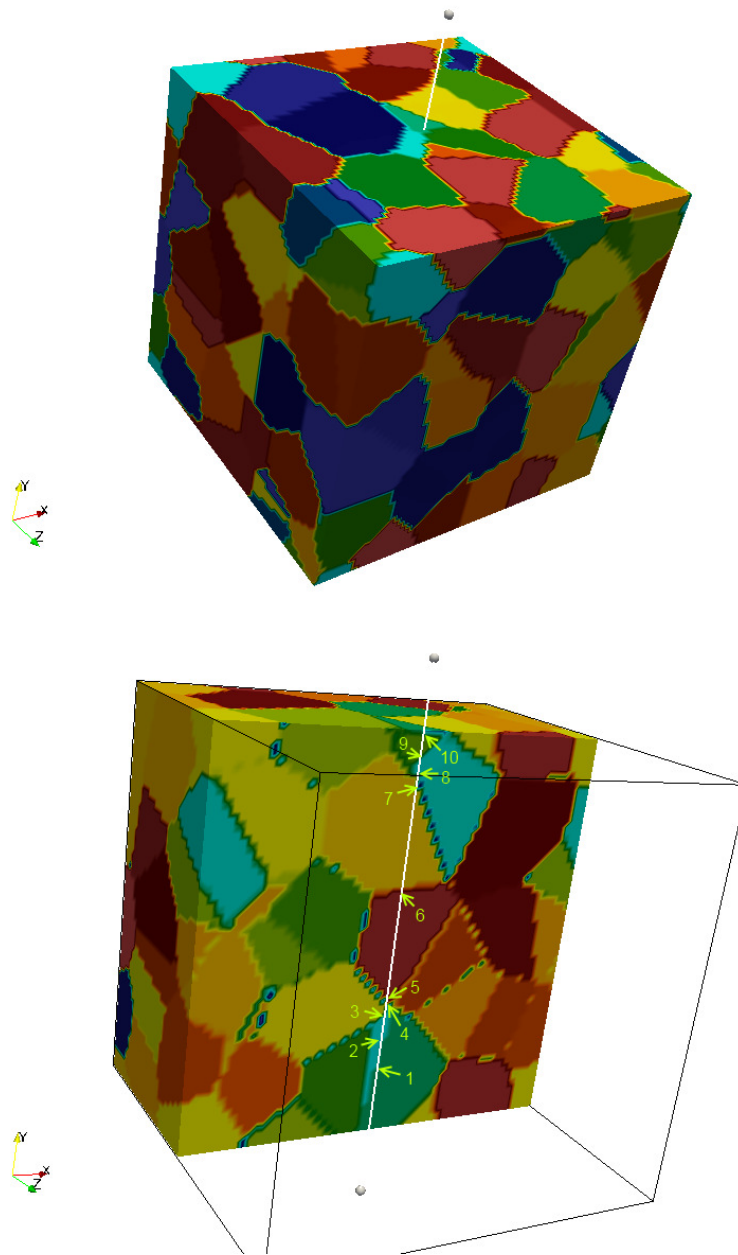
Figure 5.2: Simulated microstructure with 100 randomly oriented grains and $64 \times 64 \times 64$ Fourier points. The colors represent different grains. The stress and kinematic fields are plotted along the line passing through the center of the microstructure in the y direction. The numbers are interface identifiers indicating the positions of the intersection of the line with an interface.

compromise between accuracy and computation time is obtained using $2^6 = 64$ Fourier points in each direction.
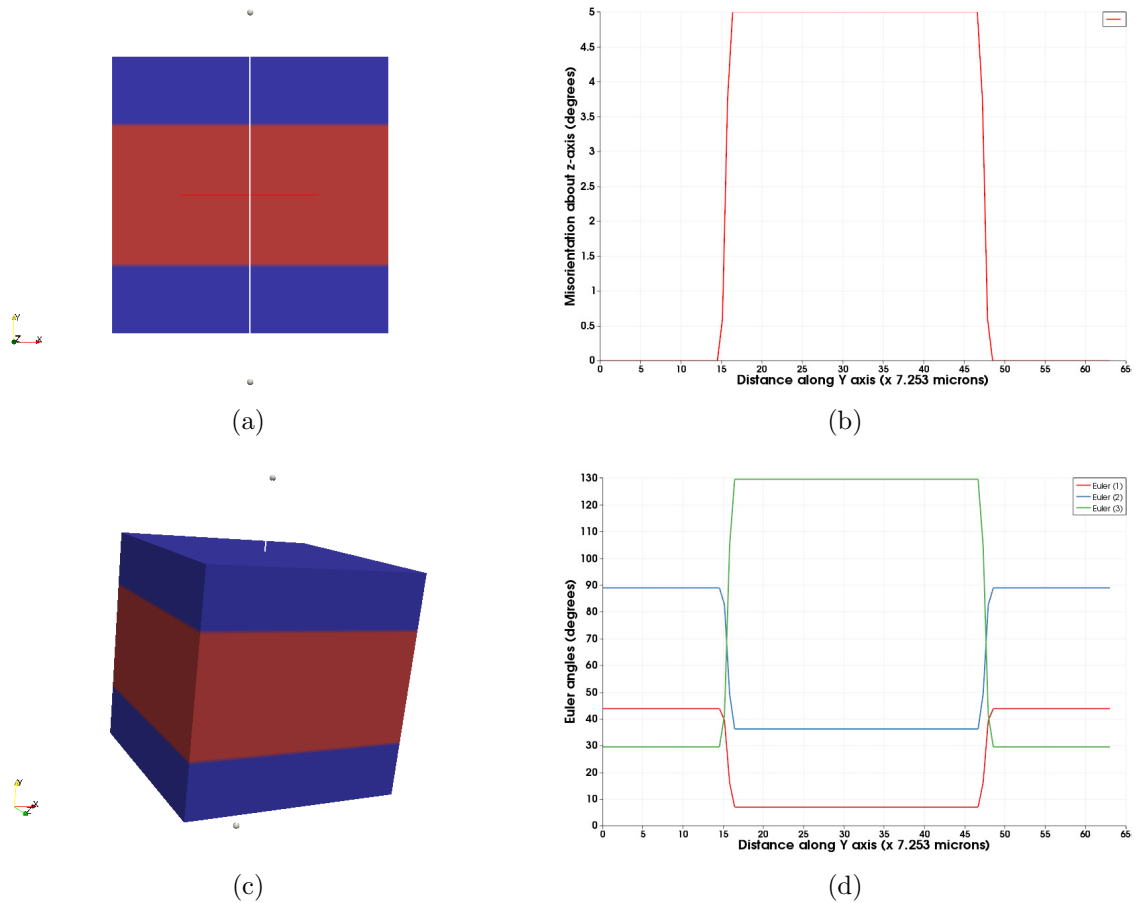
Figure 5.3: Microstructure of (a) 2-dimensional and (c) 3-dimensional columnar bicrystal with respective GB (b) misorientation of 5° about $z-axis$ and (d) randomly assigned Euler angles in degrees, plotted along the lines shown in (a) and (c).

5.3.2 Characterizing microstructures with initial curvatures

Three cases of GBs are considered: (a) the first case where the GB interface is infinitesimally thin and forms between two Fourier points belonging to two different grains. This case is identified as t_0. (b) The second case where the immediate neighbor Fourier points belonging to different grains are considered as part of the grain boundary giving it a finite thickness whose maximum value is equal to δ. This case is identified as t_1. (c) In the third case, the second neighbor Fourier points are also considered as part of the grain boundary with its largest thickness equal to 3δ. This case is identified as t_2. All the three cases are illustrated in figure 5.4.
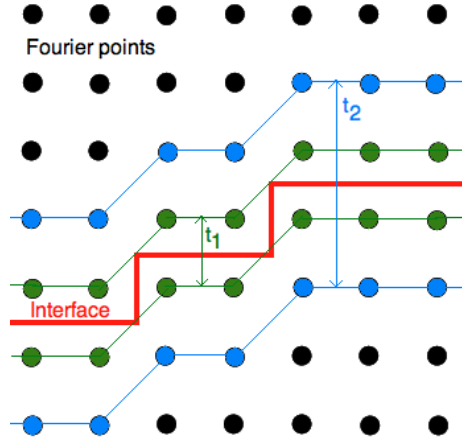
Figure 5.4: 2-dimensional illustration of an infinitesimally thin t_0 (in red), thickness $t_1 = \delta$ (in green), and thickness $t_2 = 3\delta$ (in blue), interface in the discretized Fourier grid consisting of evenly spaced Fourier points.

The GBs are not identified as separate grains but are characterized using residual elastic curvatures arising due to the disorientation of grains (refer to section 5.1). In the second case, the elastic curvatures are assigned values based on the difference in elastic rotations across the "interface". In the third case, the second neighbor Fourier points are assigned elastic curvature values that are same as the first neighbor. If there is more than one GB in the vicinity of a particular Fourier point then the elastic curvatures generated from both the boundaries are added. The GB volume fraction is the computed as the ratio of number of Fourier points having a non-zero residual elastic curvature, at the beginning of the simulation, to the total number of Fourier points in the domain. For the microstructure considered, the volume fraction occupied by the so-formed GBs in the three cases are 0 % (for t_0), 31 % (for t_1), and 55 % (for t_2), respectively.

Figure 5.5 shows the initial curvature components κ_{12} and κ_{32} plotted along the line shown in figure 5.2 for the polycrystalline case assuming an average grain size 10 nm. This is achieved by taking an inter Fourier point spacing of 0.7253 nm. This curvature is computed assuming first a thickness of t_1 and then thickness - t_2 as shown

in figure 5.4. GB interface thickness may be overestimated in the second case but the idea here is to highlight the influence of this initial curvature on the local stress response. The configuration without any initial curvature shall be referred to as t_0.

It is important to note that in the FFT framework the notion of length scale effect on Cauchy stresses is only introduced through the PMFDDM approach. In the conventional EVP FFT, the strains are dimensionless and both the strains and elastic constants of the medium do not scale with grain size. Therefore the Cauchy stresses also do not scale with grain size. Curvatures and couple stresses have an inherent length scale associated to them. This helps characterize the Cauchy stresses with respect to different grain sizes in the extended EVP framework. This is the first time that such a length scale effect on Cauchy stress evolution has been shown using either the self-consistent or FFT based polycrystalline models.

(a) κ_{12} $(1/\mu m)$ (b) κ_{32} $(1/\mu m)$
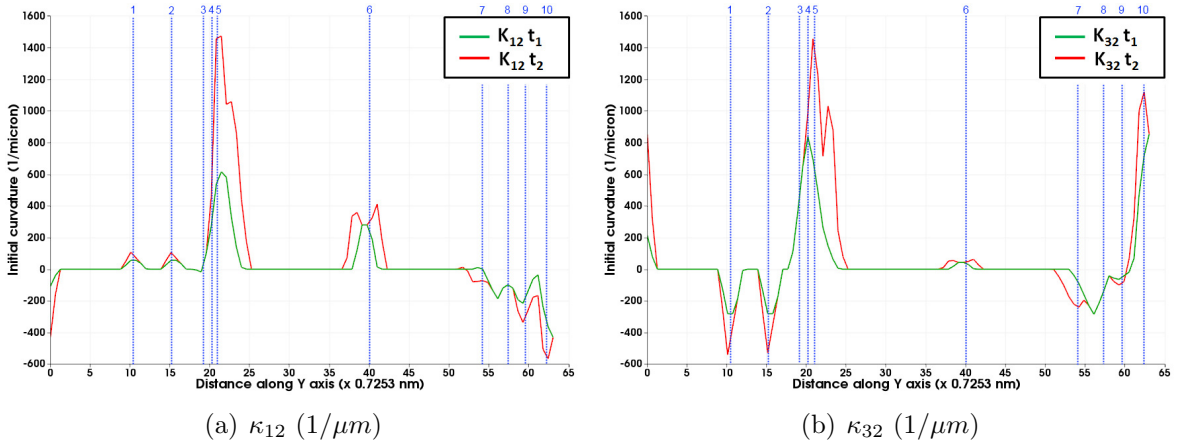
Figure 5.5: Plots over line for initial estimates of (a) κ_{12} $(1/\mu m)$ and (b) κ_{32} $(1/\mu m)$ for 10 nm polycrystal with GB thickness t_1 (in green) and t_2 (in red). Blue lines indicate the location of interfaces and the numbers in blue correspond to interface identifiers from figure 5.2.

As seen in section 5.1, initial curvatures are computed using a finite difference scheme. Therefore the sharply pointed crests and troughs are not numerical overshoot but are a result of the interpolation between discrete Fourier points. The initial curvatures form only in the vicinity of the interfaces. Orders of magnitude of the

curvatures in both cases are justified due to the very small value of Fourier grid spacing (0.7253 nm). The magnitude of curvatures are much higher for microstructure with t_2 GB thickness compared to the one with t_1 GB thickness. This is to be expected from the construction scheme associated with the t_2 approach.

Figure 5.6 shows plot over the line for the norm of initial polar dislocation and disclination densities $(\sqrt{\alpha_{ij}\alpha_{ij}})$ and $(\sqrt{\theta_{ij}\theta_{ij}})$, respectively. Note here that the initial
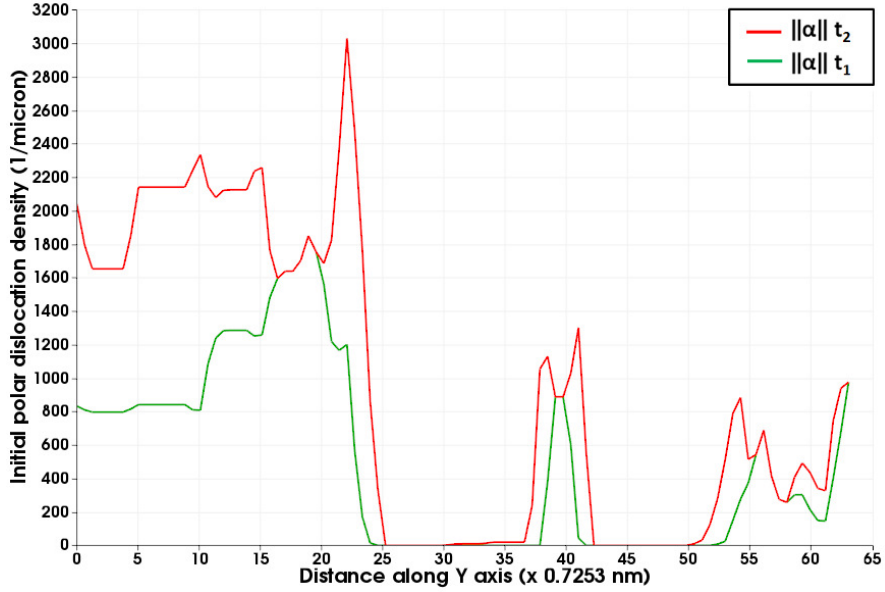
Figure 5.6: Plot over line for norm of initial polar dislocation density $(\sqrt{\alpha_{ij}\alpha_{ij}}$ in $1/\mu m)$ for a 10 nm polycrystal configuration with GB initial curvature thickness t_1 (in green) and t_2 (in red).

polar dislocation density has a contribution coming from both compatible and incompatible initial elastic curvatures. The norm of initial polar dislocation density is the same as the norm of the initial elastic curvature. From both the plots, it can be seen that the defect content is higher in the case of t_2 boundary which is to be expected.

Figure 5.7 shows plot over the same line for the norm $(\sqrt{M_{ij}M_{ij}})$ of the initial couple stress generated due to the initial curvatures. Recall that the magnitude of $\boldsymbol{A}$ is taken as Gb^2. Intra-granular couple stresses are seen to be generated, more in the case of GB thickness t_2 than t_1. These arise due to the proximity of Fourier points
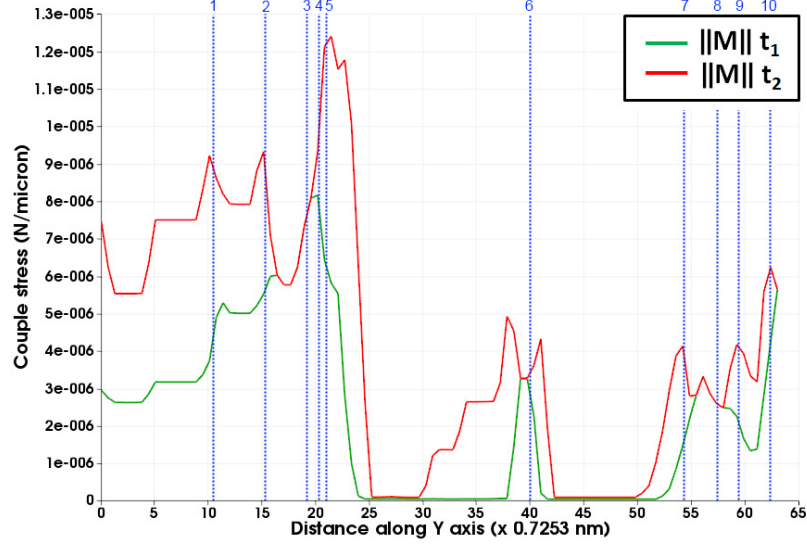
Figure 5.7: Plots over line for the norm $(\sqrt{M_{ij}M_{ij}})$ of the initial couple stress generated due to the initial elastic curvatures for 10 nm polycrystal with GB thickness t_1 (in green) and t_2 (in red). Blue lines indicate the location of interfaces traversed by the line shown in figure 5.2 and the numbers in blue correspond to interface identifiers from figure 5.2.

under consideration to other interfaces that do not lie in the plane of the line along which the couple stress norm are plotted.

5.3.3 Boundary conditions

Two types of boundary conditions are considered: (a) uniaxial tension along the y direction and (b) relaxation by holding the microstructure at constant imposed strain of 0, also along the y direction. In the first case, the prescribed applied strain component $\dot{E}_{22} = 1s^{-1}$ along with no shear $\dot{E}_{12} = \dot{E}_{13} = \dot{E}_{23} = 0$. Surfaces normal to x and z directions are traction free, therefore macroscopic Cauchy stress components $\Sigma_{11} = \Sigma_{33} = 0$. During a tensile test, the surfaces normal to the y direction are allowed to bend. Therefore, the macro couple stress components Φ_{12} and Φ_{32} are imposed to zero. The remaining surfaces are not allowed to bend and no surface is allowed to twist. Therefore, the macro curvature rates $\dot{K}_{11}$, $\dot{K}_{13}$, $\dot{K}_{21}$, $\dot{K}_{22}$, $\dot{K}_{31}$ and $\dot{K}_{33}$ are imposed to zero.

In the second case, the microstructure is held at zero strain along the y direction to study the relaxation of stresses generated from initial curvatures. The same macroscopic strain, Cauchy stress, curvature, and couple stress boundary conditions are imposed but with $\dot{E}_{22} = 0$.

5.3.4 Case studies

The case studies are divided into two parts: (a) the first part is dedicated to validating the PMFDDM model and the methodology to compute initial curvatures described in section 5.1. (b) the second part is dedicated to understanding the contributions of these initial curvatures on the local and macroscopic response of nc microstructures.

In order to validate the PMFDDM FFT numerical scheme, the model is benchmarked against the EVP FFT model. Since the latter cannot account for curvatures, therefore the benchmarking is done using the t_0 microstructure. Next, to validate the initial curvature methodology, the PMFDDM FFT model is applied to simulate uniaxial tensile loading in the bicrystalline case characterized with initial curvatures. As mentioned in section 5.1, the discontinuity in these curvatures results in unwanted oscillations (Gibbs phenomenon) in the kinematic and stress fields computed using the PMFDDM FFT approach. Corrections to these oscillations are then proposed using a DFT (discrete Fourier transform) scheme resulting in the PMFDDM DFT model.

Next, the PMFDDM DFT model along with initial curvatures is applied to study the local and macroscopic response of nc microstructures. The first step is to highlight the contribution of initial curvatures on the elastic response of nc microstructures. This will provide a deep understanding on the evolution of local stresses generated due to the presence of these initial curvatures. As shall be seen later, instantaneous Cauchy and couple stresses are generated in the presence of these initial curvatures.

The next set of simulations are performed to understand the role of plastic curvatures in relaxing these initial stresses; the microstructure with initial curvatures is relaxed in one simulation via plastic strains, and second via both plastic strains and curvatures. This opens up a question highlighting the need to parametrize the plastic curvatures. In the final set of simulations, strain based plastic deformation of nc microstructure with initial curvatures is simulated to highlight latter's role in predicting the breakdown in Hall-Petch law. Table 7 summarizes all the simulations discussed in this section.

Table 7: Simulations to highlight the contribution of residual curvatures on the local and bulk mechanical response of nc materials

Test	Description	Microstructure
(1) Benchmarking PMFDDM FFT	Comparison with EVP FFT	Polycrystalline, t_0 Coarse-grained
(2) Benchmarking PMFDDM FFT with initial curvature	Validation of initial curvature methodology Correcting oscillations	bicrystal-a, t_0 bicrystal-b, t_2
(3) Pure elastic loading	Understand role of initial curvature, uniaxial tension	Polycrystalline, t_0, t_1, t_2
(4) Relaxation of initial Cauchy and couple stresses	Role of initial curvature and (a) Strain plasticity (b) Combined strain and curvature plasticity	Polycrystalline, t_2
(5) Elasticity and strain plasticity	Understand role of initial curvature, uniaxial tension	Polycrystalline, t_0, t_1, t_2

5.4 Benchmarking and validation of PMFDDM FFT with initial curvatures

5.4.1 Comparison with EVP FFT

The first simulation performed is to benchmark the PMFDDM FFT model with respect to the EVP FFT model. To that end, the macroscopic response predicted by PMFDDM FFT model is compared with that predicted by the EVP FFT model of Lebensohn *et al.* [239] for a coarse-grained microstructure.

In order to facilitate the comparison, the microstructure is subjected to uniaxial tension along the y direction up to 0.1% strain in 40 steps of 0.000025. Initial curvatures, and consequently polar dislocation densities, are set to zero. The microstructure is allowed to deform plastically only via dislocation slip. The Hall-Petch relationship is used to estimate the CRSS; for a coarse-grained microstructure this relationship works well. The Hall-Petch relationship [170, 317] which linearly relates a material's yield strength to the inverse of the square of its average grain size:

$$\sigma_Y = \sigma_0 + \frac{k_y}{\sqrt{d_g}} \tag{5.41}$$

where σ_Y, σ_0, k_y and d_g. The Hall-Petch constants for FCC Cu, $\sigma_0 = 25$MPa and $k_y = 0.11$, are obtained from the work of Smith [375]. For a grain size of 100μm, the yield strength obtained is 36 MPa. From here the CRSS is assigned its maximum possible value of $\tau_0^s = 18$ MPa and is kept constant to obtain an elastic perfectly plastic response *i.e.* no hardening (H = 0). To obtain this average grain size, the inter-Fourier point spacing is taken as 7.253 μm.

The VM Cauchy stress vs VM strain response for this coarse-grained microstructure is plotted in figure 5.8. An excellent match is obtained between the two methods for the macroscopic response. This is to be expected because for the length scale resolution (inter Fourier point spacing 7.253 μm) the local curvatures, which
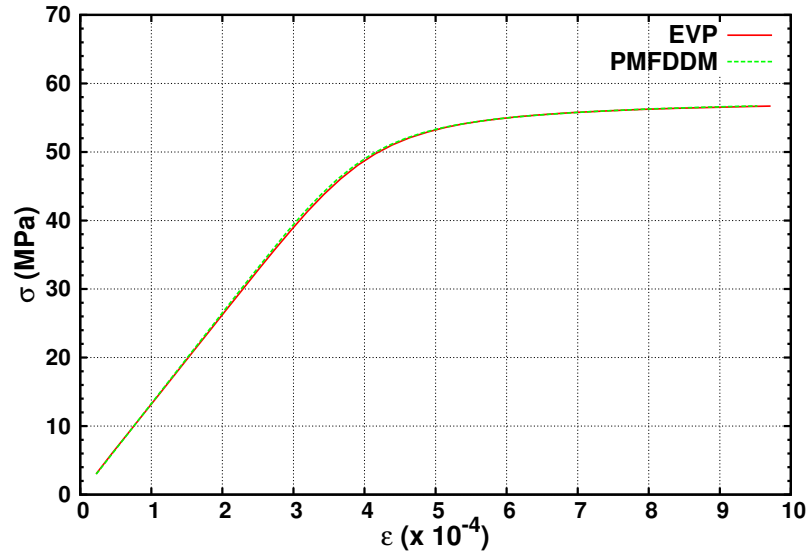
Figure 5.8: VM Cauchy stress vs. VM strain curve for a coarse grained microstructure with average grain size 100 μm subjected to uniaxial tension

are elastic in nature, and local couple stresses are not significant enough to affect the average local Cauchy stress response. In order to better understand this consider the couple stress field M_{21} in figure 5.9 plotted along the line from figure 5.2. The order of magnitude of couple stress M_{21} is $\approx 10^{-13}$ $N/\mu m$. The re-
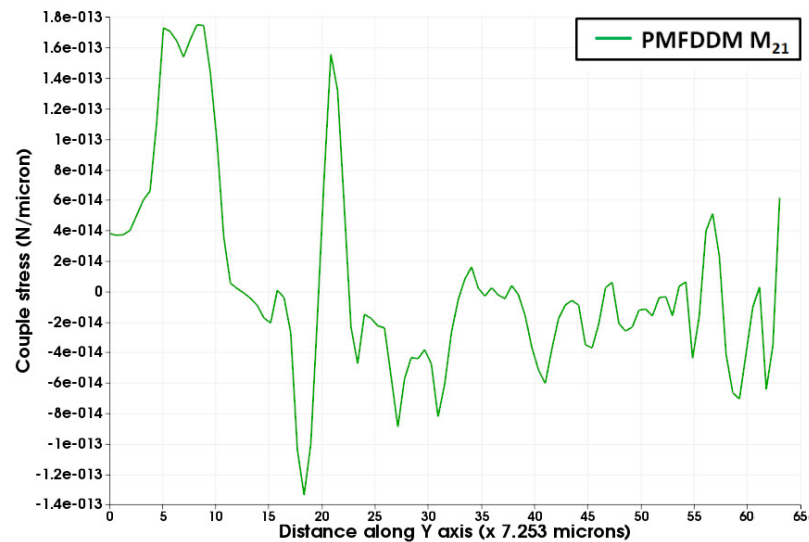
Figure 5.9: Local couple stress component M_{21} $(N/\mu m)$ generated from PMFDDM FFT at 0.1% strain along the line shown in figure 5.2

maining couple stress components (not shown here) are also in the same order of magnitude. To understand the insignificance of the couple stress contribution to local Cauchy stresses, consider the first equilibrium equation in component form: $\sigma_{11,1} + \sigma_{12,2} + \sigma_{13,3} + 0.5(M_{31,12} + M_{32,22} + M_{33,32}) - 0.5(M_{21,13} + M_{22,23} + M_{23,33})$. For an inter Fourier point spacing of 7.253 μm, the order of couple stress contribution to the equilibrium can be approximated as $10^{-13}/(7.253^2)$ $N/\mu m^3 \approx 1.9 \times 10^{-15} N/\mu m^3$ as opposed to $\approx 10^{-7} N/\mu m^3$ coming from the Cauchy stress components; the couple stress contribution is 8 orders of magnitude lower than Cauchy stresses. These are therefore not sufficient to equilibrate Cauchy stresses.

Other simulations are also performed for with larger values of the critical resolved shear stress (84 MPa and 330 MPa) to mimic smaller average grain sizes (600 nm and 30 nm, respectively). In all the cases a very good match between the VM Cauchy stress vs VM strain is obtained.

5.4.2 Gibbs phenomenon: correction using DFT

The couple stress plot-over-line shown in figure 5.9 reveals a steep change in the stress field with sharp pointed peaks close to the distance 20 (x 7.253 microns). These could represent the orientation dependence of the couple stresses across two highly misoriented grains or could be an overestimation of the couple stress field due to the fluctuations induced from Gibbs phenomenon. The purpose of this section is to identify the Gibbs phenomenon and propose corrections for it. Achieving this will provide the necessary validation for the PMFDDM FFT methdology combined with initial curvatures.

Gibbs phenomenon occurs in treating a discontinuous field using a finite series approximation of a continuous Fourier transform. It involves an overshoot in the value of the Fourier transform of a discontinuous field. Furthermore, this overshoot does not fade away with an increase in the frequency *i.e.* increase in number of Fourier

points, but converges to a non-zero value. In the continuous FFT models (both EVP and PMFDDM), the methodology ensures that the compatible displacement fields are continuous everywhere in the domain. This should imply that the derivatives of the displacement fields are also continuous everywhere. Howerver, due to the heterogeneous elasticity arising from different orientation of grains, the compatible strain and rigid body rotation fields are discontinuous across the interfaces. Taking the gradients of these discontinuous compatible fields using the continuous FFT, as is done in the case of PMFDDM FFT to the rotation field in order to get the compatible curvature fields, would induce oscillations in the vicinity of interfaces. In the present case the magnitude of the curvatures, and hence couple stresses is not significant enough to affect the Cauchy stress response. However, when initial curvatures are considered, it is possible that curvatures and couple stresses could significantly affect the Cauchy stress response. This effect could be magnified due to the Gibbs phenomenon.

In order to test and quantify if the Gibbs phenomenon is encountered when implementing the PMFDDM FFT model, the two bicrystalline cases described in figure 5.3 are considered. This is the second test described in table 7. The two bicrystals considered are: (1) bicrystal-a with tilt misorientation of $5°$ and t_0 configuration, and (2) bicrystal-b with random orientation of grains with t_2 configuration. In both the cases, the inter Fourier point spacing in each direction is taken as 0.7253 nm in order to appreciate the effect of curvature and couple stress oscillations on the Cauchy stresses. The test conditions are the same as in the studies done in previous section for microstructures undergoing uniaxial tension.

For bicrystal-a, the curvature and couple stress components, κ_{32} and M_{32} respectively, are shown in figure 5.10. The Gibbs phenomenon is clearly visible in these plots. There is an apparent overshoot of the couple stress and curvature at the interface which results in ripples in these fields deep within the two crystals. At the

first time step for the simulations, the curvature field ripples are generated which affect the equilibrium solution of the couple stresses. The couple stresses in turn induce oscillations in the couple stress polarization fields which enter the compatible solution of the strain fields resulting into ripples in the strain field. This strain field is then used to compute the Cauchy stress field that inherits these oscillations. The effect of these ripples could be diminished by taking a larger number of Fourier points but the overshooting values converge to a non-zero constant with increasing Fourier points and still pose a problem. From a different aspect, reducing the value of A by one order of magnitude reduces the magnitude of couple stresses which in turn reduces the amplitude of ripples in the Cauchy stress. However, this does not affect the relative amplitude of the ripples in curvature and couple stresses.

(a) κ_{32} $(1/\mu m)$
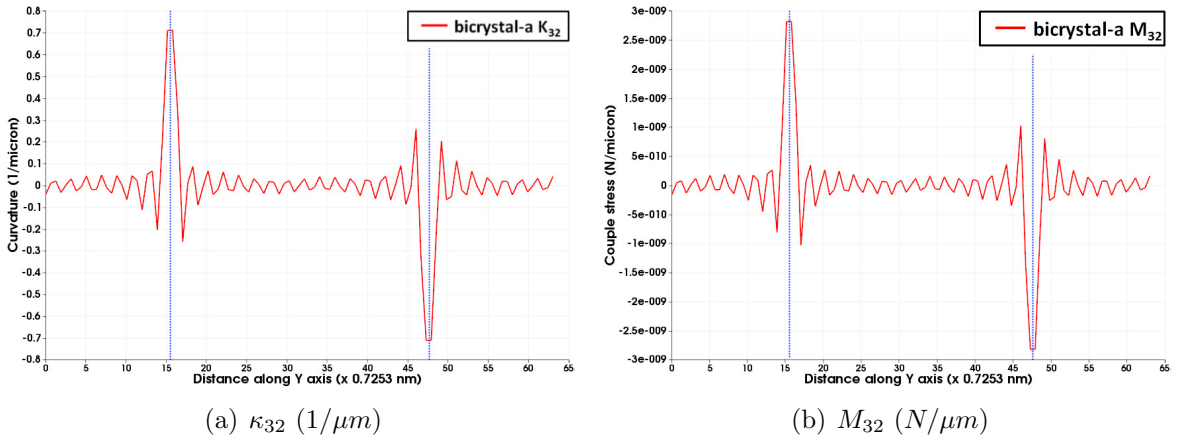
(b) M_{32} $(N/\mu m)$

Figure 5.10: (a) κ_{32} $(1/\mu m)$ and (b) M_{32} $(N/\mu m)$ plotted along line shown in figure 5.3(a) for bicrystal-a configuration at 1.2% applied strain along y.

To better understand the severity of the Gibbs phenomenon, consider the bicrystal-b case. Figure 5.12(a) shows the initial curvature component κ_{32} for bicrystal-b. The Fourier points over which the initial curvature is non-zero are shown as small pink squares. The thickness of GB interface is $t_2 \approx 2.18nm$. The initial curvature is computed as a gradient of the rotation field in crystal space, therefore there are no oscillations as can be seen from figure 5.12(b). The magnitude of initial curvature is

(a) σ_{11} (MPa)

(b) σ_{12} (MPa)
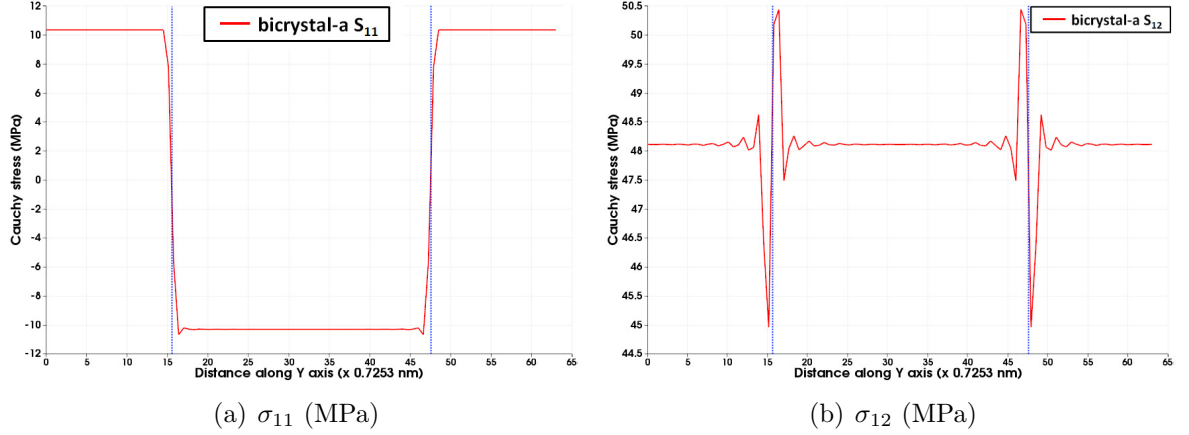
Figure 5.11: (a) σ_{11} (MPa) and (b) σ_{12} (MPa) plotted along line shown in figure 5.3(a) for bicrystal-a configuration at 1.2% applied strain along y.

much higher than the curvatures generated during the entire simulation of bicrystal-a. With such magnitudes, the initial couple stresses are in the order of $10^{-7} N/\mu m$ and could have significant contributions to the Cauchy stresses.

(a) κ_{32} (1/μm) contour

(b) κ_{32} (1/μm) plot-along-line
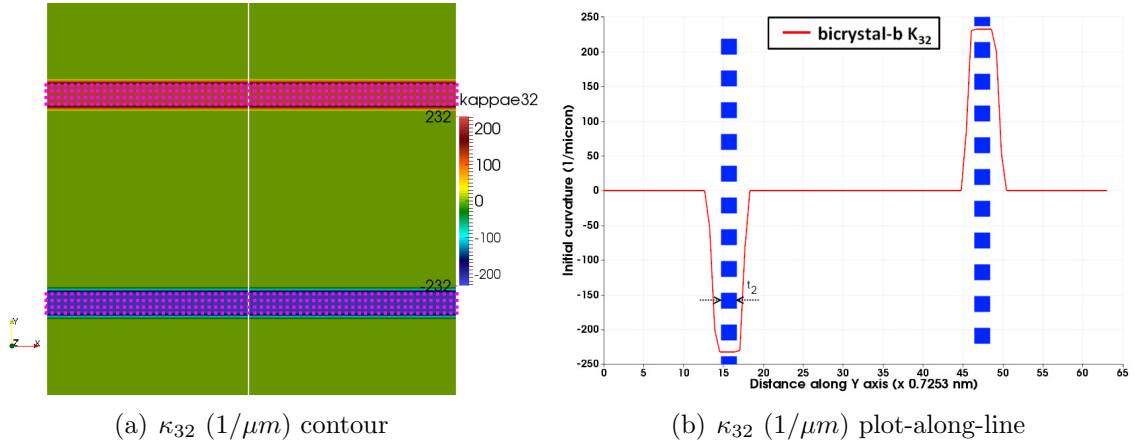
Figure 5.12: (a) Contour plot of initial curvature field κ_{32} (1/μm) highlighting (in pink) the Fourier points belonging to the GB interface of thickness $t_2 = 2.18nm$ and (b) κ_{32} (1/μm) plotted along white line shown in (a) for bicrystal-b configuration. The blue line resembles the thickness t_2 of the interface.

Bicrystal-b is then loaded in tension. Compatible total curvature κ_{32} and couple stress M_{32} at 1.2 % applied strain are plotted in figure 5.13 along the line shown in

(a) κ_{32} $(1/\mu m)$
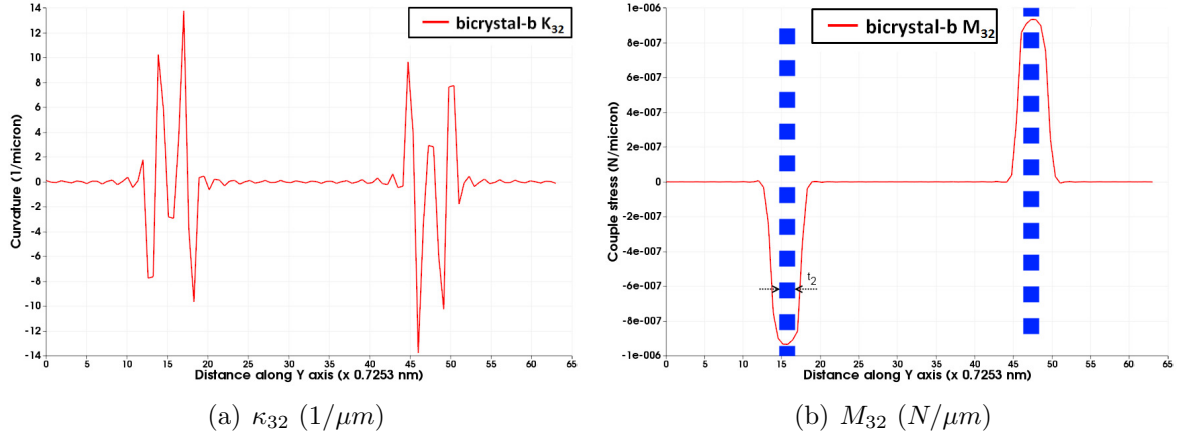
(b) M_{32} $(N/\mu m)$

Figure 5.13: Plots over line for (a) κ_{32} $(1/\mu m)$ and (b) M_{32} $(N/\mu m)$ for bicrystal-b configuration at 1.2% applied strain along y. For the sake of convenience, the blue line resembling the thickness t_2 of the interface is only shown for the couple stress.

(a) σ_{11} (MPa)

(b) σ_{12} (MPa)
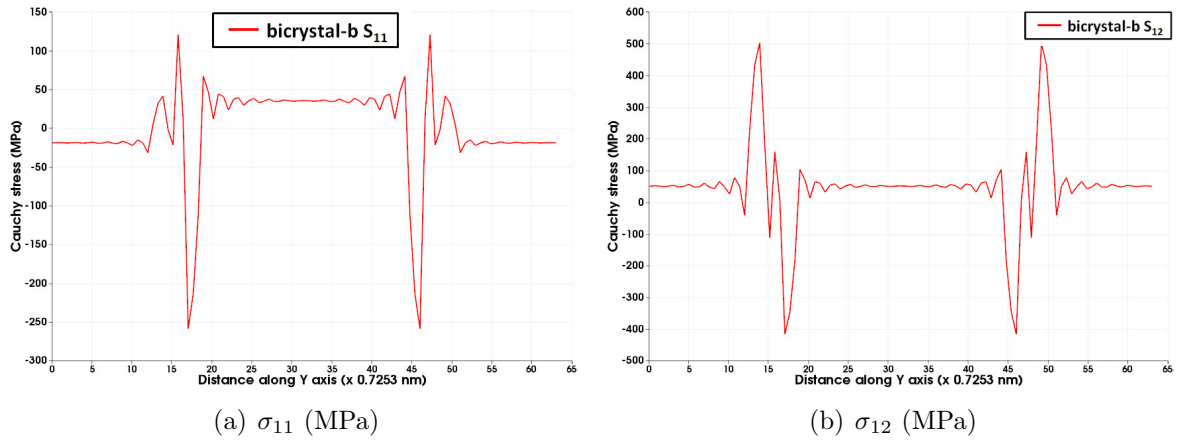
Figure 5.14: Plots over line for (a) σ_{11} (MPa) and (b) σ_{12} (MPa) for bicrystal-b configuration at 1.2% applied strain along y.

figures 5.3(b). Severe unwanted oscillations are obtained in the compatible curvature field. On the other hand, the oscillations in couple stress are not as pronounced. This is because couple stresses have a dominant contribution coming from the initial curvatures; the latter is almost two orders of magnitudes larger than the curvature generated due to loading. As the imposed strain increases, the FFT algorithm induces

unwanted oscillations of increasing amplitude in the compatible strain, and conse-
quently, Cauchy stress field. The unwanted oscillations induced in Cauchy stresses
can be observed from figure 5.14.

5.4.2.1 Correcting Gibbs phenomenon using Gaussian smoothing of initial curvatures

In the previous section it was seen that the discontinuity in initial curvatures in-
troduced spurious oscillations in the Cauchy stress and compatible total curvature
fields. In this section, correction to these oscillations is made by smoothening the
discontinuity using a Gaussian low pass filter.

The 3-dimensional columnar bicrystal-b is reconsidered but with 128 Fouier points
along the x and y directions and 16 along the z direction. This provides ample of
Fourier points to apply a Gaussian of bin width $6\tilde{\sigma} = 24\delta$, where $\tilde{\sigma}$ is the standard
deviation of the binned data. The initial curvatures are already binned along all
the directions. These have non zero gradients along the y direction. Therefore, the
Gaussian is applied to smoothen the initial curvature fields only along this direction.
Figure 5.15 shows the original unfiltered and the Gaussian filtered initial curvatures.

Uniaxial tension is then applied along the y direction and the results show that
the oscillations in both Cauchy stress and curvature fields are significantly reduced.
The compatible curvature components are also found to have significantly diminished
oscillations which further reduce with increased bin width for the Gaussian filter.
However, a non-negligible overshoot in the curvature components at the edges of the
new GB interface is obtained. This is because the Gaussian filter is only applied to
the initial curvature but the grain orientations having a rotational jump across the
GB interface remain untreated.

Gaussian filtering does reduce the long range ripples in Cauchy stress and cur-
vature fields, however it requires a significantly large bin width which is not feasible
in the polycrystalline case described in figure 5.2 without significantly increasing the

(a) Unfiltered
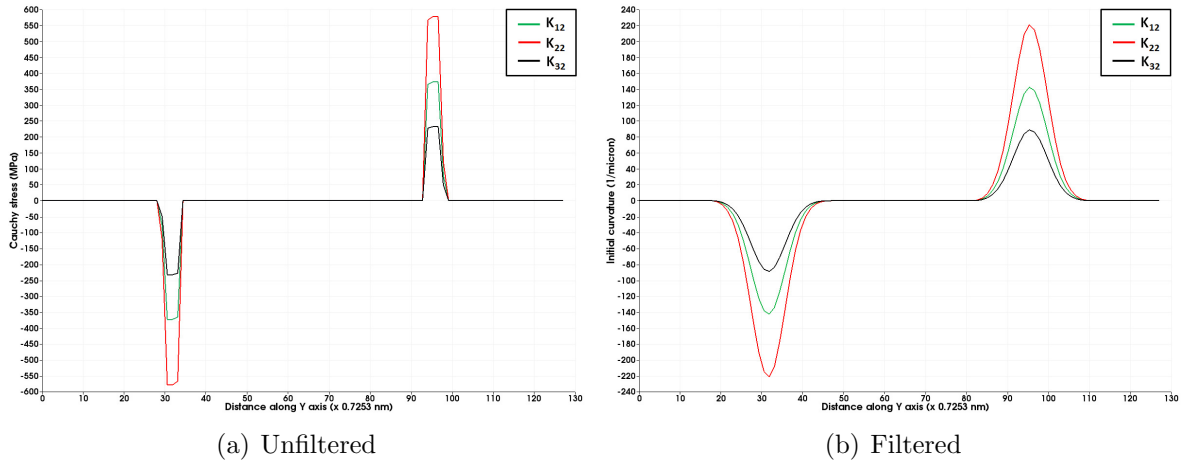
(b) Filtered

Figure 5.15: Plots over line from figure 5.2 for non-zero initial curvature components $(1/\mu m)$ κ_{22} (in red), κ_{12} (in green) and κ_{32} (in black) in the (a) unfiltered form and (b) applying a Gaussian filter of width 24δ on the modified bicrystal-b configuration with 128 Fourier points along x and y direction and 16 along z direction.
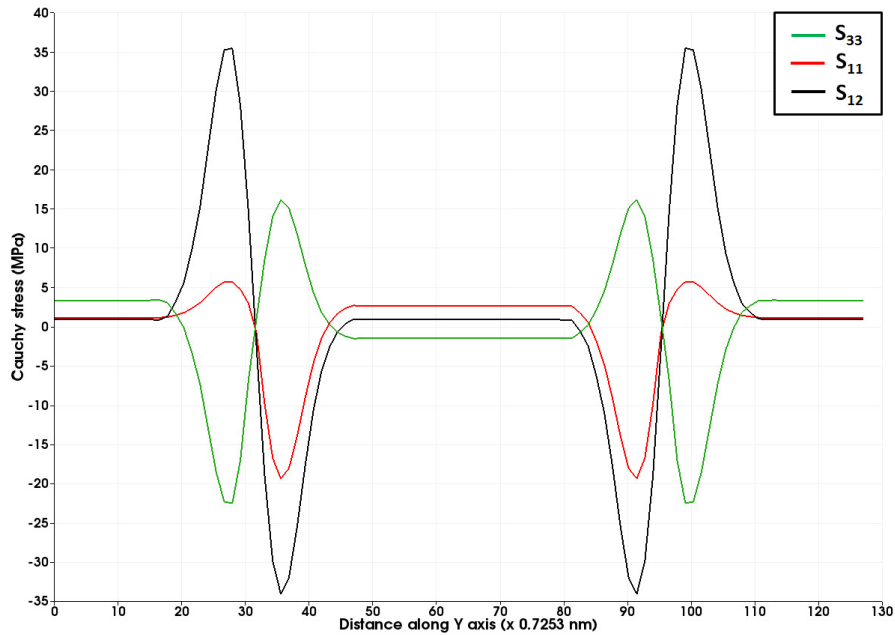
Figure 5.16: Plots over line from figure 5.2 for Cauchy stress components (MPa) σ_{11} (in red), σ_{33} (in green) and σ_{12} (in black) for the modified bicrystal-b configuration with Gaussian filtered initial curvatures.

GB interface to volume ratio.
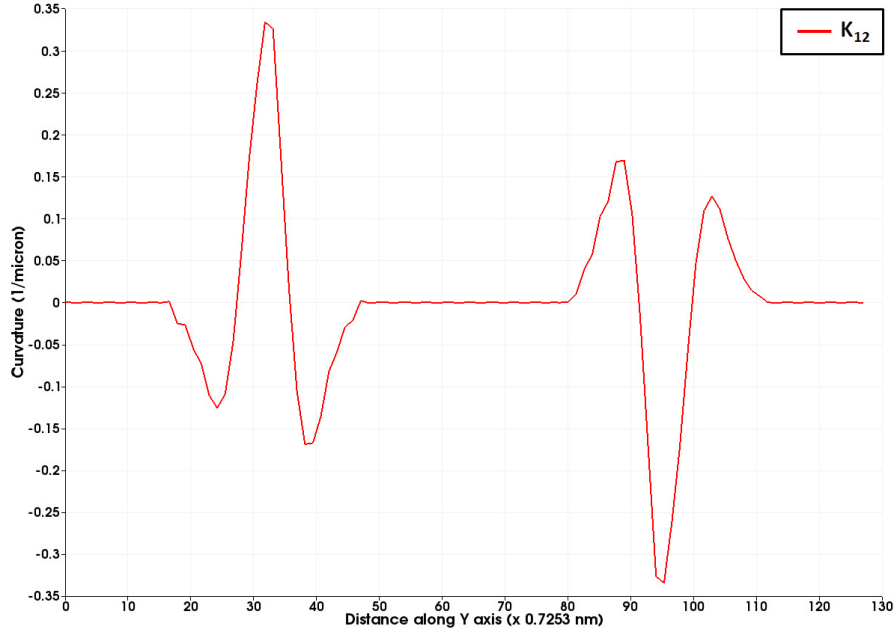
Figure 5.17: Plots over line from figure 5.2 for compatible total curvature component κ_{12} $(1/\mu m)$ for the modified bicrystal-b configuration with Gaussian filtered initial curvatures at 0.02% strain.

5.4.2.2 Correcting Gibbs phenomenon using DFT

In this section, a different numerical scheme based on DFT is developed to tackle the Gibbs phenomenon. This method derives motivation from a recent work by Berbenni *et al.* [34]. These workers encountered the Gibbs phenomenon in dealing with discontinuous polar dislocation fields prescribed as initial conditions to compute the incompatible and compatible plastic and elastic distortion field, and consequently Cauchy stresses, using the FFT technique. Their approach to solve the problem involved replacing the Fourier transforms of continuous partial derivatives of fields with the Fourier transform of the centered finite difference approximation of that field. Then using the discrete Fourier series formulation, these Fourier transformed centered finite differences of fields were used to obtain equivalent expressions for first and second order multiplications of angular frequencies. Using this approach, Berbenni *et al.* [34] were able to remove the oscillations from the kinematic and stress

232

fields.

As an illustration, consider the first order partial derivative along direction x, $\partial/\partial x$ of a continuous field $f(l, m, n)$ where l, m and n are the Fourier points in direction x, y and z, respectively. Using the convention of the "fourn" subroutine as described in appendix F, the continuous Fourier transform of this partial derivative field is $-ik_1 FT(f)$. On the other hand, the centered finite difference approximation of the partial derivative is given as $[f(l+1, m, n) - f(l-1, m, n)]/2\delta_1$, where δ_1 is the inter Fourier point spacing along direction x. Taking the Fourier transform of this expression and using the shift theorem for Fourier transforms (refer to appendix F), the corresponding DFT approximation of $-ik_1 FT(f)$ is given as $-i\sin(2\pi\xi_1/N_1)/\delta_1$, where $\xi_1 = k_1/(2\pi)$. The other partial derivatives are computed in a similar manner. Detailed derivations of this methodology are presented in the appendix F.

With the intention to apply this technique, the following method is proposed. Recall the compatible total strain and curvature solutions obtained using the Fourier transform technique.

$$\epsilon_{ij}(\mathbf{x}) = E_{ij} + \frac{1}{2} FT^{-1}\left(ik_j \left(\hat{G}_{ik}(\vec{k}) + \hat{G}_{ki}(\vec{k}) \right) \hat{f}_k(\vec{k}) \right) \tag{5.42}$$

$$\kappa_{ij}(\mathbf{x}) = K_{ij} - \frac{1}{2} e_{ikl} FT^{-1}\left(k_j k_k \hat{G}_{lm}(\vec{k}) \hat{f}_m(\vec{k}) \right) \tag{5.43}$$

Using equation (5.17) for the fictive body force and defining a modified Green's tensor $\hat{\Gamma}_{ijkl} = \xi_j \xi_l \hat{G}_{ik}(\vec{k})$, the above equations can be rewritten as:

$$\epsilon_{ij}(\mathbf{x}) = E_{ij} - \frac{1}{2} FT^{-1}\left(\left(\hat{\Gamma}_{ijkl}(\vec{k}) + \hat{\Gamma}_{kjil}(\vec{k}) \right) \left(\hat{\tau}_{kl}(\vec{k}) - \frac{1}{2} e_{klm}(ik_n) \hat{\mu}_{mn}(\vec{k}) \right) \right) \tag{5.44}$$

$$\kappa_{ij}(\mathbf{x}) = K_{ij} + \frac{1}{2} e_{ikl} FT^{-1}\left(\hat{\Gamma}_{ljmk}(\vec{k}) \left((ik_n) \hat{\tau}_{mn}(\vec{k}) + \frac{1}{2} e_{mnp}(k_n k_q) \hat{\mu}_{pq}(\vec{k}) \right) \right) \tag{5.45}$$

The continuous frequencies corresponding to first and second order partial derivatives can then be approximated using the DFT approach as a vector and a matrix of the form

$$D_i^I = [DFT(ik_1) \quad DFT(ik_2) \quad DFT(ik_3)]$$

$$D_{ij}^{II} = \begin{bmatrix} DFT(k_1^2) & DFT(k_1 k_2) & DFT(k_1 k_3) \\ DFT(k_2 k_1) & DFT(k_2^2) & DFT(k_2 k_3) \\ DFT(k_3 k_1) & DFT(k_3 k_2) & DFT(k_3^2) \end{bmatrix}$$

where $DFT(\ )$ corresponds to the DFT equivalent of frequency within the brackets. The expressions for these are given in appendix F.

Finally, the compatible total strain and curvature can be written as:

$$\epsilon_{ij}(\mathbf{x}) = E_{ij} - \frac{1}{2} FT^{-1} \left(\left(\hat{\Gamma}_{ijkl}(\vec{k}) + \hat{\Gamma}_{kjil}(\vec{k}) \right) \left(\hat{\tau}_{kl}(\vec{k}) - \frac{1}{2} e_{klm}(D_n^I)\hat{\mu}_{mn}(\vec{k}) \right) \right) \quad (5.46)$$

$$\kappa_{ij}(\mathbf{x}) = K_{ij} + \frac{1}{2} e_{ikl} FT^{-1} \left(\hat{\Gamma}_{ljmk}(\vec{k}) \left((D_n^I)\hat{\tau}_{mn}(\vec{k}) + \frac{1}{2} e_{mnp}(D_{nq}^{II})\hat{\mu}_{pq}(\vec{k}) \right) \right) \quad (5.47)$$

This method shall henceforth be known as the DFT-1 approach. Note that in DFT-I, the modified Green's tensor is still computed using the continuous Fourier transforms. This function can also be approximated using the DFT technique. Re-considering the expression for modified Green's function using equation (E.17) i.e. $\hat{\Gamma}_{ijkl}(\vec{k}) = (k_j k_l)[C_{kmin}^{\circ} k_m k_n + F_{kmnopi}^{\circ} k_m k_n k_o k_p]^{-1}$, it involves fourth order partial derivatives which appear in the form of multiplication of four frequencies. Their corresponding DFT approximations have been derived in the appendix F and are represented by the fourth order DFT tensor D_{ijkl}^{IV}. Therefore, the DFT equivalent of the modified Green's tensor can be defined as $\hat{\Gamma}_{ijkl}(\vec{k}) = D_{jl}^{II}[C_{kmin}^{\circ} D_{mn}^{II} + F_{kmnopi}^{\circ} D_{mnop}^{IV}]^{-1}$. The DFT form of modified Green's tensor can be combined with DFT-1 to obtain an extension of this method. The extended method shall henceforth be referred to as DFT-2.

The bicrystalline case bicrystal-b is re-simulated using the DFT-1 approach. Figure 5.18 shows the plot over line from figure 5.3(c) for curvature κ_{32}, couple stress M_{32}, and Cauchy stresses σ_{11} and σ_{22} obtained using the DFT-1 and CFT approaches at 1.2% imposed tensile strain (refer to figures 5.13 and 5.14). The results reveal that DFT-1 is a significant improvement over the CFT approach. The intra-granular ripples in Cauchy stress σ_{11} and σ_{12}, and curvature κ_{32} have vanished. At the GB

(a) κ_{32} $(1/\mu m)$

(b) M_{32} $(N/\mu m)$

(c) σ_{11} (MPa)

(d) σ_{12} (MPa)
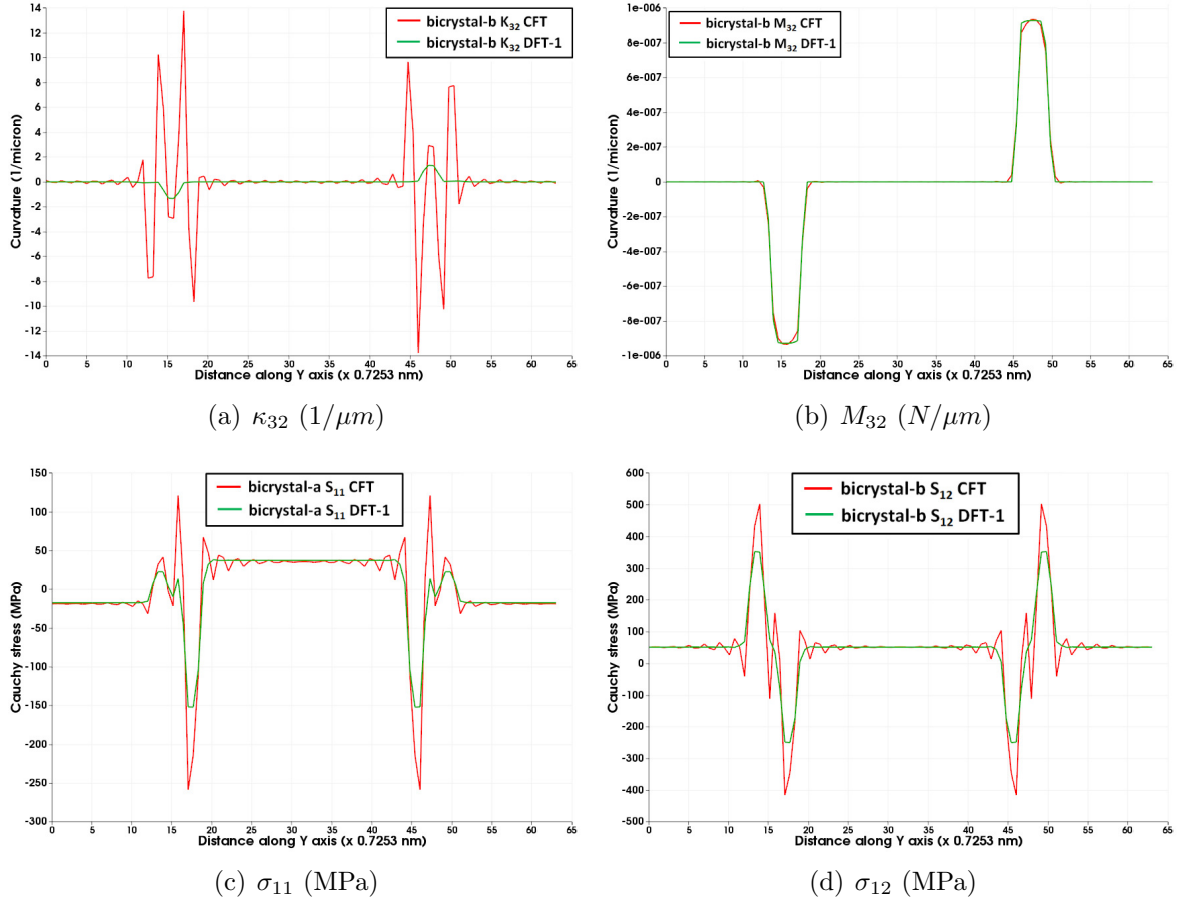
Figure 5.18: Plots over line for (a) κ_{32} $(1/\mu m)$, (b) M_{32} $(N/\mu m)$, (c) σ_{11} (MPa), and (d) σ_{12} (MPa) for bicrystal-b configuration at 1.2% tensile strain along y to compare methods DFT-1 (in green) and CFT (in red).

interface, Cauchy stress magnitudes have reduced by a factor of ≈ 1.67 for the largest value. This could significantly affect the yield stress predicted using the PMFDDM method. The strongest effect is seen on the curvature magnitude which has reduced by a huge factor of 14 confirming that the large compatible elasitc curvatures obtained in the CFT case were drastic consequences of the spurious oscillations. More importantly, overshooting curvatures obtained in the vicinity of interfaces in the CFT and in the Gaussian filtering case have vanished. Couple stresses are expected to not be affected much, although the very minor ripples close to the interface have vanished.

In order to compare all the three methods (CFT, DFT-1 and DFT-2), the bicrystal-a case is resimulated. Figure 5.19 shows the plot over line (shown in figure 5.3(a)) for curvature κ_{32}, couple stress M_{32}, and Cauchy stresses σ_{11} and σ_{22} obtained using the DFT-2 and DFT-1 approaches at 1.2% imposed tensile strain.

(a) κ_{32} $(1/\mu m)$ (b) σ_{12} (MPa)
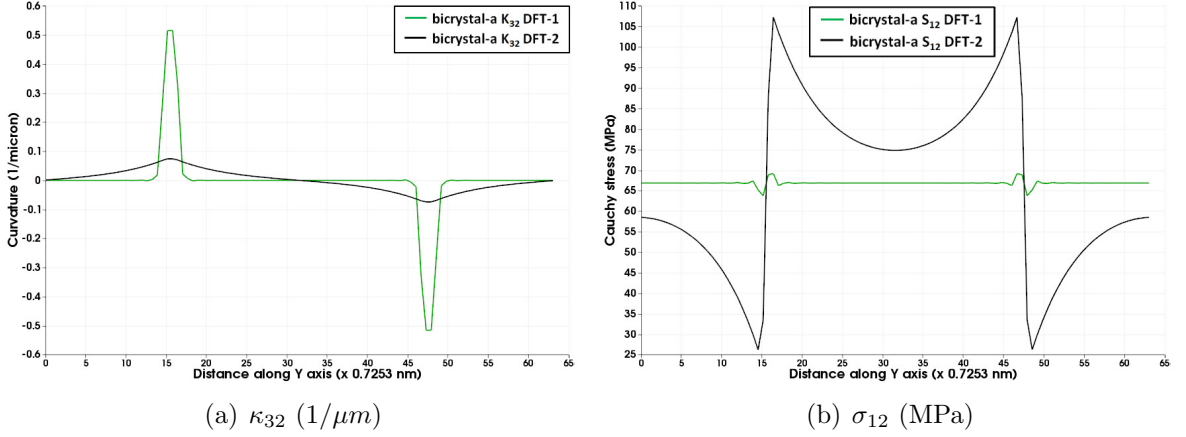
Figure 5.19: Plots over line for (a) κ_{32} $(1/\mu m)$, (b) M_{32} $(N/\mu m)$, (c) σ_{11} (MPa), and (d) σ_{12} (MPa) for bicrystal-a configuration at 1.2% tensile strain along y to compare methods DFT-2 (inblack) and DFT-1 (in green).

A stark difference between the kinematic and stress fields predicted by the two methods is immediately apparent. The DFT-2 solution is clearly not appropriate since it does not converge to the Eshelby solution in either of the two crystals. The effect comes from using the DFT approximation for the modified Green's function. One of the possible reasons could be that the accuracy $0(\delta^2)$ achieved from using the centered difference method may not be sufficient to obtain the correct solution. Interestingly, DFT-2 method removes any residual oscillations that are transferred from its DFT-1 part. Although the oscillations arising from DFT-1 are small; the ratio of relative amplitudes (with respect to the mean value) of the oscillations for bicrystal-a in σ_{11} and σ_{12} are 3.02% and 4.64%.

The above discussions provide ample support to the DFT-1 approach as the most
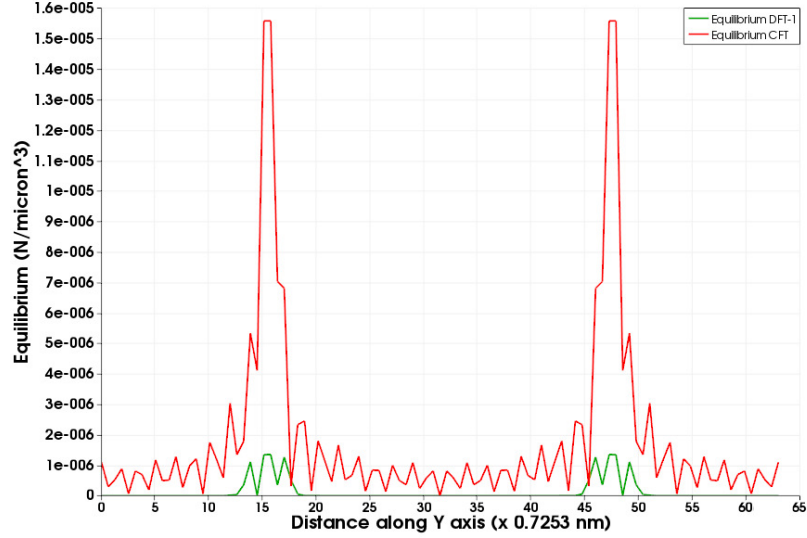
Figure 5.20: Comparison of the equilibrium vector magnitude computed from CFT and DFT-1 approaches at 1.2% tensile strain along the line shown in figure 5.3(a) for bicrystal-a configuration.

suitable available approach for solving the PMFDDM FFT problem with initial curvature. As a final test to validate the DFT-1 technique, the local equilibrium vector $\sigma_{ij,j} + 0.5e_{ijk}M_{kl,lk}$ is plotted, over the line shown in figure 5.3(a) for bicrystal-a, to compare with the CFT approach. The results are shown in figure 5.20. The equilibrium vector from the DFT-1 method is one order of magnitude lower than in the CFT case. Furthermore, the interface oscillations in the equilibrium vector decay rapidly to zero, away from the interface, as opposed to the CFT case.

In conclusion, the DFT-1 approach is the best suited for solving the PMFDDM FFT problem.

5.5 Pure elastic tensile loading: impact of initial curvatures on local elastic response

Following the validation of the PMFDDM FFT method with initial curvatures using the DFT scheme, the model can now be applied to study the role of residual curvatures on the local and macroscopic response of polycrystals. In this section, the impact

of residual curvatures on the elastic response is studied. This corresponds to the third test shown in table 7. The 100 grain microstructure (shown in figure 5.2 and henceforth known as nc100) is characterized with initial curvatures having magnitudes reflecting an average grain size of 10 nm. This is achieved by using an inter Fourier point spacing of 0.7253 nm.

The 10 nm nc100 is loaded in uniaxial tension upto 2% strain along the y-direction in 100 steps of 0.0002. Plastic deformation is not allowed. The VM Cauchy stress vs. VM strain curve is then a straight line as shown in figure 5.21. The macroscopic
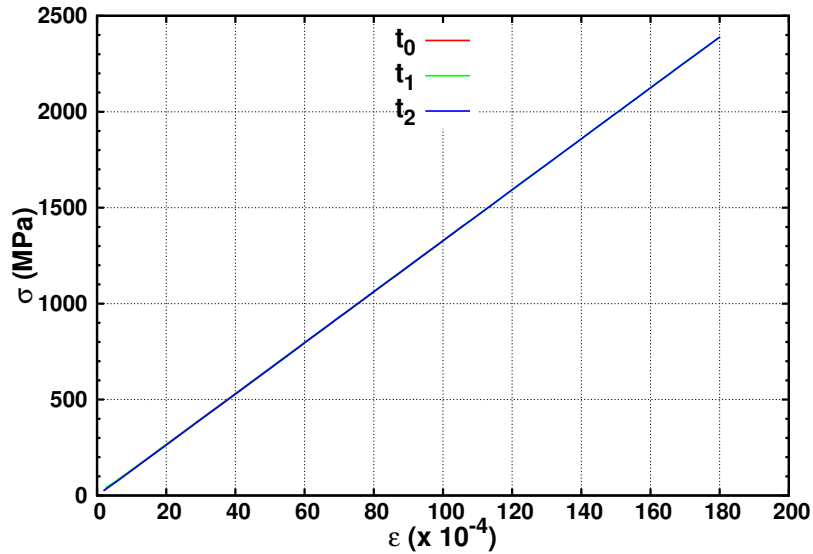
Figure 5.21: VM Cauchy stress vs. VM strain plot for 10 nm nc100 configuration with no GB initial curvature t_0, GB initial curvature thickness t_1, and t_2.

perfectly elastic response of all three configurations match very well throughtout the process of loading. Interestingly, the local responses are very different. In order to appreciate the effect of initial curvatures on the Cauchy stresses, consider the plot over line for σ_{22} shown for 10 nm nc100 with no initial curvature (t_0), GB thickness t_1 and GB thickness t_2 at 0.8% strain in figure 5.22. Here, 0.8% strain is chosen because the differences in the Cauchy stresses will be very pronounced.

Cauchy stresses of increasingly larger magnitude are obtained as the GB curvature
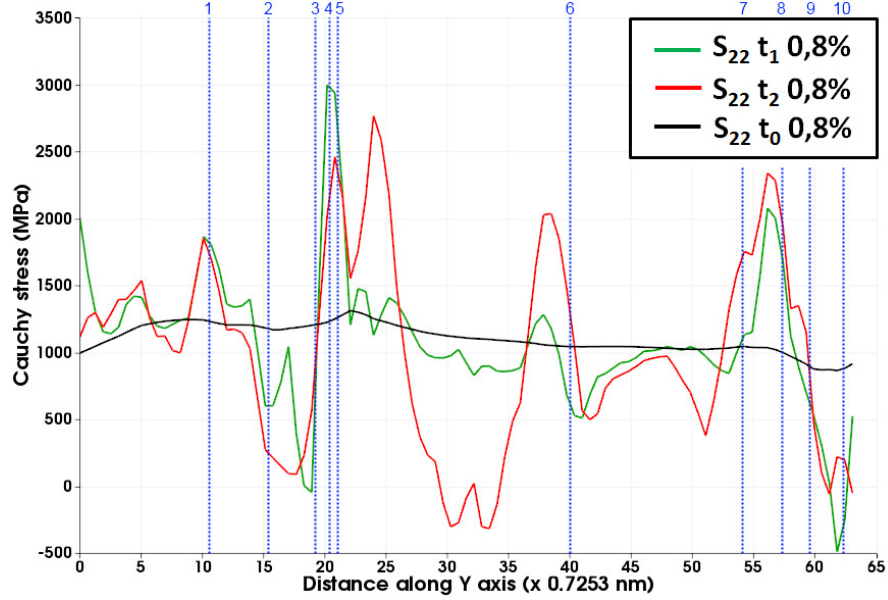
Figure 5.22: Plots over line for Cauchy stress component σ_{22}(MPa) for 10 nm nc100 configuration for t_0, t_1 and t_2 configurations at imposed strain 0.8%. Blue lines indicate the location of interfaces and the numbers in blue correspond to interface identifiers from figure 5.2.

thickness increases. These are fluctuations in the local Cauchy stresses that result from equilibrating the large couple stresses. The largest fluctuation in the case of GB thickness t_2 occurs in the σ_{11} component (not shown here) where a value that is 20 times larger than the average is attained. In general, the fluctuations in Cauchy stresses do not follow the couple stress evolution trend shown in figure 5.7 but no analogy should be drawn here because the magnitudes of both Cauchy and couple stresses are affected by other Fourier points in their vicinity. Jumps in stress fields across the interface appear as expected. These are the regions where Cauchy stress fluctuations are usually largest. However, of particular interest are the fluctuations in intra-granular stresses that are generated in between interface indicators 10-1, 5-6 and 6-7. Consider the cross sections shown in figure 5.23. These are nc100 snapshots at 1 and 2 Fourier point spacings back and forth in the direction normal to the cross section shown in figure 5.2. For the grain between 10-1, there are two interfaces

239
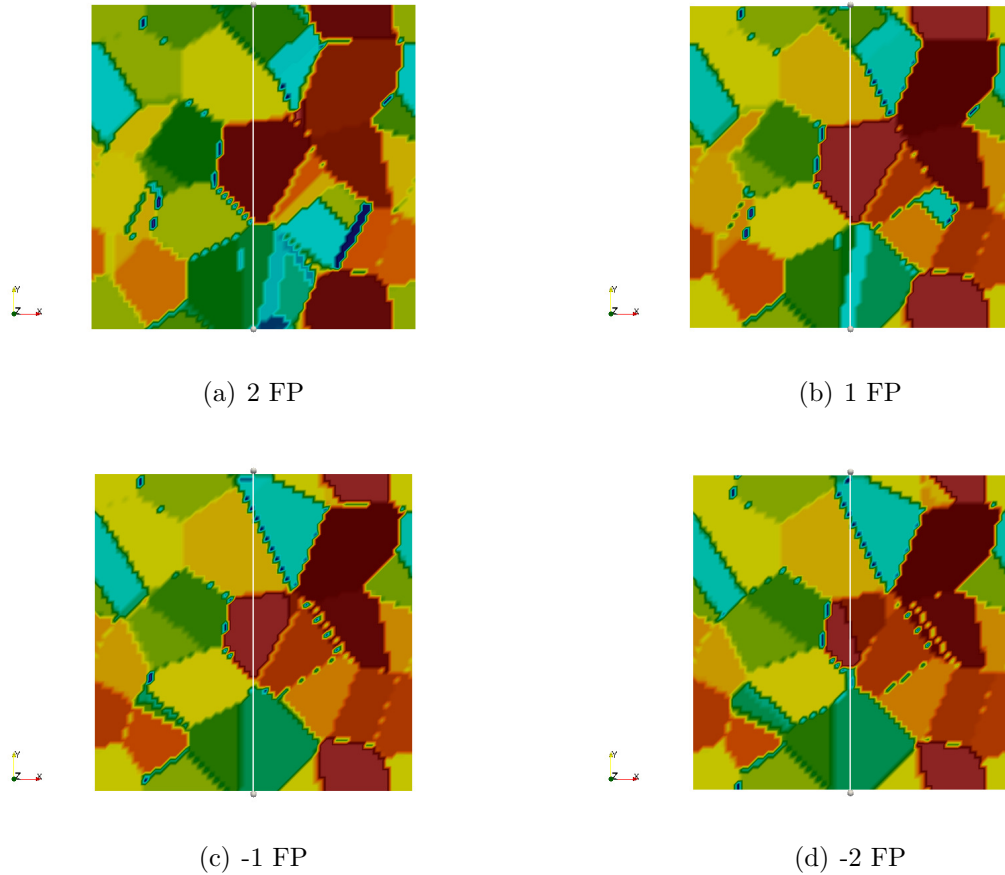
(a) 2 FP

(b) 1 FP

(c) -1 FP

(d) -2 FP

Figure 5.23: nc100 snapshots of cross sections that are (a) 2 FP, (b) 1 FP, (c) -1 FP, and (d) -2 FP spacing away in the direction normal to the cross section shown in figure 5.2 [FP = Fourier point].

and a triple junction that fall in its proximity, these are one and two Fourier point spacing away in the outward direction as can be seen from figures 5.23(a) and (b). For t_1 the interface in figure 5.23(a) induces the stress fluctuations. For t_2, both the interfaces and the triple junction initial curvatures and couple stresses contribute to the fluctuations. For 5-6, there is an interface that is at two Fourier points away in the inward direction shown in figure 5.23(d). This affects only the Cauchy stress response of t_2. This is reflected in the plots over line for Cauchy stresses where in 5-6 the fluctuations are very high for the t_2 case and relatively very low for the t_1 case. Finally, in the case of 6-7, there are no interfaces or triple junctions encountered either

for t_1 or t_2. This is reflected in nearly vanishing fluctuations in the middle zone. The conclusion of this exercise is to highlight that the results obtained are not spurious fluctuations but are a direct consequence of causality from residual curvatures.

The mean values for the σ_{22} component along the line from figure 5.2 are found to have a very close match for all three cases. This is a combined effect of the imposed strain rate component $\dot{E}_{22}$ and the line direction (parallel to loading direction) along which the kinematic and stress components are plotted.

Next, consider the time evolution of Cauchy stresses. Figure 5.24 shows the plots along line for Cauchy stress components σ_{11}, σ_{22} and σ_{12} at imposed strains of 0.02%, 0.4% and 0.8% for the GB t_2. Very large values of Cauchy stresses are developed right

(a) σ_{11} (MPa) (b) σ_{22} (MPa)
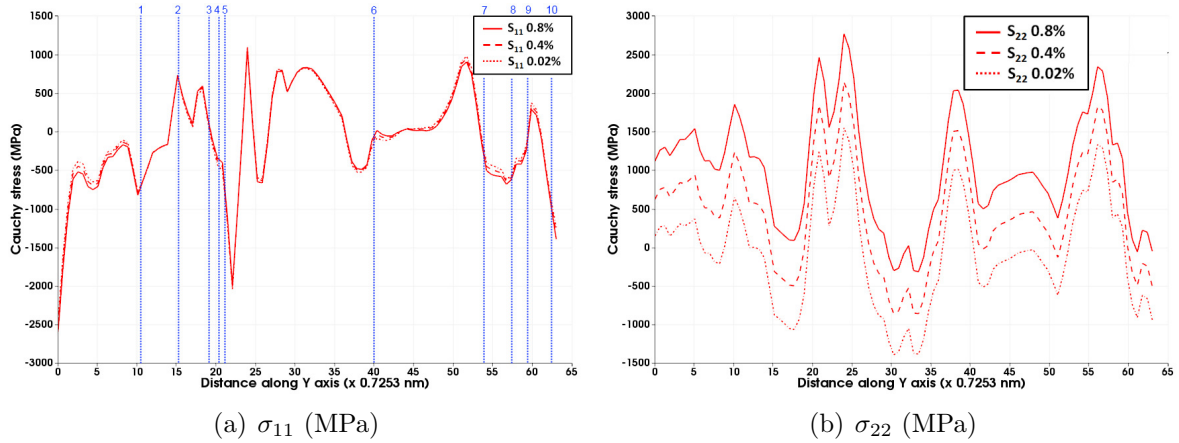
Figure 5.24: Plots over line for Cauchy stress (MPa) components (a) σ_{11} and (b) σ_{22} for 10 nm nc100 configuration with GB thickness t_2 at imposed strains 0.02% (dots), 0.4% (dashes) and 0.8% (solid line). Plasticity is not allowed. Blue lines indicate the location of interfaces and the numbers in blue correspond to interface identifiers from figure 5.2.

at 0.02% imposed strain which is the first step of loading. These are a consequence of the very large magnitudes of initial couple stresses induced due to the initial curvature. These initial couple stresses contribute to the compatible total strains and curvatures through their polarization fields resulting in fluctuations in these kinematic fields. The compatible strains in turn lead to the generation of Cauchy stresses that have

the reported large magnitudes, at the first step of loading. If plasticity were activated, these would immediately result in the relaxation of the Cauchy stresses obtaining a rather curious response of initial stress relaxation before the elastic regime.
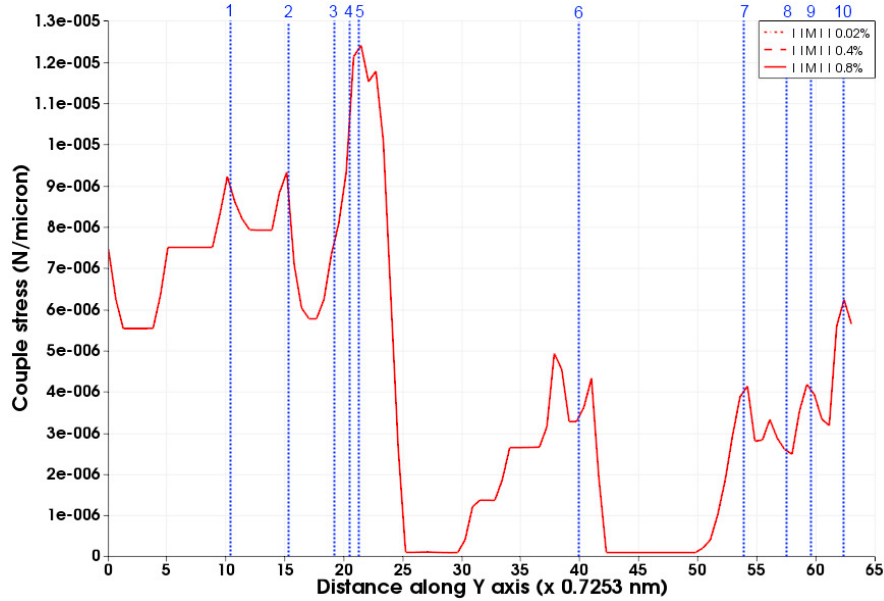
Figure 5.25: Plots over line for Couple stress norm $\sqrt{M_{ij}M_{ij}}$ (N/micron) for 10 nm nc100 configuration with GB thickness t_2 at imposed strains 0.02% (dots), 0.4% (dashes) and 0.8% (solid line). All lines are overlapping. Blue lines indicate the location of interfaces and the numbers in blue correspond to interface identifiers from figure 5.2.

Revisiting the plot over line profiles of Cauchy stresses, quite interestingly, the σ_{11} and σ_{12} Cauchy stresses hardly undergo any change during loading. This is in general true for all the other components of Cauchy stresses besides σ_{22}. The latter component increases according to the loading conditions. However, the curious stagnancy of the other components indicates that the couple stress may not be evolving at all during the loading and indeed this is the case as can be seen from figure 5.25. This implies that couple stress magnitudes have a dominating contribution coming from initial curvatures such that they are not affected by the compatible curvature generated during loading. This can be verified from figure 5.26. It can be seen that
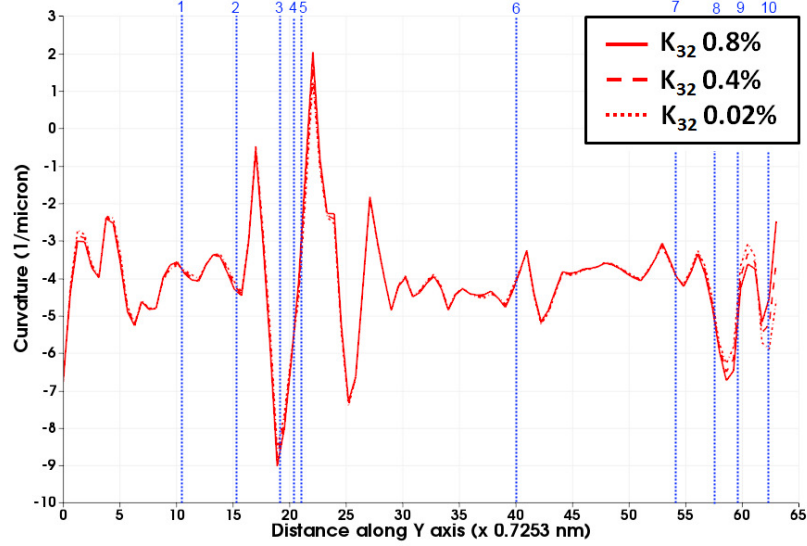
Figure 5.26: Plots over line for curvature component κ_{32} (1/micron) for 10 nm nc100 configuration with GB thickness t_2 at imposed strains 0.02% (dots), 0.4% (dashes) and 0.8% (solid line). Blue lines indicate the location of interfaces and the numbers in blue correspond to interface identifiers from figure 5.2.

the compatible total (which are elastic due to absence of curvature plasticity) curvatures generated are almost two orders of magnitude lower than the initial elastic curvatures. This means the curvature contribution resulting in very high fluctuations in Cauchy stresses predominantly arises from incompatible initial elastic curvatures.

Quite interestingly, the compatible curvature components too are found to be, in general, stagnated from the initiation of loading. This is due to the combined effect of stagnation in Cauchy and couple stress polarizations that contribute to the curvature. All these values are awaiting the activation of strain plasticity to evolve.

The conclusion of this study is that the presence of local residual curvatures induces large fluctuations in the Cauchy stress fields in the vicinity of GBs. These could significantly affect the local plastic response of nc materials.

5.6 Relaxation of initial stresses: understanding the role of curvature plasticity

5.6.1 Strain plasticity

In the previous section, simulating the elastic response of nc100 with residual curvatures is found to generate very large fluctuations in Cauchy stresses - in the order of a few GPas for the case of GB initial curvature thickness t_2. In this section, the aim is to study the relaxation of these Cauchy stresses by allowing strain plasticity. To that end, only the t_2 configuration is considered. The microstructure is held at constant zero imposed strain along the y direction. Cauchy stresses are generated in order to satisfy the local equilibrium. Due to the very large instantaneous stresses that are generated, strain plasticity is immediately activated.

Figure 5.27 shows the VM Cauchy stress vs. VM strain plot for the relaxation process. The initial decline in the VM Cauchy stress is very steep followed by a cu-
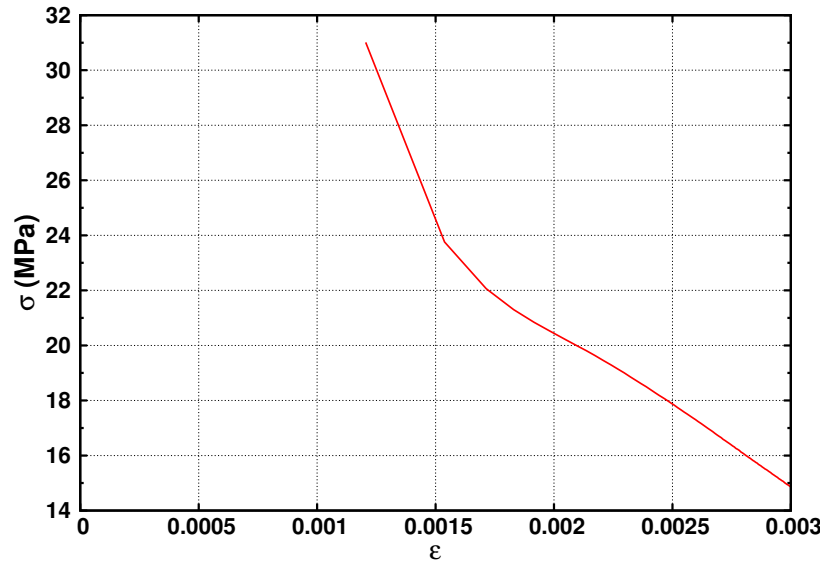
Figure 5.27: VM Cauchy stress vs. VM strain plot for 10 nm nc100 undergoing relaxation of self-stresses generated in the case of GB curvature thickness t_2.

rious linear response. With the activation of strain plasticity, the large fluctuations in Cauchy stresses are rapidly relaxed in the initial stages of the relaxation process.

The VM stress reduces until the point where all the macroscopic Cauchy stress components satisfy their respective boundary conditions. For example, the macroscopic component Σ_{11} is imposed to zero and therefore the average value of the local stress (figure 5.28) tends towards the macroscopic stress with increasing relaxation. On the other hand, the macroscopic component Σ_{22} is not imposed to zero in order for the microstructure to maintain a constant strain in the y direction. However, since the macroscopic strain is imposed to zero, the mean value of local Cauchy stresses should reduce to zero with decreasing VM stress. Quite interestingly, this is not the case. The local Cauchy stresses are found to have a drastically reduced rate of relaxation even though the macroscopic response attains a steady rate of decline.
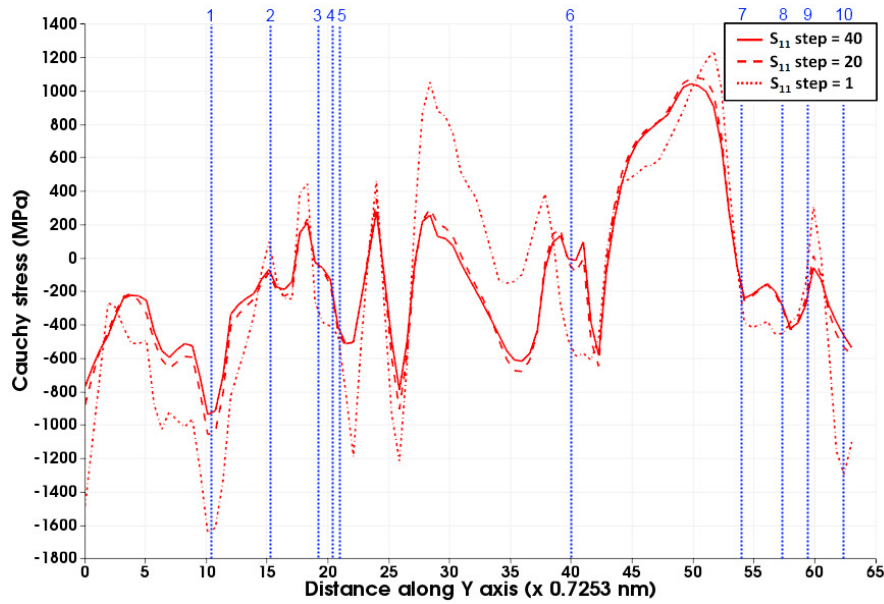
Figure 5.28: Plots over line for Cauchy stress component σ_{11} (MPa) for 10 nm nc100 configuration with GB thickness t_2 at relaxation step 1 (dots), 20 (dashes) and 40 (solid line). Blue lines indicate the location of interfaces and the numbers in blue correspond to interface identifiers from figure 5.2.

This is a consequence of couple stresses which are found to stagnate after the initial few relaxation steps (figure 5.29). The large residual curvatures remain unrelaxed in the absence of plastic curvature evolution resulting into the stagnancy.

245

The noticeably small change in couple stress magnitude is an effect of the compatible elastic curvatures that are generated to accommodate the couple stresses. On the other hand, there is an increase in compatible total strains which has the largest contribution coming from plastic strains that are generated by the relaxation of the Cauchy stresses.
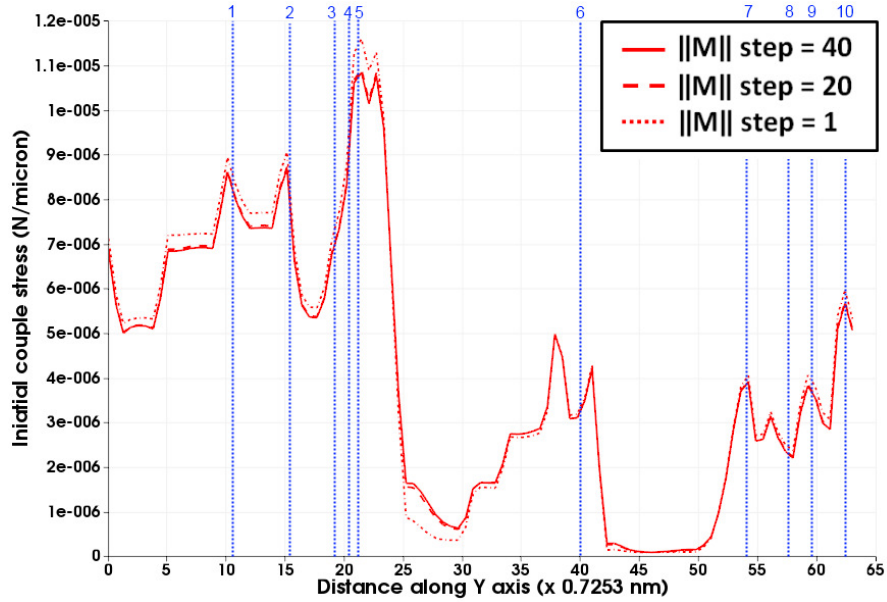
Figure 5.29: Plots over line for couple stress norm $\sqrt{M_{ij}M_{ij}}$ (N/micron) for 10 nm nc100 configuration with GB thickness t_2 at relaxation step 1 (dots), 20 (dashes) and 40 (solid line). Blue lines indicate the location of interfaces and the numbers in blue correspond to interface identifiers from figure 5.2.

The incompatible components of accumulated plastic strains lead to the generation of polar dislocations in the medium. These are in addition to those that already exist due to the presence of residual curvatures. Figure 5.30 also shows the contours plotted over microstructure for the initial and generated polar dislocation densities. The latter are found to generate close to the former due to very large Cauchy stresses in the vicinity of the interfaces.

This reproduces the effect of GB dislocation emission.

246
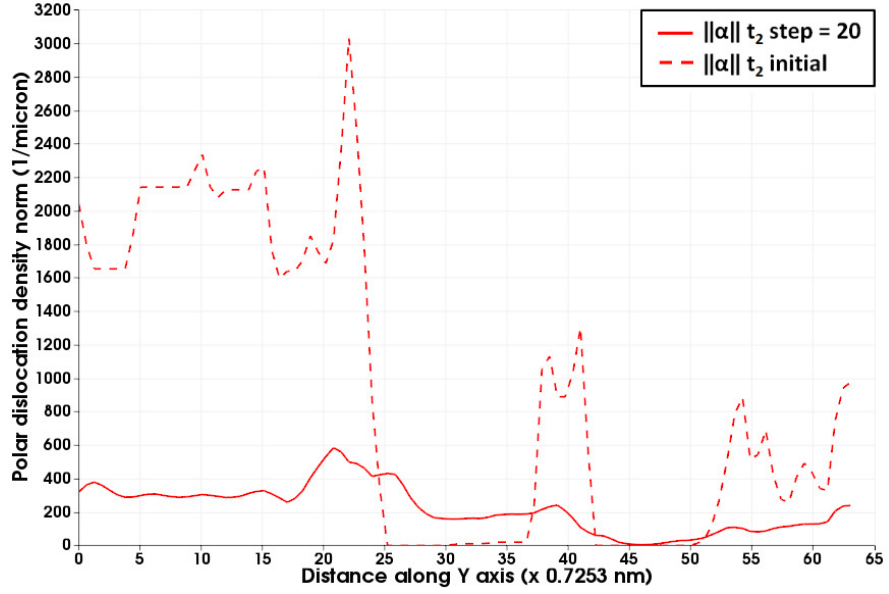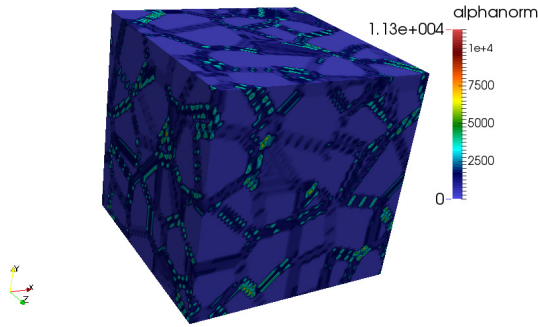
(a) $\sqrt{\alpha_{ij}\alpha_{ij}}$ (1/micron)

(b) $\sqrt{\alpha_{ij}\alpha_{ij}}$ (1/micron) initial
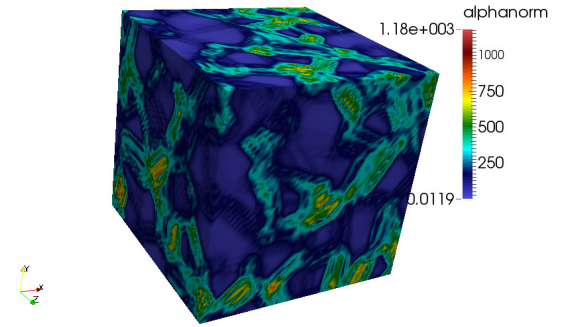
(c) $\sqrt{\alpha_{ij}\alpha_{ij}}$ (1/micron) generated at step = 20

Figure 5.30: Polar dislocation density norm $\sqrt{\alpha_{ij}\alpha_{ij}}$ (1/micron) (a) plot over line (from figure 5.2) comparison between initial density and generated density at relaxation step 20, and their respective contours over the microstructure t_2 10nm nc100 in (b) and (c).

5.6.2 Combined strain and curvature plasticity

In the previous section it is shown that couple stresses generated as a consequence of the initial curvatures are hardly relaxed through the evolution of plastic strains. The PMFDDM FFT formulation is such that the couple stresses can only be significantly affected by the evolution of plastic curvatures. In order to test this, the relaxation

of the 10nm nc100 t_2 configuration is reconsidered. For this simulation, both plastic strain and curvatures are allowed to accommodate the stresses. The plastic curvature reference rate $\dot{\kappa}_0$ is set to 100 /μm, and the reference couple stress is set to $M_0 = 10^{-7}$ N/ μm. The initial couple stress magnitudes are very large compared to this threshold, as can be seen from figure 5.25. These will lead to very large initial plastic curvature rates resulting in rapid relaxation of these stresses. As mentioned earlier, this value of M_0 is purposely chosen to observe the effect of plastic curvature rates on the local response. The plastic strain rate reference components are kept the same as in the relaxation case studied earlier.
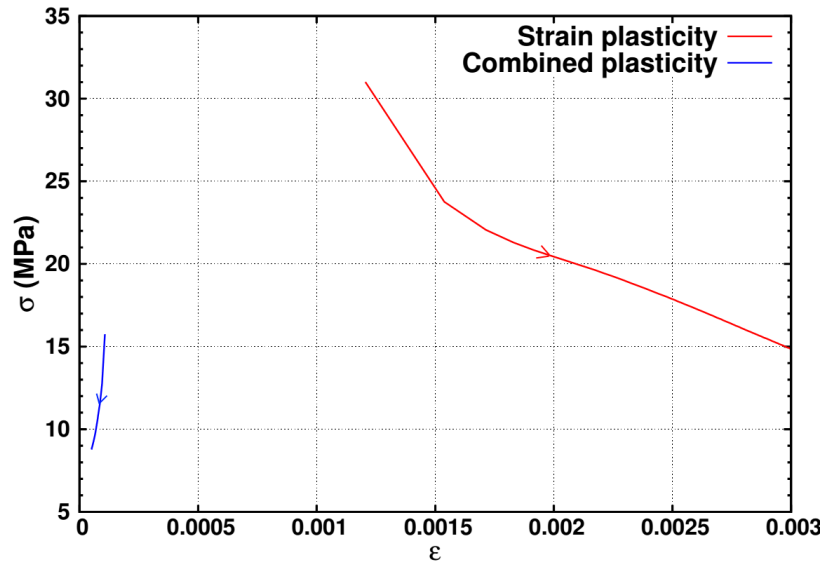
Figure 5.31: Comparison of VM Cauchy stress vs. VM strain plot for relaxation of 10 nm nc100 configuration with just strain plasticity and combined strain and curvature plasticity for GB initial curvature thickness t_2. The arrows indicate the direction of increasing number of relaxation steps.

Figure 5.31 shows the comparison between VM Cauchy stress vs VM strain curve for the relaxation cases when only strain plasticity is activated and when combined strain and curvature plasticity are activated. With the combined plasticity case the initial VM Cauchy stress is much lower than in the solely strain plasticity case. With further increase in relaxation steps a very surprising result is obtained. VM strains

are found to reduce along with reducing Cauchy stress. This implies that residual strains diminish when curvature plasticity is activated. Interestingly, the rate of decay in Cauchy stresses is much lower in the combined case than when only strain plasticity is activated. The plastic curvature evolution seems to impede the rate of Cauchy stress relaxation. The blue curve represents the VM Cauchy stress vs VM strain curve for the combined plasticity case. With respect to the VM couple stress vs VM curvature evolution, in the case when only strain plasticity is activated, it has a constant value because plastic strains do not accommodate couple stresses. In the combined case though, the VM couple stresses relax with increasing VM curvature as can be seen from figure 5.32.
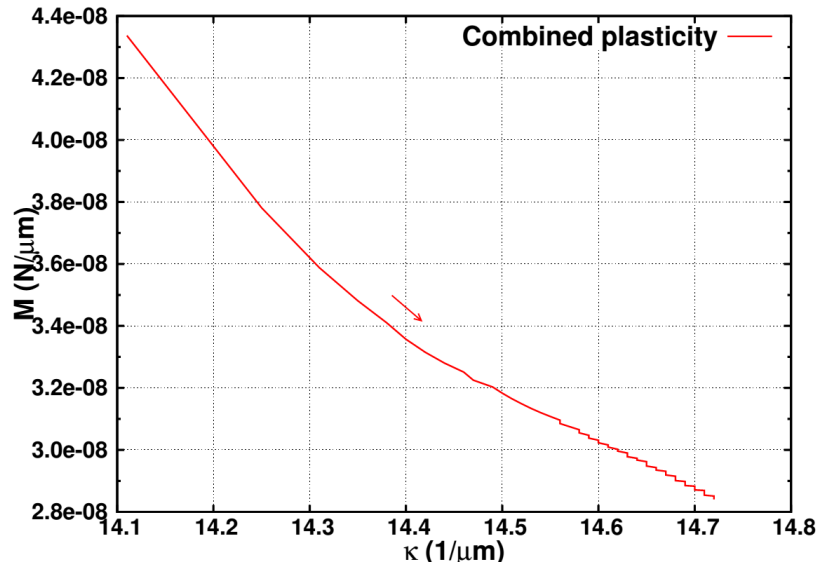
Figure 5.32: VM couple stress vs. VM cuvature plot for relaxation of 10 nm nc100 configuration with combined strain and curvature plasticity for GB initial curvature thickness t_2. The arrow indicates the direction of increasing number of relaxation steps.

This global relaxation in couple stresses is directly reflected into the local relaxations. Figure 5.33 shows the plot over line from figure 5.2 for the couple stress norm $\sqrt{M_{ij}M_{ij}}$ at different relaxation steps. As expected, the couple stresses incur a rapid drop at the first relaxation step due to the very large plastic curvature rates that are
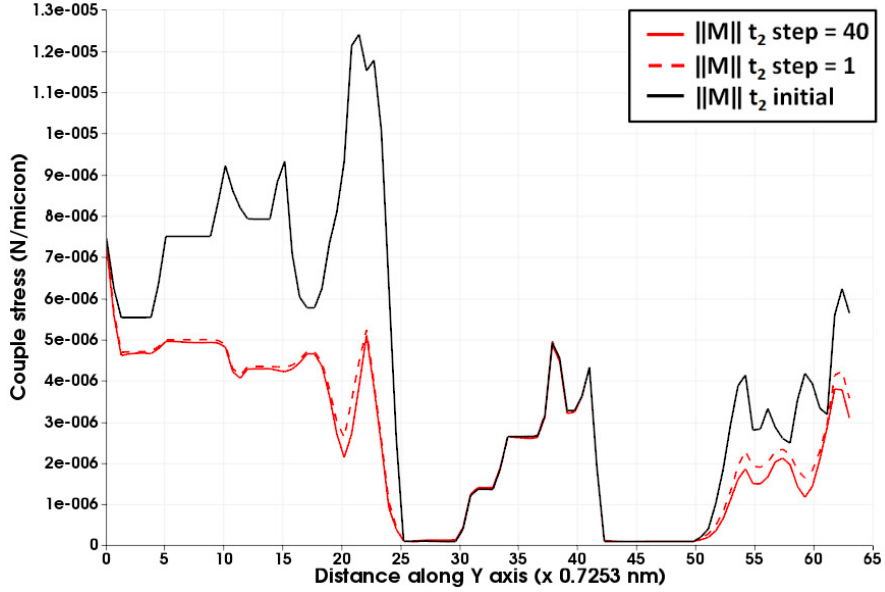
Figure 5.33: Plot over line from figure 5.2 for couple stress norm $\sqrt{M_{ij}M_{ij}}$ during relaxation of 10 nm nc100 t_2 configuration with combined strain and curvature plasticity at relaxation steps 1 and 40 compared with the initial couple stress.

generated for the low threshold of $M_0 = 10^{-7}$ N/μm. However, the couple stresses appear to saturate at values higher than this threshold. To explain this, analogy is drawn from the plastic rate response. The reference plastic curvature rate chosen is not large enough such that when the plastic curvature rate is capable to fully accommodate initial curvatures, the couple stress magnitude is already larger than the threshold.

Figure 5.34 shows the Cauchy stress component σ_{11} plot over line at relaxation steps 1 and 40 compared with the same component obtained from relaxation via just strain plasticity. Quite interestingly, the Cauchy stress fluctuations are found to be lower in the combined plasticity case. This is a combined effect of strain plasticity and the lowering in couple stress magnitude due to curvature plasticity. The plot also reveals a surprising reversal in the Cauchy stresses at some locations going from compressive to tensile.

With the activation of curvature plasticity, an increase in the total compatible
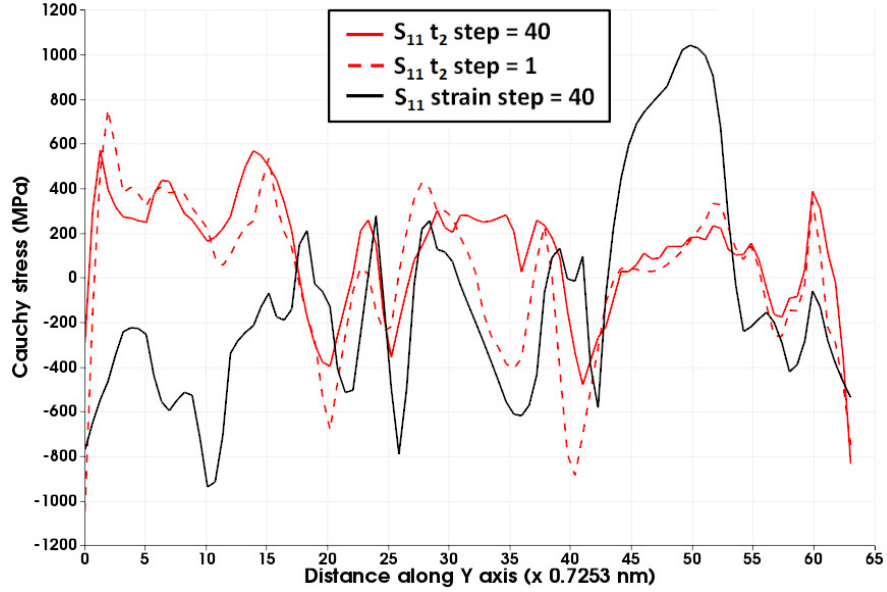
Figure 5.34: Plot over line from figure 5.2 for compatible Cauchy stress component σ_{11} during relaxation of 10 nm nc100 t_2 configuration with combined strain and curvature plasticity at relaxation steps 1 and 40 compared with the one obtained from relaxation via just strain plasticity at step 40.

curvature should be expected. Figure 5.35 shows the plot over line for the compatible total curvature at relaxation steps 1 and 40 compared with the one obtained from the relaxation case for just strain plasticity at step 40. Quite interestingly, the total curvature has much lower fluctuations in the combined plasticity case as opposed to just strain plasticity. In the former case, the total curvatures are the elastic curvatures necessary to accommodate the stagnated very large couple stresses. However with the activation of curvature plasticity, these magnitudes rapidly decrease resulting in the lower fluctuations in compatible curvatures. This is important because the larger the change in plastic curvature, higher is the associated plastic rotation. For the present case, at the step 40 the largest rotation rate is found to be about 3 radians.

The polar dislocation density evolution is very interesting (shown in figure 5.36). It is found to rapidly decrease and rapidly increase in different locations. It appears
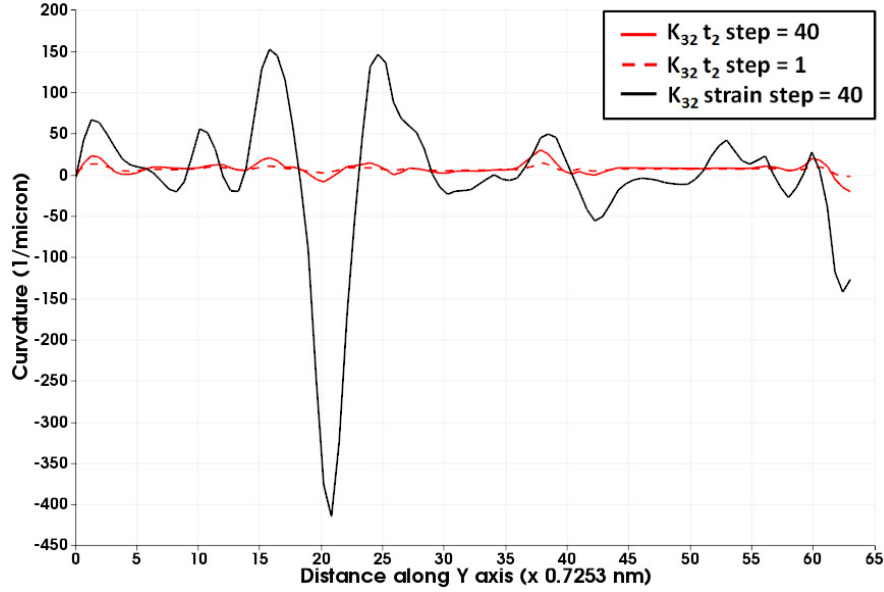
Figure 5.35: Plot over line from figure 5.2 for compatible total curvature component κ_{32} during relaxation of 10 nm nc100 t_2 configuration with combined strain and curvature plasticity at relaxation steps 1 and 40 compared with the one obtained from relaxation via just strain plasticity at step 40.

that the increases occur at locations where the couple stress is stagnated which results in the accummulation of plastic curvature that directly contributes to the polar dislocation density through equation (2.99).

Finally, the polar disclination density too evolves with the change in the plastic curvature rate. Figure 5.37 shows the plot over line for the evolution of polar disclination density norm $\sqrt{\theta_{ij}\theta_{ij}}$. The initial polar disclination density should be zero but as a consiquence of the initial curvature methodology chosen, numerical initial disclination densities are obtained. Quite interestingly, its magnitude decreases rapidly at the places where the couple stress magnitude is very large and increases at the locations where the couple stress magnitude is low enough for the plastic curvature to accummulate. Despite the increase in the polar dislocation and disclination densities, the overall Cauchy and couple stresses are decreasing over time indicating that these increase in defect polarities could result in stabler configurations.

252
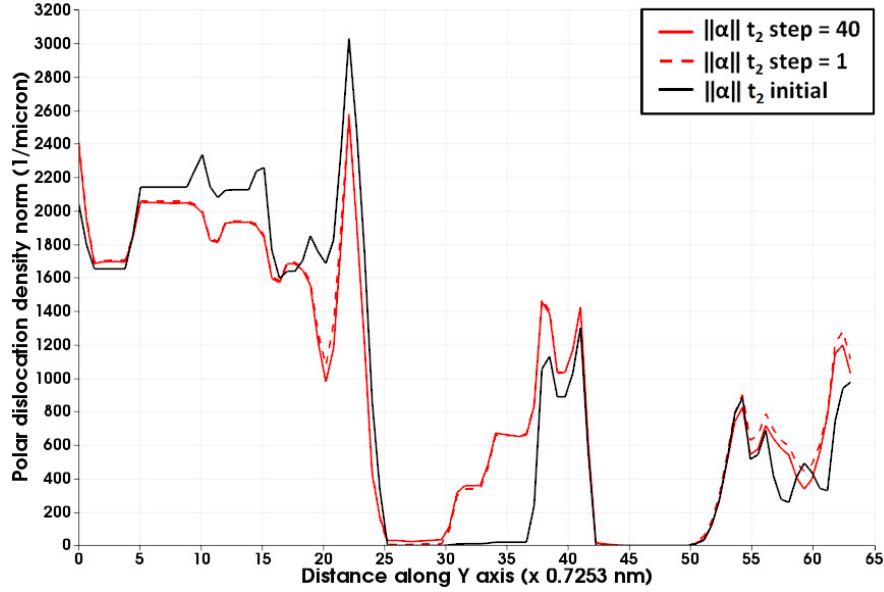
Figure 5.36: Plot over line from figure 5.2 for polar dislocation density norm $\sqrt{\alpha_{ij}\alpha_{ij}}$ during relaxation of 10 nm nc100 t_2 configuration with combined strain and curvature plasticity at relaxation steps 1 and 40 compared with the one obtained from relaxation via just strain plasticity at step 40.

5.7 Uniaxial tension: impact of residual curvature on stress-strain response

The previous study on the 10nm nc100 highlighted the impact of residual curvatures on generation of local Cauchy stresses and their role in significantly reducing the relaxation of local stresses in the microstructure. In this section, their role on the elastic-plastic response of the microstructure is studied during tensile loading. This corresponds to the final test described in table 7.

In order to avoid dealing with relaxations of initial microstrctures, the nc100 microstructure is characterized with grains of average size 30 nm by taking an inter Fourier point spacing of 2.176 nm. Cauchy stresses at the first step of loading are found to be lower the threshold stress chosen (330 MPa). Since the texture in the microstructure remains the same, the initial elastic curvatures, polar dislocation and disclination densities, and initial couple stresses all have magnitudes that are
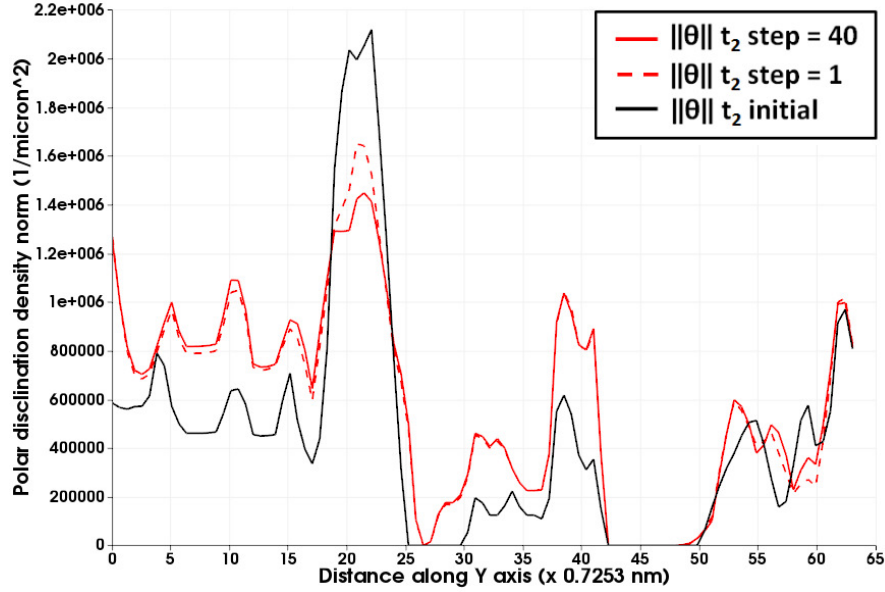
Figure 5.37: Plot over line from figure 5.2 for polar disclination density norm $\sqrt{\theta_{ij}\theta_{ij}}$ during relaxation of 10 nm nc100 t_2 configuration with combined strain and curvature plasticity at relaxation steps 1 and 40 compared with the one obtained from relaxation via just strain plasticity at step 40.

$\delta_{10nm}/\delta_{30nm} = 3$ times lower than their 10 nm nc100 counterparts.

Applying uniaxial tension in a similar way as in the case of 10 nm nc100, with no plasticity, the same type of trends are obtained for the evolution of Cauchy stresses, couple stresses and compatible elastic curvatures. Due to the reduced value of initial curvatures, the fluctuations in Cauchy stress and compatible curvatures are much lower than in the 10 nm case. The average compatible elastic curvature magnitude is found to be three times lower than in the 10 nm nc100 case. Interestingly, the Cauchy stress average value for σ_{22} is found to be the same as in the case of 10 nm nc100. This is a consequence of the couple stress theory framework and its FFT implementation. The Cauchy and couple stresses are only related to each other through their fluctuating terms which are treated in the FFT component of the algorithm. For the curvature and couple stress magnitudes to affect the average magnitude of Cauchy stresses, both stresses must be constitutively related to elastic strain and curvature

254

as shown in the section 3.1.
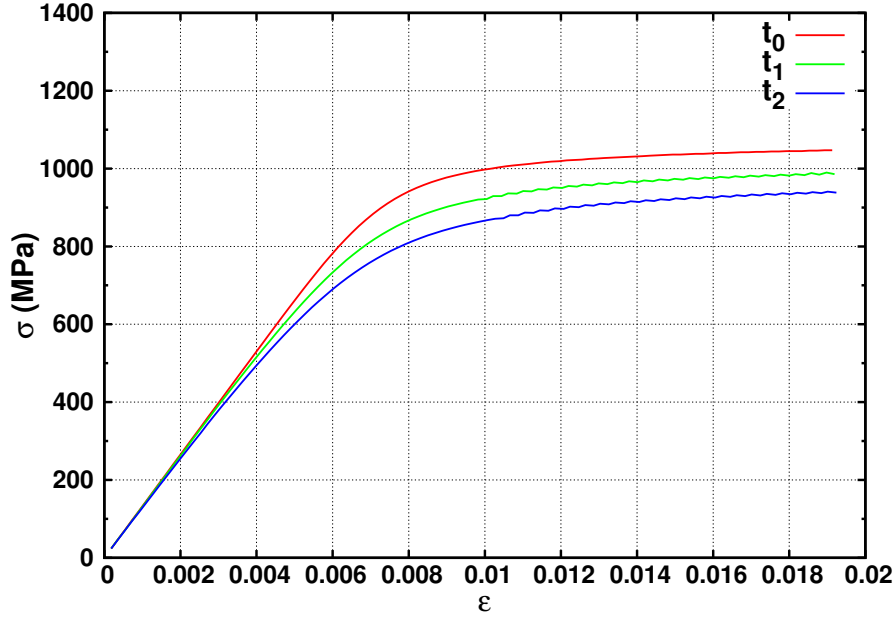
Figure 5.38: VM Cauchy stress vs. VM strain plot for 30 nm nc100 configuration with no GB initial curvature t_0, GB initial curvature thickness t_1, and t_2.

Strain plasticity is now activated with the generic $\dot{\gamma}_0 = 0.1/sec$ and $n = 10$. Figure 5.38 shows the VM Cauchy stress vs. VM strain response. As expected, in the case when GB initial curvatures are very high, the corresponding large fluctuations in Cauchy stresses are accommodated at an earlier stage. Therefore, Cauchy stresses in the t_2 case reach their saturation point faster than in the t_1 and t_0 cases. These results show an effect that resembles the breakdown in Hall-Petch law. In a separate set of simulations, the magnitude of $\boldsymbol{A}$ is taken as $0.1Gb^2$ to test the dependence of the saturation stress on this value. It is found that the VM Cauchy stress vs. VM strain response for the t_1 and t_2 cases saturates at a higher stress but still follows the same hierarchy in saturating. Therefore, this effect of the softening of the saturation point for Cauchy stresses, which is very similar to the breakdown in Hall-Petch law, is coming from the couple stresses generated to accommodate the residual curvatures.

These results show that residual curvatures in the nc GB interface have a significant contribution to the plastic response of these materials.

5.8 Discussion

In this chapter, the meso-scale PMFDDM model was numerically implemented using an FFT based approach to study the influence of residual curvatures on local and macroscopic response of bulk polycrystalline aggregates.

Validation of the numerical technique is performed in two stages. In the first stage, the model, which is based on using CFTs of parital derivatives of fields quantities, is benchmarked against the existing state-of-the-art in FFT based modelling *i.e.* the EVP FFT model. The local and macroscopic response predicted by both these models are found to have a very good match, thus validating the PMFDDM approach. The second stage involves validating the local and macroscopic response in the presence of residual curvatures. It is found that the CFT approach invokes the Gibbs phenomenon when computing the derivative of discontinuous residual curvatures, and grain rotations across interfaces. This leads to the development of the PMFDDM FFT model based on DFT.

The PMFDDM DFT model is then applied to nc aggregates with residual curvatures subjected to study the influence of residual curvatures on their (1) purely elastic, (2) strain based plastic, and (3) combined strain and curvature based plastic response. For this purpose, the nc microstructures of 0%, 31.54% and 55.95% GB interface to volume ratio are considered. Here the GB interface is characterized by imposing and spreading the residual curvatures in the vicinity of the grain boundary. The pure elastic loading case reveals a very close match in the macrscopic VM Cauchy stress vs. VM strain response for all the microstructures studied. Quite interestingly, very large fluctuations in the local Cauchy stress response are obtained

with increasing thickness of the GB residual curvatures. Activating strain plasticity results in immediate relaxation of these Cauchy stresses through the evolution of statistical dislocations and the generation of polar dislocation densities. On the other hand couple stress evolution is found to stagnate very close to their original values because of the residual curvatures that are unable to evolve in the absence of curvature plasticity. This also has a significant impact on the relaxation of Cauchy stresses. Finally, activating both curvature and strain based plasticity reveals that couple stresses are relaxed through the evolution of polar dislocation and disclinations resulting in lower Cauchy stresses.

The most significant result from this study is the softening in the yield stress obtained for microstructures characterized with residual curvatures. This is effect of the local couple stresses that are generated which relax the Cauchy stresses in the vicinity of grain boundaries that occupy a large volume of the nc microstructure. This results in the lowering of the yield stress which could help explain the breakdown in the Hall-Petch relationship.

In nc materials, couple stresses are generated in the event that a bending moment or torque acts locally or macroscopically on the material. Such moments or torques are generated during plasticity mechanisms involving GB motion. One of the effects of these local moments or torques is to induce grain rotations. The present PMFDDM FFT model is able to account for the plasticity induced by these local moments and torques through the evolution of both plastic strain and curvatures. The results show that relaxing the coule stresses changes the polarity of discinations in the microstructure thus leading to stabler configurations. This strongly indicates that evolution of plastic curvature could help understand the lack of or formation of polar disclinations, at the same time explaining why polar dislocation densities do not appear where they are expected and vice versa. Prior to understanding this, it is important to perform studies to parametrize the plastic curvature rate constants.

Application of the PMFDDM FFT model to nc aggregates has led to the opening of several potential areas of research inluding: (a) Understanding relaxation of internal stresses through the evolution of statistically stored and geometrically necessary dislocation and disclination densities plastic strain and curvature evolution. This could help shed light on the possible configurations that are favorable for nucleation of screened disclinations. (b) Study the role of Cauchy and couple stress non-locality induced through the interface tangential continuity conditions necessary to maintain the continuity of strains and curvatures at the GB interface. (c) Introducing the transport of defects to study the collective behavior of GB plasticity mechanisms. (d) Studying the effect of complex loading conditions - for example combined torsion-compression or uniaxial tension with bending - with the help of combined strain, curvature, Cauchy and couple stress based boundary conditions. (e) Understanding the role of residual curvatures and strains and their evolution on microstructures subjected to multi-axial or cyclic loading. (f) Developing expressions for the elasticity tensor $\boldsymbol{A}$ in higher order symmetres to generate heterogeneous local couple stresses in absence of initial curvatures.

5.9   Conclusion

The study performed in this chapter highlights the importance of residual curvatures on the local and bulk mechanical response of nc materials. Presence of residual curvatures results in the generation of large fluctuations in local Cauchy and couple stresses. These could play an important role in the activation of rare events such as nucleation of new grains, twins, etc. Relaxation of stresses generated from residual curvatures reproduces the effect of GB dislocation emission. Furthermore, these residual curvatures are found to lower the saturation point of the macroscopic Cauchy stress response during tensile loading; a softening effect that could explain the breakdown in the Hall-Petch relationship.

This study has led to the development of a numerical tool based on the FFT implementation of meso-scale PMFDDM model using the DFT technique. The model is based on a couple stress theory formulation through which it is capable of accounting for the evolution of geometrically necessary and statistically stored dislocations and disclinations, residual strains and curvatures, heterogeneous elasticity and complex loading conditions.

CHAPTER VI

VIRTUAL DIFFRACTION: MULTI-SCALE CHARACTERIZATION

In this chapter, the purpose is to understand if residual curvature and inompati-bilities can be characterized using X-ray diffraction. To assess this, a multi-scale numerical tool connecting the incompatible theory of defects with the kinematic the-ory of diffraction is developed for generating virtual diffraction peaks from defected microstructures. This tool is designed such that it facilitates comparison between dif-ferent plasticity models - including the multi-scale field disclination and dislocation mechanics model proposed in this work -, atomistic simulations, and experiments.

The chapter is organized as follows: Section 6.1 recalls the existing virtual diffrac-tion peak generation techniques that use either a displacement based approach [445, 446] or a strain based approah [384] to generate virtual peaks from a distorted crystal. Section 6.2 elaborates on the complexities involved in using these methods and in-troduces a new averaged strain based Fourier method for constructing virtual peaks. Section 6.3 presents the methodology used to generate diffraction peaks using all the aforementioned methods. In order to assess the agreement of these methods as a function of microstructures, different scenarios are investigated. First, the case of a single infinitely long screw dislocation, originally discussed in the work of Wilson [459, 460] is revisited. Second, the case of a low angle GB, constructed via the use of a wall of edge dislocations is studied to understand the effect of negligible higher gradients of displacement on the conformity of the three methods. Third, several microstructures built from restrictedly random distributions of dislocations are used

to generate peaks via these methods and the results are analysed. Finally, a realistic microstructure resulting from coplanar slip and generated via the use of discrete dislocation dynamics (DDD) is used to quantify the consistency of these methods for the purpose of practical applications. Section 6.4 compares the proposed virtual diffraction technique with other diffraction based characterization techniques.

6.1 Virtual diffraction peaks from a defected crystal: theoretical review

The purpose of this section is to highlight the different possible techniques to generate virtual diffraction peaks from distorted crystals. To that end, the kinematic theory of X-ray diffraction based derivations of the Fourier method of Warren [446] and the Stokes-Wilson approximation [384] are rigorously derived.

The Fourier method of Warren is an exact technique to generate diffraction peaks, albeit within the bounds of the kinematic theory of diffraction. In a coherently diffracting distorted single crystal, kinematic theory of diffraction states that the diffracting intensity I is a function of the diffraction vector $\vec{g}'$ as follows [446]:

$$I\left(\vec{g}'\right) = I_e F^2 \sum_{m'} \sum_{m} \exp\left(2\pi i \vec{g}' \cdot \left(\boldsymbol{R_{m'}} - \boldsymbol{R_m}\right)\right) \tag{6.1}$$

where I_e is the intensity of the polarized primary beam, F is the complex structure factor that is same for each unit cell, and the double summation is performed over the total number of unit cells in the crystal. $\vec{R_m}$ is the position of atoms in the $m_1 m_2 m_3{}^{th}$ cell in the crystal and is given as:

$$\vec{R_m} = m_1 \vec{a_1} + m_2 \vec{a_2} + m_3 \vec{a_3} + \vec{u}(m_1, m_2, m_3) \tag{6.2}$$

where $\vec{a_1}, \vec{a_2}, \vec{a_3}$ are the orthogonal vectors defining a unit cell in lattice space and $\vec{m} = m_1 \vec{a_1} + m_2 \vec{a_2} + m_3 \vec{a_3}$ is the position of $m_1 m_2 m_3{}^{th}$ cell in this space. The displacement vector $\vec{u}(m_1, m_2, m_3)$, which is a smooth function, accounts for the distortions within the continuous domain and in general is different for each unit cell.

Strains within the domain are assumed to be continuous, therefore any distortion within the unit cell is neglected [446]. The diffraction vector is defined as $\vec{g}' = \frac{\vec{s}-\vec{s_0}}{\lambda} = h_1\vec{b_1} + h_2\vec{b_2} + h_3\vec{b_3}$ where $\vec{s_0}$ and $\vec{s}$ are the primary and reflected beam vectors respectively and h_1, h_2 and h_3 are continuous variables in the reciprocal space $\vec{b_1}, \vec{b_2}$ and $\vec{b_3}$. Substituting equation (6.2) into (6.1) gives,

$$
\begin{aligned}
&I\left(\vec{g}'\right) \\
&= I_e F^2 \sum_{m'}\sum_{m} \exp\left(2\pi i \begin{bmatrix} h_1\left(m_1' - m_1\right) + h_2\left(m_2' - m_2\right) + h_3\left(m_3' - m_3\right) \\ +\vec{g}' \cdot \left(\vec{u}\left(m_1', m_2', m_3'\right) - \vec{u}\left(m_1, m_2, m_3\right)\right) \end{bmatrix}\right)
\end{aligned} \quad (6.3)
$$

The powder pattern theorem [446] is now recalled. This theorem provides the total power received from a powder sample (irradiated with X-rays of wavelength λ) containing M crystals and placed at a distance R from the receiving surface. The total power is a function of the intensity $I\left(\vec{g}'\right)$ integrated over a volume in the reciprocal space. Expressing in terms of power distribution, the total power received from a powder sample of M crystals is defined as

$$
I^{tot} = \int I(2\theta)d(2\theta) = \frac{MR^2\lambda^3 p(hkl)}{4v_a}\iiint \frac{I(\vec{g}')}{\sin\theta}dh_1 dh_2 dh_3 \quad (6.4)
$$

where 2θ is the diffraction angle, $I(2\theta)$ is the power distribution, $p(hkl)$ is a multiplicity factor that transforms the interference function into one equivalent region in reciprocal space. Stokes and Wilson [384] and Warren [446] have shown that aligning the diffraction vector along one of the orthogonal reciprocal space basis vectors $\vec{b}_1$, $\vec{b}_2$ or $\vec{b}_3$ gives the same expression for power distribution as obtained from a general treatment using an arbitrary diffraction vector. Following the convention from the work of Warren [446], the methodology is developed by probing along the $00l$ direction. However, for the sake of generality, the vectorial notation is retained but the diffraction vector is probed only along the direction $00l$ in the reciprocal space. Then the change in diffraction vector is given as $\Delta\vec{g} = (h_1 - h)\vec{b}_1 + (h_2 - k)\vec{b}_2 + (h_3 - l)\vec{b}_3 \approx (h_3 - l)\vec{b}_3$. Such an approximation allows for the definition $dh_3 = \frac{\cos\theta d(2\theta)}{\lambda|\vec{b}_3|}$. The expression for

262

$I(2\theta)$ can then be written as,

$I(2\theta)$

$$= \frac{KMF^2}{\sin^2\theta} \sum_{m'}\sum_{m} \exp\left(2\pi i \begin{bmatrix} (h_1 - h + h)\left(m'_1 - m_1\right) \\ + (h_2 - k + k)\left(m'_2 - m_2\right) \\ + (h_3 - l + l)\left(m'_3 - m_3\right) \\ + \vec{g'} \cdot \left(\vec{u}\left(m'_1, m'_2, m'_3\right) - \vec{u}(m_1, m_2, m_3)\right) \end{bmatrix}\right) dh_1 dh_2$$

$$= \frac{KMF^2}{\sin^2\theta} \sum_{m'}\sum_{m} \begin{bmatrix} \exp\left(2\pi i \begin{bmatrix} (h_1 - h)\left(m'_1 - m_1\right) \\ + (h_2 - k)\left(m'_2 - m_2\right) \\ + (h_3 - l)\left(m'_3 - m_3\right) \\ + \vec{g'}\cdot(\vec{u'} - \vec{u}) \end{bmatrix}\right) \times \\ \exp\left(2\pi i \begin{bmatrix} h\left(m'_1 - m_1\right) + k\left(m'_2 - m_2\right) \\ + l\left(m'_3 - m_3\right) \end{bmatrix}\right) \end{bmatrix} dh_1 dh_2 \quad (6.5)$$

where K is a constant. $m'_1, m'_2, m'_3, m_1, m_2, m_3$ and h, k, l are integers. Therefore the second exponential term becomes a complex multiple of 2π and hence equal to unity leading to:

$$I(2\theta) = \frac{KMF^2}{\sin^2\theta} \iint \sum_m \sum_{m'} \exp\left(2\pi i\left[\Delta\vec{g}\cdot(\vec{m'} - \vec{m}) + \vec{g}\cdot(\vec{u'} - \vec{u})\right]\right) \quad (6.6)$$

Warren and Averbach [448] and Bertaut [35] proposed a methodology to reduce the above equation to a simpler form. Let N be the total number of unit cells in the domain. The diffracting domain can then be divided into columns C_i (i goes from 1 to total number of columns N_c in the domain) of unit cells, aligned along the direction of the diffraction vector $\vec{g}$; these columns are perpendicular to the reflecting plane. The unit cells within each column are separated by a length $|\vec{L}| = |\vec{m'} - \vec{m}|$. Therefore $\vec{L}$ can be defined as:

$$\vec{L} = \vec{m'} - \vec{m} = t\frac{\vec{g}}{|\vec{g}|} \quad (6.7)$$

where $t = |\vec{L}|$. For a given $|\vec{L}|$, two unit cells that are separated by this distance within the same column form one N_L pair. The ratio of the summation of all such N_L pairs within the domain with respect to N_c gives the average number of N_L pairs per column (N'). The ratio of N' with respect to the average number of cells per column (N/N_c) defines the proportion ($N^* = \frac{N'N_c}{N}$) of average number of all possible unit cell pairs that are involved in forming N_L pairs within the column. Defining the difference in displacement between unit cells forming an N_L pair in a distorted crystal as $\Delta\vec{u}(\vec{L})$ and averaging the exponential term involving $\Delta\vec{u}(\vec{L})$ over the entire domain, the distributed power is reduced to a single summation over the magnitude of $\vec{L}$ gives

$$I(2\theta) = \frac{KNF^2}{\sin^2\theta} \sum_{|\vec{L}|=-\infty}^{\infty} N^* \left\langle \exp\left(2\pi i\vec{g}\cdot\Delta\vec{u}(\vec{L})\right)\right\rangle \exp\left(2\pi i\vec{L}\cdot\Delta\vec{g}\right) \quad (6.8)$$

where $\langle\rangle$ indicates averaging the exponential term involving $\Delta\vec{u}(\vec{L})$ over the entire crystal domain.

For the ease of understanding the implications of connecting theory of defects with the kinematic theory of diffraction. it is convenient to avoid dealing with the complexities associated with structure factors of the material system. Therefore a rather simpler formulation of the intensity in terms of $\Delta\vec{g}$ is adopted such that

$$I(\Delta\vec{g}) = \frac{I(2\theta)\sin^2\theta}{KNF^2} \quad (6.9)$$

This normalization generalizes the present scheme to account for both X-ray and electron diffraction; the Lorentz-polarization factor [78] that contributes to the intensity obtain from X-ray diffraction is factored out. Then separating the exponential terms in equation (6.8) into its sine and cosine components, the intensity can be written as

$$I(\Delta\vec{g}) = \sum_{|\vec{L}|=-\infty}^{\infty} \left\{ A\left(\vec{L}\right)\cos\left(2\pi\vec{L}\cdot\Delta\vec{g}\right) + B\left(\vec{L}\right)\sin\left(2\pi\vec{L}\cdot\Delta\vec{g}\right)\right\} \quad (6.10)$$

264

where the summation is carried over the Fourier length $|\vec{L}|$. This expression for $I(\Delta \vec{g})$ represents a Fourier series with $A(\vec{L})$ and $B(\vec{L})$ as the Fourier coefficients which can be interpreted as a product of the size Fourier coefficient $A^S(\vec{L}) = N^*$ and the distortion Fourier coefficients

$$
\begin{aligned}
A^D(\vec{L}) &= \left\langle \cos 2\pi \vec{g} \cdot \Delta \vec{u}(\vec{L}) \right\rangle \\
B^D(\vec{L}) &= \left\langle \sin 2\pi \vec{g} \cdot \Delta \vec{u}(\vec{L}) \right\rangle
\end{aligned} \tag{6.11}
$$

Note that the term $B^S(\vec{L})$ does not exist because the contribution of grain size is a real term and cannot be represented using an imaginary quantity. Furthermore, the size contribution is always positive. In the present work, for the sake of comparison with the Stokes-Wilson approximation, size broadening is neglected and only the distortion Fourier coefficients shown in equation (6.11) are used.

The Fourier transform method (6.10) is computationally intensive as it requires calculating the Fourier coefficients for length $|\vec{L}|$ varying from 1 cell spacing to the size of the diffracting domain along the direction of the diffraction vector. An alternative, significantly less computationally intensive approach to generate strain broadened profiles was introduced by Stokes and Wilson [384]. This approach, known as the Stokes-Wilson approximation, uses apparent strains (local strains resolved along the direction of the diffraction vector) to compute the intensity diffracted from a coherently diffracting domain. The Stokes-Wilson approximation is derived from the Fourier method; the details of which are shown in the following.

Redefining the difference in displacement in terms of a scalar component resolved along the direction of $|\vec{L}|$ as

$$
\epsilon^L = \frac{\vec{g} \cdot \Delta \vec{u}(\vec{L})}{|\vec{g}||\vec{L}|} \tag{6.12}
$$

The distortion Fourier coefficients from equation (6.11) can be redefined in terms

of a probability distribution function (PDF) of ϵ^L $\left(p_{\epsilon^L}\left(\epsilon^L\right)\right)$ [445, 101, 425, 245] as

$$A^D(\vec{L}) = \int_{-\infty}^{\infty} p_{\epsilon^L}(\epsilon^L) \cos\left(2\pi|\vec{g}|\epsilon^L|\vec{L}|\right) d\epsilon^L$$

$$B^D(\vec{L}) = \int_{-\infty}^{\infty} p_{\epsilon^L}(\epsilon^L) \sin\left(2\pi|\vec{g}|\epsilon^L|\vec{L}|\right) d\epsilon^L \tag{6.13}$$

Stokes and Wilson [384] argued that for large values of $|\vec{L}|$ the relative displacements between the unit cells will be random and hence cancel each other out. For very small values of $|\vec{L}|$ it is possible to take the power series expansion of $\vec{u}(\vec{x} + \vec{L})$ around the point $\vec{x}$ giving $\Delta\vec{u}(\vec{L}) = \vec{u}(\vec{x}) + \vec{L} \cdot \nabla\vec{u}(\vec{x}) + \vec{L}^2 : \nabla\nabla\vec{u}(\vec{x}) + \cdots - \vec{u}(\vec{x})$. Neglecting $O(\vec{L}^2)$ terms and substituting for $\vec{L}$ from equation (6.7) gives

$$\Delta\vec{u}(\vec{L}) = t\frac{\vec{g} \cdot \nabla\vec{u}}{|\vec{g}|} \tag{6.14}$$

Substituting (6.14) in the expression of $A^D(\vec{L})$ and $B^D(\vec{L})$ shown in equation (6.11) gives $A^D(\vec{L}) = \langle\cos(2\pi t\vec{g} \cdot \nabla\vec{u} \cdot \vec{g}/|\vec{g}|)\rangle$ and $B^D(\vec{L}) = \langle\sin(2\pi t\vec{g} \cdot \nabla\vec{u} \cdot \vec{g}/|\vec{g}|)\rangle$. The apparent strain is defined as $e = \boldsymbol{g} \cdot \nabla\boldsymbol{u} \cdot \boldsymbol{g}/|\boldsymbol{g}|^2$ which upon re-substituting $t = |\vec{L}|$ leads to the following definitions,

$$A^D(\vec{L}) = \left\langle\cos(2\pi|\vec{L}|e|\vec{g}|)\right\rangle$$

$$B^D(\vec{L}) = \left\langle\sin(2\pi|\vec{L}|e|\vec{g}|)\right\rangle \tag{6.15}$$

Equation (6.15) rewritten in terms of the PDF of e, $(p_e(e))$ gives,

$$A^D\left(\vec{L}\right) = \int_{-\infty}^{\infty} p_e(e) \cos\left(2\pi\left|\vec{L}\right|e\left|\vec{g}\right|\right) de$$

$$B^D\left(\vec{L}\right) = \int_{-\infty}^{\infty} p_e(e) \sin\left(2\pi\left|\vec{L}\right|e\left|\vec{g}\right|\right) de \tag{6.16}$$

Therefore the assumption of Stokes and Wilson, that for large values of $\vec{L}$ the relative displacements between the unit cells will be random and cancel each other out [384], implies that equations (6.13) and (6.16) result in the same solution for the

distortion Fourier coefficients. Comparison of the two PDF definitions in equations (6.13) and (6.16) reveals that the assumption of Stokes and Wilson also implies that the PDF of ϵ^L is independent of $|\vec{L}|$ [384, 245],

$$p_{\epsilon^L}(\epsilon^L) = p_e(e) \tag{6.17}$$

The Fourier transform of the intensity neglecting size effects may then be defined as,

$$A^D\left(\vec{L}\right) + iB^D\left(\vec{L}\right) = \int_{-\infty}^{\infty} I\left(\Delta\vec{g}\right) \exp^{\left(-2\pi i \Delta\vec{g}\cdot\vec{L}\right)} d\Delta\vec{g} \tag{6.18}$$

Taking the inverse Fourier transform gives,

$$I\left(\Delta\vec{g}\right) = \int_{-\infty}^{\infty} \left[A^D\left(\vec{L}\right) + iB^D\left(\vec{L}\right)\right] \exp\left(2\pi i \Delta\vec{g}\cdot\vec{L}\right) d\left|\vec{L}\right| \tag{6.19}$$

and from equation (6.16)

$$A^D\left(\vec{L}\right) + iB^D\left(\vec{L}\right) = \int_{-\infty}^{\infty} p_e\left(e\right) \exp\left(2\pi i \left|\vec{L}\right| e \left|\vec{g}\right|\right) de \tag{6.20}$$

Substituting (6.20) in (6.19) gives the expression [245]

$$I\left(\Delta\vec{g}\right) = \int_{-\infty}^{\infty} \int_{-\infty}^{\infty} p_e(e) \exp\left(2\pi i |\vec{L}|e|\vec{g}|\right) \exp\left(2\pi i |\Delta\vec{g}||\vec{L}|\right) d\left|\vec{L}\right| \tag{6.21}$$

The apparent strain e is also defined as $e = \frac{d-d'}{d}$ where d is the perfect lattice plane spacing along the direction of $\vec{g}$ and d' is the lattice plane spacing caused by lattice deformation. Under small strain hypothesis, the apparent strain may be approximated as $e = \frac{d-d'}{d'}$. Then similar to the work of Leineweber and Mittemeijer [245], the relationship between $\Delta\vec{g}$ and e is given as $e = -|\Delta\vec{g}|/|\vec{g}'| \approx -|\Delta\vec{g}|/|\vec{g}|$. Substituting in equation (6.21) leads to,

$$I(\Delta\vec{g}) \equiv p_{\Delta\vec{g}}(\Delta\vec{g}) = \frac{1}{|\vec{g}|} p_e(e) \tag{6.22}$$

Equation (6.22) shows that within the bounds of the Stokes-Wilson approximation the diffracted intensity distribution is proportional to the PDF of apparent strain

because the higher gradients of displacement within the coherently diffracting domain are neglected; a consequence of which results in equation (6.17) [245, 24]. The Stokes-Wilson approximation has already been used to generate diffraction peaks in the discrete dislocation dynamics simulations of Balogh *et al.* [24].

6.2 A new average-strain based Fourier method

As shown in the previous section, the displacement based Fourier transform method [446] relies on the knowledge of the displacement fields arising from a defected microstructure while that of Stokes and Wilson [384] makes use of the internal strain fields. For the displacement based Fourier method of Warren, connection with defect theory can be achieved by following the discrete approach. In the following, the methodology adopted is based on dislocations but is equally applicable to disclinations.

Assuming the medium to be elastically isotropic, it is possible to express the displacement field of equation (2.15) in the form of a line integral associated with a curved dislocation in an infinite medium [93] as,

$$\vec{u}(\vec{x}) = -\frac{\vec{b}}{4\pi} \int\limits_{C} \vec{A} \cdot d\vec{x}' + \frac{1}{8\pi} \int\limits_{C} \left(-\{\vec{b}\}\Delta|\vec{X}| + \frac{1}{1-\nu}\nabla(\nabla|\vec{X}| \times \vec{b}) \right) \cdot d\vec{x}' \quad \text{or}$$

$$u_i(\vec{x}) = -\frac{b_i}{4\pi} \int\limits_{C} A_k dx'_k + \frac{1}{8\pi} \int\limits_{C} \left(e_{ikl}b_l|\vec{X}|_{,pp} + \frac{1}{1-\nu}e_{kmn}b_n|\vec{X}|_{,mi} \right) dx'_k \qquad (6.23)$$

Here $\vec{X} = \vec{x} - \vec{x}'$ denotes the radius vector which connects the source point $\vec{x}'$ on the dislocation line to the field point $\vec{x}$. $\vec{A} = A_i$ is a vector potential corresponding to a solid angle and defined as:

$$\vec{A} = \frac{\hat{X} \times \vec{s}}{|\vec{X}|(1 + \hat{X} \cdot \vec{s})} \qquad (6.24)$$

where $\hat{X}$ denotes the unit vector $\vec{X}/|\vec{X}|$ and $\vec{s}$ is an arbitrary unit vector giving the direction of the surface cut (depicted in figures 2.3 and 2.11). The choice of this unit vector is arbitrary. Note that the surface cut is a mathematical formulation

necessary to define the displacement field of a dislocation. In reality materials do not have a surface cut at a dislocations site. Atoms in the vicinity of a dislocation are displaced from their perfect lattice position. This departure from the ideal configuration is visible to the X-rays in the form of the lattice displacement field entering in equation (6.10) through (6.11). Therefore, from the perspective of kinematic theory of diffraction, it is only the instantaneous position of atoms that is visible to the X-rays. Thus, only the elastic displacement field contributes to the scattering intensity. From the theory of dislocations, the equilibrium solution presented in equation (6.23) is in fact the multi-valued elastic displacement field. A unique separation of this multi-valued elastic displacement field is not possible due to the arbitrary nature of $\vec{s}$. Therefore, for the lack of an alternative, in the present work, as in the work of Kamminga and Delhez [198, 199], the multi-valued elastic displacement is used to generate the broadened peaks from the Fourier based method of Warren.
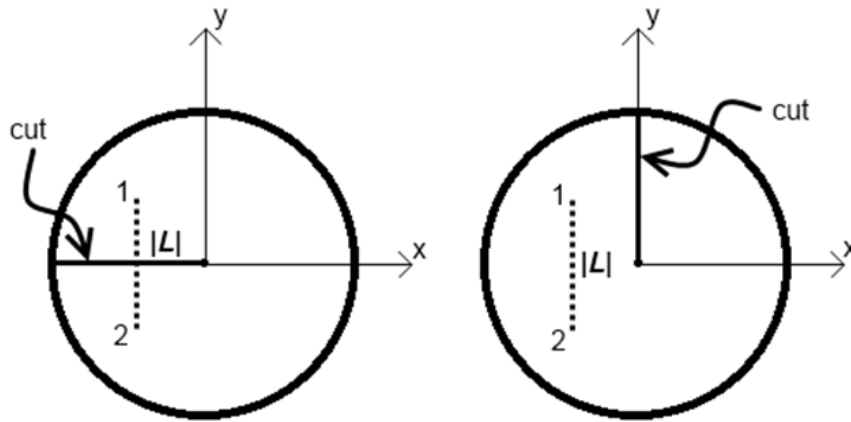
Figure 6.1: Representation of different displacement differences due to a jump at the cut surface. The two points are along the same diffraction vector separated by the same length in two equivalent cylindrical domains containing screw dislocations with equal line and Burgers vector but different orientation of the cut.

The presence of the surface cut, along with the arbitrariness associated with its orientation, may have consequences on the broadening of the diffraction peaks. With respect to virtual diffraction from a distorted crystal, depending on the orientation of

this cut, the magnitude of difference in elastic displacements entering the cosine and sine functions of distortion Fourier coefficients in equation (6.11) could be different. Consider the illustration in figure 6.1 of an infinitely long single screw dislocation placed at the center of a cylindrical domain whose axis is along the z direction. In one case the cut is aligned along the $-x$ direction and in the second case the cut is aligned along the $+y$ direction. Note that such a specific choice of cut orientations is made only for the sake of illustration and it is representative of the general problem that is discussed here. Let a beam of X-rays with diffraction vector aligned in the yz plane (so that its projection in xy plane is along the y direction) be incident on each of these cylindrical domains. For a given Fourier length $|\boldsymbol{L}|$ when the resolved component of diffraction vector crosses the surface cut, the jump leads to a relatively larger difference in displacement compared to when the surface cut is not traversed for the same two points. Therefore mathematically and computationally, for the same dislocation line, Burgers and diffraction vector, there are multiple possibilities of displacement contributions to virtual diffraction peaks depending on the orientation of the cut.

Encountering the surface cut while computing the displacement differences could have a significant effect on the broadening of the diffraction peaks. This can be mathematically demonstrated through the exponential term of the intensity in equation (6.3) or the distortion Fourier coefficients in equation (6.11). The jump in the surface cut is of the order of a lattice vector, specifically the Burgers vector. Therefore the difference in displacements taken across the surface cut would introduce an additional term, in the form of an inner product between the diffraction vector and the Burgers vector *i.e.* $\exp\left(2\pi i \vec{\boldsymbol{g}} \cdot \Delta\vec{\boldsymbol{u}}\right) = \exp\left(2\pi i \vec{\boldsymbol{g}} \cdot \Delta\vec{\boldsymbol{u}}^* + 2\pi i \vec{\boldsymbol{g}} \cdot \vec{\boldsymbol{b}}\right)$ where $\Delta\vec{\boldsymbol{u}}^*$ is the difference in displacement if the surface cut were not present between those points, and $\vec{\boldsymbol{b}}$ is the Burgers vector. This additional term $\exp\left(2\pi i \vec{\boldsymbol{g}} \cdot \vec{\boldsymbol{b}}\right)$ will contribute to the computed intensity if $2\pi \vec{\boldsymbol{g}} \cdot \vec{\boldsymbol{b}}$ is not a multiple of 2π.

270

An alternative way to generate the virtual peaks is to use strain based methods such as the Stokes-Wilson approximation [384]. Due to the discrete nature of dislocations considered here, only the out-of-core compatible elastic strains are taken into account. However, this method is applicable to both discrete and continuous approaches. The core contributions to diffraction (which include compatible elastic and incompatible elastic and plastic, strains) are neglected because the total volume occupied by the dislocation core is very small compared to the rest of the coherently diffracting domain studied in this work and would not have a significant effect on the broadening of peaks. Furthermore, this allows the application of the present model in a discrete framework without dealing with the singularity in elastic strain field associated with the dislocation line defined within the core.

Taking the gradient of the elastic displacement field given in equation (6.23), one obtains the compatible elastic distortion field. The symmetric component of the compatible elastic distortion – compatible elastic strain – associated to a curved dislocation line is given as (deWit, 1960),

$$
\begin{aligned}
e_{ij}^{\parallel}\left(\boldsymbol{x}\right) &= \frac{1}{2}\left(\boldsymbol{u}_{i,j}\left(\boldsymbol{x}\right) + \boldsymbol{u}_{j,i}\left(\boldsymbol{x}\right)\right) \\
&= \frac{1}{8\pi}\oint_{C}\left(\begin{array}{c} -\frac{1}{2}\Big(e_{jkl}(\boldsymbol{b}_i|\boldsymbol{X}|_{,l} - \boldsymbol{b}_l|\boldsymbol{X}|_{,i}) + e_{ikl}(\boldsymbol{b}_j|\boldsymbol{X}|_{,l} - \boldsymbol{b}_l|\boldsymbol{X}|_{,j})\Big)_{,pp} \\ +\frac{1}{1-\nu}e_{kmn}\boldsymbol{b}_n|\boldsymbol{X}|_{,mij}\end{array}\right) d\boldsymbol{x}_k^{'} \quad (6.25)
\end{aligned}
$$

So far, the only strain based method that has been applied to generate virtual peaks is the Stokes-Wilson approximation [384]. The underlying assumptions of this method however limit the application to microstructures having short range stresses. The Stokes-Wilson argument that relative displacement is random for large values of $|\boldsymbol{L}|$ implicitly assumes that the coherently diffracting domain is devoid of long range strain inducing defects. However, this may not be the case in material systems such as nano-crystalline aggregates. Recall from section 2.2.2, the study on nc Pd using aberration corrected transmission electron microscopy which revealed the presence of a disclination dipole along a $\Sigma 9$ GB and terminating near a $\Sigma 9$ $\Sigma 3$ $\Sigma 3$ TJ

271

[341]. Ordered strain field distribution within and around the disclination dipole may not satisfy the Stokes-Wilson approximation and therefore could have an important contribution to the diffraction profile. For very small values of $|\boldsymbol{L}|$, these distributions of strain translate into localized strain gradients, which too are neglected in the Stokes-Wilson approximation; thus the contribution coming from all the gradients of displacement except for the instantaneous elastic strain are ignored.

In what follows, a new computational technique for generating the diffraction profile is presented which, along with the strains, accounts for other gradients of the displacement without making any assumptions. First, the components of gradients of displacement that have a contribution to line broadening are identified.

Recalling the definition of ϵ^L in (6.12); it is equal to the change in displacement along the direction of the diffraction vector. For small distances, the differences in displacement, when expanded in the form of power series, become a function of their gradients. These gradients can be separated into symmetric components corresponding to elastic strain gradients and anti-symmetric components corresponding to elastic curvatures and their gradients [421]. In order to identify which of these components contribute to the broadening of intensity profiles the power series expansion is revisited: $\Delta \vec{\boldsymbol{u}}(\boldsymbol{L}) = \vec{\boldsymbol{u}}(\vec{\boldsymbol{x}}) + \vec{\boldsymbol{L}} \cdot \nabla \vec{\boldsymbol{u}}(\vec{\boldsymbol{x}}) + \vec{\boldsymbol{L}}^2 : \nabla \nabla \vec{\boldsymbol{u}}(\vec{\boldsymbol{x}}) + \cdots - \vec{\boldsymbol{u}}(\vec{\boldsymbol{x}})$ for small $|\vec{\boldsymbol{L}}|$. Rejecting $O(\vec{\boldsymbol{L}}^3)$ terms and switching to Einstein notations gives $\Delta u_i(\vec{\boldsymbol{L}}) = L_j u_{i,j} + L_j L_k u_{i,jk}$. Substituting the difference in displacement in equation (6.13) for cosine distortion Fourier coefficients and equation (6.7) for the Fourier length gives:

$$
\begin{aligned}
A^D(\vec{\boldsymbol{L}}) = \left\langle \cos(2\pi \vec{\boldsymbol{g}} \cdot \Delta \vec{\boldsymbol{u}}(\vec{\boldsymbol{L}})) \right\rangle &= \left\langle \cos(2\pi g_i \Delta u_i(\vec{\boldsymbol{L}})) \right\rangle \\
&= \left\langle \cos(2\pi \left[g_i L_j u_{i,j} + g_i L_j L_k u_{i,jk} \right]) \right\rangle \\
&= \left\langle \cos \left(\frac{2\pi t}{|\vec{\boldsymbol{g}}|} \left[g_i g_j u_{i,j} + \frac{t}{|\vec{\boldsymbol{g}}|} g_i g_j g_k u_{i,jk} \right] \right) \right\rangle
\end{aligned}
\tag{6.26}
$$

In the work of Stokes and Wilson [384] and Wilson [460] it has been shown that the double dot product of the diffraction vectors with the first gradient of the displacement

- distortion tensor - extracts the symmetric part of the distortion tensor *i.e.* the strain. The second gradient of displacement - 2-distortion tensor - is worked out in a similar way. It has been shown that the 2-distortion tensor can be sub-divided into a symmetric and anti-symmetric component with respect to any two of its indices [421]. Therefore:

$$A^D(\vec{L}) = \left\langle \cos\left(\frac{2\pi t}{|\vec{g}|}\left[g_i g_j \epsilon_{ij} + \frac{t}{|\vec{g}|}g_i g_j g_k(u_{(i,j)k} + u_{[i,j]k})\right]\right)\right\rangle \qquad (6.27)$$

From equations (2.52) and (2.51), the anti-symmetric component of the 2-distortion tensor which is the third order curvature tensor $\tilde{\kappa}_{[ij]k}$ can be represented in terms of the second order curvature tensor as $\tilde{\kappa}_{[ij]k} = -e_{ijl}\kappa_{lk}$. Substituting this in equation (6.27) gives,

$$A^D(\vec{L}) = \left\langle \cos\left(\frac{2\pi t}{|\vec{g}|}\left[g_i g_j \epsilon_{ij} + \frac{t}{|\vec{g}|}g_i g_j g_k(u_{(i,j)k} - e_{ijl}\kappa_{lk})\right]\right)\right\rangle \qquad (6.28)$$

From the definition from the Levi-Civita permutation tensor it can be easily deduced that $g_i g_j e_{ijl} = 0$. Therefore the equation from the cosine distortion Fourier coefficient reduces to,

$$A^D(\vec{L}) = \left\langle \cos\left(\frac{2\pi t}{|\vec{g}|}\left[g_i g_j \epsilon_{ij} + \frac{t}{|\vec{g}|}g_i g_j g_k \epsilon_{ij,k}\right]\right)\right\rangle \qquad (6.29)$$

Thus besides elastic strain, only the strain gradient and by analogy higher gradients of strain contribute to line profile broadening. For larger values of $\vec{L}$ this would translate into distribution of strains. The elastic rotation, curvature and its gradients have no contributions to the line profile.

Therefore ϵ^L defined in equation (6.12) as the resolved component of the difference in displacement along the direction of the diffraction vector can now be defined as the elastic strain averaged over the length $\left|\vec{L}\right|$,

$$\epsilon^L(x) = \frac{1}{\left|\vec{L}\right|} \int_{x-\frac{|\vec{L}|}{2}}^{x+\frac{|\vec{L}|}{2}} e^e(x)\,dx \qquad (6.30)$$

273

where $e(x) = \frac{\vec{g} \cdot \epsilon^e(x) \cdot \vec{g}}{|\vec{g}|^2}$ is the apparent elastic strain.

With such a definition of ϵ^L coupled with the knowledge that curvature does not contribute to broadening, the Fourier coefficients are defined as shown in equation (6.13). The intensity can then be computed by combining equations (6.13), (6.19) and (6.30) to give,

$$I(\Delta\vec{g}) = \int_{-\infty}^{\infty} \int_{-\infty}^{\infty} p_{\epsilon^L}\left(\epsilon^L\right) \exp\left(2\pi i |\vec{g}| \epsilon^L \left|\vec{L}\right|\right) \exp\left(2\pi i \vec{L} \cdot \Delta\vec{g}\right) d\epsilon^L d\left|\vec{L}\right| \quad (6.31)$$

Equation (6.31) is derived from the Fourier method without imposing any limits either on the range of the diffraction vector or on the Fourier length. This formulation is applicable in both discrete and continuous framework. Furthermore, the problem associated with multi-valued elastic displacement and the orientation of the dislocation jump surface is avoided altogether without making any assumptions. From the computational standpoint, similar to the Stokes-Wilson approximation, evaluating the intensity using equation (6.31) requires only the knowledge of the local elastic strain field in the material; however it is necessary to know the probability distribution function (PDF) of the strain averaged over the Fourier length $\left|\vec{L}\right|$ for all $\vec{L}$.

From the standpoint of kinematic theory of diffraction, equation (6.10) and equation (6.31) should give the exact same diffraction peaks since both are the exact solutions derived from equation (6.3). However, from the perspective of the theory of dislocations there is a fundamental difference stemming from the multi-valued nature of the elastic displacement field. The consequences of these are presented later in this work for the particular case of the restrictedly random distribution.

For the sake of clarity, in the remainder of the article, the Fourier method of Warren and the new averaged strain method shall be referred to as the Fourier displacement method and the Fourier averaged strain method, respectively.

6.3   Establishing domains of applicability

6.3.1   Computational methodology

In order to generate virtual diffraction peaks with the Fourier transform method of Warren (6.10), the Stokes-Wilson approximation (6.22), and the new averaged strain method (6.31), two different numerical procedures are used. To probe the differences between these methods for different microstructures, representative volumes are either seeded with infinitely long straight dislocations - for which closed formed expressions are given in section 2.1.1 - or seeded with finite length dislocations. In this second case, the idea is to generate microstructures representative of those actually generated during plastic deformation of single crystals or of polycrystals. To that end, the discrete dislocation dynamics method is employed. Dislocations are therefore discretized into segments formally defined by two end points (or nodes) whose position and tangent are used for the purpose of interpolation of the position and tangent of all points belonging to the segment [141]. Neglecting accelerations, the over-damped equations of motion of each dislocation line are then solved using an adaptive finite element scheme. For more details, the reader is referred to the work of Balogh *et al.* [24].

From a given microstructure, defined by dislocation lines, the diffraction peaks can be approximated by the method of Stokes and Wilson [384]. Recall here that, as discussed above, one of the core assumptions of the Stokes-Wilson construct of diffraction peaks is the independence of the PDF of average strains with respect to the Fourier length. Therefore, the coherently diffracting volume containing dislocations is randomly seeded with sampling points at which the apparent strain is computed. An optimized binning procedure [361] is then used to obtain the PDF of strain that is to be computed as a function of departure from the inverse of the equilibrium spacing between the planes *i.e.* $|\Delta \vec{g}| = \frac{1}{d'} - \frac{1}{d}$. The bin size is taken as: $w = 3.49 \sigma n^{-\frac{1}{3}}$ [361], where w is the bin width and σ is the standard deviation of the apparent strain for

n sampling points. The apparent elastic strain at each sampling point is computed using the superposition principle. Therefore, at a given field sampling point the elastic strain field is computed as the sum of the fields arising from each dislocation line. While closed form expressions of the elastic strain field from an infinitely long straight dislocation exist [96] and are presented in equations (2.17), the strain field due to a curved dislocation is computed via the numerical integration of the expression (6.25). To that end, a composite Gaussian integration procedure is used in which each length of a curved dislocation sub-segment does not exceed 1000 lattice spacings. For each sub segment 32 integration points are used.

In the Fourier displacement method, the heart of the numerical procedure lies in the computation of the distortion Fourier coefficients $A^D(\vec{\boldsymbol{L}})$ and $B^D(\vec{\boldsymbol{L}})$. As shown by equation (6.11), these depend on the difference in the displacement between two points separated by a Fourier length $|\vec{\boldsymbol{L}}|$ along the direction of the diffraction vector. Therefore for each $|\vec{\boldsymbol{L}}|$, N_L pairs of points are initially seeded within the volume. Every point in the N_L pair is separated by $|\vec{\boldsymbol{L}}|$ from its conjugate, along the direction of the diffraction vector. For each point, the displacement fields are either computed with use of closed form analytical expression as shown in equations (2.16) - in the case of straight dislocations - or via computation of the displacement as given by equation (6.23). In the latter case the same numerical integration procedure, prescribed for the case of elastic strain computation, is used. Finally, the cosine and sine terms in equation (6.11) are averaged over the N_L pairs to give their respective distortion Fourier coefficients.

The new averaged strain method also requires the evaluation of the Fourier coefficients $A^D(\vec{\boldsymbol{L}})$ and $B^D(\vec{\boldsymbol{L}})$ which are now defined using the equation (6.13) involving the averaged strain ϵ^L from equation (6.30). The numerical procedure begins with computing the elastic strain within the domain at points lying on a regular grid. Then for each Fourier length $\left|\vec{\boldsymbol{L}}\right|$, N_L pairs of points are randomly sampled in the domain.

ϵ^L is evaluated for each of these N_L pairs by averaging the resolved local elastic strain computed at regularly spaced points along the segment joining the two points constituting an N_L pair. The interpolation is carried out at each of these segment points by using the nodal elastic strain values of their respective associated grid element.

A dislocation core with a radius of one Burgers vector is defined so that any sampling points falling within this core are neglected from the computation of the intensity. Figure 6.2 illustrates the sampling procedure for a microstructure containing finite length screw dislocations.
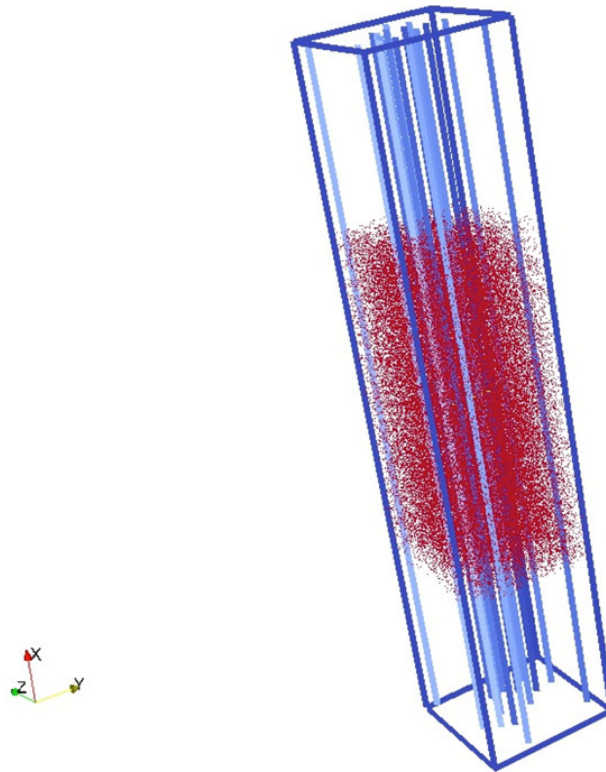
Figure 6.2: Microstructure containing finite long screw dislocations. The red dots represent sampling points.

All the simulations are performed using 5×10^6 points sampled for the Stokes-Wilson approximation, 10^4 N_L pairs for the Fourier displacement method and 4×10^4 N_L pairs for the Fourier averaged strain method, unless mentioned otherwise.

The intensities and PDFs generated are normalized with respect to their maximum values to compare their widths. In order to avoid difficulties associated with crystal anisotropy, microstructures in all four cases are taken as those of Aluminum with lattice spacing $a_0 = 4.0494$ Å, shear modulus $\mu = 26$ GPa, and Poissons ratio $\nu = 0.345$. The simulated continuous media is elastically isotropic, has cubic symmetry and it has the shear modulus and the Poissons ratio of Aluminum.

The relative difference between resulting reflections obtained by using Stokes-Wilson approximation with respect to the Fourier based methods is quantified by comparing the integral breadths of the peaks. Integral breadth of a line profile is defined as the ratio of the total intensity $I = \int I\left(\Delta\vec{g}\right) d\Delta\vec{g}$ with respect to $\left.\frac{dI}{d\Delta\vec{g}}\right|_{max}$ which translates into a ratio of the area under the $I\left(\Delta\vec{g}\right)$ vs. $\left|\Delta\vec{g}\right|$ curve with respect to the maximum value of the intensity distribution I_{max}. Since the intensity distribution is normalized with respect to its maximum value, the integral breadth in the present framework becomes equal to the area under the normalized $I\left(\Delta\vec{g}\right)$ vs $\left|\Delta\vec{g}\right|$ curve. In the following sections, for the line profiles of different microstructures studied, only the percentage difference in integral breadths will be highlighted. To compute area under the normalized $I\left(\Delta\vec{g}\right)$ vs $\left|\Delta\vec{g}\right|$ curve, the trapezoidal rule is used.

6.3.2 Applications to Dislocations in Single Crystal Microstructures

The purpose here is to apply the virtual diffraction tool to understand the contribution of ordered strain fields, that are typically observed in the vicinity of line defects, on the broadening of diffraction peaks. Generating diffraction peaks using Stokes-Wilson approximation is computationally less demanding than the Fourier displacement and the new Fourier averaged strain method, albeit at the cost of neglecting strain gradients and distributions of strain. It is therefore interesting to observe the extent of error induced in making such assumptions. This is realized by investigating four distinct cases. In the first three scenarios, infinitely long and straight dislocations are

inserted in a volume to study the cases of (1) a single screw dislocation in a cylindrical volume (2) a low angle GB - to compare the intensity profiles in presence of localized higher displacement gradients, (3) a restrictedly random distribution of dislocations - to highlight the contribution of higher displacement gradients and strain averaged over a distance $|\vec{L}|$ to intensity profiles -, and (4) the last configuration studied is a dislocation microstructure associated to coplanar slip that is generated by the discrete dislocation dynamics method.

6.3.2.1 *Single screw dislocation in a cylinder*

In this first scenario, the case of a single dislocation isolated in a cylindrical volume is revisited to further demonstrate the fundamental differences between the three methods. The screw dislocation line is aligned along the axis of an infinitely long cylinder. The origin is chosen to be at the center of the circular surface and the cylindrical axis and dislocation line are aligned along the $\vec{a}_3$ direction. The displacement field in the presence of an infinitely long screw dislocation is given as:

$$\vec{u} = \frac{b_3}{2\pi} \tan^{-1}\left(\frac{y}{x}\right)\vec{a}_3 \tag{6.32}$$

where b_3 is the Burgers vector component along the direction $\vec{a}_3$.

Following the procedure adopted by Wilson [460], an analytical description of the diffraction peak profile can be obtained by virtue of the Stokes-Wilson approximation. The apparent elastic strain resolved along the hkl direction can be derived as:

$$e = \frac{\vec{g} \cdot \nabla\vec{u} \cdot \vec{g}}{|\vec{g}|^2} = \frac{b_3 l \vec{g} \cdot (\hat{a}_3 \times \vec{r})}{2\pi |\vec{g}|^2 |\vec{r}|^2} \tag{6.33}$$

where $\vec{r} = x\hat{a}_1 + y\hat{a}_2$. It follows from equation (6.33) that the locus of the apparent strain is a circle with radius equal to $\frac{b_3 l \vec{g} \cdot (\hat{a}_3 \times \vec{r})}{4\pi |\vec{g}|^2 e}$ and center at $\left(0, -\frac{b_3 l \vec{g} \cdot (\hat{a}_3 \times \vec{r})}{2\pi |\vec{g}|^2 e}\right)$. Let E denote the largest value attained by the apparent elastic strain on the circumference of the cylinder. The PDF of apparent strain $p_e(e)$ is obtained by computing the fraction of total area of cross-section that lies between the circles of radii e and $e + de$

and is given as [460],

$$p_e(e)de = \frac{E^2}{2e^3}de \quad \text{for } e > E \text{ and}$$

$$p_e(e)de = \left(\frac{E^2}{2e^3} - \frac{E^2}{\pi e^3} \cos^{-1}\left(\frac{e}{E}\right) - \frac{\sqrt{E^2 - e^2}}{\pi e^2} \right) de \quad \text{for } e < E \qquad (6.34)$$

Analytical solutions involving Bessel functions for the intensity diffracted from a cylindrical domain containing a single screw dislocation have been provided in an earlier work of Wilson [459]. However, due to lack of rigorous proof these are not used in the present work.

The methodology discussed in section 6.3.1 is tested in the case of a single screw dislocation. Figure 6.3 shows a convergence test comparing the PDF of strain obtained from the numerical Stokes-Wilson approximation using 5×10^4, 5×10^5 and 5×10^6 sampling points and Wilsons analytical solution for a single screw dislocation of Burgers vector **001** placed at the center of a cylinder with radius equal to 1000 a_0 using diffraction vector $\vec{g} = \mathbf{402}$. Such a configuration has a dislocation density of $\approx 1.94 \times 10^{12} m^{-2}$.

The plots show that with 5×10^6 sampling points there is a reasonably good match between the analytical and numerical PDFs of strain. The percentage difference in integral breadths with respect to the analytical peak is 7.5% as opposed to 25.8% using 5×10^4 points and 21.2% using 5×10^5 points. Increasing the number of sampling points slowly improves the accuracy but with a significant increase in the computation time. Using 5×10^6 points provides a good trade-off between accuracy and computation time. Convergence studies were also performed for the displacement based Fourier method and averaged strain based Fourier method (not shown here) leading to the choice of 10^4 N^L pairs and 4×10^4 N^L pairs as mentioned in section 6.3.1.

For the sake of comparison and consistency with the ensuing applications, the coherently diffracting domain will from now on be taken as a cuboid with two square

280
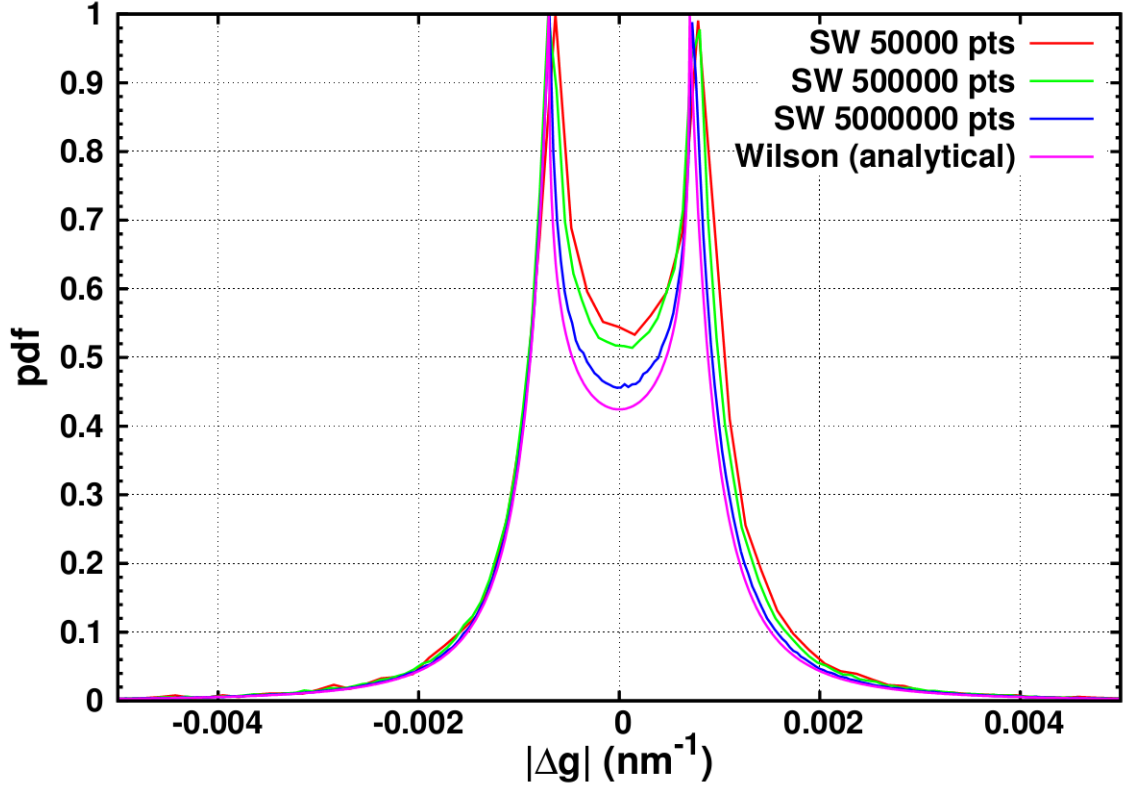
Figure 6.3: Convergence test comparing PDF of strain plotted using numerical Stokes-Wilson approximation for 3 sets of points (SW 50000 pts, SW 500000 pts, SW 5000000 pts) and Wilsons analytical solution (Wilson (analytical)) for diffraction vector $\vec{g} = \mathbf{402}$

faces perpendicular to the dislocation line. Figure 6.4 shows the comparison of intensity generated using the Fourier displacement method, Fourier averaged strain method and PDF of strain obtained from numerical Stokes-Wilson approximation for a single screw dislocation of Burgers vector $\mathbf{001}$ placed at the center of a square domain with dimensions $1000a_0$ x $1000a_0$ using diffraction vectors $\vec{g} = \mathbf{111}$, $\mathbf{222}$, $\mathbf{224}$ and $\mathbf{333}$. The dislocation density of the domain is $\approx 6.1 \times 10^{12} m^{-2}$.

The diffraction peaks obtained from the Fourier based methods are symmetric about the line $|\vec{g}| = 0$ which is consistent with the numerical solution of the Stokes-Wilson approximation. Ripples in the Fourier based solutions are an artifact caused by the fact that distortion Fourier coefficients $A^D\left(\vec{L}\right)$ and $B^D\left(\vec{L}\right)$ do not converge
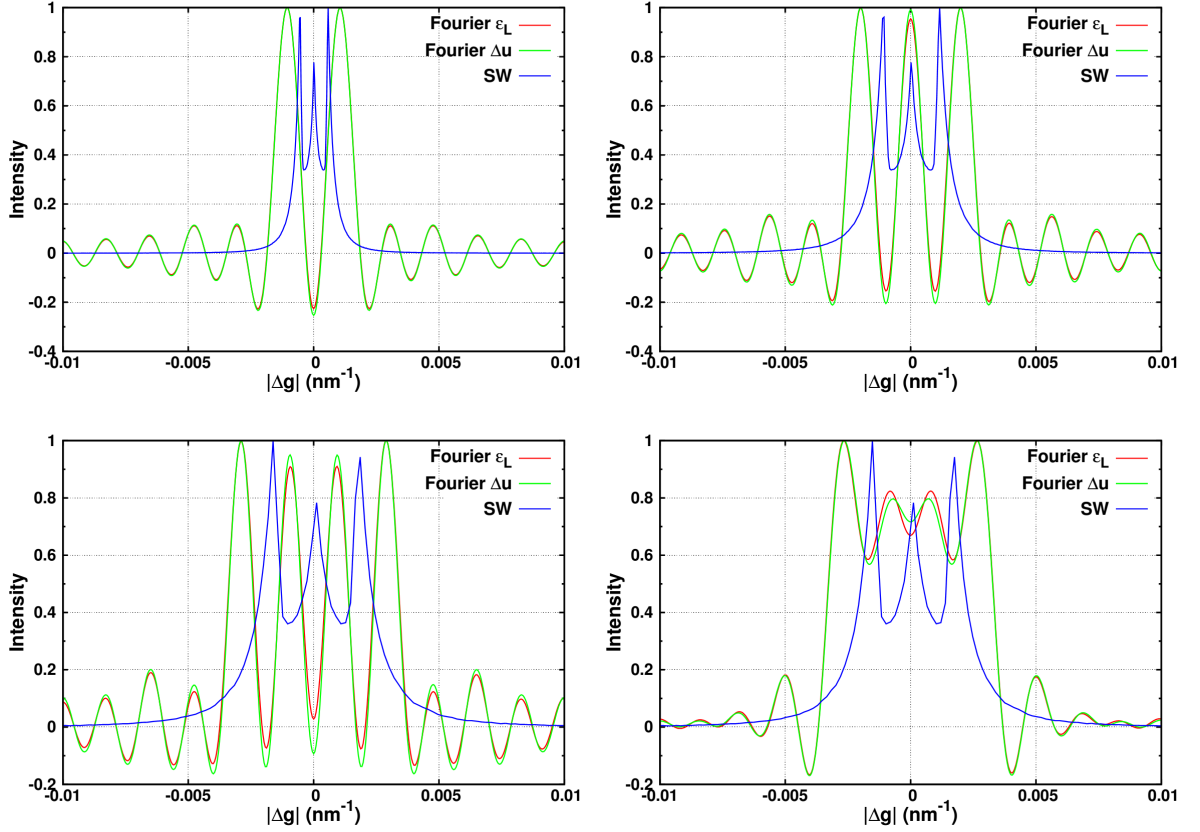
Figure 6.4: Intensity comparison between the normalized Fourier method, the Stokes-Wilson (SW) approximation and Wilson's analytical solution for diffraction vectors (a) $\vec{g} = [111]$, (a) $\vec{g} = [222]$, (a) $\vec{g} = [333]$ and (d) $\vec{g} = [224]$

to zero until the maximum $\left|\vec{L}\right|$ is reached. This effect, is referred to as termination ripples, can also be observed in figure 6.7, but there it is much less pronounced. Theoretically, $A^D\left(\vec{L}\right)$ and $B^D\left(\vec{L}\right)$ should be calculated till $\left|\vec{L}\right|$ reaches infinity as indicated by the summation limits in equation (6.11). However, for computational purposes a cut-off limit needs to be imposed. In the present work, this limit is set to be the domain size along the direction of the diffraction vector. The intensity can have negative values if the distortion Fourier coefficients do not converge to zero within the defined range of $\left|\vec{L}\right|$.

There is an excellent agreement between the Fourier displacement and averaged

strain methods for all the diffraction vectors. On the other hand, a significant difference in peak widths exists between those generated from Fourier based methods and the Stokes-Wilson approximation. The percentage difference in integral breadths of peaks obtained from Stokes-Wilson approximation with respect to those from the average strain based Fourier method for diffraction vectors $\vec{g} = \mathbf{111}$, $\mathbf{222}$ and $\mathbf{333}$ are 41.69%, 26.31% and 20.19%, respectively, whereas for $\vec{g} = \mathbf{224}$ the difference is 48.79%. These differences come from the Stokes-Wilson assumption that the PDF of apparent elastic strain is equal to the PDF of averaged apparent elastic strain which neglects the uniform distribution arising from the decay of strain field away from the dislocation line.

Comparison of the Fourier based methods in figure 6.4 shows that in the case of a single screw dislocation, the displacement difference across the jump surface does not affect the diffraction profile. This can be explained as follows. As seen in section 2.1.1, the surface cut for a single screw dislocation in 2-dimensions is bounded by the z-axis $(-\infty, \infty)$ and the x-axis $(-\infty, 0]$ which in the xy plane is represented by the line $y = 0$ bounded by the points $x = -\infty$ and $x = 0$ [96]. Therefore the differences in displacements, taken along the xy plane projection of all the diffraction vectors, encounter this surface cut. Following the reasoning from section 6.2, these differences in displacement across a surface cut introduce an additional term in the form of $\exp\left(2\pi i \vec{g} \cdot \vec{b}\right)$. For all the diffraction vectors used here *i.e.* $\vec{g} = \mathbf{111}$, $\mathbf{222}$, $\mathbf{224}$ and $\mathbf{333}$, and the Burgers vector of the screw dislocation $\vec{b} = \mathbf{001}$, the inner product $\vec{g} \cdot \vec{b}$ is an integer which leads to an even multiple of pi that has no effect on the exponential term.

The significance of distribution of strains to broadening of the diffraction peaks obtained from the Fourier method may be appreciated by comparing the PDF of average apparent elastic strain $p_{\epsilon^L}\left(\epsilon^L\right)$ over a distance with the PDF of apparent elastic strain $p\left(e\right)$ as shown in figure 6.4. The comparison is made for three Fourier
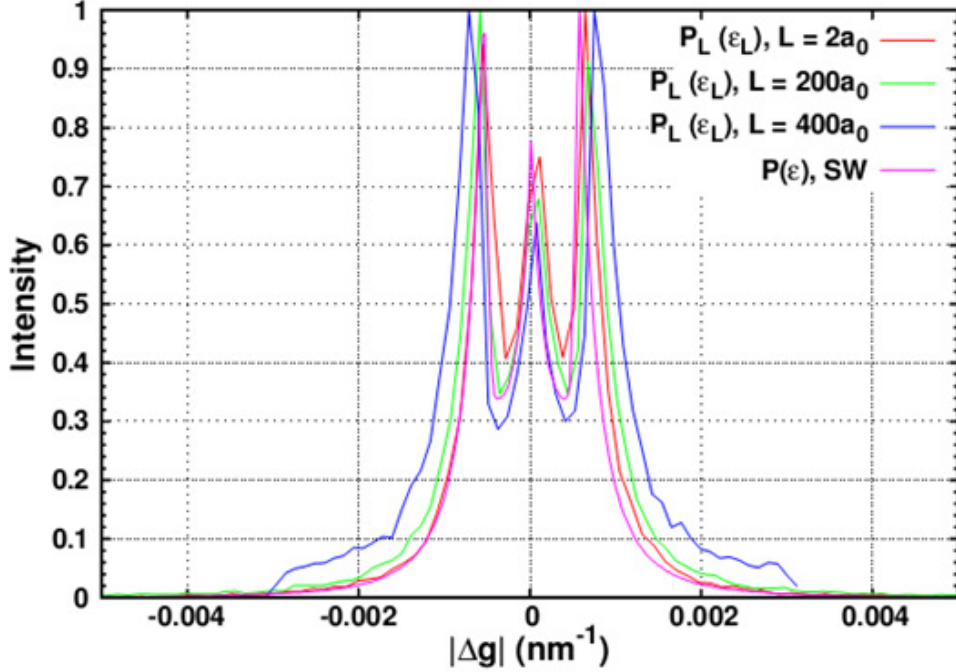
Figure 6.5: Comparison of normalized PDFs of elastic strain averaged over lengths $|\vec{L}| = 2a_0$, $200a_0$ and $400a_0$ with the normalized PDFs of apparent elastic strain

lengths viz. $|\vec{L}| = 2a_0$, $200a_0$ and $400a_0$ for the diffraction vector $\vec{g} = \mathbf{111}$. From figure 6.4, for $|\vec{L}| = 2a_0$ the PDF of ϵ^L compares well with the PDF of apparent strain. Such a result is to be expected. More interestingly, an unmistakable broadening of the PDF of averaged strain occurs with the increase in $|\vec{L}|$ highlighting the importance of the distribution of strain.

6.3.2.2   Low angle symmetric tilt GB

Low angle symmetric tilt GBs (LAGBs) are particularly interesting because of the inhomogeneous strain distribution and sharp second and higher order displacement gradients localized in the vicinity of the GB. With such a configuration, a stark difference in the intensity generated from displacement based Fourier method, averaged strain based Fourier method and the PDF of strain from Stokes-Wilson approximation may be expected. To test this hypothesis, the Fourier intensities and $p_e(e)$ are computed for [001] tilt LAGB with misorientation of 2° using two diffraction vectors;
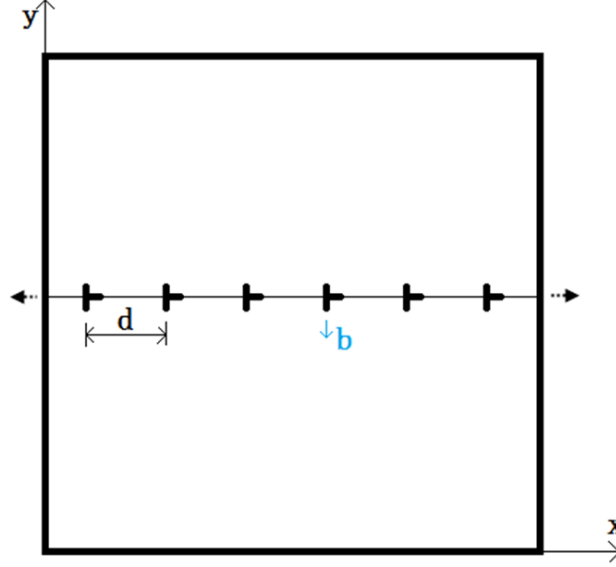
Figure 6.6: Low angle STGB represented using dislocations with Burgers vector $\vec{b}$ and periodic spacing of d. Periodic boundary conditions are imposed along x-axis

$\vec{g} = \mathbf{131}$ and $\mathbf{311}$. The GB is represented as a dislocation wall aligned parallel to the x-axis and centered in a square domain of size $1000\ a_0 \times 1000\ a_0$ giving a dislocation density of $\approx 2.1 \times 10^{14} m^{-2}$. Periodic boundary conditions are imposed along the X-axis as shown in figure 6.6. The spacing d between the dislocations is computed using the Franks formula $d = \frac{|\vec{b}|/2}{\sin(\omega/2)}$ where ω is the tilt angle.

The results are illustrated in figure 6.7. To facilitate a better comparison of peak tails, the $I(\Delta\vec{g})$ vs. $|\Delta\vec{g}|$ curves are re-plotted on a semi-log scale. A positive constant shift, equal to the magnitude of the global minimum intensity of all three peaks, is added to each of these peaks in order to facilitate the illustration of negative values in tail ripples; for $\vec{g} = \mathbf{131}$ and $\mathbf{311}$, the shifts are equal to 0.0015866 and 0.10808, respectively. The peaks are then renormalized and plotted as shown in figure 6.7(c) and 6.7(f).

Contrary to expectation, the shape and broadening of the three profiles are in good agreement as seen in plots 6.7(b) and 6.7(d); percentage differences in integral breadths obtained from Stokes-Wilson approximation and average strain based
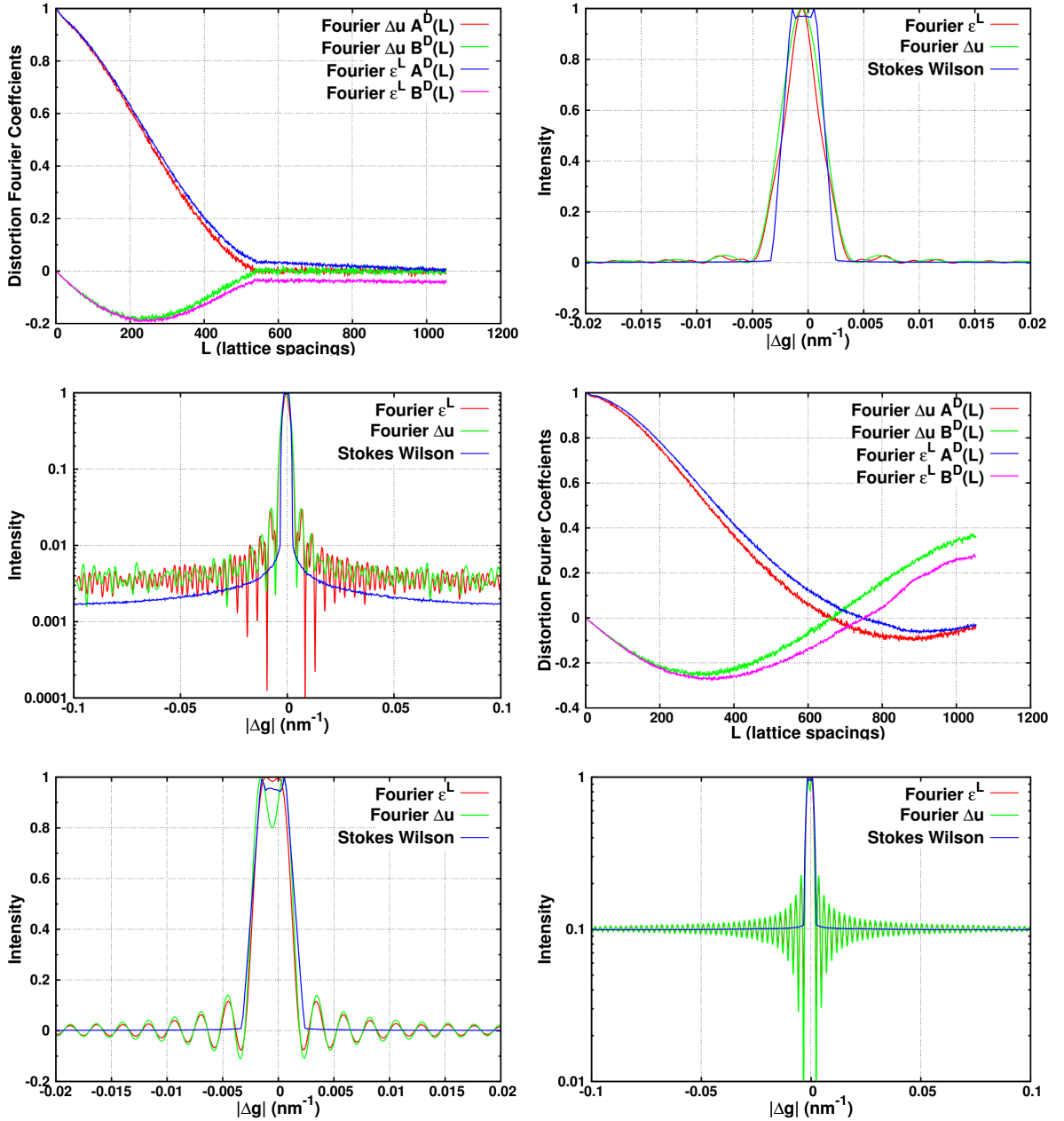
Figure 6.7: Distortion Fourier coefficients from the Fourier displacement and averaged strain methods a) and d) and comparison of intensities from the Fourier displacement (Fourier) method, Fourier averaged strain (Fourier $\Delta\vec{u}$) method and the Stokes-Wilson (Stokes-Wilson) approximation in the case of a 2° [001] STGB b) and e) for diffraction vectors $\vec{g} = \mathbf{131}$ and $\mathbf{311}$. Plots c) and f) are the same intensities in semi-log format, renormalized after a positive shift by a constant (0.0015866 and 0.10808, respectively, for $\vec{g} = \mathbf{131}$ and $\mathbf{311}$) equal to the magnitude of the minimum of intensity of all three peaks combined, to facilitate illustration of the negative values.

Fourier method equal to 14.54% for $\vec{g} = \mathbf{131}$ and 4.89% for $\vec{g} = \vec{\mathbf{3}}\mathbf{11}$. Similar to the case of single dislocation, tail ripples are generated due to the distortion Fourier coefficients not converging to zero for the chosen range of $\left|\vec{L}\right|$.

Elastic strains are localized in the vicinity of the GB and the displacements in each crystal forming the GB interface are constant and equal in their respective lattices. Accounting for the highly localized but non-negligible residual elastic strain distribution within the GB interface leads to $p_{\epsilon^L}\left(\epsilon^L\right) \approx p_e\left(e\right)$. Also, the strain gradients are inhomogeneously distributed and restricted to the GB interface. Therefore their contribution to the peak profile generated using the Fourier method is not significant.

Figure 6.7(b) and 6.7(d) further reveal symmetric peaks but with a distinct peak shift for both the diffraction vectors. It is well known that the presence of GBs can cause a shift in the diffraction peaks from their mean positions [414]. Peak shifting occurs due to the elastic strains generated in the presence of dislocation walls and is factored into the virtual peaks from the non-zero values of the distortion Fourier sine coefficient $B^D(\vec{L})$. Peak symmetry is attributed to the highly localized strains and strain gradients occupying a very small domain area in the neighborhood of the GB interface along the direction of diffraction vector.

With the limit on $\left|\vec{L}\right|$ set to be the maximum distance in the domain along the direction of $\vec{g}$, for some diffraction vectors such as $\vec{g} = \mathbf{311}$ the values of $A^D(\vec{L})$ and $B^D(\vec{L})$ do not necessarily converge to zero in the permissible range. Comparison of the distortion Fourier coefficients in figure 6.7 reveals that high amplitudes of termination ripples occur when $A^D(\vec{L})$ and $B^D(\vec{L})$ do not converge to 0 within the range of $|\vec{L}|$ values, as mentioned also for figure 6.4.

Increasing the magnitude of the diffraction vector component along the direction of the Burgers vector leads to a faster convergence of the distortion Fourier coefficients and broadens the diffraction peaks. On the other hand, increasing the magnitude of diffraction vector component along the GB ($\vec{b} \times \vec{l}$) leads to a much slower

convergence to zero for the distortion Fourier coefficients, meaning a less broadened diffraction peak. This effect is analogous to the well-known phenomenon of strain anisotropy, where the broadening of strain profiles in a dislocated crystal is scaled for *hkl* dependence by dislocation contrast factors [417]. Such a result could be helpful in identifying the direction of the GB without a priori knowledge about its orientation in the sample.

6.3.2.3   *Restrictedly random distribution of dislocations*

Wilkens [450, 451, 452] introduced the concept of restrictedly random distribution (RRD) of dislocations as an energetically admissible representative volume element alternative to the completely random distribution chosen in the work of Krivoglaz [214]. In the context of present work, the RRD configuration is interesting because of the associated homogeneous distribution of strain and higher order displacement gradients.

In the RRD configuration, the two-dimensional domain is divided into sub domains of equal areas. Equal amount of dislocations with opposite Burgers vectors are randomly distributed within these sub areas such that the net Burgers vector is equal to zero and the dislocation density in each sub domain is equal to that of the entire domain. With the help of this configuration, Wilkens [450, 451, 452] provided an analytical expression for the variance of averaged square strain, which is used to calculate theoretical diffraction profiles based on his dislocation model using the Warren-Averbach equation [447, 448]. Theoretical profile functions based on the Wilkens model are used by the modern full pattern diffraction line profile analysis methods, like eCMWP, to evaluate strain broadening caused by dislocations [326].

The RRD has been studied by Kamminga and co-workers [198, 199, 200] who used the displacement based Fourier method to perform simulations for single slip and multi-slip in 2D in order to test the domains of applicability of the Wilkens model

[450, 451, 452]. Traditionally [451, 452, 198, 199], the two-dimensional coherently diffracting domain is taken as an infinitely long cylinder. However it is difficult to divide the cylindrical domain into equal areas of equal size without either overlapping sub-domains or eliminating sub-domains with smaller areas [199]. In the context of the aim of this work *i.e.* study of the effects of strains, their distributions and higher order strain gradients on diffraction profile and to avoid the alterations to domain size and consequently dislocation density, an infinitely long rectangular cuboid with two square faces is chosen as the domain. A set of 32 infinitely long straight screw dislocations with Burgers vector $\vec{b} = \pm\frac{1}{2} [\mathbf{110}]$ are placed in the domain perpendicular to the square face of an area $2000a_0 \times 2000a_0$ resulting in a dislocation density of $4.88 \times 10^{13} m^{-2}$. Dislocations with such a Burgers vector are typically found in FCC materials. The domain is divided into 16 sub domains of areas $500a_0 \times 500a_0$. Each of these sub domains has 2 randomly placed dislocations with opposite Burgers vector. Such a configuration ensures that the sub domains have equal areas, same dislocation density and a zero net Burgers vector. A similar RRD configuration is used in a detailed statistical analysis to study dislocation screening effects on diffraction peaks in the works of Kaganer and Sabelfeld [196], and Levine and Thompson [246]. In the present work performing such an analysis is not intended; instead the microstructural configuration is used to show the differences between the three diffraction profile calculation methods.

The simulations are performed for 5 diffraction vectors allowed by the selection rules of an FCC lattice viz. $\mathbf{131}$, $\mathbf{11\bar{3}}$, $\mathbf{31\bar{3}}$, $\mathbf{311}$ and $\mathbf{31\bar{1}}$. A Gaussian filter is applied to the Fourier coefficients to dampen the termination ripples, and thus facilitate comparison with the reflections obtained by the Stokes-Wilson method. Applying a Gaussian filter is equivalent to convoluting the Fourier transform of that Gaussian to the peak shape. This convolution can be thought of as adding a computational instrumental broadening to the peak shapes. The standard deviation (σ) used in the

Gaussian is computed using the $I(\Delta\vec{g})$ and $|\Delta\vec{g}|$ values from the Fourier displacement method and the same Gaussian filter, with a range $[-3\sigma,3\sigma]$ with 150 binning intervals, is applied to all the intensities. For the sake of brevity however, only the intensities obtained from diffraction vectors $\mathbf{11\bar{3}}$ and $\mathbf{31\bar{3}}$ are illustrated in figure 6.8.
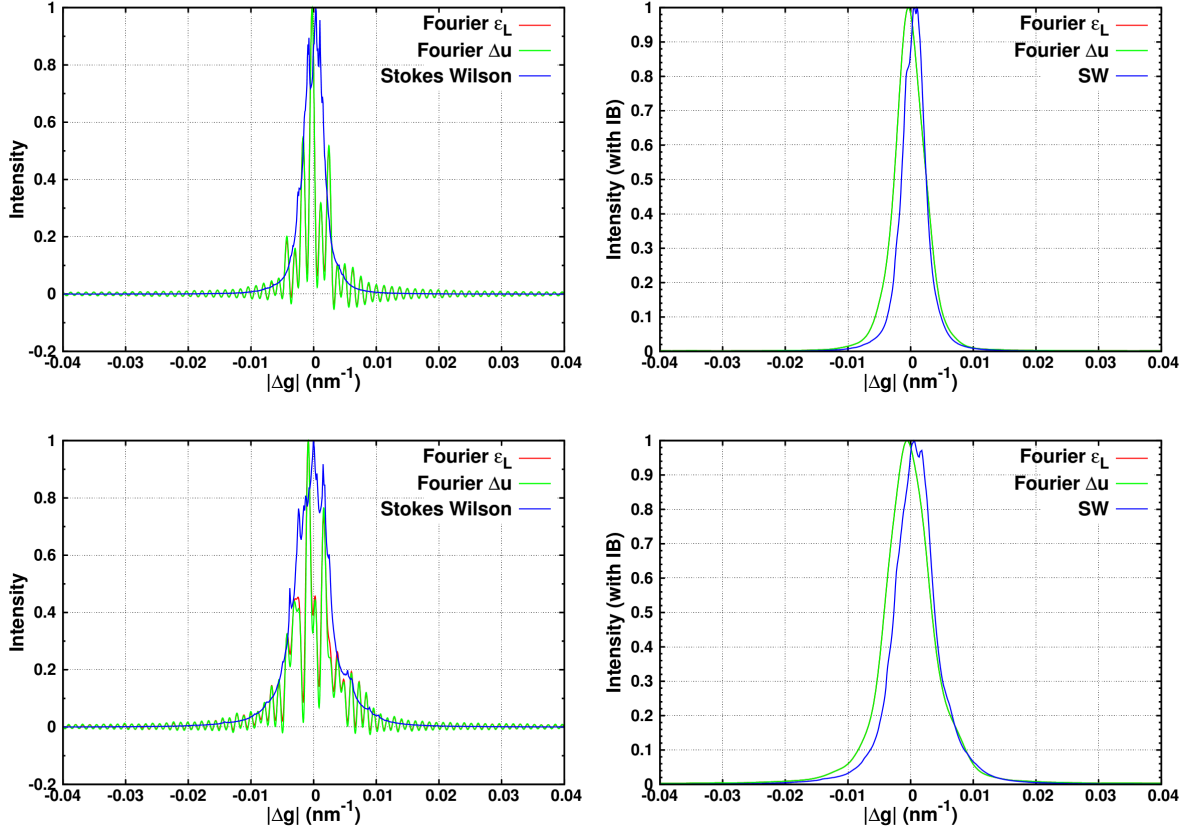
Figure 6.8: Comparison of normalized unfiltered and filtered i.e. with instrumental broadening - intensity from Fourier averaged strain (Fourier ϵ^L), Fourier displacement (Fourier $\Delta\vec{u}$) method, and PDF of strain from Stokes-Wilson approximation (SW) for RRD of 32 screw dislocations with Burgers vector $\vec{b} = \pm\frac{1}{2}[\mathbf{110}]$ in a 2000 a_0 x 2000 a_0 simulation box divided in 16 sub domains for diffraction vectors (a), (b) $\vec{g} = \mathbf{11\bar{3}}$, and (c), (d) $\vec{g} = \mathbf{31\bar{3}}$.

The plots show that for diffraction vectors $\vec{g} = \mathbf{11\bar{3}}$ and $\mathbf{31\bar{3}}$, there is an excellent match between the diffraction peaks generated using the Fourier based methods; in fact an overlap of these peaks is observed after filtering. Following the discussion in section 6.3, this similarity occurs because the additional exponential term

$\exp\left(2\pi i \vec{\boldsymbol{g}} \cdot n\vec{\boldsymbol{b}}\right)$ does not contribute to the diffraction peaks; here n is an integer representing the number of surface cuts between two particular points that are used to compute the difference in displacement for a given $\vec{\boldsymbol{L}}$. With the diffraction vectors $\vec{\boldsymbol{g}} = \mathbf{11\bar{3}}$ and $\mathbf{31\bar{3}}$ and Burgers vector $\vec{\boldsymbol{b}} = \frac{1}{2}\,[\mathbf{110}]$ the inner product $2\pi\vec{\boldsymbol{g}} \cdot n\vec{\boldsymbol{b}}$ becomes a multiple of $2\pi n$ and therefore it does not contribute to the diffraction peaks.

With respect to the intensity obtained from Stokes-Wilson approximation, the conformity with peaks obtained from Fourier strain based method for the studied diffraction vectors $\vec{\boldsymbol{g}} = \mathbf{11\bar{3}}$ and $\mathbf{31\bar{3}}$, is better than the single dislocation case but not as good as in the case of LAGB; the percentage difference in integral breadths being 15.54% and 19.72%, respectively for the aforementioned diffraction vectors. These conformities in profiles can be attributed to the variation in strain along the direction of the diffraction vector. In the direction of diffraction vectors used here the apparent strain distributions and the gradients may not be significant to have a large contribution to broadening of the peak generated from the Fourier methods. It is not just the presence of a particular strain distribution or strain gradients that warrants for peak broadening, but also their visibility along the direction of the diffraction vector; a phenomenon that can be explained by the dislocation contrast factors [417, 415].

Asymmetry of the profiles is caused by the elastic strains induced in presence of dislocations [419, 287, 416]. This effect is captured by the peaks generated using the Stokes-Wilson approximation but becomes more pronounced in the peaks generated using the Fourier based methods, especially in the tails, highlighting the influence of strain distributions and strain gradients of displacement on the diffraction profiles.

Comparing the LAGB and RRD microstructures, the two main differences are the arrangement of dislocations and the nature of dislocations. The LAGB has geometrically necessary dislocations with net Burgers vector not equal to zero and the RRD has statistically stored dislocations with the net Burgers vector equal to zero.

Simulations were performed on the RRD to test if modifying the net Burgers vector has a consequence on the diffraction peaks generated. In the modified RRD configuration all dislocations were assigned the same Burgers vector such that the net Burgers vector magnitude was now equal to $16\sqrt{2}a_0$. Similar to the original RRD configuration, results (not shown here to avoid redundancy) revealed a good match for the diffraction profiles, however no effect of the non-zero net Burgers vector could be extrapolated. Simulations were repeated for the original and modified RRD with edge dislocations, but similar to the previous case no dependence of the diffraction peak shape on the net Burgers vector could be extrapolated. Strain distribution arising from screening of the stress fields of dislocations - depending on their arrangement - is the dominating factor in determining the evolution of diffraction profiles.

6.3.3 Dislocation discontinuity surface cut

In the previous section, all the reflections that were studied correspond to the allowed reflections in cubic crystals. It is observed that for the reflections studied there is no difference between the two Fourier based methods indicating that the dislocation discontinuity surface cut does not contribute to broadening of peaks. In fact, for all combinations of allowed reflections and Burgers vectors in cubic crystals, the exponential term $\exp\left(2\pi i \vec{\boldsymbol{g}} \cdot \vec{\boldsymbol{b}}\right)$ and hence the surface cut do not contribute to the broadening of peaks.

In order to study the significance of the surface cut and its orientation in the case when $\exp\left(2\pi i \vec{\boldsymbol{g}} \cdot \vec{\boldsymbol{b}}\right) \neq 1$, $I(\Delta\vec{\boldsymbol{g}})$ vs. $\Delta\vec{\boldsymbol{g}}$ profiles are re-plotted in the case of RRD simulations (similar to the ones in section 6.3) for one forbidden reflection in cubic crystals corresponding to $\vec{\boldsymbol{g}} = \boldsymbol{101}$. This forbidden reflection yields $\exp\left(2\pi i \vec{\boldsymbol{g}} \cdot \vec{\boldsymbol{b}}\right) \neq 1$ and is compared with two allowed reflection $\vec{\boldsymbol{g}} = \boldsymbol{11\bar{3}}$ and $\boldsymbol{31\bar{3}}$. Three simulations are performed for these diffraction vectors: 1) the surface cuts associated with all dislocations are oriented at 0º, similar to the work of deWit [96], 2) all surface cuts

oriented at 50° and 3) each dislocation has its own surface cut randomly assigned. The peaks are calculated using the Fourier displacement method and the Stokes-Wilson approximation. As expected the peaks obtained for the allowed reflections, $11\bar{3}$ and $31\bar{3}$, matched perfectly for all three surface cut orientation cases. Furthermore, there was no difference in the PDF of apparent elastic strain obtained from the Stokes-Wilson approximation for any of the above cases. For the sake of illustration, only one allowed reflection corresponding to g = $31\bar{3}$ is compared with the forbidden reflection g = 101 in figure 6.9.
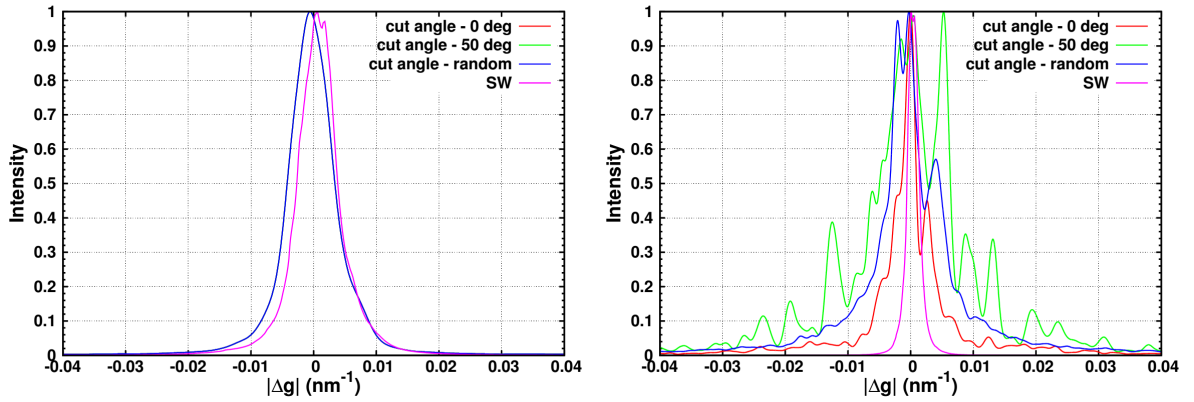
Figure 6.9: Comparison of filtered diffraction peaks obtained from an RRD with 32 screw dislocations along the [110] slip direction and Burgers vector $\frac{1}{2}[\mathbf{110}]$ for the allowed reflection with diffraction vector a) $\vec{g} = \mathbf{31\bar{3}}$ and the forbidden reflection with diffraction vector b) $\vec{g} = \mathbf{101}$ using the Fourier displacement method for surface cuts oriented at 0° (cut angle 0 deg), 50° (cut angle - 50 deg) and randomly (cut angle - random) assigned for each dislocation with the Stokes-Wilson approximation (SW)

Interestingly, there are significant differences found between the peaks obtained for the diffraction vector g = 101 for which $\exp\left(2\pi i \vec{g} \cdot \vec{b}\right) \neq 1$. These differences illustrate the mathematical uncertainty associated with assigning an orientation to the surface cut and the corresponding error in using the displacement based Fourier method to generate diffraction peaks for the cases where $\exp\left(2\pi i \vec{g} \cdot \vec{b}\right) \neq 1$. Note that in FCC crystals, such differences in peak shapes associated with the surface cut are found only in the case of a few forbidden reflections. However, the presented

mathematical scenario can become a physical reality for certain structures; for example, some of the super-structure reflections of an L1$_2$ ordered alloy having superlattice dislocations would be susceptible to the problem. In L1$_2$ cubic structures the Burgers vector of a superlattice dislocation is $\vec{b} = \frac{1}{2}[\mathbf{110}]$ [84] and the $\mathbf{101}$ reflection is permitted: thus using the displacement based Fourier method to generate diffraction peaks for this particular case would be problematic.

An indirect consequence of the presence of surface cuts is the contribution of plastic strain history to the diffraction profiles. In order to understand this, reconsider the integral in equation (6.30) for the averaged apparent elastic strain: $\epsilon^L(x) = \frac{1}{|\vec{L}|} \int_{x-\frac{L}{2}}^{x+\frac{L}{2}} e^e(x)\, dx$. The methodology adopted in this work involves performing the integration over a straight line joining two points separated by the distance $\left|\vec{L}\right|$. Such a straight line integral is allowed because the apparent elastic strain used in this work is compatible *i.e.* $e = e^{\|}$. This compatible elastic strain is a state variable independent of the path of dislocation and hence unaffected by the presence and orientation of the surface cut. However, if incompatible strains are considered then dislocation path dependence is necessarily induced. From the incompatible theory of dislocations, incompatible elastic strains $e^{e\perp}$ are induced in the material due to the incompatible plastic strains $e^{p\perp}$ associated with the presence of dislocations with the necessary condition $e^{e\perp} = -e^{p\perp}$ to maintain the continuity of the material [2]. These incompatible plastic strains are associated with the surface cut through the symmetric component of the incompatible plastic distortion tensor ($\boldsymbol{U}^{p\perp}$) where the latter is defined as $U_{kl}^{p\perp}(\vec{r}) = -\delta_k\left(\vec{S}\right)b_l$, as shown in equation (2.14). The symbol $\vec{S}$ corresponds to a 3-dimensional surface bounding the dislocation line which in the static 2-dimensional case for an infinitely long straight dislocation becomes the semi-infinite surface cut, r is a point in space and δ is the Dirac-Delta function on the surface $\vec{S}$. The relationship of this 3-dimensional surface $\vec{S}$ with the plastic distortion $U^{p\perp}$ indicates that its shape and orientation may depend on the history of

294

plastic strain in the material; a hypothesis that remains to be rigorously proven. If such dependence were to be obtained then the integral in equation (6.30) could yield different results depending on the path chosen, provided the incompatible elastic strains are accounted for.

In the displacement based Fourier method where the equilibrium solution of multi-valued elastic displacements is taken, the only possible way that the path dependence could affect the diffraction profile is through the surface cuts. However, in the 2-dimensional static formulation adopted here, since the surface cut orientations can be arbitrarily assigned, the displacement based Fourier method may not be reliable for those combinations of diffraction and Burgers vectors where $\exp\left(2\pi i \vec{g} \cdot \vec{b}\right) \neq 1$. This problem of orienting the surface cut can be avoided by using the out of core compatible elastic strains in the average strain based Fourier method to obtain the diffraction profile. To account for the presence of surface cuts and consequently the plastic strain history in the average strain based Fourier method, the in-core incompatible elastic strains need to be considered. Interestingly, in the case of FCC crystal lattices one finds that all the combinations of allowed reflections and dislocation Burgers vectors lead to $\exp\left(2\pi i \vec{g} \cdot \vec{b}\right) = 1$, indicating that in this very particular case the diffraction peaks are independent of the surface cut and hence the plastic strain history.

6.4 Diffraction as a characterization technique

The work considers existing diffraction peak generating methods that link the kinematic theory of diffraction to the theory of defects. From a continuum standpoint, generating virtual diffraction peaks from distorted crystals has so far been achieved using either the displacement based Fourier transform method or the Stokes-Wilson approximation. In the case of dislocation microstructures, Kamminga [198, 199] used the closed form equilibrium solution of elastic displacements of infinitely long straight

dislocations in the Fourier transform method to simulate X-ray diffraction peaks associated with the presence of RRDs of infinitely long and straight dislocations - similar to those assumed by Wilkens [450] -. The numerical and semi-analytical models showed relatively good agreement. However, the present study has revealed that in using the displacement based method, there is a degree of complexity and uncertainty involved due to the multi-valued nature of elastic displacements induced in presence of line crystal defects. This precludes the use of the displacement based method for specific material systems. Furthermore, this method cannot be applied to the a fully continuous framework where the displacement fields are undefined. On the other hand, the approximate Stokes-Wilson method has been used by Wilson [459] to derive an analytical expression of diffraction line profiles due to the presence of an infinitely long screw dislocation contained in a cylindrical volume. In another work, Wilson [460] adopted the Stokes-Wilson approximation to provide a simple strain based expression of the intensity. Similarly, the case of a single edge dislocation was treated in the work of Vassamillet [431]. The Stokes-Wilson method, however, uses a stringent approximation in neglecting the effects of strain gradients on broadening and therefore limit their applibility to selected cases. A recent work by Kaganer and Sabelfeld [197] has shown that the Stokes-Wilson approximation is applicable only in cases where long-range order in strain distributions is absent.

A new average strain based method is developed that avoids the problem of multi-valued displacements, accounts for the higher gradients of strains and has a wider domain of applicability. The method can be used to generate virtual diffraction peaks from both fine and meso-scale plasticity models that are based either on a discrete representation of defects such as discrete dislocatio dynamics models [224, 92, 479, 360, 142, 449, 53, 36] or a fully continuous approach based on incompatibilities such as the one presented in this work.

The trade-off between the accuracy and the demand for computational power of

the three methods is discussed based on the applications to (1) a single screw dislocation, (2) a low angle symmetric tilt grain boundary and (3) restrictedly random distribution of dislocations. The Stokes-Wilson approximation is computatationally the fastest but least accurate method, while the Fourier method based on average strains is the slowest but accurate and the most robust. Virtual peak profiles generated from simulation cells of known dislocation configurations can be evaluated by various line profile analysis procedures: either by methods based on the Wilkens approach [451, 452, 476, 404, 229, 152, 418, 413, 413, 414], or by moment based methods [151, 48], or by early techniques like the Warren-Averbach method [447, 448]. The characteristics of the dislocation structure determined using the above mentioned methods can then be compared with the known values from the simulated configurations in order to explore the boundaries and capabilities of the evaluation methods for various microstructural scenarios.

The three aforementioned methods can be thought of as bottom-up approaches where virtual diffraction peaks are developed from a known microstructure. On the other hand, top-down approaches such as the X-ray and neutron diffraction line profile analysis (LPA) exist and are widely used to extract statistical microstructural features, such as sub-grain (coherently diffracting domain) size, dislocations, twinning and stacking faults, from the shape of diffraction peaks. Because LPA provides information about dislocation density and dislocation configurations, it is a valuable tool for both experimental material characterization and for benchmarking constitutive models based on dislocation densities.

The LPA technique was introduced in the fundamental work of Krivoglaz [214], Wilkens [450, 451, 452] and Groma and co-workers [152, 150] who intended to develop analytical or semi-analytical links between dislocation densities, their arrangements and the diffraction line profile. These developments typically establish first (1) a relationship between diffraction line profile and strain fields [384, 444, 445, 446] and

then, (2) a relationship between moments of the strain fields (*i.e.* average, variance) and dislocation density distributions [214, 450, 451, 452, 152, 150].

The first steps along this path are found in the work of Warren and Averbach [447, 448] who separated the strain and diffracting domain size contributions to the diffraction peaks using the Fourier transform of intensity. Their idea was to deconvolute the measured intensities into contributions coming from crystallite size effects and lattice distortions by simplifying the expression of the distortion Fourier coefficient. They argued that for small values of $\vec{g} \cdot \Delta \vec{u}$, the distortion Fourier coefficient which is the average of cosine function can be expanded as a power series $A^D(\vec{L}) = < \cos\left(2\pi\vec{g} \cdot \Delta\vec{u}(\vec{L})\right) >= 1 - 2\pi^2|\vec{g}|^2|\Delta\vec{u}(\vec{L})|^2 + O(|\vec{g}|^4)$. For small values of $|\vec{g}|$ and $|\vec{L}|$, $O(|\vec{g}|^4)$ may be neglected. Taking the natural log of $A^D(\vec{L})$ and performing a binomial expansion along with rejection of higher order terms gives the following expression

$$\ln A^D(\vec{L}) = -2\pi^2|\vec{g}|^2 \left\langle |\Delta\vec{u}(\vec{L})| \right\rangle^2 \tag{6.35}$$

The difference in displacement can be defined in terms of ϵ^L from equation (6.12) as

$$\ln A^D(\vec{L}) = -2\pi^2|\vec{g}|^2 \left\langle \epsilon \right\rangle^2 |\vec{L}|^2 \tag{6.36}$$

Equations (6.35) and (6.36) are both known as the Warren Averbach solutions. In general, they are only valid for very small values of $\vec{g} \cdot \vec{L}$. However, if a Gaussian strain distribution is assumed then they are valid for any value of $\vec{g} \cdot \vec{L}$ [446]. It should be noted that the Warren Averbach method assumes the sine distortion Fourier coefficient is equal to zero.

Based on these developments, Krivoglaz [214] proposed a relationship between mean square strain and dislocation density for a random set of infinitely long and straight dislocations. However, the deficiency of Krivoglazs approach is that the random set of dislocations leads to a diverging mean square strain and thus a diverging

stored energy density if the size of the crystal is increased while the dislocation density is constant. Wilkens [450, 451, 452] solved this problem by introducing the concept of RRD as a representative microstructure for material systems. However, the dislocation distribution used by Wilkens has several limitations; the most severe being the prediction of symmetrical line profiles which led to the development of other models.

Reliability of the Warren Averbach method for LPA purposes in case of dislocation structures has also been questioned in the work of Wilkens [453] and Langford *et al.* [229]. For a particular diffraction vector it is possible that there are large variations in strain for distances. These effects can be captured by only if is allowed to scale the entire domain. Besides these, other errors Treatment for some of the errors such as truncation of intensity profiles, background determination, counting statistics, etc. are dealt in the work of Young *et al.* [475], Delhez *et al.* [86], among others. Improvement procedures for this method are also discussed in the work of Zorn and Aust [485] and Delhez *et al.* [87].

X-ray line broadening in plastically deformed [001] Cu crystals [419] was studied based on Wilkens theoretical work and a new composite model of dislocations introduced by Mughrabi [285]. Following which, Groma and coworkers [152, 418] developed a theory to interpret the asymmetric line broadening of plastically deformed crystals and applied it to [001] Cu crystals. Groma and Székely [151] showed that it was possible to obtain dislocation density from tails of line profiles without assuming any particular dislocation distribution. More recently, the extended Convolutional Multiple Whole Profile (eCMWP) procedure, has been very effectively used to characterize the microstructure and dislocation structure of polycrystals and single crystals [48, 326, 327].

In the more recent work of Balogh *et al.* [24], the Stokes-Wilson approximation was used to perform diffraction simulations of more realistic microstructures resulting

from co-planar slip of dislocations in face centered cubic (FCC) systems. Discrete dislocation dynamics was used to generate the microstructures and the diffraction peaks, calculated using the Stokes-Wilson approximation, were analyzed with the eCMWP software package [326]. An error in the range of 20% was reported for the evaluated dislocation densities. However, it is unclear whether the error contributions came solely from the line profile analysis or a part is induced at an earlier stage while generating the diffraction peaks using the Stokes-Wilson approximation which neglects the contribution of strain distributions and gradients. The fact that peaks represent information originating from different regions within a grain and from several grains suggests that details of the underlying structure may be lost in the averaging process used in eCWMP. The accuracy of LPA models can be tested using the averaged strain based model presented in this work.

The averaged strain based model in its present state is incapable of accounting for the size Fourier coefficient $A^S(\vec{L})$ contributions to the broadening of peaks. The problem mainly arises due to the continuum approach chosen where the position of atoms, which is necessary to account for the size effect, cannot be uniquely known. To that end motivation can be taken from a recent work by Coleman *et al.* [78], who developed an algorithm to generate virtual diffraction peaks during atomistic simulations of [010] STGBs via the explicit evaluation of the structure factor in equation (6.5) without *a priori* knowledge of the GB unit cell. On one hand this method is similar to the averaged strain based method with respect to its applicability to both electron and x-ray diffraction conditions. On the other hand, unlike the new averaged strain based formulation, the atomistic method incorporates both the size and strain contributions to broadening. However, these contributions cannot be separated like in the continuum model. For domain sizes in the nano-meter range where the size effects are dominant, the size coefficient $A^S(\vec{L})$ contribution can be separated from the total Fourier coefficient $A(\vec{L})$ obtained from the atomistic model by removing the

300

distortion Fourier coefficient $A^D(\vec{L})$ contribution from it. This will be pursued in a future study.

6.5 Conclusion

The present study is performed for two main purposes, 1) to better understand the fundamental implications on virtual diffraction peak generation coming from combining the incompatible theory of dislocations with the kinematic theory of diffraction and, 2) to understand the domains of applicability of these three virtual diffraction peak generation techniques and their similarities and differences. In order to study this, a numerical tool to generate virtual diffraction profiles from continuous crystalline media containing line defects is developed based on: (1) the approximation of Stokes and Wilson [384], (2) the Fourier method based on displacements [444, 445, 446], and (3) a new Fourier method based on average strains.

From a theoretical standpoint, firstly, it is found that only elastic strains and their gradients contribute to broadening of diffraction profiles; elastic rotation, curvature and its gradients, have no contribution to broadening. Secondly, with respect to the static formulation of incompatible theory of dislocations, a fundamental difference arises between the two Fourier methods. The displacement based Fourier method requires the definition of an arbitrarily oriented surface representative of the displacement discontinuity induced in presence of a dislocation. Interestingly, in the specific case of FCC lattices studied here, changing the orientation does not affect the reflections. However, in the case of certain systems this mathematical issue would persist: for example, some super-structure reflections of $L1_2$ ordered alloys having super lattice dislocations would be susceptible to the problem. The average strain based Fourier method is not affected by the orientation of this surface and therefore gives the exact solution.

Application to FCC crystals having infinitely long straight defects in the form of i)

a single screw dislocation, ii) low angle tilt GB, iii) RRD of dislocations highlights the importance of spatial distributions of strain and their gradients to the diffraction profiles and help identify those microstructural configurations where the Stokes-Wilson approximation [384] does not provide an accurate diffraction profile. Furthermore, it is found that for the combination of allowed reflections and Burgers vectors in FCC lattice, the displacement based Fourier method and the average strain based Fourier method provide the exact same solution. The results shown in this chapter generally agree with the results in the literature, in that in the presence of crystal lattice defects internal strain fields are induced which lead to broadening or shifts in diffraction peaks [419, 287, 416, 414].

CHAPTER VII

CONCLUSIONS

The present research aimed at using a continuous constitutive framework to investigate the role of incompatibilities in strains and curvatures – defined at the inter-atomic, fine, and meso scales– on the local energy and microstructure, and the bulk mechanical response of nc/ufg materials. The idea was to test if incompatibilities in geometric fields, specifically in lattice curvature, could be used as multi-scale metrics for capturing information on local energy and microstructure at the inter-atomic and fine scales and transmit it to meso scale. The methodology used to achieve this is rather counter-intuitive because it involves using a continuous approach to model the dynamics of defects at a length scale where the matter's nature is inherently discrete. The challenges faces during this thesis were to (1) research and adopt/develop a kinematically and thermodynamically rigorous framework to account for the incompatibilties in strain and curvature at the inter-atomic, fine and meso scales, (2) understand the role of these incompatibilities on the geometry and energy of the local microstructure, (3) understand the contribution of residual curvatures on the meso and macro scale bulk mechanical response, (4) test if these incompatibilities can be characterized using X-ray or neutron diffraction, and (5) based on all the results obtained from the above challenges, assess whether curvatures can be treated as multi-scale metrics for nc plasticity.

The first challenge highlights the need for a kinematically and thermomechanically rigorous theoretical formulation for capturing the role of incompatibilities at inter-atomic, fine and meso scales. To that end, the modelling framework adopted was based on continuous representation of dislocations and disclinations. This approach

which accounts for the incompatibilities in lattice strains and curvatures is found to be the most appropriate to achieve the aim of this thesis. New higher order/grade elastic constitutive laws, based on the incompatible framework were proposed to account for the Cauchy and couple stress contributions coming from incompatibilities in elastic strain and curvature at the fine and meso scales. These laws form an integral part of the fine scale field disclination and dislocation mechanics theory that accounts for polar dislocation and disclination contributions to local plasticity. At the meso-scale, a phenomenological field disclination and dislocation mechanics model is proposed that accounts for statistical dislocation and disclination contributions to plasticity, in addition to those coming from polar defect densities. The fine and meso scale models allow for a kinematically rigorous continuous treatment of interfaces and junctions at both these scales by respecting compatibility conditions on elastic and plastic strain and curvature at the interfaces.

In order to understand the role of strain and curvature incompatibilities on the geometry and energy of the local microstructure, the multi-scale model is applied at the fine scale to the case of <001> STGBs and TJs. Incompatible elastic strains that manifest themselves within the defect cores are found to have the most significant contribution to the elastic energy. Their contribution to the elastic energy is captured through the higher order/grade elastic constitutive laws developed in this work. On the other hand, the energetic contrbution of incompatible curvatures is negligible. However, curvatures incompatibilities are necessary to characterize the GB geometry.

Static simulations were performed to generate TJ energy vs. misorientation maps for TJs constructed from <001> STGBs. Results revealed that TJ configurations corresponding to Herring's relationship, respecting kinematic constraints, and compatibility conditions on elastic strain and curvature, did not belong to a global minimum. Quite interestingly, the global minimum excess energy TJ configuration conisted of high angle GBs. Some TJ configurations were found to have a negative

excess energy contribution. For these triple junctions the elastic curvature, and consequently couple stress, contribution to the elastic energy was notably large compared to higher energy TJ configurations. This suggests that elastic curvatures could be generated as a consequence of relaxation mechanisms possibly through the nucleation of sub-grain boundaries, new grains, disclinations, twins.

Using the knowledge gained from fine-scale applications, the multi-scale model was then applied at the meso-scale to study the importance of residual curvatures on the local and macro scale mechanical response of nc materials. Presence of residual curvatures results in the generation of large fluctuations in local Cauchy and couple stresses. These could play an important role in the activation of rare events such as nucleation of new grains, twins, etc. Furthermore, these residual curvatures are found to lower the saturation point of the macroscopic Cauchy stress response; a softening effect that could explain the breakdown in the Hall-Petch relationship.

Finally, tests were then performed to see if incompatibilities can be characterized using X-ray or neutron diffraction. It is found that only elastic strains and their gradients contribute to broadening of diffraction profiles; elastic rotation, curvature and its gradients, have no contribution to broadening.

Assessing the results obtained from each study, it can be concluded that lattice curvatures definitely qualify to be treated as multi-scale metrics for nc plasticity.

APPENDIX A

G-DISCLINATIONS: ELASTIC LAWS

Generalized disclinations or g-disclinations are a new type of line crystal defects, introduced in the work of Acharya and Fressengeas [5], that go beyond the Volterra construct of dislocations and conventional disclinations; henceforth Volterra's disclinations shall be addressed as conventional disclinations. In the presence of g-disclinations, a discontinuity in the entire elastic distortion tensor $[\boldsymbol{U}^e]$ is induced. This concept was introduced to model phase transformations where a discontinuity in elastic distortion across the inter-phase boundaries cannot be appropriately described using dislocations and conventional disclinations. In this chapter, the aim is to develop elastic constitutive laws that can account for the presence of g-disclinations. First, the geometric fields related to g-disclinations in simply connected body are derived in a fully continuous framework. Second, the expressions for elastic constitutive laws in linear anisotropic elasticity are then proposed.

A.1 Geometric fields of g-disclinations

Let $\boldsymbol{G}$ - the 2-distortion tensor - define the second gradient of the compatible total dislocation field:

$$\boldsymbol{G} = \mathbf{grad\ grad\ } \boldsymbol{u} = \mathbf{grad\ } \boldsymbol{U} \quad \text{or} \quad G_{ijk} = u_{i,jk} = U_{ij,k} \tag{A.1}$$

It can be decomposed into a symmetric tensor and a third-order anti-symmetric curvature tensor as,

$$\boldsymbol{G} = \boldsymbol{G}^s + \tilde{\boldsymbol{\kappa}}^a \quad \text{or} \quad G_{ijk} = G_{(ij)k} + \tilde{\kappa}_{[ij]k} \tag{A.2}$$

In the presence of g-disclinations, the total 2-distortion tensor can be decomposed

306

into elastic and plastic components:

$$\boldsymbol{G} = \boldsymbol{G}^e + \boldsymbol{G}^p \quad \text{or} \quad G_{ijk} = G_{ijk}^e + G_{ijk}^p \tag{A.3}$$

The elastic and plastic components of the 2-distortion tensor can be decomposed into compatible and incompatible contributions in presence of g-disclinations using the Stokes-Helmholtz decomposition,

$$\boldsymbol{G}^e = \boldsymbol{G}^{e\|} + \boldsymbol{G}^{e\perp} \quad \text{or} \quad G_{ijk}^e = G_{ijk}^{e\|} + G_{ijk}^{e\perp} \tag{A.4}$$

$$\boldsymbol{G}^p = \boldsymbol{G}^{p\|} + \boldsymbol{G}^{p\perp} \quad \text{or} \quad G_{ijk}^p = G_{ijk}^{p\|} + G_{ijk}^{p\perp} \tag{A.5}$$

The compatibility of the total 2-distortion requires that the sum of the incompatible elastic and plastic 2-distortions is equal to zero:

$$\boldsymbol{G}^{e\perp} + \boldsymbol{G}^{p\perp} = 0 \quad \text{or} \quad G_{ijk}^{e\perp} + G_{ijk}^{p\perp} = 0 \tag{A.6}$$

Using equations (2.98) and (A.2) the following relationship between the 2-distortion tensor the dislocation density field can be derived

$$\boldsymbol{\alpha} = 2\mathbf{X}(\boldsymbol{G}^e) \quad \text{or} \quad \alpha_{ij} = e_{mni} G_{mnj}^e \tag{A.7}$$

The polar g-disclination density can be defined as,

$$\mathbf{curl}\,\boldsymbol{G}^e = -\mathbf{curl}\,\boldsymbol{G}^p = \boldsymbol{\pi} \quad \text{or} \quad e_{kmn} G_{ijn,m}^e = -e_{kmn} G_{ijn,m}^p = \pi_{ijk} \tag{A.8}$$

Then the compatibility condition on this density is given as:

$$\mathbf{div}\,\boldsymbol{\pi} = \nabla \cdot \boldsymbol{\pi} = 0 \quad \text{or} \quad \pi_{ijk,k} = 0 \tag{A.9}$$

The incompatible plastic 2-distortion should vanish identically throughout the body when the polar disclination density is equal to zero. This enforces augmented conditions on the incompatible plastic 2-distortion:

$$\mathbf{div}\,\boldsymbol{G}^{p\perp} = 0 \quad \text{or} \quad G_{ijk,k}^{p\perp} = 0, \quad \text{in } V \quad \text{and}$$

$$\boldsymbol{G}^{p\perp} \cdot \vec{\boldsymbol{n}} = 0 \quad \text{or} \quad G_{ijk}^{p\perp} n_k = 0, \quad \text{on } \boldsymbol{S} \tag{A.10}$$

A.2 Elastic laws for a simply connected body subjected to surface tractions and surface hyper-traction tensors

Let a simply connected body containing an arbitrary distribution of dislocations and g-disclinations be subjected to elastic deformation under the action of a surface traction vector $\vec{t}$ and a surface hyper-traction tensor $\boldsymbol{\lambda}$ whose anti-symmetric part corresponds to the moment on its surface. This tensor $\boldsymbol{\lambda}$ is related to the surface moments and third order hyper-stress tensor M as

$$\boldsymbol{\lambda} = \tilde{\boldsymbol{M}} \cdot \vec{n} \tag{A.11}$$

$$\vec{m} = \boldsymbol{X}\left(\boldsymbol{\lambda}\right) \tag{A.12}$$

The equations of balance of mass (3.1), momentum (3.2) and moment of momentum (3.9) and correspondingly the equilibrium equation (3.14) are always respected. Under the action of the traction and surface hyper-traction tensor, the dissipation is given by

$$D = \int_{S} \left(\vec{v}^{t} \cdot \vec{t} + \dot{\boldsymbol{U}} : \boldsymbol{\lambda} \right) dS - \int_{V} \dot{\psi} dV = 0 \tag{A.13}$$

where $\boldsymbol{U}$ is the second order distortion tensor induced under the action of surface hyper-traction tensor. Substituting equations (A.11) and (A.12) in (A.13) gives

$$D = \int_{S} \left(\vec{v} \cdot \boldsymbol{\sigma} \cdot \vec{n} + \dot{\boldsymbol{U}} : \tilde{\boldsymbol{M}} \cdot \vec{n} \right) dS - \int_{V} \dot{\psi} dV = 0 \tag{A.14}$$

Applying the divergence theorem gives

$$\begin{aligned} D &= \int_{V} \mathbf{div}\left(\vec{v} \cdot \boldsymbol{\sigma} + \dot{\boldsymbol{U}} : \tilde{\boldsymbol{M}} \right) dV - \int_{V} \dot{\psi} dV = 0 \\ &= \int_{V} \left(\vec{v} \cdot \mathbf{div}\,\boldsymbol{\sigma} + \mathbf{grad}\,\vec{v} : \boldsymbol{\sigma} + \mathbf{grad}\,\dot{\boldsymbol{U}} : \tilde{\boldsymbol{M}} + \dot{\boldsymbol{U}} : \mathbf{div}\,\tilde{\boldsymbol{M}} \right) dV - \int_{V} \dot{\psi} dV \end{aligned} \tag{A.15}$$

Using the equilibrium equation (3.7) and (3.10) gives

$$D = \int_{V} \left(\mathbf{grad}\,\vec{v}^{t} : \boldsymbol{\sigma} + \mathbf{grad}\,\dot{\boldsymbol{U}}^{t} : M + \dot{\boldsymbol{U}}^{t} : \mathbf{div} M \right) dV - \int_{V} \dot{\psi} dV = 0 \tag{A.16}$$

The force stress and third order hyper stress tensors can be separated into symmetric and anti-symmetric parts. Recall that the symmetric part of the gradient of velocity vector is the strain rate tensor which extracts the symmetric Cauchy stress from the asymmetric force stress tensor through the inner product. The anti-symmetric part of the gradient of velocity is the rotation rate tensor which extracts the anti-symmetric component of the force stress tensor. Similarly, the symmetric and anti-symmetric components of the gradient of distortion rate tensor extract the symmetric and anti-symmetric components of the third order hyper-stress tensor, respectively.

$$D = \int_V \left(\begin{array}{c} \dot{\boldsymbol{\epsilon}}^t : \boldsymbol{\sigma}^s + \dot{\boldsymbol{\omega}}^t : \boldsymbol{\sigma}^a + \mathbf{grad}\,\dot{\boldsymbol{\epsilon}}^t \vdots \tilde{\boldsymbol{M}}^s \\ + \mathbf{grad}\,\dot{\boldsymbol{\omega}}^t \vdots \tilde{\boldsymbol{M}}^a + \dot{\boldsymbol{\epsilon}}^t : \mathbf{div}\,\tilde{\boldsymbol{M}}^s + \dot{\boldsymbol{\omega}}^t : \mathbf{div}\,\tilde{\boldsymbol{M}}^a \end{array} \right) dV - \int_V \dot{\psi}\, dV = 0 \quad \text{(A.17)}$$

The gradient of elastic strain is symmetric with respect to its first two indices, i.e. $\epsilon_{(ij),k}$, therefore its conjugate, the third order hyper-stress component is also symmetric with respect to its first two indices $\tilde{M}_{(ij)k}$. Similarly, the components of third order hyper-stress tensor associated with the gradient of elastic rotation tensor are anti-symmetric with respect to its first two indices, i.e. $\tilde{M}_{[ij]k}$. Using equations (2.39) and (2.40) and rearranging the terms gives,

$$D = \int_V \left(\begin{array}{c} \dot{\boldsymbol{\epsilon}} : \boldsymbol{\sigma}^s + \dot{\vec{\boldsymbol{\omega}}} \cdot 2\boldsymbol{X}(\boldsymbol{\sigma}^a) + \mathbf{grad}\,\dot{\boldsymbol{\epsilon}} \vdots \tilde{\boldsymbol{M}}^s + \mathbf{grad}\,\dot{\vec{\boldsymbol{\omega}}} : 2\boldsymbol{X}\left(\tilde{\boldsymbol{M}}^a\right) \\ + \dot{\boldsymbol{\epsilon}} : \mathbf{div}\,\tilde{\boldsymbol{M}}^s + \dot{\vec{\boldsymbol{\omega}}} \cdot 2\boldsymbol{X}(\mathbf{div}\,\boldsymbol{M}^a) \end{array} \right) dV$$

$$- \int_V \dot{\psi}\, dV = 0 \quad \text{(A.18)}$$

In the absence of the symmetric part of the surface distortion tensor $\boldsymbol{U}$, the body is subjected only to surface tractions and moments. Thus the symmetric component of the third order hyper-stress tensor vanishes and equation (A.18) is to be compared with the dissipation equation (3.22). The correlation of the work conjugates of the gradient of rotation vector in these equations leads to the relationship between second order couple stresses and the anti-symmetric part of third order hyper-stresses given

309

by equations (3.35) and (3.36). Substituting for the anti-symmetric third order hyper-stress tensor, the term $2\boldsymbol{X}\left(\mathbf{div}\tilde{\boldsymbol{M}}^{a}\right)$ becomes $\mathbf{div}\boldsymbol{M}$. The gradient of the elastic strain tensor can be defined as the symmetric part of the third order 2-distortion tensor. As we only deal with the elastic deformations, the plastic strain rate is zero. Therefore only the elastic strain rate enters the expression of dissipation. The gradient of the rotation vector is the deviatoric second order curvature tensor; it extracts only the deviatoric component of the second order curvature tensor. Using the equilibrium equation (3.10) for couple stresses, the final expression of the dissipation reads

$$D = \int_{V} \left(\dot{\boldsymbol{\epsilon}}^{e} : \left(\boldsymbol{\sigma}^{s} + \mathbf{div}\ \tilde{\boldsymbol{M}}^{s} \right) + \left(\dot{\boldsymbol{G}}^{e} \right)^{s} : \boldsymbol{M}^{s} + \dot{\boldsymbol{\kappa}}^{e} : \boldsymbol{M} \right) dV - \int_{V} \dot{\psi} dV = 0 \quad (A.19)$$

In the absence of defects, the field variables - elastic strain, symmetric part of elastic 2-distortion tensor and the elastic curvature, are all compatible. In the sole presence of dislocations, the elastic strain has an additional incompatible component while the other state variables are compatible. In the presence of both dislocations and conventional disclinations, the elastic strain and curvature both have additional incompatible components, whereas the symmetric part of 2-distortion is compatible. In the presence of dislocations and G-disclinations, all the state variables have an additional incompatible component. An interesting peculiarity of equation (A.19) is the coupling of the symmetric part of the third order hyper-stress tensor with the elastic strain. The simplest form of free elastic energy density is chosen as:

$$\psi = \psi \left(\boldsymbol{\epsilon}^{e}, (\boldsymbol{G}^{e})^{s}, \tilde{\boldsymbol{\kappa}}^{e} \right) \quad (A.20)$$

Following the analogy from equations (3.25) and (3.26), the elastic constitutive laws are,

$$\boldsymbol{\sigma}^{s} + \mathbf{div}\ \tilde{\boldsymbol{M}}^{s} = \frac{\partial \psi \left(\boldsymbol{\epsilon}^{e}, (\boldsymbol{G}^{e})^{s}, \boldsymbol{\kappa}^{e} \right)}{\partial \boldsymbol{\epsilon}^{e}} \quad (A.21)$$

$$\tilde{\boldsymbol{M}}^{s} = \frac{\partial \psi \left(\boldsymbol{\epsilon}^{e}, (\boldsymbol{G}^{e})^{s}, \boldsymbol{\kappa}^{e} \right)}{\partial (\boldsymbol{G}^{e})^{s}} \quad (A.22)$$

$$\boldsymbol{M}^{D} = \frac{\partial \psi \left(\boldsymbol{\epsilon}^{e}, (\boldsymbol{G}^{e})^{s}, \boldsymbol{\kappa}^{e} \right)}{\partial \boldsymbol{\kappa}^{e}} \quad (A.23)$$

It directly follows from the form of dissipation equation (A.19) and the elastic laws (A.21) and (A.22) that the elastic strains tensor and the symmetric part of the 2-distortion tensor are coupled. When the distortion of the body is compatible, or when only dislocations are present, the symmetric part of the 2-distortion tensor $(\boldsymbol{G}^e)^s$ is the gradient of the elastic strain $(\mathbf{grad}\,\boldsymbol{\epsilon}^e)$. The anti-symmetric part of the 2-distortion tensor $(\boldsymbol{G}^e)^a$ equals the anti-symmetric third order curvature tensor $\boldsymbol{\kappa}^a$ and is related to the second order curvature tensor via equations (2.52) and (2.51). If g-disclinations are not present in the body, then the expressions of the Cauchy and couple stresses reduce to (3.25) and (3.26).

In order to derive the elastic laws in a linear case, the following quadratic form of free energy density is adopted

$$
\begin{aligned}
\psi = {} & \frac{1}{2}U^e_{(ij)}C_{(ij)(kl)}U^e_{(kl)} + U^e_{(ij)}B_{(ij)[kl]m}\kappa^e_{[kl]m} + \kappa^e_{[ij]k}D_{[ij]k(lm)}U^e_{(lm)} \\
& + \frac{1}{2}\kappa^e_{[ij]k}A_{[ij]k[lm]n}\kappa^e_{[lm]n} + U^e_{(ij)}E_{(ij)(kl)m}G^e_{(kl)m} + G^e_{(ij)k}F_{(ij)k(lm)}U^e_{(lm)} \\
& + \kappa^e_{[ij]k}H_{[ij]k(lm)n}G^e_{(lm)n} + G^e_{(ij)k}J_{(ij)k[lm]n}\kappa^e_{(lm)n} + \frac{1}{2}G^e_{(ij)k}K_{(ij)k(lm)n}G^e_{(lm)n}
\end{aligned} \qquad \text{(A.24)}
$$

The elastic constitutive laws are obtained by taking partial derivatives of the free energy density with respect to $U^e_{(pq)}$, $G^e_{(pq)r}$ and $\kappa^e_{[pq]r}$,

$$
\begin{aligned}
\sigma_{(pq)} + \tilde{M}_{(pq)r,r} = {} & C_{(pq)(kl)}U^e_{(kl)} + B_{(pq)[kl]m}\kappa^e_{[kl]m} \\
& + \kappa^e_{[ij]k}D_{[ij]k(pq)} + E_{(pq)(kl)m}G^e_{(kl)m} + G^e_{(ij)k}F_{(ij)k(pq)} \qquad \text{(A.25)}
\end{aligned}
$$

$$
\begin{aligned}
\tilde{M}_{(pq)r} = {} & U^e_{(ij)}E_{(ij)(pq)r} + F_{(pq)r(lm)}U^e_{(lm)} \\
& + \tilde{\kappa}^e_{[ij]k}H_{[ij]k(pq)r} + J_{(pq)r[lm]n}\kappa^e_{(lm)n} + K_{(pq)r(lm)n}G^e_{(lm)n} \qquad \text{(A.26)}
\end{aligned}
$$

$$
\begin{aligned}
\tilde{M}_{[pq]r} = {} & U^e_{(ij)}B_{(ij)[pq]r} + D_{[pq]r(lm)}U^e_{(lm)} \\
& + A_{[pq]r[lm]n}\kappa^e_{[lm]n} + H_{[pq]r(lm)n}G^e_{(lm)n} + G^e_{(ij)k}J_{(ij)k[pq]r} \qquad \text{(A.27)}
\end{aligned}
$$

The elastic field variables are compatible in absence of defects, the elastic strain has an additional incompatible contribution in the sole presence of dislocations, and in the presence of both dislocations and G-disclinations all the field variables have an

additional incompatible component. The elastic constants $\boldsymbol{A}$, $\boldsymbol{B}$, $\boldsymbol{C}$ and $\boldsymbol{D}$ fulfil the conditions (3.29) - (3.32) imposed by the symmetries of the associated field variables and the positive definiteness of the free energy density. Similar conditions can be extrapolated for the constants $\boldsymbol{E}$, $\boldsymbol{F}$, $\boldsymbol{H}$, $\boldsymbol{J}$ and $\boldsymbol{K}$.

APPENDIX B

HIGHER ORDER ELASTICITY TENSORS

B.1 Isotropic elasticity tensors

The expressions for isotropic tensors of order greater than 4 presented in [230, 192] and derived in [385] are revisited here. In the following, first the expressions for 5th order elasticity tensors $\boldsymbol{B}$ and $\boldsymbol{D}$ are developed following the methodology of Suiker and Chang [385]. This is followed by the expression of 6th order tensor $\boldsymbol{A}$

The relationship between the 5th order isotropic tensor B_{ijklm} and the formal orthogonal invariant polynomial function $\boldsymbol{B}\left(\boldsymbol{u^{(1)}}, \boldsymbol{u^{(2)}}, \boldsymbol{u^{(3)}}, \boldsymbol{u^{(4)}}, \boldsymbol{u^{(5)}}\right)$ associated with vectors $\boldsymbol{u^{(1)}}$, $\boldsymbol{u^{(2)}}$, $\boldsymbol{u^{(3)}}$, $\boldsymbol{u^{(4)}}$ and $\boldsymbol{u^{(5)}}$ is,

$$\boldsymbol{B}\left(\boldsymbol{u^{(1)}}, \boldsymbol{u^{(2)}}, \boldsymbol{u^{(3)}}, \boldsymbol{u^{(4)}}, \boldsymbol{u^{(5)}}\right) = B_{ijklm}u_i^{(1)}u_j^{(2)}u_k^{(3)}u_l^{(4)}u_m^{(5)} \tag{B.1}$$

The function $\boldsymbol{B}\left(\boldsymbol{u^{(1)}}, \boldsymbol{u^{(2)}}, \boldsymbol{u^{(3)}}, \boldsymbol{u^{(4)}}, \boldsymbol{u^{(5)}}\right)$ can be written as a linear combination of the independent basic invariants [385] as:

$$
\begin{aligned}
B&(u^{(1)}, u^{(2)}, u^{(3)}, u^{(4)}, u^{(5)}) \\
&= \mathrm{B_1} \det\left[u^{(1)}, u^{(2)}, u^{(3)}\right] F\left(u^{(4)}, u^{(5)}\right) + \mathrm{B_2} \det\left[u^{(1)}, u^{(2)}, u^{(4)}\right] F\left(u^{(3)}, u^{(5)}\right) \\
&+ \mathrm{B_3} \det\left[u^{(1)}, u^{(2)}, u^{(5)}\right] F\left(u^{(3)}, u^{(4)}\right) + \mathrm{B_4} \det\left[u^{(1)}, u^{(3)}, u^{(4)}\right] F\left(u^{(2)}, u^{(5)}\right) \\
&+ \mathrm{B_5} \det\left[u^{(1)}, u^{(3)}, u^{(5)}\right] F\left(u^{(2)}, u^{(4)}\right) + \mathrm{B_6} \det\left[u^{(1)}, u^{(4)}, u^{(5)}\right] F\left(u^{(2)}, u^{(3)}\right) \\
&+ \mathrm{B_7} \det\left[u^{(2)}, u^{(3)}, u^{(4)}\right] F\left(u^{(1)}, u^{(5)}\right) + \mathrm{B_8} \det\left[u^{(2)}, u^{(3)}, u^{(5)}\right] F\left(u^{(1)}, u^{(4)}\right) \\
&+ \mathrm{B_9} \det\left[u^{(2)}, u^{(4)}, u^{(5)}\right] F\left(u^{(1)}, u^{(3)}\right) + \mathrm{B_{10}} \det\left[u^{(3)}, u^{(4)}, u^{(5)}\right] F\left(u^{(1)}, u^{(2)}\right)
\end{aligned}
\tag{B.2}
$$

Substituting the equations $\det\left[u^{(i)}u^{(j)}...u^{(m)}\right] = e_{ij...k}u_i^{(1)}u_j^{(2)}...u_k^{(m)}$ and the Kronecker delta gives,

$$
B_{ijklm} = \left(
\begin{aligned}
&B_1 e_{ijk}\delta_{lm} + B_2 e_{ijl}\delta_{km} + B_3 e_{ijm}\delta_{kl} + B_4 e_{ikl}\delta_{jm} + B_5 e_{ikm}\delta_{jl} \\
&+ B_6 e_{ilm}\delta_{jk} + B_7 e_{jkl}\delta_{im} + B_8 e_{jkm}\delta_{il} + B_9 e_{jlm}\delta_{ik} + B_{10} e_{klm}\delta_{ij}
\end{aligned}
\right)
\tag{B.3}
$$

In the general case, the tensor B_{ijklm} has $3^5 = 243$ non-zero independent coefficients. However in the isotropic case these reduce to only 10 independent non-zero coefficients. This is derived from the principle of objectivity.

Following a similar spectral decomposition with respect to the coefficients ij and kl as for C_{ijkl} gives,

$$B_{ijklm} = B_{(ij)(kl)m} + B_{(ij)[kl]m} + B_{[ij](kl)m} + B_{[ij][kl]m} \qquad \text{(B.4)}$$

A spectral decomposition of such a kind involving only the specific pairs of indices ij and kl is obtained from the knowledge of the symmetries of the terms associated with it. From the adopted form of free energy density (3.28) the only contribution of the cross term involving $\boldsymbol{B}$ comes from the 2nd term in the above relationship. Considering the symmetry of $\boldsymbol{B}$ with respect to the indices ij gives

$$B_{(ij)klm} = \frac{1}{2}\left(B_{ijklm} + B_{jiklm}\right) \qquad \text{(B.5)}$$

Recall that,

$$B_{ijklm} = \begin{pmatrix} B_1 e_{ijk}\delta_{lm} + B_2 e_{ijl}\delta_{km} + B_3 e_{ijm}\delta_{kl} + B_4 e_{ikl}\delta_{jm} + B_5 e_{ikm}\delta_{jl} \\ + B_6 e_{ilm}\delta_{jk} + B_7 e_{jkl}\delta_{im} + B_8 e_{jkm}\delta_{il} + B_9 e_{jlm}\delta_{ik} + B_{10} e_{klm}\delta_{ij} \end{pmatrix} \text{(B.6)}$$

Interchanging the indices i and j gives

$$B_{jiklm} = \begin{pmatrix} B_1 e_{jik}\delta_{lm} + B_2 e_{jil}\delta_{km} + B_3 e_{jim}\delta_{kl} + B_4 e_{jkl}\delta_{im} + B_5 e_{jkm}\delta_{il} \\ + B_6 e_{jlm}\delta_{ik} + B_7 e_{ikl}\delta_{jm} + B_8 e_{ikm}\delta_{jl} + B_9 e_{ilm}\delta_{jk} + B_{10} e_{klm}\delta_{ij} \end{pmatrix} \text{(B.7)}$$

Substituting the above in equation (B.5) gives;

$$B_{(ij)klm} = \frac{1}{2}\begin{bmatrix} (B_4 + B_7)e_{ikl}\delta_{jm} + (B_5 + B_8)e_{ikm}\delta_{jl} + (B_6 + B_9)e_{ilm}\delta_{jk} \\ +(B_4 + B_7)e_{jkl}\delta_{im} + (B_5 + B_8)e_{jkm}\delta_{il} + (B_6 + B_9)e_{jlm}\delta_{ik} \\ +2B_{10}e_{klm}\delta_{ij} \end{bmatrix} \text{(B.8)}$$

Note that the coefficients B_1, B_2, and B_3 have vanished due to the symmetry

conditions and there are only 4 independent coefficients and 7 terms that exist. Considering the anti-symmetry with respect to the k and l indices gives,

$$B_{(ij)lkm} = \frac{1}{2} \begin{bmatrix} (B_4 + B_7)e_{ilk}\delta_{jm} + (B_5 + B_8)e_{ilm}\delta_{jk} + (B_6 + B_9)e_{ikm}\delta_{jl} \\ +(B_4 + B_7)e_{jlk}\delta_{im} + (B_5 + B_8)e_{jlm}\delta_{ik} + (B_6 + B_9)e_{jkm}\delta_{il} \\ +2B_{10}e_{lkm}\delta_{ij} \end{bmatrix} \quad \text{(B.9)}$$

From equations (B.8) and (B.9) and using,

$$B_{(ij)[kl]m} = \frac{1}{2}\left(B_{(ij)klm} - B_{(ij)lkm}\right) \quad \text{(B.10)}$$

the expression for $B_{(ij)[kl]m}$ can be derived

$$B_{(ij)[kl]m} = \frac{1}{4} \begin{bmatrix} 2(B_4 + B_7)e_{ikl}\delta_{jm} + (B_5 + B_8 - B_6 - B_9)e_{ikm}\delta_{jl} \\ -(B_5 + B_8 - B_6 - B_9)e_{ilm}\delta_{jk} + 2(B_4 + B_7)e_{jkl}\delta_{im} \\ +(B_5 + B_8 - B_6 - B_9)e_{jkm}\delta_{il} - (B_5 + B_8 - B_6 - B_9)e_{jlm}\delta_{ik} \\ +4B_{10}e_{klm}\delta_{ij} \end{bmatrix} \quad \text{(B.11)}$$

Note that the number of independent coefficients have now reduced to 3. Let the terms be denoted as $B_1' = 2(B_4 + B_7)$, $B_2' = (B_5 + B_8 - B_6 - B_9)$ and $B_3' = 4B_{10}$. Then,

$$B_{(ij)[kl]m} = \frac{1}{4} \begin{bmatrix} B_1'\left(e_{ikl}\delta_{jm} + e_{jkl}\delta_{im}\right) \\ +B_2'\left(e_{ikm}\delta_{jl} - e_{ilm}\delta_{jk} + e_{jkm}\delta_{il} - e_{jlm}\delta_{ik}\right) \\ +B_3'e_{klm}\delta_{ij} \end{bmatrix} \quad \text{(B.12)}$$

Following the same analogy as for B_{ijklm} the non-zero terms for D_{ijklm} in the isotropic case are given as,

$$D_{ijklm} = d_1 e_{ijk}\delta_{lm} + d_2 e_{ijl}\delta_{km} + d_3 e_{ijm}\delta_{kl} + d_4 e_{ikl}\delta_{jm} + d_5 e_{ikm}\delta_{jl} + d_6 e_{ilm}\delta_{jk}$$
$$+ d_7 e_{jkl}\delta_{im} + d_8 e_{jkm}\delta_{il} + d_9 e_{jlm}\delta_{ik} + d_{10} e_{klm}\delta_{ij} \quad \text{(B.13)}$$

Following a similar spectral decomposition with respect to the coefficients ij and lm gives;

$$D_{ijklm} = D_{(ij)k(lm)} + D_{(ij)k[lm]} + D_{[ij]k(lm)} + D_{[ij]k[lm]} \quad \text{(B.14)}$$

315

From the constitutive relationship on couple stresses [281], the tensor $\boldsymbol{D}$ extracts the symmetric part of the distortion tensor and the anti-symmetric part of the gradient of distortion tensor. Hence, D_{ijklm} is symmetric with respect to lm and anti-symmetric with respect to ij.

The anti-symmetry with respect to ij is considered first;

$$
D_{[ij]klm} = \frac{1}{2} \begin{bmatrix} 2d_1 e_{ijk}\delta_{lm} \ + \ 2d_2 e_{ijl}\delta_{km} \ + \ 2d_3 e_{ijm}\delta_{kl} \\[2mm] + (d_4 - d_7) e_{ikl}\delta_{jm} + (d_5 - d_8) e_{ikm}\delta_{jl} + (d_6 - d_9) e_{ilm}\delta_{jk} \\[2mm] - (d_4 - d_7) e_{jkl}\delta_{im} - (d_5 - d_8) e_{jkm}\delta_{il} - (d_6 - d_9) e_{jlm}\delta_{ik} \end{bmatrix} \quad \text{(B.15)}
$$

The total number of coefficients has reduced from 10 to 6. Let $a = d_4 - d_7$, $b = d_8 - d_5$ and $c = D_9 - D_6$. Considering the symmetry with respect to the indices lm gives,

$$
D_{[ij]k(lm)} = \frac{1}{4} \begin{bmatrix} 4d_1 e_{ijk}\delta_{lm} \ + \ 2(d_2 + d_3) e_{ijl}\delta_{km} \ + \ 2(d_2 + d_3) e_{ijm}\delta_{kl} \\[2mm] - (a + b) e_{ikl}\delta_{jm} - (a + b) e_{ikm}\delta_{jl} \\[2mm] + (a + b) e_{jkl}\delta_{im} + (a + b) e_{jkm}\delta_{il} \end{bmatrix} \quad \text{(B.16)}
$$

Only 3 independent coefficients remain. Let $D_1' = d_1$, $D_2' = \frac{1}{2}(d_2 + d_3)$ and $D_3' = -(a + b)/4$, then

$$
\begin{aligned}
D_{[ij]k(lm)} &= D_1' e_{ijk}\delta_{lm} \ + D_2'(e_{ijl}\delta_{km} \ + \ e_{ijm}\delta_{kl}) \\
&\quad + D_3'(e_{ikl}\delta_{jm} + e_{ikm}\delta_{jl} - e_{jkl}\delta_{im} - e_{jkm}\delta_{il})
\end{aligned} \quad \text{(B.17)}
$$

Similarly for the 6th order isotropic constant A_{ijklmn}, a spectral decomposition into symmetric and anti-symmetric part with respect to the indices ij and lm gives

$$
A_{ijklmn} = A_{(ij)k(lm)n} + A_{(ij)k[lm]n} + A_{[ij]k(lm)n} + A_{[ij]k[lm]n} \quad \text{(B.18)}
$$

In the general case, the tensor $\boldsymbol{A}$ has $3^6 = 729$ non-zero terms. However in the

isotropic case this reduces to only 15 independent non-zero terms.

$$
A_{ijklmn} = \begin{bmatrix} a_1\delta_{ij}\delta_{kl}\delta_{mn} + a_2\delta_{ij}\delta_{km}\delta_{\ln} + a_3\delta_{ij}\delta_{kn}\delta_{lm} + a_4\delta_{ik}\delta_{jl}\delta_{mn} \\[6pt] +a_5\delta_{ik}\delta_{jm}\delta_{\ln} + a_6\delta_{ik}\delta_{jn}\delta_{lm} + a_7\delta_{il}\delta_{jk}\delta_{mn} + a_8\delta_{il}\delta_{jm}\delta_{kn} \\[6pt] +a_9\delta_{il}\delta_{jn}\delta_{km} + a_{10}\delta_{im}\delta_{jk}\delta_{\ln} + a_{11}\delta_{im}\delta_{jl}\delta_{kn} + a_{12}\delta_{im}\delta_{jn}\delta_{kl} \\[6pt] +a_{13}\delta_{in}\delta_{jk}\delta_{lm} + a_{14}\delta_{in}\delta_{jl}\delta_{km} + a_{15}\delta_{in}\delta_{jm}\delta_{kl} \end{bmatrix} \quad (B.19)
$$

Considering the first anti-symmetry in A_{ijklmn} with respect to the ij indices,

$$
A_{[ij]klmn} = \frac{1}{2}\left[A_{ijklmn} - A_{jiklmn}\right] \quad (B.20)
$$

Interchanging the indices i and j gives,

$$
A_{jiklmn} = \begin{bmatrix} a_1\delta_{ij}\delta_{kl}\delta_{mn} + a_2\delta_{ij}\delta_{km}\delta_{\ln} + a_3\delta_{ij}\delta_{kn}\delta_{lm} + a_4\delta_{jk}\delta_{il}\delta_{mn} \\[6pt] +a_5\delta_{jk}\delta_{im}\delta_{\ln} + a_6\delta_{jk}\delta_{in}\delta_{lm} + a_7\delta_{jl}\delta_{ik}\delta_{mn} + a_8\delta_{jl}\delta_{im}\delta_{kn} \\[6pt] +a_9\delta_{jl}\delta_{in}\delta_{km} + a_{10}\delta_{jm}\delta_{ik}\delta_{\ln} + a_{11}\delta_{jm}\delta_{il}\delta_{kn} + a_{12}\delta_{jm}\delta_{in}\delta_{kl} \\[6pt] +a_{13}\delta_{jn}\delta_{ik}\delta_{lm} + a_{14}\delta_{jn}\delta_{il}\delta_{km} + a_{15}\delta_{jn}\delta_{im}\delta_{kl} \end{bmatrix} \quad (B.21)
$$

Substituting equations (B.19) and (B.21) in equation (B.20) gives,

$A_{[ij]klmn}=$

$$
\frac{1}{2}\begin{bmatrix} (a_7 - a_4)\delta_{il}\delta_{jk}\delta_{mn} + (a_6 - a_{13})\delta_{ik}\delta_{jn}\delta_{lm} + (a_5 - a_{10})\delta_{ik}\delta_{jm}\delta_{nl} \\[6pt] -(a_7 - a_4)\delta_{ik}\delta_{jl}\delta_{mn} + (a_8 - a_{11})\delta_{il}\delta_{jm}\delta_{kn} + (a_9 - a_{14})\delta_{il}\delta_{jn}\delta_{km} \\[6pt] -(a_5 - a_{10})\delta_{im}\delta_{jk}\delta_{nl} - (a_8 - a_{11})\delta_{im}\delta_{jl}\delta_{kn} + (a_{12} - a_{15})\delta_{im}\delta_{jn}\delta_{kl} \\[6pt] -(a_6 - a_{13})\delta_{in}\delta_{jk}\delta_{lm} - (a_9 - a_{14})\delta_{in}\delta_{jl}\delta_{km} - (a_{12} - a_{15})\delta_{in}\delta_{jm}\delta_{kl} \end{bmatrix} \quad (B.22)
$$

The original 15 non-zero independent coefficients have reduced to 6 with 12 different terms. Next consider the anti-symmetry over the indices lm.

$$
A_{[ij]k[lm]n} = \frac{1}{2}\left[A_{[ij]klmn} - A_{[ij]kmln}\right] \quad (B.23)
$$

Interchanging the indices l and m gives

$A_{[ij]kmln}=$

$$\frac{1}{2}\begin{bmatrix} (a_7 - a_4)\delta_{im}\delta_{jk}\delta_{ln} + (a_6 - a_{13})\delta_{ik}\delta_{jn}\delta_{lm} + (a_5 - a_{10})\delta_{ik}\delta_{jl}\delta_{nm} \\[2mm] -(a_7 - a_4)\delta_{ik}\delta_{jm}\delta_{ln} + (a_8 - a_{11})\delta_{im}\delta_{jl}\delta_{kn} + (a_9 - a_{14})\delta_{im}\delta_{jn}\delta_{kl} \\[2mm] -(a_5 - a_{10})\delta_{il}\delta_{jk}\delta_{nm} - (a_8 - a_{11})\delta_{il}\delta_{jm}\delta_{kn} + (a_{12} - a_{15})\delta_{il}\delta_{jn}\delta_{km} \\[2mm] -(a_6 - a_{13})\delta_{in}\delta_{jk}\delta_{lm} - (a_9 - a_{14})\delta_{in}\delta_{jm}\delta_{kl} - (a_{12} - a_{15})\delta_{in}\delta_{jl}\delta_{km} \end{bmatrix} \quad \text{(B.24)}$$

For the sake of simplicity let us rename some of the coefficients as $\alpha = a_7 - a_4$, $\beta = a_6 - a_{13}$, $\gamma = a_5 - a_{10}$, $\kappa = a_8 - a_{11}$, $\xi = a_9 - a_{14}$ and $\mu = a_{12} - a_{15}$.

From (B.22), (B.23) and (B.24),

$$A_{[ij]k[lm]n} = \frac{1}{4}\begin{bmatrix} (\alpha + \gamma)\delta_{il}\delta_{jk}\delta_{mn} + (\alpha + \gamma)\delta_{ik}\delta_{jm}\delta_{nl} - (\alpha + \gamma)\delta_{ik}\delta_{jl}\delta_{nm} \\[2mm] -(\alpha + \gamma)\delta_{im}\delta_{jk}\delta_{\mathrm{ln}} + (\xi - \mu)\delta_{il}\delta_{jn}\delta_{km} + (\xi - \mu)\delta_{in}\delta_{jm}\delta_{kl} \\[2mm] -(\xi - \mu)\delta_{im}\delta_{jn}\delta_{kl} - (\xi - \mu)\delta_{in}\delta_{jl}\delta_{km} \\[2mm] +2\kappa\delta_{il}\delta_{jm}\delta_{kn} - 2\kappa\delta_{im}\delta_{jl}\delta_{kn} \end{bmatrix} \quad \text{(B.25)}$$

Replacing $A'_1 = (\alpha + \gamma)/4$, $A'_2 = (\xi - \mu)/4$ and $A'_3 = \kappa/2$

$$\begin{aligned} A_{[ij]k[lm]n} =\ & A'_1 \left(\delta_{il}\delta_{jk}\delta_{mn} + \delta_{ik}\delta_{jm}\delta_{nl} - \delta_{ik}\delta_{jl}\delta_{nm} - \delta_{im}\delta_{jk}\delta_{\mathrm{ln}}\right) \\ & + A'_2 \left(\delta_{il}\delta_{jn}\delta_{km} + \delta_{in}\delta_{jm}\delta_{kl} - \delta_{im}\delta_{jn}\delta_{kl} - \delta_{in}\delta_{jl}\delta_{km}\right) \\ & + A'_3 \left(\delta_{il}\delta_{jm}\delta_{kn} - \delta_{im}\delta_{jl}\delta_{kn}\right) \end{aligned} \quad \text{(B.26)}$$

Finally, this gives just 3 non-zero coefficients and 10 terms. The quadratic form of elastic energy density imposes another symmetry condition on $\boldsymbol{A}$ i.e. $A_{ijklmn} = A_{lmnijk}$ which is implicit in equation (B.26).

B.1.1 Transforming 5th and 6th order elasticity tensors to 4th order

For the sake of rigor, the elastic constitutive laws presented in section (3.1.1) are developed here using second order elastic curvatures. Using the relationship between second and third order elastic curvatures and couple stresses from equation (2.51) and (3.35), respectively, the elastic laws (3.43) and (3.44) can be rewritten as:

$$\sigma_{(pq)} = C_{(pq)(kl)}\epsilon_{(kl)}^{e(\|+\perp)} - B_{(pq)[kl]m}e_{kln}\kappa_{nm}^{e(\|+\perp)} - e_{ijn}D_{[ij]m(pq)}\kappa_{nm}^{e(\|+\perp)}$$

318

$$M_{sr}^D = -e_{spq}\epsilon_{(lm)}^{e(\|+\perp)}B_{(lm)[pq]r} - e_{spq}D_{[pq]r(lm)}\epsilon_{(lm)}^{e(\|+\perp)} + e_{spq}A_{[pq]r[lo]m}e_{lon}\kappa_{nm}^{e(\|+\perp)} \quad \text{(B.27)}$$

Without the loss of generality, the following relationships can be defined:

$$B_{(pq)nm}\kappa_{nm}^{e(\|+\perp)} = -B_{(pq)[kl]m}e_{kln}\kappa_{nm}^{e(\|+\perp)} - e_{ijn}D_{[ij]m(pq)}\kappa_{nm}^{e(\|+\perp)}$$

$$D_{sr(nm)}\epsilon_{nm}^{e(\|+\perp)} = -e_{spq}\epsilon_{(lm)}^{e(\|+\perp)}B_{(lm)[pq]r} - e_{spq}D_{[pq]r(lm)}\epsilon_{(lm)}^{e(\|+\perp)}$$

$$A_{srnm}\kappa_{nm}^{e(\|+\perp)} = e_{spq}A_{[pq]r[lo]m}e_{lon}\kappa_{nm}^{e(\|+\perp)} \quad \text{(B.28)}$$

Finally, the elastic constitutive laws can be written in terms of 4th order elasticity tensors and second order elastic curvature tensors as,

$$\boldsymbol{\sigma}^s = \boldsymbol{C} : \boldsymbol{\epsilon}^{e(\|+\perp)} + \boldsymbol{B} : \boldsymbol{\kappa}^{e(\|+\perp)} \quad \text{or} \quad \sigma_{(pq)} = C_{(pq)(kl)}\epsilon_{(kl)}^{e(\|+\perp)} + B_{(pq)nm}\kappa_{nm}^{e(\|+\perp)}$$

$$\boldsymbol{M}^D = \boldsymbol{D} : \boldsymbol{\epsilon}^{e(\|+\perp)} + \boldsymbol{A} : \boldsymbol{\kappa}^{e(\|+\perp)} \quad \text{or} \quad M_{sr}^D = D_{sr(nm)}\epsilon_{nm}^{e(\|+\perp)} + A_{srnm}\kappa_{nm}^{e(\|+\perp)} \quad \text{(B.29)}$$

APPENDIX C

MULTI-SCALE DESCRIPTIONS OF INTERFACES IN CONTINUOUS MEDIA

Thus far, the implications of using a continuous approach as opposed to a discrete approach have been discussed with respect to the representation of line crystal defects. In this section, the implications of modelling interfaces - specifically GBs -, and TJs in a continuum are discussed.

A continuous description of GB interfaces may be attributed a finite volume at the interatomic length scale whereby individual defects can be represented by their respective polar density fields. This is in accordance with the atomistic description of GBs which features elementary structures spreading over a finite-width (non-singular) layer - sometimes as thin as a nano-meter [387]. On the other hand, at the meso-scopic scale resolution these interfaces are modelled as singular surfaces *i.e.* having an infinitesimal thickness. Prominent amongst the models describing singular interfaces are those using a surface defect description - for example, Frank-Bilby surface dislocations [131, 38]. Such a description becomes necessary when modelling singular interfaces across which there is a discontinuity of elastic/plastic strain and/or curvature fields. In this section, the specific intent is to clarify the issue of continuity vs. discontinuity of the elastic/plastic strain and curvature tensor fields across a surface of discontinuity, in the framework of both, the fine scale FDDM model and the meso-scale PMFDDM model. Although discontinuities in these fields are allowed, necessary tangential continuity conditions on the elastic strain and curvature tensors will be derived at smooth interfaces, and some of their implications investigated. This forthcoming work derives motivation from an earlier investigation of the continuity

conditions on the plastic distortion rate in the field theory of dislocations [3].

C.0.2 Tangential continuity of elastic/plastic strain and curvature fields at Interfaces

In the following, the tangential continuity conditions on elastic/plastic strain and curvature fields necessary for a fully continuous treatment of interfaces. These have been discussed in detail in the works of Fressengeas *et al.* [136] and Upadhyay *et al.* [420].

C.0.2.1 Compatibility condition for a single interface

Consider a smooth surface of discontinuity $\mathcal{I}$, separating the body D into two domains D^+ and D^-. A smooth surface is the one without any discontinuities in its tangent plane orientation field. For the sake of simplicity, this interface $\mathcal{I}$ is assumed to remain attached to the material. At any point P on $\mathcal{I}$, let the normal vector $\vec{n}$ to the interface is oriented from D^- toward D^+. Also, let $\vec{l}$ and $\vec{t} = \vec{n} \times \vec{l}$ be two unit vectors belonging to the tangent plane to the interface as shown in figure C.1. $\mathcal{I}$ may be used to model
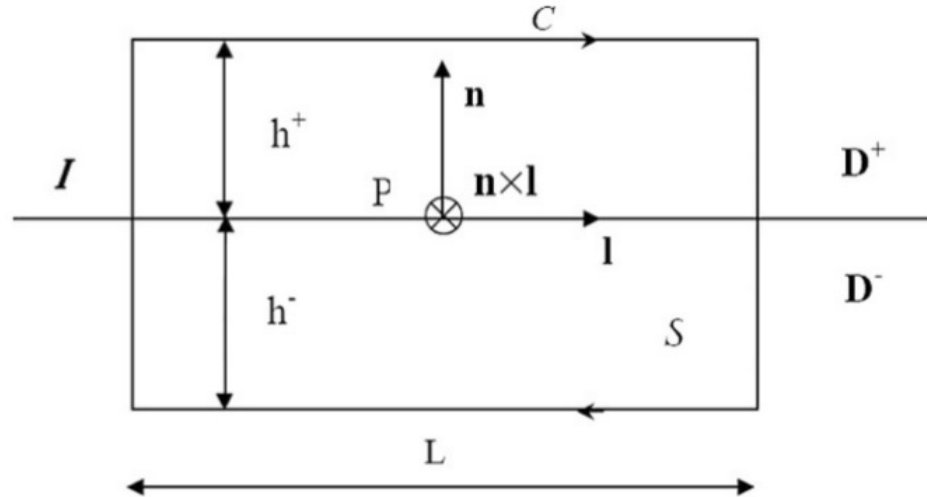
Figure C.1: Burgers circuit across an interface $\mathcal{I}$ separating the body D into domains D^-, D^+. $\vec{n}$ is the unit normal to the interface, and $\vec{t} = \vec{n} \times \vec{l}$ the normal to the bounded surface S.

a GB in a polycrystal. In this case, the GB is seen as having no width. Continuum

mechanics requires that the displacement $\vec{u}$ and traction vector $\boldsymbol{\sigma}.\vec{n}$ be continuous across the interface. Hence $[\vec{u}] = 0$ and $[\boldsymbol{\sigma}.\vec{n}] = 0$. The continuity of the traction vector is also reflected by the continuity of the normal part, $\boldsymbol{\sigma}_n = \boldsymbol{\sigma}\cdot\vec{n}\otimes\vec{n}$, of the stress tensor: $[\boldsymbol{\sigma}_n] = 0$. However, the tangential part of the stress tensor, $\boldsymbol{\sigma}_t = \boldsymbol{\sigma} - \boldsymbol{\sigma}_n$, can be discontinuous across the interface. This discontinuity is expressed by:

$$\exists \vec{l} \in \mathcal{I}, \quad [\boldsymbol{\sigma}] \cdot \vec{l} \neq 0 \tag{C.1}$$

which implies that:

$$[\boldsymbol{\sigma}] \times \vec{n} \neq 0 \tag{C.2}$$

In contrast, the continuity of the displacement at the interface requires tangential continuity of the total distortion $\boldsymbol{U}$:

$$\forall \vec{l} \in \mathcal{I}, \quad [\boldsymbol{U}] \cdot \vec{l} = 0 \tag{C.3}$$

a condition also rendered as:

$$[\boldsymbol{U}] \times \vec{n} = 0 \tag{C.4}$$

or, in terms of the normal and tangential parts of the distortion, $[\boldsymbol{U}_n]$ and $[\boldsymbol{U}_t]$, as:

$$[\boldsymbol{U}_t] = [\boldsymbol{U}] - [\boldsymbol{U}_n] = [\boldsymbol{U}] - [\boldsymbol{U}] \cdot \vec{n} \otimes \mathbf{n} = 0 \tag{C.5}$$

This tangential continuity condition is known as Hadamard's compatibility condition [168]. It does not impose any requirement on the normal discontinuity $[\boldsymbol{U}_n]$ across the interface. Furthermore, it does not deal with the continuity vs. discontinuity of the elastic/plastic curvature and strain tensors at the interface. In the following it will be shown that if the choice is made to represent the incompatibility arising from the presence of lattice defects in the interface area in a continuous manner, additional continuity conditions on the elastic curvature and strain at the interface need to be accounted for.

Consider a rectangular closed circuit C lying across the interface and bounding a surface S oriented by $\vec{t}$, in the manner shown in figure C.1. Rewriting equations

(2.106) and (2.108) in the present context, the net Frank's vector $\boldsymbol{\Omega}$ of the disclinations threading S is such that:

$$\forall \vec{l} \in \mathcal{I}, \quad \boldsymbol{\Omega} = \int_C \boldsymbol{\kappa}^e \cdot d\vec{r} = \int_S \boldsymbol{\theta} \cdot \vec{t}dS \tag{C.6}$$

Provisionally, the distribution of disclinations in S is assumed to include not only a continuous distribution of disclinations $\boldsymbol{\theta}$ in each domain D^- and D^+, but also a singular distribution $\boldsymbol{\theta}(\mathcal{I})$ along the interface $\mathcal{I}$. This singular term represents "surface-disclinations" through a density of (adimensional) Frank's vectors per m in the direction $\vec{l}$. If the circuit C is collapsed onto point P by letting h^+ and h^- tend to zero, and L shrinks along the direction $\vec{l}$, equation (C.6) becomes:

$$\forall \vec{l} \in \mathcal{I}, \quad \left[\boldsymbol{\kappa}^e\right] \cdot \vec{l} = \boldsymbol{\theta}(\mathcal{I}) \cdot \vec{t} \tag{C.7}$$

Essentially, the bulk density $\boldsymbol{\theta}$ distributed in D^+ and D^- disappears in this limit. Thus, equation (C.7) provides the density $\boldsymbol{\theta}(\mathcal{I})$ of surface-disclinations needed to accommodate a tangential discontinuity of the elastic curvature $\left[\boldsymbol{\kappa}^e\right]$ in no width across the interface. It has no implication on its normal discontinuity. However, if the choice is made to describe the interface in a continuous manner and a small resolution length scale is used to render the fine structure of the boundary, then the surface-disclination concept must be surrendered. This modeling choice amounts to acknowledging that the accommodation of a finite variation of the tangential part of the elastic curvature takes place in a finite material layer, perhaps as thin as a few nano-meters and containing a few atomic rows, but non discrete. In this case, equation (C.7) becomes:

$$\forall \vec{l} \in \mathcal{I}, \quad \left[\boldsymbol{\kappa}^e\right] \cdot \vec{l} = 0 \tag{C.8}$$

The meaning of equation (C.8) is that, in the absence of surface-disclinations, tangential continuity of the elastic curvature tensor is required in a continuous model. Equation (C.8) is equally transcribed as:

$$\left[\boldsymbol{\kappa}^e\right] \times \vec{n} = 0 \tag{C.9}$$

or in terms of its normal and tangential components, $\left[\boldsymbol{\kappa}^e\right]_n$ and $\left[\boldsymbol{\kappa}^e\right]_t$, as:

$$\left[\boldsymbol{\kappa}^e\right]_t = \left[\boldsymbol{\kappa}^e\right] - \left[\boldsymbol{\kappa}^e\right]_n = \left[\boldsymbol{\kappa}^e\right] - \left[\boldsymbol{\kappa}^e\right] \cdot \mathbf{n} \otimes \vec{\boldsymbol{n}} = 0 \qquad (C.10)$$

Continuity of the normal component of the elastic curvature tensor is not required by equation (C.9), nor is it accommodated by the surface-disclination density in equation (C.7).[1] The continuity of the tangential component of the elastic curvature implies that spatial correlations are existing between the lattice rotations of the neighbouring grains, because limiting values of the curvature from the left and from the right of the interface must be equal. Since it is not accommodated at the interface by surface-disclinations, a finite variation of the tangential component of the elastic curvature over the boundary area must be accommodated by the bulk disclination density $\boldsymbol{\theta}$ in a layer across the interface. However, the width of this layer is not implied by equation (C.9). Experimental evidence of such a length scale was provided in various materials after diverse strain paths, in the form of the scaling range for the power law dependence of the probability density of a certain grain misorientation vs. the inter-granular distance [31].

Similar continuity constraints can be obtained for the plastic curvature and plastic curvature rate. Since the total rotation $\vec{\boldsymbol{\omega}}$ is compatible, taking the line integral of the total curvature described in equation (2.90) along the closed circuit C shows that:

$$\forall \vec{\boldsymbol{l}} \in \mathcal{I}, \quad \int_C \boldsymbol{\kappa}^p.d\vec{\boldsymbol{r}} = - \int_C \boldsymbol{\kappa}^e.d\vec{\boldsymbol{r}}. \qquad (C.11)$$

Hence, it is straightforward to show from equations (C.8), (C.9) and (C.11) that tangential continuity of the plastic curvature is also required:

$$\left[\boldsymbol{\kappa}^p\right] \times \vec{\boldsymbol{n}} = 0 \qquad (C.12)$$

---

[1] The occurrence of a normal discontinuity of the elastic curvature tensor implies that the continuity required in equation (2.92) for the calculation of the disclination density tensor may not be satisfied for three of its components. Thus, discontinuity of the involved disclination densities may occur at the interface.

when surface-disclinations are absent. For small rotations, the derivation with respect to time of equation (C.12) involves only partial time derivatives. Thus, tangential continuity also holds for the plastic curvature rate:

$$\left[\dot{\boldsymbol{\kappa}}^p\right] \times \mathbf{n} = 0 \tag{C.13}$$

This rate condition may also be obtained by integrating the transport equation of disclinations (3.97) over a "pillbox" set across an arbitrary area patch, in the limit when such a patch contracts onto a surface of discontinuity in the material (see a derivation in [3], in the context of dislocation transport).

The conservation of the Burgers vectors content across the interface also gives rise to additional tangential continuity conditions. Using equations (2.107) and (2.109), the net Burgers vector $\mathbf{b}$ of the dislocations threading S is such that:

$$\forall \vec{l} \in \mathcal{I}, \quad \mathbf{b} = \int_C (\boldsymbol{\epsilon}^e - \boldsymbol{\kappa}^e \times \mathbf{r}).d\vec{r} = \int_S (\boldsymbol{\alpha} - \boldsymbol{\theta} \times \vec{r}) \cdot \vec{t} dS \tag{C.14}$$

It is assumed that a continuous distribution of dislocations and disclinations is existing in the domains D^- and D^+ and also, provisionally, singular distributions $\boldsymbol{\alpha}(\mathcal{I})$ and $\boldsymbol{\theta}(\mathcal{I})$ along the interface $\mathcal{I}$. The term $\boldsymbol{\alpha}(\mathcal{I})$ represents surface-dislocations through a density of Burgers vectors per m in the direction $\vec{l}$. When the circuit C collapses onto point P in the limit, when H^+, h^- and L tend to zero, equation (C.14) becomes

$$\forall \vec{l} \in \mathcal{I}, \quad \left[\boldsymbol{\epsilon}^e - \boldsymbol{\kappa}^e \times \vec{r}_0\right] \cdot \vec{l} = (\boldsymbol{\alpha}(\mathcal{I}) - \boldsymbol{\theta}(\mathcal{I}) \times \vec{r}_0) \cdot \vec{t} \tag{C.15}$$

where $\vec{r}_0$ denotes the location of point P in the reference frame. In a way similar to equation (C.7), equation (C.15) provides information on the density of surface-dislocations and surface-disclinations needed to accommodate a discontinuity in the elastic displacement across the singular interface $\mathcal{I}$. Now, if choice is made to describe the interface in a continuous manner, the surface-defect concept must be surrendered and equation (C.15) reduces to:

$$\forall \vec{l} \in \mathcal{I}, \quad \left[\boldsymbol{\epsilon}^e - \boldsymbol{\kappa}^e \times \vec{r}_0\right] \cdot \vec{l} = 0 \tag{C.16}$$

325

Equation (C.16) describes the tangential continuity of the tensor $\boldsymbol{\epsilon}^e - \boldsymbol{\kappa}^e \times \vec{r}_0$ at the interface. An equivalent form, similar to equation (C.9), is:

$$\left[\boldsymbol{\epsilon}^e - \boldsymbol{\kappa}^e \times \vec{r}_0 \right] \times \vec{n} = 0 \tag{C.17}$$

or in terms of the normal and tangential components $\left[\boldsymbol{\epsilon}^e - \boldsymbol{\kappa}^e \times \vec{r}_0 \right]_n$ and $\left[\boldsymbol{\epsilon}^e - \boldsymbol{\kappa}^e \times \vec{r}_0 \right]_t$:

$$\left[\boldsymbol{\epsilon}^e - \boldsymbol{\kappa}^e \times \vec{r}_0 \right]_t = \left[\boldsymbol{\epsilon}^e - \boldsymbol{\kappa}^e \times \vec{r}_0 \right] - \left[\boldsymbol{\epsilon}^e - \boldsymbol{\kappa}^e \times \vec{r}_0 \right]_n = \left[\boldsymbol{\epsilon}^e - \boldsymbol{\kappa}^e \times \vec{r}_0 \right] - \left[\boldsymbol{\epsilon}^e - \boldsymbol{\kappa}^e \times \vec{r}_0 \right] \cdot \vec{n} \otimes \vec{n} = 0 \tag{C.18}$$

The normal component $\left[\boldsymbol{\epsilon}^e - \boldsymbol{\kappa}^e \times \vec{r}_0 \right]_n$ is left unconstrained by equation (C.17). Note that, since the total displacement and rotation of the body are compatible, the following integral is zero:

$$\forall \vec{l} \in \mathcal{I}, \quad \int_C (\boldsymbol{\epsilon} - \mathbf{grad}\ \vec{\omega} \times \vec{r}) \cdot d\vec{r} = 0 \tag{C.19}$$

Substracting equation (2.107) from equation (C.19), it is found that an alternative form of the Burgers vector is:

$$\mathbf{b} = -\int_C (\boldsymbol{\epsilon}^p - \boldsymbol{\kappa}^p \times \vec{r}).d\vec{r}. \tag{C.20}$$

Then, following the above line of reasoning, an alternative relation to equation (C.17), using the plastic strain and curvature tensors is found:

$$\left[\boldsymbol{\epsilon}^p - \boldsymbol{\kappa}^p \times \vec{r}_0 \right] \times \vec{n} = 0. \tag{C.21}$$

At small transformations, a derivation of equation (C.21) with respect to time involves only partial time derivatives, and the following result on the plastic strain rate and curvature rate is obtained:

$$\left[\dot{\boldsymbol{\epsilon}}^p - \dot{\boldsymbol{\kappa}}^p \times \vec{r}_0 \right] \times \vec{n} = 0. \tag{C.22}$$

If the reference point is chosen in the interface, such that $\vec{r}_0 = 0$, equations (C.17), (C.21) and (C.22) condense into simpler relations involving only the strain component

of the incompatibility. Note that equation (C.21) was given in this simplified form by Hirth [186], on the basis of heuristic arguments. The curvature-induced incompatible plastic displacement $\boldsymbol{\kappa}^p \times \vec{r}_0$ and the related disclinations were not considered in this paper, where dislocation-based modeling of GBs was discussed. In such context, tangential continuity should apply not only to the symmetric part of the plastic distortion rate tensor (the plastic strain rate tensor) but also to its skew-symmetric part (the plastic rotation rate tensor) [3]. The tangential continuity conditions (C.17), (C.21) and (C.22) differ from their counterparts in the theory of dislocation fields [3, 31, 260] because the elastic/plastic rotation and rotation rate tensors are undefined in a theory of crystal defects involving disclinations. Stated differently, the tangential continuity conditions (C.9), (C.12) and (C.13) do not hold in the theory of dislocation fields because the elastic/plastic curvature and curvature rate tensors are assumed to be integrable in the latter.

In the framework of the meso-scale phenomenological field disclination and dislocation mechanics model, the conservation of the Frank's and Burgers vectors also implies jump conditions on the meso-scopic plastic curvature rate and strain rate, respectively, at the interface. At the meso-scale, the latter are always seen as surfaces of discontinuity. In the simple case of a material surface of discontinuity, stationary with respect to the material, the tangential continuity conditions are:

$$\left[\dot{\boldsymbol{\kappa}}^p + \dot{\boldsymbol{\kappa}}^{p*}\right] \times \vec{n} = 0 \tag{C.23}$$

$$\left[\dot{\boldsymbol{\epsilon}}^p + (\boldsymbol{L}^p)^s - (\dot{\boldsymbol{\kappa}}^p + \dot{\boldsymbol{\kappa}}^{p*}) \times \vec{r}_0\right] \times \vec{n} = 0, \tag{C.24}$$

The conditions (C.23) and (C.24) imply that the incremental plastic tangential rotation and displacement are continuous at the surface of discontinuity. When the resolution length scale becomes large enough: $\dot{\boldsymbol{\kappa}}^p = 0$ and $\dot{\boldsymbol{\epsilon}}^p = 0$ and the averaged theory reduces to crystal plasticity. However, appending the residual tangential continuity conditions, $\left[\dot{\boldsymbol{\kappa}}^{p*}\right] \times \vec{n} = 0$ and $\left[(\boldsymbol{L}^p)^s - \dot{\boldsymbol{\kappa}}^{p*} \times \vec{r}_0\right] \times \vec{n} = 0$, to the latter makes

this conventional theory non-local, as limiting values of fields from the two sides of the surface of discontinuity are required to have some relationship. Such a non-locality is expected to affect the distribution of plastic strain and rotation rates in the vicinity of GBs (see [330] in the case of pure dislocations). In the work of Richeton *et al.* [330] grain-to-grain interactions are modeled, which allowed retrieving size effects and loading path-dependency in particle-reinforced alloys. However, the features of GB in relation with the non-locality of elasticity are lost in the coarse-graining process, because their characteristic length-scale is much too small to be perceived at this scale of resolution.

C.0.2.2 *Compatibility condition for multiple junctions*

Consider a multiple junction J where N interfaces, with respective discontinuities in the elastic curvature $\left[\boldsymbol{\kappa}_e\right]_i; i \in (1, N)$, connect along a single line. In practice, mostly triple-junctions ($N = 3$) are observed when the interfaces represent GBs. If the choice of continuous modeling is made, closure requires that the sum of all discontinuities vanish at the multiple junction:

$$\sum_{i=1}^{N} \left[\boldsymbol{\kappa}_e\right]_i = 0 \tag{C.25}$$

$$\sum_{i=1}^{N} \left[\boldsymbol{\epsilon}_e - \boldsymbol{\kappa}_e \times \vec{\boldsymbol{r}}_0\right]_i = 0 \tag{C.26}$$

A reference grain is used to start and finish a closed circuit about a multiple junction. Summing the relations (C.10) for all interfaces, and using equation (C.25), it is seen that the normal discontinuities in the elastic curvature need to satisfy a Kirchhoff-like compatibility condition at the multiple junction:

$$\sum_{i=1}^{N} \left[\boldsymbol{\kappa}_e\right]_i \cdot \mathbf{n}_i \otimes \vec{\boldsymbol{n}}_i = 0 \tag{C.27}$$

Similarly, for a multiple junction located at $\vec{\boldsymbol{r}}_0$, it can be shown from equations (C.18) and (C.26) that the normal discontinuities $\left[\boldsymbol{\epsilon}_e - \boldsymbol{\kappa}_e \times \vec{\boldsymbol{r}}_0\right]_n$ must satisfy the

compatibility condition:

$$\sum_{i=1}^{N} \left[\boldsymbol{\epsilon}_e - \boldsymbol{\kappa}_e \times \vec{r}_0 \right]_i \cdot \vec{n}_i \otimes \mathbf{n}_i = 0 \tag{C.28}$$

Additional compatibility conditions are obtained for the normal discontinuities in the plastic curvature and curvature rate:

$$\sum_{i=1}^{N} \left[\boldsymbol{\epsilon}_p - \boldsymbol{\kappa}_p \times \vec{r}_0 \right]_i \cdot \vec{n}_i \otimes \mathbf{n}_i = 0 \tag{C.29}$$

$$\sum_{i=1}^{N} \left[\dot{\boldsymbol{\epsilon}}_p - \dot{\boldsymbol{\kappa}}_p \times \vec{r}_0 \right]_i \cdot \mathbf{n}_i \otimes \vec{n}_i = 0 \tag{C.30}$$

C.1 Power dissipation from a bicrystal with a singular interface

Consider a bicrystal of volume V bounded by a surface S undergoing elastic deformation under the action of surface tractions $\vec{t}$ and moments $\vec{m}$. Let this bicrystal consist of an infinitesimally thin interface Ω separating volumes D^- and D^+ as shown in figure C.1 and no other defects. Since the interface is infinitesimally thin, therefore $D = D^+ + D^-$. The power dissipated during elastic deformation of this bicrystal is:

$$D = \int_S \left(\vec{v} \cdot \vec{t} + \dot{\vec{\omega}} \cdot \vec{m} \right) dS - \int_D \dot{\psi} dV \tag{C.31}$$

which is similar to equation (3.15). The equilibrium condition requires that the traction and moment vectors be continuous in the direction normal to the interface Ω. Therefore,

$$\boldsymbol{\sigma}^+ \cdot \vec{n} = \boldsymbol{\sigma}^- \cdot \vec{n} = \boldsymbol{\sigma} \cdot \vec{n} = \vec{t} \quad \text{on } \Omega \tag{C.32}$$

$$\boldsymbol{\sigma}^+ \cdot \vec{n} = \boldsymbol{\sigma}^- \cdot \vec{n} = \boldsymbol{\sigma} \cdot \vec{n} = \vec{t} \quad \text{on } \Omega \tag{C.33}$$

where $\boldsymbol{\sigma}^+$, $\boldsymbol{\sigma}^-$ and $\boldsymbol{M}^+$, $\boldsymbol{M}^-$ are the Cauchy and couple stress tensors from the side D^+ and D^-, respectively, at the interface. These continuity equations can be used to obtain the following relationships

$$\left[\vec{v} \cdot \vec{t} \right] = \left[\vec{v} \cdot \boldsymbol{\sigma} \cdot \vec{n} \right] = \left[\vec{v} \right] \cdot \boldsymbol{\sigma} \cdot \vec{n} \tag{C.34}$$

$$\left[\vec{\dot{\omega}} \cdot \vec{m}\right] = \left[\vec{\dot{\omega}} \cdot \boldsymbol{M} \cdot \vec{n}\right] = \left[\vec{\dot{\omega}}\right] \cdot \boldsymbol{M} \cdot \vec{n} \tag{C.35}$$

Traction and moment continuity also implies that $\boldsymbol{sigma} \cdot \vec{n} = \frac{1}{2}\left(\boldsymbol{\sigma}^+ + \boldsymbol{\sigma}^-\right) \cdot \vec{n}$ and $\boldsymbol{M} \cdot \vec{n} = \frac{1}{2}\left(\boldsymbol{M}^+ + \boldsymbol{M}^-\right) \cdot \vec{n}$ at the interface. In order to satisfy the Hadamard compatibility condition i.e. satisfying the tangential continuity along the interface, velocity jump $[\vec{v}]$ at the interface can be related to jump in total strain tensor $[\boldsymbol{\epsilon}]$ as [346]:

$$[\vec{v}] = -[\boldsymbol{\epsilon}] \cdot \vec{n} v_n \tag{C.36}$$

where v_n is the component of velocity normal to the interface. Similarly, tangential continuity requires that the jump in rotation rate $\left[\vec{\dot{\omega}}\right]$ be related to the jump in total curvature field as:

$$\left[\vec{\dot{\omega}}\right] = -[\boldsymbol{\kappa}] \cdot \vec{n} \dot{\omega}_n \tag{C.37}$$

where $\dot{\omega}_n$ is the component of rotation rate normal to the interface. The tangential continuity also implies that the tangential component of the jump in strain and curvature field is equal to zero, therefore,

$$[\boldsymbol{\epsilon}] = -[\boldsymbol{\epsilon}] \, \vec{n} \otimes \vec{n} = [\boldsymbol{\epsilon}_n] \tag{C.38}$$

$$[\boldsymbol{\kappa}] = -[\boldsymbol{\kappa}] \, \vec{n} \otimes \vec{n} = [\boldsymbol{\kappa}_n] \tag{C.39}$$

These relationships can be substituted in equations for velocity and rotation rate to obtain

$$[\vec{v}] = -\left([\boldsymbol{\epsilon}] \, \vec{n} \otimes \vec{n}\right) \cdot \vec{n} v_n \tag{C.40}$$

$$\left[\vec{\dot{\omega}}\right] = -\left([\boldsymbol{\kappa}] \, \vec{n} \otimes \vec{n}\right) \cdot \vec{n} \dot{\omega}_n \tag{C.41}$$

Finally,

$$[\vec{v}] \cdot \boldsymbol{\sigma} \cdot \vec{n} = -\left\{\left([\boldsymbol{\epsilon}] \, \vec{n} \otimes \vec{n}\right) \cdot \vec{n} v_n\right\} \cdot (\boldsymbol{\sigma} \cdot \vec{n}) = [\boldsymbol{\epsilon}] : \boldsymbol{\sigma} v_n \tag{C.42}$$

330

$$\left[\dot{\vec{\omega}}\right] \cdot \boldsymbol{M} \cdot \vec{n} = -\left\{\left([\boldsymbol{\kappa}]\,\vec{n} \otimes \vec{n}\right) \cdot \vec{n}\dot{\omega}_n\right\} \cdot (\boldsymbol{M} \cdot \vec{n}) = [\boldsymbol{\kappa}] : \boldsymbol{M}\dot{\omega}_n \qquad \text{(C.43)}$$

Using the divergence theorem, the dissipation can now be written as

$$D = \int_D \left(\boldsymbol{\sigma} : \boldsymbol{\epsilon} + \boldsymbol{M} : \boldsymbol{\kappa}\right) dV$$

$$+ \int_\Omega \left(\frac{1}{2}\left(\boldsymbol{\sigma}^+ + \boldsymbol{\sigma}^-\right) : [\boldsymbol{\epsilon}] + \frac{1}{2}\left(\boldsymbol{M}^+ + \boldsymbol{M}^-\right) : [\boldsymbol{\kappa}]\right) dS - \int_V \dot{\psi}\,dV \qquad \text{(C.44)}$$

Note here that due to the singular interface, the Helmholtz free energy density rate $\dot{\psi}$ has contributions coming only from internal energy stored in volume D. In the presence of dislocations and disclinations, the non-locality associated with elastic and plastic curvatures and their rates need to be accounted for in the above equation.

APPENDIX D

KELVIN DECOMPOSITION OF AN ELASTICITY TENSOR

In this section, the basis tensors obtained from the Kelvin decomposition of the elasticity tensors $\boldsymbol{C}$ and $\boldsymbol{A}$ are developed. For the sake of simplicity, the superscript D for the deviatoric couple stress and elastic curvatures tensor along with the s for the symmetric Cauchy stress tensor and e for the elastic strain and curvature tensors, are dropped.

D.1 Kelvin decomposition in classical elasticity

In the following the methodology for Kelvin decomposition of the classical elasticity problem as outlined in the work of Desmorat and Marull [89, 265] is recalled.

The elasticity fourth rank tensor $\boldsymbol{C}$ (the corresponding Voigt matrix representation is $[C]$) has eigenvalues $\Lambda^{(I)}$ and corresponding second rank symmetric eigentensors $e^{(I)}$ (with eigenvectors $\hat{e}^{(I)}$) solutions of the eigenproblem

$$\boldsymbol{C} : \boldsymbol{e}^{(I)} = \Lambda^{(I)} \boldsymbol{e}^{(I)}, \qquad \boldsymbol{e}^{(I)} : \boldsymbol{e}^{(J)} = \delta_{IJ}$$

$$[C]\hat{e}^{(I)} = \Lambda^{(I)}\hat{e}^{(I)}, \qquad \hat{e}^{(I)} \cdot \hat{e}^{(J)} = \delta_{IJ} \tag{D.1}$$

with δ_{IJ} the Kronecker delta symbol. The couples $(\Lambda^{(I)}, \boldsymbol{e}^{(I)}$ or $\hat{e}^{(I)})$ are the Kelvin modes and the eigenvalues $\Lambda^{(I)}$ are the Kelvin moduli. These moduli are at most six (in the general anisotropic case in classical elasticity). In an isotropic case these reduce to only two $i.e.$ $3K$ and $2G$ where K and G are the bulk and shear moduli. The Kelvin decomposition of the elasticity tensor $\boldsymbol{C}$ is then given as

$$\boldsymbol{C} = \sum_{I=1}^{6} \Lambda^{(I)} \boldsymbol{e}^{(I)} \otimes \boldsymbol{e}^{(I)} \quad \Leftrightarrow \quad [C] = \sum_{I=1}^{6} \Lambda^{(I)} \hat{e}^{(I)} \otimes \left(\hat{e}^{(I)}\right)^{T} \tag{D.2}$$

332

There is always a family of six orthogonal eigentensors $e^{(I)}$ but some eigenvalues can be repeated - making the family of eigentensors, non-unique - depending on the material symmetry. The terms of identical moduli $\Lambda^{(I)} = \Lambda^K$ can be conveniently grouped as,

$$C = \sum_{K=1}^{N \le 6} \Lambda^K P^K \qquad P^K = \sum_{I/\Lambda^{(I)}=\Lambda^K} e^{(I)} \otimes e^{(I)} \qquad (\text{D.3})$$

with N being the number of different Kelvin moduli. The projectors P^K are unique for a given elasticity tensor C and they naturally lead to the definition of Kelvin stresses

$$\sigma^K = P^K : \sigma \qquad (\text{D.4})$$

For a given material symmetry, the above equation defines the Kelvin stress σ^K as the projection of the Cauchy stress tensor on K^{th} Kelvin model in a unique and objective manner. If the same projection is made for the elastic strain, *i.e.* $\epsilon^K = P^K : \epsilon$, the elasticity law $\sigma = C : \epsilon$ is equivalent to

$$\sigma^K = \Lambda^K P^K \quad \forall K \qquad (\text{D.5})$$

D.2 Kelvin decomposition in couple stress theory

In the following, a Kelvin type decomposition is introduced for the 4th order elasticity tensor A that enters in the elastic law relating couple stresses to elastic curvatures.

Recall that the elastic constitutive law in the couple stress theory relates the generally asymmetric and deviatoric couple stresses and elastic curvatures. Therefore, the equivalent Kelvin and Voigt vector and tensor representations will have 9 components, in lieu of 6 for the classical elasticity case.

The elasticity fourth rank tensor A (the corresponding Voigt matrix representation is $[A]$) has eigenvalues $\Phi^{(I)}$ and corresponding second rank symmetric eigentensors $e^{(I)}$ (with eigenvectors $\hat{e}^{(I)}$) solutions of the eigenproblem

$$A : e^{(I)} = \Phi^{(I)} e^{(I)}, \qquad e^{(I)} : e^{(J)} = \delta_{IJ}$$

333

$$[A]\hat{e}^{(I)} = \Phi^{(I)}\hat{e}^{(I)}, \qquad \hat{e}^{(I)} \cdot \hat{e}^{(J)} = \delta_{IJ} \tag{D.6}$$

The eigenvalues $\Phi^{(I)}$ can at most attain nine different values. The extended Kelvin decomposition of the elasticity tensor $\boldsymbol{A}$ is then given as

$$\boldsymbol{A} = \sum_{I=1}^{9} \Phi^{(I)} \boldsymbol{e}^{(I)} \otimes \boldsymbol{e}^{(I)} \quad \Leftrightarrow \quad [A] = \sum_{I=1}^{9} \Phi^{(I)} \hat{e}^{(I)} \otimes \left(\hat{e}^{(I)} \right)^{T} \tag{D.7}$$

It can be deduced that while a family of nine orthogonal eigentensors $\boldsymbol{e}^{(I)}$ is always existing, some of the eigenvalues can be repeated - making the family of eigentensors, non-unique - depending on the material symmetry. The terms of identical moduli $\Phi^{(I)} = \Phi^{K}$ can be conveniently grouped as,

$$\boldsymbol{A} = \sum_{K=1}^{N \leq 9} \Phi^{K} \boldsymbol{P}^{K} \qquad \boldsymbol{Q}^{K} = \sum_{I/\Phi^{(I)}=\Phi^{K}} \boldsymbol{e}^{(I)} \otimes \boldsymbol{e}^{(I)} \tag{D.8}$$

The projectors $\boldsymbol{Q}^{K}$ are unique for a given elasticity tensor $\boldsymbol{A}$ and they naturally lead to the definition of Kelvin couple stresses,

$$\boldsymbol{M}^{K} = \boldsymbol{Q}^{K} : \boldsymbol{M} \tag{D.9}$$

For a given material symmetry, the above equation defines the Kelvin couple stress $\boldsymbol{M}^{K}$ as the projection of the couple stress tensor on the Kth Kelvin mode in a unique and objective manner. If the same projection is made for the elastic curvature, *i.e.* $\boldsymbol{\kappa}^{K} = \boldsymbol{Q}^{K} : \boldsymbol{\epsilon}$, the elasticity law $\boldsymbol{M} = \boldsymbol{A} : \boldsymbol{\kappa}$ is equivalent to

$$\boldsymbol{M}^{K} = \Phi^{K} \boldsymbol{Q}^{K} \quad \forall K \tag{D.10}$$

D.3 Kelvin decomposition for cubic symmetry

In the following, the eigenvectors and tensors related to Cauchy stresses and elastic strains are developed in the case of cubic symmetry. On the other hand, due to limited knowledge on the symmetries of the elasticity tensor $\boldsymbol{A}$, the eigenvectors and tensors related to the couple stresses and elastic curvatures are developed in the case of isotropic symmetry.

Cubic material symmetry, encountered for instance in FCC single and poly crystals, allows for an easy Kelvin decomposition of the elasticity tensor and ends up to simple Kelvin stresses. If the Cauchy stresses and elastic strains are rewritten in the Voigt notation as

$$\hat{\sigma} = \left(\sigma_{xx}, \sigma_{yy}, \sigma_{zz}, \sqrt{2}\sigma_{yz}, \sqrt{2}\sigma_{zx}, \sqrt{2}\sigma_{xy} \right)^T$$
$$\hat{\epsilon} = \left(\epsilon_{xx}, \epsilon_{yy}, \epsilon_{zz}, \sqrt{2}\epsilon_{yz}, \sqrt{2}\epsilon_{zx}, \sqrt{2}\epsilon_{xy} \right)^T \tag{D.11}$$

the elasticity law $\boldsymbol{\sigma} = \boldsymbol{C} : \boldsymbol{\epsilon}$ takes the canonical form (in the natural anisotropy basis),

$$\hat{\sigma} = [C]\hat{\epsilon} \quad [C]^{-1} = \begin{bmatrix} \frac{1}{E} & -\frac{\nu}{E} & -\frac{\nu}{E} & 0 & 0 & 0 \\ -\frac{\nu}{E} & \frac{1}{E} & -\frac{\nu}{E} & 0 & 0 & 0 \\ -\frac{\nu}{E} & -\frac{\nu}{E} & \frac{1}{E} & 0 & 0 & 0 \\ 0 & 0 & 0 & \frac{1}{2G} & 0 & 0 \\ 0 & 0 & 0 & 0 & \frac{1}{2G} & 0 \\ 0 & 0 & 0 & 0 & 0 & \frac{1}{2G} \end{bmatrix}_{(\vec{b}_1,\vec{b}_2,\vec{b}_3)} \tag{D.12}$$

with E the Young's modulus. There are $N = 3$ Kelvin moduli,

$$\Lambda^{K=1} = \Lambda^{(1)} = 3K = \frac{E}{1 - 2\nu},$$
$$\Lambda^{K=2} = \Lambda^{(2)} = \Lambda^{(3)} = \frac{E}{1 + \nu},$$
$$\Lambda^{K=3} = \Lambda^{(4)} = \Lambda^{(5)} = \Lambda^{(6)} = 2G \tag{D.13}$$

The 6 corresponding eigentensors in the basis $(\vec{b}_1, \vec{b}_2, \vec{b}_3)$

$$e^{(1)} = \frac{1}{\sqrt{3}}\mathbf{I}, \quad e^{(2)} = \frac{\vec{b}_1 \otimes \vec{b}_1 - \vec{b}_2 \otimes \vec{b}_2}{\sqrt{2}}, \quad e^{(3)} = \frac{\vec{b}_1 \otimes \vec{b}_1 + \vec{b}_2 \otimes \vec{b}_2 - 2\vec{b}_3 \otimes \vec{b}_3}{\sqrt{6}}$$
$$e^{(4)} = \frac{\vec{b}_2 \otimes \vec{b}_3 + \vec{b}_3 \otimes \vec{b}_2}{\sqrt{2}}\mathbf{I}, \quad e^{(5)} = \frac{\vec{b}_3 \otimes \vec{b}_1 + \vec{b}_1 \otimes \vec{b}_3}{\sqrt{2}}, \quad e^{(6)} = \frac{\vec{b}_1 \otimes \vec{b}_2 + \vec{b}_2 \otimes \vec{b}_1}{\sqrt{2}} \tag{D.14}$$

These can be represented in tensorial forms using six basis B tensors. In the following these tensors are renamed such that the first 5 tensors upon performing an

inner product with the Cauchy stress tensor, extract its deviatoric component and the sixth one extracts it hydrostatic component as,

$$B^{(1)} = \frac{1}{\sqrt{2}} \begin{bmatrix} -1 & 0 & 0 \\ 0 & 1 & 0 \\ 0 & 0 & 0 \end{bmatrix} ; B^{(2)} = \frac{1}{\sqrt{6}} \begin{bmatrix} -1 & 0 & 0 \\ 0 & -1 & 0 \\ 0 & 0 & 2 \end{bmatrix} ; B^{(3)} = \frac{1}{\sqrt{2}} \begin{bmatrix} 0 & 0 & 0 \\ 0 & 0 & 1 \\ 0 & 1 & 0 \end{bmatrix} ;$$

$$B^{(4)} = \frac{1}{\sqrt{2}} \begin{bmatrix} 0 & 0 & 1 \\ 0 & 0 & 0 \\ 1 & 0 & 0 \end{bmatrix} ; B^{(5)} = \frac{1}{\sqrt{2}} \begin{bmatrix} 0 & 1 & 0 \\ 1 & 0 & 0 \\ 0 & 0 & 0 \end{bmatrix} ; B^{(6)} = \frac{1}{\sqrt{3}} \begin{bmatrix} 1 & 0 & 0 \\ 0 & 1 & 0 \\ 0 & 0 & 1 \end{bmatrix} ; \tag{D.15}$$

The projectors can be defined as

$$\boldsymbol{P}^{K=1} = \boldsymbol{e}^{(1)} \otimes \boldsymbol{e}^{(1)}$$

$$\boldsymbol{P}^{K=2} = \boldsymbol{e}^{(2)} \otimes \boldsymbol{e}^{(2)} + \boldsymbol{e}^{(3)} \otimes \boldsymbol{e}^{(3)}$$

$$\boldsymbol{P}^{K=3} = \boldsymbol{e}^{(4)} \otimes \boldsymbol{e}^{(4)} + \boldsymbol{e}^{(5)} \otimes \boldsymbol{e}^{(5)} + \boldsymbol{e}^{(6)} \otimes \boldsymbol{e}^{(6)} \tag{D.16}$$

The Kelvin stresses $\boldsymbol{\sigma}^K = \boldsymbol{P}^K : \boldsymbol{\sigma}$ are then obtained as:

1) $\boldsymbol{\sigma}^{K=1} = \boldsymbol{\sigma}^H$ is the hydrostatic stress $\frac{1}{3}\mathrm{tr}(\boldsymbol{\sigma})\mathbf{I}$ associated to the Kelvin modulus $3K$

2) $\boldsymbol{\sigma}^{K=2} = \boldsymbol{\sigma}^d$ is the diagonal part of the deviatoric stress in natural anisotropy basis and is associated to the Kelvin modulus $\frac{E}{(1+\nu)}$

3) $\boldsymbol{\sigma}^{K=3} = \boldsymbol{\sigma}^{\bar{d}}$ is the off-diagonal deviatoric tensor in this same basis and is associated to the Kelvin modulus $2G$

The two deviatoric tensors are then naturally obtained from the Kelvin analysis as

$$\boldsymbol{\sigma}^D = \boldsymbol{\sigma}^d + \boldsymbol{\sigma}^{\bar{d}} \quad \text{and} \quad \boldsymbol{\sigma} = \boldsymbol{\sigma}^D + \boldsymbol{\sigma}^H \tag{D.17}$$

It can be noted that Kelvin decomposition applied to isotropic materials exhibits two modes that are the classical hydrostatic and deviatoric parts of the stress tensor.

The couple stresses and elastic curvatures can be treated in a similar fashion as the Cauchy stresses and elastic strains. If the couple stresses and elastic curvatures are written in the Voigt notation, then they would be as follows:

$$\hat{M} = \left(M_{xx}, M_{yy}, M_{zz}, M_{yz}, M_{xz}, M_{xy}, M_{zy}, M_{zx}, M_{yx} \right)^T$$

$$\hat{\kappa} = \left(\kappa_{xx}, \kappa_{yy}, \kappa_{zz}, \kappa_{yz}, \kappa_{xz}, \kappa_{xy}, \kappa_{zy}, \kappa_{zx}, \kappa_{yx} \right)^T \qquad (D.18)$$

the elasticity law $\boldsymbol{M} = \boldsymbol{A} : \boldsymbol{\kappa}$ takes the form (in the natural anisotropy basis),

$$\hat{M} = [A]\hat{\kappa} \quad [A]^{-1} = \begin{bmatrix} A_1 & 0 & 0 & 0 & 0 & 0 & 0 & 0 & 0 \\ 0 & A_1 & 0 & 0 & 0 & 0 & 0 & 0 & 0 \\ 0 & 0 & A_1 & 0 & 0 & 0 & 0 & 0 & 0 \\ 0 & 0 & 0 & A_1 & 0 & 0 & 0 & 0 & 0 \\ 0 & 0 & 0 & 0 & A_1 & 0 & 0 & 0 & 0 \\ 0 & 0 & 0 & 0 & 0 & A_1 & 0 & 0 & 0 \\ 0 & 0 & 0 & 0 & 0 & 0 & A_1 & 0 & 0 \\ 0 & 0 & 0 & 0 & 0 & 0 & 0 & A_1 & 0 \\ 0 & 0 & 0 & 0 & 0 & 0 & 0 & 0 & A_1 \end{bmatrix}_{(\vec{b}_1,\vec{b}_2,\vec{b}_3)} \qquad (D.19)$$

here A_2 is assumed to be zero in the isotropic case. Also note that both couple stress and elastic curvature in the constitutive relationship are deviatoric in nature, therefore the above form of the tensor automatically deals with these. There is only one non-zero Kelvin moduli,

$$\Phi^{K=1} = \Phi^{(1)} = \Phi^{(2)} = \Phi^{(3)} = \Phi^{(4)} = \Phi^{(5)} = \Phi^{(6)} = \Phi^{(7)} = \Phi^{(8)} = \Phi^{(9)} = A_1 \quad (D.20)$$

The 9 corresponding eigentensors in the basis $(\vec{b}_1, \vec{b}_2, \vec{b}_3)$ are

$$\boldsymbol{e}^{(1)} = \frac{1}{\sqrt{3}}\mathbf{I}, \quad \boldsymbol{e}^{(2)} = \frac{\vec{b}_1 \otimes \vec{b}_1 - \vec{b}_2 \otimes \vec{b}_2}{\sqrt{2}}, \quad \boldsymbol{e}^{(3)} = \frac{\vec{b}_1 \otimes \vec{b}_1 + \vec{b}_2 \otimes \vec{b}_2 - 2\vec{b}_3 \otimes \vec{b}_3}{\sqrt{6}}$$

$$\boldsymbol{e}^{(4)} = \vec{b}_2 \otimes \vec{b}_3, \quad \boldsymbol{e}^{(5)} = \vec{b}_1 \otimes \vec{b}_3, \quad \boldsymbol{e}^{(6)} = \vec{b}_1 \otimes \vec{b}_2,$$

$$\boldsymbol{e}^{(7)} = \vec{b}_3 \otimes \vec{b}_2, \quad \boldsymbol{e}^{(8)} = \vec{b}_3 \otimes \vec{b}_1, \quad \boldsymbol{e}^{(9)} = \vec{b}_2 \otimes \vec{b}_1 \qquad (D.21)$$

337

These can be represented in tensorial forms using nine basis B_2 tensors. In the following these tensors are renamed such that the first 8 tensors upon performing an inner product with the couple stress tensor, extract its deviatoric component and the ninth one extracts it hydrostatic component (which is zero) as,

$$B_2^{(1)} = \frac{1}{\sqrt{2}} \begin{bmatrix} -1 & 0 & 0 \\ 0 & 1 & 0 \\ 0 & 0 & 0 \end{bmatrix} ; B_2^{(2)} = \frac{1}{\sqrt{6}} \begin{bmatrix} -1 & 0 & 0 \\ 0 & -1 & 0 \\ 0 & 0 & 2 \end{bmatrix} ; B_2^{(3)} = \begin{bmatrix} 0 & 0 & 0 \\ 0 & 0 & 1 \\ 0 & 0 & 0 \end{bmatrix} ;$$

$$B_2^{(4)} = \begin{bmatrix} 0 & 0 & 1 \\ 0 & 0 & 0 \\ 0 & 0 & 0 \end{bmatrix} ; B_2^{(5)} = \begin{bmatrix} 0 & 1 & 0 \\ 0 & 0 & 0 \\ 0 & 0 & 0 \end{bmatrix} ; B_2^{(6)} = \begin{bmatrix} 0 & 0 & 0 \\ 0 & 0 & 0 \\ 0 & 1 & 0 \end{bmatrix} ;$$

$$B_2^{(7)} = \begin{bmatrix} 0 & 0 & 0 \\ 0 & 0 & 0 \\ 1 & 0 & 0 \end{bmatrix} ; B_2^{(8)} = \begin{bmatrix} 0 & 0 & 0 \\ 1 & 0 & 0 \\ 0 & 0 & 0 \end{bmatrix} ; B_2^{(9)} = \frac{1}{\sqrt{3}} \begin{bmatrix} 1 & 0 & 0 \\ 0 & 1 & 0 \\ 0 & 0 & 1 \end{bmatrix} \qquad \text{(D.22)}$$

The projectors can be defined as

$$\boldsymbol{Q}^{K=1} = \boldsymbol{e}^{(1)} \otimes \boldsymbol{e}^{(1)}$$

$$\boldsymbol{Q}^{K=2} = \boldsymbol{e}^{(2)} \otimes \boldsymbol{e}^{(2)} + \boldsymbol{e}^{(3)} \otimes \boldsymbol{e}^{(3)}$$

$$\boldsymbol{Q}^{K=3} = \boldsymbol{e}^{(4)} \otimes \boldsymbol{e}^{(4)} + \boldsymbol{e}^{(5)} \otimes \boldsymbol{e}^{(5)} + \boldsymbol{e}^{(6)} \otimes \boldsymbol{e}^{(6)}$$

$$+ \boldsymbol{e}^{(7)} \otimes \boldsymbol{e}^{(7)} + \boldsymbol{e}^{(8)} \otimes \boldsymbol{e}^{(8)} + \boldsymbol{e}^{(9)} \otimes \boldsymbol{e}^{(9)} \qquad \text{(D.23)}$$

The Kelvin stresses $\boldsymbol{M}^K = \boldsymbol{Q}^K : \boldsymbol{M}$ are then obtained as:

1) $\boldsymbol{M}^{K=1} = \boldsymbol{M}^H$ is the hydrostatic component of the deviatoric couple stress and is therefore equal to zero.

2) $\boldsymbol{M}^{K=2} = \boldsymbol{M}^d$ is the diagonal part of the deviatoric couple stress in natural anisotropy basis and is associated to the Kelvin modulus A_1.

3) $\boldsymbol{M}^{K=3} = \boldsymbol{M}^{\bar{d}}$ is the off-diagonal deviatoric couple stress in this same basis and is also associated to the Kelvin modulus A_1.

The two deviatoric tensors are then naturally obtained from the Kelvin analysis as

$$\boldsymbol{M} = \boldsymbol{M}^D = \boldsymbol{M}^d + \boldsymbol{M}^{\bar{d}} \tag{D.24}$$

APPENDIX E

STATIC FDDM FFT IN HETEROGENEOUS ELASTICITY

E.0.1 A Fourier transform based approach

In the following, a Fourier transform based methodology is developed to solve the static field disclination and dislocation mechanics problem presented in section 3.2.1. The main idea is to separate the compatible and incompatible contributions from elastic strains and curvatures by performing operations in the Fourier space. This method derives motivation from the Fourier transform based static field dislocation mechanics method for homogeneous elasticity proposed in the work of Brenner *et al.* [50], and extends it to disclinations in heterogeneous elasticity.

Consider a heterogeneous periodic medium defined using a discrete Fourier grid of equi-distant Fourier points. Each of these points are allowed to have their own elastic properties. Let the medium contain an arbitrary distribution of continuously distributed dislocations and disclinations which are defined using their respective defect densities in such a manner that each zone of incompatibility is associated with an individual defect. This highlights that the present framework is developed at the fine scale. The compatible and incompatible elastic strain and curvature induced in the presence of these defects, along with externally imposed conditions, results in the generation of Cauchy and couple stresses in the medium. In order to represent these stresses, the isotropic elastic laws developed in section 3.1.4.4 are recalled,

$$\sigma_{ij}^s = C_{ijkl}\left(\epsilon_{kl}^{e\parallel} + \epsilon_{kl}^{e\perp}\right) + B_{ijkl}\kappa_{kl}^{e\perp Ds} \tag{E.1}$$

$$M_{ij}^D = D_{ijkl}\epsilon_{kl}^{e\perp D} + A_{ijkl}\left(\kappa_{kl}^{e\parallel D} + \kappa_{kl}^{e\perp D}\right) \tag{E.2}$$

Let A°, B°, C° and D° be the elasticity tensors for a reference medium and δA,

340

δB, δC and δD be their local variations then,

$$\sigma^s = (C^\circ + \delta C) : \left(\epsilon^{e\|} + \epsilon^{e\perp}\right) + (B^\circ + \delta B) : \kappa^{e\perp Ds} \tag{E.3}$$

$$M^D = (A^\circ + \delta A) : \left(\kappa^{e\|} + \kappa^{e\perp}\right) + (D^\circ + \delta D) : \epsilon^{e\perp D} \tag{E.4}$$

Then the Cauchy and couple stress polarization tensors, τ and μ respectively, can be defined as,

$$\tau = \delta C : \left(\epsilon^{e\|} + \epsilon^{e\perp}\right) + \delta B : \kappa^{e\perp Ds} \tag{E.5}$$

$$\mu = \delta A : \left(\kappa^{e\|} + \kappa^{e\perp}\right) + \delta D : \epsilon^{e\perp D} \tag{E.6}$$

Replacing the local variations in elasticity tensors with the reference elasticity tensors gives,

$$\tau = -C^\circ : \epsilon^{e\|} + C^\circ : \epsilon^{p\perp} + B^\circ : \kappa^{p\perp Ds} + \sigma^s \tag{E.7}$$

$$\mu = -A^\circ : \kappa^{e\|} + A^\circ : \kappa^{p\perp} + D^\circ : \epsilon^{p\perp D} + M^D \tag{E.8}$$

Recall the Stokes-Helmholtz decomposition of elastic strains and curvatures,

$$\epsilon^e = \epsilon^{e\|} + \epsilon^{e\perp} = \left(\nabla \tilde{u}\right)_{sym} + \epsilon^{e\perp} \tag{E.9}$$

$$\kappa^e = \kappa^{e\|} + \kappa^{e\perp} = \left(\nabla \tilde{\omega}\right)_{sym} + \kappa^{e\perp} \tag{E.10}$$

where $\nabla \tilde{u}$ and $\nabla \tilde{\omega}$ are arbitrary elastic displacement and rotation vector belonging to the null space of the curl operator. Without the loss of generality it can be assumed that the elastic rotation vector is a function of the elastic displacement as $\tilde{\omega}_i = \frac{1}{2} e_{ijk} \tilde{u}_{l,k}$. The polarization tensors in equations (E.5) and (E.6) can then be rewritten as,

$$\tau_{ij} = -C^\circ_{ijkl} \tilde{u}_{k,l} + C^\circ_{ijkl} \epsilon^{p\perp}_{kl} + B^\circ_{ijkl} \kappa^{p\perp Ds}_{kl} + \sigma^s_{ij} \tag{E.11}$$

$$\mu_{ij} = -\frac{1}{2} A^\circ_{ijkl} e_{kmn} \tilde{u}_{n,ml} + A^\circ_{ijkl} \kappa^{p\perp}_{kl} + D^\circ_{ijkl} \epsilon^{p\perp D}_{kl} + M^D_{ij} \tag{E.12}$$

Substituting the above equations into the equilibrium equation (3.14) gives,

$$\sigma^s_{ij,j} + \frac{1}{2} e_{ica} M^D_{ab,bc} = \left[C^\circ_{ijkl} \tilde{u}_{k,lj} + \frac{1}{2} e_{ica} A^\circ_{abmn} e_{mpk} \tilde{u}_{k,pnbc} \right]$$

341

$$+ \begin{bmatrix} -C^{\circ}_{ijkl}\epsilon^{p\perp}_{kl,j} - B^{\circ}_{ijkl}\kappa^{p\perp}_{kl,j} - \dfrac{1}{2}e_{ica}A^{\circ}_{abmn}\kappa^{p\perp}_{mn,bc} \\[2mm] -\dfrac{1}{2}e_{ica}D^{\circ}_{abmn}\epsilon^{p\perp}_{mn,bc} + \dfrac{1}{2}e_{ica}\mu_{ab,bc} + \tau_{ij,j} \end{bmatrix} = 0 \quad \text{(E.13)}$$

Defining $F^{\circ}_{icbnpk} = \frac{1}{2}e_{ica}A^{\circ}_{abmn}e_{mpk}$ and $\hat{f}_i$ as a fictive body force representing the remainder of equation (E.13).

$$\sigma^{s}_{ij,j} + \frac{1}{2}e_{ica}M^{D}_{ab,bc} = C^{\circ}_{ijkl}\tilde{u}_{k,lj} + F^{\circ}_{icbnpk}\tilde{u}_{k,pnbc} + f_i = 0 \quad \text{(E.14)}$$

This can be transformed into a Navier type equation using periodic Green's function as follows,

$$C^{\circ}_{ijkl}\tilde{G}_{kr,lj}\left(x - x'\right) + F^{\circ}_{icbnpk}\tilde{G}_{kr,pnbc}\left(x - x'\right) + \delta_{ir}\delta\left(x - x'\right) = 0 \quad \text{(E.15)}$$

Taking its Fourier transform gives,

$$\left[(i)^2\xi_j\xi_l C^{\circ}_{ijkl} + (i)^4\xi_c\xi_b\xi_n\xi_p F^{\circ}_{icbnpk}\right]\hat{\tilde{G}}_{kr}\left(\vec{k}\right) = -\delta_{ir} \quad \text{(E.16)}$$

Rearranging the terms gives the expression for the periodic Green's function in the Fourier space as

$$\hat{\tilde{G}}_{ki}\left(\vec{k}\right) = \left[\xi_j\xi_l C^{\circ}_{ijkl} - \xi_c\xi_b\xi_n\xi_p F^{\circ}_{icbnpk}\right]^{-1} \quad \text{(E.17)}$$

Focusing on the fictive body force,

$$\hat{f}_i\left(\vec{k}\right) = \begin{bmatrix} -\left(i\xi_j\right)C^{\circ}_{ijkl}\hat{\epsilon}^{p\perp}_{kl}\left(\vec{k}\right) - \left(i\xi_j\right)B^{\circ}_{ijkl}\hat{\kappa}^{p\perp}_{kl}\left(\vec{k}\right) \\[2mm] +\dfrac{1}{2}\xi_b\xi_c e_{ica}A^{\circ}_{abmn}\hat{\kappa}^{p\perp}_{mn}\left(\vec{k}\right) + \dfrac{1}{2}\xi_b\xi_c e_{ica}D^{\circ}_{abmn}\hat{\epsilon}^{p\perp}_{mn}\left(\vec{k}\right) \\[2mm] -\dfrac{1}{2}\xi_b\xi_c e_{ica}\hat{\mu}_{ab}\left(\vec{k}\right) + \left(i\xi_j\right)\hat{\tau}_{ij}\left(\vec{k}\right) \end{bmatrix} \quad \text{(E.18)}$$

recall from equation (2.92) that $\boldsymbol{\theta} = \mathbf{curl}\,\boldsymbol{\kappa}^{p\perp}$. Taking curl on both sides of this equation gives,

$$\mathbf{curl}\,\boldsymbol{\theta} = -\mathbf{curl}\left(\mathbf{curl}\,\boldsymbol{\kappa}^{p\perp}\right) = -\mathbf{grad}\left(\mathbf{div}\,\boldsymbol{\kappa}^{p\perp}\right) + \nabla^2\boldsymbol{\kappa}^{p\perp} \quad \text{(E.19)}$$

As a consequence of the Stokes-Helmholtz decomposition, $\boldsymbol{\kappa}^{p\perp}$ belongs to the curl space. Therefore its divergence is equal to zero which gives $\mathbf{curl}\,\boldsymbol{\theta} = \nabla^2 \boldsymbol{\kappa}^{p\perp}$ or, in component form, $e_{jkl}\theta_{il,k} = \kappa^{p\perp}_{ij,mm}$. Taking its Fourier transform and rearranging terms gives,

$$\hat{\kappa}^{p\perp}_{ij}\left(\vec{\boldsymbol{k}}\right) = -\frac{i\xi_k e_{jkl}\hat{\theta}_{il}\left(\vec{\boldsymbol{k}}\right)}{\left\|\vec{\boldsymbol{k}}\right\|^2} \tag{E.20}$$

where $\vec{\boldsymbol{k}}$ is a vector in Fourier space with ξ_k being its equivalent component form. For a given disclination density, the incompatible component of the plastic curvature can be obtained in Fourier space using the above equation.

In a similar manner, an expression can be derived for the incompatible plastic strain as a function of dislocation density in Fourier space. Recall from equation (2.99) that $-e_{jkl}\epsilon^{p\perp}_{il,k} - \kappa^{p(\|+\perp)}_{kk}\delta_{ij} + \kappa^{p(\|+\perp)}_{ji} = \alpha_{ij}$. Transferring the terms containing plastic curvature on the other side of the expression, taking the curl of the equation and then the Fourier transform gives,

$$\hat{\epsilon}^{p\perp}_{ij}\left(\vec{\boldsymbol{k}}\right) = -\frac{i\xi_k e_{jkl}\left(\hat{\alpha}_{il}\left(\vec{\boldsymbol{k}}\right) - \hat{\kappa}^{p\perp}_{li}\left(\vec{\boldsymbol{k}}\right) + \hat{\kappa}^{p(\|+\perp)}_{mm}\left(\vec{\boldsymbol{k}}\right)\delta_{il}\right)}{\left\|\vec{\boldsymbol{k}}\right\|^2} \tag{E.21}$$

Note that the curl of the compatible component of plastic curvature is equal to zero. Therefore only the incompatible component is shown in the second term within the rounded brackets in the numerator. This does not apply to the third term involving the trace (an invariant) of the plastic curvature; both compatible and incompatible components have a contribution. In this case, the curl is taken over the Kronecker delta function which introduces the partial derivative of the latter *i.e.* $\delta_{ij,k}$. It can be shown that $\delta_{ij,k}$ is equal to zero. Recall the definition of the Kronecker delta functions in terms of the Heaviside function as

$$\delta_{ij} = H\left(x_i - x_j\right) - H\left(x_j - x_i\right) - 1 \tag{E.22}$$

where

$$H\left(\vec{\pmb{x}} - \vec{\pmb{x}}'\right) = \begin{cases} 0, \ \vec{\pmb{x}} < \vec{\pmb{x}}' \\ 1, \ \vec{\pmb{x}} \geq \vec{\pmb{x}}' \end{cases} \tag{E.23}$$

Recalling the definition of the Dirac delta function $\delta(\vec{\pmb{x}}) = -\delta(-\vec{\pmb{x}})$, the partial derivative of the Kronecker delta is,

$$\begin{aligned} \delta_{ij,k} &= \delta\left(x_i - x_j\right)\delta_{ik} - \delta\left(x_i - x_j\right)\delta_{jk} - \delta\left(x_j - x_i\right)\delta_{jk} + \delta\left(x_j - x_i\right)\delta_{ik} \\ &= \delta\left(x_i - x_j\right)\delta_{ik} - \delta\left(x_i - x_j\right)\delta_{jk} + \delta\left(x_i - x_j\right)\delta_{jk} - \delta\left(x_i - x_j\right)\delta_{ik} \\ &= 0 \end{aligned} \tag{E.24}$$

Therefore, equation (E.21) can be reduced to

$$\hat{\epsilon}_{ij}^{p\perp}\left(\vec{\pmb{k}}\right) = -\frac{i\xi_k e_{jkl}\left(\hat{\alpha}_{il}\left(\vec{\pmb{k}}\right) - \hat{\kappa}_{li}^{p(\|+\perp)}\left(\vec{\pmb{k}}\right)\right)}{\left\|\vec{\pmb{k}}\right\|^2} \tag{E.25}$$

Finally, the equations (E.20) and (E.25) for incompatible plastic strain and curvature can be substituted in equation (E.18) for the fictive body force to obtain the following compatible elastic displacements, strains and curvatures as,

$$\tilde{u}_i^{\|} = FT^{-1}\left(\hat{\tilde{G}}_{ij}\left(\vec{\pmb{k}}\right)\hat{\tilde{f}}_j\left(\vec{\pmb{k}}\right)\right) \tag{E.26}$$

$$\epsilon_{ij}^{e\|} = FT^{-1}\left(i\left(\xi_j\hat{\tilde{G}}_{ik}\left(\vec{\pmb{k}}\right)\right)_{sym}\hat{\tilde{f}}_k\left(\vec{\pmb{k}}\right)\right) \tag{E.27}$$

$$\kappa_{ij}^{e\|} = \frac{1}{2}e_{ikl}FT^{-1}\left(-\xi_j\xi_k\hat{\tilde{G}}_{lm}\left(\vec{\pmb{k}}\right)\hat{\tilde{f}}_m\left(\vec{\pmb{k}}\right)\right) \tag{E.28}$$

These expressions are the periodic solutions to the fluctuations in compatible fields. These need to augmented with the mean compatible fields which can be derived from the boundary conditions.

These expressions, which are dependent on the expressions of the Green's function and the fictive body force, can attain different forms depending on the type of incompatibility in the material, and heterogeneous or homogeneous elasticity. To that end, table 8 proposes the expressions for the Green's function and fictive body force that

344

can be deduced from equations (E.17) and (E.18) based on type of incompatibility and heterogeneous or homogeneous elasticity.

Table 8: Green's function and fictive body force

INCOMPA-TIBILITY	ELASTICITY	GREEN'S FUNCTION & FICTIVE BODY FORCE
NO	Heterogeneous	$\hat{\tilde{G}}_{ki}\left(\vec{\boldsymbol{k}}\right) = \left[\xi_j\xi_l C^\circ_{ijkl}\right]^{-1}$ $\hat{f}_i\left(\vec{\boldsymbol{k}}\right) = \left[\left(i\xi_j\right)\hat{\tau}_{ij}\left(\vec{\boldsymbol{k}}\right)\right]$
Dislocations	Homogeneous	$\hat{\tilde{G}}_{ki}\left(\vec{\boldsymbol{k}}\right) = \left[\xi_j\xi_l C^\circ_{ijkl}\right]^{-1}$ $\hat{f}_i\left(\vec{\boldsymbol{k}}\right) = \left[-\left(i\xi_j\right)C^\circ_{ijkl}\hat{U}^{p\perp}_{kl}\left(\vec{\boldsymbol{k}}\right)\right]$
Dislocations	Heterogeneous	$\hat{\tilde{G}}_{ki}\left(\vec{\boldsymbol{k}}\right) = \left[\xi_j\xi_l C^\circ_{ijkl}\right]^{-1}$ $\hat{f}_i\left(\vec{\boldsymbol{k}}\right) = \left[-\left(i\xi_j\right)C^\circ_{ijkl}\hat{U}^{p\perp}_{kl}\left(\vec{\boldsymbol{k}}\right) + \left(i\xi_j\right)\hat{\tau}_{ij}\left(\vec{\boldsymbol{k}}\right)\right]$
Dislocations & Disclinations	Homogeneous	$\hat{\tilde{G}}_{ki}\left(\vec{\boldsymbol{k}}\right) = \left[\xi_j\xi_l C^\circ_{ijkl} - \xi_c\xi_b\xi_n\xi_p F^\circ_{icbnpk}\right]^{-1}$ $\hat{f}_i\left(\vec{\boldsymbol{k}}\right) = \begin{bmatrix} -\left(i\xi_j\right)C^\circ_{ijkl}\hat{\epsilon}^{p\perp}_{kl}\left(\vec{\boldsymbol{k}}\right) \\ -\left(i\xi_j\right)B^\circ_{ijkl}\hat{\kappa}^{p\perp}_{kl}\left(\vec{\boldsymbol{k}}\right) \\ +\frac{1}{2}\xi_b\xi_c e_{ica}A^\circ_{abmn}\hat{\kappa}^{p\perp}_{mn}\left(\vec{\boldsymbol{k}}\right) \\ +\frac{1}{2}\xi_b\xi_c e_{ica}D^\circ_{abmn}\hat{\epsilon}^{p\perp}_{mn}\left(\vec{\boldsymbol{k}}\right) \end{bmatrix}$
Dislocations & Disclinations	Heterogeneous	$\hat{\tilde{G}}_{ki}\left(\vec{\boldsymbol{k}}\right) = \left[\xi_j\xi_l C^\circ_{ijkl} - \xi_c\xi_b\xi_n\xi_p F^\circ_{icbnpk}\right]^{-1}$ $\hat{f}_i\left(\vec{\boldsymbol{k}}\right) = \begin{bmatrix} -\left(i\xi_j\right)C^\circ_{ijkl}\hat{\epsilon}^{p\perp}_{kl}\left(\vec{\boldsymbol{k}}\right) \\ -\left(i\xi_j\right)B^\circ_{ijkl}\hat{\kappa}^{p\perp}_{kl}\left(\vec{\boldsymbol{k}}\right) \\ +\frac{1}{2}\xi_b\xi_c e_{ica}A^\circ_{abmn}\hat{\kappa}^{p\perp}_{mn}\left(\vec{\boldsymbol{k}}\right) \\ +\frac{1}{2}\xi_b\xi_c e_{ica}D^\circ_{abmn}\hat{\epsilon}^{p\perp}_{mn}\left(\vec{\boldsymbol{k}}\right) \\ -\frac{1}{2}\xi_b\xi_c e_{ica}\hat{\mu}_{ab}\left(\vec{\boldsymbol{k}}\right) \\ +\left(i\xi_j\right)\hat{\tau}_{ij}\left(\vec{\boldsymbol{k}}\right) \end{bmatrix}$

E.1 Iterative procedure

In this section, an algorithm to solve the static FDDM FFT problem of finding compatible elastic strain and curvature fields and corresponding Cauchy and couple stresses for prescribed polar densities of disclinations and dislocations.

The algorithm begins by computing the incompatible plastic curvature $\kappa_{ij}^{p\perp}$ from the prescribed disclination density θ_{ij} using equation (E.20). The dislocation density is also prescribed and along with the incompatible plastic curvature it provides the incompatible plastic strain field through equation (E.25).

In the homogeneous elasticity case where $\boldsymbol{A}^\circ = \boldsymbol{A}$, $\boldsymbol{B}^\circ = \boldsymbol{B}$, $\boldsymbol{C}^\circ = \boldsymbol{C}$ and $\boldsymbol{D}^\circ = \boldsymbol{D}$, these field quantities are sufficient to obtain the values for compatible elastic displacement, strain and curvature through equations (E.26) – (E.28). Cauchy and couple stresses can then be directly obtained using equations (E.1) and (E.2).

In the case of heterogeneous elasticity, the compatible elastic displacements, strains, and curvatures are dependent on the Cauchy and couple stress polarization tensors and vice versa. In this case, an iterative procedure needs to be adopted to solve the problem. Let the compatible elastic displacement, strain and curvature be initialized to zero at iteration $I = 0$, i.e. $\tilde{u}_i^{I=0} = 0$, $\epsilon_{ij}^{e,I=0} = 0$ and $\kappa_{ij}^{e,I=0} = 0$. If λ^I and ϕ^I represent the Cauchy and couple stress guesses at iteration I, then at step $I = 0$ these can be estimated as:

$$\lambda_{ij}^{(I=0)} = C_{ijkl}\epsilon_{kl}^{e\perp} + B_{ijkl}\kappa_{kl}^{e\perp Ds} = -C_{ijkl}\epsilon_{kl}^{p\perp} - B_{ijkl}\kappa_{kl}^{p\perp Ds} \tag{E.29}$$

$$\phi_{ij}^{D(I=0)} = D_{ijkl}\epsilon_{kl}^{e\perp D} + A_{ijkl}\kappa_{kl}^{e\perp D} = -D_{ijkl}\epsilon_{kl}^{p\perp D} - A_{ijkl}\kappa_{kl}^{p\perp D} \tag{E.30}$$

Then for an iteration step I, the polarization tensor can be defined as

$$\tau_{ij}^{(I)} = -C_{ijkl}^\circ \tilde{u}_{k,l}^{(I-1)} + C_{ijkl}^\circ \epsilon_{kl}^{p\perp} + B_{ijkl}^\circ \kappa_{kl}^{p\perp Ds} + \lambda_{ij}^{(I-1)} \tag{E.31}$$

$$\phi_{ij}^{(I)} = -\frac{1}{2}A_{ijkl}^\circ e_{kmn}\tilde{u}_{n,ml}^{(I-1)} + D_{ijkl}^\circ \epsilon_{kl}^{p\perp D} + A_{ijkl}^\circ \kappa_{kl}^{p\perp D} + \mu_{ij}^{(I-1)} \tag{E.32}$$

346

The Green's function can either be computed beforehand or during the iterative procedure using equation (E.17). The fictive body force at step I is computed as:

$$\hat{f}_i^{(I)}\left(\vec{k}\right) = \begin{bmatrix} -\left(i\xi_j\right) C^\circ_{ijkl}\hat{\epsilon}^{p\perp}_{kl}\left(\vec{k}\right) - \left(i\xi_j\right) B^\circ_{ijkl}\hat{\kappa}^{p\perp}_{kl}\left(\vec{k}\right) \\ +\frac{1}{2}\xi_b\xi_c e_{ica} A^\circ_{abmn}\hat{\kappa}^{p\perp}_{mn}\left(\vec{k}\right) + \frac{1}{2}\xi_b\xi_c e_{ica} D^\circ_{abmn}\hat{\epsilon}^{p\perp}_{mn}\left(\vec{k}\right) \\ -\frac{1}{2}\xi_b\xi_c e_{ica}\hat{\mu}_{ab}\left(\vec{k}\right) + \left(i\xi_j\right)\hat{\tau}_{ij}\left(\vec{k}\right) \end{bmatrix} \qquad \text{(E.33)}$$

The I iteration estimates for compatible elastic strain $e_{ij}^{e\|(I)}$ and curvature $k_{ij}^{e\|(I)}$ fields can be obtained as

$$e_{ij}^{e\|(I)} = FT^{-1}\left(i\left(\xi_j\hat{\tilde{G}}_{ik}\left(\vec{k}\right)\right)_{sym}\hat{\tilde{f}}_k^{(I)}\left(\vec{k}\right)\right) \qquad \text{(E.34)}$$

$$\tilde{k}_{ij}^{e\|(I)} = \frac{1}{2}e_{ikl}FT^{-1}\left(-\xi_j\xi_k\hat{\tilde{G}}_{lm}\left(\vec{k}\right)\hat{\tilde{f}}_m^{(I)}\left(\vec{k}\right)\right) \qquad \text{(E.35)}$$

Then the Ith guesses for Cauchy and couple stresses can be obtained by

$$\lambda_{ij}^{(I=0)} = C_{ijkl}(\epsilon_{kl}^{e\|} - \epsilon_{kl}^{p\perp}) + B_{ijkl}(\kappa_{kl}^{e\|Ds} - \kappa_{kl}^{p\perp Ds}) \qquad \text{(E.36)}$$

$$\phi_{ij}^{D(I=0)} = D_{ijkl}(\epsilon_{kl}^{e\|D} - \epsilon_{kl}^{p\perp}D) + A_{ijkl}(\kappa_{kl}^{e\|D} - \kappa_{kl}^{p\perp D}) \qquad \text{(E.37)}$$

The algorithm then repeats itself from equation (E.31) until convergence is achieved. An accelerated procedure, such as the augmented Lagrangian scheme, can be used to achieve faster convergence.

APPENDIX F

DISCRETE FOURIER TRANSFORMS

In this section, a 3-dimensional discrete Fourier transform (DFT) based framework is proposed as a solution to overcome the Gibbs phenomenon associated in taking continuous Fourier transforms of discontinuous fields. The method is motivated from a recent work by Berbenni *et al.* [34] on a 2-dimensional DFT approach introduced to solve Poisson and Navier type equations associated with incompatibilities introduced in presence of dislocations and G-disclinations. The microstrcture is discretized into a regular grid of $N_1 \times N_2 \times N_3$ voxels with equal spacing in all three dimensions with periodic boundary conditions along all the surfaces. The position vectors is defined as $\vec{x} = ((l-1)\,\delta_1, (m-1)\,\delta_2, (n-1)\,\delta_3)$, where $l = 1 \rightarrow N_1, m = 1 \rightarrow N_2, n = 1 \rightarrow N_3$ and δ_1, δ_2 and δ_3 are the voxel sizes in directions 1, 2 and 3 respectively. The total number of voxels are $N_{tot} = N_1 N_2 N_3$.

In the following the derivations are with respect to the "fourn" subroutine in FORTRAN obtained from the open source "Numerical Recipes 77" book. In the convention adopted by the book, the discrete Fourier transform is defined as:

$$\hat{f}(\xi_1, \xi_2, \xi_3) = \sum_{l=1}^{N_1} \sum_{m=1}^{N_2} \sum_{n=1}^{N_3} f(i,j,k)\, e^{2\pi i (l-1)(\xi_1-1)/N_1} e^{2\pi i (m-1)(\xi_2-1)/N_2} e^{2\pi i (n-1)(\xi_3-1)/N_3} \tag{F.1}$$

and

$$f(l,m,n) = \sum_{l=1}^{N_1} \sum_{m=1}^{N_2} \sum_{n=1}^{N_3} \frac{\hat{f}(\xi_1, \xi_2, \xi_3)\, e^{-2\pi i (l-1)(\xi_1-1)/N_1} e^{-2\pi i (m-1)(\xi_2-1)/N_2} e^{-2\pi i (n-1)(\xi_3-1)/N_3}}{N_{tot}} \tag{F.2}$$

where $i = \sqrt{-1}$. ξ_1, ξ_2 and ξ_3 are the frequencies corresponding to l, m and n, respectively.

In the following the shift theorem for Fourier transforms will be utilized to compute the partial derivatives of functions approximated using the centered difference scheme.

348

With the Fourier transform convention adopted here, the shift theorem is defined as:

$$FT\left(f(l+P, m+Q, n+R)\right) = e^{-2\pi i P\xi_1/N_1} e^{-2\pi i Q\xi_2/N_2} e^{-2\pi i R\xi_3/N_3} FT\left(f(l, m, n)\right) \quad \text{(F.3)}$$

where FT represents the Fourier transform operator and P, Q, R are some integers.

Also, the partial derivative in the adopted convention is given as:

$$FT\left(\frac{\partial^3 f(l, m, n)}{\partial x_1 \partial x_2 \partial x_3}\right) = (-ik_1)(-ik_2)(-ik_3) FT\left(f(l, m, n)\right) \quad \text{(F.4)}$$

where $k_1 = 2\pi\xi_1$, $k_2 = 2\pi\xi_2$ and $k_3 = 2\pi\xi_3$ are the angular frequencies.

F.1 Differentiation rules

Let $\partial^{a+b+c} f(l, m, n)/\partial x_1^a \partial x_2^b \partial x_3^c$ correspond to the ath, bth and cth partial derivative of a funtion $f(l, m, n)$ with respect to x_1, x_2 and x_3, respectively. In the present work, only the partial dervatives corresponding to $a + b + c = 1$, 2, 3 and 4 are considered. The first to fourth order partial derivates are computed on the discrete grid based on the 27-voxel finite difference approximation of partial derivatives using centered differences. The accuracy achieved is of the order $O(\delta_1^2, \delta_2^2, \delta_3^2)$.

F.1.1 First order partial derivatives

The first order partial derivatives are approximated as

$$\frac{\partial f(l, m, n)}{\partial x_1} = \frac{f(l+1, m, n) - f(l-1, m, n)}{2\delta_1}$$
$$\frac{\partial f(l, m, n)}{\partial x_2} = \frac{f(l, m+1, n) - f(l, m-1, n)}{2\delta_2} \quad \text{(F.5)}$$
$$\frac{\partial f(l, m, n)}{\partial x_3} = \frac{f(l, m, n+1) - f(l, m, n-1)}{2\delta_3}$$

The continuous Fourier transforms of the above equations are $-ik_1$, $-ik_2$ and $-ik_3$. The equivalent discrete Fourier transforms are given as

$$-ik_1 \leftrightarrow \frac{e^{-2\pi i(\xi_1-1)/N_1} - e^{2\pi i(\xi_1-1)/N_1}}{2\delta_1} = -\frac{i}{\delta_1}\sin\left(\frac{2\pi(\xi_1-1)}{N_1}\right)$$
$$-ik_2 \leftrightarrow \frac{e^{-2\pi i(\xi_2-1)/N_2} - e^{2\pi i(\xi_2-1)/N_2}}{2\delta_2} = -\frac{i}{\delta_2}\sin\left(\frac{2\pi(\xi_2-1)}{N_2}\right)$$
$$-ik_3 \leftrightarrow \frac{e^{-2\pi i(\xi_3-1)/N_3} - e^{2\pi i(\xi_3-1)/N_3}}{2\delta_3} = -\frac{i}{\delta_3}\sin\left(\frac{2\pi(\xi_3-1)}{N_3}\right) \quad \text{(F.6)}$$

F.1.2 Second order partial derivatives

The second order partial derivatives are approximated as

$$\frac{\partial^2 f(l,m,n)}{\partial x_1^2} = \frac{f(l+1,m,n) - 2f(l,m,n) + f(l-1,m,n)}{\delta_1^2}$$

$$\frac{\partial^2 f(l,m,n)}{\partial x_2^2} = \frac{f(l,m+1,n) - 2f(l,m,n) + f(l,m-1,n)}{\delta_2^2}$$

$$\frac{\partial^2 f(l,m,n)}{\partial x_3^2} = \frac{f(l,m,n+1) - 2f(l,m,n) + f(l,m,n-1)}{\delta_3^2}$$

$$\frac{\partial^2 f(l,m,n)}{\partial x_1 \partial x_2} = \frac{\left[\begin{array}{c} f(l+1,m+1,n) - f(l+1,m-1,n) \\ -f(l-1,m+1,n) + f(l-1,m-1,n) \end{array}\right]}{4\delta_1\delta_2}$$

$$\frac{\partial^2 f(l,m,n)}{\partial x_1 \partial x_3} = \frac{\left[\begin{array}{c} f(l+1,m,n+1) - f(l+1,m,n-1) \\ -f(l-1,m,n+1) + f(l-1,m,n-1) \end{array}\right]}{4\delta_1\delta_3}$$

$$\frac{\partial^2 f(l,m,n)}{\partial x_2 \partial x_3} = \frac{\left[\begin{array}{c} f(l,m+1,n+1) - f(l,m+1,n-1) \\ -f(l,m-1,n+1) + f(l,m-1,n-1) \end{array}\right]}{4\delta_2\delta_3}$$

The continuous Fourier transform and the corresponding discrete Fourier transform are:

$$-k_1^2 \leftrightarrow \frac{2}{\delta_1^2}\left(1 - \cos\left(\frac{2\pi(\xi_1 - 1)}{N_1}\right)\right)$$

$$-k_2^2 \leftrightarrow \frac{2}{\delta_2^2}\left(1 - \cos\left(\frac{2\pi(\xi_2 - 1)}{N_2}\right)\right)$$

$$-k_3^2 \leftrightarrow \frac{2}{\delta_3^2}\left(1 - \cos\left(\frac{2\pi(\xi_3 - 1)}{N_3}\right)\right)$$

$$-k_1 k_2 \leftrightarrow -\frac{1}{\delta_1\delta_2}\sin\left(\frac{2\pi(\xi_1 - 1)}{N_1}\right)\sin\left(\frac{2\pi(\xi_2 - 1)}{N_2}\right)$$

$$-k_1 k_3 \leftrightarrow -\frac{1}{\delta_1\delta_3}\sin\left(\frac{2\pi(\xi_1 - 1)}{N_1}\right)\sin\left(\frac{2\pi(\xi_3 - 1)}{N_3}\right)$$

$$-k_2 k_3 \leftrightarrow -\frac{1}{\delta_2\delta_3}\sin\left(\frac{2\pi(\xi_2 - 1)}{N_2}\right)\sin\left(\frac{2\pi(\xi_3 - 1)}{N_3}\right) \tag{F.7}$$

F.1.3 Third order partial dervatives

Let D_{pqr} represent the third order partial derivatives with respect to $\partial x_p, \partial x_q, \partial x_r$ where p, q and r can all attain values 1, 2 and 3. There are 27 third order partial derivatives of a function possible in the 3-dimensional space. By virtue of Clairaut's theorem where the order of the partial derivatives can be exchanged, the following dependencies can be derived for D_{pqr}:

$$D_{111}$$
$$D_{112} = D_{121} = D_{211}$$
$$D_{113} = D_{131} = D_{311}$$
$$D_{122} = D_{212} = D_{221}$$
$$D_{123} = D_{132} = D_{213} = D_{231} = D_{312} = D_{321}$$
$$D_{133} = D_{313} = D_{331}$$
$$D_{222}$$
$$D_{223} = D_{232} = D_{322}$$
$$D_{233} = D_{232} = D_{332}$$
$$D_{333} \tag{F.8}$$

The above partial derivatives can be grouped together with respect to the types of indices as follows:

$$(1) D_{111}, D_{222}, D_{333}$$
$$(2) D_{112}, D_{113}, D_{122}, D_{133}, D_{223}, D_{233}$$
$$(3) D_{123} \tag{F.9}$$

Only the first three derivatives (D_{111}, D_{112} and D_{123}) of the above types will be computed in the following, the remaining can be obtained by cycling through the

indices. The third order partial derivatives are given as follows:

$$D_{111} = \frac{\partial^3 f(l,m,n)}{\partial x_1^3} = \frac{\begin{bmatrix} f(l+2,m,n) - 2f(l+1,m,n) \\ -2f(l-1,m,n) + f(l-2,m,n) \end{bmatrix}}{2\delta_1^3}$$

$$D_{112} = \frac{\partial^3 f(l,m,n)}{\partial x_1^2 \partial x_2} = \frac{\begin{bmatrix} f(l+1,m+1,n) - f(l+1,m-1,n) - 2f(l,m+1,n) \\ +2f(l,m-1,n) + f(l-1,m+1,n) - f(l-1,m-1,n) \end{bmatrix}}{2\delta_1^2 \delta_2}$$

$$D_{123} = \frac{\partial^3 f(l,m,n)}{\partial x_1 \partial x_2 \partial x_3} = \frac{\begin{bmatrix} f(l+1,m+1,n+1) - f(l+1,m+1,n-1) \\ -f(l+1,m-1,n+1) + f(l+1,m-1,n-1) \\ -f(l-1,m+1,n+1) + f(l-1,m+1,n-1) \\ +f(l-1,m-1,n+1) - f(l-1,m-1,n-1) \end{bmatrix}}{8\delta_1 \delta_2 \delta_3} \qquad \text{(F.10)}$$

The continuous Fourier transform and the corresponding discrete Fourier transform are given as:

$$ik_1^3 \leftrightarrow i\frac{2}{\delta_1^3} \sin\left(\frac{2\pi(\xi_1 - 1)}{N_1}\right)\left(1 - \cos\left(\frac{2\pi(\xi_1 - 1)}{N_1}\right)\right)$$
$$ik_1^2 k_2 \leftrightarrow i\frac{2}{\delta_1^2 \delta_2} \sin\left(\frac{2\pi(\xi_2 - 1)}{N_2}\right)\left(1 - \cos\left(\frac{2\pi(\xi_1 - 1)}{N_1}\right)\right)$$
$$ik_1 k_2 k_3 \leftrightarrow \frac{i}{\delta_1 \delta_2 \delta_3} \sin\left(\frac{2\pi(\xi_1 - 1)}{N_1}\right)\sin\left(\frac{2\pi(\xi_2 - 1)}{N_2}\right)\sin\left(\frac{2\pi(\xi_3 - 1)}{N_3}\right) \quad \text{(F.11)}$$

F.2   Fourth order partial derivatives

Let D_{pqrs} represent the third order partial derivatives with respect to $\partial x_p, \partial x_q, \partial x_r, \partial x_s$ where p, q, r and s can all attain values 1, 2 and 3. There are 81 fourth order partial derivatives of a function possible in the 3-dimensional space. From Clairaut's theorem, the following dependencies can be derived for D_{pqrs}:

D_{1111}

$D_{1112} = D_{1121} = D_{1211} = D_{2111}$

$$D_{1113} = D_{1131} = D_{1311} = D_{3111}$$

$$D_{1122} = D_{1212} = D_{1221} = D_{2112} = D_{2121} = D_{2211}$$

$$D_{1133} = D_{1313} = D_{1331} = D_{3113} = D_{3131} = D_{3311}$$

$$D_{1123} = D_{1132} = D_{1213} = D_{1231} = D_{1312} = D_{1321} = D_{2113} = D_{2311} = D_{2131} = D_{3112}$$

$$= D_{3121} = D_{3211}$$

$$D_{1222} = D_{2122} = D_{2212} = D_{2221}$$

$$D_{1223} = D_{1232} = D_{1322} = D_{2132} = D_{2213} = D_{2231} = D_{2312} = D_{2321} = D_{3122} = D_{3212}$$

$$= D_{3221} = D_{2123}$$

$$D_{1233} = D_{1323} = D_{1332} = D_{2133} = D_{2313} = D_{2331} = D_{3123} = D_{3132} = D_{3213} = D_{3231}$$

$$= D_{3312} = D_{3321}$$

$$D_{1333} = D_{3133} = D_{3313} = D_{3331}$$

$$D_{2222}$$

$$D_{2223} = D_{2232} = D_{2322} = D_{3222}$$

$$D_{2233} = D_{2323} = D_{2332} = D_{3223} = D_{3232} = D_{3322}$$

$$D_{2333} = D_{3233} = D_{3323} = D_{3332}$$

$$D_{3333} \tag{F.12}$$

The above partial derivatives can be grouped together with respect to the types of indices as follows:

$$(1) D_{1111}, \; D_{2222}, \; D_{3333}$$

$$(2) D_{1112}, \; D_{1113}, \; D_{1222}, \; D_{1333}, \; D_{2223}, \; D_{2333}$$

$$(3) D_{1122} = D_{1133} = D_{2233}$$

$$(4) D_{1123} = D_{1223} = D_{1233} \tag{F.13}$$

Only the first four derivatives (D_{1111}, D_{1112}, D_{1122} and D_{1123}) of the above types will be computed in the following, the remaining can be obtained by cycling through

the indices. The fourth order partial derivatives are given as follows:

$$D_{1111} = \frac{\partial^4 f(l,m,n)}{\partial x_1^4} = \frac{\begin{bmatrix} f(l+2,m,n) - 4f(l+1,m,n) + 6f(l,m,n) \\ -4f(l-1,m,n) + f(l-2,m,n) \end{bmatrix}}{\delta_1^4}$$

$$D_{1112} = \frac{\partial^4 f(l,m,n)}{\partial x_1^3 \partial x_2} = \frac{\begin{bmatrix} f(l+2,m+1,n) - f(l+2,m-1,n) \\ -2f(l+1,m+1,n) + 2f(l+1,m-1,n) \\ +2f(l-1,m+1,n) - 2f(l-1,m-1,n) \\ -f(l-2,m+1,n) + f(l-2,m-1,n) \end{bmatrix}}{4\delta_1^3 \delta_2}$$

$$D_{1122} = \frac{\partial^4 f(l,m,n)}{\partial x_1^2 \partial x_2^2} = \frac{\begin{bmatrix} f(l+1,m+1,n) - 2f(l+1,m,n) \\ +f(l+1,m-1,n) - 2f(l,m+1,n) \\ +4f(l,m,n) - 2f(l,m-1,n) + f(l-1,m+1,n) \\ -2f(l-1,m,n) + f(l-1,m-1,n) \end{bmatrix}}{\delta_1^2 \delta_2^2}$$

$$D_{1123} = \frac{\partial^4 f(l,m,n)}{\partial x_1^2 \partial x_2 \partial x_3} = \frac{\begin{bmatrix} f(l+1,m+1,n+1) - f(l+1,m+1,n-1) \\ -f(l+1,m-1,n+1) + f(l+1,m-1,n-1) \\ -2f(l,m+1,n+1) + 2f(l,m+1,n-1) \\ +2f(l,m-1,n+1) - 2f(l,m-1,n-1) \\ +f(i-1,j+1,k+1) - f(i-1,j+1,k-1) \\ -f(i-1,j-1,k+1) + f(i-1,j-1,k-1) \end{bmatrix}}{4\delta_1^2 \delta_2 \delta_3} \quad \text{(F.14)}$$

The continuous Fourier transform and the corresponding discrete Fourier transform are given as:

$$k_1^4 \leftrightarrow \frac{4}{\delta_1^4}\left(1 - \cos\left(\frac{2\pi(\xi_1 - 1)}{N_1}\right)\right)^2$$

$$k_1^3 k_2 \leftrightarrow \frac{2}{\delta_1^3 \delta_2} \sin\left(\frac{2\pi(\xi_1 - 1)}{N_1}\right) \sin\left(\frac{2\pi(\xi_2 - 1)}{N_2}\right)\left(1 - \cos\left(\frac{2\pi(\xi_1 - 1)}{N_1}\right)\right)$$

$$k_1^2 k_2^2 \leftrightarrow \frac{4}{\delta_1^2 \delta_2^2} \left(1 - \cos\left(\frac{2\pi(\xi_1 - 1)}{N_1}\right)\right) \left(1 - \cos\left(\frac{2\pi(\xi_2 - 1)}{N_2}\right)\right)$$

$$k_1^2 k_2 k_3 \leftrightarrow \frac{2}{\delta_1^2 \delta_2 \delta_3} \sin\left(\frac{2\pi(\xi_2 - 1)}{N_2}\right) \sin\left(\frac{2\pi(\xi_3 - 1)}{N_3}\right) \left(1 - \cos\left(\frac{2\pi(\xi_1 - 1)}{N_1}\right)\right) \quad \text{(F.15)}$$

F.3 Discrete Fourier transforms of multi-ordered partial derivatives in multi-dimensions

From the previous section, a specific pattern can be detected in the appearance of sine and cosine terms along with the imaginary number i and the inter Fourier point spacings δ_1, δ_2 and δ_3. The sine terms and the imaginary number i appear at every odd derivative in one particular direction. The cosine terms appear for every higher order derivative after the first derivative. An additional cosine term is introduced at every even ordered partial derivative in one particular direction. The power of the inter Fourier point spacings corresponds to the order of the partial derivative. For example, consider an ath (an integer greater than 0) order derivative along the x_1 direction. The continuous Fourier transform and its corresponding discrete Fourier transform can be written as:

$$(ik_1)^a$$

$$\leftrightarrow \frac{1}{\delta_1^a} \left(i \sin\left(\frac{2\pi(\xi_1 - 1)}{N_1}\right)\right)^{\frac{1-(-1)^a}{2}} \left(2\left[1 - \cos\left(\frac{2\pi(\xi_1 - 1)}{N_1}\right)\right]\right)^{\frac{n}{2}\frac{1+(-1)^a}{2} + \frac{n-1}{2}\left(\frac{1-(-1)^a}{2}\right)}$$

The above expression can be extended to 3-dimensions as:

$$(ik_1)^a (ik_2)^b (ik_3)^c$$

$$\leftrightarrow \frac{1}{\delta_1^a} \left(i \sin\left(\frac{2\pi(\xi_1 - 1)}{N_1}\right)\right)^{\frac{1-(-1)^a}{2}} \left(2\left[1 - \cos\left(\frac{2\pi(\xi_1 - 1)}{N_1}\right)\right]\right)^{\frac{a}{2}\left(\frac{1+(-1)^a}{2}\right) + \frac{a-1}{2}\left(\frac{1-(-1)^a}{2}\right)}$$

$$\times \frac{1}{\delta_2^b} \left(i \sin\left(\frac{2\pi(\xi_2 - 1)}{N_2}\right)\right)^{\frac{1-(-1)^b}{2}} \left(2\left[1 - \cos\left(\frac{2\pi(\xi_2 - 1)}{N_2}\right)\right]\right)^{\frac{b}{2}\left(\frac{1+(-1)^b}{2}\right) + \frac{b-1}{2}\left(\frac{1-(-1)^b}{2}\right)}$$

$$\times \frac{1}{\delta_3^c} \left(i \sin\left(\frac{2\pi(\xi_3 - 1)}{N_3}\right)\right)^{\frac{1-(-1)^c}{2}} \left(2\left[1 - \cos\left(\frac{2\pi(\xi_3 - 1)}{N_3}\right)\right]\right)^{\frac{c}{2}\left(\frac{1+(-1)^c}{2}\right) + \frac{c-1}{2}\left(\frac{1-(-1)^c}{2}\right)}$$

Finally, the above expression can be generalized in m dimensions to obtain the discrete Fourier transform of the finite difference approximation with accuracy $O(h^2)$

of partial derivatives of order $a + b + c + \cdots + d$ in j dimensions as:

$$(ik_1)^a (ik_2)^b (ik_3)^c \ldots (ik_j)^d$$

$$\leftrightarrow \frac{1}{\delta_1^a} \left(i \sin \left(\frac{2\pi(\xi_1 - 1)}{N_1} \right) \right)^{\frac{1-(-1)^a}{2}} \left(2 \left[1 - \cos \left(\frac{2\pi(\xi_1 - 1)}{N_1} \right) \right] \right)^{\frac{a}{2} \left(\frac{1+(-1)^a}{2} \right) + \frac{a-1}{2} \left(\frac{1-(-1)^a}{2} \right)}$$

$$\times \frac{1}{\delta_2^b} \left(i \sin \left(\frac{2\pi(\xi_2 - 1)}{N_2} \right) \right)^{\frac{1-(-1)^b}{2}} \left(2 \left[1 - \cos \left(\frac{2\pi(\xi_2 - 1)}{N_2} \right) \right] \right)^{\frac{b}{2} \left(\frac{1+(-1)^b}{2} \right) + \frac{b-1}{2} \left(\frac{1-(-1)^b}{2} \right)}$$

$$\times \frac{1}{\delta_3^c} \left(i \sin \left(\frac{2\pi(\xi_3 - 1)}{N_3} \right) \right)^{\frac{1-(-1)^c}{2}} \left(2 \left[1 - \cos \left(\frac{2\pi(\xi_3 - 1)}{N_3} \right) \right] \right)^{\frac{c}{2} \left(\frac{1+(-1)^c}{2} \right) + \frac{c-1}{2} \left(\frac{1-(-1)^c}{2} \right)}$$

$$\cdots$$

$$\times \frac{1}{\delta_j^d} \left(i \sin \left(\frac{2\pi(\xi_j - 1)}{N_j} \right) \right)^{\frac{1-(-1)^d}{2}} \left(2 \left[1 - \cos \left(\frac{2\pi(\xi_j - 1)}{N_j} \right) \right] \right)^{\frac{d}{2} \left(\frac{1+(-1)^d}{2} \right) + \frac{d-1}{2} \left(\frac{1-(-1)^d}{2} \right)}$$

APPENDIX G

PMFDDM ALGORITHM

In the following, the iterative procedure for PMFDDM FFT developed in section 5.2.2 is described in the form of a pseudocode algorithm (see algorithm 1). The notations used in the algorithm are described in table 9.

Table 9: Legend for algorithm 1

NOTATION	DESCRIPTION
E	Macro strain
K	Macro curvature
$\Delta E = \dot{E}\Delta t$	Macro strain increment
$\Delta K = \dot{K}\Delta t$	Macro curvature increment
t	Previous time step
$t + \Delta t$	Current time step
N_{tot}	Total number of time steps
ε	Threshold value for error
ERR	Normalized error
N_{iter}	Maximum number of iterations
ΔK	Macro curvature increment
re, im	Real and imaginary components in Fourier space
ξ_i	Fourier space vector in component form
σ^{err}, M^{err}	Threshold errors in Cauchy and couple stresses
A, B	Normalized errors in Cauchy and couple stresses

Continued on next page

357

Table 9 – *Continued from previous page*

NOTATION	DESCRIPTION
wgt	volumetric weight function
VM	VM component
BCs	Boundary conditions
EA	Euler Angles
N1, N2, N3	Fourier points

Algorithm 1 : PMFDDM FFT simple

Require: Files containing RVE dimensions, Boundary conditions, test and run conditions, microstructural information such as Euler angles, elastic and plastic properties

Ensure: Output local and macro stresses, strains, curvatures, displacements, polar defect densities

1: Input N1; N2; N3; ΔE; ΔK; Σ; Φ; ε; σ^{err}; M^{err}; EA; C°; A°; τ_0^s; n; M_0; $\dot{\gamma}_0$; $\dot{\kappa}_0$

2: $E^{t+\Delta t} \leftarrow \Delta E$; $K^{t+\Delta t} \leftarrow \Delta K$, $u \leftarrow 0$; $\epsilon \leftarrow 0$; $\kappa \leftarrow 0$; $\epsilon^{pt} \leftarrow 0$; $\kappa^{pt} \leftarrow 0$; $\dot{\epsilon}^{pt} \leftarrow 0$; $\dot{\kappa}^{pt} \leftarrow 0$; $wgt \leftarrow 1/(N1 \times N2 \times N3)$; ▷ Initialization at t = 0

3: $\lambda \leftarrow C^0 : E$; $\phi \leftarrow A^0 : K$; ▷ Guesses for local stresses for $t = \Delta t$, $i = 0$

4: **for** $t \leftarrow \Delta t, N_{tot}$ **do**

5:     $i \leftarrow 1$;

6:     $ERR(\sigma, \epsilon, \kappa, M) \leftarrow 2\varepsilon$; ▷ Initialize error criteria for while loop on i

7:     **while** $(i < N_{iter}; ERR(\lambda, \epsilon, \kappa, \phi) > \varepsilon)$ **do**

8:         **for** each Fourier pt. **do**

9:             $\hat{\tau}^{re}(\hat{\boldsymbol{k}}), \hat{\tau}^{im}(\hat{\boldsymbol{k}}) \leftarrow FFT\ (\tau = -C^{\circ} : \epsilon^{t+\Delta t,i-1} + \lambda^{t+\Delta t,i-1})$;

10:            $\hat{\mu}^{re}(\hat{\boldsymbol{k}}), \hat{\mu}^{im}(\hat{\boldsymbol{k}}) \leftarrow FFT\ (\mu = -A^{\circ} : \kappa^{t+\Delta t,i-1} + \phi^{t+\Delta t,i-1})$;

11:            $\hat{f}^{re}(\hat{\boldsymbol{k}}) \leftarrow -\xi_j \hat{\tau}_{ij}^{im}(\hat{\boldsymbol{k}}) - \hat{\mu}_{jk}^{re}(\hat{\boldsymbol{k}}) e_{ilj} \xi_k \xi_l / 2$;

12:            $\hat{f}^{im}(\hat{\boldsymbol{k}}) \leftarrow \xi_j \hat{\tau}_{ij}^{re}(\hat{\boldsymbol{k}}) - \hat{\mu}_{jk}^{im}(\hat{\boldsymbol{k}}) e_{ilj} \xi_k \xi_l / 2$;

13:            $\hat{G}_{ki}(\hat{\boldsymbol{k}}) \leftarrow \left(C_{ijkl}^{\circ} \xi_l \xi_j - F_{icbqrk}^{\circ} \xi_r \xi_q \xi_b \xi_c \right)^{-1}$;

14:            $u_k^i \leftarrow FFT^{-1}(\hat{G}_{kl}(\hat{\boldsymbol{k}}) \hat{f}_l(\hat{\boldsymbol{k}}))$;

15:            $U_{ij}^i \leftarrow FFT^{-1}\left(i\xi_j \hat{G}_{ik}(\hat{\boldsymbol{k}}) \hat{f}_k(\hat{\boldsymbol{k}}) \right)$;

16:            $\epsilon_{ij}^i \leftarrow E_{ij}^i + \frac{1}{2} \left(U_{ij}^i + U_{ji}^i \right)$;

17:            $\kappa_{ij}^i \leftarrow K_{ij} + \frac{1}{2} e_{ikl} FFT^{-1}\left(-\xi_j \xi_k \hat{G}_{lm}(\hat{\boldsymbol{k}}) \hat{f}_m(\hat{\boldsymbol{k}}) \right)$;

18:         **if** Mixed BC prescribed **then**

19:            $E_{ij}^i = E_{ij}^{i-1} + C_{ijkl}^{\circ-1} \alpha^{kl} \left(\Sigma_{kl} - \left\langle \lambda_{kl}^{(i)}(\boldsymbol{x}) \right\rangle \right) \Delta E$;

20:            $K_{ij}^i = K_{ij}^{i-1} + A_{ijkl}^{\circ-1} \beta^{kl} \left(\Phi_{kl} - \left\langle \phi_{kl}^{(i)}(\boldsymbol{x}) \right\rangle \right) \Delta K$;

21:         **end if**

22:         **end for**

23:     $ERR(\lambda,\epsilon,\kappa,\phi) \leftarrow 0$; ▷ Initialization for cumulative addition in NR loop

24:         **for** each Fourier pt. **do**

25:             $(\lambda^{i-1} \leftarrow \sigma^{i-1}), (\phi^{i-1} \leftarrow M^{i-1}), (e^i \leftarrow \epsilon^i), (\tilde{\kappa}^i \leftarrow \kappa^i)$

26:             A $\leftarrow 2\sigma^{err}$, B $\leftarrow 2M^{err}$; ▷ Initializing error criteria for NR loop

27:             $j \leftarrow 0$

28:         **while** $(j < N_{iter2}$; A $< \sigma^{err}$; B $< M^{err})$ **do**

29:             Evaluate $\dot{\epsilon}^{p(i,j)}(\sigma^{i,j-1}), \frac{\partial \dot{\epsilon}^p}{\partial \sigma}|_{\sigma^{i,j-1}}$

30:             Evaluate $\dot{\kappa}^{p(i,j)}(M^{i,j-1}), \frac{\partial \dot{\kappa}^p}{\partial M}|_{M^{i,j-1}}$

Algorithm 1 continued...

31:     $R_k(\sigma^i) \leftarrow \sigma_k^{i,j-1} + C_{kl}^0 \epsilon_l^i - \lambda_k^{i-1} - C_{kl}^0 e_l^i$; $k = 1, 6$;

32:     $R_k(M^i) \leftarrow M_k^{i,j-1} + A_{kl}^0 \kappa_l^i - \mu_k^{i-1} - A_{kl}^0 \tilde{\kappa}_l^i$; $k = 7, 15$;

33:     $\frac{\partial R_k}{\partial \sigma_l}|_{\sigma^{i,j-1}} \leftarrow \delta_{kl} + C_{km}^0 \frac{\partial \epsilon_m}{\partial \sigma_l}$; $k = 1, 6$; $l = 1, 6$;

34:     $\frac{\partial R_k}{\partial \sigma_l}|_{\sigma^{i,j-1}} \leftarrow 0$; $k = 7, 15$; $l = 1, 6$;

35:     $\frac{\partial R_k}{\partial M_l}|_{M^{i,j-1}} \leftarrow 0$; $k = 1, 6$; $l = 7, 15$;

36:     $\frac{\partial R_k}{\partial M_l}|_{M^{i,j-1}} \leftarrow \delta_{kl} + A_{km}^0 \frac{\partial \kappa_m}{\partial M_l}$; $k = 7, 15$; $l = 7, 15$;

37:     $\sigma_k^{i,j} \leftarrow \sigma_k^{i,j-1} - \left[\frac{\partial R_k}{\partial \sigma_l}|_{\sigma^{i,j-1}} \right]^{-1} R_l(\sigma^{i,j-1})$;

38:     $M_k^{i,j} \leftarrow M_k^{i,j-1} - \left[\frac{\partial R_k}{\partial M_l}|_{M^{i,j-1}} \right]^{-1} R_l(M^{i,j-1})$;

39:     $\text{A} \leftarrow \frac{||\sigma^j - \sigma^{j-1}||}{||\sigma^{j-1}||}$; $\text{B} \leftarrow \frac{||M^j - M^{j-1}||}{||M^{j-1}||}$

40:     $j \leftarrow j + 1$

41:     **end while**

42:     $\lambda_k^i \leftarrow \lambda_k^{i-1} + C_{kl}^0 (e_l^i - \epsilon_l^i)$

43:     $\phi_k^i \leftarrow \phi_k^{i-1} + A_{kl}^0 (\tilde{\kappa}_l^i - \kappa_l^i)$;

44:     $ERR(\sigma,\epsilon,\kappa,M) \leftarrow ERR(\sigma,\epsilon,\kappa,M) + (||\sigma^i - \lambda^i||, ||\epsilon^i - e^i||, ||M^i - \phi^i||,$
        $||\kappa^i - \tilde{\kappa}^i||) \times wgt$

45:     **end for**

46:     $ERR(\sigma,\epsilon,\kappa,M) \leftarrow ERR(\sigma,\epsilon,\kappa,M)/\text{VM}(\sigma,\epsilon,\kappa,M)$;

47:     $i \leftarrow i + 1$

48:     **end while**

49:     **if** $t > \Delta t$ **then**

50:         $\tau^s \leftarrow \tau^s + \Delta \tau$

51:     **end if**

52:     $E^{t+\Delta t} \leftarrow E^t + \Delta E$; $K^{t+\Delta t} \leftarrow K^t + \Delta E$;

53:     $\epsilon^{p(t+\Delta t)} = \epsilon^{pt} + \dot{\epsilon}^{p(t+\Delta t)} \Delta t$;

54:     $\kappa^{p(t+\Delta t)} = \kappa^{pt} + \dot{\kappa}^{p(t+\Delta t)} \Delta t$;

55:     Update Euler angles using $\dot{\epsilon}^{p(t+\Delta t)}$, $\dot{\kappa}^{p(t+\Delta t)}$

56:     $\epsilon^{e(t+\Delta t)} \leftarrow U^{t+\Delta t} - \epsilon^{p(t+\Delta t)}$;

57:     $\kappa^{e(t+\Delta t)} \leftarrow \kappa^{t+\Delta t} - \kappa^{p(t+\Delta t)}$;

58:     $\alpha^{t+\Delta t} = -\text{curl}\epsilon^{p(t+\Delta t)} + \kappa^{pT(t+\Delta t)} - tr(\kappa^{p(t+\Delta t)})I$;

59:     $\theta^{t+\Delta t} = -\text{curl}\kappa^{p(t+\Delta t)}$

60: **end for**

360

REFERENCES

[1] ABRAHAM, F., BROUGHTON, J., BERNSTEIN, N., and KAXIRAS, E., "Spanning the continuum to quantum length scales in a dynamic simulation of brittle fracture," *Europhysics Letters*, vol. 44, pp. 783 – 787, 1998.

[2] ACHARYA, A., "A model of crystal plasticity based on the theory of continuously distributed dislocations," *Journal of the Mechanics and Physics of Solids*, vol. 49, pp. 761–784, 2001.

[3] ACHARYA, A., "Jump condition on gnd evolution as a constraint on slip transmission at grain boundaries," *Philosophical Magazine*, vol. 87, pp. 1349 – 1359, 2007.

[4] ACHARYA, A. and BASSANI, J., "Incompatibility and crystal plasticity," *Journal of the Mechanics and Physics of Solids*, vol. 48, pp. 1565 – 1595, 2000.

[5] ACHARYA, A. and FRESSENGEAS, F., "Coupled phase transformations and plasticity as a field theory of deformation incompatibility," vol. 174, pp. 87–94, 2012.

[6] ACHARYA, A. and ROY, A., "Size effects and idealized dislocation microstructure at small scales: Predictions of a phenomenological model of mesoscopic field dislocation mechanics: Part i," *Journal of the Physics and Mechanics of Solids*, vol. 54, pp. 1687–1710, 2006.

[7] AGIASOFITOU, E. and LAZAR, M., "On the nonlinear continuum theory of dislocations: A gauge field theoretical approach," *Journal of Elasticity*, vol. 99, pp. 163–178, 2010.

[8] AIFANTIS, E. C., "Update on a class of gradient theories," *Mechanics of Materials*, vol. 35, pp. 259–280, 2003.

[9] AIFANTIS, E., "On the microstructural origin of certain inelastic models," *Transactions of the American Society of Mechanical Engineers: Journal of Engineering Materials and Technology*, vol. 106, pp. 326 – 330, 1984.

[10] ALIVISATOS, A. P., "Semiconductor clusters, nanocrystals, and quantum dots," *Science*, vol. 271, pp. 933–937, 1996.

[11] ALLEN, S. M. and CAHN, J. W., "A microscopic theory for antiphase boundary motion and its application to antiphase domain coarsening," *Acta Metallurgica*, vol. 27, pp. 1085–1095, 1979.

[12] ALLEN, S. and CAHN, J., "Ground state structures in ordered binary alloys with second neighbor interactions," *Acta Metallurgica*, vol. 20, p. 423, 1972.

[13] AMELINCKX, S., "Etchpits and dislocations along grain boundaries, sliplines and polygonization walls," *Acta Metallurgica*, vol. 2, no. 6, pp. 848 – 853, 1954.

[14] AMODEO, R. and GHONIEM, N., "Dislocation dynamics. i. a proposed methodology for deformation micromechanics," *Physical Review B*, vol. 41, p. 6958 6967, 1990.

[15] ANTHONY, K.-H., "Die theorie der disklinationen," *Archive for Rational Mechanics and Analysis*, vol. 39, pp. 43 – 88, 1950.

[16] ARSENLIS, A. and PARKS, D., "Crystallographic aspects of geometrically-necessary and statistically-stored dislocation density," *Acta Materialia*, vol. 47, pp. 1597 – 1611, 1999.

[17] ARSENLIS, A., PARKS, D., BECKER, R., and BULATOV, V., "On the evolution of crystallographic dislocation density in non-homogeneously deforming crystals," *Journal of the Mechanics and Physics of Solids*, vol. 52, pp. 1213 – 1246, 2004.

[18] ASARO, R., "Crystal plasticity," *Journal of Applied Mechanics*, vol. 50, pp. 921 – 934, 1983.

[19] ASLAN, O., CORDERO, N. M., GAUBERT, A., and FOREST, S., "Micromorphic approach to single crystal plasticity and damage," *International Journal of Engineering Science*, vol. 49, pp. 1311–1325, 2011.

[20] AULD, B., *Acoustic Fields and Waves in Solids.* New York: Wiley, 1973.

[21] AUST, K. T. and CHALMERS, B., "The specific energy of crystal boundaries in tin," *Proceedings of the Royal Society of London. Series A, Mathematical and Physical Sciences*, vol. 201, pp. 210–215, 1950.

[22] BABIC, M., "Average balance equations for granular materials," *International Journal of Engineering Science*, vol. 35, pp. 523 – 548, 1997.

[23] BACHURIN, D. V., MURZAEV, R. T., and NAZAROV, A. A., "Atomistic computer and disclination simulation of [001] tilt boundaries in nickel and copper," *The Physics of Metals and Metallography*, vol. 96, pp. 555–561, 2003.

[24] BALOGH, L., CAPOLUNGO, L., and TOM, C., "On the measure of dislocation densities from diffraction line profiles: A comparison with discrete dislocation methods," *Acta Materialia*, vol. 60, pp. 1467–1477, 2012.

[25] BAMMANN, D. and JOHNSON, G., "On the kinematics of finite deformation plasticity," *Acta Mechanica*, vol. 70, pp. 1 – 13, 1987.

[26] BARAI, P. and WENG, G. J., "A micro-continuum model for creep behavior of complex nano-crystalline materials," *International Journal of Engineering Science*, vol. 49, no. 155-174, p. 155, 2011.

[27] BASSANI, J., *Plastic Flow of Crystals*, vol. 30, pp. 191 – 258. Academic Press, New York, 1994.

[28] BASSANI, J., NEEDLEMAN, A., and VAN DER GIESSEN, E., "Plastic flow in a composite: A comparison of nonlocal continuum and discrete dislocation predictions," *International Journal of Solids and Structures*, vol. 38, pp. 833 – 853, 2001.

[29] BASSANI, J. L. and WU, T.-Y., "Latent hardening in single crystals ii. analytical characterization and predictions," *Proceedings of the Royal Society of London. Series A: Mathematical and Physical Sciences*, vol. 435, no. 1893, pp. 21–41, 1991.

[30] BEAUSIR, B. and FRESSENGEAS, C., "Disclination densities from ebsd orientation mapping," *International Journal of Solids and Structures*, vol. 50, pp. 137 – 146, 2013.

[31] BEAUSIR, B., FRESSENGEAS, C., GURAO, N., TOTH, L. S., and SUWAS, S., "Spatial correlation in grain misorientation distribution," *Acta Materialia*, vol. 57, pp. 5382 – 5395, 2009.

[32] BECKER, A. A., HYDE, T. H., SUN, W., and ANDERSON, P., "Benchmark for finite element analysis of creep continuum damage mechanis," *Computational Materials Science*, vol. 25, pp. 34–41, 2002.

[33] BERBENNI, S., PALIWAL, B., and CHERKAOUI, M., "A micromechanics-based model for shear-coupled grain boundary migration in bicrystals," *International Journal of Plasticity*, vol. 44, pp. 68 – 94, 2013.

[34] BERBENNI, S., TAUPIN, V., DJAKA, K., and FRESSENGEAS, C., "A numerical spectral approach for solving elasto-static field dislocation and g-disclination mechanics," *International Journal of Solids and Structures*, pp. –, 2014.

[35] BERTAUT, E. F., "Raies de debye-scherrer et rpartition des dimensions des domains de braggs dans les poudres polycrystallines," *Acta Crystallographica*, vol. 3, pp. 14–18, 1950.

[36] BERTIN, N., CAPOLUNGO, L., and BEYERLEIN, I., "Hybrid dislocation dynamics based strain hardening constitutive model," *International Journal of Plasticity*, vol. 49, no. 0, pp. 119 – 144, 2013.

[37] BILBY, B., *Continuous Distribution of Dislocations*, vol. 1-4 of *Progress in Solid Mechanics*, pp. 331 – 400. North Holland Publishing Company, Amsterdam, 1960.

[38] BILBY, B., BULLOUGH, R., and SMITH, E., "Continuous distributions of dislocations: A new application of the methods of non-riemannian geometry," *Proceedings of the Royal Society of London: Series A, Mathematical and physical sciences*, vol. 231, pp. 263 – 273, 1955.

[39] BILBY, B., GARDNER, L., and STROH, A., "Continuous distributions of dislocations and the theory of plasticity," in *Proceedings of the 9th Internation Congress on Applied Mechanics*, vol. 8, (Bruxelles 1956), pp. 41 – 47, Université de Bruxelles, 1957.

[40] BILBY, B. and SMITH, E., "Continuous distributions of dislocations iii," *Proceedings of the Royal Society of London: Series A, Mathematical and physical sciences*, vol. 232, pp. 481 – 505, 1956.

[41] BISHOP, C. M., CANNON, R. M., and CARTER, W. C., "A diffuse interface model of interfaces: Grain boundaries in silicon nitride," *Acta Materialia*, vol. 53, no. 4755-4764, p. 4755, 2005.

[42] BISHOP, G. and CHALMERS, B., "A coincidence ledge dislocation description of grain boundaries," *Scripta Metallurgica*, vol. 2, pp. 133 – 139, 1968.

[43] BOBYLEV, S. V., MOROZOV, N. F., and OVID'KO, I. A., "Cooperative grain boundary sliding and migration process in nanocrystalline solids," *Physical Review Letters*, vol. 105, pp. 055504–1 – 055504–4, 2010.

[44] BOLLMANN, W., "Triple lines in polycrystalline aggregates as disclinations," *Philosophical Magazine A*, vol. 49, pp. 73–79, 1984.

[45] BOLLMANN, W., "Triple-line disclinations representations, continuity and reactions," *Philosophical Magazine A*, vol. 57, pp. 637–649, 1988.

[46] BOLLMANN, W., "Triple-line disclinations in polycrystalline material," *Materials Science and Engineering A*, vol. 113, pp. 129 – 138, 1989.

[47] BOLLMANN, W., "The stress field of a model triple-line disclination," *Materials Science and Engineering A*, vol. 136, pp. 1 – 7, 1991.

[48] BORBÉLY, A. and UNGÁR, T., "X-ray line profiles analysis of plastically deformed metals," *Comptes Rendus Physique*, vol. 13, no. 3, pp. 293–306, 2012.

[49] BOURKE, M., DUNAND, D., and USTUNDAG, E., "Smarts – a spectrometer for strain measurement in engineering materials," *Applied Physics A*, vol. 74, pp. s1707–s1709, 2002.

[50] BRENNER, R., BEAUDOIN, A., SUQUET, P., and ACHARYA, A., "Numerical implementation of static field dislocation mechanics theory for periodic media," *Philosophical Magazine*, vol. 94, pp. 1764–1787, 2014.

[51] Brown, D. W., Sisneros, T. A., Clausen, B., Abeln, S., Bourke, M. A. M., Smith, B. G., Steinzig, M. L., Tom, C., and Vogel, S. C., "Development of intergranular thermal residual stresses in beryllium during cooling from processing temperatures," *Acta Materialia*, vol. 57, pp. 972–979, 2009.

[52] Bulatov, V., Cai, W., Fier, J., Hiratani, M., Hommes, G., Pierce, T., Tang, M., Rhee, M., Yates, K., and Arsenlis, T., "Scalable line dynamics in paradis," in *Proceedings of the 2004 ACM/IEEE Conference on Supercomputing*, SC '04, (Washington DC, USA), IEEE Computer Society, 2004.

[53] Bulatov, V. and W., C., *Computer Simulations of Dislocations*. Oxford: Oxford University Press, 2006.

[54] Burgers, J. *Proceedings of the Koninklijke Nederlandse Akademie van Wetenschappen*, vol. 42, pp. 293–378, 1939.

[55] Burgers, J., "Geometrical considerations concerning the structural irregularities to be assumed in a crystal," *Proceedings of the Physical Society*, vol. 52, pp. 23–33, 1940.

[56] Busso, E., Meissonneir, F., and O'Dowd, N., "Gradient-dependent deformation of two-phase single crystals," *Journal of the Mechanics and Physics of Solids*, vol. 48, pp. 2333 – 2362, 2000.

[57] Cahn, J. W. and Hilliard, J. E., "On the equilibrium segregation at a grain boundary," *Acta Metallurgica*, vol. 7, pp. 219–221, 1959.

[58] Cahn, J. W., Mishin, Y., and Suzuki, A., "Coupling grain boundary motion to shear deformation," *Acta Materialia*, vol. 54, pp. 4953–4975, 2006.

[59] Cahn, J. W. and Taylor, J. E., "A unified approach to motion of grain boundaries, relative tangential translation along grain boundaries and grain rotation," *Acta Materialia*, vol. 54, pp. 4887–4898, 2004.

[60] Cahn, J. and Hilliard, J., "Free energy of a nonuniform system. i. interfacial free energy," *Journal of Chemical Physics*, vol. 28, p. 258, 1958.

[61] Cai, W. and Bulatov, V., "Mobility laws in dislocation dynamics simulations," *Materials Science and Engineering A - Structural Materials Properties Microstructure and Processing*, vol. 387, pp. 277–281, 2004.

[62] Capolungo, L., Beyerlein, I., and Qwang, Z., "The role of elastic anisotropy on plasticity in hcp metals: A three-dimensional dislocation dynamics study," *Modelling and Simulation in Materials Science and Engineering*, vol. 18, p. 25, 2010.

[63] Chakravarthy, S. and Curtin, W., "Stress gradient plasticity," *Proceedings of the National Academy of Sciences*, vol. 108, pp. 15716 – 15720, 2011.

[64] CHAKRAVARTHY, S. and CURTIN, W., "Stress gradient plasticity: Concept and applications," *Procedia IUTAM: 23rd International Congress of Theoretical and Applied Mechanics*, vol. 10, pp. 453 – 461, 2014.

[65] CHALMERS, B. and GLEITER, H., "A re-interpretation of the coincidence model for grain boundaries," *Philosophical Magazine*, vol. 23, pp. 1541–1546, 1971.

[66] CHEN, J., LU, L., and LU, K., "Hardness and strain rate sensitivity of nanocrystalline cu," *Scripta Materialia*, vol. 54, pp. 1913 – 1918, 2006.

[67] CHEN, J., WANG, W., QIAN, L., and LU, K., "Critical shear stress for onset of plasticity in a nanocrystalline cu determined by using nanoindentation," *Scripta Materialia*, vol. 49, pp. 645–650, 2003.

[68] CHEN, L.-Q. and FAN, D., "Possibility of spinodal decomposition in zrO_2-Y_2O_3 alloys – a theoretical investigation," *Journal of the American Ceramic Society*, vol. 78, p. 769, 1995.

[69] CHEN, L.-Q. and WANG, Y., "The continuum field approach to modeling micro-structural evolution," *JOM-Journal of the Minerals Metals & Materials Society*, vol. 48, pp. 13 – 18, 1996.

[70] CHEN, L., "Phase-field models for microstructure evolution," *Annual Reviews of Materials Reserach*, vol. 32, pp. 113 – 140, 2002.

[71] CHEN, M., MA, E., HEMKER, K., SHENG, H., WANG, Y., and CHENG, X., "Deformation twinning in nanocrystalline aluminium," *Science*, vol. 300, pp. 1275–1277, 2003.

[72] CHERKAOUI, M. and CAPOLUNGO, L., *Atomistic and Continuum Modeling of Nanocrystalline Materials: Deformation Mechanisms and Scale Transition.* New York: Springer, 2009.

[73] CHOU, T.-W. and MALASKY, H. J., "A crystal defect theory approach to faulting in geological structures," *Journal of Geophysical Research: Solid Earth*, vol. 84 B, pp. 6083–6089, 1979.

[74] CHUNG, S. W., LEE, C. S., and KIM, S. J., "Large-scale simulaiton of crack propogation based on continuum damage mechanics and two-step mech partitioning," *Mechanics of Materials*, vol. 38, no. 76-87, p. 76, 2006.

[75] CLAYTON, J., *Homogenization and Incompatibility Fields in Finite Strain Elastoplasticity.* PhD dissertation, Georgia Institute of Technology, Department of Mechanical Engineering, September 2002.

[76] CLAYTON, J., "Homogenization and incompatibility fields in finite strain elastoplasticity," tech. rep., Department of Mechanical Engineering, Georgia Institute of Technology, Atlanta, Georgia, September 2002.

[77] CLAYTON, J., McDOWELL, D. L., and BAMMANN, D. J., "Modeling dislocations and disclinations with finite micropolar elasticity," *International Journal of Plasticity*, vol. 22, pp. 210–256, 2006.

[78] COLEMAN, S., SPEAROT, D., and CAPOLUNGO, L., "Virtual diffraction analysis of ni [010] symmetric tilt grain boundaries," *Modelling and Simulation in Materials Science and Engineering*, vol. 21, p. 055020, 2013.

[79] CORDIER, P., DEMOUCHY, S., BEAUSIR, B., TAUPIN, V., BAROU, F., and FRESSENGEAS, C., "Disclinations provide the missing mechanism for deforming olivine-rich rocks in the mantle," *Nature*, vol. 507, pp. 51 – 56, 2014.

[80] COSSERAT, E. and COSSERAT, F., *Théorie des corps dformables.* Paris: Hermann, 1909.

[81] CUITIÑO, A. and ORTIZ, M., "A material-independent method for extending stress update algorithms from small-strain plasticity to finite plasticity with multiplicative kinematics," *Engineering Computations*, vol. 9, pp. 437 – 452, 1992.

[82] DAFALIAS, Y., "Plastic spin: Necessity or redundancy?," *International Journal of Plasticity*, vol. 14, pp. 909–931, 1998.

[83] DAO, M., LU, L., ASARO, R. J., HOSSON, J. T. M. D., and MA, E., "Toward a quantitative understanding of mechanical behavior of nanocrystalline metals," *Acta Materialia*, vol. 55, pp. 4041 – 4065, 2007.

[84] DE HOSSON, J. T. M., "Superlattice dislocations in l12 ordered alloys and in alloys containing l12 ordered precipitates," *Mat. Sci. Engg.*, vol. 81, pp. 515 – 523, 1986.

[85] DEKEYSER, W. and AMELINCKX, S., *Les Dislocations et la Croissance des Crystauxs.* Paris: Masson, 1955.

[86] DELHEZ, R., DE KEIJSER, T. H., and MITTEMEIJER, E. J. Accuracy in Powder diffraction, National Bureau of Science: Washington DC: National Bureau of Science Special Publication Number 567, 1980.

[87] DELHEZ, R., DE KEIJSER, T. H., MITTEMEIJER, E. J., and LANGFORD, J. I., "Size and strain parameters from peak profiles: Sense and nonsense," *Australian Journal of Physics*, vol. 41, pp. 213–227, 1988.

[88] DELLINGER, L., VASICEK, D., and SONDERGELD, C., "Kelvin notation for stabilizing elastic constant inversion," *Revue de l'Institute Francaise de Petrol*, vol. 53, pp. 709 – 719, 1998.

[89] DESMORAT, R., "Décomposition de kelvin et concept de contraintes effectives multiples pour les matériaux anisotropes," *Comptes Rendus Mécanique*, vol. 337, pp. 733 – 738, 2009.

[90] DEVINCRE, B., HOC, T., and KUBIN, L., "Dislocation mean free paths and strain hardening of crystals," *Science*, vol. 320, pp. 1745 – 1748, 2008.

[91] DEVINCRE, B., KUBIN, L., and HOC, T., "Physical analyses of crystal plasticity by {DD} simulations," *Scripta Materialia*, vol. 54, pp. 741 – 746, 2006.

[92] DEVINCRE, B., PONTIKIS, V., BRECHET, Y., CANOVA, G., CONDAT, M., and KUBIN, L., "Three-dimensional simulations of plastic flow in crystals," in *Microscopic Simulations of Complex Hydrodynamic Phenomena* (MARESCHAL, M. and HOLIAN, B., eds.), vol. 292 of *NATO ASI Series*, pp. 413–423, Springer US, 1992.

[93] DEWIT, R., "The continuum of stationary dislocations," *Solid State Physics*, vol. 10, pp. 249–292, 1960.

[94] DEWIT, R., "Linear theory of static disclinations," in *Fundamental Aspects of Dislocation Theory* (SIMMONS, J., DEWIT, R., and BULLOUGH, R., eds.), vol. 1, pp. 651–680, National Bureau of Standards Special Publication 317, Washington D.C., 1970.

[95] DEWIT, R., "Theory of disclinations: Ii. continuous and discrete disclinations in anisotropic elasticity," *Journal of Research of the National Bureau of Standards - A. Physics and Chemistry*, vol. 77A, pp. 49–100, 1973.

[96] DEWIT, R., "Theory of disclinations: Iii. continuous and discrete disclinations in isotropic elasticity," *Journal of Research of the National Bureau of Standards - A. Physics and Chemistry*, vol. 77A, pp. 359–368, 1973.

[97] DEWIT, R., "Theory of disclinations: Iv. straight disclinations," *Journal of Research of the National Bureau of Standards - A. Physics and Chemistry*, vol. 77A, pp. 607–658, 1973.

[98] DIMITRAKOPULOS, G., KARAKOSTAS, T., and POND, R., "The defect character of interface junction lines," *Interface Science*, vol. 4, pp. 129 – 138, 1996.

[99] DINGREVILLE, R., QU, J., and CHERKAOUI, M., "Surface free energy and its effects on the elastic behavior of nano-sized particles, wires and films," *Journal of the Mechanics and Physics of Solids*, vol. 53, pp. 1827–1854, 2005.

[100] DRUYAMOV, B. and ROMAN, I., "A continuum model for grain junctions in polycrystalline aggregate," *Mechanics of Materials*, vol. 30, pp. 31–40, 1998.

[101] EASTABROOK, J. N. and WILSON, A. J. C., "The diffraction of x-rays by distorted-crystal aggregates iii: Remarks on the interpretation of the fourier coefficients," *Proceedings of the Physical Society B*, vol. 65, pp. 67–75, 1952.

[102] ECKART, C., "The thermodynamics of irreversible processes iv. the theory of elasticity and anelasticity," *Physical Review*, vol. 73, pp. 373 – 382, 1948.

[103] EL-DASHER, B., ADAMS, B., and ROLLETT, A., "Viewpoint: experimental recovery of geometrically necessary dislocation density in polycrystals," *Scripta Materialia*, vol. 48, pp. 141–145, 2003.

[104] ERB, U., "Electrodeposited nanocrystals: Synthesis, properties and industrial applications," *Nanostructured Materials*, vol. 6, pp. 533 – 538, 1995.

[105] ERINGEN, A. C., "Linear theory of micropolar elasticity," *Journal of Mathematics and Mechanics*, vol. 15, 1966.

[106] ERINGEN, A. C., "Linear theory of nonlocal elasticity and dispersion of plane waves," *International Journal of Engineering Science*, vol. 10, pp. 425–435, 1972.

[107] ERINGEN, A. C., "Plane waves in nonlocal micropolar elasticity," *International Journal of Engineering Science*, vol. 22, pp. 1113–1121, 1984.

[108] ERINGEN, A. C., *Nonlocal continuum field theories*. New York: Springer-Verlag New York, Inc., 2002.

[109] ERINGEN, A. C. and EDELEN, D. G. B., "On nonlocal elasticity," *International Journal of Engineering Science*, vol. 10, pp. 233–248, 1972.

[110] ERINGEN, A. C. and SUHUBI, E. S., "Nonlinear theory of simple micro-elastic solids - i," *International Journal of Engineering Science*, vol. 2, pp. 189–203, 1964.

[111] ESHELBY, J., *The Continuum Theory of Lattice Defects*, vol. 3, pp. 79 – 144. Academic Press, 1956.

[112] ESHELBY, J., *Elastic Inclusions and Inhomogeneities*, vol. 2, pp. 89 – 140. North Holland Publishing Company, Amsterdam, 1961.

[113] EVANS, A. and HUTCHINSON, J., "A critical assessment of theories of strain gradient plasticity," *Acta Materialia*, vol. 57, pp. 1675 – 1688, 2009.

[114] FALK, F., "One-dimensional model of shape memory alloy," *Archives of Mechanics*, vol. 15, pp. 63 – 84, 1983.

[115] FAN, D. and CHEN, L. Q., "Computer simulation of grain growth using a continuum field model," *Acta Materialia*, vol. 45, pp. 611–622, 1997.

[116] FARKAS, D., "Grain-boundary structures in hexagonal materials: Coincident and near coincident grain boundaries," *Metallurgical and Materials Transactions A*, vol. 25, pp. 1337 – 1346, 1994.

[117] FARKAS, D., FROSETH, A., and VAN SWYGENHOVEN, H., "Grain boundary migration during room temperature deformation of nanocrystalline ni," *Scripta Materialia*, vol. 55, pp. 695–698, 2006.

[118] FARKAS, D., MOHANTY, S., and MONK, J., "Strain-driven grain boundary motion in nanocrystalline materials," *Materials Science and Engineering A*, vol. 493, pp. 33–40, 2008.

[119] FIELD, D., TRIVEDI, P., WRIGHT, S., and KUMAR, M., "Analysis of local orientation gradients in deformed single crystals," *Ultramicroscopy*, vol. 103, pp. 33–39, 2003.

[120] FLECK, N. A. and HUTCHINSON, J. W., "A phenomenological theory for strain gradient effects in plasticity," *Journal of the Mechanics and Physics of Solids*, vol. 41, pp. 1825–1857, 1993.

[121] FLECK, N. A. and HUTCHINSON, J. W., *Strain Gradient Plasticity*, vol. 33, pp. 295–361. Academic Press, New York, 1997.

[122] FLECK, N. and HUTCHINSON, J., "A reformulation of strain gradient plasticity," *Journal of the Mechanics and Physics of Solids*, vol. 49, pp. 2245 – 2272, 2001.

[123] FLECK, N., MULLER, G., ASHBY, M., and HUTCHINSON, J., "Strain gradient plasticity: Theory and experiment," *Acta Metallurgica et Materialia*, vol. 42, pp. 475 – 487, 1994.

[124] FOREST, S., "Some links between cosserat, strain gradient crystal plasticity and the statistical theory of dislocations," *Philosophical Magazine*, vol. 88, pp. 3549–3563, 2008.

[125] FOREST, S., CAILLETAUD, G., and SIEVERT, R., "A cosserat theory for elasto-viscoplastic single crystals at finite deformation," *Archives of Mechanics*, vol. 4, pp. 705–736, 1997.

[126] FOREST, S. and SIEVERT, R., "Elastoviscoplastic constitutive frameworks for generalized continua," *Acta Mechanica*, vol. 160, pp. 71–111, 2003.

[127] FOREST, S. and SIEVERT, R., "Nonlinear microstrain theories," *International Journal of Solids and Structures*, vol. 43, pp. 7224–7245, 2006.

[128] FORTIER, P., PALUMBO, G., BRUCE, G., MILLER, W., and AUST, K., "Triple line energy determination by scanning tunneling microscopy," *Scripta Metallurgica et Materialia*, vol. 25, pp. 177 – 182, 1991.

[129] FORTY, A., "Direct observations of dislocations in crystals," *Advances in Physics*, vol. 3, pp. 1–25, 1954.

[130] FOSTER, C. M., POMPE, W., DAYKIN, A. C., and SPECK, J. S., "Relative coherency strain and phase transformation history in epitaxial ferroelectric thin films," *Journal of Applied Physics*, vol. 79, pp. 1405–1415, 1996.

[131] Frank, F. C., "The resultant content of dislocations in an arbitrary intercrystalline boundary," in *Symposium on The Plastic Deformation of Crystalline Solids*, (Pittsburg), p. 150, Mellon Institute, 1950.

[132] Frank, F. C., "I. liquid crystals. on the theory of liquid crystals," *Discussions of the Faraday Society*, vol. 25, pp. 19–28, 1958.

[133] Frank, F., "Crystal growth and dislocations," *Advances in Physics*, vol. 1, pp. 91–109, 1952.

[134] Fressengeas, C., Taupin, V., and Capolungo, L., "An elasto-plastic theory of dislocation and disclination fields," *International Journal of Solids and Structures*, vol. 48, pp. 3499–3509, 2011.

[135] Fressengeas, C., Taupin, V., and Capolungo, L., "Continuous modeling of the structure of symmetric tilt boundaries," *International Journal of Solids and Structures*, vol. 51, pp. 1434 – 1441, 2014.

[136] Fressengeas, C., Taupin, V., Upadhyay, M., and Capolungo, L., "Tangential continuity of elastic/plastic curvature and strain at interfaces," *International Journal of Solids and Structures*, vol. 49, pp. 2660 – 2667, 2012.

[137] Gal, I., "Effect of dislocation distribution on the x-ray scattering from deformed metals," *Proceedings of 5th International Symposium on Metallurgy and Material Science*, pp. 249–254, 1984.

[138] Gao, H., Huang, Y., Nix, W., and Hutchinson, J., "Mechanism based strain gradient plasticity - i. theory," *Journal of the Mechanics and Physics of Solids*, vol. 47, pp. 1239 – 1263, 1999.

[139] Gertsman, V. Y., Nazarov, A. A., Romanov, A. E., Valiev, R. Z., and Vladimirov, V. I., "Disclination-structural unit model of grain boundaries," *Philosophical Magazine A*, vol. 59, pp. 1113–1118, 1989.

[140] Ghoniem, N., Huang, J., and Wang, Z., "Affine covariant-contravariant vector forms for the elastic field of parametric dislocations in isotropic crystals," *Philosophical Magazine Letters*, vol. 82, pp. 55–63, 2002.

[141] Ghoniem, N. and Sun, L., "Fast-sum method for the elastic field of three-dimensional ensembles," *Physical Review B*, vol. 60, p. 128, 1999.

[142] Ghoniem, N., Tong, S.-H., and Sun, L., "Parametric dislocation dynamics: A thermodynamics-based approach to investigations of mesoscopic plastic deformation," *Physical Review B*, vol. 61, pp. 1–15, 2000.

[143] Gilman, J. J. and Johnston, W. G., "Observations of dislocation glide and climb in lithium fluoride crystals," *Journal of Applied Physics*, vol. 27, pp. 1018–1022, 1956.

[144] GJOSTEIN, N. and RHINES, F., "Absolute interfacial energies of [001] tilt and twist grain boundaries in copper," *Acta Metallurgica*, vol. 7, pp. 319 – 330, 1959.

[145] GLAZOFF, M., BARLAT, F., and WEILAND, H., "Continuum physics of phase and defect microstructures: Bridging the gap between physical metallurgy and plasticity of aluminum alloys," *International Journal of Plasticity*, vol. 20, pp. 363 – 402, 2004.

[146] GLEITER, H., "Nanocrystalline materials," *Progress in Materials Science*, vol. 33, pp. 223 – 315, 1989.

[147] GLEITER, H., "Nanostructured materials: Basic concepts and microstructure," *Acta Materialia*, vol. 48, pp. 1 – 29, 2000.

[148] GORKAYA, T., MOLODOV, D., and GOTTSTEIN, G., "Stress-driven migration of smmetrical <100> tilt grain boundaries in al bicrystals," *Acta Materialia*, vol. 57, pp. 5396 – 5405, 2009.

[149] GROH, S., DEVINCRE, B., KUBIN, L., ROOS, A., FEYEL, F., and CHABOCHE, J., "Dislocations and elastic anisotropy in heteroepitaxial metallic thin films," *Philosophical Magazine Letters*, vol. 83, pp. 303–313, 2003.

[150] GROMA, I. and MONNET, G., "Analysis of asymmetric broadening of x-ray diffraction peak profiles caused by randomly distributed polarized dislocation dipoles and dislocation walls," *Journal of Applied Crystallography*, vol. 35, pp. 589–593, 2002.

[151] GROMA, I. and SZKELY, F., "Analysis of the asymptotic properties of x-ray line broadening caused by dislocations," *Journal of Applied Crystallography*, vol. 33, pp. 1329–1334, 2000.

[152] GROMA, I., UNGR, T., and WILKENS, M., "Asymmetric x-ray line broadening of plastically deformed crystals. i. theory," *Journal of Applied Crystallography*, vol. 21, pp. 47–53, 1988.

[153] GUDMUNDSON, P., "A unified treatment of strain gradient plasticity," *Journal of the Mechanics and Physics of Solids*, vol. 52, pp. 1379 – 1406, 2004.

[154] GUNTHER, W., "Zur statik und kinematik des cosseratschen kontinuums," *Abhandlungen der Braunschweigischen Wissenschaftlichen Gesellschaft*, vol. 10, pp. 195–213, 1958.

[155] GUO, Y., WANG, J., WANG, Z., TANG, S., and ZHOU, Y., "Phase field crystal modeling of grain rotation with small initial misorientations in nanocrystalline materials," *Computational Materials Science*, vol. 88, pp. 163 – 169, 2014.

[156] GURTIN, M. E., "On the plasticity of single crystals: Free energy, micro-forces, plastic-strain gradients," *Journal of the Mechanics and Physics of Solids*, vol. 48, pp. 989–1036, 2000.

[157] GURTIN, M. E., "A gradient theory of single crystal viscoplasticity that accounts for geometrically necessary dislocations," *Journal of the Mechanics and Physics of Solids*, vol. 50, pp. 5–32, 2002.

[158] GURTIN, M. E., "A finite-deformation, gradient theory of single-crystal plasticity with free energy dependent on densities of geometrically necessary dislocations," *International Journal of Plasticity*, vol. 24, pp. 702–725, 2008.

[159] GURTIN, M. E., ANAND, L., and LELE, S. P., "A gradient single-crystal plasticity with free energy dependent on dislocation densities," *Journal of the Mechanics and Physics of Solids*, vol. 55, pp. 1853–1878, 2007.

[160] GURTIN, M., "Generalized ginzburg-landau and cahn-hilliard equations based on a microforce balance," *Physica D*, vol. 92, pp. 178 – 192, 1996.

[161] GURTIN, M. and ANAND, L., "Nanocrystalline grain boundaries that slip and separate: A gradient theory that accounts for grain-boundary stress and conditions at a triple-junction," *Journal of the Mechanics and Physics of Solids*, vol. 56, pp. 184 – 199, 2008.

[162] GUTKIN, M. Y., "Nanoscopics of dislocations and disclinations in gradient elasticity," *Reviews on Advanced Materials Science*, vol. 1, pp. 27–60, 2000.

[163] GUTKIN, M. Y. and AIFANTIS, E. C., "Dislocations in gradient elasticity," *Scripta Materialia*, vol. 40, pp. 559–566, 1999.

[164] GUTKIN, M. Y., MIKAELYAN, K., ROMANOV, A., and KLIMANEK, P., "Disclination models of misorientation band generation and propagation," *Physica Status Solidi A*, vol. 193, pp. 35–52, 2002.

[165] GUTKIN, M. Y. and OVID'KO, I. A., *Plastic Deformation in Nanocrystalline Materials*. Berlin: Springer, 2004.

[166] GUTKIN, M. Y., OVID'KO, I. A., and PANDE, C. S., "Theoretical models of plastic deformation processes in nanocrystalline materials," *Reviews on Advanced Materials Science*, vol. 2, pp. 80–102, 2001.

[167] GUTKIN, M., OVID'KO, I., and SKIBA, N., "Transformations of grain boundaries due to disclination motion and emission of dislocation pairs," *Materials Science and Engineering A*, vol. 339, pp. 73 – 80, 2003.

[168] HADAMARD, J., *Leçon sur la Propagation des Ondes et les Equations de l'Hydrodrnamique*. Paris: Hermann, 1909.

[169] HADJESFANDIARI, A. R. and DARGUSH, G. F., "Couple stress theory for solids," *International Journal of Solids and Structures*, vol. 48, pp. 2496–2510, 2011.

[170] HALL, E. O., "The deformation and ageing of mild steel: Iii discussion of results," *Proceedings of the Physical Society*, vol. B 64, pp. 747–753, 1951.

[171] HAN, W., CERRETA, E., MARA, N., BEYERLEIN, I., CARPENTER, J., ZHENG, S., TRUJILLO, C., DICKERSON, P., and MISRA, A., "Deformation and failure of shocked bulk cunb nanolaminates," *Acta Materialia*, vol. 63, pp. 150 – 161, 2014.

[172] HASHIMOTO, H. and UYEDA, R., "Detection of dislocation by the moiré pattern in electron micrographs," *Acta Crystallographica*, vol. 10, pp. 143–144, 1957.

[173] HASLAM, A. J., MOLDOVAN, D., PHILLPOT, S. R., WOLF, D., and GLEITER, H., "Combined atomistic and mesoscale simulation of grain growth in nanocrystalline thin films," *Computational Materials Science*, vol. 23, pp. 15 – 32, 2002.

[174] HASSON, G., BOOS, J.-Y., HERBEUVAL, I., BISCONDI, M., and GOUX, C., "Theoretical and experimental determinations of grain boundary structures and energies: Correlation with various experimental results," *Surface Science*, vol. 31, pp. 115 – 137, 1972.

[175] HAVNER, K. S., WU, S. C., and FUH, S., "On symmetric bicrystals at the yield point in (110) channel die compression," *Journal of the Mechanics and Physics of Solids*, vol. 42, pp. 361–379, 1994.

[176] HAVNER, K. S. and YU, P., "On the stress state at the yield point in symmetric bicrystals in (110) channel die compression," *Mechanics of Materials*, vol. 27, pp. 211–227, 1998.

[177] HAVNER, K., *Finite Plastic Deformation of Crystalline Solids*. Cambridge: Cambridge University Press, 1992.

[178] HECHT, F., "New development in freefem++," *Journal of Numerical Mathematics*, vol. 20, pp. 251 – 266, 2012.

[179] HECKER, M. and ROMANOV, A., "The stress fields of edge dislocations near wedge-shaped boundaries and bonded wedges," *Materials Science and Engineering: A*, vol. 164, pp. 411 – 414, 1993.

[180] HERRING, C., *Surface Tension as a Motivation for Sintering*, pp. 143 – 179. McGraw-Hill Book Co., New York, 1951.

[181] HIBBARD, G. D., RADMILOVIC, V., AUST, K. T., and ERB, U., "Grain boundary migration during abnormal grain growth in nanocrystalline ni," *Materials Science and Engineering A*, vol. 494, pp. 232–238, 2008.

[182] HILL, R. and HAVNER, K., "Perspectives in the mechanics of elastoplastic crystals," *Journal of the Mechanics and Physics of Solids*, vol. 30, pp. 5 – 22, 1982.

[183] HILLIARD, J., *Spinodal Decomposition.* American Society for Metals, Metals Park, Ohio, 1992.

[184] HIRSCH, P. B., HORNE, R. W., and WHELAN, M. J., "Lxviii. direct observations of the arrangement and motion of dislocations in aluminium," *Philosophical Magazine*, vol. 1, pp. 677–684, 1956.

[185] HIRSCH, P. B., SILCOX, J., SMALLMAN, R. E., and WESTMACOTT, K. H., "Dislocation loops in quenched aluminium," *Philosophical Magazine*, vol. 3, pp. 897–908, 1958.

[186] HIRTH, J. P., "The influence of grain boundaries on mechanical properties," *Metallurgical and Materials Transactions*, vol. 3, pp. 3047 – 3067, 1972.

[187] HIRTH, J. and LOTHE, J., *Theory of Dislocations.* New York: John Wiley and Sons, 1982.

[188] HOLT, D., "Dislocation cell formation in metals," *Journal of Applied Physics*, vol. 41, pp. 3197 – 3201, 1970.

[189] HOWE, J., MORI, H., and WANG, Z., "In situ high resolution transmission electron microscopy in the study of nanomaterials," *MRS Bulletin*, vol. 33, pp. 115 – 121, 2008.

[190] HULL, D. and BACON, D., *Introduction to Dislocations.* New York: John Wiley and Sons, 5 ed., 1965.

[191] JACQUET, P., "Recherches expérimentales sur la microstructure de la solution solide cuivre-zinc 6535 polycristalline très faiblement déformée par traction et sur son evolution au recuit entre 200 et 600 c," *Acta Metallurgica*, vol. 2, pp. 752 – 769, 1954.

[192] JAUNZEMIS, W., *Continuum Mechanics.* New York: MacMillan, 1967.

[193] JIN, Y., ARTEMEV, A., and KHACHATURYAN, A., "Three-dimensional phase field model of low-symmetry martensitic transformation in polycrystal: Simulation of ζ'_2 martensite in aucd alloys," *Acta Materialia*, vol. 49, p. 2309, 2001.

[194] JUN, S., JANG, E., and LIM, J., "Synthesis of multi-shell nanocrystals by a single step coating process," *Nanotechnology*, vol. 17, pp. 3892 – 3896, 2006.

[195] KACHER, J., LANDON, C., ADAMS, B., and FULLWOOD, D., "Braggs law diffraction simulations for electron backscatter diffraction analysis," *Ultramicroscopy*, vol. 109, pp. 1148–1156, 2009.

[196] KAGANER, V. M. and SABELFELD, K. K., "X-ray diffraction peaks from correlated dislocations: Monte carlo study of dislocation screening," *Acta Crystallographica*, vol. A66, pp. 703–716, 2010.

[197] KAGANER, V. and SABELFELD, K., "Strain distributions and diffraction peak profiles from crystals with dislocations," *Acta Crystallographica Section A*, vol. 70, 2014.

[198] KAMMINGA, J. D. and DELHEZ, R., "Calculation of diffraction line profiles from specimens with dislocations. a comparison of analytical models with computer simulations," *Journal of Applied Crystallography*, vol. 33, pp. 1122–1127, 2000.

[199] KAMMINGA, J. D. and DELHEZ, R., "Measurement of dislocation distributions by means of x-ray diffraction," *Materials Science and Engineering A*, vol. 309-310, pp. 55–59, 2001.

[200] KAMMINGA, J. D. and SEIJBEL, L. J., "Diffraction line broadening analysis if broadening is caused by both dislocations and limited crystallite size," *Journal of the Research of the National Institute of Standards and Technology*, vol. 109, pp. 65–74, 2004.

[201] KANJARLA, A., LEBENSOHN, R., BALOGH, L., and TOMÉ, C., "Study of internal lattice strain distributions in stainless steel using a full-field elasto-viscoplastic formulation based on fast fourier transforms," *Acta Materialia*, vol. 60, pp. 3094 – 3106, 2012.

[202] KATO, M., SATO, T., and ANDO, K., "Determination of the higher-order elastic compliance constants of metals from measurements of the dependence of ultrasound velocity on stress," *Journal of the Acoustical Society of America*, vol. 101, pp. 2111–2121, 1996.

[203] KLEINERT, H., *Multivalued fields in Condensed Matter, Electromagnetism, and Gravitation*. Singapore: World Scientific Publishing Co. Pte. Ltd., 2008.

[204] KLEMAN, M. and FRIEDEL, J., "Disclinations, dislocations, and continuous defects: A reappraisal," *Reviews of Modern Physics*, vol. 80, pp. 61–115, 2008.

[205] KLEMM, V., KLIMANEK, P., and MOTYLENKO, M., "Tem identification of disclinations in plastically deformed crystals," in *Local Lattice Rotations and Disclinations in Microstructure of Distorted Crystalline Materials* (KLIMANEK, P., ROMANOV, A. E., and SEEFELDT, B. M., eds.), vol. 87 of *Solid State Phenomena*, pp. 57 – 72, 2002.

[206] KLEMM, V., KLIMANEK, P., and MOTYLENKO, M., "Transmission electron microscopy analysis of disclination structures in plastically deformed metals," *Materials Science and Engineering A*, vol. 324, pp. 174 – 178, 2002.

[207] Klemm, V., Klimanek, P., and Seefeldt, M., "A microdiffraction method for the characterization of partial disclinations in plastically deformed metals by tem," *physica status solidi (a)*, vol. 175, pp. 569–576, 1999.

[208] Knapp, J. A. and Follstaedt, D. M., "Hall-petch relationship in pulsed-laser deposited nickel films," *Journal of Materials Research*, vol. 19, pp. 218 – 227, 2004.

[209] Kobayashi, R., Warren, J. A., and Carter, W. C., "A continuum model of grain boundaries," *Physica D*, vol. 140, pp. 141–150, 2000.

[210] Koch, C. C., Ovid'ko, I. A., Seal, S., and Veprek, S., *Structural Nanocrystalline Materials: Fundamentals and Applications*. Cambridge: Cambridge University Press, 2007.

[211] Kondo, K., "On the geometrical and physical foundations of the theory of yielding," in *Proceedings of the 2nd Japan Congress on Applied Mechanics*, (Tokyo), pp. 41 – 47, Japan National Committee for Theoretical and Applied Mechanics, Science Council of Japan, 1953.

[212] Krakow, W., "Structural multiplicity observed at a $\Sigma = 5/[001]53.1°$ tilt boundary in gold," *Philosophical Magazine A - Physics of Condensed Matter Structure*, vol. 63, pp. 233 –240, 1991.

[213] Krallics, G. and Lenard, J. G., "An examination of the accumulative roll-bonding process," *Journal of Materials Processing Technology*, vol. 152, pp. 154 – 161, 2004.

[214] Krivoglaz, M. A., *X-ray and neutron diffraction in nonideal crystals*. New York: Plenum, 1969.

[215] Kröner, E., "Dislocations and the biot-savart law," *Proceedings of the Physical Society A*, vol. 68, p. 53 55, 1955.

[216] Kröner, E., "Kontinuumstheorie der versetzungen und eigenspannungen," *Ergebnisse der Angewandten Mathematik*, vol. 5, pp. 1–179, 1958.

[217] Kröner, E., "Allgemeine kontinuumstheorie der versetzungen und eigenspannungen," *Archive for Rational Mechanics and Analysis*, vol. 4, pp. 273 – 334, 1960.

[218] Kröner, E., "On the physical reality of torque stresses in continuum mechanics," *International Journal of Engineering Science*, vol. 1, pp. 261–278, 1963.

[219] Kröner, E., "Elasticity theory of nonlocal elasticity and dispersion of plane waves," *International Journal of Engineering Science*, vol. 3, pp. 731–742, 1967.

[220] Kröner, E., "Incompatibility, defects, and stress functions in the mechanics of generalized continua," *International Journal of Solids and Structures*, vol. 21, pp. 747 – 756, 1985.

[221] KRÖNER, E., "Dislocations in crystals and in continua: A confrontation," *International Journal of Engineering Science*, vol. 33, pp. 2127–2135, 1995.

[222] KRÖNER, E. and SEEGER, A., "Nicht-lineare elastizitatstheorie der versetzungen und eigenspannungen," *Archives for Rational Mechanics and Analysis*, vol. 3, pp. 97–119, 1959.

[223] KROUPA, F. and LEJČEK, "Development of the disclination concept," in *Local Lattice Rotations and Disclinations in Microstructure of Distorted Crystalline Materials* (KLIMANEK, P., ROMANOV, A. E., and SEEFELDT, B. M., eds.), vol. 87 of *Solid State Phenomena*, pp. 1–14, 2002.

[224] KUBIN, L. and CANOVA, G., "The modelling of dislocation patterns," *Scripta Metallurgica*, vol. 27, pp. 957–962, 1992.

[225] KUMAR, K. S., SWYGENHOVEN, H. V., and SURESH, S., "Mechanical behavior of nanocrystalline metals and alloys," *Acta Materialia*, vol. 51, pp. 5743 – 5774, 2003.

[226] LAKES, R., "Elastic and viscoelastic behavior of chiral materials," *International Journal of Mechanical Sciences*, vol. 43, pp. 1579–1589, 2001.

[227] LANDAU, L. and LIFSHITZ, E., *The Classical Theory of Fields*. Addison-Wesley, 1961.

[228] LANGER, J., *An Introduction to the Kinetics of First Order Phase Transitions*. Cambridge University Press, Cambridge, 1992.

[229] LANGFORD, J. I., DELHEZ, R., DE KEIJSER, T. H., and MITTEMEIJER, E. J., "Profile analysis for microcrystalline properties by the fourier and other methods," *Australian Journal of Physics*, vol. 41, pp. 173–187, 1988.

[230] LAZAR, M., "On the higgs mechanism and stress functions in the translational gauge theory of dislocations," *Physics Letters A*, vol. 373, pp. 1578–1582, 2009.

[231] LAZAR, M. and MAUGIN, G. A., "Defects in gradient micropolar elasticity: I. screw dislocation," *Journal of the Mechanics and Physics of Solids*, vol. 52, pp. 2263–2284, 2004a.

[232] LAZAR, M. and MAUGIN, G. A., "Defects in gradient micropolar elasticity: Ii. edge dislocation and wedge disclination," *Journal of the Mechanics and Physics of Solids*, vol. 52, pp. 2285–2307, 2004b.

[233] LAZAR, M. and MAUGIN, G. A., "Nonsingular stress and strain fields of dislocations and disclinations in first strain gradient elasticity," *International Journal of Engineering Science*, vol. 43, pp. 1157–1184, 2005.

[234] LAZAR, M. and MAUGIN, G. A., "Dislocations in gradient elasticity revisited," *Proceedings of the Royal Society of London A*, vol. 462, pp. 3465–3480, 2006.

[235] LAZAR, M. and MAUGIN, G. A., "On microcontinuum field theories: the eshelby stress tensor and incompatibility conditions," *Philosophical Magazine*, vol. 25, pp. 3853–3870, 2007.

[236] LAZAR, M., MAUGIN, G. A., and AIFANTIS, E. C., "Dislocations in second strain gradient elasticity," *International Journal of Solids and Structures*, vol. 43, pp. 1787–1817, 2006.

[237] LAZAR, M., MAUGIN, G. A., and AIFANTIS, E. C., "On dislocations in a special class of generalized elasticity," *Physica Status Solidi (b)*, vol. 242, pp. 2365–2390, 2006.

[238] LEBENSOHN, R., "N-site modeling of a 3d viscoplastic polycrystal using fast fourier transform," *Acta Materialia*, vol. 49, pp. 2723 – 2737, 2001.

[239] LEBENSOHN, R., KANJARLA, A., and EISENLOHR, P., "An elasto-viscoplastic formulation based on fast fourier transforms for the prediction of micromechanical fields in polycrystalline materials," *International Journal of Plasticity*, vol. 32 - 33, pp. 59 – 69, 2012.

[240] LEBENSOHN, R. and TOMÉ, C., "A self-consistent viscoplastic model: Prediction of rolling textures of anisotropic polycrystals," *Materials Science and Engineering A*, vol. 175, pp. 71 – 82, 1994.

[241] LEBENSOHN, R., TURNER, P., SIGNORELLI, J., CANOVA, G., and TOMÉ, "Calculation of intergranular stresses based on a large-strain viscoplastic self-consistent polycrystal model," *Modelling and Simulations in Materials Science and Engineering*, vol. 6, pp. 447 – 465, 1998.

[242] LEE, E., "Some comments on elastic-plastic analysis," *International Journal of Solids and Structures*, vol. 17, pp. 859 – 872, 1981.

[243] LEE, E. and LIU, D., "Elastic-plastic theory with application to plane-wave analysis," *Journal of Applied Physics*, vol. 38, pp. 19 – 27, 1967.

[244] LEI, R., WANG, M., LI, Z., and WEI, H., "Disclination dipoles observation and nanocrystallizatoin mechanism in ball milled cu-nb powders," *Materials Letters*, vol. 65, pp. 3044 – 3046, 2011.

[245] LEINEWEBER, A. and MITTEMEIJER, E. J., "Notes on the order-of-reflection dependence of microstrain broadening," *Journal of Applied Crystallography*, vol. 43, pp. 981–989, 2010.

[246] LEVINE, L. E. and THOMSON, R., "X-ray scattering by dislocations in crystal. general theory and application to screw dislocations," *Acta Crystallographica*, vol. A53, pp. 590–602, 1997.

[247] LEVITAS, V., "Phase-field theory for martensitic phase transformations at large strains," *International Journal of Plasticity*, vol. 49, pp. 85 – 118, 2013.

[248] LEVITAS, V. and LEE, D.-W., "Athermal resistance to an interface motion in phase field theory of microstructure evolution," *Physical Review Letters*, vol. 99, p. 245701, 2007.

[249] LEVITAS, V., PRESTON, D., and LEE, D.-W., "Three-dimensional landau theory for multivariant stress-induced martensitic phase transformations iii. alternative potentials, critical nuclei, kink solutions, and dislocation theory," *Physical Review B*, vol. 68, p. 134201, 2003.

[250] LI, J., "Some elastic properties of an edge dislocation wall," *Acta Metallurgica*, vol. 8, pp. 563–574, 1960.

[251] LI, J., "Disclination model of high angle grain boundaries," *Surface Science*, vol. 31, pp. 12–26, 1972.

[252] LI, J., UMEMOTO, M., TODAKA, Y., and TSUCHIYA, K., "Role of strain gradient on the formation of nanocrystalline structure produced by severe plastic deformation," *Journal of Alloys and Compounds*, vol. 434 - 435, pp. 290 – 293, 2007.

[253] LIU, B., EISENLOHR, P., ROTERS, F., and RAABE, D., "Simulation of dislocation penetration through a general low-angle grain boundary," *Acta Materialia*, vol. 60, pp. 5380–5390, 2012.

[254] LIU, P., MAO, S., WANG, L., HAN, X., and ZHANG, Z., "Direct dynamic atomic mechanisms of strain-induced grain rotation in nanocrystalline, txtured, columnar-structured thin gold films," *Scripta Materialia*, vol. 64, pp. 343 – 346, 2011.

[255] LOOKMAN, T., SAXENA, A., and ALBERS, R., "Phonon mechanisms and transformation paths in pu," *Physical Review Letters*, vol. 100, p. 145504, 2008.

[256] LU, L., SHEN, Y. F., CHEN, X. H., QIAN, L. H., and LU, K., "Ultrahigh strength and high electrical conductivity in copper," *Science*, vol. 304, pp. 422 – 426, 2004.

[257] LUBARDA, V. A., "The effects of couple stresses on dislocation strain energy," *International Journal of Solids and Structures*, vol. 40, pp. 3807–3826, 2003.

[258] M., F., *Discrete Dislocation Dynamics: Principles and Recent Applications*, pp. 17–36. ISTE, London, 2010.

[259] MA, A., ROTERS, F., and RAABE, D., "On the consideration of interactions between dislocations and grain boundaries in crystal plasticity finite element modeling theory, experiments, and simulations," *Acta Materialia*, vol. 54, pp. 2181–2194, 2006.

[260] MACH, J., BEAUDOIN, A. J., and ACHARYA, A., "Continuity in the plastic strain rate and its influence on texture evolution," *Journal of the Physics and Mechanics of Solids*, vol. 58, pp. 105 – 128, 2010.

[261] MADEC, R., DEVINCRE, B., and KUBIN, L., "Simulations of dislocation pattern in multislip," *Scripta Materialia*, vol. 47, pp. 689–695, 2002.

[262] MADEC, R., DEVINCRE, B., KUBIN, L., HOC, T., and RODNEY, D., "The role of collinear interaction in dislocation-induced hardening," *Science*, vol. 301, pp. 1879–1882, 2003.

[263] MAJID, K., NYILAS, R., and SPOLENAK, R., "Metal plasticity by grain rotation - microdiffraction case studies," *Materials Science and Engineering A*, vol. 524, pp. 33–39, 2009.

[264] MARANGANTI, R. and SHARMA, P., "A novel atomistic approach to determine strain-gradient elasticity constants: Tabulation and comparison for various metals, semiconductors, silica, polymers and the (ir) relevance for nanotechnologies," *Journal of the Mechanics and Physics of Solids*, vol. 55, pp. 1823 – 1852, 2007.

[265] MARULL, R. and DESMORAT, R., "Kelvin modes based cubic plasticity and induced anisotropic damage: Application to creep of am1 single crystal," in *Advanced Materials Modelling for Structures* (ALTENBACH, H. and KRUCH, S., eds.), vol. 19, pp. 217–227, Springer Berlin Heidelberg, 2013.

[266] MATHEW, V. M., MENON, C. S., and JAYACHANDRAN, K. P., "Third-order elastic constants and pressure derivatives of the second-order elastic constants of beta-tin," *Journal of Physics and Chemistry of Solids*, vol. 63, pp. 1835–1838, 2002.

[267] MAYEUR, J., MCDOWELL, D. L., and BAMMANN, D. J., "Dislocation-based micropolar single crystal plasticity: Comparison of multi- and single criterion theories," *Journal of the Mechanics and Physics of Solids*, vol. 59, pp. 398–422, 2011.

[268] MCDOWELL, D. L., "Viscoplasticity of heterogeneous metallic materials," *Materials Science and Engineering: R: Reports*, vol. 62, pp. 67 – 123, 2008.

[269] MCDOWELL, D., MILLER, M., and BAMMANN, D., "Some additional considerations for coupling of material and geometric nonlinearities for polycrystalline metals," in *Proceedings of the International Seminar on Large Plastic Deformations*, (Fontainebleau, France), MECAMAT 1991, 1991.

[270] MENTER, J. W., "The direct study by electron microscopy of crystal lattices and their imperfections," *Proceedings of the Royal Society of London. Series A, Mathematical and Physical Sciences*, vol. 236, pp. 119–135, 1956.

[271] MICHEL, J., MOULINEC, H., and SUQUET, P., "A computational method based on augmented lagrangians and fast fourier transforms for composites with high contrast," *Computer Modelling in Engineering & Sciences*, vol. 1, pp. 79 – 88, 2000.

[272] MICHEL, J., MOULINEC, H., and SUQUET, P., "A computational scheme for linear and non-linear composites with arbitrary phase contrast," *International Journal for Numerical Methods in Engineering*, vol. 52, pp. 139 – 160, 2001.

[273] MICHLER, J., VON KAENEL, Y., STIEGLER, J., and BLANK, E., "Complementary application of electron microscopy and micro-raman spectroscopy for microstructure, stress, and bonding defect investigation of heteroepitaxial chemical vapor deposited diamond films," *Journal of Applied Physics*, vol. 83, pp. 187–197, 1998.

[274] MIEHE, C., "Eshelby stress in elastoplasticity and ductile fracture," *International Journal of Plasticity*, vol. 10, pp. 393 – 408, 1994.

[275] MIEHE, C., "On the representation of prandtl-reuss tensors within the framework of multiplicative elastoplasticity," *International Journal of Plasticity*, vol. 10, pp. 609 – 621, 1994.

[276] MIKAELYAN, K., OVID'KO, I., and ROMANOV, A., "Disclination-structural-unit model of quasiperiodic tilt boundaries of finite extent," *Materials Science and Engineering A*, vol. 288, pp. 61 – 65, 2000.

[277] MIKKELSEN, L., "Necking in rectangular tensile bars approximated by 2-d gradient dependent plasticity model," *European Journal of Mechanics A: Solids*, vol. 18, pp. 805 – 818, 1999.

[278] MINDLIN, R. D., "Microstructure in linear elasticity," *Archive for rational mechanics and analysis*, vol. 16, pp. 51–78, 1964.

[279] MINDLIN, R. D., "Second gradient of strain and surface-tension in linear elasticity," *International Journal of Solids and Structures*, vol. 1, pp. 417–438, 1965.

[280] MINDLIN, R. D. and ESHEL, N. N., "On first strain-gradient theories in linear elasticity," *International Journal of Solids and Structures*, vol. 4, pp. 109–124, 1968.

[281] MINDLIN, R. D. and TIERSTEN, H. F., "Effects of couple stresses in linear elasticity," *Archive for rational mechanics and analysis*, vol. 11, pp. 415–448, 1962.

[282] MOMPIOU, F., CAILLARD, D., and LEGROS, M., "Grain boundary shear-migration coupling - i. in situ tem straining experiments in al polycrystals," *Acta Materialia*, vol. 57, pp. 2198–2209, 2009.

[283] MOULINEC, H. and SUQUET, P., "A fast numerical method for computing the linear and nonlinear properties of composites," *Comptes Rendus de l'Académie des Sciences Paris II*, vol. 318, pp. 1417 – 1423, 1994.

[284] MOULINEC, H. and SUQUET, P., "A numerical method for computing the overall response of nonlinear composites with complex microstructure," *Computer Methods in Applied Mechanics and Engineering*, vol. 157, pp. 69 – 94, 1998.

[285] MUGHRABI, H., "Dislocation wall and cell structures and long-range internal stresses in deformed metal crystals," *Acta Metallurgica*, vol. 31, pp. 1367–1379, 1983.

[286] MUGHRABI, H., "On the current understanding of strain gradient plasticity," *Materials Science and Engineering: A*, vol. 387-389, pp. 209 – 213, 2004.

[287] MUGHRABI, H., UNGÁR, T., KIENLE, W., and WILKENS, M., "Long-range intenal stresses and asymmetric x-ray line-broadening in tensile-deformed [001]-orientated copper single crystals," *Philosophical Magazine A*, vol. 53, pp. 793–813, 1986.

[288] MURA, T., "Continuous distribution of moving dislocations," *Philosophical Magazine*, vol. 8, p. 843857, 1963.

[289] MURA, T., "The elastic field of moving dislocations and disclinations," in *Fundamental Aspects of Dislocation Theory* (SIMMONS, J., DEWIT, R., and BULLOUGH, R., eds.), vol. 2, pp. 977–998, National Bureau of Standards Special Publication 317, Washington D.C., 1970.

[290] MURA, T., "Semi-microscopic plastic distortion disclinations," *Archives of Mechanics*, vol. 24, pp. 449–456, 1972.

[291] MURAYAMA, M., HOWE, J. M., HIDAKA, H., and TAKAKI, S., "Atomic-level observation of disclination dipoles in mechanically milled nanocrystalline fe," *Science*, vol. 295, pp. 2433 – 2435, 2002.

[292] MURNAGHAN, F., *Finite Deformation of an Elastic Solid.* New York: John Wiley and Sons, Inc., 1951.

[293] NABARRO, F. R. N., "Dislocations in a simple cubic lattice," *Proceedings of the Physical Society*, vol. 59, pp. 256–272, 1947.

[294] NABARRO, F., *Theory of crystal dislocations.* Oxford: Clarendon Press, 1967.

[295] NADEAU, G., *Introduction to Elasticity.* New York: Holt, Rinehart and Winston, 1964.

[296] NAZAROV, A. A., SHENDEROVA, O. A., and BRENNER, D. W., "Elastic models of symmetric ¡001¿ and ¡011¿ tilt grain boundaries in diamond," *Physical Review B*, vol. 61, pp. 928–936, 2000.

[297] NAZAROV, A. A., SHENDEROVA, O. A., and BRENNER, D. W., "On the disclination-structural unit model of grain boundaries," *Materials Science and Engineering A*, vol. 281, pp. 148–155, 2000.

[298] NAZAROV, A., "Disclinations in bulk nanostructured materials: Their origin, relaxation and role in material properties," *Advances in Natural Sciences: Nanoscience and Nanotechnology*, vol. 4, pp. 033002:1–11, 2013.

[299] NAZAROV, A., ENIKEEV, N., ROMANOV, A., ORLOVA, T., ALEXANDROV, I., BEYERLEIN, I., and VALIEV, R., "Analysis of substructure evolution during simple shear of polycrystals by means of a combined viscoplastic self-consistent and disclination modeling approach," *Acta Materialia*, vol. 54, pp. 985–995, 2006.

[300] NAZAROV, A., ROMANOV, A., and VALIEV, R., "On the structure, stress fields and energy of nonequilibrium grain boundaries," *Acta Metallurgica et Materialia*, vol. 41, pp. 1033–1040, 1993.

[301] NAZAROV, A., ROMANOV, A., and VALIEV, R., "On the nature of high internal stresses in ultrafine grained materials," *Nanostructured Materials*, vol. 4, pp. 93 – 101, 1994.

[302] NAZAROV, A., ROMANOV, A., and VALIEV, R., "Models of the defect structure and analysis of the mechanical behavior of nanocrystals," *Nanostructured Materials*, vol. 6, pp. 775 – 778, 1995.

[303] NAZAROV, A., ROMANOV, A., and VALIEV, R., "Random disclination ensembles in ultrafine-grained materials produced by severe plastic deformation," *Scripta Materialia*, vol. 34, pp. 729–734, 1996.

[304] NIX, W. and GAO, H., "Indentation size effects in crystalline materials: a law for strain gradient plasticity," *Journal of the Mechanics and Physics of Solids*, vol. 46, pp. 411 – 425, 1998.

[305] NYE, J. F., "Polarization effects in the diffraction of electromagnetic waves: The role of disclinations," *Proceedings of the Royal Society of London. Series A, Mathematical and Physical Sciences*, vol. 387, pp. 105–132, 1983.

[306] NYE, J., "Some geometrical relations in dislocated crystals," *Acta Metallurgica*, vol. 1, pp. 153–, 1953.

[307] OONO, Y. and PURI, S., "Computationally efficient modeling of ordering of quenched phases," *Physical Review Letters*, vol. 58, p. 836, 1987.

[308] OROWAN, E., "Zur kristallplastizität. i-iii," *Zeitschrift für Physik*, vol. 89, pp. 605–659, 1934.

[309] Palumbo, G. and Aust, K., "Localized corrosion at grain boundary intersections in high purity nickel," *Scripta Metallurgica*, vol. 22, pp. 847 – 852, 1988.

[310] Palumbo, G. and Aust, K., "Triple-line corrosion in high purity nickel," *Materials Science and Engineering A*, vol. 113, pp. 139 – 147, 1989.

[311] Pantleon, W., "Resolving the geometrically necessary dislocation content by conventional electron backscattering diffraction," *Scripta Materialia*, vol. 58, pp. 994–997, 2008.

[312] Pashley, D. W., Menter, J. W., and Bassett, G. A., "Observation of dislocations in metals by means of moiré patterns on electron micrographs," *Nature*, vol. 179, pp. 752–755, 1957.

[313] Peach, M. and Koehler, J., "The forces exerted on dislocations and the stress fields produced by them," *Physical Review*, vol. 80, p. 436 , 1950.

[314] Peierls, R., "The size of a dislocations," *Proceedings of the Physical Society*, vol. 52, pp. 34 – 37, 1940.

[315] Peirce, D., Asaro, R., and Needleman, A., "Material rate dependence and localization in crystalline solids," *Acta Metallurgica*, vol. 31, pp. 1951 – 1976, 1983.

[316] Pertsev, N. A., Romanov, A. E., and Vladimirov, V. I., "Rectangular disclination loops i. a universal technique," *Philosophical Magazine A*, vol. 49, pp. 591–609, 1984.

[317] Petch, N. J., "The cleavage strength of polycrystals," *Journal of the Iron and Steel Institute*, vol. 174, pp. 25–28, 1953.

[318] Polanyi, M., "Über eine art gitterstrung, die einen kristall plastisch machen könnte," *Zeitschrift für Physik*, vol. 89, pp. 660–664, 1934.

[319] Poulsen, H. F., Margulies, L., Schmidt, S., and Winther, G., "Lattice rotations of individual bulk grains: Part i: 3d x-ray characterization," *Acta Materialia*, vol. 51, pp. 3821–3830, 2003.

[320] Protasova, S. G., Gottstein, G., Molodov, D. A., Sursaeva, V. G., and Shvindlerman, L. S., "Triple junction motion in aluminium tricrystals," *Acta Materialia*, vol. 49, pp. 2519–2525, 2001.

[321] Puri, S., Das, A., and Acharya, A., "Mechanical response of multicrystalline thin films in mesoscale field dislocation mechanics," *Journal of the Physics and Mechanics of Solids*, vol. 59, pp. 2400 – 2417, 2011.

[322] Rabkin, E., Amouyal, Y., and Klinger, L., "Scanning probe microscopy study of grain boundary migration in nial," *Acta Materialia*, vol. 52, pp. 4953–4959, 2004.

[323] READ, W. T. and SHOCKLEY, W., "Dislocation models of crystal grain boundaries," *Physical Review*, vol. 78, pp. 275 – 289, 1950.

[324] READ, W., *Dislocations in Crystals*. New York: McGraw-Hill, 1954.

[325] REIßNER, H., "Eigenspannungen und eigenspannungsquellen," *ZAMM - Journal of Applied Mathematics and Mechanics / Zeitschrift für Angewandte Mathematik und Mechanik*, vol. 11, pp. 1 – 8, 1931.

[326] RIBÁRIK, G., GUBICKZA, J., and UNGÁR, T., "Correlation between strength and microstructure of ball-milled al-mg alloys determined by x-ray diffraction," *Materials Science and Engineering A*, vol. 387-389, pp. 343–347, 2004.

[327] RIBÁRIK, G. and UNGÁR, T., "Characterization of the microstructure in random and textured polycrystals and single crystals by diffraction line profile analysis," *Materials Science and Engineering A*, vol. 528, pp. 112–121, 2010.

[328] RIBÁRIK, G., UNGÁR, T., and GUBICZA, J., "Mwp-fit: a program for multiple whole-profile fitting of diffraction peak profiles by ab initio theoretical functions," *Journal of Applied Crystallography*, vol. 34, pp. 669–676, 2001.

[329] RICE, J., "Inelastic constitutive relations for solids: An internal-variable theory and its application to metal plasticity," *Journal of the Mechanics and Physics of Solids*, vol. 19, pp. 433 – 455, 1971.

[330] RICHETON, T., WANG, G. F., and FRESSENGEAS, C., "Continuity constraints at interfaces and their consequences on the work hardening of metal-matrix composites," *Journal of the Physics and Mechanics of Solids*, vol. 59, pp. 2023 – 2043, 2011.

[331] RIETVELD, H. M., "Line profiles of neutron powder-diffraction peaks for structure refinement," *Acta Crystallographica*, vol. 22, pp. 151–152, 1967.

[332] ROBINSON, C., WARD, J. C., and BEEVERS, R. B., "Liquid crystalline structure in polypeptide solutions. part 2," *Discussions of the Faraday Society*, vol. 25, pp. 29–42, 1958.

[333] ROMANOV, A. E. and KOLESNIKOVA, A. L., "Application of disclination concept to solid structures," *Progress in Materials Science*, vol. 54, pp. 740–769, 2009.

[334] ROMANOV, A., "Continuum theory of defects in nanoscaled materials," *Nanostructured Materials*, vol. 6, pp. 125 – 134, 1995.

[335] ROMANOV, A., "Fundamentals of disclination theory: Development of disclination-dislocation structures in deformed materials," *Solid State Phenomena*, vol. 87, pp. 47 – 56, 2002.

[336] Romanov, A., "Importance of disclinations in severe plastically deformed materials," *Advanced Engineering Materials*, vol. 5, pp. 301–307, 2003.

[337] Romanov, A., "Mechanics and physics of disclinations in solids," *European Journal of Mechanics*, vol. 22, pp. 727 – 741, 2003.

[338] Romanov, A., Kolesnikova, A., Ovid'ko, I., and Aifantis, E., "Disclinations in nanocrystalline materials: Manisfestation of the relay mechanism of plastic deformation," *Materials Science and Engineering A*, vol. 503, pp. 62 – 67, 2009.

[339] Romanov, A. and Vladimirov, V., *Disclinations in Crystalline Solids*, vol. 9, p. 191. North-Holland, Amsterdam, 1992.

[340] Romanov, A. E., "Screened disclinations in solids," *Materials Science and Engineering A*, vol. 164, pp. 58 – 68, 1993.

[341] Rösner, H., Kübel, C., Ivanisenko, Y., Kurmanaeva, L., Divinski, S. V., Peterlechner, M., and Wilde, G., "Strain mapping of a triple junction in nanocrystalline pd," *Acta Materialia*, vol. 59, pp. 7380–7387, 2011.

[342] Roy, A. and Acharya, A., "Finite element approximation of field dislocation mechanics," *Journal of the Mechanics and Physics of Solids*, vol. 53, pp. 143 – 170, 2005.

[343] Roy, A. and Acharya, A., "Size effects and idealized dislocation microstructure at small scales: Predictions of a phenomenological model of mesoscopic field dislocation mechanics: Part ii," *Journal of the Physics and Mechanics of Solids*, vol. 54, pp. 1711–1743, 2006.

[344] Rybin, V., *Large Plastic Deformations and Fracture of Metals*. Moscow: Metalurgica, 1986.

[345] Rybin, V., Zisman, A., and Zolotorevsky, N., "Junction disclinations in plastically deformed crystals," *Acta Metallurgica et Materialia*, vol. 41, pp. 2211–2217, 1993.

[346] Saillard, A., Cherkaoui, M., Capolungo, L., and Busso, E., "Stress influence on high temperature oxide scale growth: Modeling and investigation on a thermal barrier coating system," *Philosophical Magazine*, vol. 90, pp. 2651 – 2676, 2010.

[347] Saito, Y., Tsuji, N., Utsunomiya, H., Sakai, T., and Hong, R. G., "Ultra-fine grained bulk aluminum produced by accumulative roll-bonding process," *Scripta Materialia*, vol. 39, pp. 1221 – 1227, 1998.

[348] Sanders, P. G., Eastman, J. A., and Weertman, J. R., "Elastic and tensile behavior of nanocrystalline copper and palladium," *Acta Materialia*, vol. 45, pp. 4019 – 4025, 1997.

[349] SANDERS, P. G., FOUGERE, G. E., THOMPSON, L. J., EASTMAN, J. A., and WEERTMAN, J. R., "Improvements in the synthesis and compaction of nanocrystalline materials," *Nanostructured Materials*, vol. 8, pp. 243 – 252, 1997.

[350] SAXENA, A., WU, Y., LOOKMAN, T., SHENOY, S., and BISHOP, A., "Hierarchial pattern formation in elastic materials," *Physica A*, vol. 239, pp. 18 – 34, 1997.

[351] SCARDI, P. and LEONI, M., "Fourier modelling of the anisotropic line broadening of x-ray diffraction profiles due to line and plane lattice defects," *Journal of Applied Crystallography*, vol. 32, pp. 671–682, 1999.

[352] SCHEIDLER, M. and WRIGHT, T., "A continuum framework for finite viscoplasticity," *International Journal of Plasticity*, vol. 17, pp. 1033 – 1085, 2001.

[353] SCHIØTZ, J. and JACOBSEN, K. W., "A maximum in the strength of nanocrystalline copper," *Science*, vol. 301, pp. 1357 – 1359, 2003.

[354] SCHMID, E., "Ueber die schubverfestigung von einkristallen bei plasticher deformation," *Zeitschrift fur Physik*, vol. 40, p. 54 74, 1926.

[355] SCHOBER, T. and BALLUFFI, R. W., "Quantative observation of misfit dislocation arrays in low and high angle twist grain boundaries," *Philosophical Magazine*, vol. 21, pp. 109–123, 1970.

[356] SCHONFELDER, B., GOTTSTEIN, G., and SHVINDLERMAN, L. S., "Comparative study of grain-boundary migration and grain-boundary self-diffusion of [001] twist-grain boundaries in copper by atomistic simulations," *Acta Materialia*, vol. 53, pp. 1597–1609, 2005.

[357] SCHUH, C. A., NIEH, T. G., and IWASAKI, H., "The effect of solid solution w additions on the mechanical properties of nanocrystalline ni," *Acta Materialia*, vol. 51, pp. 431 – 443, 2003.

[358] SCHUH, C. A., NIEH, T. G., and YAMASAKI, T., "Hall-petch breakdown manifested in abrasive wear resistance of nanocrystalline nickel," *Scripta Materialia*, vol. 46, pp. 735 – 740, 2002.

[359] SCHWARTZ, D., VITEK, V., and SUTTON, A., "Atomic-structure of (001) twist boundaries in fcc metals - structural unit model," *Philosophical Magazine A - Physics of Condensed Matter Structure*, vol. 51, pp. 499 – 520, 1985.

[360] SCHWARZ, K., "Simulation of dislocations on the mesoscopic scale. i. methods and examples," *Journal of Applied Physics*, vol. 85, pp. 108–119, 1999.

[361] SCOTT, D. W., "On optimal and data-based histograms," *Biometrika*, vol. 66, no. 3, pp. 605–610, 1979.

[362] Seefeldt, M., "Disclinations in large-strain plastic deformation and work-hardening," *Reviews on Advanced Materials Science*, vol. 2, pp. 44–79, 2001.

[363] Segal, V. M., "Materials processing by simple shear," *Materials Science and Engineering A*, vol. 197, pp. 157 – 164, 1995.

[364] Sharma, P., "Size-dependent elastic fields of embedded inclusions in isotropic chiral solids," *International Journal of Solids and Structures*, vol. 41, pp. 6317–6333, 2004.

[365] Shekhar, S. and King, A. H., "Strain fields and energies of grain boundary triple junctions," *Acta Materialia*, vol. 56, pp. 5728 – 5736, 2008.

[366] Shih, K. and Li, J., "Energy of grain boundaries between cusp misorientations," *Surface Science*, vol. 50, pp. 109–124, 1975.

[367] Shilkrot, L., Curtin, W., and Miller, R., "A coupled atomistic/continuum model of defects in solids," *Journal of the Mechanics and Physics of Solids*, vol. 50, pp. 2085 – 2106, 2002.

[368] Shilkrot, L., Miller, R., and Curtin, W., "Coupled atomistic and discrete dislocation plasticity," *Physical Review Letters*, vol. 89, pp. 025501 – 025504, 2002.

[369] Shu, J. Y. and Fleck, N. A., "Strain gradient crystal plasticity: size-dependent deformation of bicrystals," *Journal of the Mechanics and Physics of Solids*, vol. 47, pp. 297–324, 1999.

[370] Shu, J., Fleck, N., Van der Giessen, E., and Needleman, A., "Boundary layers in constrained plastic flow: Comparison of nonlocal and discrete dislocation plasticity," *Journal of the Mechanics and Physics of Solids*, vol. 49, pp. 1361 – 1395, 2001.

[371] Simmons, G. and Wang, H., *Single Crystal Elastic Constants and Calculated Aggregate Properties: A Handbook*. Cambridge: MIT press, 1971.

[372] Sindhu, S. and Menon, C. S., "Higher order elastic constants and generalized grneisen parameters of elastic waves and low temperature thermal expansion of dysprosium," *Journal of Physics and Chemistry of Solids*, vol. 58, pp. 2001–2006, 1997.

[373] Sinner, E.-K. and Knoll, W., "Functional tethered membranes," *Current Opinion in Chemical Biology*, vol. 5, pp. 705 – 711, 2001.

[374] Sluys, L. and Estrin, Y., "The analysis of shear banding with a dislocation based gradient plasticity model," *International Journal of Solids and Structures*, vol. 37, pp. 7127 – 7142, 2000.

[375] SMITH, W. and HASHEMI, J., *Foundations of Materials Science and Engineering.* New York: McGraw-Hill, 2006.

[376] SMYSHLYAEV, V. and FLECK, N., "Bounds and estimates for the overall plastic behavior of composites with strain gradient effects," *Proceedings of the Royal Society of London A*, vol. 451, pp. 795 – 810, 1994.

[377] SMYSHLYAEV, V. and FLECK, N., "The role of strain gradients in the grain size effect for polycrystals," *Journal of the Mechanics and Physics of Solids*, vol. 44, pp. 465 – 495, 1996.

[378] SPEAROT, D. E., TSCHOPP, M. A., and MCDOWELL, D. L., "Orientation and rate dependence of dislocation nucleation stress computed using molecular dynamics," *Scripta Materialia*, vol. 60, pp. 675–678, 2009.

[379] SPEAROT, D., JACOB, K., and MCDOWELL, D., "Nucleation of dislocations from [001] bicrystal interfaces in aluminum," *Acta Materialia*, vol. 53, pp. 3579–3589, 2005.

[380] SPEAROT, D. and SANGID, M., "Insights on slip transmission at grain boundaries from atomistic simulations," *Current Opinion in Solid State and Materials Science*, in press.

[381] STEINBACH, I. and APEL, M., "Multiphase field model for solid state transformation with elastic strain," *Physica D*, vol. 217, pp. 153–160, 2006.

[382] STEINMANN, P., "Views on multiplicative elastoplasticity and the continuum theory of dislocations," *International Journal of Engineering Science*, vol. 34, pp. 1717–1735, 1996.

[383] STOKES, A. R. and WILSON, A. J. C., "A method of calculating the integral breadths of debye-scherrer lines," *Mathematical Proceedings of the Cambridge Philosophical Society*, vol. 38, pp. 313–322, 1942.

[384] STOKES, A. R. and WILSON, A. J. C., "The diffraction of x rays by distorted crystal aggregates - i," *Proceedings of the Physical Society*, vol. 56, pp. 174–181, 1944.

[385] SUIKER, A. S. J. and CHANG, C. S., "Aplpication of higher-order tensor theory for formulating enhanced continuum models," *Acta Mechanica*, vol. 142, pp. 223–234, 2000.

[386] SUTTON, A. P., BALLUFFI, R. W., and VITEK, V., "On intrinsic secondary grain boundary dislocation arrays in high angle symmetrical tilt grain boundaries," *Scripta Metallurgica*, vol. 15, pp. 989–994, 1981.

[387] SUTTON, A. P. and VITEK, V., "On the structure of tilt grain boundaries in cubic metals i. symmetrical tilt boundaries," *Philosophical Transactions of the Royal Society of London Series A*, vol. 309, pp. 1–36, 1983.

[388] Sutton, A. P. and Vitek, V., "On the structure of tilt grain boundaries in cubic metals ii. asymmetrical tilt boundaries," *Philosophical Transactions of the Royal Society of London Series A*, vol. 309, pp. 37–54, 1983.

[389] Sutton, A. P. and Vitek, V., "On the structure of tilt grain boundaries in cubic metals iii. generalization of the structural study and implications for the properties of grain boundaries," *Philosophical Transactions of the Royal Society of London Series A*, vol. 309, pp. 55–68, 1983.

[390] Swygenhoven, H. V., "Footprints of plastic deformation in nanocrystalline metals," *Materials Science and Engineering A*, vol. 483-484, pp. 33 – 39, 2008.

[391] Swygenhoven, H. V., Karo, A., and Farkas, D., "Grain boundary structure and its influence on plastic deformation of polycrystalline fcc metals at the nanoscale: A molecular dynamics study," *Scripta Materialia*, vol. 44, pp. 1513 – 1516, 2001.

[392] Tadmor, E., Ortiz, M., and Phillips, R., "Quasicontinuum analysis of defects in solids," *Philosophical Magazine A*, vol. 73, pp. 1529 – 1563, 1996.

[393] Taupin, V., Berbenni, S., and Fressengeas, C., "Size effects on the hardening of channel type microstructures: a field dislocation mechanics-based approach," *Acta Materialia*, vol. 60, pp. 664 – 673, 2012.

[394] Taupin, V., Capolungo, L., and Fressengeas, C., "Disclination mediated plasticity in shear-coupled boundary migration," *International Journal of Plasticity*, vol. 53, pp. 179 – 192, 2014.

[395] Taupin, V., Capolungo, L., Fressengeas, C., Das, A., and Upadhyay, M., "Grain boundary modeling using an elasto-plastic theory of dislocation and disclination fields," *Journal of the Mechanics and Physics of Solids*, vol. 61, pp. 370 – 384, 2013.

[396] Taupin, V., Fressengeas, C., Ventura, P., Lebyodkin, M., and Gornakov, V., "A field theory of piezoelectric media containing dislocations," *Journal of Applied Physics*, vol. 115, p. 144902, 2014.

[397] Taylon, G., "Plastic strain in metals," *Journal of the Institute of Metals*, vol. 62, p. 307 324, 1938.

[398] Taylon, G. and Elam, C., "The distortion of an aluminium crystal during a tensile test," *Proceedings of the Royal Society of London A*, vol. 102, p. 643 667, 1923.

[399] Taylon, G. and Elam, C., "The plastic extension and fracture of aluminium single crystals," *Proceedings of the Royal Society of London A*, vol. 108, p. 28 51, 1925.

[400] TAYLOR, G. I., "The mechanism of plasic deformation of crystals. part i. theoretical," *Proceedings of the Royal Society of London. Series A, Containing Papers of a Mathematical and Physical Character*, vol. 145, pp. 362–387, 1934.

[401] TEODOSIU, C. and SIDOROFF, F., "A finite theory of the elastoviscoplasticity of single crystals," *International Journal of Engineering Science*, vol. 14, pp. 713 – 723, 1976.

[402] THIBAULT, J., PUTAUX, J., JACQUES, A., GEORGE, A., MICHAUD, H., and BAILLIN, X., "Structure and characterization of the dislocations in tilt grain boundaries between $\Sigma = 1$ and $\Sigma = 3$: A high resolution electron microscopy study," *Materials Science and Engineering A*, vol. 164, pp. 233 –240, 1993.

[403] THOMPSON, W. K., *Encyclopedia Britannica*. Edinburg: Adam and Charles Black, 1878.

[404] TORAYA, H., "Whole-powder-pattern fitting without reference to a structure model: Application to x-ray powder diffractometer data," *Journal of Applied Crystallography*, vol. 19, pp. 440–447, 1986.

[405] TÓTH, L., BEAUSIR, B., GU, C., ESTRIN, Y., SCHEERBAUM, N., and DAVIS, C., "Effect of grain refinement by severe plastic deformation on the next-neighbor misorientation distribution," *Acta Materialia*, vol. 58, pp. 6706 – 6716, 2010.

[406] TOUPIN, R. A., "Elatic materials with couple stresses," *Archive for rational mechanics and analysis*, vol. 11, pp. 385–414, 1962.

[407] TRAUTT, Z. T. and MISHIN, Y., "Grain boundary migration and grain rotation studied by molecular dynamics," *Acta Materialia*, vol. 60, pp. 15 – 32, 2002.

[408] TSCHOPP, M. A. and McDOWELL, D. L., "Grain boundary dislocation sources in nanocrystalline copper," *Scripta Materialia*, vol. 58, pp. 299–302, 2008.

[409] TSCHOPP, M., TUCKER, G., and McDOWELL, D., "Structure and free volume of <110> symmetric tilt grain boundaries with the e structural units," *Acta Materialia*, vol. 55, pp. 3959 – 3969, 2007.

[410] TUCKER, G. J., ZIMMERMAN, J. A., and McDOWELL, D. L., "Continuum metrics for deformation and microrotation from atomistic simulations: Application to grain boundaries," *International Journal of Engineering Science*, vol. 49, pp. 1424–1434, 2011.

[411] TUCKER, G. J., TSCHOPP, M. A., and McDOWELL, D. L., "Evolution of structure and free volume in symmetric tilt grain boundaries during dislocation nucleation," *Acta Materialia*, vol. 58, pp. 6464 – 6473, 2010.

[412] UCHIC, M., DIMIDUK, D., FLORANDO, J., and NIX, W., "Sample dimensions influence strength and crystal plasticity," *Science*, vol. 305, pp. 986 – 989, 2004.

[413] UNGÁR, T., "Dislocation densities, arrangements and character from x-ray diffraction experiments," *Materials Science and Engineering A*, vol. 309-310, pp. 14–22, 2001.

[414] UNGÁR, T., "Microstructural parameters from x-ray diffraction peak broadening," *Scripta Materialia*, vol. 51, pp. 777–781, 2004.

[415] UNGÁR, T., "Dislocation model of strian anisotropy," *Powder Diffraction*, vol. 23, pp. 125–132, 2008.

[416] UNGÁR, T., BIERMANN, H., and MUGHRABI, H., "Dislocation distributions as seen by x-ray line profiles," *Materials Science and Engineering A*, vol. 164, pp. 175–179, 1993.

[417] UNGÁR, T. and BORBÉLY, A., "The effect of dislocation contrast on x-ray line broadening, a new approach to line profile analysis," *Applied Physics Letters*, vol. 69, pp. 3173–3175, 1996.

[418] UNGÁR, T., GROMA, I., and WILKENS, M., "Asymmetric x-ray line broadening of plastically deformed crystals ii. evaluation procedure and application to [001]-cu crystals," *Journal of Applied Crystallography*, vol. 22, pp. 26–34, 1989.

[419] UNGÁR, T., MUGHRABI, H., RÖNNPAGEL, D., and WILKENS, M., "X-ray line-broadening study of the dislocation cell structure in deformed [001]-orientated copper single crystals," *Acta Metallurgica*, vol. 32, pp. 333–342, 1984.

[420] UPADHYAY, M., CAPOLUNGO, L., TAUPIN, V., and FRESSENGEAS, C., "Grain boundary and triple junction energies in crystalline media: A disclination based approach," *International Journal of Solids and Structures*, vol. 48, pp. 3176–3193, 2011.

[421] UPADHYAY, M., CAPOLUNGO, L., TAUPIN, V., and FRESSENGEAS, C., "Elastic constitutive laws for incompatible crystalline media: the contributions of dislocations, disclinations and g-disclinations," *Philosophical Magazine*, vol. 93, pp. 794–832, 2013.

[422] UPMANYU, M., SROLOVITZ, D. J., LOBKOVSKY, A. E., WARREN, J. A., and CARTER, W. C., "Simultaneous grain boundary migration and grain rotation," *Acta Materialia*, vol. 54, pp. 1707–1719, 2006.

[423] UPMANYU, M., SROLOVITZ, D. J., SHVINDLERMAN, L. S., and GOTTSTEIN, G., "Molecular dynamics simulation of triple junction migration," *Acta Materialia*, vol. 50, pp. 1405–1420, 2002.

[424] VALIEV, R., ISLAMGALIEV, R., and ALEXANDROV, I., "Bulk nanostructured materials from severe plastic deformation," *Progress in Materials Science*, vol. 45, pp. 103–189, 2000.

[425] VAN BERKUM, J. G. M., DELHEZ, R., DE KEIJSER, T. H., and MITTEMEIJER, E. J., "Diffraction-line broadening due to strain fields in materials; fundamental aspects and methods of analysis," *Acta Crystallographica*, vol. A52, pp. 730–747, 1996.

[426] VAN SWYGENHOVEN, H., DERLET, P., and FROSETH, A., "Nucleation and propogation of dislocations in nanocrystalline fcc metals," *Acta Materialia*, vol. 54, pp. 1975–1983, 2006.

[427] VAN SWYGENHOVEN, H., SPACZER, M., CARO, A., and FARKAS, D., "Competing plastic deformation mechanisms in nanophase metals," *Physical Review B: Condensed Matter*, vol. 60, pp. 22–25, 1999.

[428] VAN SWYGENHOVEN, H. and WEERTMAN, J. R., "Deformation in nanocrystalline metals," *Materials Today*, vol. 9, pp. 24–31, 2006.

[429] VARADHAN, S., BEAUDOIN, A. J., and FRESSENGEAS, C., "Lattice incompatibility and strain-aging in single crystals," *Journal of the Mechanics and Physics of Solids*, vol. 57, pp. 1733–1748, 2009.

[430] VARADHAN, S., BEAUDOIN, A., ACHARYA, A., and FRESSENGEAS, C., "Dislocation transport using an explicit galerkin/least-qquares formulation," *Modelling and Simulation in Materials Science and Engineering*, vol. 14, pp. 1245 – 1270, 2006.

[431] VASSAMILLET, L. F., "Dislocations and their effect on x-ray diffraction," *Il Nuovo Cimento*, vol. 13, no. 6, pp. 1133–1142, 1959.

[432] VERMA, A., *Crystal Growth and Dislocations*. London: Butterworths, 1953.

[433] VILLERT, S., MAURICE, C., and WYON, X., "Accuracy assessment of elastic strain measurement by ebsd," *Journal of Microscopy*, vol. 233, pp. 290–301, 2009.

[434] VLIET, K. J. V., TSIKATA, S., and SURESH, S., "Model experiments for direct visualization of grain boundaty deformation in nanocrystalline metals," *Applied Physics Letters*, vol. 83, pp. 1441 – 1443, 2003.

[435] VOGEL, F. L., PFANN, W. G., COREY, H. E., and THOMAS, E. E., "Observations of dislocations in lineage boundaries in germanium," *Physical Review*, vol. 90, pp. 489–490, 1953.

[436] VOLTERRA, V., "Sur léquilibre des corps élastiques multiplement connexes," *Annales Scientifiques de lÉcole Normale Supérieure*, vol. 24, pp. 401–517, 1907.

[437] WANG, G. J., SUTTON, A. P., and VITEK, V., "A computer simulation study of ¡001¿ and ¡111¿ tilt boundaries: the multiplicity of sstructures," *Acta Metallurgica*, vol. 32, pp. 1093–1104, 1984.

[438] WANG, J. and MISRA, A., "An overview of interface-dominated deformation mechanisms in metallic multilayers," *Current Opinion in Solid State and Materials Science*, vol. 15, pp. 20 – 28, 2011.

[439] WANG, Y. and KHACHATURYAN, A., "Three-dimensional field model and computer modeling of martensitic transformations," *Acta Materialia*, vol. 45, pp. 759 – 773, 1997.

[440] WANG, Y. and LI, J., "Phase field modeling of defects and deformation," *Acta Materialia*, vol. 58, pp. 1212–1235, 2010.

[441] WANG, Z., YANG, R., ZHOU, J., QIN, Y., XU, C., HU, Y., and XU, S., "Lateral nanowire/nanobelt based nanogenerators, piezotronics and piezo-phototronics," *Materials Science and Engineering R*, vol. 70, pp. 320 – 329, 2010.

[442] WANG, Z., BEYERLEIN, I., and LESAR, R., "Dislocation motion in high strain-rate deformation," *Philosophical Magazine*, vol. 87, pp. 2263–2279, 2007.

[443] WANG, Z., BEYERLEIN, I., and LESAR, R., "The importance of cross-slip in high-rate deformation," *Modelling and Simulation in Materials Science and Engineering*, vol. 15, pp. 675–690, 2007.

[444] WARREN, B. E., "A generalized treatment of cold work in powder patterns," *Acta Crystallographica*, vol. 8, pp. 483–486, 1955.

[445] WARREN, B. E., "X-ray studies of deformed metals," *Progress in Metal Physics*, vol. 8, no. 1, pp. 147–202, 1959.

[446] WARREN, B. E., *X-Ray Diffraction.* New York: Dover Publications, Inc., 1990.

[447] WARREN, B. E. and AVERBACH, B. L., "The effect of cold-work distortion on x-ray patterns," *Journal of Applied Physics*, vol. 21, pp. 595–599, 1950.

[448] WARREN, B. E. and AVERBACH, B. L., "The separation of cold-work distortion and particle size broadening in x-ray patterns," *Journal of Applied Physics*, vol. 23, no. 4, pp. 497–498, 1952.

[449] WEYGAND, D., FRIEDMAN, L., DER GIESSEN E., V., and NEEDLEMAN, A., "Aspects of boundary-value problem solutions with three-dimensional dislocation dynamics,," *Modelling and Simulations and Materials Science and Engineering*, vol. 10, pp. 437–468, 2002.

[450] WILKENS, M., "Das mittlere spannungsquadrat ¡s2¿ begrenzt regellos verteilter versetzungen in einem zylinderformigen korper," *Acta Metallurgica*, vol. 17, pp. 1155–1159, 1969.

[451] WILKENS, M., "The determination of density and distribution of dislocations in deformed single crystals from broadened x-ray diffraction profiles," *Physica Status Solidi A*, vol. 2, pp. 359–370, 1970.

[452] WILKENS, M., *Theoretical Aspects of Kinematical X-ray Diffraction Profiles from Crystals Containing Dislocation Distributions*, vol. 2 of *Fundamental Aspects of Dislocation Theory*. USA: National Bureau of Standards Special Publication 312, Washington DC: US Government Printing Office, 1970.

[453] WILKENS, M., "X-ray diffraction line broadening of crystals containing small-angle boundaries," *Journal of Applied Crystallography*, vol. 12, pp. 119–125, 1979.

[454] WILKINSON, A., MEADEN, G., and DINGLEY, D., "High-resolution elastic strain measurement from electron backscatter diffraction patterns: new levels of sensitivity," *Ultramicroscopy*, vol. 106, pp. 307–313, 2006.

[455] WILLIAMSON, G. K. and HALL, W. H., "X-ray line broadening from files aluminium and wolfram," *Acta Metallurgica*, vol. 1, pp. 22–31, 1953.

[456] WILLIS, J., "Second-order effects of dislocations in anisotropic crystals," *International Journal of Engineering Science*, vol. 5, pp. 171 – 190, 1967.

[457] WILLIS, J., "Stress fields produced by dislocations in anisotropic media," *Philosophical Magazine*, vol. 17, pp. 1033 – 1085, 1970.

[458] WILSON, A. J. C., "The reflection of x-rays from the 'anti-phase nuclei' of aucu3," *Proceedings of the Royal Society of London. Series A, Mathematical and Physical Sciences*, vol. 181, pp. 360–368, 1943.

[459] WILSON, A. J. C., "The diffraction of x-rays by distorted-crystal aggregates. iv. diffraction by a crystal with an axial screw dislocation," *Acta Crystallographica*, vol. 5, pp. 318–322, 1952.

[460] WILSON, A. J. C., "The effects of dislocations on x-ray diffraction," *Il Nuovo Cimento*, vol. 1, no. 2, pp. 277–283, 1955.

[461] WOLF, D. and KLUGE, M., "elationship between shear resistance and local atomic structure at grain boundaries in fcc metals," *Scripta Materialia*, vol. 24, pp. 907–914, 1990.

[462] WOLF, D. and LUTSKO, J. F., "Structurally-induced elastic anomalies in a superlattice of (001) twist grain boundaries," *Journal of Materials Research*, vol. 4, pp. 1427–1443, 1989.

[463] WOLF, D., YAMAKOV, V., PHILLPOT, S. R., MUKHERJEE, A., and GLEITER, H., "Deformation of nanocrystalline materials by molecular-dynamics simulation: Relation to experiments?," *Acta Materialia*, vol. 53, pp. 1 – 40, 2005.

[464] Wu, K.-A. and Voorhees, P., "Phase field crystal simulations of nanocrystalline grain growth in two dimensions," *Acta Materialia*, vol. 60, pp. 407 – 419, 2012.

[465] Wu, M., "Stress and strain energy of a periodic array of interfacial wedge disclination dipoles in a transversely isotropic bicrystal," *International Journal of Engineering Science*, vol. 40, pp. 873 – 897, 2002.

[466] Wu, M., Nazarov, A., and Zhou, K., "Misorientation dependence of the energy of [1$\bar{1}$00] symmetrical tilt boundaries in hcp metals: Prediction by the disclination-structural unit model," *Philosophical Magazine*, vol. 84, pp. 785 – 806, 2004.

[467] Wu, S. C. and Havner, K. S., "Analytical and numerical investigation of nonuniform straining and subgrain initiation in bicrystals in channel die compression," *Philosophical Transactions of the Royal Society of London Series A*, vol. 355, pp. 1905–1943, 1997.

[468] Xiong, L., Deng, Q., Tucker, G., McDowell, D., and Chen, Y. *Acta Materialia*, vol. 60, pp. 899 – 913, 2012.

[469] Xiong, L., Deng, Q., Tucker, G., McDowell, D., and Chen, Y., "Coarse-grained atomistic simulations of dislocations in al, ni and cu crystals," *International Journal of Plasticity*, vol. 38, pp. 86 – 101, 2012.

[470] Xiong, L., McDowell, D., and Chen, Y., "Nucleation and growth of dislocation loops in cu, al and si by a concurrent atomistic-continuum method," *Scripta Materialia*, vol. 67, pp. 633 – 636, 2012.

[471] Xiong, L., Tucker, G., McDowell, D., and Chen, Y. *Journal of the Mechanics and Physics of Solids*, vol. 59, pp. 160 – 177, 2011.

[472] Yamakov, V., Wolf, D., Phillpot, S. R., and Gleiter, H., "Grain-boundary diffusion creep in nanocrystalline palladium by molecular-dynamics simulation," *Acta Materialia*, vol. 50, pp. 61 – 73, 2002.

[473] Yamakov, V., Wolf, D., Phillpot, S. R., Mukherjee, A. K., and Gleiter, H., "Deformation-mechanism map for nanocrystalline metals by molecular-dynamics simulation," *Nature Materials*, vol. 3, pp. 43–47, 2004.

[474] Yang, R., Qin, Y., Dai, L., and Wang, Z., "Power generation with laterally packaged piezoelectric fine wires," *Nature Nanotechnology*, vol. 4, pp. 34 – 39, 2009.

[475] Young, R. A., Gerdes, R. J., and Wilson, A. J. C., "Propogation of some systematic errors in x-ray line profile analysis," *Acta Crystallographica*, vol. 22, pp. 155–162, 1967.

[476] YOUNG, R. A. and WILES, D. B., "Profile shape functions in rietveld refinements," *Journal of Applied Crystallography*, vol. 15, pp. 430–438, 1982.

[477] YOUSSEF, K. M., SCATTERGOOD, R. O., MURTY, K. L., and KOCK, C. C., "Ultratough nanocrystalline copper with a narrow grain size distribution," *Applied Physics Letters*, vol. 85, pp. 929 – 931, 2004.

[478] ZBIB, H. and AIFANTIS, E., "On the localization and post-localization behavior of plastic deformation. i, ii, iii," *Res Mechanica*, vol. 23, pp. 261 – 277, 279 – 292, 293 – 305, 1989.

[479] ZBIB, H., RHEE, M., and HIRTH, J., "On plastic deformation and the dynamics of 3d dislocations," *International Journal of Mechanical Sciences*, vol. 40, pp. 113–127, 1998.

[480] ZHANG, G. and LOU, X., "Controlled growth of nico2o4 nanorods and ultrathin nanosheets on carbon nanofibers for high-performance supercapacitors," *Scientific Reports*, vol. 3, 2013.

[481] ZHANG, K., WEERTMAN, J. R., and EASTMAN, J. A., "The influence of time, temperature, and grain size on indentation creep in high-purity nanocrystalline and ultrafine grain copper," *Applied Physics Letters*, vol. 85, pp. 5197 – 5199, 2004.

[482] ZHANG, K., WEERTMAN, J. R., and EASTMAN, J. A., "Rapid stress-driven grain coarsening in nanocrystalline cu at ambient and cryogenic temperatures," *Applied Physics Letters*, vol. 87, pp. 061921–1 – 061921–3, 2005.

[483] ZHILYAEV, A. P. and LANGDON, T. G., "Using high-pressure torsion for metal processing: Fundamentals and applications," *Progress in Materials Science*, vol. 53, pp. 893 – 979, 2008.

[484] ZHOU, K., WU, M., and NAZAROV, A., "Relaxation of a disclinated tricrystalline nanowire," *Acta Materialia*, vol. 56, pp. 5828 – 5836, 2008.

[485] ZORN, G., "Pitfalls in the evaluation of x-ray diffraction line shape," *Australian Journal of Physics*, vol. 41, pp. 237–249, 1988.